



Provided by the author(s) and University of Galway in accordance with publisher policies. Please cite the published version when available.

Title	Physicochemical and biological functionalisation strategies of the neuroelectrode interface to promote neural integration through the modulation of reactive gliosis
Author(s)	Vallejo Giraldo, Catalina
Publication Date	2017-12-05
Item record	http://hdl.handle.net/10379/7015

Downloaded 2024-05-18T03:29:44Z

Some rights reserved. For more information, please see the item record link above.





Physicochemical and Biological Functionalisation Strategies of the Neuroelectrode Interface to Promote Neural Integration through the Modulation of Reactive Gliosis

A thesis submitted to the National University of Ireland for the degree of Doctor of
Philosophy

Catalina Vallejo Giraldo

November 2017

Centre for Research in Medical Devices (CÚRAM),

National University of Ireland Galway.

Research Supervisor: Dr Manus Biggs

Co-supervisors: Dr Eilís Dowd and Prof. Abhay Pandit

TABLE OF CONTENTS

TABLE OF CONTENTS	i
PUBLICATIONS AND PRESENTATIONS	viii
LIST OF FIGURES	xii
LIST OF TABLES	xxxii
ACKNOWLEDGEMENTS	xxxiv
LIST OF ABBREVIATIONS	xxxix
ABSTRACT	xlili
Chapter 1	1
INTRODUCTION	1
1.1 Neuro- Electrically Active Devices.....	1
1.2 Glial Scar Formation	2
1.3 Functionalisation of Neuroelectrodes: Electrically Active Devices.....	4
1.3.1 Mechanical Functionalisation	5
1.3.2 Topographical Functionalisation.....	6
1.3.2.1 Anodisation in Biomedical Applications	7
1.3.3 Biological Functionalisation	8
1.4 Conducting Polymers	9
1.4.1 Fabrication of Polymer Electrode Coatings	10
1.5 Poly(3,4-ethylene dioxythiophene) (PEDOT).....	12
1.5.1 Morphological and Topographical Functionalisation of PEDOT	13
1.5.2 Biological Functionalisation of PEDOT	14
1.5.2.1 Extracellular Matrix (ECM) Protein, Peptides	16

1.5.2.2	Glycosaminoglycan's (GAGs)	17
1.6	Hypothesis and Objectives	22
1.6.1	Objective One (Chapter two)	24
1.6.2	Objective Two (Chapter Three)	24
1.6.3	Objective Three (Chapter Four)	25
1.7	References	25
Chapter 2		53
ANODISATION OF MAGNETRON-SPUTTERED INDIUM-TIN OXIDE (ITO) FILMS		53
2.1	Preamble	53
2.2	Introduction	55
2.3	Materials and Methods	57
2.3.1	Anodic Oxidation of ITO	57
2.3.2	Physical Characterisation	58
2.3.2.1	Surface Morphology	58
2.3.2.2	Thickness Measurements	59
2.3.2.3	UV- visible Spectroscopy	59
2.3.2.4	Stability and Durability through Accelerated Ageing Study	59
2.3.3	Chemical Characterisation	60
2.3.4	Electrochemical Characterisation	61
2.3.4.1	Electrochemical Measurements	61
2.3.5	Biological Characterisation	61
2.3.5.1	Cell Culture	61
2.3.5.2	Metabolic Analysis	64
2.3.5.3	Immunofluorescent Labelling	64

2.3.5.4	Microscopy and Image Analysis	66
2.3.6	Protein Antibody Microarray	67
2.3.6.1	Protein Extraction.....	67
2.3.6.2	Protein Quantification of Cell Lysates	67
2.3.6.3	Construction of Gliosis Antibody Microarray.....	68
2.3.7	Electrophysiological Recordings	72
2.3.8	Calcium Imaging and Substrate Stimulation.....	72
2.3.9	Statistical Analysis	74
2.4	Results and Discussion.....	74
2.4.1	Physical Characterisation of Anodised ITO Films.....	76
2.4.2	Chemical characterisation	82
2.4.3	Electrochemical Characterisation.....	83
2.4.4	Biological Characterisation.....	89
2.4.5	Functional Characterisation	98
2.5	Conclusion.....	104
2.6	References	104
Chapter 3		115
TOPOGRAPHICALLY FUNCTIONALISED POLY(3,4-ETHYLENEDIOXYTHIOPHENE):P-TOLUENE SULPHONATE (PEDOT:PTS) NEUROELECTRODES VIA MICROIMPRINT LITHOGRAPHY		115
3.1	Preamble.....	115
3.2	Introduction	116
3.3	Materials and Methods	118
3.3.1	Fabrication of Microelectrode Arrays.....	118
3.3.2	Imprinting and Die Fabrication.....	118

3.3.2.1	Photo Lithography.....	118
3.3.2.2	Nickel Die.....	119
3.3.2.3	Imprinting Process.....	119
3.3.3	Physical Characterisation.....	119
3.3.3.1	Surface Morphology.....	119
3.3.3.2	Thickness Measurements.....	120
3.3.4	Chemical Characterisation.....	120
3.3.5	Electrochemical Characterisation.....	121
3.3.5.1	Preparation of PEDOT:PTS Samples.....	121
3.3.5.2	Electrochemical Measurements.....	121
3.3.6	Biological Characterisation.....	123
3.3.6.1	Cell Culture.....	123
3.3.6.2	Immunofluorescent Labelling.....	128
3.3.6.3	Microscopy and Image Analysis.....	129
3.3.6.4	Cytokine Inflammatory Panel.....	130
3.3.7	Calcium Imaging.....	131
3.3.8	Statistical Analysis.....	132
3.4	Results and Discussion.....	132
3.4.1	Physical Characterisation.....	132
3.4.2	Electrochemical Characterisation.....	139
3.4.3	Biological Characterisation.....	147
3.4.4	Calcium Imaging.....	161
3.5	Conclusion.....	163
3.6	References.....	163

Chapter 4	179
ANALYSIS OF THE NEUROTROPIC AND ANTI-INFLAMMATORY EFFECTS OF NEUROELECTRODE FUNCTIONALISATION WITH A HEPARAN SULPHATE MIMETIC	179
4.1 Preamble	179
4.2 Introduction	180
4.3 Materials and Methods	181
4.3.1 Physical Characterisation	181
4.3.1.1 Surface Morphology	181
4.3.1.2 Thickness Measurements	182
4.3.2 Chemical Characterisation	182
4.3.2.1 Contact Angle Measurement	182
4.3.2.2 Attenuated Total Reflectance Infra-Red Spectroscopy (ATR-IR) ..	183
4.3.2.3 Raman Spectroscopy	183
4.3.2.4 X Ray Photoelectron Spectroscopy	183
4.3.3 Electrochemical Characterisation.....	184
4.3.3.1 Preparation of PEDOT:PTS and PEDOT:PTS:F6 samples	184
4.3.3.2 Electrochemical Measurements.....	185
4.3.4 Biological Characterisation.....	186
4.3.4.1 Bioactivity Elution Profiles	186
4.3.5 Cell Culture	188
4.3.6 Immunofluorescent Labelling	189
4.3.7 Microscopy and Image Analysis.....	189
4.3.8 Cytokine Inflammatory Panel	190

4.3.9	Glycosaminoglycans Competition Assay Towards FGF-2 and VEGF Binding	190
4.3.10	Protein Antibody Microarray and Lectin Array	191
4.3.10.1	Protein Extraction of Primary VM Cell Mixed Population and Labelling	191
4.3.10.2	Construction of Antibody and Lectin Hybrid Microarray	192
4.3.10.3	Profiling Samples on Hybrid Microarrays, Data Extraction and Analysis	196
4.3.11	Statistical Analysis	197
4.4	Results and Discussion	197
4.4.1	Physical and Chemical Characterisation	203
4.4.2	Electrochemical Characterisation	214
4.4.3	Biological Characterisation	219
4.5	Conclusion	240
4.6	References	241
	Chapter 5	259
	FUTURE DIRECTIONS	259
5.1	Platform Development	261
5.1.1	Dual Functionalisation	261
5.1.2	The influence of Electrochemical Modification on the Surface Properties of ITO (Chapter 2)	262
5.1.3	Topographical Cues for The Modulation of Reactive Astrocyte Phenotype and Neurite outgrowth for Neural Interfaces Application (Chapter 3)	264

5.1.3.1	The Neural response to Topographically Functionalised Neuroelectrode Surfaces with Vertical Silicon Nanowires (<i>Manuscript in preparation</i>).....	265
5.1.4	Chemically Modified Conducting Coatings for Neural Applications (Chapter 4).....	266
5.1.5	<i>Ex vivo</i> Whole Rat Brain Slice Model	268
5.1.5.1	Material and Methods.....	270
5.1.5.2	Preliminary Results: Important Observations	272
5.2	References	276
APPENDICES		277

PUBLICATIONS AND PRESENTATIONS

Full Papers

1. **Vallejo-Giraldo, C.**, Ouidja, M., Huyng, Minh Bao., Krukiewicz, K., Calaresu, Ivo., Pallipurath, A.R., Flannery, A., Trotier, A., Kilcoyne, M., Dowd, E., Ballerini, L., Garcia-Papy, Dulce., Abhay, P., Biggs, M.J.P. 'Analysis of the Neurotropic and Anti-inflammatory Effects of Neuroelectrode Functionalization with a Heparan Sulphate Mimetic'. *In preparation*
2. **Vallejo-Giraldo, C.**, Krukiewicz, K., Calaresu, Ivo., Zhu, J, Koo., B.S., Fernandez-Yague, M., Thomas, D., Peixoto, N., McNamara, K., Syed, T., Palma, M., Farid, N., O'Connor, Gerard., Dowd, E., Ballerini, L., Abhay, P., Biggs, M.J.P. 'The Neural Response to PEDOT:PTS Neuroelectrodes Topographically Functionalized via Microimprint Lithography'. *In preparation*
3. Tsimbouri, Monica P., P. G. C., Pemberton, Gabriel D., Yang, Jingli., Jayawarna, Vineetha., Oripiriyakul, Wich., Burgess, Karl., Gonzalez-Garcia, Cristina., Blackburn, Gavin., Thomas, Dilip. **Vallejo-Giraldo, C.**, Biggs, MJ, Curtis, Adam S.G., Salmeron-Sanchez, Manuel., Reid, Stuart., Dalby, Matthew J. (2017). Stimulation of 3D Osteogenesis by Mesenchymal Stem Cells via a Nanovibrational Bioreactor. *Nature Biomedical Engineering, in press*
4. **Vallejo-Giraldo, C.**, Pampaloni, N. P., Pallipurath, A. R., Mokarian-Tabari, P., O'Connell, J., Holmes, J. D, Trotier, A., Krukiewicz, K., Operlla-Aceret, G., Pugliese, E., Ballerini, L., Kilcoyne, M., Dowd, E., Quinlan, Leo R., Pandit, A., Biggs, MJ. (2017). Preparation of Cytocompatible ITO Neuroelectrodes with Enhanced Electrochemical Characteristics Using a Facile Anodic Oxidation Process. *Advanced Functional Materials. 10.1002/adfm.201605035*
5. **Vallejo-Giraldo, C.**, Pugliese, E., Larrañaga, A., Fernandez-Yague, M. A., Britton, J.J., Trotier, A., Tadayyon, G., Kelly, A., Rago, I., Sarasua, Jose-Ramon., Dowd, E., Quinlan, Leo R. Pandit, A., Biggs, MJ. (2016). Polyhydroxyalkanoate/Carbon Nanotube Nanocomposites: Flexible Electrically Conducting Elastomers for Neural Applications. *Nanomedicine, 11(19), 2547-2563.*

6. Mokarian-Tabari, P., **Vallejo-Giraldo, C.**, Fernandez-Yague, M., Cummins, C., Morris, M. A., and Biggs, MJ. (2015). Nanoscale Neuroelectrode Modification via Sub-20 nm Silicon Nanowires through Self-Assembly of Block Copolymers. *Journal of Materials Science: Materials in Medicine*, 26(2), 120.
7. Biggs, MJ., Parisi Capdevila, E., **Vallejo-Giraldo, C.**, and J Wind, S. (2014). Cellular Response to Ferroelectric PVDF-TrFE Nanoscale Surfaces Formed by Varying Polymer Concentration. *Pharmaceutical Nanotechnology*, 2(1), 42-48.
8. **Vallejo-Giraldo, C.**, Kelly, A. and Biggs, MJ. (2014). Biofunctionalisation of Electrically Conducting Polymers. *Drug discovery today*, 19(1), 88-94.

Book Chapter

9. Fernandez-Yague, M. A., **Vallejo-Giraldo, C.**, Aceret, G. O., Pandit, A., and Biggs, M. J. (2016). Biological Activity on Piezoelectric PVDF. *In Electrically Active Materials for Medical Devices* (pp. 167-176). Imperial College Press, London.

Conference Proceedings

10. **Vallejo-Giraldo, C.**, Dowd, E., Papy-Garcia, D., Pandit, A and Biggs MJ (2016). Functionalized PEDOT Polymeric Coatings for Neuroelectrodes: Topographical and Biological Strategies. *Front. Bioeng. Biotechnol. Conference Abstract: 10th World Biomaterials Congress*. doi: 10.3389/conf.FBIOE.2016.01.01369
11. Biggs, MJ., Mokarian-Tabari, P., **Vallejo-Giraldo, C.**, Thomas, D., Morris, MA., and Pandit, A (2016). Nanopillar Modified Neuroelectrodes through Block Copolymer Self-Assembly. *Front. Bioeng. Biotechnol. Conference Abstract: 10th World Biomaterials Congress*. doi: 10.3389/conf.FBIOE.2016.01.02560
12. Tadayyon, G., **Vallejo-Giraldo, C.**, and Biggs, MJ (2016). Electrically Conducting Polymers in Next Generation Neuroelectrode Design. *Front. Bioeng. Biotechnol. Conference Abstract: 10th World Biomaterials Congress*. doi: 10.3389/conf.FBIOE.2016.01.00687
13. Peixoto, N., Silue, T., **Vallejo-Giraldo, C.**, and Biggs, MJ (2016). Electrochemical Analysis of Accelerated Aging of PEDOT-PTS Coated Screen-printed Electrodes. In *BIODEVICES* pp. 76-82. 10.5220/0005700600760082.

14. **Vallejo-Giraldo, C., Pandit, A., and Biggs, MJ (2016).** The Effects of Electrodeposition Current Density on the Morphology, Electrochemical and Biological Characteristics of Poly (3, 4ethylenedioxythiophene): Poly (Styrenesulfonate) (PEDOT-PSS) Neural Interfaces. In *Irish Journal of Medical Science (Vol. 185, pp. S21-S21)*.
15. Biggs, M.J., **Vallejo-Giraldo, C., and Pandit, A (2014).** Morphological Modification of Conducting Polymers. In *Journal of Tissue Engineering and Regenerative Medicine (Vol. 8, pp. 137-137)*.

Presentations at International and Local Conferences

1. Biointerfaces -Gordon Research Seminar (GRS) on June 11th -12th, **2016**. Les Diablerets, Switzerland, ***Awarded Oral presentation***
2. Biointerfaces -Gordon Research Conference (GRC) on June 12th -17th, **2016**. Les Diablerets, Switzerland, ***Poster Presentation***
3. 10th World Biomaterials Congress on May 17th - 22nd, **2016**. Montreal, Canada, ***Oral presentation. Trainee Award***
4. 9th International Conference on Biomedical Electronics and Devices on February 21st -23rd, **2016**. Rome, Italy, ***Oral presentation. Best paper award***
5. Bioengineering in Ireland. Biomedical Science Section (RAMI) on January 22nd-23rd, **2015**. Galway, Ireland, ***Oral presentation***
6. Biochemical Society Irish Area Section Annual Meeting in Galway-Protein Interactions in Biology on December 7th **2015**. Galway, Ireland, ***Oral presentation***
7. Galway Neuroscience Research Day on December 4th **2015**, ***Oral presentation***
8. 27th European Conference on Biomaterials (ESB) on August 30th-September 3rd, **2015**. Cracow, Poland, ***Oral presentation***
9. Advanced Functional Polymers for Medicine (AFPM) on March 23rd-25th, **2015**. Galway, Ireland, ***Poster presentation. Best poster from NUI, Galway***
10. Bioengineering in Ireland. Biomedical Science Section (RAMI) on January 16th-17th, **2015**. Carton House, Maynooth, Ireland, ***Oral presentation***
11. The European Materials Research Society Conference on September 15th-18th, **2014**. Warsaw, Poland, ***Poster Presentation***
12. 26th European Conference on Biomaterials (ESB) on August 31st -September 3rd, **2014**. Liverpool, UK, ***Oral presentation***
13. The Royal Academy of Medicine Ireland, RAMI, Biomedical Science Section on June 19th, **2014**. Dublin, Ireland, ***Oral presentation. Donegan Medal awarded for best oral presentation***

14. Tissue Engineering and Regenerative Medicine Society (TERMIS) on June 10th -13th, **2014**. Genova, Italy, *Oral presentation*
15. Physics of Soft and Biological Matters on April 14th-16th, **2014**. Cambridge, UK, *Poster presentation*.
16. Galway Neuroscience Research Day on December 5th, **2013**, *Oral presentation*
17. Annual NFB retreat on July 2nd and 3rd, **2013** in the National Museum of Ireland, Country Life. Westport, Co Mayo, Ireland, *Oral presentation*

LIST OF FIGURES

- Figure 1.1** *Electrically stimulating systems consist of a number of electrodes which transmit signals via electrical and ionic conduction in bodily fluids.* 2
- Figure 1.2** *The cellular response and onset of gliosis following neuroelectrode implantation. A) Acute inflammatory response after probe implantation leads to the recruitment and activation of microglia, and astrocytes in response to locally released soluble signaling factors. B) Chronic inflammation follows and is maintained by populations of reactive astrocytes in response to injury, leading to the deposition of a fibrous network. Image modified from Vallejo-Giraldo et al.[165].....* 3
- Figure 1.3** *Common techniques used in the modification of conducting polymers (CPs). Modifications to alter the chemical/electrical, morphological and biological properties in CPs, have been accomplished using methods such as click chemistry, covalent and non-covalent methods, electrospinning, and micro and nanopatterning, among others. Image taken from [165].* 10
- Figure 1.4** *Structural characteristics of glycosaminoglycan's. Image taken from Papy-Garcia et al. [297].* 18
- Figure 1.5** *Heparan sulphate proteoglycans have many roles in cell physiology. HSPGs function as co-receptors for growth factors and their receptor tyrosine kinases, which are present either on the same cell (a) or on adjacent cells (b). They transport chemokines across cells (c) and present them at the cell surface (d). Proteolytic processing leads to the shedding of syndecans and glypicans from the cell surface (e), and heparanase cleave the HS chains (f), liberating bound ligands (such as growth factors). Cell surface HSPGs are actively taken up by endocytosis (g) and can recycle back to the surface or be degraded in lysosomes (h). HSPGs also facilitate cell adhesion to the extracellular matrix (i) and form bridges to the cytoskeleton (j). Secreted HSPGs are involved in the formation of organised extracellular matrices that form physiological barriers (k) and sequester growth factors and morphogens for later release (l). Serglycin carrying highly sulphated heparin chains is packaged into secretory granules (m). Finally, some experiments*

suggest that HS chains exist in the nucleus (n), although their function in this location is unknown. Image taken from Bishop et al [300]. 20

Figure 2.1 Schematic of the electrochemical set-up used for the anodisation process of ITO. Pristine ITO coated glass slides were placed at the anode electrode and constant current densities of 0.4 mA cm^{-2} , 4 mA cm^{-2} and 43 mA cm^{-2} over a constant time of 450 seconds were applied to pristine ITO coated glass through a PSS/PBS electrolyte. Within this process, hydrogen is released from the cathode (platinum) and oxygen forms on the surface of the anode (ITO) by the variation of the current densities (galvanostatic anodisation). This results in ITO oxide films growing on the ITO surface, called the anodised films. 58

Figure 2.2 Expression of dopamine in SH-SY5Y neuroblastoma cell line. A) Fluorescent micrographs of immune-labelled cultures at day fourteen on pristine ITO glass and anodised ITO films with resulting roughness of 19 nm, 61 nm and 81nm. No RA supplementation (top) with RA supplementation films (bottom). Scale bar = $20\mu\text{m}$, objective $60\times$. Dopamine expression is visualised by anti- Anti-Tyrosine Hydroxylase (TH) in green, F-actin in red by rhodamine-conjugated phalloidin and in blue nuclei by DAPI. B) Mean fluorescence intensity quantification of dopamine expression using a threshold method. The TH dopamine marker was significantly upregulated following fourteen days of RA exposure, coupled with the induction of a neuronal phenotype. In addition, TH dopamine mean fluorescence intensity was significantly increased by day fourteen on the cells cultured on anodised films with the lowest roughness profile of 19 nm, which corresponds to the films formed at 0.4 mA cm^{-2} current density compared to control and the other experimental groups. Results are $\pm \text{STD}$, $\star = p < 0.05$ 62

Figure 2.3 Methodology of focal adhesion (FA) analysis through ImageJ. Cells were labelled with anti-paxillin for FA imaging (Green), rhodamine conjugated phalloidin for actin imaging (red) and DAPI for nuclear imaging (blue) A. The paxillin channel was subsequently isolated and individual FA sites were scored with

a 4 pixel wide line B. The individual lines were analysed by length and number C. as described previously in [51]. 66

Figure 2.4 Representative images from slides surface chemistries. A) Microarray experiments were carried out using three replicate slides. Alexa Fluor® 555 labelled healthy rat brain lysate ($5 \mu\text{g mL}^{-1}$) and soybean agglutinin (SBA) lectin ($10 \mu\text{g mL}^{-1}$) were used as internal controls and incubated in two separate subarrays on every slide to confirm retained antibody performance and printing, respectively. B). Individual representation image from a slide surface chemistry showing the subarrays. The subarrays were incubated and printed with each antibody following the order detailed in C) at a range of concentrations of 0.1 to 1 mg mL^{-1} 71

Figure 2.5 Optimisation of current densities lower than 0.4 mA cm^{-2} through the impedance measurements at 1 kHz. Left, Plot of impedance magnitudes at 1 kHz of pristine ITO control and anodised films formed using current densities between 0.1 mA cm^{-2} and 0.5 mA cm^{-2} . Right, tabulated impedance magnitude values measured at 1 kHz for each of the films formed between 0.1 mA cm^{-2} and 0.5 mA cm^{-2} current densities. Overall, the anodised films formed at 0.4 mA cm^{-2} current density showed the lowest impedance magnitude at 1 kHz. 75

Figure 2.6 Particle size and distribution are significantly affected by current density. A). Scanning electron micrograms of control pristine ITO coated glass (A) and ITO anodised films with (B). 0.4 mA cm^{-2} ; (C). 4 mA cm^{-2} ; and (D). 43 mA cm^{-2} current densities. Scale bar = $1 \mu\text{m}$ B). Corresponding roughness (R_a) measurements of the pristine ITO glass and the anodised ITO films with different current densities, 0.4 mA cm^{-2} , 4 mA cm^{-2} ; and 43 mA cm^{-2} and, representative line profiles C) from each of the films. R_a indicates the mean surface roughness, calculated on $10 \mu\text{m}^2$ regions. 77

Figure 2.7 Morphological characterisation of the anodised ITO films. A) TEM images showing the structure and distribution of each of the anodised films and the pristine ITO glass control, scale bar = 500 nm B) Tabulated porosity percentages values for each of the experimental groups as an indication of the compactness of the particles forming each film. 78

Figure 2.8 Optical transmission spectra of the pristine ITO coated glass and the anodic oxidised films formed at 0.4 mA cm⁻², 4 mA cm⁻² and 43 mA cm⁻² current densities. 80

Figure 2.9 The impact of the accelerated ageing study on durability and electrical stability of the anodised ITO films. A) On top, scanning electron micrograms of control pristine ITO glass (A) and ITO anodised films with (B). 0.4 mA cm⁻²; (C). 4 mA cm⁻²; and (D). 43 mA cm⁻² current densities. Scale bar = 200µm. After four weeks under biologically relevant ageing, important film delamination was observed on anodised films formed using high current densities (4 mA cm⁻² and 43 mA cm⁻²). Partial micro-cracks were observed in films formed at 0.4 mA cm⁻² and control ITO. On bottom, corresponding photographs showing the final visual appearance of control and anodised films (E-H) after four weeks of ageing study. B) Plot of percentage loss of charge storage capacity (CSC) after four weeks of accelerated ageing study simulating four years of implant equivalence in the body. Important significant differences between the ITO control and the anodised films were observed. The ITO anodised films formed at 0.4 mA cm⁻² were the most stable films compared to control and to the films formed using high current densities. Results are ± STD, ★ = p < 0.05. 81

Figure 2.10 Electrochemical analysis of anodised films. Cyclic voltammograms of ITO (blue) and ITO anodised films formed with current densities; 0.4 mA cm⁻² (black), 4 mA cm⁻² (green) and 43 mA cm⁻² (purple). CVs recorded in 50mM phosphate buffer, scan rate 100 mV s⁻¹ A) and in 50mM phosphate buffer containing 2mM [Ru(NH₃)₆]³⁺ B), scan rate 100 mV s⁻¹. Bode C) and Nyquist D) plots comparing the EIS spectra of pristine ITO glass (blue filled asterisks), bare gold glass (red filled diamonds), and anodised ITO films formed using 0.4 mA cm⁻² (black filled triangles), 4 mA cm⁻² (green filled squares) and 43 mA cm⁻² (purple filled circles). (E) represents the electrical equivalent circuit used to analyse experimental data..... 84

Figure 2.11 Cyclic voltammograms of (A) pristine ITO glass, and anodised ITO films formed at current densities of (B) 0.4 mA cm⁻², (C) 4 mA cm⁻² and (D) 43 mA

cm^{-2} , in 50 mM phosphate buffer, pH 7.8, containing 2mM $[\text{Ru}(\text{NH}_3)_6]_3^+$. Scan rates are 500, 400, 300, 200, and 100 mV s^{-1} , from outside inwards. (Inset: Plot of the square root of scan rate versus anodic peak (ipa) currents). 88

Figure 2.12 *The presence of the polymer PSS in the solution is important for the anodisation process. Films formed without the presence of PSS at 0.4 mA cm^{-2} , 4 mA cm^{-2} and 43 mA cm^{-2} current densities revealed a linear increase in impedance compared to pristine ITO. 89*

Figure 2.13 *Cytocompatibility analysis of anodised ITO films of different roughness (R_a) formed by varying the current density. Fluorescent images of SH-SY5Y cells following one, seven and fourteen days in culture on anodised films displaying 19 nm, 61 nm and 81 nm over $10 \mu\text{m}^2$ (R_a) roughness relative to pristine ITO control (R_a 1 nm over $10 \mu\text{m}^2$). Green, live; red, dead. Bar = $50 \mu\text{m}$ A). A significant ($p < 0.05$) decrease in cell viability was observed in anodised films with an average roughness of 61 nm and 81 nm relative to control and 19 nm film roughness. B). Metabolic activity of SH-SY5Y cells compared with pristine ITO coated glass control as measured by the AlamarBlue assay ($p < 0.05$) C). Metabolic activity was significantly elevated in cells cultured on anodised ITO films with 19 nm roughness relative to anodised films with 61 and 81 nm roughness respectively by day seven and day fourteen. Results are \pm STD, $\star = p < 0.05$ 90*

Figure 2.14 *Focal adhesion formation of SH-SY5Y cell grown roughness. Immunofluorescent imaging was employed to quantify FA length and number in cells cultured on pristine ITO coated glass and experimental anodised films of different roughness (A-D), (green: paxillin, red: actin, blue: nucleus, bar: $40 \mu\text{m}$). Cells cultured on control ITO coated glass generated less FA complexes over time, whilst this trend was reversed in cells on experimental anodised ITO films of all roughness E). SH-SY5Y cells grown on 19 nm, and 81 nm roughness of anodised films were associated with a significant increase in FA length relative to cells cultured on pristine ITO coated glass ($R_a = 1 \text{ nm}$). There was a significant reduction in FA length of the cells cultured on 61 nm roughness compared to the cells grown on 19 nm, and*

81 nm experimental roughnesses F). For all analysis, results are \pm STD, ★ = $p < 0.05$ 93

Figure 2.15 Focal adhesions were sub-grouped into focal adhesions proper (FAs) and nascent focal complexes (FX). FXs were the predominant adhesion complex subtype observed on all anodised ITO films and the pristine ITO coated glass up to day seven. However, FXs were displaced by the FA subtype by day fourteen in cells cultured on all experimental and control materials. A significant increase in the mean number of focal adhesions per cell on all of the experimental anodised ITO films compared to control pristine ITO group was observed on day fourteen. 95

Figure 2.16 Unsupervised clustering of all experimental anodised films normalised by control pristine ITO. This analysis clearly defined a group between the anodised films with nano roughness of 61 nm and 81 nm respectively, and a single cluster for the films formed with the lowest roughness profile of 19 nm; sharing only 1% similarity with the rest of the experimental substrates. The gliosis response of the films formed with 0.4 mA cm^{-2} current density which exhibit the lowest roughness profile of 19 nm showed a remarkable intensity downregulation of reactive astrocytes, microglia and calcium influx markers. The resulting roughness factor of the anodised films was predominant on the differential intensity expression of the antibodies evaluated. $N=3$, 18 data points 96

Figure 2.17 Synaptic network formation on anodised film formed at a current density of 0.4 mA cm^{-2} . A) Left, current tracings from two sample neurons (in grey control and in black anodised film) showing heterogeneous post-synaptic currents (PSCs; inward deflections) recorded at a holding potential of -56 mV. Right, Superimposed traces show isolated PSCs recorded from Control (top; the average is superimposed in grey) and 0.4 mA cm^{-2} (bottom; the average is superimposed in black) neurons. Bar plots in B) summarise PSC amplitude (left) and PSC frequency (right) values. Although not statistically significant, on anodised films PSC frequency was slightly higher ($0.9 \pm 0.6 \text{ Hz}$ in controls and $1.5 \pm 0.9 \text{ Hz}$ in anodised films, $N=8$ and $N=7$, respectively), while the average values for PSC amplitude were similar ($40.8 \pm 25.9 \text{ pA}$ controls and $40.5 \pm 50.7 \text{ pA}$ in anodised films). C) Bar plots

summarise the values measured for the input resistance (top, $1195 \pm 368 \text{ M}\Omega$ controls and $946 \pm 229 \text{ M}\Omega$ anodised films) and membrane capacitance (bottom, $75 \pm 20 \text{ pF}$ controls and $85 \pm 19 \text{ pF}$ anodised film). D) Fluorescent micrographs of immune-labelled cultures, control (left) and anodised films (right), at low (top panels, objective $10\times$) and high (bottom panels objective $40\times$) magnifications. Neurons are visualised by anti β -tubulin III, in red, glial cells by anti-GFAP, in green and nuclei are visualised by Hoeschst, in blue. The plots in E) summarise neuronal densities in all conditions. 100

Figure 2.18 Calcium imaging and substrate stimulation. Left snapshots of representative fields of VM cells grown on anodised ITO film formed at 0.4 mA cm^{-2} (top) and control pristine ITO glass (bottom) and stained with calcium-sensitive fluorescent probe Fluo-4. Five regions of interest (ROI) per image were selected (highlighted in different colours), each representing a single neuron. Right, fluorescence tracings show the appearance of Ca^{2+} episodes, calcium events were measured from the relative ROI in the corresponding recording filed in both conditions (each cell is identified by the colour). Stimulation was delivered to the films as biphasic voltage pulses (2V cm^{-2} , 0.1s pulse, 0.2 Hz). Dashed lines highlight the corresponding evoked calcium response in both groups. Note that all selected cells displayed calcium transients in response to the stimulus in the 0.4 mA cm^{-2} condition, while the same stimulus did not elicit any responses in control cultures. 102

Figure 2.19 Calcium imaging and substrate stimulation. Left, snapshots of representative fields of neuronal cultures grown on 0.4 mA cm^{-2} (top) and control (bottom) and stained with the Oregon Green 488-BAPTA-1 AM. Six regions of interest (ROI) per image were selected (highlighted in different colours), each representing a single neuron, ROIs were selected at least $100 \mu\text{m}$ apart. Right, fluorescence tracings show the appearance of Ca^{2+} episodes, calcium events were measured from the relative ROI in the corresponding recording filed in both conditions (each cell is identified by the colour). In these experiments, voltage stimuli were delivered (every 60 seconds, arrows) via the substrate. Dashed lines highlight the corresponding evoked calcium response in both groups. Note that all selected

cells displayed calcium transients in response to the stimulus in the 0.4 mA cm^{-2} condition, while the same stimulus did not elicit any responses in control cultures. 103

Figure 3.1 Schematic of conductive AFM (PF-TUNA) used for the evaluation of the micro-functionalised microelectrodes conductive profile. By using the moving probe as mobile electrode, the current was flowing through the metal-coated tip and the conducting sample which was grounded..... 123

Figure 3.2 CellROX® expression on primary ventral mesencephalic (VM) mixed cell population grown on sterile Thermanox® Plastic Coverslips with 13 mm diameter (NUNCTM brand products). Cultures were stimulated with interleukin- 1β (IL- 1β) at 1, 10 and 50 ng ml^{-1} and control. A) Fluorescent images of VM mixed cell population grown on sterile Thermanox® Plastic Coverslip over a period of three, seven and ten days showing CellROX® expression in green, actin in red rhodamine-conjugated phalloidin and nuclei in blue, DAPI. Bar = $20 \mu\text{m}$, objective $60\times$ magnification. (B-D) show the percentage of CellROX® nuclei colocalisation quantified after stimulus with interleukin- 1β (IL- 1β) at 1, 10 and 50 ng ml^{-1} and control. Elevated levels of CellROX® on VM mixed cell population were seen after a stimulus of 10 ng ml^{-1} of IL- 1β and 50 ng ml^{-1} over ten days in culture, resulting in an increase of oxidative stress species presence as a response of inflammation. ★ = $p < 0.05$ 125

Figure 3.3 Morphological characterisation of activated microglia population from primary ventral mesencephalic (VM) mixed cells under stimulus of interleukin- 1β (IL- 1β) at 1, 10 and 50 ng ml^{-1} and control concentrations after 21 days in culture. A) Fluorescent images of astrocytes and microglia from VM mixed cell population grown on sterile Thermanox® Plastic Coverslips with 13 mm diameter (NUNCTM) brand products over a period of 21 days. Astrocytes are visualised by anti-GFAP, in green and microglia are visualised by Iba-1, in red, and nuclei are visualised by DAPI, in blue. Bar = $20 \mu\text{m}$, objective $60\times$ magnification. The number of microglia ramifications B) and their length C) were quantified following methods detailed in [67] as indicators of activated microglia. Significant differences ($p < 0.05$) were

observed in the number and length of microglia ramifications cultured under stimulus of 10 ng ml⁻¹ IL-1 β compared to controls and to the other IL-1 β concentrations used. Overall, microglia morphologies under stimulus of 10 ng ml⁻¹ IL-1 β resemble microglia amoeboid morphologies. ★ = $p < 0.05$ 126

Figure 3.4 Microelectrode functionalisation process. Upper panel A) describes the sequential steps taken on the bare platinum electrodes (a) electrodeposition of PEDOT:PTS coating (b), followed by the optical micrograph of the coated PEDOT:PTS microelectrode ready for the functionalisation with the topography (c) Scale bar= 2mm, 10 \times . Bottom panel B) outlines the low temperature three-step die imprinting lithography process. This process starts with the micro-pit nickel die master and the PEDOT:PTS coated electrode (a). The nickel die was then pressed against the PEDOT:PTS coated microelectrode at a localised constant pressure of 1.9 tons per cm² for fifteen minutes at room temperature using parallel pressing plates. Finally, a scanning electron micrograph (SEM) of the micro-topographically functionalised PEDOT:PTS coated microelectrode is shown (c). 134

Figure 3.5 Micro-topographically functionalised microelectrodes. Upper panel A) Scanning electron micrographs (SEM) of the nickel die master utilised for the low temperature three-step die imprinting lithography process (a) the micro-topographically functionalised substrate with ordered array of micro-pits produced on PEDOT:PTS coated microelectrodes by low temperature three-step die imprinting lithography process (b). Scale bar = 10 μ m. In the insets, the pit, interpit and depth dimensions are detailed. B) Atomic-force microscopy (AFM) sectional analysis of the micro-topographically functionalised PEDOT:PTS coated microelectrode over a region of 10 μ m² area reflecting the vertical distance of the pit patterned transferred of 0.96 \pm 0.07 μ m. Fifteen measurements were taken from three different replicas. Results are \pm STD. 135

Figure 3.6 Bare platinum (Pt) morphological characterisation. A). Scanning electron micrograph (SEM) of bare platinum (Pt) microelectrodes, and corresponding mean surface roughness (R_a) B). Scale bar = 3 μ m. 137

Figure 3.7 Microelectrode morphological physical characterisation. Upper panel A). Scanning electron micrographs (SEM) (a-c) of pristine PEDOT:PTS, flattened PEDOT:PTS and the micro-topographically functionalised PEDOT:PTS coated microelectrodes. Scale bar = 3 μ m. B) Corresponding surface plots (d-f) of pristine PEDOT:PTS, flattened PEDOT:PTS and the micro-topographically functionalised microelectrodes on 10 μ m² regions. 137

Figure 3.8 Electrochemical analysis of functionalised PEDOT:PTS coated microelectrodes. A) Cyclic voltammograms (CVs) bare platinum (Pt) and gold coated (Au) microelectrodes and pristine PEDOT:PTS, flattened PEDOT:PTS and micro-topographically functionalised PEDOT:PTS coated microelectrodes. CVs were recorded in 0.01 M phosphate-buffered saline (PBS) at a scan rate of 100 mV s⁻¹. B) Relative electrode surface area calculated based on cyclic voltammograms (CVs) in 2.5 mol dm⁻³ K₄[Fe(CN)₆] in 0.1 M KCl solution at a scan rate of 100 mV s⁻¹. The relative electrode surface area was estimated according to the Randles-Sevcik equation and the bare platinum (Pt) microelectrode was used as a reference. Bode C) and Nyquist D) plots comparing the EIS spectra of bare platinum (Pt) and gold coated (Au) microelectrodes and pristine PEDOT:PTS, flattened PEDOT:PTS and micro-topographically functionalised PEDOT:PTS coated microelectrodes. E) represents the electrical equivalent circuit used to analyse experimental data. Results are \pm STD, ★ = $p < 0.05$ 141

Figure 3.9 Electrochemical analysis of functionalised PEDOT:PTS coated macro electrode (1.6 cm²). A) Cyclic voltammograms (CVs) bare platinum (Pt) and pristine PEDOT:PTS, flattened PEDOT:PTS and micro-topographically functionalised PEDOT:PTS coated electrodes. CVs were recorded in 1X phosphate-buffered saline (PBS) at a scan rate of 100 mV s⁻¹. B) Bode plots comparing the EIS spectra of bare platinum (Pt) and pristine PEDOT:PTS, flattened PEDOT:PTS and micro-topographically functionalised PEDOT:PTS coated electrodes. C) Table summarising the charge storage capacity (CSC) of large bare platinum (Pt) and pristine PEDOT:PTS, flattened PEDOT:PTS and micro-topographically functionalised PEDOT:PTS coated electrodes. CSC was evaluated from the cathodic region of cyclic voltammograms (CVs) recorded in 1X phosphate-buffered saline

(PBS) at 100 mV s^{-1} scan rate (Potential range: -1 V to 0.4 V vs. Ag/AgCl). Results are $\pm \text{STD}$, $\star = p < 0.05$ 143

Figure 3.10 Conductive-AFM (C-AFM) (in PeakForce Tuna mode, PF Tuna, Bruker) of micro-topographically functionalised PEDOT:PTS coated microelectrodes. A) C-AFM micrograph of micro-topographically functionalised PEDOT:PTS coated microelectrode used for analysis. B) I-V curves were recorded at selective positions, non-patterned region and patterned region (pit) on the micro-topographically functionalised microelectrode. C-AFM tips (coated with Platinum/Iridium) were used as the mobile counter electrode to contact the SWCNTs (PeakForce-TUNA tips, Bruker). For a schematic of the set-up, see Figure 3.1. The voltage bias was ramped between -500mV and 500mV . The data was then analysed by NanoScope Analysis (version 1.5, Bruker) and Matlab (version 2016 a)..... 146

Figure 3.11 Ventral mesencephalic cells (VM) adhered on micro-topographically functionalised electrodes. Scanning electron micrograph (SEM) of primary VM mixed cell population adhered on micro-topographically functionalised PEDOT:PTS coated electrodes. Scale bar= $50 \mu\text{m}$ 147

Figure 3.12 Cytocompatibility of functionalised electrodes. A) Fluorescent images of primary ventral mesencephalic (VM) mixed cell population grown on each of the bare platinum (Pt) and functionalised PEDOT:PTS coated electrodes for three, seven and ten days in culture. Neurons are visualised by anti β -tubulin III, in red, astrocyte cells by anti-GFAP, in green and nuclei are visualised by DAPI, in blue. Bar = $20 \mu\text{m}$, objective $60\times$ magnification. Cell density (%) analysis of astrocytes and neurons presence on each of the electrodes is presented in B). An overall significant ($p < 0.05$) decrease in viability of neurons and astrocytes density was observed in flattened PEDOT:PTS coated electrodes. Neural length analysis of electrodes presented in C) showed with significant ($p < 0.05$) longer neurite lengths the neurons grown on micro-topographically functionalised PEDOT:PTS coated electrodes. $\star = p < 0.05$ 149

Figure 3.13 Morpho-adhesion characteristics of astrocyte presence in the functionalised electrodes towards astrocyte reactivity indication. A) Selective

fluorescent images of astrocytes from primary ventral mesencephalic (VM) mixed cell population grown on each of the bare platinum (Pt) and functionalised PEDOT:PTS coated electrodes for three, seven and ten days in culture. Astrocytes are visualised by anti-GFAP, in green, formation of focal adhesion contacts by anti-Paxillian, in red and nuclei are visualized by DAPI, in blue. Bar = 20 μm , objective 60 \times magnification. Frequency distribution in time (three, seven, and ten days) of cytoplasm astrocyte areas (μm^2) on bare platinum (Pt) and functionalised PEDOT:PTS coated electrodes is presented in B). The frequency distribution of astrocyte areas on micro-topographically functionalised PEDOT:PTS coated electrodes showed the lowest frequencies over time. C) represents the frequency distribution of the astrocyte focal adhesion contact numbers per cell and their corresponding length frequency distribution over time in D)..... 153

Figure 3.14. Comparative gliosis derived cytokines and chemokine factor profiling for interferon- γ (IFN- γ ;A), tumor necrosis factor- α (TNF- α ;B), chemokine factor CXCL-1 (KC/GRO;C), interleukin-6 (IL-6;D) and interleukin-5 (IL-5;E). The release expression of each of the signaling molecules is analysed from primary ventral mesencephalic (VM) mixed cell population supernatants collected at day three, seven and ten days on bare platinum (Pt) and functionalised PEDOT:PTS coated electrodes. An important effect is seen on the micro-topographically functionalised PEDOT:PTS coated electrodes, which presented significantly and consistently low release profiles for each cytokine and chemokine factor analysed. Results are \pm STD, $\star = p < 0.05$ 159

Figure 3.15 Molecular network induced by cytokines TNF α , IL-6, IL-5 and IFN γ secreted by primary ventral mesencephalic (VM) mixed cells. Each node represents a single protein molecule encoded by genes. Coloured nodes indicate query proteins and first shell of interactors. The lines between the nodes indicate high confidence (>0.7) predicted interactions based on experimentally determined databases, co-expression, and co-occurrence. 161

Figure 3.16 Neuronal network activity in bare platinum (Pt), pristine PEDOT:PTS and micro-topographically functionalised PEDOT:PTS coated electrodes. A)

snapshot of representative field used for Ca^{2+} imaging recording with highlighted regions of interest (ROI), indicating the neurons selected for the measurements. B) spontaneous repetitive Ca^{2+} events (two sample neurons were selected from the same field for each electrode) recorded in hippocampal cultures grown on the three different conditions. C) inter event interval (IEI) values are summarised for the different electrodes. Note the similar occurrence of spontaneous calcium events, due to ongoing synaptic activity. 162

Figure 4.1 Calibration curve showing the linear relationship of the fluorescence heparan sulphate mimetic-F6 -Cy5 tagged versus its concentration. A linear relationship is observed between $0.5 \mu\text{g ml}^{-1}$ and $500 \mu\text{g ml}^{-1}$ satisfying the equation $y = 1.35x + 2.56$ ($R^2 = 0.9994$). 187

Figure 4.2 Images from a representative scanned microarray slide after incubation and washing. A) Incubations were carried out on three replicate microarray slides. Alexa Fluor® 555 labelled healthy rat brain lysate (5 mg mL^{-1}) and SNA-I lectin (10 mg mL^{-1}) were used as controls to confirm retained antibody performance and printing, respectively, and were incubated in two separate subarrays on every slide. B) Individual subarray from a representative scanned microarray slide after incubation with healthy rat brain lysate and subsequent washing. The subarrays were printed with antibodies and lectins in replicates of six following the order detailed in C). 196

Figure 4.3 Biochemical functionalisation of the neuroelectrode surface with PEDOT:PTS:F6 thin films. A) F6 is a dextran T5 (M_w 5,000 Daltons) derivative containing sulphate, carboxymethyl, and phenylalanine methyl ester groups. For an easy representation, three differently substituted glucosidic units (A, B, and C) are depicted and arranged in an arbitrary combination. The relative content of each unit was calculated according to the nature of the group substituted at position 2 of each unit (C2). R represents the proportion of each substituted group at C3 and C4, which total substitution corresponds to 200%. F6 was synthesised and analysed as in [44]. B) Pictorial representation of PEDOT:PTS:F6 functionalised electrodes from the

electrophysical arrangement to the cell level interaction with growth factors binding, i.e FGF-2..... 199

Figure 4.4 Cytocompatibility effects of heparan sulphate mimetic-F6 – concentrations in solution. Live and dead assay was carried out using primary ventral mesencephalic (VM) mixed neural cell population under the presence of bulk F6 at 1, 10, 50, 100 and 1000 $\mu\text{g ml}^{-1}$. An early time of three days in culture A) and late time of ten days B) were evaluated. A maintained cell viability was achieved when bulk F6 was present in the cell culture media at concentrations below 50 $\mu\text{g ml}^{-1}$. Results are \pm STD. ★ = $p < 0.05$ 201

Figure 4.5 Electrochemical quartz crystal microbalance (EQCM) measurements of the masses recorded of PEDOT:PTS:F6 coatings at 1, 10, 50, 100 and 1000 $\mu\text{g ml}^{-1}$. PEDOT:PTS:F6 at 1000 $\mu\text{g ml}^{-1}$ of heparan sulphate mimetic- F6 was found to possess the highest mass immobilised of F6 within the polymer matrix with a mass recorded of 807.2 $\mu\text{g cm}^{-2}$ 203

Figure 4.6 Scanning electron micrographs (SEM) of the bare platinum/iridium (PtIr) microelectrode A) and PEDOT:PTS:F6 coated microelectrode B) are shown, respectively. Scale bar = 200 μm . In the inset, the PEDOT:PTS:F6 coating is detailed, showing the nodular formation of electrodeposited coatings. 204

Figure 4.7 Morphological changes with different concentrations of F6. A) Scanning electron micrographs (SEM) of pristine PEDOT:PTS coated microelectrodes and the PEDOT:PTS:F6 coated microelectrodes at 1, 10, 50, 100 and 1000 $\mu\text{g ml}^{-1}$ of heparan sulphate mimetic-F6. B) FT-MIR spectra of powdered F6 (black), pristine PEDOT:PTS coated microelectrodes (red) and PEDOT:PTS:F6 coated microelectrodes at 1, 10, 50, 100 and 1000 $\mu\text{g ml}^{-1}$ of F6. Blue dotted lines show bands that belong to only F6, while red dotted lines show bands contributed by just PEDOT:PTS polymer. It can be seen that with an increase in the concentration of F6 in the PEDOT:PTS matrix, the bands become sharper suggesting a greater rigidity in the structure. 206

Figure 4.8 Chemical characterisation of the PEDOT:PTS:F6 coated microelectrode. A) Contact angle on pristine PEDOT:PTS and PEDOT:PTS:F6

coated microelectrodes, showing the decrease in a water contact angle suggesting an increase in hydrophilicity. B) Raman spectra of PEDOT:PTS microelectrodes, with and without incorporated F6, and powdered F6. Peaks assigned solely to F6 are indicated by an * on the pure F6 and of PEDOT:PTS:F6 coated microelectrodes spectra. (C-F) Raman mapping of pristine PEDOT:PTS and PEDOT:PTS:F6 coated microelectrodes. C) shows the component DLS analysis, where red pixels represent the F6 component and green pixels represent the PEDOT:PTS component. D) and E) show the intensity of the Raman bands at 1021 cm^{-1} and 997 cm^{-1} , respectively, and indicate the presence of F6 evenly distributed on coated PEDOT:PTS microelectrodes. F) shows the band intensity at 585 cm^{-1} and indicates the presence of PEDOT:PTS in the coating. (G-I) X-ray photoelectron spectra of G) pristine PEDOT:PTS, H) PEDOT:PTS:Dextran, and I) PEDOT:PTS:F6 coated microelectrodes, showing the presence of sulphur in various chemical environments corresponding to S-C bonding ($2p$ neutral state) and $2p_{3/2}$ and $2p_{1/2}$ states in both sulphonates and sulphates. The * in G) denotes the presence of possible impurities from the electrolyte. 208

Figure 4.9 FT-MIR spectra of powdered dextran (black), pristine PEDOT:PTS coated microelectrodes (red) and PEDOT:PTS:Dextran coated microelectrodes. Blue dotted lines show bands that belong to only dextran, while red dotted lines show bands contributed just by PEDOT:PTS matrix. 211

Figure 4.10 The positions of C peaks and the relative compositions. A) X-ray photoelectron spectra of (a) pristine PEDOT:PTS coated microelectrode, (b) PEDOT:PTS:Dextran coated microelectrode, and (c) PEDOT:PTS:F6 coated microelectrode showing the presence of carbon in various oxidation states. The C-N bond cannot be used to discern the percentage of alanine moiety present as a substitution on heparan sulphate mimetic-F6, because trace amounts of acetonitrile from the electrolyte could be present contributing to this peak in all three coated microelectrodes. C* denotes partially oxidised carbon. Table giving the relative atomic percentages of these bonds in coated microelectrodes is presented in B) the relative increase in the percentages of $C^*O,S/C^*N$ and $C^*O,S(-COO)/C^*N$ bonds

between PEDOT:PTS:Dextran and PEDOT:PTS:F6 (highlighted in bold), shows the increase in N possibly due to presence of phenylalanine component in F6. 214

Figure 4.11 Electrochemical analysis of PEDOT:PTS:F6 coated microelectrodes.

A) Cyclic voltammograms (CVs) of bare Platinum/Iridium (PtIr) microelectrodes, pristine PEDOT:PTS and PEDOT:PTS:F6 coated microelectrodes. CVs were recorded in 1X phosphate-buffered saline (PBS) at a scan rate of 100 mV s^{-1} . Bode B) and Nyquist C) plots comparing the EIS spectra of bare Platinum/Iridium (PtIr) microelectrodes, pristine PEDOT:PTS, and PEDOT:PTS:F6 coated microelectrodes. D) and E) represent the electrical equivalent circuit used to analyse experimental data of the coated microelectrodes and bare Platinum/Iridium (PtIr) microelectrodes, respectively. Results are $\pm \text{STD}$ 218

Figure 4.12 Concentration profile of heparan sulphate mimetic- F6 released from PEDOT:PTS:F6 coated electrodes in the passive (orange squares) and active (red dots) modes for a period of 21 days under simulating in vivo conditions (constant agitation under 37° degrees).

For the active release mode, 50 stimulation cycles were applied every day over 21 days which resulted in approx. 1000 stimulations over this period. The stimulation regime was a biphasic potential pulse, consisting of a 5-second application of a reduction potential (-0.5 V) followed by a 5-second application of an oxidative potential (+0.5 V). Results are $\pm \text{STD}$ 221

Figure 4.13 Electrical stability of the PEDOT:PTS:F6 microelectrodes.

Plot of percentage loss of charge storage capacity (CSC) after 1000 continuous stimulation cycles of biphasic potential pulses, consisting of a 5-second application of a reduction potential (-0.5 V) followed by a 5-second application of an oxidative potential (+0.5 V). Important significant differences between the bare Platinum/Iridium (PtIr) microelectrodes and the PEDOT-based coated microelectrodes were observed. PEDOT:PTS:F6 coated microelectrodes were the most stable followed by pristine PEDOT:PTS coated microelectrodes and bare Platinum/Iridium (PtIr) microelectrodes after. Results are $\pm \text{STD}$, $\star = p < 0.05$ 222

Figure 4.14 Cytocompatibility of PEDO:PTS:F6 coated electrodes.

A) Fluorescent images of primary ventral mesencephalic (VM) mixed cell population grown on each

of the bare platinum (Pt) electrodes and pristine PEDOT:PTS, PEDOT:PTS:Dextran and PEDOT:PTS:F6 coated electrodes for three, seven and ten days in culture. Neurons are visualised by anti β -tubulin III, in red, astrocyte cells by anti-GFAP, in green and nuclei are visualised by DAPI, in blue. Bar = 20 μ m, objective 60 \times magnification. Cell density (%) analysis of astrocytes and neurons presence on each of the electrodes is presented in B). An overall significant ($p < 0.05$) enhancement in viability of neurons was observed in PEDOT:PTS:F6 coated electrodes. Neural length analysis of electrodes presented in C) showed with significant ($p < 0.05$) longer neurite lengths the neurons grown on PEDOT:PTS:F6 coated electrodes, suggesting on an overall neurotrophic effect of these electrodes owing to the presence of heparan sulphate mimetic-F6. Results are \pm STD. $\star = p < 0.05$ 225

Figure 4.15 Comparative pro-inflammatory derived cytokines and chemokine factor profiling for interferon- γ (IFN- γ ;A), tumor necrosis factor- α (TNF- α ;B), chemokine factor CXCL-1 (KC/GRO;C), interleukin-6 (IL-6;D) and interleukin-5 (IL-5;E). The release expression of each of the signaling molecules is analysed from primary ventral mesencephalic (VM) mixed cell population supernatants collected at day three, seven and ten days on bare platinum (Pt) electrodes, pristine PEDOT:PTS, PEDOT:PTS:Dextran and PEDOT:PTS:F6 coated electrodes. An important effect is seen on the PEDOT:PTS functionalised with the heparan sulphate mimetic-F6 coated electrodes, which presented significantly low release profiles for each cytokine and chemokine factor analysed after ten days in culture. Results are \pm STD, $\star = p < 0.05$ 228

Figure 4.16 Glycosaminoglycans competition assay towards FGF-2 and VEGF binding. F6 shows a strong binding capacity to FGF2 and VEGF in a heparin-like manner. 232

Figure 4.17 Unsupervised clustering of all experimental and control groups and inflamed control, respectively. This analysis clearly defined interestingly hierarchical clusters between experimental sulphated groups: the chemical sulphated pristine PEDOT:PTS coated electrodes and the biological modified PEDOT:PTS:F6 coated electrodes with the heparan sulphate mimetic-F6, and between controls

groups with non-sulphated patterns: control material bare platinum, the negative control for sulphation PEDOT:PTS:Dextran coated electrodes and tissue culture plastic as inflamed control, at both days three A) and ten B) respectively. PEDOT:PTS:F6 coated electrodes showed a remarkable intensity downregulation of reactive astrocytes, microglia and calcium influx markers with an important upregulation of neural response compared to all groups and controls at day three and day ten, respectively. N = 3, 18 data points..... 234

Figure 4.18 Histograms representing the differences in recognition of printed lectins by each of the experimental groups and controls at day three A) and day seven B) respectively. Microarray experiments were carried out using three replicate slides. The subarrays were printed with each lectin following the order detailed in Figure 4.2 and incubated with fluorescently labelled protein preparations. Results are average \pm standard error. N = 3, 18 data points 238

Figure 5.1 Multidisciplinary approaches for neural interfaces applications. A) Anodisation of ITO, B) Micro-pit and C) GAG-mimetic functionalised electrodes, respectively, as electrochemical, surface morphology, and cytocompatibility strategies for the generation of neural interfaces with superior electrical and biological characteristics..... 260

Figure 5.2 Involvement of both biological and topographical functionalisation strategies as interdisciplinary efforts for neural interface applications. 261

Figure 5.3 Pictorial representation of flexible ITO microelectrode arrays for the fabrication of anodised electrodes 263

Figure 5.4 Schematic of the fabrication process for the topographical functionalisation of conducting polymer coatings for the modulation of reactive astrocytes adhesion and function to be further evaluated through signalling and interaction pathways. 264

Figure 5.5 The neural response to topographically functionalised neuroelectrode surfaces with vertical silicon nanowires...... 266

Figure 5.6 Biomimetic conducting coatings for the presentation of glycochemistries at the neural interface. 267

Figure 5.7 Organotypic whole brain slice cultures as ex vivo models. Brain slice cultures can be effective models of neurodegenerative diseases and an important translational step forward in simulating more in vivo-like conditions. 269

Figure 5.8 Whole brain sagittal slice after 21 days in culture. In a unique slice many anatomical structures are conserved. Scale bar =5 mm. 270

Figure 5.9 Characterisation of whole brain slice viability. A) Fluorescent micrographs showing the overall tissue viability at day 21 in culture through the live/dead assay B) and LDH analysis in C) Live cells are shown in green, dead cells in red. Scale bar 100 μ m. 273

Figure 5.10 Immunohistochemical characterisation of striatum region from a whole brain slice cultures. A) Representative images demonstrating the presence of general neuronal and dopaminergic neurons at 14 and 21 days in culture B). Scale bar= 40 μ m. 274

Figure 5.11 Immunohistochemical characterisation of whole brain slice cultures of microglial presence. A) Representative images demonstrating the presence of astrocytes (in green) and microglia (in red). A presence of microglia in the whole brain slice was observed by day 21 in culture B). Length analysis of the microglia ramifications showed that there is an increase in length over time C). Scale bar= 40 μ m...... 275

LIST OF TABLES

Table 1.1 General summary of PEDOT and their derivatives and biological modifications for neural applications. 16

Table 2.1 Summary of the commercial antibodies used for the construction of gliosis antibody microarray..... 69

Table 2.2 Physical properties of anodised ITO films formed with different deposition currents. Values of experimental thickness and mean particle diameter of pristine and anodised films formed with 0.4 mA cm⁻², 4 mA cm⁻² and 43 mA cm⁻² current densities over a constant time of 450 seconds. The data represent the mean of 15 measurements for film thickness plus >200 measurements for particle diameter. Results are ± SD, N=3. 79

Table 2.3 XPS analysis of the elemental composition of the Pristine ITO and anodised ITO films. 83

Table 2.4 Electrochemical characteristics of ITO anodised films. Non-faradaic charge density evaluated from cathodic region of cyclic voltammograms recorded in 50 mM phosphate buffer at 0.1 V s⁻¹ scan rate (Potential range: -1 V to 0.4 V vs. Ag/AgCl). Faradaic charge density and peak current density (ipa) evaluated from voltammograms recorded in 50mM phosphate buffer containing 2 mM [Ru(NH₃)₆]₃⁺ at 0.1 V s⁻¹ scan rate..... 85

Table 2.5 Summary of the calculated resistance values (R₃) for each of the anodised ITO films after equivalent circuit analysis. 86

Table 3.1 X-ray photoelectron spectroscopy (XPS) analysis of the elemental composition of the micro-topographically functionalised PEDOT:PTS coated microelectrodes looking at the nickel residual presence from nickel die master used

<i>in the low temperature three-step die imprinting lithography process. Ni 2p atomic percentage was at the noise level. N=3.</i>	136
Table 3.2 Microelectrode physical properties. Values of experimental mean surface roughness (R_a) and mean surface area (SA) measurements over $10 \mu\text{m}^2$ regions. The data represent the mean of 15 measurements from three different replicas. Results are $\pm SD$, $N=3$	138
Table 3.3 Electrochemical performance and stability of functionalised PEDOT:PTS coated microelectrodes. The initial and the final charge storage capacity (CSC) was evaluated from the cathodic region of cyclic voltammograms (CVs) recorded in 1X phosphate-buffered saline (PBS) at 100 mV s^{-1} scan rate (Potential range: -1 V to 0.4 V vs. Ag/AgCl). The corresponding loss was calculated after 500 cycles. Results are $\pm SD$, $N=3$	142
Table 3.4 Summary of the calculated resistance values (R_m) of bare platinum (Pt) and gold coated (Au) microelectrodes and pristine PEDOT:PTS, flattened PEDOT:PTS and micro-topographically functionalised PEDOT:PTS coated microelectrodes after equivalent circuit analysis. Results are $\pm STD$. $N=3$	145
Table 4.1 Summary of all the commercial antibodies used for the gliosis antibody microarray.	193
Table 4.2 Lectins, their sources, common names, binding specificities, print sugars and the manufacturer.	194
Table 4.3 Passive mode concentration profile of heparan sulphate mimetic-F6 released from PEDOT:PTS:F6 coated electrodes at a concentration of 1, 10, 50, 100 and $1000 \mu\text{g ml}^{-1}$ for a period of 21 days. Results are $\pm STD$. $N=3$	202
Table 4.4 Values of experimental mean surface roughness (R_a) and mean thickness measurements of pristine PEDOT:PTS coated microelectrodes and PEDOT:PTS:F6 coated microelectrodes at 1, 10, 50, 100 and $1000 \mu\text{g ml}^{-1}$ of heparan sulphate mimetic-F6. The data represent the mean of 15 measurements from three different replicas. Results are $\pm SD$, $N=3$	205

Table 4.5 Tentative assignments of the peaks observed in the Raman spectra. 210

Table 4.6 Tentative assignments of the peaks observed in the ATR-IR spectra. ... 211

Table 4.7 Electrochemical performance of PEDOT:PTS:F6 coated microelectrodes. The charge storage capacity (CSC) was evaluated from the cathodic region of cyclic voltammograms (CVs) recorded in 1X phosphate-buffered saline (PBS) at 100 mV s⁻¹ scan rate (potential range: -0.8 V to 1 V vs. Ag/AgCl). The calculated resistance values (R₃) of bare Platinum/Iridium (PtIr) microelectrodes, pristine PEDOT:PTS and PEDOT:PTS:F6 coated microelectrodes after equivalent circuit analysis. Results are ± STD. N=3..... 218

ACKNOWLEDGEMENTS

It may sound strange to some people, but for me it is always been quite normal that my family is involved in all that I do, and, yes, this includes Science. It has been usual for me during all my academic appointments to have meetings with my family to discuss ideas, data, graphs and presentations. Or just to have meetings to structure my pathway, to stop and to recharge my energy to continue working on what we like to call, my ‘Personal Life Project’. Thanks to the articulate and appropriate advice from my *Papo*, for the spiritual help and faith given by my *Mamo*, and for the grounded help from my *Sis*. All of my achievements are possible because of each of them, especially because of the patience and full time support of my sister, who brings a special touch to whatever I do in life. I can say that through her, I can perceive the enlightenment and inspiration needed from the Holy Spirit. Therefore, this thesis is our thesis because without her I cannot do things with the same level of happiness and conviction.

Thanks to *Borji*, who has always been there to calm me down and keep me going with his terrific sense of humour and patient love.

Thanks for the good vibes and prayers across continents, for the innumerable cups of coffee, and support from the people around me.

Thanks to the old and new bosses, for all opportunities given and well taken, for showing me that I am able to do whatever I commit to and set my mind to, especially to Dr Windebank and Dr Yaszemski for never failing to believe in me. For telling me that the **only** and **simple** thing to do is to make things to happen, and to keep my head up. Thanks to Professor Abhay Pandit for helping me structure my learning process and for the deadlines to reach my goals. Thanks to Dr Eilis Dowd for listening to me at all times and helping me to clearly outline my ideas.

A warm and deep thank you to Dr Manus Biggs for allowing me to come and start anew, for the immense guidance and support, for the encouragement in all my phases of my PhD life and of course for the unimaginable tons of work given ☺. Most importantly for showing me step by step and little by little how to work towards my goals, even if the goals were not reached as planned, you always helped me to

appreciate other ways and methods that were ready to be explored. I greatly appreciate your confidence in me, your great sense of humour even in the hard moments and even more for the good words and good temper during the whole process, your first journey as a PhD supervisor, especially when I have been super desperate and crying as crazy.

Thanks to each of the members of the now expanded Biggs's group, and Pandit's group, to Dr Oliver Carroll, Mr. Anthony Sloan, Mr. Maciej Doczyk, Dr Stefania Spada, Mr. Derek Whelan, and Mrs. Tara Cosgrave for their valuable assistance and never saying no. Kind thanks to each of the members of the administrative team at CURAM and NFB for being so caring and always willing to help. Big thanks to Mrs. Claire Riordan, Mrs. Andrea Fitzpatrick and Mrs. Joanna Hopkins for being awesome.

Great thanks to the collaborators along these years, Professor Laura Ballerini and her group at SISSA, especially PhD student Mr. Niccolò Paolo Pampaloni, who kindly showed me all the techniques during my internship at SISSA and continues to work on the project with PhD student Mr. Ivo Calaresu. Thanks to Professor Dulce Papy-Garcia and her team at CRRET, especially to Dr Idir for his help during my staying at CRRET and Dr Minh Bao Huynh for his further help with the project. Thanks to Dr Anuradha R. Pallipurath at University of Bath for all the long helpful discussions and further involvement in the project, as well as Dr Parvaneh Mokarian-Tabari at Trinity College. Thanks to Dr Nathalia Peixoto at George Mason University and her team for her great dynamic explanations, thanks to Dr Matteo Palma and his PhD student Mr. Jingyuan Zhu. Thanks to the collaborators at NUIG, Dr Michelle Kilcoyne and her PhD student Mrs. Andrea Flannery, to Dr Gerard O'Connor, Dr Nazar Farid and Dr Una Fitzgerald and her group. My gratitude and appreciation to Dr Paul Kavanagh and Dr Leo R Quinlan for teaching, guiding and supporting through the years with their good Irish vibes.

My PhD journey has been a mixture of good and bad moments, of big and small steps, of nice people and not so nice people, of good and bad communication, of bustle, of stops, of lazy moments. But, in the end, a journey lived to fullest because it

always has made sense to me in my hard work and full passion impregnated it on purpose.

Thanks for everything and to everyone.

Suena muy curioso para muchos, para mí siempre ha sido lo más normal del mundo tener a mi familia muy cercana en todo lo que hago, y sí, esto incluye Ciencias desde varios campos. Desde tener reuniones para discutir datos, ideas, graficas o hacer presentaciones o para simplemente, parar, recuperar las ganas y seguir de nuevo con los consejos siempre acertados y bien dichos de mi *Papo*, de la espiritualidad de mi *Mamo* y de los pies en la tierra de mi hermanita. Es por ellos, y especialmente al apoyo y guía de mi hermanita que siempre lo que hago tiene otro toque. Es por eso que con mi *Sis* todo está lleno para mí y me vasta. Sé que en ella tengo la expresión más clara de querer hacer las cosas bien a través de la inspiración del Espíritu Santo. Es por eso que esta tesis es NUESTRA tesis, porque sola nunca puedo llegar a cubrir todo con tan buen ánimo e integridad.

Como parte activa de mi familia en estos cuatro años está mi *Borji*, que ha llegado para darme tranquilidad y ánimos para continuar, parar y terminar. Por su buen humor y amor paciente. También están las oraciones y buenas vibras desde varios continentes, junto a los múltiples cafés y palabras de ánimo de los que me rodean.

A los viejos y nuevos jefes, por las oportunidades y porque siempre me han mostrado que soy capaz de hacer lo que quiero y que lo único que tengo que hacer es *make things happen*, así de sencillo, como diría el Doctor Manus. Gracias al Profesor Abhay por darme estructura y *deadlines* para lograr objetivos, Doctor Eilis por escucharme siempre.

Un sentido y especial agradecimiento es para el Doctor Manus, por la cantidad inimaginable de trabajo asignado ☺ que al final me muestra que el *multitasking* existe en su máximo nivel de expresión, pero sabiendo que lo más importante es hacer las cosas bien y con el máximo esfuerzo, así no se llegue al objetivo esperado. Por mostrarme que durante el hacer, siempre hay nuevas maneras e ideas para ser exploradas. Agradezco su confianza, y mucho más por las buenas maneras y buen ambiente que me ha brindado, inclusive cuando me he desesperado y llorado como loca.

Al final, como todo en la vida, mi doctorado se ha compuesto de pasos grandes y pequeños, de cosas malas y buenas, de personas agradables y no tan agradables, de

comunicar, de negociar, de llegar, de parar, de querer y no querer, pero que siempre recobra vida en mi trabajo duro y hecho con pasión.

Gracias por todo y a todos.

LIST OF ABBREVIATIONS

AFM - Atomic Force Microscopy
Ag/AgCl - Silver chloride
ANSCs - Adult Neural Stem Cells
Asn – Asparagine
BCA - Bicinchoninic Acid
BDBF - Brain-Derived Neurotrophic Factor
BSA - Bovine Serum Albumin
Ca²⁺ - Calcium
CaCl₂ – Calcium Chloride
C-AFM – Conductive-Atomic Force Microscopy
CE – Counter Electrode
CHs- Conducting Hydrogels
ClO₄- Perchlorate
CNS – Central Nervous System
CNTs – Carbon Nanotubes
CO₂ –Carbon Dioxide
CPs – Conducting Polymers
CS – Chondroitin Sulphate
CSC- Charge Storage Capacity
CV - Cyclic Voltammogram
Cy3 – Cyanine
DAPI- (4',6-diamidino-2-phenylindole)
Dex-P –Dexamethasone Phosphate
DI – Distilled
DIV-Days *in vitro*
DMSO- Dimethyl Sulphoxide
D_o – Diffusion Coefficient
DS – Dermatan Sulphate
ECM – Extracellular Matrix
EDOT – 3,4-Ethylenedioxythiophene
EGTA- Ethylene Glycol-Bis(β-aminoethyl ether)-N,N,N',N'-Tetracetic Acid)
EIS – Electrical Impedance Spectroscopy
ESA – Electroactive surface area
FA- Focal Adhesion
FCS – Fetal Calf Serum
FDA – Fluorescein Diacetate

FITC-Fluorescein Isothiocyanate
GAGs – Glycosaminoglycans
Gal – Galactose
GalNAc – N-acetylgalactosamine
GFAP – Anti-Glial Fibrillary Acidic Protein
GlcA – Glucuronic Acid
GlcNAc – N-acetylglucosamine
GPI – Glycosylphosphatidylinositol
H₂O₂ – Hydrogen Peroxide
H₂SO₄ – Sulphuric Acid
HA – Hyaluronic Acid
HBSS – Hank’s Balanced Salt Solution
HDMS – Hexamethyldisilazane
HEPES – (4-(2-hydroxyethyl)-1-piperazineethanesulfonic acid)
HF – Hydrofluoric Acid
HMs - Heparan Mimetics
HNO₃ – Nitric Acid
HS – Heparan Sulphate
HSPG – HS proteoglycan
I.D – Internal Diameter
IdoA - Iduronic Acid
IEI – Inter-Event Interval
i_{pa} – Anodic Peak Currents
ITO – Indium-Tin Oxide
KCl – Potassium Chloride
KS - Keratan Sulphates
LDH – Lactate dehydrogenase
LiClO₄ – Lithium Perchlorate
LRM55 – Mixed Glioma Cells
MgCl₂ – Magnesium Chloride
MWCNTs – Multiple-Walled Carbon Nanotube
N- Nitrogen
Na₂ATP – Adenosine 5'-Triphosphate Disodium Salt Hydrate
NaCl – Sodium Chloride
NaOH – Sodium Hydroxide
ND – Neutral Density
NFB – Neutral Formalin Buffer
NGF – Nerve Growth Factor
Ni – Nickel
np-Au - Nanoporous Gold

O – Oxygen
P0- Postnatal Rats at an Age of 0 days
P2- Postnatal Rats at an Age of 2 days
P3- Postnatal Rats at an Age of 3 days
P4 -Postnatal Rats at an Age of 4days
P11 - Postnatal Rats at an Age of 11 days
PANI - Polyaniline
PBS - 1X Phosphate-Buffered Saline Solution
PC12 – Pheochromocytoma Cells
PDMS – Polydimethylsiloxane
PEDOT - Poly(3, 4-ethylenedioxythiophene)
PEDOT:PTS - Poly (3,4- ethylenedioxythiophene):P-Toluene Sulphonate
PF-TUNA - PeakForce Tunneling Atomic Force Microscopy
PI - Propidium Iodide
PIPES - 0.1 M piperazine-N,N'-bis(2-ethanesulfonic acid)
PLL - Poly-Lysine
PO - Poly-L-Ornithine
PPy-Polypyrrole
PS - Penicillin-Streptomycin
PSCs - Spontaneous Postsynaptic Currents
PSS - Poly(sodium 4-styrenesulphonate)
Pt - Platinum
PT – Polythiophene
PTS - Paratoluene Sulphonate
R_a - Roughness Average
RA- Retinoic Acid
RGTA - Regenerating Agents
RIPA-Radioimmunoprecipitation
ROI - Regions of Interest
ROS - Reactive Oxygen Species
RT- Room Temperature
SAT - Semitool Spray Acis Tool
SBA - Soybean Agglutinin
SCE - Saturated Calomel Electrode
SEM - Scanning Electron Microscopy
Ser – Serine
SMEA - Stretchable Microelectrode Array
STS-ASE - Surface Technology Systems-Advanced Silicon Etching
SWNT - Single-Walled Nanotubes
TBS-T - Tris-Buffered Saline-Tween 20

TBS-Tris – Tris Buffered Saline
TH- Tyrosine Hydroxylase
Thr – Threonine
Tris-HCl - Tris Hydrochloride
TTX –Tetrodotoxin
VM -Ventral Mesencephalic
WE -Working Electrode
XPS - X-Ray Photoelectron Spectroscopy

ABSTRACT

Implanted neuroprosthetics and neuroelectrode systems have been under investigation for a number of decades and have been proven to be safe and efficacious as treatments for several neurological disorders including paralysis, epilepsy and Parkinson's disease as well as for biosensor systems. Neuroelectrode technologies are typically fabricated from metallic conductors such as platinum, iridium and its oxides, materials that while chemically inert and excellent electrical conductors, are often not intrinsically cytocompatible and do not promote integration with neural tissue. The performance of the electrode-tissue interface ultimately rests on the optimisation of the material substrate, to enable chronic functionality. Thus, neural electrodes should present a degree of biomimicry and provide electrical, chemical and physicochemical properties analogous to neural tissues, with an ultimate goal of mitigating electrode deterioration via reactive host cell response and glial scar-induced encapsulation, which drives neural loss and increases signal impedance, compromising the efficiency of implanted neuromodulation systems.

Over several decades of research, studies with conducting polymers as electrode coatings have shown enhanced tissue integration and electrode performance *in situ* through physicochemical and biochemical functionalisation. In this thesis, findings on novel topographical and biological functionalisation strategies of conducting polymers, are provided in the context of neurospecific biomaterials, shedding light on the valuable impact of multi-functionalised strategies for biomedical applications. Further, new functionalisation approaches employing an anodisation process of indium-tin oxide (ITO) are outlined as potential electrode materials.

At first, a bench-top electrochemical process to formulate anodised ITO films with altered roughness, electrochemical properties and bioactivity was explored. The systematic study shows that anodisation of magnetron sputtered ITO with a current density of 0.4 mA cm^{-2} results in a well distributed surface morphology, relatively low impedance, electrochemical stability and supported cell viability and neural

network activity. Using this current density of 0.4 mA cm^{-2} , PEDOT:PTS neural coating(s) were then electrodeposited for topographical functionalisation via microimprint lithography. The topographical functionalised electrodes reduced adhesion of reactive astrocytes *in vitro*, as is evident from morphological changes in cell area, focal adhesion formation and the synthesis of pro-inflammatory cytokines and chemokine factors. This work describes the role of micro-topographically modified neural interfaces in the development of stable microelectrode interfaces and reduced gliosis response. Further in the search for biomimicry of the properties analogous to neural tissues, and with an ultimate goal of mitigating electrode deterioration via reactive host cell response and glial scar formation, PEDOT:PTS neural coating were functionalised with the heparan mimetic called F6, first use as a biological dopant in neural coatings. The bio-functionalised PEDOT:PTS:F6 coating show promise as functional neural electrodes and open up opportunities for the use of other glycanic signatures towards the attenuation of inflammation and gliosis with neural trophic characteristics.

The biomaterial-tissue interface is not a simple description of a boundary but rather a dynamic interface involving both the localised reaction of the surrounding tissue to the materials, and the material adaptations within the physiological environment. Current research has focused on both the foreign body reaction and the long-term performance of biomaterials in a combined effort to drive the functionalisation of next generation implantable devices. As a result, the improved functionalisation of electrode systems is expected to prompt advancements in the design and development of implantable neural prosthetic devices and medical therapies for neurological disorders.

CHAPTER 1

INTRODUCTION

Part of this chapter has been previously published in:

Vallejo-Giraldo, C.; Kelly, A.; Biggs, M. J., Drug Discov. Today 2014, 19 (1), 88-94.

DOI: 10.1016/j.drudis.2013.07.022

1.1 Neuro- Electrically Active Devices

The physiology of electrically responsive tissues has captured popular attention since the development of the physical investigations of electricity by Luigi Galvani [1] in the 18th century and by the electrical excitability of the dog motor cortex using platinum wires by Fritsch & Hitzig [2]. Their findings opened new avenues to explore the electro-stimulation and electro-recording *in situ* [2, 3]. One of these, the creation of platform-interfaces to identify the effects of electrical stimulation/recording in both cellular systems and nervous tissues, was enhanced [4, 5].

Neuro-electrical devices have been under investigation for several decades [6-11] and are proven to be safe and efficacious as gauged by two criteria: 1) a capacity to evoke an optimum physiological response at an anatomical site of therapy and 2) a regulated specific stimulation threshold that avoids damage to the stimulated tissue as well as to the stimulating electrode thereby ensuring its functional integrity is maintained [5].

Implantable, electrically stimulating systems consist of a number of electrodes which transmit signals via electrical and ionic conduction in bodily fluids [12]. (**Figure 1.1**) While microfabricated neuro-electrodes have facilitated electrical connections with living tissue and work reasonably well in acute applications, implanted electrodes for chronic requirements have had limited success [11, 13-17].

Research has shown that over time, four weeks after post-implantation, there is consistent accumulation of hypertrophic astrocytes, fibroblasts and meningeal cells that create an activated macrophage/microglial/foreign body giant cell core found

adjacent to the electrode termed the glial scar [14, 18-21]. This inflammatory response around the neuro-electrode system increases to such an extent that it not only affects the generation of neural processes, causing neural loss, but also affects the stimulation-recording stability of the electrodes at the implantation site [21-24].

To produce functional neuroelectrodes that support intimate contact with the tissue of the nervous system for long-term recording performance and therapy, they should remain functionally stable *in situ* to achieve optimum therapeutic benefit [25].

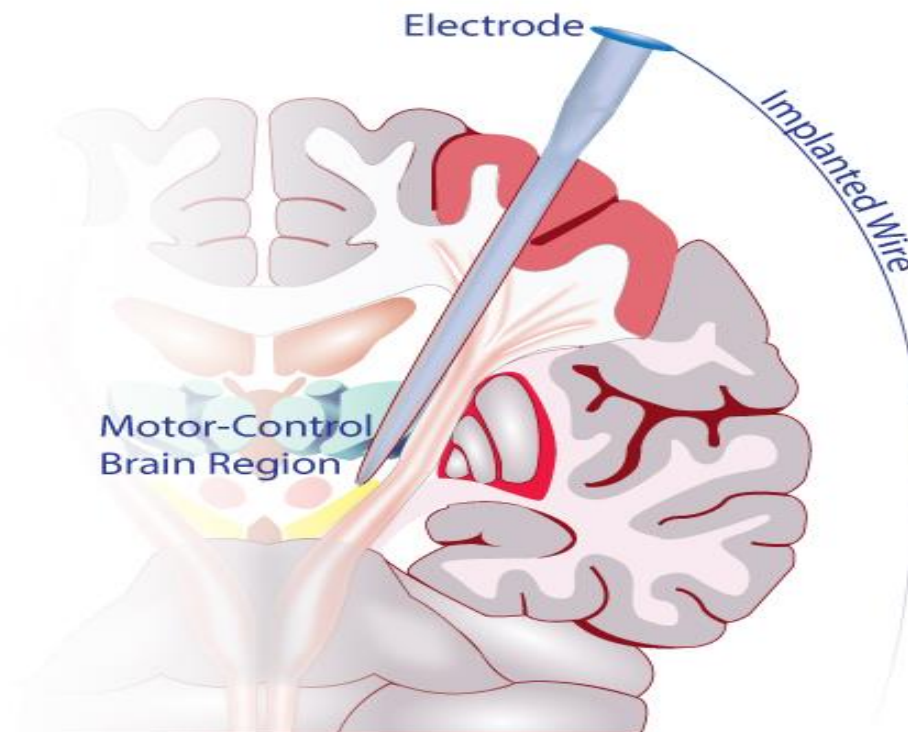


Figure 1.1 Electrically stimulating systems consist of a number of electrodes which transmit signals via electrical and ionic conduction in bodily fluids.

1.2 Glial Scar Formation

Studies indicate that *in situ*, both neuronal recording and charge delivery decrease with time in implanted electrode active systems [18, 26-29]. This loss of function has been linked to an adverse tissue response characterised by glial scar formation and electrode encapsulation, causing the signal strength to decrease and adjacent neurons to move away from the electrode due to the surrounding region of gliosis [18, 21, 30,

31]. It is evident that an understanding of these parameters is required for optimal biomimetic configurations/functional design for improved chronic performance of electrically active neural interfaces. (**Figure 1.2**)

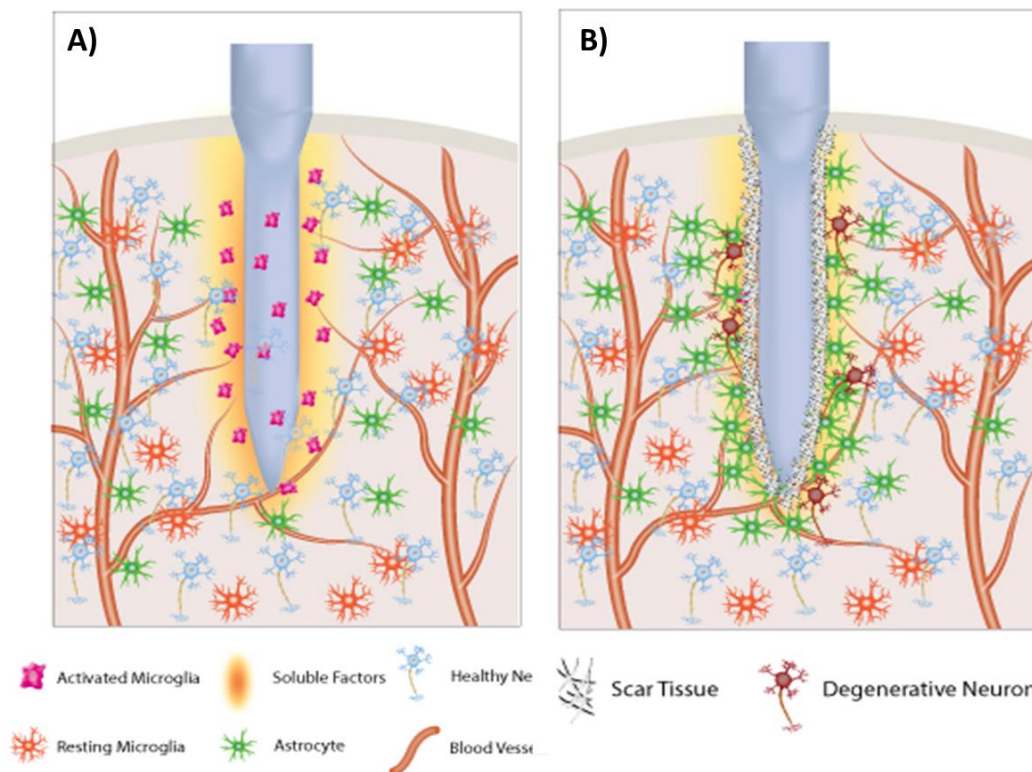


Figure 1.2 *The cellular response and onset of gliosis following neuroelectrode implantation.* A) Acute inflammatory response after probe implantation leads to the recruitment and activation of microglia, and astrocytes in response to locally released soluble signaling factors. B) Chronic inflammation follows and is maintained by populations of reactive astrocytes in response to injury, leading to the deposition of a fibrous network. Image modified from Vallejo-Giraldo et al.[165]

Gliosis or reactive astrogliosis is defined by astroglial cells undergoing reactive molecular and morphological changes that lead to *scar glial formation* responding to central nervous system (CNS) injury and other neurological diseases [14, 19, 32]. The initiation and progression of gliosis is dependent on the bioelectrochemical as well as the physicochemical properties of the implanted material [22, 31, 33]. It has been observed that reducing the amount of protein adsorbed on the polymeric coating

surface, concomitantly with the adsorption of specific cells in the transition stage from inflammatory to the proliferative and repair phase of the wound healing process, results in a better signal from recording electrodes in the long term [34, 35]. This is due to the decrease in reactive astrocyte adhesion, minimising scar formation. The proliferative phase allows the migration of cells to the wound site releasing chemo-attractant factors to trigger the activation of cell membrane receptors, supporting cell growth and protein adsorption. This phase, as part of a timely cascade of events within the healing process, takes place during the first days after implantation and may last for several weeks [30, 35]. However, alterations in the time period of these events may occur depending on extension of the injury or other complications. Biocompatibility efforts have sought to establish enhanced integration of the electrical device with the tissue interface through an attenuated foreign body response [36, 37]. At the forefront of current strategies to reduce reactive gliosis is physicochemical modification through adaptive materials which may be exploited to functionalise electrically active devices for neural applications [38-40].

1.3 Functionalisation of Neuroelectrodes: Electrically Active Devices

Neural tissue engineering has achieved a great success in offering a way to treat central nervous system disorders such as deafness [41, 42], paralysis [43], epilepsy [44] and Parkinson's disease [45-49]. To be integrated with surrounding tissue, bioactive devices, neural electrodes have to provide electrical, chemical and physical properties analogous to the properties typical of the natural extracellular microenvironment and the naturally occurring translating signals, with the ultimate goal of offering the best signal to noise ratio (SNR) and mitigating electrode deterioration via reactive host cell response and glial scar-induced encapsulation [44, 46, 50, 51].

The performance of the electrode-tissue interface ultimately depends on the optimisation at the brain machine interface, to enable chronic functionality. The challenge for materials science is to apply biomaterials strategies and develop innovative biocompatible materials that mimic neural tissue characteristics, cause minimal inflammation and neuronal cell loss, and are functional for a long period of

time [51-53]. To achieve this, functionalisation schemes have been proposed with biomimetic mechanical, topographical and biological properties.

1.3.1 Mechanical Functionalisation

Neuroelectrode technologies are typically fabricated from metallic conductors such as platinum, iridium and its oxides, materials that although chemically inert and excellent electrical conductors, are often not intrinsically cytocompatible and do not promote optimal integration with neural tissue [7, 52, 54, 55].

For a majority of neural electrode applications, a threshold material stiffness must be maintained for the implant to penetrate the neural tissue to the final insertion point [21], a process in itself associated with an acute tissue response, characterised by glial scar formation and electrode encapsulation [18, 22, 52], but further inflammation is often initiated due to a mechanical mismatch at the interface [56] and relative micromotion [57, 58].

Although the brain's shear modulus is reported to be in a range between 200-1500 Pa [59] and soft polymers such as polydimethylsiloxane (PDMS) possess an elastic modulus of between 100 kPa and 3 MPa [60, 61], elastomeric polymers and their variations may offer a viable strategy to reduce the mechanical mismatch at the neuroelectrode interface [52, 62, 63], promoting chronic electrode performance and enhanced integration of the device with the adjacent tissue. McClain and colleagues [64] have produced electrically-functional characterised electrodes composed of PDMS and thin-film gold with a high-level of compliance well suited for neural *in vivo* applications. A low Young's modulus was reported because of the thin, non-continuous morphology of the gold film and the low-modulus PDMS substrate [64]. Furthermore, an elastically stretchable microelectrode array (SMEA) has been reported by Yu et al. [65] with a design that allows stimulation and detection of electrical activity from cultured brain tissue (hippocampal slices), before, during, and after large biaxial deformation. Moreover, relative micromotion can be reduced using flexible materials [66-68], which can accommodate relative movement, maintaining electrodes in close contact with the cortical surface, and improve the charge transfer capability [69]. Likewise, in the pursuit of enhanced biomimicry and long-term

performance at the implantation site, conducting hydrogels (CHs) [50, 70-72] have been explored as three-dimensional polymeric networks to modulate mechanical properties of brain tissue. Blending hydrogels with conductive components such as carbon nanotubes (CNTs) or conducting polymers (CPs) has provided an avenue for maintaining the desired electrical characteristics of a coated electrode while imparting reduced stiffness [50].

1.3.2 Topographical Functionalisation

In order to overcome the challenge associated with cytocompatibility and long-term functionality *in situ*, recent studies have also focused on the creation of modified surface architecture, increasing the surface area and roughness of the electrode surface through topographical means [73-79].

A range of techniques has been explored to create defined microstructures on the electrode surface [80] including laser ablation [81, 82], focused ion beam [83, 84], hot embossing [85, 86], and electron beam lithography [87, 88] resulting in a significant increase in surface area in relation to volume ratio, and enhancing cellular growth [79, 86, 89-92].

Important systematic studies have been performed using topographies to control astrocyte adhesion while promoting high neuron coverage as a strategy to reduce gliosis [77, 93, 94]. For instance, a very recent work by Seker and colleagues [94] demonstrated, through a focal adhesion study, the reduction in adhesion of astrocytes while maintaining neural presence on np-Au surfaces when larger features sizes were used (170 nm and greater). Also, a study performed by Qi et al. [95] showed that the use of micro-patterned topographies, specifically, linear, circular and dot features with widths of 2 μm and 10 μm , and 4 μm in depth could influence the differentiation of adult neural stem cells (ANSCs) into neurons, but may discourage the differentiation into astrocytes *in vitro*. Moreover, Turner et al. [96] presented the use of microscale isotropic topographies such as pillars and wells as modulator cues for astrocyte adhesion. Their findings showed that using micro-wells of 1 μm in depth resulted in less LRM55 astroglial cell adhesion. It can be agreed however, that studies into topographies as modulators of reactive astrocytes presence towards attenuation

of the astroglial scarring response while promoting neural outgrowth require further in-depth research [86].

Considering functionalisation strategies of neural interfaces reported to date, control of topography from the micro [97-100] to the nanoscale range [93, 101-103] has shown promise, not only because it imparts a low impedance profile at the tissue-electrode interface through a large effective surface area [78, 79, 101, 104-106], but also because topography itself has proven to be critical in influencing cell adhesion of specific cell types through altering integrin distribution [107-109], as well as in modulating the activation of intrinsic cellular signaling that leads to more quiescent or reactive cell phenotypes and the onset of a pro-inflammatory response [101, 107-110].

1.3.2.1 Anodisation in Biomedical Applications

Electrochemical activation or passivation via the anodic oxidation (anodisation process) [111, 112], is a technique devised at the beginning of the last century [113] and widely used in biomedical engineering due to its relative simplicity [113-118]. As with the electrochemical polymerisation process, this surface treatment technique facilitates the oxidation of ions at the substrate-electrolyte interface to produce passive thin-film coatings [51, 119] but, because in this system the surface to be treated forms the anode, the process is referred to as the anodising or an anodisation process.

Metal oxide dielectrics for electrical devices [120, 121] and protective and decorative films on metallic surfaces to increase corrosion resistance can be obtained with this simple surface treatment [51, 122]. Furthermore, the anodic oxidation technique can be employed in conjunction with mask strategies for the generation of biologically passive layers or nano features on titanium [113-118] and alumina [123, 124] to improve cell adhesion and implant integration assembly [125] and to produce micro-porous titanium oxide films on implant surfaces for orthopedic applications [126]. In turn, these template strategies have been used in the neural interfaces field for the fabrication of topographies for enhancement of high aspect ratio on microelectrodes [127-130]. However, the impact of anodised metals or semiconductors has not been

investigated thus far in the development of bio-functional neural interfaces applications [131].

1.3.3 Biological Functionalisation

Applicability and biocompatibility of the implantable neural devices are attributed to the biomimicry of the properties analogous to neural tissues [132]. Neural interfaces that promote neural integration, with a minimal inflammation response, are the main persistent challenges for the material science and the fabrication technology fields [50, 63, 132]. This need has given rise to functionalisation strategies with biochemical cues [133-140], to elicit desired biomimetic response at the soft tissue interface [45, 141, 142].

Moreover, local delivery of biological molecules through device stimulation has great promise for maintaining a stable chronic neural interface through on-demand delivery of bioactive molecules, promoting favorable electrode integration and reducing local inflammation [114, 143-146].

Due to ongoing difficulties in stable and persistent biochemical functionalisation of metallic electrodes, alternative materials which can be readily biochemically functionalised have come to the forefront of neuroelectrode design. For example, despite the debate around the cytotoxic properties of carbon nanotubes, studies have demonstrated a reduced cytotoxicity to single-walled nanotubes (SWNT) and multiple-walled carbon nanotube (MWCNTs) networks when biochemically functionalised, and CNTs have been shown to be promising materials as neurospecific biomaterials, with potential 2D and 3D applications. For example, Zhou et al. [147] have described a 3D nanofibrous matrix with the inclusion of heparin in combination with poly-L-lysine (PLL). Here, the biomodification was shown to support neuronal regeneration [147]. Likewise, 3D hydrogels incorporated with anti-inflammatory agents have been shown to reduce *in vitro* glial cell adhesion and cell spreading [148, 149], proving them to be powerful modulators of neural inflammatory cell function and gliosis.

1.4 Conducting Polymers

Conducting polymers (CPs), also called intrinsically conducting polymers (ICPs), are categorised as organic polymers, with a delocalised conjugated backbone structure [105, 150]. The interactions between the carbon atoms comprise single and double bonds where every bond in the backbone contains a localised sigma bond (strong bond), and a pi bond (less strong localised bond). Conductivity is produced through the use of dopant ions which neutralise the unstable backbone of the polymer in its oxidised state by donating or accepting electrons [151-153].

Since the discovery of the first conducting polymer in 1960 [154], the development of conducting polymers has considerably expanded, and they have shown promise not only in a wide range of applications including biomedical uses [50, 105, 139, 155-157], but also in electronics-solar cells [158, 159], chemical sensors [160, 161], and in the microphotonics industry among others [162, 163]. Of particular importance in neuroelectrode design are the organic polyheterocycles (polymers possessing aromatic conjugated backbones) semiconductors such as polythiophene (PT), polyaniline (PANI), the functionalised thiophene, poly(3, 4-ethylenedioxythiophene) (PEDOT), polypyrrole (PPY) and poly(para-phenylene-vinylenes). However, at present, PPy and PEDOT including their derivatives are considered the most promising semiconducting polymers for neural applications and specifically as coatings for neural recording/stimulating systems [46, 105, 164-167, 168]. Their use in tissue engineering has been shown to facilitate tissue integration and to enhance the performance of the electrode *in situ* through surface modifications [40, 100, 156, 169]. (**Figure 1.3**)

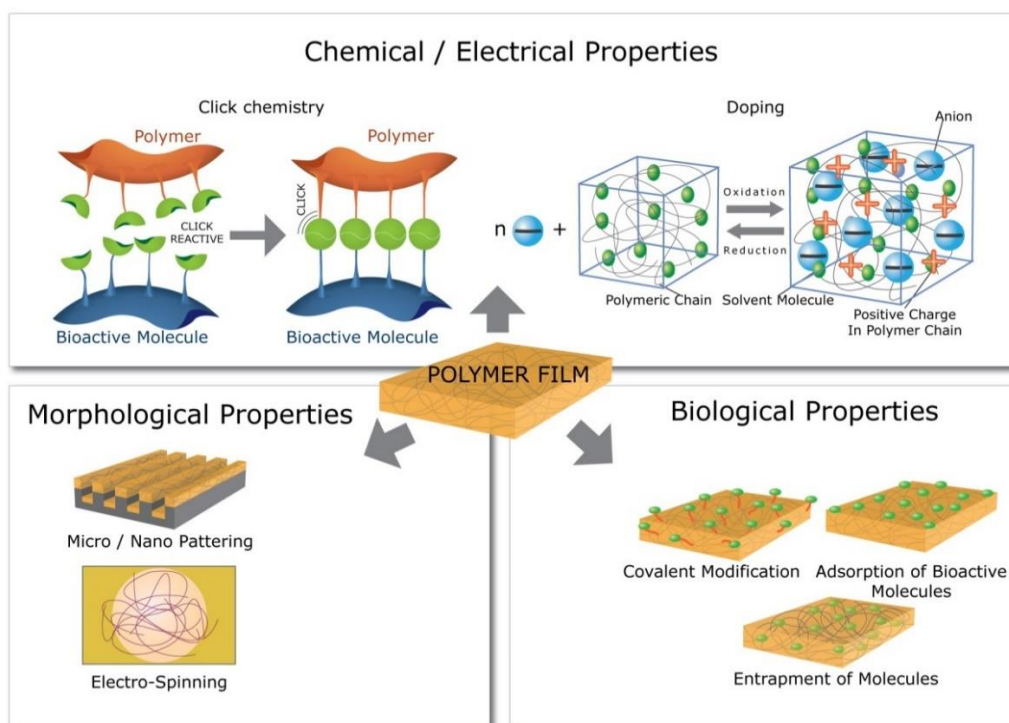


Figure 1.3 Common techniques used in the modification of conducting polymers (CPs). Modifications to alter the chemical/electrical, morphological and biological properties in CPs, have been accomplished using methods such as click chemistry, covalent and non-covalent methods, electrospinning, and micro and nanopatterning, among others. Image taken from [165].

1.4.1 Fabrication of Polymer Electrode Coatings

Although there are different ways to formulate thin-film coatings to an electrode surface [170-173], electrochemical polymerisation [25, 167, 174-177] is emerging as the preferred technique for the fabrication of electrode coatings due to its general simplicity, the fact that it requires only small amounts of monomer, is deposited only on conducting surfaces and because it can be readily modified to control the film's physicoelectrical properties for further functionalisation process [50, 104, 174, 178, 179]. In this context, the electrochemical formation of conducting polymers is a unique process where the experimental conditions i.e galvanostatic or potentiostatic deposition, solvent-electrolyte composition, deposition time, monomer and dopant choice [153, 180], facilitate the mass transfer of oxidised monomers at the substrate-

solution interface to produce conductive coatings. Furthermore, electrochemical and chemical follow-up reactions are possible which can be employed to subsequently further modulate the physicochemical and cytocompatibility properties of the deposited coatings [50, 105].

Systematic studies of semiconducting polymers in neuroelectrode systems have focused on galvanostatic electrodeposition processes for the formation of uniform PEDOT coatings onto the electrode surface [25, 175, 176]. The deposition process of PEDOT involves oxidation of an EDOT monomer, adsorbed onto an electrode surface by generating a constant electric current between the counter and working electrodes. This provides a uniform charge to the electrode surface, and through mass transport principles, leads to diffusion of the oxidised monomers and oligomerisation, resulting in the formation of PEDOT clusters and eventually film growth. By varying the time over which electrodeposition occurs, the thickness and roughness of the electropolymerised coatings can be controlled, correlating with a transition between impedance profiles, roughness, and mechanical properties [25, 50, 105, 176].

Of particular importance in electrochemical deposition are the electrolyte dopants, as they are shown to impact the electrical, chemical and morphological characteristics of electropolymerised coating [181] and dopant selection is critical in electrode coating design [182, 183]. The nature of the dopant influences physical properties of the formed coating stability, surface structure, permeability and wettability [105, 167, 179, 184]. Common counterion dopants extensively investigated for the electropolymerisation process include poly(styrene sulfonate) (PSS), paratoluene sulphonate (PTS), dexamethasone phosphate (Dex-P), and perchlorate (ClO_4) [50, 153, 176, 185]. In particular, conducting coatings produced from PEDOT doped with small sulfonate ions, namely PTS, have been shown to have the highest charge storage capacity, lowest impedance and highest injection limit, with significant biological benefits over both PEDOT/PSS and PEDOT/ ClO_4 giving rise to an overall coating stability [50, 91, 176, 186].

1.5 Poly(3,4-ethylene dioxythiophene) (PEDOT)

As one of the most widely explored of the synthetic semiconducting polymers, PEDOT is a derivative of polythiophene and an attractive alternative to PPy in bioengineering and other applications due to its relatively high degree of conductivity and environmental stability [50, 105, 139, 156, 187]. Owing to its chemical/oxidation and thermal stability, it possesses excellent film formation and transparency in its doped state, and is well-suited for use as an electrode material [45, 188-190]. It provides low interfacial impedance on electrodes and can increase charge delivery capacity through hybrid ionic transfer (mixed conductivity) [7, 91, 175, 181, 182].

Depending on the nature, size and concentration of the dopant used in its electrical polymerisation [176, 184, 191, 192], properties such as physical, mechanical, chemical and biological [105, 177, 193-197] are variable to a great extent, allowing functionalisation of this material so as to be suitable for commercial and biomedical applications.

For example, experimentally, studies have reported good cytocompatibility of PEDOT as a polymeric substrate, either pristine or tailored by chemical [196, 198-200], morphological [100, 201-203] and biochemical [12, 204-206] modifications to elicit a desired functional response. Luo et al. [207] proposed the use of carbon nanotubes as dopants during the polymerisation of PEDOT to impart structural reinforcement while preserving biocompatibility during chronic neural stimulation [207]. Other studies investigating improved implant - tissue interface stability postulate the use of PEDOT combined with RGD (Arg-Gly-Asp)-modified alginate hydrogel loaded with brain-derived neurotrophic factor (BDNF) as coatings for cochlear stimulating devices [208]. These studies indicated that PEDOT can be employed to reduce electrode impedance, improved charge delivery and maintain spiral ganglion neuron survival both *in vitro* and *in vivo* [208]. The feasibility of using *in situ* polymerisation of PEDOT as a useful alternative to investigate reduction in glial scar formation in neural prosthesis and long-term electrode functionality was reported by Ouyang et al. [209]. They showed successful *in vivo* polymerisation of PEDOT in the rat cerebral cortex with lower impedance and improved recording

quality on implanted neuroelectrodes. Furthermore, PEDOT was also successfully integrated with the brain tissue, extending a junction of more than 1 mm to the electrode, promoting integration at the electrode/tissue interface with healthy neurons and minimising the gliosis region [209].

To date, PEDOT has been studied extensively [50, 139, 157, 210-220] and verified experimentally as an electrode coating material for *in vitro* applications. However PEDOT is susceptible to delamination from the electrode substrate *in situ* following long term device implantation *in vivo* [39, 50]. To address this issue, studies are conducted on functionalisation approaches through morphological and biological cues [13, 105, 197, 203, 216, 221, 222].

1.5.1 Morphological and Topographical Functionalisation of PEDOT

Morphological functionalisation of PEDOT-based materials has been performed as a technique for the preparation of the conductive biomaterials with neural applications [50, 105, 167]. Of particular interest is the electrochemical polymerisation (electrodeposition) process where a number of important variables controlling film-coating growth conditions are taken into account. Deposition time, solvent system, electrolyte, and deposition charge have been shown to impact directly film morphology (thickness and topography), which directly modulates cellular adhesion and interaction [50, 156, 167]. Thus, in this regard, the employed dopant in the electrodeposition process is critical in the resulting film topographical properties [105, 167]. For instance, the inherent smooth and rough surface conformation obtained using PTS and PSS as dopants respectively has been shown to impart differential cellular response due to the differences in the microstructure of polymer films [13, 50, 176]. Furthermore, recent studies have identified the use of chemical surfactants as templates to precisely control PEDOT-based polymer structures [223-225]. However, this technique required washes to carefully remove residual surfactants from the films, which therefore reduces the possibility of the biocompatibility of the polymeric coatings or further functionalisation.

An innovative approach to templated electropolymerisation was described by Richardson-Burns et al. [226] where PEDOT was deposited around living neural cells

cultured on an electrode site. Cells were subsequently removed from the deposited polymer to produce a surface with cell shaped cavities. Further, a recent study by Wan et al. [227] reported on the fabrication of PEDOT-based three dimensional (3D) macroporous scaffolds using an ice-templating method. The resulted scaffolds possessed a tunable pore size and morphology, and were electrochemically active, enabling further biochemical functionalisation.

Current research has focused on a multi-functionalisation approaches to PEDOT-based coatings facilitating structural and topographical modifications, achieved using micro and nanopatterning templates [222, 227, 228], nanofibers [229, 230] and laser micromachining [82]. Although there are important systematic studies presenting morphological-topographical functionalisation strategies for PEDOT-based coatings, critical further study is required for the implementation of other technologies that allow controlled topographical modification on cytocompatibility and astrogliosis towards the generation of neural interfaces with chronic functionality.

1.5.2 Biological Functionalisation of PEDOT

The entrapment or surface functionalisation of PEDOT with biological elements [20, 206, 231-233], and anti-inflammatory drugs [234-237], with the aim of reducing inflammation while promoting neural tissue integration with maintained low impedance profile at the material coating interface, has moved the field towards the use of combinational strategies to reduce gliosis [135, 145, 146, 208, 236, 238-242].

The incorporation and delivery of therapeutic agents through carriers such as vesicles, micelles, nanotubes, nanospheres and nanocapsules have been widely employed as functional modifiers to PEDOT-based approaches with varying success [237, 243-245]. Owing to their mechanical/structural reinforcement, electrical, and thermal properties, the use of carbon-based nanotubes or graphene as an electrically conducting surface or in conjugation with PEDOT-based polymers has gained considerable interest, with promising results *in vivo* [216, 246-250]. Together, these properties elicit stability and enhanced electrode performance under continuous stimulation for chronic stimulating systems.

However, the most successful techniques implemented for the immobilisation of biomolecules with PEDOT-based chemistries are entrapment and adsorption methods, as well as covalent attachment and doping techniques, which are used together to support polymerisation and to enable the insertion of functional groups into the backbone of the PEDOT polymer [50, 100, 105, 156, 200].

In vitro and *in vivo* studies compiled in an excellent review [241], show the release kinetics and the elution profile of peptides, neural factors and drugs from PEDOT-based polymers and in general conducting and semiconducting polymers used as coatings for stimulating interfaces. Nevertheless, despite the vast research on the incorporation of biomolecules in PEDOT-based polymers for neural applications [12, 25, 135, 145, 146, 208, 236, 240-242, 249-252], concepts such as optimal concentrations for a physiological response, use of immobilised concentration gradients versus homogeneous concentrations, molecule lifespan bioactivity, stability and loading efficiency continue to be the subject of experimental investigation [253-255]. Further, it is important to note that chemical elution is dependent on time, surface area, loading concentration and depletion by electrical stimulation, and so direct comparison among studies might not always be appropriate.

Currently, in the pursuit of enhanced biomimicry and long-term performance of neuroelectrodes following implantation, hydrogels have also been explored in conjunction with semiconducting polymers as three-dimensional and mechanically soft polymeric networks to serve as drug delivery vehicles with tunable degradability [72, 256]. PEDOT-based/hydrogel composite materials have been studied as biphasic scaffolds to encourage cellular infiltration/nutrient diffusion and to deliver encapsulated bioactive molecules, cells and drugs [183, 205, 208, 214, 252, 257, 258]. Conducting hydrogel systems exhibit multiple advantageous properties over traditional bulk conducting polymer formulations including: 1) a high water content that facilitates the loading of water soluble molecules, 2) tailored degradability which allows controlled regeneration, 3) a reduction in protein adsorption at the biomaterial interface providing a low fouling substrate, 4) increased diffusion of bioactive molecules, 5) biomimetic mechanical properties, as well as a relatively high surface

area. The reader is referred to an excellent topical review on conducting hydrogels for medical electrode applications [214].

The general use of PEDOT and their derivatives in a summary of the current applications and biological modifications used to achieve optimal biointegration at the biomaterial interface, is presented in *Table 1.1*.

Table 1.1 General summary of PEDOT and their derivatives and biological modifications for neural applications.

Derivative	Application	Modification	Reference
PEDOT-COOH	Cancer Therapeutic Neural Stimulation Drug delivery	Nanodots functionalised with captured antibodies, peptide coupling.	[256, 259-265]
PEDOT-TsO, PEDOT-OH:TsO	Biosensors	Affinity to antibiotics, cell-based and viruses.	[266-271]
PEDOT-OH, PEDOT-N ₃	Medical electrodes Neural Tissue Drug delivery	Peptides	[272-275]
PEDOT:PSS-co- MA	Medical electrodes, Neural tissue Neural Stimulation Drug delivery	Biomimetics, Growth factors and anti-inflammatory drugs.	[206, 244, 251, 276]
PEDOT-PSS	Neural Tissue Neural Stimulation Drug delivery	Biomimetics, Growth factors and anti-inflammatory drugs	[137, 208, 236, 240, 250, 277, 278]
PEDOT-PTS	Neural Tissue Neural Stimulation	Biomimetics, Growth factors and anti-inflammatory drugs.	[162 194, 245, 279-281]

1.5.2.1 Extracellular Matrix (ECM) Protein, Peptides

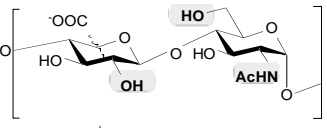
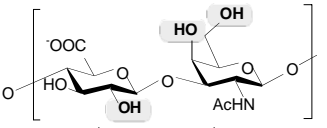
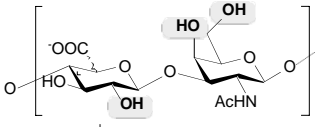
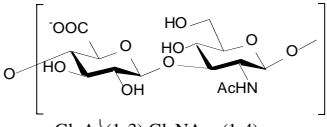
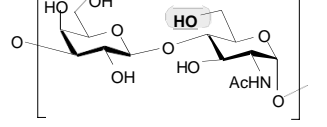
The ECM is a mixture of proteins and polysaccharides that provides biochemical and biophysical cues to govern cell behavior and consequent biological cascades [143, 282]. PEDOT scaffolds represent a powerful platform for ECM proteins such as collagen, fibronectin, and laminin to enhance cell attachment and neurite extension [227, 283, 284]. For instance, PEDOT/collagen system studied by Xiao and

colleagues showed preferentially growth of PC12 cells than that observed in the PEDOT/LiClO₄ system. Their results showed that collagen is highly bioactive for cell adhesion, supporting a network structure with nano-silks surface morphology [283]. An interesting recent PEDOT-based brushes approach detailed in [285] was used to tailor the level of cell adhesion to the interface with pre-adsorption of fibronectin on the system. Modulation of cell adhesion with brush composition was observed for very short brushes, while the longest brushes had impaired cell adhesion. Moreover, peptide sequences such as laminin derived peptide sequences have been extensively studied as PEDOT dopants [50, 142, 286]. Important work done by Cui et al. [200, 278] and later by Green et al. [184, 279], has shown the efficacy of doped peptide sequences, such as DCDPGYIGSR from the $\beta(1)$ and DEDEDYFQRYLI from $\alpha(1)$ of laminin chains [286, 287] respectively, with PEDOT-based polymers. Their results indicated a superior neural cell adhesion relative to pristine PEDOT. In contrast, DEDEDYFQRYL (YFQRYLI) peptide, has been shown by Green and colleagues [184, 279] as an important point of comparison between the effects observed with the former DCDPGYIGSR (YIGSR) sequence, that YFQRYLI active sequence supported a higher proportion of neurite outgrowth, but not cell attachment. This is, significant as it indicates that regardless of the peptide sequence, doping with ECM derived sequences can be employed to increase both cell attachment and neurite outgrowth, indicating the efficacy of ECM derivatives as key biological elements for neuroelectrode functionalisation [142, 251, 288, 289].

1.5.2.2 Glycosaminoglycan's (GAGs)

Complex glycanic ECM components like anionic GAGs are known to play essential roles in human physiology and pathology. GAGs are a major class of polysaccharides initially known as mucopolysaccharides [290-292] and are the glycan moiety of proteoglycans which are one of the main constituents of the ECM. Proteoglycans and GAGs have elicited scientific interest due to the ample amount of biological information that they enclose [293]. This information is known to be carried on the GAGs chains, making these polysaccharides the major responsible factor for most biological activities conferred to proteoglycans [294].

GAGs can be characterised by possessing a vast variety of sulphated patterns whose expression appear to be finely controlled during their biosynthesis in cells [295, 296]. From their structural perspectives, four GAG sub-families have been identified based on the GAG saccharidic composition, these include heparan sulphates (HS) and heparin, chondroitin sulphates (CS), keratan sulphates (KS) and hyaluronic acid (HA). These linear molecules are formed of repeating disaccharidic units linked by glycosidic bounds. Each disaccharide consists of one hexosamine moiety, either N-acetylglucosamine (GlcNAc) or N-acetylgalactosamine (GalNAc), and an uronic acid, either glucuronic (GlcA) or iduronic acid (IdoA) except for KS, which consists of a galactose (Gal) in place of the uronic acid. [297] (**Figure 1.4**)

GAG	Uronic acid/ Galactose	Hexosamine	Disaccharide *
Heparin (HP) Heparan Sulfate (HS)	D-Glucuronic acid L-iduronic acid	D-Glucosamine	 GlcA β (1-4) GlcNAc α (1-4) IdoA α (1-4) GlcNAc α (1-4)
Chondroitin sulfate (CS)	D-Glucuronic acid	D-Galactosamine	 GlcA β (1-3) GalNAc β (1-4)
Dermatan Sulfate (DS)	D-Glucuronic acid L-iduronic acid	D-Galactosamine	 GlcA β (1-3) GalNAc α (1-4) IdoA α (1-3) GalNAc α (1-4)
Hyaluronic Acid (HA)	D-Glucuronic acid	D-Glucosamine	 GlcA β (1-3) GlcNAc α (1-4)
Keratan Sulfate (KS)	D-Galactose	D-Glucosamine	 Gal β (1-4) GlcNAc α (1-3)

*In shaded are represented the sugar positions susceptible of being sulfated.

Figure 1.4 Structural characteristics of glycosaminoglycan's. Image taken from Papy-Garcia et al. [297].

Heparin is a HS structural analogue that can be placed in the HS sub-family of GAGs, although it is only produced by mast cells and characterised for being extremely sulphated compared to any other HS [298]. CS is another important family of GAGs showing some particularities. The CS family includes CS-A, -B, -C, -D and -E. CS - B is also known as dermatan sulphate (DS). Heparin, HS and DS together with CS-E, are in following way the most sulphated GAG family members compared to KS. In the ECM and as carbohydrate moieties on proteoglycans, these classes of GAGs exist as O-linked to Ser residues in the contrary to KS which is N-linked to Asn and O-linked to Ser or Thr residues in the core protein. An exception is HA which is the only non sulphated GAG characterised by not been attached to any core protein [293, 299]. Once attached to the core protein, the existing proteoglycan with GAGs like HS, CS and KS are secreted in granules to the ECM to exert multiple biological functions [300] **Figure 1.5**

The majority of proteoglycans located at the cell surfaces or in the ECM are HS proteoglycans (HSPG), although in some cases the presence of small proportions of CS have been described in their chains. HSPG families are syndecans, glypicans and perlecans. Syndecans are transmembrane HSPG, glypicans are inserted into membranes by a lipid anchor (GPI), and perlecans are not linked to cell membranes but reside in the ECM [300]. Most of the biological actions conferred to these proteoglycans are now known to be assured by their HS or CS chains.

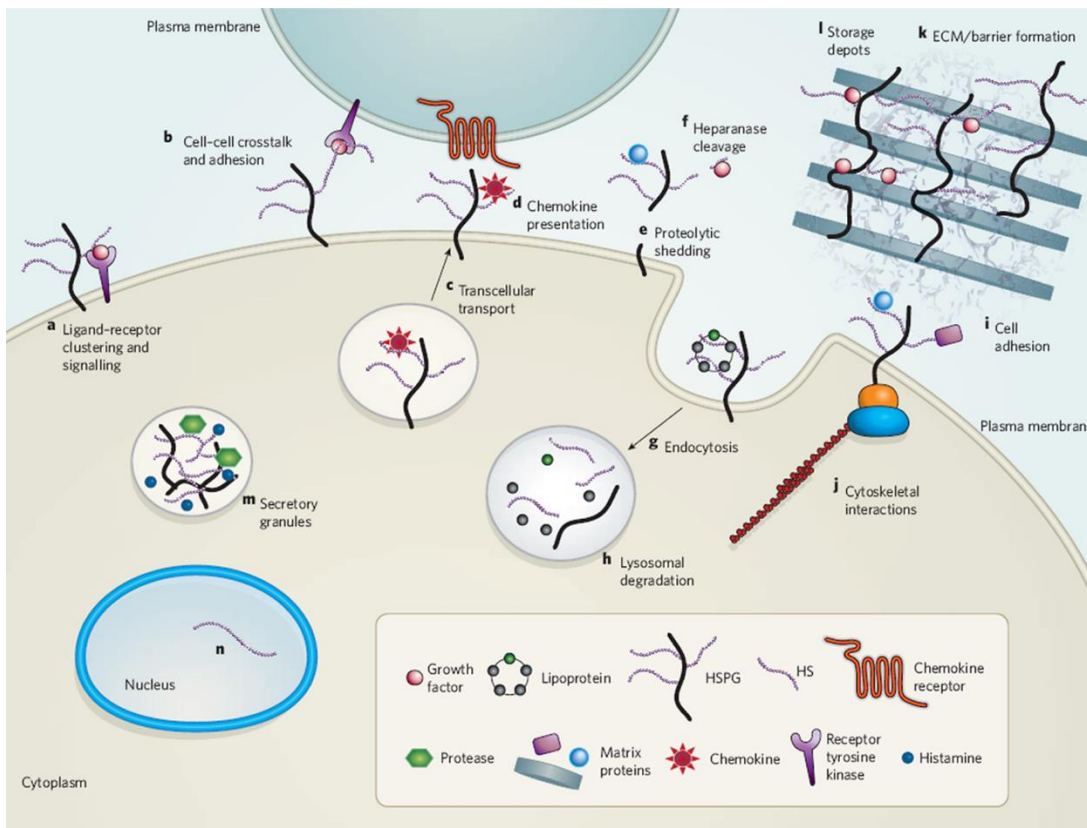


Figure 1.5 Heparan sulphate proteoglycans have many roles in cell physiology. HSPGs function as co-receptors for growth factors and their receptor tyrosine kinases, which are present either on the same cell (a) or on adjacent cells (b). They transport chemokines across cells (c) and present them at the cell surface (d). Proteolytic processing leads to the shedding of syndecans and glypicans from the cell surface (e), and heparanase cleave the HS chains (f), liberating bound ligands (such as growth factors). Cell surface HSPGs are actively taken up by endocytosis (g) and can recycle back to the surface or be degraded in lysosomes (h). HSPGs also facilitate cell adhesion to the extracellular matrix (i) and form bridges to the cytoskeleton (j). Secreted HSPGs are involved in the formation of organised extracellular matrices that form physiological barriers (k) and sequester growth factors and morphogens for later release (l). Serglycin carrying highly sulphated heparin chains is packaged into secretory granules (m). Finally, some experiments suggest that HS chains exist in the nucleus (n), although their function in this location is unknown. Image taken from Bishop et al [300].

- Anionic GAG in ECM

The main structural difference between the different GAG sub-families concerns the identity of their constitutive disaccharides. Although each GAG is formed of only one or two particular disaccharide units, differential sulphation of HS and CS sugar moieties can generate a great number of differently sulphated blocks within a single GAG chain making these molecules highly complex and thus highly information dense [301]. The high sulphate content in GAGs is known to favour its interaction with several heparin binding proteins resulting often in protein activity potentiation. GAG chains can contain multiple protein-specific binding sites in a single chain [302]. This is in part due to the capacity of their sulphated sequence to bind and regulate the activity of effector proteins as growth factors and cytokines; GAGs potentialise their biological activities and protect them from proteolytic degradation [303]. It is well known that HS possess complex structures that may vary in a spatiotemporal manner [298] and that in function of their sulphation patterns, HS may interact, as epitopes in proteins, with particular host matrix proteins. These HS-protein interactions are known to play key roles in the control of a number of biological processes such as cell differentiation, proliferation, migration and survival [304].

The therapeutic potential of GAGs as functionalisation approaches in neural applications has been extensively investigated [12, 50, 105, 233, 250, 289, 305-308].

The use of GAGs as electroactive coatings for neural applications is favorable for two reasons: Firstly, GAGs as naturally occurring molecules in neural tissues, impart biological mimicry and have been shown to provide stealth properties with respect to the foreign body response [297]. Secondly, GAGs are charged biomolecules that may act as counterions in the electrochemical polymerisation of PEDOT [250]. Experimentally, Asplund et al. showed in their work that the incorporation of heparin as a counter ion for EDOT deposition in water soluble conditions enhanced the biocompatibility and electrochemical stability of these electrodes when compared to PEDOT:PSS films [12, 250]. Moreover, an interesting study by Teixeira et al. [309] showed the efficacy of PEDOT:heparin/growth factor scaffolds as potential

electroactive materials to modulate the bioavailability of growth factors through electrochemical oxidation of PEDOT. Critically, in this study it was identified that GAG-functionalised biomaterials can be employed to promote stem cell differentiation *in vitro* [305]. Furthermore, a recent study by Mantione and colleagues reported on the use of HA, heparin, and CS as dopants within a PEDOT matrix to support neuroregeneration [233].

New avenues in GAG functionalisation through synthetic glycochemistry and glycomimetics have recently emerged which have been explored to present structural mimicry of specific carbohydrate moieties, addressing the drawbacks of commercially available carbohydrate [289, 310-312].

Papy-Garcia et al. functionalised different libraries of synthetic GAGs through a series of chemical modifications to produce so called GAG mimetics including the RGTA (regenerating agents) and heparan mimetics (HMs) that exhibit increase stability and resistance to glycanase activity [313, 314]. The growing body of experimental findings *in vitro* and *in vivo* has placed these HMs as current therapeutic strategies within the broad spectrum of tissue engineering applications [315-326].

However, GAG-mimetic materials as functional coatings of neural electrodes remain under experimental investigation.

1.6 Hypothesis and Objectives

The biomaterial-tissue interface is not a simple description of aboundary, but rather a dynamic interface involving both the localised reaction of the surrounding tissue to the materials, and the material adaptations within the physiological environment. Current research has focused on both the foreign body reaction and the long-term performance of biomaterials in a combined effort to drive the functionalisation of next generation implantable devices. As a result, the improved functionalisation of electrode systems is expected to prompt advancements in the design and development of implantable neural prosthetic devices and medical therapies for neurological disorders.

The availability of a great variety of synthetic materials has invigorated the conducting polymers field and their functionalisation, and in particular the

stimulating neural devices area. Multifunctional innovative manufacturing and polymer synthesis methods have driven the development of physicochemical modification, facilitating the delivery of bioactive molecules and drugs that can be immobilised on the substrates, further diversifying the potential of neuroelectrode biomedical applications.

More recently, increased attention has been directed to hierarchically structured or composite materials that have been developed from the integration of conducting polymers with organic and naturally occurring hydrogels and carbon based materials or through geometric/topographical modification. These hybrid materials contribute to significant progress in the development of integral engineered designs for electrode interfaces. It is interesting to consider that topographical alteration or modification to the 3D structure of conducting polymers and its role in influencing cellular proliferation and migration has yet to be resolved.

Despite the great number of studies conducted on the biofunctionalisation of conductive polymers and their derivatives, substantial progress has yet to be made to confirm the efficacy of improved functionalisation of bioelectrodes *in vivo*. This is crucial if functionalised conducting polymers are to have a significant impact on a wide spectrum of bioapplications and therapies. Certainly, this is an exciting area of research.

Conducting polymers and the process of biofunctionalisation is still an emerging technology and many questions with regard to specific strategies to provide enhanced functionality remain to be explored. Hence, the ultimate aim of this thesis was to develop novel physical, chemical and biochemical approaches electrodes for neural interfaces applications, aiming for stimulation systems such as deep brain stimulation, to enhance neuron/electrode interfacing *in vitro*, opening the way for functionalisation strategies for subsequent *ex-vivo* and *in vivo* evaluation.

To achieve this general objective, the work of this thesis was attributed to three phases:

- The first phase focuses on develop highly conducting metal oxide surfaces with enhanced electrochemical and cytocompatibility through an anodisation process of thin-film ITO.
- The second phase of this work was to functionalise electrochemically deposited PEDOT:PTS coated electrodes using the topographical approach.
- The third and final phase was to investigate PEDOT:PTS functionalisation with a heparan-mimetic (HM) F6 as a biological dopant.

The main objectives and hypothesis of each phase are described below.

1.6.1 Objective One (Chapter two)

To formulate anodised thin-film ITO neuroelectrode interfaces through a facile electrochemical process employing the application of current densities ranging from 0.4 mA cm^{-2} to 43 mA cm^{-2} and to evaluate the physical, electrochemical and cytocompatibility properties of anodised ITO *in vitro*.

Hypothesis:

ITO anodisation can be employed as a functionalisation approach to increase surface roughness and oxygen content for the generation of cytocompatible and functional thin-film electrode interfaces for neural applications.

1.6.2 Objective Two (Chapter Three)

To topographically functionalise PEDOT:PTS coated electrodes via a low-temperature microimprint-lithography process for the development of cytocompatible anti-adhesive neural interfaces.

Hypothesis:

Topographical functionalisation of PEDOT:PTS electrode coatings with arrays of micropits will increase the electrode active surface area and will enhance electrode integration by minimising astrocyte cell adhesion and the onset of subsequent

astrocyte reactivity. This will provide long-term stability and enhanced charge transfer for neural simulation.

1.6.3 Objective Three (Chapter Four)

To biologically functionalise PEDOT:PTS coated electrodes using an electrodeposition process for the incorporation of the heparan sulphate mimetic F6 for the development of cytocompatible and stable neural interfaces.

Hypothesis:

The use of a sulphated heparan mimetic polyanion termed F6 can be employed as a potential biological dopant for neural interfaces leading to enhanced electrode integration, and a minimised glial response through an indirect neurotropic effect of F6 mediated by growth factor binding.

1.7 References

1. Piccolino, M., Trends in Neurosciences 1997, 20 (10), 443-448.
2. Gross, C. G., J Hist Neurosci 2007, 16 (3), 320-31. DOI 10.1080/09647040600630160.
3. Carlson, C.; Devinsky, O., Epilepsy Behav 2009, 15 (2), 131-2. DOI 10.1016/j.yebeh.2009.03.002.
4. Agnew, W. F.; Yuen, T. G.; Pudenz, R. H.; Bullara, L. A., Surgical neurology 1975, 4 (5), 438-48.
5. Hambrecht, F. T., in W.F. Agnew, D.B. McCreery (Eds.), Neural Prostheses, Prentice Hall International, Englewood Cliffs (1990) 1990, 2-23.
6. Gage, G. J.; Stoetzner, C. R.; Richner, T.; Brodnick, S. K.; Williams, J. C.; Kipke, D. R., JoVE (Journal of Visualized Experiments) 2012, (60), e3565-e3565.
7. Cogan, S. F., Annu. Rev. Biomed. Eng. 2008, 10, 275-309.
8. Schendel, A. A.; Eliceiri, K. W.; Williams, J. C., Current Opinion in Solid State and Materials Science 2014, 18 (6), 301-307.

9. Lu, Y.; Lyu, H.; Richardson, A. G.; Lucas, T. H.; Kuzum, D., *Sci Rep-Uk* 2016, 6.
10. Meyer, R. D.; Cogan, S. F.; Nguyen, T. H.; Rauh, R. D., *IEEE Trans. Neural Syst. Rehabil. Eng.* 2001, 9 (1), 2-11.
11. Du, Z. J.; Kolarcik, C. L.; Kozai, T. D.; Luebben, S. D.; Sapp, S. A.; Zheng, X. S.; Nabity, J. A.; Cui, X. T., *Acta Biomater* 2017, 53, 46-58.
12. Asplund, M.; Thaning, E.; Lundberg, J.; Sandberg-Nordqvist, A. C.; Kostyszyn, B.; Inganas, O.; von Holst, H., *Biomed Mater* 2009, 4 (4), 045009. DOI 10.1088/1748-6041/4/4/045009.
13. Kim, D. H.; Richardson-Burns, S.; Povlich, L.; Abidian, M. R.; Spanninga, S.; Hendricks, J. L.; Martin, D. C., *Soft, Fuzzy, and Bioactive Conducting Polymers for Improving the Chronic Performance of Neural Prosthetic Devices*. In *Indwelling Neural Implants: Strategies for Contending with the In Vivo Environment*, Reichert, W. M., Ed. Boca Raton (FL), 2008.
14. Polikov, V. S.; Tresco, P. A.; Reichert, W. M., *J Neurosci Methods* 2005, 148 (1), 1-18. DOI <https://doi.org/10.1016/j.jneumeth.2005.08.015>.
15. Kook, G.; Lee, S. W.; Lee, H. C.; Cho, I.-J.; Lee, H. J., *Micromachines* 2016, 7 (10), 179.
16. Kozai, T. D.; Eles, J. R.; Vazquez, A. L.; Cui, X. T., *J Neurosci Methods* 2016, 258, 46-55.
17. Kuwabara, M.; Tashiro, H.; Terasawa, Y.; Osawa, K.; Tokuda, T.; Ohta, J.; Fujikado, T., *Advanced Biomedical Engineering* 2017, 6, 59-67.
18. Polikov, V. S.; Block, M. L.; Fellous, J. M.; Hong, J. S.; Reichert, W. M., *Biomaterials* 2006, 27 (31), 5368-76. DOI 10.1016/j.biomaterials.2006.06.018.
19. Sofroniew, M. V., *Trends Neurosci.* 2009, 32 (12), 638-647. DOI <https://doi.org/10.1016/j.tins.2009.08.002>.
20. Eles, J. R.; Vazquez, A. L.; Snyder, N. R.; Lagenaur, C.; Murphy, M. C.; Kozai, T. D.; Cui, X. T., *Biomaterials* 2017, 113, 279-292.

21. Spencer, K. C.; Sy, J. C.; Falcón-Banchs, R.; Cima, M. J., *Lab Chip* 2017, 17 (5), 795-804.
22. Griffith, R. W.; Humphrey, D. R., *Neurosci Lett* 2006, 406 (1), 81-86.
23. Gutowski, S. M.; Templeman, K. L.; South, A. B.; Gaulding, J. C.; Shoemaker, J. T.; LaPlaca, M. C.; Bellamkonda, R. V.; Lyon, L. A.; García, A. J., *Journal of Biomedical Materials Research Part A* 2014, 102 (5), 1486-1499.
24. McCreery, D.; Cogan, S.; Kane, S.; Pikov, V., *J. Neural Eng.* 2016, 13 (3), 036012.
25. Green, R. A.; Lovell, N. H.; Wallace, G. G.; Poole-Warren, L. A., *Biomaterials* 2008, 29 (24-25), 3393-9. DOI 10.1016/j.biomaterials.2008.04.047.
26. McConnell, G. C.; Rees, H. D.; Levey, A. I.; Gutekunst, C.-A.; Gross, R. E.; Bellamkonda, R. V., *J. Neural Eng.* 2009, 6 (5), 056003.
27. Spencer, K. C.; Sy, J. C.; Cima, M. J., Systems and methods for reducing scar formation about a neural implant. Google Patents: 2016.
28. Yin, Y.; Xia, K.; Li, Y.; Wu, T.-Z.; Tang, M.-H. In Composite process to fabricate low impedance and long electrical stability platinum gray microelectrodes using iridium oxide, *Nano/Micro Engineered and Molecular Systems (NEMS)*, 2016 IEEE 11th Annual International Conference on, IEEE: 2016; pp 442-445.
29. Seymour, J.; Gulari, M. N.; Lahann, J.; Kipke, D., Method for manufacturing an implantable electronic device. Google Patents: 2016.
30. Pekny, M.; Pekna, M., *Biochimica et Biophysica Acta (BBA)-Molecular Basis of Disease* 2016, 1862 (3), 483-491.
31. Gilmour, A. D.; Woolley, A. J.; Poole-Warren, L. A.; Thomson, C. E.; Green, R. A., *Biomaterials* 2016, 91, 23-43.
32. Pekny, M.; Pekna, M., *Physiol. Rev.* 2014, 94 (4), 1077-98. DOI 10.1152/physrev.00041.2013.
33. Roitbak, T.; Syková, E., *Glia* 1999, 28 (1), 40-48.

34. Dee, K. C.; Puleo, D. A.; Bizios, R., Protein-Surface Interactions. In *An Introduction To Tissue-Biomaterial Interactions*, John Wiley & Sons, Inc.: 2003; pp 37-52.
35. Dee, K. C.; Puleo, D. A.; Bizios, R., Wound Healing. In *An Introduction To Tissue-Biomaterial Interactions*, John Wiley & Sons, Inc.: 2003; pp 127-147.
36. He, W.; Bellamkonda, R. V., A Molecular Perspective on Understanding and Modulating the Performance of Chronic Central Nervous System (CNS) Recording Electrodes. In *Indwelling Neural Implants: Strategies for Contending with the In Vivo Environment*, Reichert, W. M., Ed. Boca Raton (FL), 2008.
37. Liu, B.; Kim, E.; Meggo, A.; Gandhi, S.; Luo, H.; Kallakuri, S.; Xu, Y.; Zhang, J., *J. Neural Eng.* 2017, 14 (2), 026008.
38. Di, L.; Wang, L. P.; Lu, Y. N.; He, L.; Lin, Z. X.; Wu, K. J.; Ren, Q. S.; Wang, J. Y., *Acta Biomater* 2011, 7 (10), 3738-45. DOI 10.1016/j.actbio.2011.06.009.
39. Venkatraman, S.; Hendricks, J.; King, Z. A.; Sereno, A. J.; Richardson-Burns, S.; Martin, D.; Carmena, J. M., *IEEE transactions on neural systems and rehabilitation engineering : a publication of the IEEE Engineering in Medicine and Biology Society* 2011, 19 (3), 307-16. DOI 10.1109/TNSRE.2011.2109399.
40. Chen, N.; Tian, L.; Patil, A. C.; Peng, S.; Yang, I. H.; Thakor, N. V.; Ramakrishna, S., *Nano Today* 2017.
41. Lenarz, T.; Lim, H. H.; Reuter, G.; Patrick, J. F.; Lenarz, M., *Otol. Neurotol.* 2006, 27 (6), 838-843.
42. Engineer, N. D.; Riley, J. R.; Seale, J. D.; Vrana, W. A.; Shetake, J. A.; Sudanagunta, S. P.; Borland, M. S.; Kilgard, M. P., *Nature* 2011, 470 (7332), 101-104.
43. Lahr, J.; Schwartz, C.; Heimbach, B.; Aertsen, A.; Rickert, J.; Ball, T., *J. Neural Eng.* 2015, 12 (4), 043001.

44. Vanleer, A. C.; Blanco, J. A.; Wagenaar, J. B.; Viventi, J.; Contreras, D.; Litt, B., *J. Neural Eng.* 2016, 13 (2), 026015.
45. Fattahi, P.; Yang, G.; Kim, G.; Abidian, M. R., *Adv Mater* 2014, 26 (12), 1846-1885.
45. Durand, D. M.; Ghovanloo, M.; Krames, E., *J. Neural Eng.* 2014, 11 (2), 020201.
46. Zhou, Z.; Yu, P.; Geller, H. M.; Ober, C. K., *Biomacromolecules* 2013, 14 (2), 529-537.
47. Dorval, A. D.; Russo, G. S.; Hashimoto, T.; Xu, W.; Grill, W. M.; Vitek, J. L., *Journal of neurophysiology* 2008, 100 (5), 2807-2818.
48. Lempka, S. F.; Johnson, M. D.; Miocinovic, S.; Vitek, J. L.; McIntyre, C. C., *Clinical Neurophysiology* 2010, 121(12), 2128-2133.
49. Paek, S. B.; Kale, R. P.; Wininger, K. M.; Lujan, J. L., *Emerging Trends in Neuro Engineering and Neural Computation*, Springer (2017), 81-97.
50. Aregueta-Robles, U. A.; Woolley, A. J.; Poole-Warren, L. A.; Lovell, N. H.; Green, R. A., *Front. Neuroengineering* 2014, 7 (15). DOI 10.3389/fneng.2014.00015.
51. Vallejo-Giraldo, C.; Pampaloni, N. P.; Pallipurath, A. R.; Mokarian-Tabari, P.; O'Connell, J.; Holmes, J. D.; Trotier, A.; Krukiewicz, K.; Orpella-Aceret, G.; Pugliese, E.; Ballerini, L.; Kilcoyne, M.; Dowd, E.; Quinlan, L. R.; Pandit, A.; Kavanagh, P.; Biggs, M. J. P., *Adv Funct Mater* 2017, 1605035 DOI 10.1002/adfm.201605035.
52. Vallejo-Giraldo, C.; Pugliese, E.; Larranaga, A.; Fernandez-Yague, M. A.; Britton, J. J.; Trotier, A.; Tadayyon, G.; Kelly, A.; Rago, I.; Sarasua, J. R.; Dowd, E.; Quinlan, L. R.; Pandit, A.; Biggs, M. J., *Nanomedicine (Lond)* 2016, 11 (19), 2547-63. DOI 10.2217/nnm-2016-0075.
53. Schmidt, C. E.; Leach, J. B., *Annu. Rev. Biomed. Eng.* 2003, 5 (1), 293-347.
54. Rose, T.; Robblee, L., *IEEE Trans. Biomed. Eng.* 1990, 37 (11), 1118-1120.

55. Stein, R. B., *The Quarterly Review of Biology* 1990, 65 (4), 527-527. DOI 10.1086/417023.
56. Thelin, J.; Jörntell, H.; Psouni, E.; Garwicz, M.; Schouenborg, J.; Danielsen, N.; Linsmeier, C. E., *PLoS One* 2011, 6 (1), e16267.
57. Hamzavi, N.; Tsang, W. M.; Shim, V. P. W. In *Nonlinear elastic brain tissue model for neural probe-tissue mechanical interaction*, 2013 6th International IEEE/EMBS Conference on Neural Engineering (NER), 6-8 Nov. 2013; 2013; pp 1119-1122.
58. Leach, J. B.; Achyuta, A. K. H.; Murthy, S. K., *Front. Neuroengineering* 2009, 2.
59. Miller, K.; Chinzei, K.; Orssengo, G.; Bednarz, P., *J Biomech* 2000, 33 (11), 1369-1376. DOI Doi 10.1016/S0021-9290(00)00120-2.
60. Lotters, J. C.; Olthuis, W.; Veltink, P. H.; Bergveld, P., *J Micromech Microeng* 1997, 7 (3), 145-147. DOI Doi 10.1088/0960-1317/7/3/017.
61. Palchesko, R. N.; Zhang, L.; Sun, Y.; Feinberg, A. W., *PLoS One* 2012, 7 (12), e51499. DOI 10.1371/journal.pone.0051499.
62. Keohan, F.; Wei, X. F. F.; Wongsarnpigoon, A.; Lazaro, E.; Darga, J. E.; Grill, W. M., *J Biomat Sci-Polym E* 2007, 18 (8), 1057-1073. DOI 10.1163/156856207781494395.
63. Kozai, T. D. Y.; Langhals, N. B.; Patel, P. R.; Deng, X.; Zhang, H.; Smith, K. L.; Lahann, J.; Kotov, N. A.; Kipke, D. R., *Nat. Mater.* 2012, 11 (12), 1065-1073.
64. McClain, M. A.; Clements, I. P.; Shafer, R. H.; Bellamkonda, R. V.; LaPlaca, M. C.; Allen, M. G., *Biomedical microdevices* 2011, 13 (2), 361-373.
65. Yu, Z.; Graudejus, O.; Tsay, C.; Lacour, S. P.; Wagner, S.; Morrison III, B., *J Neurotrauma* 2009, 26 (7), 1135-1145.
66. Harris, J. P.; Hess, A. E.; Rowan, S. J.; Weder, C.; Zorman, C. A.; Tyler, D. J.; Capadona, J. R., *Journal of neural engineering* 2011, 8 (4). DOI Artn 046010
Doi 10.1088/1741-2560/8/4/046010.

67. Hassler, C.; Guy, J.; Nietzsche, M.; Staiger, J. F.; Stieglitz, T. In Chronic intracortical implantation of saccharose-coated flexible shaft electrodes into the cortex of rats, Engineering in Medicine and Biology Society, EMBC, 2011 Annual International Conference of the IEEE, IEEE: 2011; pp 644-647.
68. Heo, D. N.; Kim, H.-J.; Lee, Y. J.; Heo, M.; Lee, S. J.; Lee, D.; Do, S. H.; Lee, S. H.; Kwon, I. K., *Acs Nano* 2017, 11 (3), 2961-2971.
69. Khodagholy, D.; Doublet, T.; Gurfinkel, M.; Quilichini, P.; Ismailova, E.; Leleux, P.; Herve, T.; Sanaur, S.; Bernard, C.; Malliaras, G. G., *Advanced materials* 2011, 23 (36), H268-72. DOI 10.1002/adma.201102378.
70. Mario Cheong, G. L.; Lim, K. S.; Jakubowicz, A.; Martens, P. J.; Poole-Warren, L. A.; Green, R. A., *Acta Biomater* 2014, 10 (3), 1216-1226. DOI <http://dx.doi.org/10.1016/j.actbio.2013.12.032>.
71. Dai, T.; Qing, X.; Lu, Y.; Xia, Y., *Polymer* 2009, 50 (22), 5236-5241. DOI <http://dx.doi.org/10.1016/j.polymer.2009.09.025>.
72. Goding, J.; Gilmour, A.; Martens, P.; Poole-Warren, L.; Green, R., *Advanced healthcare materials* 2017, 6 (9). DOI 10.1002/adhm.201601177.
73. Zhong, C.; Ke, D.; Wang, L.; Lu, Y.; Wang, L., *Electrochem. Commun.* 2017.
74. Simitzi, C.; Ranella, A.; Stratakis, E., *Acta Biomater* 2017.
75. Shi, X.; Xiao, Y.; Xiao, H.; Harris, G.; Wang, T.; Che, J., *Colloids and Surfaces B: Biointerfaces* 2016, 145, 768-776.
76. Yiannakou, C.; Simitzi, C.; Manousaki, A.; Fotakis, C.; Ranella, A.; Stratakis, E., *Biofabrication* 2017, 9 (2), 025024. DOI 10.1088/1758-5090/aa71c6.
77. Ereifej, E. S.; Matthew, H. W.; Newaz, G.; Mukhopadhyay, A.; Auner, G.; Salakhutdinov, I.; VandeVord, P. J., *Journal of Biomedical Materials Research Part A* 2013, 101 (6), 1743-1757.
78. Mokarian-Tabari, P.; Vallejo-Giraldo, C.; Fernandez-Yague, M.; Cummins, C.; Morris, M. A.; Biggs, M. J., *J. Mater. Sci.: Mater. Med.* 2015, 26 (2), 120.
79. Boehler, C.; Stieglitz, T.; Asplund, M., *Biomaterials* 2015, 67, 346-353.

80. Leber, M.; Shandhi, M.; Hogan, A.; Solzbacher, F.; Bhandari, R.; Negi, S., *Appl. Surf. Sci.* 2016, 365, 180-190.
81. Corey, J.; Wheeler, B.; Brewer, G., *IEEE Trans. Biomed. Eng.* 1996, 43 (9), 944-955.
82. Chung, C.-K.; Tseng, S.-F.; Hsiao, W.-T.; Chiang, D.; Lin, W.-C., *JOURNAL OF LASER MICRO NANOENGINEERING* 2016, 11 (3), 395-399.
83. Thakar, R.; Weber, A. E.; Morris, C. A.; Baker, L. A., *Analyst* 2013, 138 (20), 5973-82. DOI 10.1039/c3an01216f.
84. Bass, R. B.; Clark, W. W.; Zhang, J. Z.; Lichtenberger, A. W., *IEEE Transactions on Applied Superconductivity* 2001, 11 (1), 92-94. DOI 10.1109/77.919292.
85. Hof, L. A.; Guo, X.; Seo, M.; Wüthrich, R.; Greener, J., *Micromachines* 2017, 8 (1), 29.
86. Ereifej, E. S.; Cheng, M. M.-C.; Mao, G.; VandeVord, P. J., *J Neurosci Methods* 2013, 217 (1), 17-25.
87. Hoshino, T.; Miyazako, H.; Nakayama, A.; Wagatsuma, A.; Mabuchi, K., *Sensors and Actuators B: Chemical* 2016, 236, 659-667.
88. Gomez, N.; Lee, J. Y.; Nickels, J. D.; Schmidt, C. E., *Adv Funct Mater* 2007, 17 (10), 1645-1653. DOI 10.1002/adfm.200600669.
89. Kai, D.; Prabhakaran, M. P.; Jin, G. R.; Ramakrishna, S., *Journal of Biomedical Materials Research Part A* 2011, 99A (3), 376-385. DOI 10.1002/Jbm.A.33200.
90. Weng, B.; Liu, X.; Shepherd, R.; Wallace, G. G., *Synthetic Met* 2012, 162 (15-16), 1375-1380. DOI 10.1016/j.synthmet.2012.05.022.
91. Green, R. A.; Hassarati, R. T.; Bouchinet, L.; Lee, C. S.; Cheong, G. L. M.; Yu, J. F.; Dodds, C. W.; Suaning, G. J.; Poole-Warren, L. A.; Lovell, N. H., *Biomaterials* 2012, 33 (25), 5875-5886. DOI <http://dx.doi.org/10.1016/j.biomaterials.2012.05.017>.

92. Ortmann, V., Biostable neuroelectrode. Google Patents: 2013.
93. Chapman, C. A.; Chen, H.; Stamou, M.; Biener, J.; Biener, M. M.; Lein, P. J.; Seker, E., *ACS Appl Mater Interfaces* 2015, 7 (13), 7093-7100.
94. Chapman, C. A.; Wang, L.; Chen, H.; Garrison, J.; Lein, P. J.; Seker, E., *Adv Funct Mater* 2017, 27 (3).
95. Qi, L.; Li, N.; Huang, R.; Song, Q.; Wang, L.; Zhang, Q.; Su, R.; Kong, T.; Tang, M.; Cheng, G., *PLoS One* 2013, 8 (3), e59022.
96. Turner, A. M.; Dowell, N.; Turner, S. W.; Kam, L.; Isaacson, M.; Turner, J. N.; Craighead, H. G.; Shain, W., *J Biomed Mater Res* 2000, 51 (3), 430-41.
97. Pearce, T. M.; Williams, J. C., *Lab Chip* 2007, 7 (1), 30-40.
98. HajjHassan, M.; Chodavarapu, V.; Musallam, S., *Sensors* 2008, 8 (10), 6704-6726.
99. Donoghue, J. P., *Nat Neurosci* 2002, 5, 1085-1088.
100. Uppalapati, D.; Boyd, B. J.; Garg, S.; Travas-Sejdic, J.; Svirskis, D., *Biomaterials* 2016, 111, 149-162.
101. Kotov, N. A.; Winter, J. O.; Clements, I. P.; Jan, E.; Timko, B. P.; Campidelli, S.; Pathak, S.; Mazzatenta, A.; Lieber, C. M.; Prato, M., *Adv Mater* 2009, 21 (40), 3970-4004.
102. Brüggemann, D.; Michael, K. E.; Wolfrum, B.; Offenhäusser, A., *International Journal of Nano and Biomaterials* 17 2012, 4 (2), 108-127.
103. Pancrazio, J. J., *Future Medicine*, 2008, 823-830.
104. Cui, X.; Hetke, J. F.; Wiler, J. A.; Anderson, D. J.; Martin, D. C., *Sensors and Actuators A: Physical* 2001, 93 (1), 8-18.
105. Asplund, M.; Nyberg, T.; Inganäs, O., *Polym Chem-Uk* 2010, 1 (9), 1374-1391.
106. Streich, C.; Koenen, S.; Lelle, M.; Peneva, K.; & Barcikowski, S.; *Applied Surface Science*, 2015, 348, 92-99

107. Biggs, M. J. P.; Richards, R. G.; Dalby, M. J., *Nanomedicine: Nanotechnology, Biology and Medicine* 2010, 6 (5), 619-633.
108. Biggs, M. J.; Richards, R. G.; Gadegaard, N.; McMurray, R. J.; Affrossman, S.; Wilkinson, C. D.; Oreffo, R. O.; Dalby, M. J., *J Biomed Mater Res A* 2009, 91 (1), 195-208. DOI 10.1002/jbm.a.32196.
109. Biggs, M. J.; Richards, R.; Gadegaard, N.; Wilkinson, C.; Dalby, M., *J. Orthop. Res.* 2007, 25 (2), 273-282.
110. Morgan, J. T.; Murphy, C. J.; Russell, P., *Exp. Eye Res.* 2013, 115, 1-12.
111. Robinson, J. L.; King, P. F., *J. Electrochem. Soc.* 1961, 108 (1), 36-41. DOI Doi 10.1149/1.2428007.
112. Cabrera, N.; Mott, N. F., *Rep Prog Phys* 1948, 12, 163-184.
113. McNamara, L. E.; Sjostrom, T.; Burgess, K. E. V.; Kim, J. J. W.; Liu, E.; Gordonov, S.; Moghe, P. V.; Meek, R. M. D.; Oreffo, R. O. C.; Su, B.; Dalby, M. J., *Biomaterials* 2011, 32 (30), 7403-7410. DOI 10.1016/j.biomaterials.2011.06.063.
114. Tsuchiya, H.; Macak, J. M.; Ghicov, A.; Taveira, L.; Schmuki, P., *Corros. Sci.* 2005, 47 (12), 3324-3335. DOI 10.1016/j.corsci.2005.05.041.
115. Ghicov, A.; Tsuchiya, H.; Macak, J. M.; Schmuki, P., *Electrochem. Commun.* 2005, 7 (5), 505-509. DOI 10.1016/j.elecom.2005.03.007.
116. Mahshid, S.; Dolati, A.; Goodarzi, M.; Askari, M.; Ghahramaninezhad, A., *Nanotechnology (General) - 217th Ecs Meeting 2010*, 28 (7), 67-74. DOI 10.1149/1.3491775.
117. Tian, T.; Xiao, X. F.; Liu, R. F.; She, H. D.; Hu, X. F., *J. Mater. Sci.* 2007, 42 (14), 5539-5543. DOI 10.1007/s10853-006-1104-6.
118. Bauer, S.; Kleber, S.; Schmuki, P., *Electrochem. Commun.* 2006, 8 (8), 1321-1325. DOI 10.1016/j.elecom.2006.05.030.
119. Diamanti, M. V.; Del Curto, B.; Pedferri, M., *J. Appl. Biomater. Biomech.* 2011, 9 (1), 55-69. DOI 10.5301/JABB.2011.7429.

120. Cho, S. W.; Jeong, J. G.; Park, S. H.; Cho, M. H.; Jeong, K.; Whang, C. N.; Yi, Y., *Appl. Phys. Lett.* 2008, 92 (21). DOI Artn 213302
10.1063/1.2931697.
121. Schueller, G. R. T.; Taylor, S. R.; Hajcsar, E. E., *J. Electrochem. Soc.* 1992, 139 (10), 2799-2805. DOI Doi 10.1149/1.2068982.
122. Blawert, C.; Dietzel, W.; Ghali, E.; Song, G. L., *Adv Eng Mater* 2006, 8 (6), 511-533. DOI 10.1002/adem.200500257.
123. Swan, E. E. L.; Popat, K. C.; Grimes, C. A.; Desai, T. A., *Journal of Biomedical Materials Research Part A* 2005, 72A (3), 288-295. DOI 10.1002/jbm.a.30223.
124. Foong, T. R. B.; Sellinger, A.; Hu, X., *Acs Nano* 2008, 2 (11), 2250-2256. DOI 10.1021/nn800435n.
125. Ho, P. K. H.; Granstrom, M.; Friend, R. H.; Greenham, N. C., *Adv Mater* 1998, 10 (10), 769-774. DOI Doi 10.1002/(Sici)1521-4095(199807)10:10<769::Aid-Adma769>3.3.Co;2-V.
126. Yao, C.; Webster, T. J., *J Nanosci Nanotechnol* 2006, 6 (9-10), 2682-2692. DOI 10.1166/jnn.2006.447.
127. Nick, C.; Quednau, S.; Sarwar, R.; Schlaak, H.; Thielemann, C., *Microsystem technologies* 2014, 20 (10-11), 1849-1857.
128. Yoon, H.; Deshpande, D. C.; Ramachandran, V.; Varadan, V. K., *Nanotechnology* 2007, 19 (2), 025304.
129. Rosengren, A.; Wallman, L.; Danielsen, N.; Laurell, T.; Bjursten, L. M., *IEEE Trans. Biomed. Eng.* 2002, 49 (4), 392-399.
130. Sun, T.; Tsang, W. M.; Park, W.-T., *Appl. Surf. Sci.* 2014, 292, 843-851.
131. Graham, A. H.; Bowen, C. R.; Robbins, J.; Taylor, J., *Sensors and Actuators B: Chemical* 2009, 138 (1), 296-303.

132. Moulton, S. E.; Higgins, M. J.; Kapsa, R. M. I.; Wallace, G. G., *Adv Funct Mater* 2012, 22 (10), 2003-2014.
133. Doménech, A.; Navarro, P.; Arán, V. J.; Muro, B.; Montoya, N.; García-España, E., *Analyst* 2010, 135 (6), 1449-1455.
134. Hofmann, G. A.; Gilbert, R. A.; Hayakawa, Y.; Heller, R.; Jaroszeski, M. J., *Needle electrodes for mediated delivery of drugs and genes*. Google Patents: 1997.
135. Boulahneche, S.; Jijie, R.; Barras, A.; Chekin, F.; Singh, S. K.; Bouckaert, J.; Medjram, M. S.; Kurungot, S.; Boukherroub, R.; Szunerits, S., *J Mater Chem B* 2017.
136. Zanganeh, S.; Khosravi, S.; Namdar, N.; Amiri, M. H.; Gharooni, M.; Abdolahad, M., *Anal. Chim. Acta* 2016, 938, 72-81.
137. Heo, D. N.; Song, S.-J.; Kim, H.-J.; Lee, Y. J.; Ko, W.-K.; Lee, S. J.; Lee, D.; Park, S. J.; Zhang, L. G.; Kang, J. Y., *Acta Biomater* 2016, 39, 25-33.
138. Zhang, Z.; Li, Q.; Han, L.; Zhong, Y., *Biomed Mater* 2015, 10 (5), 055006.
139. Balint, R.; Cassidy, N. J.; Cartmell, S. H., *Acta Biomater* 2014, 10 (6), 2341-2353.
140. Pacelli, S.; Acosta, F.; Chakravarti, A. R.; Samanta, S. G.; Whitlow, J.; Modaresi, S.; Ahmed, R. P.; Rajasingh, J.; Paul, A., *Acta Biomater* 2017.
141. Kim, B.; Gwon, K.; Lee, S.; Kim, Y. H.; Yoon, M.-H.; Tae, G., *Rsc Adv* 2016, 6 (91), 88038-88041.
142. Hardy, J. G.; Lee, J. Y.; Schmidt, C. E., *Curr. Opin. Biotechnol.* 2013, 24 (5), 847-854.
143. Weaver, C. L.; LaRosa, J. M.; Luo, X.; Cui, X. T., *Acs Nano* 2014, 8 (2), 1834-1843.
144. Luo, X.; Matrangola, C.; Tan, S.; Alba, N.; Cui, X. T., *Biomaterials* 2011, 32 (26), 6316-6323.
145. Abidian, M. R.; Kim, D. H.; Martin, D. C., *Adv Mater* 2006, 18 (4), 405-409.

146. Ge, J.; Neofytou, E.; Cahill III, T. J.; Beygui, R. E.; Zare, R. N., *Acs Nano* 2011, 6 (1), 227-233.
147. Zhou, K.; Thouas, G. A.; Bernard, C. C.; Nisbet, D. R.; Finkelstein, D. I.; Li, D.; Forsythe, J. S., *ACS Appl Mater Interfaces* 2012, 4 (9), 4524-31. DOI 10.1021/am3007565.
148. Jeffery, A. F.; Churchward, M. A.; Mushahwar, V. K.; Todd, K. G.; Elias, A. L., *Biomacromolecules* 2014, 15 (6), 2157-2165.
149. Gutowski, S. M.; Shoemaker, J. T.; Templeman, K. L.; Wei, Y.; Latour, R. A.; Bellamkonda, R. V.; LaPlaca, M. C.; García, A. J., *Biomaterials* 2015, 44, 55-70. DOI <http://dx.doi.org/10.1016/j.biomaterials.2014.12.009>.
150. Guarino, V.; Zuppolini, S.; Borriello, A.; Ambrosio, L., *Polymers-Basel* 2016, 8 (5), 185.
151. Skotheim, T. A., *Handbook of conducting polymers*. CRC press: 1997.
152. Aldissi, M., *Intrinsically conducting polymers: an emerging technology*. Springer Science & Business Media: 2013; Vol. 246.
153. Baek, S.; Green, R. A.; Poole-Warren, L. A., *Journal of Biomedical Materials Research Part A* 2014, 102 (8), 2743-2754.
154. Bolto, B.; McNeill, R.; Weiss, D., *Australian Journal of Chemistry* 1963, 16 (6), 1090-1103. DOI <http://dx.doi.org/10.1071/CH9631090>.
155. Guo, B.; Glavas, L.; Albertsson, A.-C., *Prog Polym Sci* 2013, 38 (9), 1263-1286.
156. Hackett, A. J.; Malmström, J.; Travas-Sejdic, J., *Prog Polym Sci* 2017.
157. Aqrave, Z.; Montgomery, J.; Travas-Sejdic, J.; Svirskis, D., *Trends Biotechnol.* 2017, 35 (2), 93-95.
158. Im, S.; Kim, S.; Kim, S.; Kim, F. S.; Kim, J. H., *Applied Chemistry for Engineering* 2015, 26 (6), 640-647.

159. Cardona, C. M.; Li, W.; Kaifer, A. E.; Stockdale, D.; Bazan, G. C., *Adv Mater* 2011, 23 (20), 2367-2371.
160. Ates, M., *Materials Science and Engineering: C* 2013, 33 (4), 1853-1859.
161. Gerard, M.; Chaubey, A.; Malhotra, B., *Biosens. Bioelectron.* 2002, 17 (5), 345-359.
162. Lenz, A.; Kariis, H.; Pohl, A.; Persson, P.; Ojamae, L., *Chem Phys* 2011, 384 (1-3), 44-51. DOI Doi 10.1016/J.Chemphys.2011.05.003.
163. Hide, F.; Díaz-García, M. A.; Schwartz, B. J.; Heeger, A. J., *Acc. Chem. Res.* 1997, 30 (10), 430-436.
164. Temmer, R.; Maziz, A.; Plesse, C.; Aabloo, A.; Vidal, F.; Tamm, T., *Smart Materials and Structures* 2013, 22 (10), 104006.
165. Vallejo-Giraldo, C.; Kelly, A.; Biggs, M. J., *Drug Discov. Today* 2014, 19 (1), 88-94. DOI 10.1016/j.drudis.2013.07.022.
166. Bendrea, A. D.; Cianga, L.; Cianga, I., *J Biomater Appl* 2011, 26 (1), 3-84. DOI Doi 10.1177/0885328211402704.
167. Guimard, N. K.; Gomez, N.; Schmidt, C. E., *Prog Polym Sci* 2007, 32 (8), 876-921.
168. Schmidt, C. E.; Shastri, V. R.; Vacanti, J. P.; Langer, R., *Proc Natl Acad Sci U S A* 1997, 94(17), 8948-8953
169. Kondratiev, V. V.; Malev, V. V.; Eliseeva, S. N., *Russ. Chem. Rev.* 2016, 85 (1), 14.
170. Chen, Z.; Ren, W.; Gao, L.; Liu, B.; Pei, S.; Cheng, H.-M., *Nat. Mater.* 2011, 10 (6), 424-428.
171. Gabay, T.; Ben-David, M.; Kalifa, I.; Sorkin, R.; Ze'ev, R. A.; Ben-Jacob, E.; Hanein, Y., *Nanotechnology* 2007, 18 (3), 035201.
172. Schuettler, M.; Stiess, S.; King, B. V.; Suaning, G. J., *J. Neural Eng.* 2005, 2 (1), S121.

173. Cheng, X.-e.; Shi, W., *J. Therm. Anal. Calorim.* 2010, 103 (1), 303-310.
174. Cui, X.; Wiler, J.; Dzaman, M.; Altschuler, R. A.; Martin, D. C., *Biomaterials* 2003, 24 (5), 777-787.
175. Cui, X.; Martin, D. C., *Sensors and Actuators B: Chemical* 2003, 89 (1), 92-102.
176. Baek, S.; Green, R. A.; Poole-Warren, L. A., *Acta Biomater* 2014, 10 (7), 3048-3058.
177. Green, R.; Abidian, M. R., *Adv Mater* 2015, 27 (46), 7620-7637.
178. Baek, S.; Green, R.; Granville, A.; Martens, P.; Poole-Warren, L., *J Mater Chem B* 2013, 1 (31), 3803-3810.
179. Fonner, J. M.; Forciniti, L.; Nguyen, H.; Byrne, J. D.; Kou, Y.-F.; Syeda-Nawaz, J.; Schmidt, C. E., *Biomed Mater* 2008, 3 (3), 034124.
180. El-Enany, G.; Ghanem, M.; El-Ghaffar, M., *Portugaliae Electrochimica Acta* 2010, 28 (5), 336-348.
181. King, Z. A.; Shaw, C. M.; Spanninga, S. A.; Martin, D. C., *Polymer* 2011, 52 (5), 1302-1308. DOI DOI 10.1016/j.polymer.2011.01.042.
182. Ismail, Y. A.; Martinez, J. G.; Al Harrasi, A. S.; Kim, S. J.; Otero, T. F., *Sensor Actuat B-Chem* 2011, 160 (1), 1180-1190. DOI DOI 10.1016/j.snb.2011.09.044.
183. Green, R. A.; Hassarati, R. T.; Goding, J. A.; Baek, S.; Lovell, N. H.; Martens, P. J.; Poole-Warren, L. A., *Macromol Biosci* 2012, 12 (4), 494-501. DOI DOI 10.1002/mabi.201100490.
184. Green, R. A.; Lovell, N. H.; Poole-Warren, L. A., *Acta Biomater* 2010, 6 (1), 63-71.
185. Harris, A. R.; Morgan, S. J.; Chen, J.; Kapsa, R. M.; Wallace, G. G.; Paolini, A. G., *J. Neural Eng.* 2012, 10 (1), 016004.

186. Green, R.; Matteucci, P.; Hassarati, R.; Giraud, B.; Dodds, C.; Chen, S.; Byrnes-Preston, P.; Suaning, G.; Poole-Warren, L.; Lovell, N., *J. Neural Eng.* 2013, 10 (1), 016009.
187. del Agua, I.; Mantione, D.; Casado, N.; Sanchez-Sanchez, A.; Malliaras, G. G.; Mecerreyes, D., *ACS Macro Letters* 2017, 6 (4), 473-478.
188. Cai, G.; Darmawan, P.; Cui, M.; Wang, J.; Chen, J.; Magdassi, S.; Lee, P. S., *Advanced Energy Materials* 2016, 6 (4).
189. Alamro, T.; Ram, M. K., *Electrochim Acta* 2017, 235, 623-631.
190. Cui, X. T.; Zhou, D. D., *IEEE transactions on neural systems and rehabilitation engineering : a publication of the IEEE Engineering in Medicine and Biology Society* 2007, 15 (4), 502-8. DOI 10.1109/TNSRE.2007.909811.
191. Shi, W.; Zhao, T.; Xi, J.; Wang, D.; Shuai, Z., *J Am Chem Soc* 2015, 137 (40), 12929-12938.
192. Gueye, M. N.; Carella, A.; Massonnet, N.; Yvenou, E.; Brenet, S.; Faure-Vincent, J. r. m.; Pouget, S. p.; Rieutord, F. o.; Okuno, H.; Benayad, A., *Chem Mater* 2016, 28 (10), 3462-3468.
193. Chiu, W. W.; Travaš-Sejdić, J.; Cooney, R. P.; Bowmaker, G. A., *J. Raman Spectrosc.* 2006, 37 (12), 1354-1361.
194. Harris, A. R.; Molino, P. J.; Paolini, A. G.; Wallace, G. G., *Electrochim Acta* 2016, 197, 99-106. DOI <http://dx.doi.org/10.1016/j.electacta.2016.03.038>.
195. Harman, D. G.; Gorkin, R.; Stevens, L.; Thompson, B.; Wagner, K.; Weng, B.; Chung, J. H. Y.; in het Panhuis, M.; Wallace, G. G., *Acta Biomater* 2015, 14, 33-42. DOI <http://dx.doi.org/10.1016/j.actbio.2014.11.049>.
196. Culebras, M.; Gomez, C.; Cantarero, A., *Journal of Materials Chemistry A* 2014, 2 (26), 10109-10115.
197. Martin, D. C.; Wu, J.; Shaw, C. M.; King, Z.; Spanninga, S. A.; Richardson-Burns, S.; Hendricks, J.; Yang, J., *Polym. Rev. (Philadelphia, PA, U. S.)* 2010, 50 (3), 340-384.

198. Szczepanski, C. R.; Darmanin, T.; Guittard, F., *Rsc Adv* 2015, 5 (109), 89407-89414.
199. Wei, Q.; Mukaida, M.; Kirihaara, K.; Naitoh, Y.; Ishida, T., *Materials* 2015, 8 (2), 732-750.
200. Xiao, Y.; Martin, D. C.; Cui, X.; Shenai, M., *Appl Biochem Biotechnol* 2006, 128 (2), 117-30.
201. Zhu, Z.; Mankowski, T.; Balakrishnan, K.; Shikoh, A. S.; Touati, F.; Benammar, M. A.; Mansuripur, M.; Falco, C. M., *ACS Appl Mater Interfaces* 2015, 7 (30), 16223-16230.
202. Wei, B.; Liu, J.; Ouyang, L.; Kuo, C.-C.; Martin, D. C., *ACS Appl Mater Interfaces* 2015, 7 (28), 15388-15394.
203. Deng, H.; Lin, L.; Ji, M.; Zhang, S.; Yang, M.; Fu, Q., *Prog Polym Sci* 2014, 39 (4), 627-655.
204. Vara, H.; Collazos-Castro, J. E., *ACS Appl Mater Interfaces* 2015, 7 (48), 27016-27026.
205. Kim, D.-H.; Wiler, J. A.; Anderson, D. J.; Kipke, D. R.; Martin, D. C., *Acta Biomater* 2010, 6 (1), 57-62.
206. Collazos-Castro, J. E.; Hernandez-Labrado, G. R.; Polo, J. L.; Garcia-Rama, C., *Biomaterials* 2013, 34 (14), 3603-17. DOI 10.1016/j.biomaterials.2013.01.097.
207. Luo, X.; Weaver, C. L.; Zhou, D. D.; Greenberg, R.; Cui, X. T., *Biomaterials* 2011, 32 (24), 5551-7. DOI 10.1016/j.biomaterials.2011.04.051.
208. Chikar, J. A.; Hendricks, J. L.; Richardson-Burns, S. M.; Raphael, Y.; Pfingst, B. E.; Martin, D. C., *Biomaterials* 2012, 33 (7), 1982-1990.
209. Ouyang, L.; Green, R.; Feldman, K. E.; Martin, D. C., *Prog Brain Res* 2011, 194, 263-71. DOI 10.1016/B978-0-444-53815-4.00001-7.
210. Lövenich, W., *Polymer Science Series C* 2014, 56 (1), 135-143. DOI 10.1134/s1811238214010068.

211. Ravichandran, R.; Sundarrajan, S.; Venugopal, J. R.; Mukherjee, S.; Ramakrishna, S., *J R Soc Interface* 2010, 7 Suppl 5, S559-79. DOI 10.1098/rsif.2010.0120.focus.
212. Kaur, G.; Adhikari, R.; Cass, P.; Bown, M.; Gunatillake, P., *Rsc Adv* 2015, 5 (47), 37553-37567.
213. Dhandayuthapani, B.; Yoshida, Y.; Maekawa, T.; Kumar, D. S., *International Journal of Polymer Science* 2011, 2011.
214. Green, R. A.; Baek, S.; Poole-Warren, L. A.; Martens, P. J., *Sci Technol Adv Mat* 2010, 11 (1), 014107.
215. Wen, Y.; Xu, J., *Journal of Polymer Science Part A: Polymer Chemistry* 2017, 55 (7), 1121-1150.
216. Ryu, M.; Yang, J. H.; Ahn, Y.; Sim, M.; Lee, K. H.; Kim, K.; Lee, T.; Yoo, S.-J.; Kim, S. Y.; Moon, C., *ACS Appl Mater Interfaces* 2017, 9 (12), 10577-10586.
217. Pacheco-Moreno, C. M.; Schreck, M.; Scaccabarozzi, A. D.; Bourgun, P.; Wantz, G.; Stevens, M. M.; Dautel, O. J.; Stingelin, N., *Adv Mater* 2017, 29 (4).
218. Koutsouras, D. A.; Hama, A.; Pas, J.; Gkoupidenis, P.; Hivert, B.; Faivre-Sarrailh, C.; Di Pasquale, E.; Owens, R. M.; Malliaras, G. G., *MRS Communications* 2017, 1-7.
219. Castagnola, E.; Marrani, M.; Maggiolini, E.; Maita, F.; Pazzini, L.; Polese, D.; Pecora, A.; Maiolo, L.; Fortunato, G.; Fadiga, L. In *Recording High Frequency Neural Signals Using Conformable and Low-Impedance ECoG Electrodes Arrays Coated with PEDOT-PSS-PEG*, *Advances in Science and Technology*, Trans Tech Publ: 2017; pp 77-85.
220. Malliaras, G., *Bulletin of the American Physical Society* 2017, 62.
221. Luo, S.-C.; Mohamed Ali, E.; Tansil, N. C.; Yu, H.-h.; Gao, S.; Kantchev, E. A.; Ying, J. Y., *Langmuir* 2008, 24 (15), 8071-8077.
222. Kleber, C.; Bruns, M.; Lienkamp, K.; Rhe, J.; Asplund, M., *Acta Biomater* 2017.

223. Zhao, Q.; Jamal, R.; Zhang, L.; Wang, M.; Abdiryim, T., *Nanoscale research letters* 2014, 9 (1), 557. DOI 10.1186/1556-276x-9-557.
224. Yang, J.; Kim, D. H.; Hendricks, J. L.; Leach, M.; Northey, R.; Martin, D. C., *Acta Biomater* 2005, 1 (1), 125-136.
225. Lee, Y. H.; Oh, J.; Lee, S.-S.; Kim, H.; Son, J. G., 2017.
226. Richardson-Burns, S. M.; Hendricks, J. L.; Foster, B.; Povlich, L. K.; Kim, D.-H.; Martin, D. C., *Biomaterials* 2007, 28 (8), 1539-1552.
227. Wan, A. M.-D.; Inal, S.; Williams, T.; Wang, K.; Leleux, P.; Estevez, L.; Giannelis, E. P.; Fischbach, C.; Malliaras, G. G.; Gourdon, D., *J Mater Chem B* 2015, 3 (25), 5040-5048.
228. Moyen, E.; Hama, A.; Ismailova, E.; Assaud, L.; Malliaras, G.; Hanbücken, M.; Owens, R. M., *Nanotechnology* 2016, 27 (7), 074001.
229. Lee, H.; Kim, M.; Kim, I.; Lee, H., *Adv Mater* 2016, 28 (22), 4541-4548.
230. Chen, C.; Zhang, T.; Zhang, Q.; Chen, X.; Zhu, C.; Xu, Y.; Yang, J.; Liu, J.; Sun, D., *ACS Appl Mater Interfaces* 2016, 8 (16), 10183-10192.
231. Kim, D. H.; Richardson-Burns, S. M.; Hendricks, J. L.; Sequera, C.; Martin, D. C., *Adv Funct Mater* 2007, 17 (1), 79-86.
232. Povlich, L. K.; Cho, J. C.; Leach, M. K.; Corey, J. M.; Kim, J.; Martin, D. C., *Biochimica et Biophysica Acta (BBA)-General Subjects* 2013, 1830 (9), 4288-4293.
233. Mantione, D.; del Agua, I.; Schaafsma, W.; Diez-Garcia, J.; Castro, B.; Sardon, H.; Mecerreyes, D., *Macromol Biosci* 2016, 16 (8), 1227-1238.
234. Park, S. J.; Lee, Y. J.; Heo, D. N.; Kwon, I. K.; Yun, K.-S.; Kang, J. Y.; Lee, S. H., *Sensors and Actuators B: Chemical* 2015, 215, 133-141.
235. Krukiewicz, K.; Cichy, M.; Ruszkowski, P.; Turczyn, R.; Jarosz, T.; Zak, J. K.; Lapkowski, M.; Bednarczyk-Cwynar, B., *Materials Science and Engineering: C* 2017, 73, 611-615.

236. Boehler, C.; Kleber, C.; Martini, N.; Xie, Y.; Dryg, I.; Stieglitz, T.; Hofmann, U.; Asplund, M., *Biomaterials* 2017, 129, 176-187.
237. Catt, K.; Li, H.; Hoang, V.; Beard, R.; Cui, X. T., *Nanomedicine: Nanotechnology, Biology and Medicine* 2017.
238. Krukiewicz, K.; Zak, J., *J. Mater. Sci.* 2014, 49 (16).
239. Jeon, G.; Yang, S. Y.; Byun, J.; Kim, J. K., *Nano Lett.* 2011, 11 (3), 1284-1288. DOI Doi 10.1021/Nl104329y.
240. Esrafilzadeh, D.; Razal, J. M.; Moulton, S. E.; Stewart, E. M.; Wallace, G. G., *J Control Release* 2013. DOI 10.1016/j.jconrel.2013.01.022.
241. Yue, Z.; Moulton, S. E.; Cook, M.; O'Leary, S.; Wallace, G. G., *Adv Drug Deliv Rev* 2013, 65 (4), 559-69. DOI 10.1016/j.addr.2012.06.002.
242. Löffler, S.; Melican, K.; Nilsson, K.; Richter-Dahlfors, A., *J. Intern. Med.* 2017.
243. Chen, C.; Chen, X.; Zhang, H.; Zhang, Q.; Wang, L.; Li, C.; Dai, B.; Yang, J.; Liu, J.; Sun, D., *Acta Biomater* 2017, 55, 434-442.
244. Cantu, T.; Walsh, K.; Pattani, V. P.; Moy, A. J.; Tunnell, J. W.; Irvin, J. A.; Betancourt, T., *Int. J. Nanomedicine* 2017, 12, 615.
245. Castagnola, E.; De Faveri, S.; Ansaldo, A.; Maggiolini, E.; Benfenati, F.; Ricci, D.; Fadiga, L. In *Nanostructured microsphere coated with living cells and tethered with low-stiffness wire: a possible solution to brain tissue reactions*, *Neural Engineering (NER), 2015 7th International IEEE/EMBS Conference on*, IEEE: 2015; pp 390-393.
246. Kozai, T. D.; Catt, K.; Du, Z.; Na, K.; Srivannavit, O.; Razi-ul, M. H.; Seymour, J.; Wise, K. D.; Yoon, E.; Cui, X. T., *IEEE Trans. Biomed. Eng.* 2016, 63 (1), 111-119.
247. Charkhkar, H.; Knaack, G. L.; McHail, D. G.; Mandal, H. S.; Peixoto, N.; Rubinson, J. F.; Dumas, T. C.; Pancrazio, J. J., *Acta Biomater* 2016, 32, 57-67.
248. Young, A. T.; Cornwell, N.; Daniele, M. A., *Adv Funct Mater* 2017.

249. Xiao, Y.; Cui, X.; Hancock, J. M.; Bouguettaya, M.; Reynolds, J. R.; Martin, D. C., *Sensors and Actuators B: Chemical* 2004, 99 (2), 437-443.
250. Asplund, M.; von Holst, H.; Ingnas, O., *Biointerphases* 2008, 3 (3), 83-93. DOI Doi 10.1116/1.2998407.
251. Alves-Sampaio, A.; Garcia-Rama, C.; Collazos-Castro, J. E., *Biomaterials* 2016, 89, 98-113. DOI 10.1016/j.biomaterials.2016.02.037.
252. Nagamine, K.; Sato, H.; Kai, H.; Kaji, H.; Nishizawa, M. In Hydrogel-based electrical stimulation culture system to control the engineered cellular activities driven by nano biomolecules, *Nanotechnology (IEEE-NANO)*, 2016 IEEE 16th International Conference on, IEEE: 2016; pp 232-233.
253. Cosnier, S., *Biosens. Bioelectron.* 1999, 14 (5), 443-456.
254. Nicolas, J.; Mura, S.; Brambilla, D.; Mackiewicz, N.; Couvreur, P., *Chem Soc Rev* 2013, 42 (3), 1147-1235.
255. Kamaly, N.; Yameen, B.; Wu, J.; Farokhzad, O. C., *Chem. Rev* 2016, 116 (4), 2602-2663.
256. Kuo, C.-c. Optimizing the performance of neural interface devices with hybrid poly (3, 4-ethylene dioxythiophene)(PEDOT). University of Delaware, 2017.
257. Nyberg, T.; Inganäs, O.; Jerregård, H., *Biomedical microdevices* 2002, 4 (1), 43-52.
258. Morin, E. A.; Tang, S.; Rogers, K. L.; He, W., *ACS Appl Mater Interfaces* 2016, 8 (8), 5737-5745.
259. Sekine, J.; Luo, S. C.; Wang, S.; Zhu, B.; Tseng, H. R.; Yu, H. H., *Adv Mater* 2011, 23 (41), 4788-92. DOI 10.1002/adma.201102151.
260. Chen, W.; Weng, S.; Zhang, F.; Allen, S.; Li, X.; Bao, L.; Lam, R. H.; Macoska, J. A.; Merajver, S. D.; Fu, J., *Acs Nano* 2012, 7 (1), 566-575.
261. Wang, W.; Cui, H.; Zhang, P.; Meng, J.; Zhang, F.; Wang, S., *ACS Appl Mater Interfaces* 2017, 9 (12), 10537-10543.

262. Lin, M.; Chen, J.-F.; Lu, Y.-T.; Zhang, Y.; Song, J.; Hou, S.; Ke, Z.; Tseng, H.-R., *Acc. Chem. Res.* 2014, 47 (10), 2941-2950.
263. Zhang, F.; Jiang, Y.; Liu, X.; Meng, J.; Zhang, P.; Liu, H.; Yang, G.; Li, G.; Jiang, L.; Wan, L.-J., *Nano Lett.* 2015, 16 (1), 766-772.
264. Qu, J. *Electrochemically deposited conducting polymers for reliable biomedical interfacing materials: formulation, mechanical characterization, and failure analysis.* University of Delaware, 2017.
265. Povlich, L. K.; Cho, J. C.; Leach, M. K.; Corey, J. M.; Kim, J.; Martin, D. C., *Biochim Biophys Acta* 2012. DOI 10.1016/j.bbagen.2012.10.017.
266. Dapra, J.; Lauridsen, L. H.; Nielsen, A. T.; Rozlosnik, N., *Biosens Bioelectron* 2013, 43, 315-20. DOI 10.1016/j.bios.2012.12.058.
267. Kiilerich-Pedersen, K.; Poulsen, C. R.; Jain, T.; Rozlosnik, N., *Biosens. Bioelectron.* 2011, 28 (1), 386-392.
268. Kiilerich-Pedersen, K.; Rozlosnik, N., *Diagnostics* 2012, 2 (4), 83-96.
269. Kiilerich-Pedersen, K.; Daprà, J.; Cherré, S.; Rozlosnik, N., *Biosens. Bioelectron.* 2013, 49, 374-379.
270. Rosati, G.; Daprà, J.; Cherré, S.; Rozlosnik, N., *Electroanal* 2014, 26 (6), 1400-1408.
271. Piro, B.; Shi, S.; Reisberg, S.; Noël, V.; Anquetin, G., *Biosensors* 2016, 6 (1), 7.
272. Lind, J. U.; Acikgoz, C.; Daugaard, A. E.; Andresen, T. L.; Hvilsted, S.; Textor, M.; Larsen, N. B., *Langmuir* 2012, 28 (15), 6502-11. DOI 10.1021/la300503p.
273. Godeau, G.; N'Na, J.; El Kout, E.; Ben Trad, R.; Darmanin, T.; El Kateb, M.; Beji, M.; Guittard, F., *Polym. Adv. Technol.* 2016, 27 (8), 993-998.
274. Blatz, T.; Fry, M.; James, E.; Albin, T.; Pollard, Z.; Kowalczyk, T.; Murphy, A., *J Mater Chem B* 2017.

275. Hsiao, Y.-S.; Liao, Y.-H.; Chen, H.-L.; Chen, P.; Chen, F.-C., *ACS Appl Mater Interfaces* 2016, 8 (14), 9275-9284.
276. Hernández-Balaguera, E.; Vara, H.; Polo, J., *J. Electroanal. Chem.* 2016, 775, 251-257.
277. Amorini, F.; Zironi, I.; Marzocchi, M.; Gualandi, I.; Calienni, M.; Cramer, T.; Fraboni, B.; Castellani, G., *ACS Appl Mater Interfaces* 2017, 9 (8), 6679-6689.
278. Cui, X.; Lee, V. A.; Raphael, Y.; Wiler, J. A.; Hetke, J. F.; Anderson, D. J.; Martin, D. C., *J Biomed Mater Res* 2001, 56 (2), 261-72.
279. Green, R. A.; Lovell, N. H.; Poole-Warren, L. A., *Biomaterials* 2009, 30, 3637-3644. DOI 10.1016/j.biomaterials.2009.03.043.
280. Harris, A. R.; Molino, P. J.; Paolini, A. G.; Wallace, G. G., *Synthetic Met* 2016, 222, 338-343.
281. Green, R. A.; Poole-warren, L. A.; Sungchul, B.; Martens, P. J., *Polymeric material. Google Patents: 2016.*
282. Frantz, C.; Stewart, K. M.; Weaver, V. M., *J. Cell Sci.* 2010, 123 (24), 4195-4200.
283. Xiao, Y.; Li, C. M.; Wang, S.; Shi, J.; Ooi, C. P., *Journal of Biomedical Materials Research Part A* 2010, 92 (2), 766-772.
284. Fabregat, G.; Ballano, G.; Armelin, E.; del Valle, L. J.; Cativiela, C.; Alemán, C., *Polym Chem-Uk* 2013, 4 (5), 1412-1424.
285. Malmström, J.; Hackett, A. J.; Feisst, V.; Travas-Sejdic, J., *International Journal of Nanotechnology* 2017, 14 (1-6), 235-250.
286. Bhagwat, N.; Murray, R. E.; Shah, S. I.; Kiick, K. L.; Martin, D. C., *Acta Biomater* 2016, 41, 235-246.
287. Matsuda, K.; Tashiro, K.; Hayashi, Y.; Monji, A.; Yoshida, I.; Mitsuyama, Y., *Dement. Geriatr. Cogn. Disord.* 2002, 14 (3), 113-22. DOI 63601.

288. Shi, Z.; Gao, X.; Ullah, M. W.; Li, S.; Wang, Q.; Yang, G., *Biomaterials* 2016, 111, 40-54.
289. Wang, M.; Liu, X.; Lyu, Z.; Gu, H.; Li, D.; Chen, H., *Colloids and Surfaces B: Biointerfaces* 2017, 150, 175-182. DOI <https://doi.org/10.1016/j.colsurfb.2016.11.022>.
290. Trowbridge, J. M.; Gallo, R. L., *Glycobiology* 2002, 12 (9), 117R-25R.
291. Tumova, S.; Woods, A.; Couchman, J. R., *Int J Biochem Cell Biol* 2000, 32 (3), 269-88.
292. Sugahara, K.; Mikami, T.; Uyama, T.; Mizuguchi, S.; Nomura, K.; Kitagawa, H., *Curr Opin Struct Biol* 2003, 13 (5), 612-20.
293. Raman, R.; Sasisekharan, V.; Sasisekharan, R., *Chem Biol* 2005, 12 (3), 267-77. DOI S1074-5521(05)00042-6 [pii]
10.1016/j.chembiol.2004.11.020.
294. Yung, S.; Chan, T. M., *Perit Dial Int* 2007, 27 Suppl 2, S104-9.
295. Sugahara, K.; Kitagawa, H., *Curr Opin Struct Biol* 2000, 10 (5), 518-27. DOI S0959-440X(00)00125-1 [pii].
296. Sugahara, K.; Kitagawa, H., *IUBMB Life* 2002, 54 (4), 163-75.
297. Papy-Garcia, D.; Christophe, M.; Minh Bao, H.; Fernando, S.; Ludmilla, S.; Diaz Julia Elisa, S.; Rita, R.-V., *Curr. Protein Pept. Sci.* 2011, 12 (3), 258-268.
298. Jenniskens, G. J.; Veerkamp, J. H.; van Kuppevelt, T. H., *J Cell Physiol* 2006, 206 (2), 283-94. DOI 10.1002/jcp.20450.
299. Prydz, K.; Dalen, K. T., *J Cell Sci* 2000, 113 Pt 2, 193-205.
300. Bishop, J. R.; Schuksz, M.; Esko, J. D., *Nature* 2007, 446 (7139), 1030-7. DOI nature05817 [pii]
10.1038/nature05817.
301. Lindahl, U.; Li, J. P., *Int Rev Cell Mol Biol* 2009, 276, 105-59. DOI S1937-6448(09)76003-4 [pii]

10.1016/S1937-6448(09)76003-4.

302. Chu, C. L.; Goerges, A. L.; Nugent, M. A., *Biochemistry* 2005, 44 (36), 12203-13. DOI 10.1021/bi050241p.

303. Bottaro, D. P., *Ann N Y Acad Sci* 2002, 961, 158.

304. Ori, A.; Wilkinson, M. C.; Fernig, D. G., *Front Biosci* 2008, 13, 4309-38. DOI 3007 [pii].

305. Wang, S.; Guan, S.; Wang, J.; Liu, H.; Liu, T.; Ma, X.; Cui, Z., *J. Biosci. Bioeng.* 2017, 123 (1), 116-125.

306. Suzuki, M.; Nakayama, M.; Tsuji, K.; Adachi, T.; Shimono, K., *Electrochemistry* 2016, 84 (5), 354-357.

307. Collazos-Castro, J. E.; García-Rama, C.; Alves-Sampaio, A., *Acta Biomater* 2016, 35, 42-56.

308. Wang, S.; Guan, S.; Zhu, Z.; Li, W.; Liu, T.; Ma, X., *Materials Science and Engineering: C* 2017, 71, 308-316.

309. Herland, A.; Persson, K. M.; Lundin, V.; Fahlman, M.; Berggren, M.; Jager, E. W. H.; Teixeira, A. I., *Angew Chem Int Edit* 2011, 50 (52), 12529-12533. DOI DOI 10.1002/anie.201103728.

310. Ernst, B.; Magnani, J. L., *Nat. Rev. Drug Discov.* 2009, 8 (8), 661-677.

311. Mehanna, A.; Mishra, B.; Kurschat, N.; Schulze, C.; Bian, S.; Loers, G.; Irintchev, A.; Schachner, M., *Brain* 2009, awp128.

312. Wang, M.; Lyu, Z.; Chen, G.; Wang, H.; Yuan, Y.; Ding, K.; Yu, Q.; Yuan, L.; Chen, H., *Chem. Commun.* 2015, 51 (84), 15434-15437.

313. Papy-Garcia, D.; Barbier-Chassefière, V.; Rouet, V.; Kerros, M.-E.; Klochendler, C.; Tournaire, M.-C.; Barritault, D.; Caruelle, J.-P.; Petit, E., *Macromolecules* 2005, 38 (11), 4647-4654.

314. Papy-Garcia, D.; Huynh, M. B.; Soussi-Yanicostas, N.; Vozari, R.; Sineriz, F.; Yanicostas, C., Method of diagnosis, prognostic or treatment of neurodegenerative diseases. Google Patents: 2014.
315. Ikeda, Y.; Charef, S.; Ouidja, M.-O.; Barbier-Chassefière, V.; Sineriz, F.; Duchesnay, A.; Narasimprakash, H.; Martelly, I.; Kern, P.; Barritault, D., *Biomaterials* 2011, 32 (3), 769-776.
316. Tong, M.; Zbinden, M. M.; Hekking, I. J.; Vermeij, M.; Barritault, D.; Van Neck, J. W., *Wound Repair. Regen.* 2008, 16 (2), 294-299.
317. Chevalier, F.; Lavergne, M.; Negroni, E.; Ferratge, S.; Carpentier, G.; Gilbert-Sirieix, M.; Sineriz, F.; Uzan, G.; Albanese, P., *Stem Cell Res.* 2014, 12 (3), 703-15. DOI 10.1016/j.scr.2014.03.001.
318. Frescaline, G.; Boudierlique, T.; Mansoor, L.; Carpentier, G.; Baroukh, B.; Sineriz, F.; Trouillas, M.; Saffar, J.-L.; Courty, J.; Lataillade, J.-J., *Tissue Eng Pt A* 2013, 19 (13-14), 1641-1653.
319. Barbier-Chassefière, V.; Garcia-Filipe, S.; Yue, X.; Kerros, M.; Petit, E.; Kern, P.; Saffar, J.; Papy-Garcia, D.; Caruelle, J.; Barritault, D., *Journal of Biomedical Materials Research Part A* 2009, 90 (3), 641-647.
320. Barritault, D.; Caruelle, J. In *Regenerating agents (RGTA): a new therapeutic approach*, *Ann. Pharm. Fr.*, 2006; pp 135-144.
321. Colombier, M.; Lafont, J.; Blanquaert, F.; Caruelle, J.; Barritault, D.; Saffar, J., *Cells Tissues Organs* 1999, 164 (3), 131-140.
322. Rouet, V.; Meddahi-Pellé, A.; Miao, H. Q.; Vlodysky, I.; Caruelle, J. P.; Barritault, D., *Journal of Biomedical Materials Research Part A* 2006, 78 (4), 792-797.
323. Friand, V.; Haddad, O.; Papy-Garcia, D.; Hlawaty, H.; Vassy, R.; Hamma-Kourbali, Y.; Perret, G.-Y.; Courty, J.; Baleux, F.; Oudar, O., *Glycobiology* 2009, 19 (12), 1511-1524.

324. Albanese, P.; Caruelle, D.; Frescaline, G.; Delbé, J.; Petit-Cocault, L.; Huet, E.; Charnaux, N.; Uzan, G.; Papy-Garcia, D.; Courty, J., *Exp. Hematol.* 2009, 37 (9), 1072-1083.
325. Papy-Garcia, D.; Albanese, P., *Glycoconj J* 2017, 34 (3), 377-391. DOI 10.1007/s10719-017-9773-8.
326. Holmes, B. B.; DeVos, S. L.; Kfoury, N.; Li, M.; Jacks, R.; Yanamandra, K.; Ouidja, M. O.; Brodsky, F. M.; Marasa, J.; Bagchi, D. P.; Kotzbauer, P. T.; Miller, T. M.; Papy-Garcia, D.; Diamond, M. I., *Proceedings of the National Academy of Sciences* 2013, 110 (33), E3138-E3147. DOI 10.1073/pnas.1301440110.

CHAPTER 2

ANODISATION OF MAGNETRON-SPUTTERED INDIUM-TIN OXIDE (ITO) FILMS

2.1 Preamble

During my first year, I was entirely dedicated to learning the basics of electrochemistry and electrodeposition so as to investigate the process of electrodeposition of poly(3,4-ethylenedioxythiophene) (PEDOT) conducting polymer materials and characterise them in terms of their physical, electrical and biological properties. Indium-tin oxide (ITO) was the conductive substrate selected for this preliminary work due to its low cost relative to platinum (Pt) materials, and thanks to the collaboration with Professor Donal Leech and his laboratory, Dr Manus Biggs and I began the journey of galvanostatic electrodeposition with a three-electrode set-up with the invaluable help of Dr Paul Kavanagh, a Senior Postdoc at that time in professor Donal Leech's lab. We were also assisted by the knowledge gained from the scientific reading of the well-known researchers in the field of conducting polymers and neural interfaces including Dr Rylie Green et al, Dr David Martin et al and Dr Collazos et al, to mention some.

At Professor Donal Leech's lab, I was given access to a very old but hardly used Potentiostat, a Princeton Applied Research electrochemical Potentiostat/Galvanostat model 263A running Verastudio software. At this stage, I was introduced by Dr Paul Kavanagh to the basic concepts of movement of ions and electron transfer in a three electrode set-up and how to operate the old machine. However, it was only after putting together the chemical data, obtained from the large amount of films made with this machine and submitting our work to a journal in the field, that I realised that certainly there were lots of matters to address; and while the comments were negative, they were extremely helpful in illuminating concepts such as overoxidation of the deposited films. In retrospect and in reviewing the set-up and by using our own Potentiostat acquired that year, I came to understand that the Princeton Applied Research electrochemical Potentiostat/Galvanostat model 263A was programmed

with a reversed electrode configuration. This resulted in the anodisation of the ITO films and not the electrodeposition of PEDOT. At that point, my electrochemistry experience could be summarised in a comment made to me by Professor Donal Leech in this desperate period: “electrochemistry can be a black hole at times”.

It may be true that the ITO process was confusing, frustrating and quite demotivating at the time, but in the end proved a valuable learning experience. Therefore, in celebration of serendipitous discovery and enlightening errors, the anodisation of ITO is described below. This work was not only crucial in helping to illuminate the basics of my work in conducting polymers, but also resulted in the generation of a bench-top electrochemical process to formulate anodised ITO films with altered roughness, conducting profiles and modulation of glial scar formation and neural network activity. Work which is still ongoing at the Biggs’ lab.

This chapter has been previously published in:

Vallejo-Giraldo, C.; Pampaloni, N. P.; Pallipurath, A. R.; Mokarian-Tabari, P.; O’Connell, J.; Holmes, J. D.; Trotier, A.; Krukiewicz, K.; Orpella-Aceret, G.; Pugliese, E., Ballerini, L; Kilcoyne, M; Dowd, E; Quinlan, Leo R; Pandit, Abhay; Kavanagh, Paul; and Biggs, M. J . Adv Funct Mater 2017. DOI: 10.1002/adfm.201605035

Important contribution was received from:

- Pampaloni, N., Ballerini, L.* performed the electrophysiological recordings and calcium imaging and substrate stimulation using Hippocampi cells.
- Mokarian-Tabari, P. O’Connell, J.; Holmes, J. D.* performed XPS analysis.
- Kilcoyne, M.*, contributed with the analytic tools for the construction of the antibody gliosis array.
- Quinlan, Leo R.* contributed with the analytic tools for the substrate stimulation using Ventral Mesencephalic cells.
- Kavanagh, Paul.* contributed with electrochemical analysis and important discussion of the electrochemical process of the anodised ITO films.
- *Lalor, Pierce.* performed transmission electron microscopy (TEM)

Hypothesis: ITO anodisation can be employed as a functionalisation approach to increase surface roughness and oxygen content for the generation of cytocompatible and functional thin-film electrode interfaces for neural applications.

2.2 Introduction

The modification of implantable electrodes for neural stimulation and recording through electrochemical, biochemical, morphological and topographical functionalisation has been a major focus of neural engineering over the past five years [1, 2]. A common occurrence following electrode implantation is reactive gliosis and the formation of a glial scar. This encapsulating scar forms at the electrode–tissue interface and accelerates neural loss, increases electrical signal impedance and thereby compromises the efficacy of a stimulating/recording system *in situ* [1]. Biomimetic interfaces with multiple functionalities that facilitate stable charge transfer *in vivo* while promoting enhanced cell interaction, selection and attachment are critical in chronic neuroelectrode functionality and the development of advanced neural stimulation systems and brain/machine interfaces [3]. In turn, important contributions in organic bioelectronics as neural interface platforms possessing favourable electrochemical properties for neural recording and stimulation have been reported [4-7].

Ongoing strategies in biomimetic design of the neural interface have focused on morphological, mechanical and biochemical modification of the electrode-tissue interface to reduce tissue damage and promote electrode integration through device miniaturisation, the development of flexible polymer systems and the localised delivery of anti-fibrotic or neurotropic chemistries [8, 9]. Traditionally, chemically inert conductors such as gold, platinum and iridium as well as semiconductors such as silicon have been widely employed as electrode systems in both clinical and research settings and have been found to perform well under non-chronic settings [10, 11]. Recently however, non-metallic electrically conducting materials including inherently conducting and semiconducting polymers and polymer composites have been explored as neuroelectrode alternatives in an effort to promote chronic functionality and enhanced biocompatibility [12, 13].

In the field of conducting metal oxide electronics, indium-tin oxide (ITO) is one of the most intensively investigated materials because of its relatively low electrical resistivity, its optical transparency and its thermal stability, making it well-suited for

use as an electrode or sensor material [14]. Specifically, ITO thin-films have been employed successfully in the fabrication of optoelectronic and electrochromic devices [15], electroluminescent devices [16], photovoltaic cells [17], and waveguide sensors [18].

Recent studies indicate the potential of electrically conducting ITO thin-films for biosensor applications *in vitro* [19-25]. Selvakumaran et al. [26] demonstrated the efficacy of ITO electrodes as sensing electrodes *in vitro* for bioassays, and potential physiological measurements. Here it was concluded that ITO offered a compromise between promoting cell growth while adsorbing significantly less protein than titanium control substrates [22, 27]. Further, Tanamoto and colleagues [21] developed micropatterned ITO glass electrode devices to facilitate electrical stimulation of neural cells coupled with fluorescent imaging processes. The device was observed to uniformly stimulate multiple single cells with and the authors noted potential *in vivo* applications.

It has been shown that ITO can be physically and chemically modified to locally tailor its electrical and optical and properties [28], and in particular, the modification of ITO electrodes with semiconducting polymer thin-films via electropolymerisation techniques have been explored as a method to enhance the electrode conductivity [28]. Further, surface treatments such as acid etching [29], and layer-by-layer assembly [30] have been used to modulate and alter the performance of ITO for commercial applications. Electrochemical activation or passivation via anodic oxidation (anodisation process) [31, 32] is widely used in biomedical engineering to grow metal oxide dielectrics for electrical devices [33, 34] and to obtain protective and decorative films on metallic surfaces to increase corrosion resistance [35]. The experimental conditions, i.e galvanostatic or potentiostatic anodisation deposition, electrolyte composition, and deposition time facilitate the oxidation of ions at the substrate-solution interface to produce thin-film coatings [36]. Several research groups [37-42] have demonstrated that the anodic oxidation technique can be employed in conjunction with mask strategies for the generation of biologically passive layers or nano features on titanium [37-42] and alumina [43, 44] to improve cell adhesion and implant integration. Surface modification of ITO via anodisation

however has not yet been explored as a method to enhance cytocompatibility, cell adhesion and functionality in implantable systems. Furthermore, the effects of ITO anodisation on film electrochemical impedance and topography remain unknown.

In this chapter, ITO anodisation as a functionalisation approach for the generation of cytocompatible and functional thin-film electrodes for potential neural applications is explored for the first time. Anodised ITO thin-films were formulated through a facile electrochemical process employing the application of current densities ranging from 0.4 mA cm^{-2} to 43 mA cm^{-2} . Subsequently, the physical, chemical, electrochemical and cytocompatibility effects of ITO anodisation were explored. Our results elucidate important material effects with regard to anodisation current densities on ITO film surface morphology, electrochemistry and cytocompatibility for the generation of neural interfaces with superior electrical and biological characteristics.

2.3 Materials and Methods

2.3.1 Anodic Oxidation of ITO

The anodic oxidation of ITO was conducted under ambient conditions in a solution of $10 \text{ }\mu\text{M}$ poly(sodium 4-styrenesulphonate) (PSS) (Sigma Aldrich, Ireland, $70,000 \text{ g mol}^{-1}$ MW) prepared in 1X phosphate-buffered saline solution (PBS) with a platinum foil as a counter electrode (cathode). The electrolyte solution was placed in an in-house fabricated electrochemical cell, connected to a Princeton Applied Research Potentiostat/Galvanostat model 2273 controlled with Power Suite software. Pristine ITO coated glass slides were purchased from Diamond Coatings, UK. These were provided as thin-films sputter-coated onto glass substrates with a nominal thickness of 750 nm and sheet resistivity of $8 - 10 \text{ Ohms sq}^{-1}$. Pristine ITO coated glass slides were individually cleaned in acetone, dried with a stream of nitrogen and moved to a desiccating chamber to remove moisture for 24 hours prior to use. Galvanostatic anodisation was performed applying constant current densities of 0.4 mA cm^{-2} , 4 mA cm^{-2} and 43 mA cm^{-2} over a constant time of 450 seconds to pristine ITO coated glass. A schematic representation of the anodisation process of the ITO is presented in *Figure 2.1*.

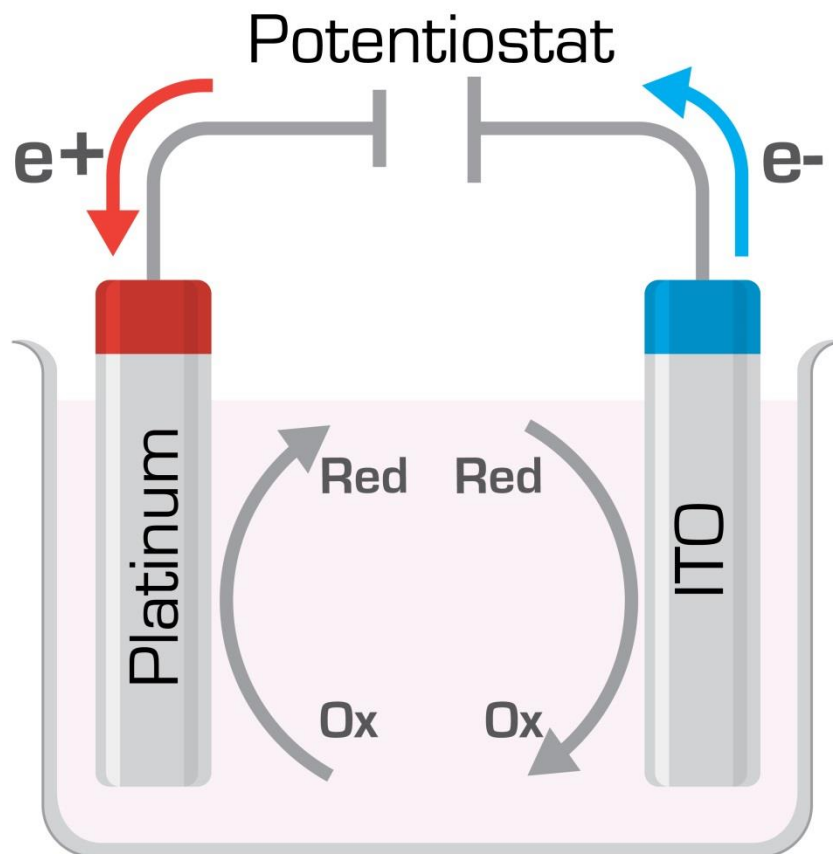


Figure 2.1 Schematic of the electrochemical set-up used for the anodisation process of ITO. Pristine ITO coated glass slides were placed at the anode electrode and constant current densities of 0.4 mA cm^{-2} , 4 mA cm^{-2} and 43 mA cm^{-2} over a constant time of 450 seconds were applied to pristine ITO coated glass through a PSS/PBS electrolyte. Within this process, hydrogen is released from the cathode (platinum) and oxygen forms on the surface of the anode (ITO) by the variation of the current densities (galvanostatic anodisation). This results in ITO oxide films growing on the ITO surface, called the anodised films.

2.3.2 Physical Characterisation

2.3.2.1 Surface Morphology

Scanning electron microscopy (SEM) was carried out using a Hitachi S-4700 Cold Field Emission Gun Scanning Electron Microscope (CFE-SEM). The SEM images

were taken using an accelerating voltage of 15 kV and spot current of 10 μ A. Gold sputtering was carried out before testing the samples using an EMSCOPE SC500 to deposit 10 nm of gold.

Atomic Force Microscopy (AFM) was performed to analyse the roughness of the samples. All measurements were taken on a Vico Dimension 3100 AFM using TESPA Tips (NanoWorld) (Si <8 nm tip radius, 42 N/m spring constant, 320 kHz nominal resonance frequency), in tapping mode over an area of 10 μ m² and 10 μ m² respectively with a 0.5 - 1 Hz scan rate.

Transmission Electron Microscopy (TEM) was performed using a H-7000 Electron Microscope to analyse inner particle distribution of the films. The samples were fixed into Epon base low viscosity resin (Agar Scientific R1078) so as to release the samples from the glass surface slide and be embedded in the resin. Thereafter, all samples were sectioned at 100 nm thickness and collected on Formvar-carbon 200 mesh copper grids (Agar Scientific – 62200N- 200 Square Mesh Nickel 3.95 mm). Images were taken at 75.kV with direct magnification of 20000x.

2.3.2.2 Thickness Measurements

The thickness of the anodised films was measured using a Zygo Newview 100 surface profilometer controlled by MicroPlus software. A pattern of bright and dark lines - fringes was created as incoming light was split from the limited region between the anodised film and the pristine ITO glass. This pattern difference was translated to calculate the height information, resulting in the thickness of the film. The size of the testing area was 1.6 cm².

2.3.2.3 UV- visible Spectroscopy

The optical transmittance of the ITO coated glass and the anodised films was assessed by using a Thermo Scientific Varios- Kan Flash microplate reader at the visible-light wavelengths (400–800 nm).

2.3.2.4 Stability and Durability through Accelerated Ageing Study

The stability of the pristine ITO glass and the anodised ITO films was determined using a long-term passive degradation through an accelerated ageing study.

Anodisation of Magnetron-Sputtered Indium-Tin Oxide (ITO) Films

Following the ASTM international guidelines for accelerated aging of medical devices [45] as well as the procedure detailed by Green et al. [46] and Hukins et al. [47], the experimental parameters were determined using *Equation 2. 1*.

$$t_{37} = t_T \times Q10^{(T-37)/10} \quad \text{Equation 2. 1}$$

where t_{37} is the simulated time at 37°C, t_T is time samples are placed at the elevated temperature, T is the elevated temperature, and $Q10$ is the accelerated factor equal to 2.0 as per the ASTM specification. Three experimental replicas for each group were placed in an oven at 95 °C and immersed in 0.9% saline for four weeks simulating 1560 days (four years) of implantation. Cyclic voltammetry was performed before and after the ageing study and used to calculate the percentage of loss in charge storage capacity (CSC). SEM pictures were taken after the ageing study to show morphological changes. The SEM sample preparation and imaging were performed following the details in 2.3.2.1 of this section.

2.3.3 Chemical Characterisation

X-ray photoelectron spectroscopy (XPS) spectra were acquired on an Oxford Applied Research Escabase XPS system equipped with a CLASS VM 100 mm mean radius hemispherical electron energy analyser with a triple-channel detector arrangement in an analysis chamber with a base pressure of 5.0×10^{-10} mbar. Survey scans were acquired between 0-1100 eV with a step size of 0.7 eV, dwell time of 0.5 s and pass energy of 100 eV. Core level scans were acquired at the applicable binding energy range with a step size of 0.1 eV, dwell time of 0.5s and pass energy of 50 eV averaged over 50 scans. A non-monochromated Mg- α x-ray source at 200 W power was used for all scans. All spectra were acquired at a take-off angle of 90° with respect to the analyser axis and were charge corrected with respect to the C1s photoelectric line by rigidly shifting the binding energy scale to 285 eV. Data were processed using CasaXPS software where a Shirley background correction was employed and peaks were fitted to Voigt profiles. To ensure accurate quantification, atomic sensitivity factors were taken from the instrument spectrum acquisition software and manually input into the data processing software.

2.3.4 Electrochemical Characterisation

2.3.4.1 Electrochemical Measurements

Cyclic voltammetry was performed using a CH Instruments 620 series potentiostat. Measurements were recorded in a custom-made electrochemical cell (2 mL volume) containing the pristine ITO coated glass as working electrode (1.6 cm²), an Ag/AgCl reference electrode (3 M KCl) (Bioanalytical Systems) and a platinum foil counter electrode (Goodfellow) in 50 mM phosphate buffer solution (pH 7.8) or saline solution [48]. Prior to measurements, solutions were purged with N₂ to avoid O₂ reduction at low potentials (< -0.4 V vs. Ag/AgCl).

Electrical impedance spectroscopy (EIS) was performed using a Princeton Applied Research Potentiostat/Galvanostat model 2273 running with Power Suite software with a four electrode set-up as described in [12]. Briefly, the signal was to the anodised films with a surface area of 1.6 cm², along with a platinum foil counter-electrode (CE) and controlled by a saturated Ag/AgCl reference electrode. An AC sine wave of 40 mV amplitude was applied with 0 V DC offset. The impedance magnitude and phase angle were calculated at 1, 10, 100, 1000, 10000 Hz, as it is reported that most of the neural cell communication occurs between 300 Hz and 1 kHz [49].

Values were presented on Bode and Nyquist plots and compared to those of a pristine ITO coated glass slide and to bare gold coated glass. The data fitting analysis was performed using EIS Spectrum Analyser 1.0 software.

2.3.5 Biological Characterisation

2.3.5.1 Cell Culture

The human neuroblastoma cell line SH-SY5Y was cultured in Dulbecco's Modified Eagles Medium nutrient mixture F12 (DMEM/F12) medium and supplemented with 10% fetal bovine serum (FBS), 1% penicillin/streptomycin and all-trans retinoic acid (RA) at a final concentration of 10 µM for differentiation into a neuronal phenotype. Immunofluorescence micrographs showing the neuronal phenotype of SH-SY5Y as a response to RA supplementation are shown in **Figure 2.2**

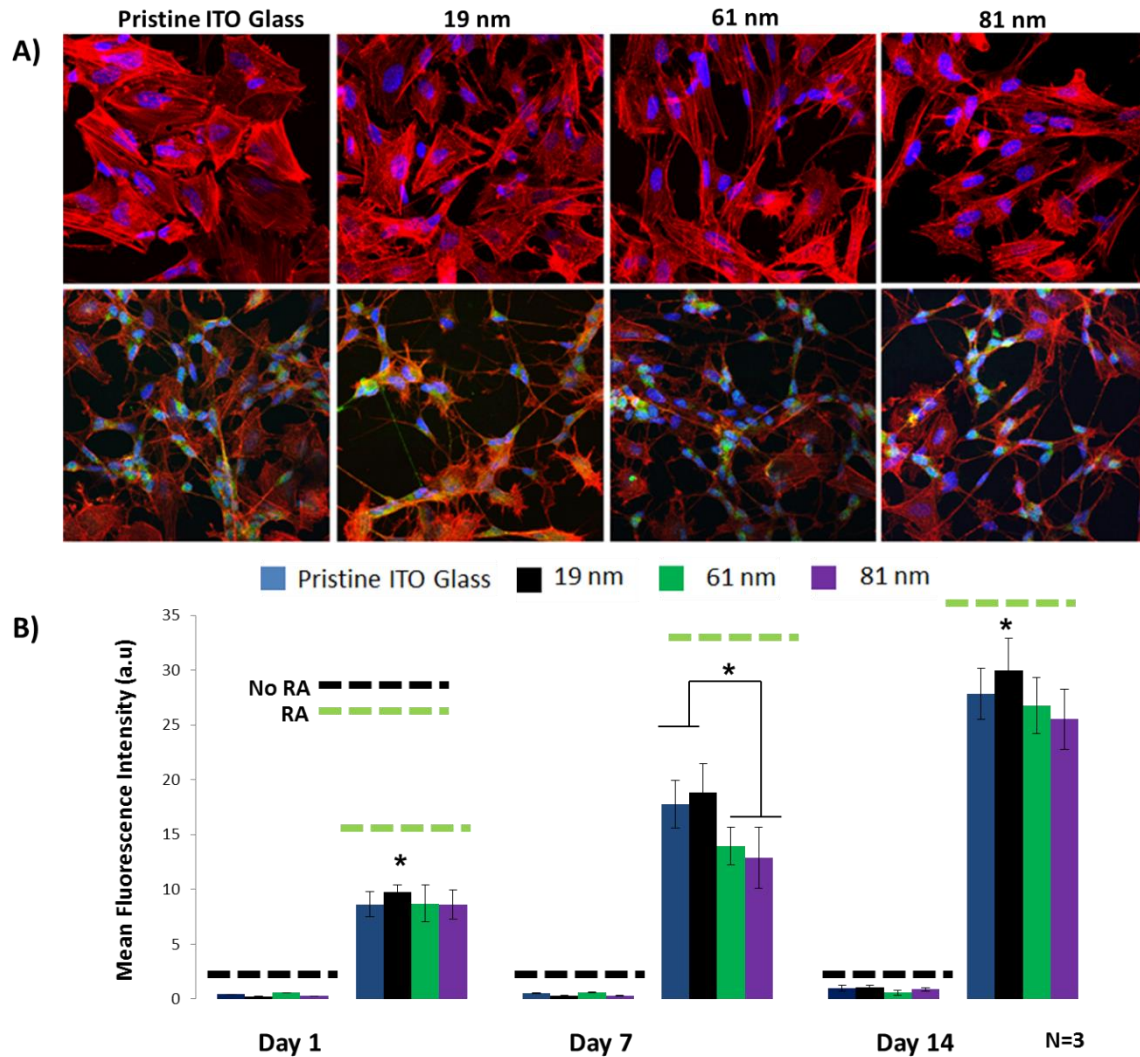


Figure 2.2 Expression of dopamine in SH-SY5Y neuroblastoma cell line. A) Fluorescent micrographs of immune-labelled cultures at day fourteen on pristine ITO glass and anodised ITO films with resulting roughness of 19 nm, 61 nm and 81nm. No RA supplementation (top) with RA supplementation films (bottom). Scale bar = 20 μ m, objective 60 \times . Dopamine expression is visualised by anti- Anti-Tyrosine Hydroxylase (TH) in green, F-actin in red by rhodamine-conjugated phalloidin and in blue nuclei by DAPI. B) Mean fluorescence intensity quantification of dopamine expression using a threshold method. The TH dopamine marker was significantly upregulated following fourteen days of RA exposure, coupled with the induction of a neuronal phenotype. In addition, TH dopamine mean fluorescence intensity was significantly increased by day fourteen on the cells cultured on anodised films with

the lowest roughness profile of 19 nm, which corresponds to the films formed at 0.4 mA cm⁻² current density compared to control and the other experimental groups. Results are ± STD, ★ = p < 0.05.

To control the surface area of culture, the pristine ITO coated glass and the anodised films were placed in customised silicone Ace O-rings with wall dimension of 1.78 mm and internal diameter (I.D) of 10.8 mm and were sealed around the borders of the surface area with silicone elastomer (Sylgard 184). The materials were placed in six well culture plates and sterilised by 100% ethanol for two hours, and subsequently washed repeatedly with Hank's balanced salt solution (HBSS) and incubated overnight at 37°C, 5% CO₂ for neural cell culture. A quantity of 50,000 or 2,000 cells cm⁻² was plated on each film, and then 200 µl of the culture medium was added to each well, and changed with fresh media every day for a period of one, seven or fourteen days. Control Thermanox® Plastic Coverslips with 13 mm diameter (NUNC™ brand products) were also bonded with silicone Ace O-rings as above.

Primary hippocampal cultures were prepared from two-three days postnatal (P₂-P₃) rats as previously reported by Cellot et al. [50]. Briefly, hippocampi were dissected and enzymatically digested. Cells were plated on poly-L-ornithine coated glass coverslips (control) or on anodised ITO substrates formed at 0.4 mA cm⁻² current density. Coverslips were placed in petri dishes and cultured in serum-containing medium in a 5% CO₂- humidified incubator for eight to ten days. Cell morphology was analysed by immunofluorescence experiments and epifluorescence microscopy to gain insights into cell health and shape. Briefly, cell densities were quantified at 20× (0.5 NA) magnification using a DM6000 Leica microscope (Leica Microsystems GmbH, Wetzlar, Germany), with random sampling of visual fields (713 × 532 µm).

Ethical Statement (Primary hippocampal cultures)

All experiments were performed in accordance with the EU guidelines (2010/63/UE) and Italian law (decree 26/14) and were approved by the local authority veterinary service and by our institution (SISSA-ISAS) ethical committee. Every effort was made to minimise animal suffering and to reduce the number of animals used. Animal

use was approved by the Italian Ministry of Health, in accordance with the EU Recommendation 2007/526/CE.

Primary cultures of ventral mesencephalic neurons (VM) were obtained from the mesencephalon of embryonic Sprague–Dawley rats in accordance with methods previously described by Vallejo-Giraldo et al. [12]. Briefly, the ventral mesencephalon were dissected from embryonic fourteen-day rat brains and then mechanically dissociated with a pipette, until the tissue was dispersed. Cells were grown in a humidified atmosphere of 5% CO₂ at 37°C and culture in media (Dulbecco's modified Eagle's medium/F12, 33 mM D-glucose, 1 % L-glutamine, 1% PS, 1 % FCS, supplemented with 2 % B27). The pristine ITO glass and the anodised films were cultured for 21 days in six well culture plates and sterilised in 70% ethanol for two hours, and subsequently washed repeatedly with HBSS. They were then rinsed three times with distilled (DI) water and left to dry overnight. A quantity of 50,000 cells cm⁻² was plated on each film, and then 3 ml of the culture medium was added to each well and changed with fresh media every two days for a period of 21 days.

2.3.5.2 Metabolic Analysis

The alamarBlue® Assay (Life Technologies, UK) was used to assess cell metabolism and was carried out at day one, day seven and day fourteen. For this purpose, 10% of the alamarBlue® solution was added to the culture media, in accordance with the provided protocols. Sample absorbance was measured in a 96 well plate at 544 excitation and 590 emission wave lengths using a Thermo Scientific Varios- Kan Flash microplate reader.

2.3.5.3 Immunofluorescent Labelling

Indirect double-immunofluorescent labelling was performed to visualise focal adhesion sites. SH-SY5Y cells on experimental and control substrates were fixed with 4% paraformaldehyde and 1% of sucrose for fifteen minutes at room temperature (RT) at each time point. Once fixed, the samples were washed with PBS and permeabilised with buffered 0.5% Triton X-100 within a buffered isotonic solution (10.3 g sucrose, 0.292 g NaCl, 0.06 g MgCl₂, 0.476 g HEPES buffer, 0.5 ml

Triton X-100, in 100 ml water, pH 7.2) at 4°C for five minutes. Non-specific binding sites were blocked with 1% bovine serum albumin (BSA) in PBS at 37°C for five minutes and subsequently incubated for two hours with a 1:100 concentration anti-vinculin (Rb mAb to Paxillin (Y113) (Life Technologies, 1:100). Samples were washed three times with 0.05% Tween 20/PBS and then incubated for one hour in the secondary antibody Alexa Fluor® 488 goat anti-Rabbit IgG (H+L) (Life Technologies, 1:100) combined with rhodamine-conjugated phalloidin (Life Technologies, 1:100) to stain F-actin. Non-specific charges (e.g. remaining aldehyde) were neutralised with 0.5% Tween 20/PBS (5 min ×3) to minimise background labelling. Samples were mounted on microscope cover slides and counterstained with slowfade^R gold antifade reagent with DAPI for nuclear staining.

For immunofluorescence experiments on primary hippocampal neurons, cultures were fixed with 4% formaldehyde (prepared from fresh paraformaldehyde) in PBS for 60 minutes at RT and then washed in PBS. The samples were permeabilised with 0.3% Triton X-100 and subsequently incubated with primary antibodies for 30 min at RT, washed with PBS and incubated with secondary antibodies for 45 minutes. Cultures were then mounted in Vectashield (Vector Laboratories) on 1 mm thick microscope slides. To visualise neurons, rabbit anti β -tubulin III, 1:250 (Sigma), primary antibody was used and Alexa 594 goat anti rabbit secondary antibody, 1:500 (Invitrogen); to visualise astrocytes mouse anti Glial-Fibrillary acidic protein (GFAP) 1:250 (Sigma) primary antibody was used and Alexa 488 goat anti mouse secondary antibody 1:500 (Invitrogen), and Hoechst 1:10000 (Invitrogen) was used to visualise cell nuclei.

Expression of dopamine by the presence of tyrosine hydroxylase (TH) in human neuroblastoma cell line SH-SY5Y cultures was evaluated by indirect double-immunofluorescent labelling as detailed for the visualisation of focal adhesion sites in this section. SH-SY5Y cells on experimental and control ITO substrates were incubated for two hours with a 1:1000 concentration of Anti-Tyrosine Hydroxylase (TH) (MAB318, Merck Millipore, 1:1000) washed three times with 0.05% Tween 20/PBS and then incubated for one hour in the secondary antibody Alexa Fluor® 488

Anodisation of Magnetron-Sputtered Indium-Tin Oxide (ITO) Films

(Life Technologies, 1:1000) combined with rhodamine-conjugated phalloidin (Life Technologies, 1:100) to stain F-actin. Samples were mounted on microscope cover slides and counterstained with slowfade^R gold antifade reagent with DAPI for nuclear staining.

2.3.5.4 Microscopy and Image Analysis

After immunostaining, samples were viewed with an Olympus IX 81 fluorescence microscope with filters for FITC (excitation 490 nm; emission 520 nm), Texas Red (excitation 596 nm; emission 615 nm) and DAPI (excitation 358 nm; emission 461 nm). At least twenty randomly selected images at 60 \times magnification were taken from each test group and the control group. The total number of focal adhesion points per cell and their length were quantified by direct scoring with a 4 pixel-wide line on the FITC channel as previously described in [51] using ImageJ software (National Institutes of Health, USA) (*Figure 2.3*).

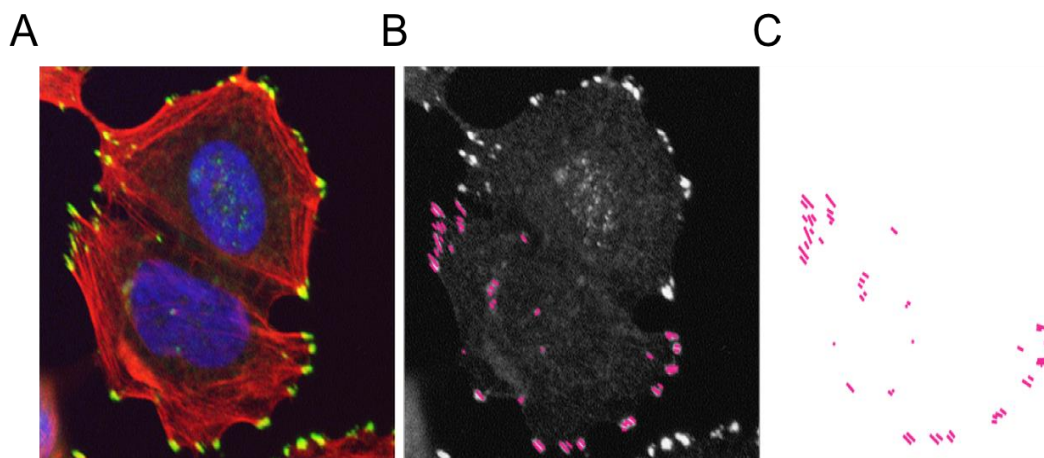


Figure 2.3 Methodology of focal adhesion (FA) analysis through ImageJ. Cells were labelled with anti-paxillin for FA imaging (Green), rhodamine conjugated phalloidin for actin imaging (red) and DAPI for nuclear imaging (blue) A. The paxillin channel was subsequently isolated and individual FA sites were scored with a 4 pixel wide line B. The individual lines were analysed by length and number C. as described previously in [51].

Anodisation of Magnetron-Sputtered Indium-Tin Oxide (ITO) Films

Cell densities were quantified at 20× (0.5 NA) magnification using a DM6000 Leica microscope (Leica Microsystems GmbH, Wetzlar, Germany), with random sampling of seven to ten fields (713 × 532 μm; control and anodised film, N=3 culture series).

2.3.6 Protein Antibody Microarray

2.3.6.1 Protein Extraction

For protein extraction and collection, samples were carefully placed on ice and the cells were washed twice with cold PBS. After the complete aspiration of cold PBS, 100 μl of cold lysis buffer was added. The lysis buffer was composed of RIPA lysis buffer (Sigma) supplemented with 1% of protease inhibitors (Life Science-Roche) and 1% of phosphatase inhibitors cocktails I & III (Sigma). Thereafter, the adherent cells were scraped off using Corning® cell scrapers (Sigma) and then the cell suspension was gently transferred into microcentrifuge tubes and placed on ice. Microcentrifuge tubes were centrifuged for fifteen minutes at 14000 rpm at 4°C, and afterwards gently removed from the centrifuge and placed on ice. Without disturbing the pellet, the supernatant was carefully aspirated and placed in a fresh clean tube, kept on ice, and stored at -80 °C to be quantified. The pellet was discarded.

2.3.6.2 Protein Quantification of Cell Lysates

Protein quantification of the VM cell lysates collected from pristine ITO glass and the ITO anodised films was done using Bio-Rad Protein Assay Dye Reagent (#5000006). As per manufacturer's instructions, the dye working solution was prepared and filtered in a concentration of 1:4 in distilled water followed by the preparation of protein standard BSA at concentrations of 0.25 mg ml⁻¹, 0.5 mg ml⁻¹, 0.75 mg ml⁻¹ and 0.9 mg ml⁻¹. After this, 5 μl of each BSA standard and sample solution were mixed in a clean, dry tube together with 250 μl of dye working solution. This solution was vortexed and incubated for five minutes at RT and finally read using NanoDrop 8000 software with the Protein Bradford module.

2.3.6.3 Construction of Gliosis Antibody Microarray

Nexterion® slide H microarray slides were purchased from Schott AG (Mainz, Germany). Alexa Fluor® 555 carboxylic acid succinimidyl ester was obtained from Life Technologies (Carlsbad, CA, USA).

Protein samples were labelled with Alexa Fluor® 555 carboxylic acid succinimidyl ester according to manufacturer's instructions. Excess label was removed and buffer was exchanged with PBS, pH 7.4 by centrifugation through 3 kDa molecular weight cut off filters. Absorbance at 555 and 280 nm was measured for labelled samples and calculations were performed according to manufacturer's instructions using an arbitrary extinction coefficient of 100,000 and molecular mass of 100,000 to enable quantification of relative protein concentration and label substitution efficiency.

All commercial antibodies (**Table 2.1**) were buffer exchanged in to PBS and quantified by bicinchoninic acid BCA assay [52]. Antibodies were diluted to print concentration in PBS and printed in six replicates on Nexterion® H amine reactive, hydrogel coated glass slides using a SciFLEXARRAYER S3 piezoelectric printer (Scienion, Berlin, Germany) under constant humidity (62% +/- 2%) at 20 °C. Each feature was printed using approximately 1 nL of diluted antibody utilising an uncoated 90 µm glass nozzle with eight replicated subarrays per microarray slide. After printing, slides were incubated in a humidity chamber overnight at room temperature to facilitate complete conjugation. The slides were then blocked in 100 mM ethanolamine in 50 mM sodium borate, pH 8.0, for one hour at RT. Slides were washed in PBS with 0.05% Tween® 20 three times for two minutes each wash followed by one wash in PBS, dried by centrifugation (470 x g, five minutes) and then stored with desiccant at 4 °C until use.

Table 2.1 Summary of the commercial antibodies used for the construction of gliosis antibody microarray

Order	Probe	Conc (mg/mL)	Information	Company	Catalogue Number
1	Anti-Glial Fibrillary Acidic Protein (GFAP)	0.25	Mouse anti-rat immunoglobulins, monoclonal	Sigma®	G3893
2	nestin (Rat-401)	1	Mouse anti-rat immunoglobulins, monoclonal	SantaCruz®	sc-33677
3	nestin (Rat-401)	0.5	Mouse anti-rat immunoglobulins, monoclonal	SantaCruz®	sc-33677
4	nestin (Rat-401)	0.25	Mouse anti-rat immunoglobulins, monoclonal	SantaCruz®	sc-33677
5	CD81 (H-121)	1	Rabbit anti-rat immunoglobulins, polyclonal	SantaCruz®	sc-9158
6	CD81 (H-121)	0.5	Rabbit anti-rat immunoglobulins, polyclonal	SantaCruz®	sc-9158
7	CD81 (H-121)	0.25	Rabbit anti-rat immunoglobulins, polyclonal	SantaCruz®	sc-9158
8	Integrin alphaM (OX42)	1	Mouse anti-rat immunoglobulins, monoclonal	SantaCruz®	sc-53086
9	Integrin alphaM (OX42)	0.5	Mouse anti-rat immunoglobulins, monoclonal	SantaCruz®	sc-53086
10	Integrin alphaM (OX42)	0.25	Mouse anti-rat immunoglobulins, monoclonal	SantaCruz®	sc-53086
11	Anti Iba1	2.5	Rabbit anti-rat immunoglobulins, polyclonal	WAKO®	019-19741
12	Anti Iba1	1	Rabbit anti-rat immunoglobulins, polyclonal	WAKO®	019-19741
13	Anti Iba1	0.5	Rabbit anti-rat immunoglobulins, polyclonal	WAKO®	019-19741
14	Anti Iba1	0.25	Rabbit anti-rat immunoglobulins, polyclonal	WAKO®	019-19741
15	Anti Iba1	0.1	Rabbit anti-rat immunoglobulins, polyclonal	WAKO®	019-19741
16	Paxillin antibody [Y113]	1	Rabbit anti-rat immunoglobulins, monoclonal	Abcam	ab32084
17	Paxillin antibody [Y113]	0.5	Rabbit anti-rat immunoglobulins, monoclonal	Abcam	ab32084
18	Paxillin antibody [Y113]	0.25	Rabbit anti-rat immunoglobulins, monoclonal	Abcam	ab32084
19	cleaved spectrin alpha II (h1186)	0.5	Rabbit anti-rat immunoglobulins, polyclonal	SantaCruz®	sc-23464
20	cleaved spectrin alpha II (h1186)	0.25	Rabbit anti-rat immunoglobulins, polyclonal	SantaCruz®	sc-23464
21	cleaved spectrin alpha II (h1186)	0.1	Rabbit anti-rat immunoglobulins, polyclonal	SantaCruz®	sc-23464
22	Anti-Smad3 antibody [EP568Y]	1	Rabbit anti-rat immunoglobulins, monoclonal	Abcam	ab40854
23	Anti-Smad3 antibody [EP568Y]	0.5	Rabbit anti-rat immunoglobulins, monoclonal	Abcam	ab40855
24	Anti-Smad3 antibody [EP568Y]	0.25	Rabbit anti-rat immunoglobulins, monoclonal	Abcam	ab40856
25	Anti-Chondroitin Sulfate antibody	0.1	Mouse anti-rat immunoglobulins, monoclonal	Sigma®	C8035
26	Anti-Chondroitin Sulfate antibody	0.05	Mouse anti-rat immunoglobulins, monoclonal	Sigma®	C8036
27	PBS		Phosphate buffered saline, pH 7.4		
28	Anti-rat_0.5	0.5	Rabbit anti-rat immunoglobulins, polyclonal	DAKO	
29	Anti-sheep_0.5	0.5	Rabbit anti-sheep immunoglobulins, polyclonal	DAKO	
30	VR1 (H-150)	1	Rabbit anti-human immunoglobulins, polyclonal	SantaCruz®	sc-20813
31	VR1 (H-150)	0.5	Rabbit anti-human immunoglobulins, polyclonal	SantaCruz®	sc-20813

Anodisation of Magnetron-Sputtered Indium-Tin Oxide (ITO) Films

Order	Probe	Conc (mg/mL)	Information	Company	Catalogue Number
32	VR1 (H-150)	0.25	Rabbit anti-human immunoglobulins, polyclonal	SantaCruz®	sc-20813
33	VR1 (H-150)	0.1	Rabbit anti-human immunoglobulins, polyclonal	SantaCruz®	sc-20813
34	Anticorps L-type Ca++ CP α1C (H-280)	1	Rabbit anti-human immunoglobulins, polyclonal	SantaCruz®	sc-25686
35	Anticorps L-type Ca++ CP α1C (H-280)	0.5	Rabbit anti-human immunoglobulins, polyclonal	SantaCruz®	sc-25686
36	Anticorps L-type Ca++ CP α1C (H-280)	0.25	Rabbit anti-human immunoglobulins, polyclonal	SantaCruz®	sc-25686
37	Anticorps L-type Ca++ CP α1C (H-280)	0.1	Rabbit anti-human immunoglobulins, polyclonal	SantaCruz®	sc-25686
38	PIEZO1 Antibody (N-15)	1	Goat anti-human immunoglobulins, monoclonal	SantaCruz®	sc-164319
39	PIEZO1 Antibody (N-15)	0.5	Goat anti-human immunoglobulins, monoclonal	SantaCruz®	sc-164319
40	PIEZO1 Antibody (N-15)	0.25	Goat anti-human immunoglobulins, monoclonal	SantaCruz®	sc-164319
41	PIEZO1 Antibody (N-15)	0.1	Goat anti-human immunoglobulins, monoclonal	SantaCruz®	sc-164319
42	PIEZO2 Antibody (G-20)	1	Rabbit anti-human immunoglobulins, polyclonal	SantaCruz®	sc-84763
43	PIEZO2 Antibody (G-20)	0.5	Rabbit anti-human immunoglobulins, polyclonal	SantaCruz®	sc-84763
44	PIEZO2 Antibody (G-20)	0.25	Rabbit anti-human immunoglobulins, polyclonal	SantaCruz®	sc-84763
45	PIEZO2 Antibody (G-20)	0.1	Rabbit anti-human immunoglobulins, polyclonal	SantaCruz®	sc-84763
46	ANKTM1 (C-19)	1	Goat anti-human immunoglobulins, polyclonal	SantaCruz®	sc-32353
47	ANKTM1 (C-19)	0.5	Goat anti-human immunoglobulins, polyclonal	SantaCruz®	sc-32353
48	ANKTM1 (C-19)	0.25	Goat anti-human immunoglobulins, polyclonal	SantaCruz®	sc-32353
49	ANKTM1 (C-19)	0.1	Goat anti-human immunoglobulins, polyclonal	SantaCruz®	sc-32353
50	TREK-1 Antibody (C-20)	1	Goat anti-human immunoglobulins, polyclonal	SantaCruz®	sc-11557
51	TREK-1 Antibody (C-20)	0.5	Goat anti-human immunoglobulins, polyclonal	SantaCruz®	sc-11557
52	TREK-1 Antibody (C-20)	0.25	Goat anti-human immunoglobulins, polyclonal	SantaCruz®	sc-11557

Incubations were carried out under dark conditions. Microarray slides were incubated as previously described [53]. Initially, one labelled sample was titrated (2.5 - 15 $\mu\text{g mL}^{-1}$) for optimal signal to noise ratio and all samples were subsequently incubated for one hour at 23 °C at 5 $\mu\text{g mL}^{-1}$ in Tris-buffered saline (TBS; 20 mM Tris-HCl, 100 mM NaCl, 1 mM CaCl₂, 1 mM MgCl₂, pH 7.2) with 0.05% Tween® 20 (TBS-T). All microarray experiments were carried out using three replicate slides. Alexa Fluor® 555 labelled healthy rat brain lysate (5 $\mu\text{g mL}^{-1}$) and soybean agglutinin (SBA) lectin (10 $\mu\text{g mL}^{-1}$) were incubated in two separate subarrays on every slide to confirm retained antibody performance and printing, respectively (**Figure 2.4**). After incubation, slides were washed three times in TBS-T for two minutes per wash, once

Anodisation of Magnetron-Sputtered Indium-Tin Oxide (ITO) Films

in TBS and then centrifuged dry as above. Dried slides were scanned immediately on an Agilent G2505 microarray scanner using the Cy3 channel (532 nm excitation, 90% PMT, 5 μm resolution) and intensity data was saved as a .tif file. Antibody microarrays were verified to remain active for at least two weeks after printing and all incubations were carried out within that timeframe.

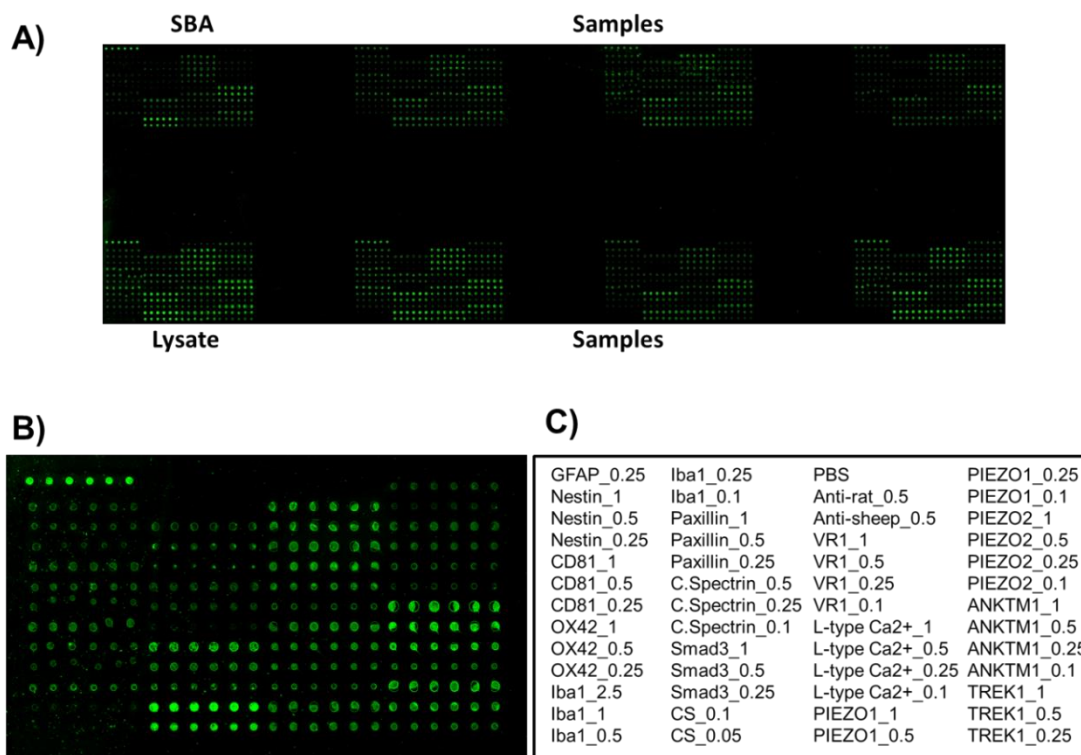


Figure 2.4 Representative images from slides surface chemistries. A) Microarray experiments were carried out using three replicate slides. Alexa Fluor® 555 labelled healthy rat brain lysate ($5 \mu\text{g mL}^{-1}$) and soybean agglutinin (SBA) lectin ($10 \mu\text{g mL}^{-1}$) were used as internal controls and incubated in two separate subarrays on every slide to confirm retained antibody performance and printing, respectively. B). Individual representation image from a slide surface chemistry showing the subarrays. The subarrays were incubated and printed with each antibody following the order detailed in C) at a range of concentrations of 0.1 to 1 mg mL^{-1} .

Data extraction from .tif files was performed as previously described [53]. Data were normalised to the mean of three replicate microarray slides (subarray by subarray using subarray total intensity, $N = 3$, 18 data points). Unsupervised hierarchical

clustering of normalised data was performed using Hierarchical Clustering Explorer v3.0 (<http://www.cs.umd.edu/hcil/hce/hce3.html>) using the parameters no pre-filtering, complete linkage, and Euclidean distance. Statistical analysis was performed as detailed in the experimental section 2.3.9.

2.3.7 Electrophysiological Recordings

Single whole-cell recordings were obtained at RT with pipettes (5-7 M Ω) containing (in mM): 120 K gluconate, 20 KCl, 10 HEPES, 10 EGTA, 2 MgCl₂, 2 Na₂ATP, pH 7.3; osmolarity was adjusted to 300 mOsm. The extracellular solution contained (in mM): 150 NaCl, 4 KCl, 1 MgCl₂, 2 CaCl₂, 1 MgCl₂, 10 HEPES, 10 glucose (all Sigma), pH 7.4. Coverslips with cultures were positioned in a Perspex chamber mounted on an inverted microscope (Eclipse TE-200, Nikon, Japan). Data were collected by Multiclamp 700B patch amplifier (Axon CNS, Molecular Devices) and digitised at 10 kHz with the pClamp 10.2 acquisition software (Molecular Devices LLC, US). The spontaneous synaptic activity was recorded clamping the membrane voltage at -56 mV holding potential (not corrected for liquid junction potential that was 14 mV). All recorded events were analysed off-line with the AxoGraph 1.4.4 (Axon Instrument) event detection software (Axon CNS, Molecular Devices)

2.3.8 Calcium Imaging and Substrate Stimulation

Stimulation of anodised films formed at 0.4 mA cm⁻² was performed with two different primary cultures: primary cultures of ventral mesencephalic neurons (embryonic primary culture) and primary hippocampal neurons (mature primary culture).

Changes in intracellular calcium ([Ca²⁺]_i) of VM neurons were measured as described previously [12]. Briefly, cells grown on pristine ITO glass as a control and on ITO anodised films formed at 0.4 mA cm⁻² were loaded with the calcium-sensitive fluorescent probe Fluo-4 AM (Life Technologies) (5 μ M in DMSO) for 30 minutes at 37°C, washed, followed by 30 minutes at 37°C in the dark. After dye loading was completed, cells were bathed in culture media (Dulbecco's modified Eagle's medium/F12, 33 mM D-glucose, 1 % L-glutamine, 1% PS, 1 % FCS, supplemented with 2 % B27) and transferred to a custom built chamber that allowed electrical

stimulation to be applied directionally to the films. Stimulation was achieved by the delivery of biphasic voltage pulses, using a software controlled constant voltage stimulator (AD Instruments, LabChart 7 software) connected to the custom built chamber via Pt contacts. The chamber was mounted on the stage of a Zeiss Axiovert 200 inverted microscope. The microscope was equipped with a 10 position Orbit I filterwheel (Improvision), for excitation (488nm) and emission (510nm LP filter). The emission light was collected every second with an Orca 285 camera (Hamamatsu). The system was controlled by the Openlab system version 5.5. Changes in Ca^{2+}_i in response to external electrical stimulation were expressed as changes in background subtracted fluorescence intensity expressed as $\Delta F/F_0$ (F_0 is the baseline fluorescence level and ΔF is the rise over baseline).

For Ca^{2+} imaging experiments using primary hippocampal neurons, cultures were loaded with cell permeable Ca^{2+} dye Oregon Green 488 BAPTA-1 AM (Molecular Probes) in DMSO (Sigma-Aldrich) with a final concentration of 4 μM for twenty minutes at 37°C in the cell culture incubator [54]. The samples were then placed in a recording chamber mounted on an inverted microscope (Nikon TE-200) where they were continuously superfused at RT with the extracellular solution (see 2.3.7 Electrophysiological Recordings). Cultures were observed with a 20 \times objective (0.45 NA, PlanFluor, Nikon). Images (1024 \times 1024 pixels) were acquired continuously for seven minutes (at 6.67 frame/seconds) by a Hamamatsu Orca-Flash 4.0 digital camera, exciting the Ca^{2+} -dye with a 488 nm wavelength light generated by a mercury lamp. Excitation light was separated from the light emitted from the sample using a 395 nm dichroic mirror and ND filter (1/16). Images of emitted fluorescence >480 nm were displayed on a colour monitor controlled by an integrating imaging software package (HC Image, Hamamatsu) using a personal computer. Recorded images were analysed off-line with the Clampfit software (pClamp suite, 10.2 version; Axon Instruments). Intracellular Ca^{2+} transients were expressed as fractional amplitude increase ($\Delta F/F_0$, where F_0 is the baseline fluorescence level and ΔF is the rise over baseline); the onset time of neuronal activation was determined by detecting those events in the fluorescence signal that exceed at least five times the standard deviation of the noise. For stimulation, voltage stimuli were delivered using a Constant Voltage

Isolated Stimulator (DS2A-Mk.II, Digitimer, England) connected to silver electrodes through insulated silver wires. One electrode was placed in contact with the upper part of the anodised film formed at 0.4 mA cm^{-2} or glass (control) sample in a dry environment; the reference electrode was in the extracellular solution. Under such conditions, neurons could only be extracellularly stimulated through the electrolyte-anodised film interface. During Ca^{2+} imaging recording session, 500ms long high-voltages were delivered (1/60 seconds).

2.3.9 Statistical Analysis

All data presented here was confirmed using at least three replicates for each of the test groups and control group. The results are expressed as the mean of the values \pm standard error of the mean. One-way ANOVA followed by a Bonferroni test were performed to determine the statistical significance ($p < 0.05$), unless otherwise stated.

For the hippocampal cultures electrophysiology and immunofluorescence analysis, all values from samples subjected to the same experimental protocols were pooled and expressed as mean \pm S.D. with N=number of cells, unless otherwise specified. Where not otherwise indicated, statistically significant differences between datasets were assessed by Student's t test (after validation of variances homogeneity by Levene's test) for parametric data at a minimum significance level of $p < 0.05$.

2.4 Results and Discussion

When subjected to anodic [55-59] and cathodic [58-61] polarisation, ITO electrodes undergo changes in chemical composition [55-61], surface morphology [55, 56, 58-61], conductivity [55, 56, 58-61] and optical transparency [57-61]. Such effects are largely influenced by i) the electrochemical parameters selected for electrode polarisation and ii) composition of the electrolyte solution [55-61]. For example, polarisation at high positive potentials ($> 1.5 \text{ V}$ vs. saturated calomel electrode (SCE)) in aqueous electrolyte can cause substantial structural changes to the ITO electrode [61]. Similarly, polarisation in strong acid (1 M HNO_3) or strong base (1 M NaOH) can result in a dramatic reduction in electrochemical activity, electrical conductivity and optical transparency of the ITO electrode [61]. Such effects are normally attributed to structural and/or chemical changes within the ITO film induced

by the polarisation process [55, 56], which, under harsh electrochemical conditions, may result in partial or complete dissolution of ITO coating [55-59].

In this chapter a method for the facile fabrication of bioactive ITO substrates with enhanced electrochemical properties as neural interfaces is reported. Due to the detrimental effects on ITO films resulting from anodisation in harsh chemical conditions detailed above, the anodisation process was performed in a relatively mild electrolyte consisting of PBS and 10 μM PSS. Constant current densities of 0.4 mA cm^{-2} , 4 mA cm^{-2} and 43 mA cm^{-2} applied for 450 seconds were used to prepare modified ITO films through anodisation in this electrolyte. The optimisation process of the current densities employed in this work are indicated in **Figure 2.5**.

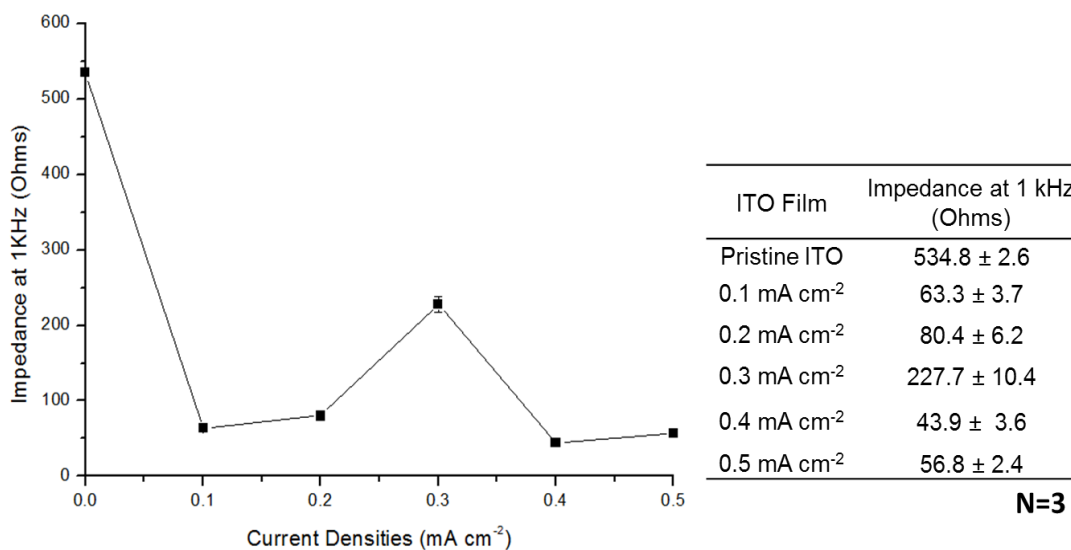


Figure 2.5 Optimisation of current densities lower than 0.4 mA cm^{-2} through the impedance measurements at 1 kHz. Left, Plot of impedance magnitudes at 1 kHz of pristine ITO control and anodised films formed using current densities between 0.1 mA cm^{-2} and 0.5 mA cm^{-2} . Right, tabulated impedance magnitude values measured at 1 kHz for each of the films formed between 0.1 mA cm^{-2} and 0.5 mA cm^{-2} current densities. Overall, the anodised films formed at 0.4 mA cm^{-2} current density showed the lowest impedance magnitude at 1 kHz.

2.4.1 Physical Characterisation of Anodised ITO Films

Systematic studies of thin-film ITO post-deposition processing in optoelectronic device fabrication have focused on the processing effects on surface roughness and on the generation of defined nanostructures. To a great extent, techniques such as chemical-bath deposition (CBD) [62] and thermal annealing [63] respectively have been utilised to modify film physicochemical properties with resulting films showing considerable morphological changes which translate into the optical transmittance and electrical conductivity. While a number of studies have explored anodisation processes to produce micro-porous titanium oxide films on implant surfaces for orthopedic applications [64], the impact of anodisation on the physical properties of ITO substrates for neural interfaces has not been investigated thus far.

Figure 2.6A shows representative SEM images of anodised ITO films using 0.4 mA cm^{-2} , 4 mA cm^{-2} and 43 mA cm^{-2} current densities over a constant time of 450 seconds, and pristine ITO coated glass as a control substrate. It is interesting to note that pristine ITO films possess a surface morphology composed of a random assembly of nanoparticles that is developed into a nanoparticulate/granular morphology in films anodised under our experimental conditions. The quantification of the degree of nodularity revealed significant differences in nodule diameter when subjected to different deposition current densities. Film growth using higher current densities yielded less-dense, non-uniform films than those of anodised films formed with lower current densities [65].

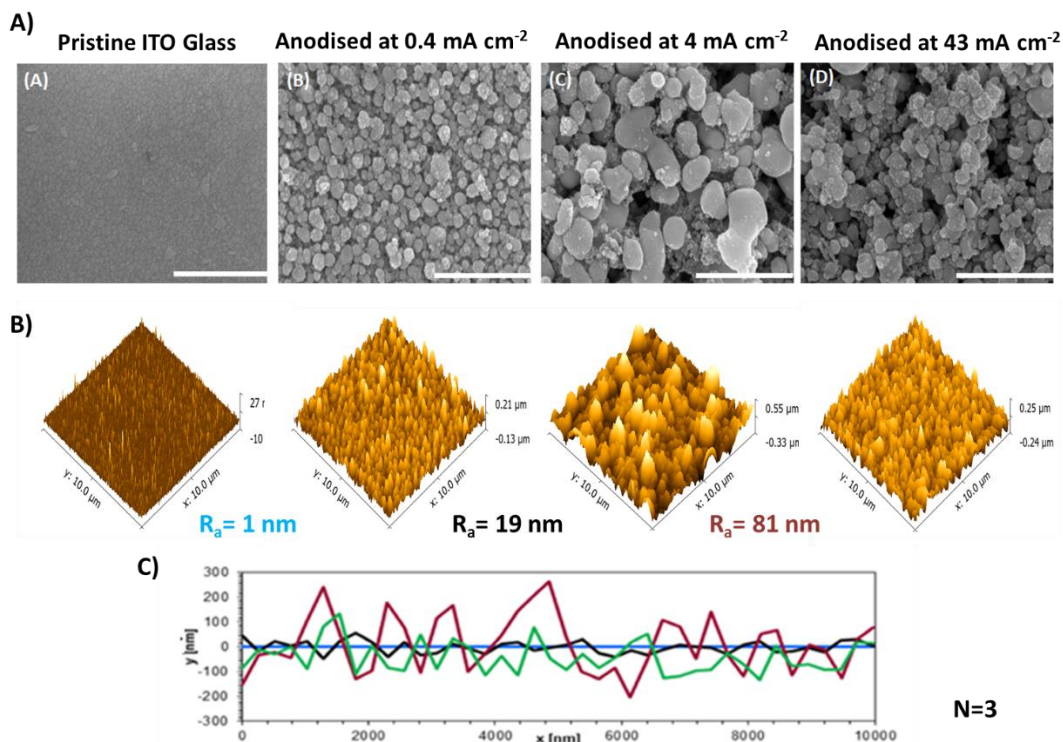


Figure 2.6 Particle size and distribution are significantly affected by current density. A). Scanning electron micrograms of control pristine ITO coated glass (A) and ITO anodised films with (B). 0.4 mA cm^{-2} ; (C). 4 mA cm^{-2} ; and (D). 43 mA cm^{-2} current densities. Scale bar = $1 \mu\text{m}$ B). Corresponding roughness (R_a) measurements of the pristine ITO glass and the anodised ITO films with different current densities, 0.4 mA cm^{-2} , 4 mA cm^{-2} ; and 43 mA cm^{-2} and, representative line profiles C) from each of the films. R_a indicates the mean surface roughness, calculated on $10 \mu\text{m}^2$ regions.

Experimentally, pristine ITO films reported a mean particle size of 86 nm, films formed with 0.4 mA cm^{-2} were associated with a mean particle size of 89 nm; and mean particle diameters of 152 nm, and 112 nm were observed in films formed using 4 mA cm^{-2} and 43 mA cm^{-2} current densities respectively. At 0.4 mA cm^{-2} , the observed nodular distribution was uniform and compact. However, at 4 mA cm^{-2} and 43 mA cm^{-2} current densities, a more clustered grain-like structure and a non-homogeneous distribution of particles were evident. This trend in distribution was further observed as an increase in porosity percentage in films formed using higher current densities than in films formed at 0.4 mA cm^{-2} and the pristine ITO coated

Anodisation of Magnetron-Sputtered Indium-Tin Oxide (ITO) Films

glass (**Figure 2.7**). This suggests that current deposition strongly affects the processes of surface diffusion of atoms, nucleation and coalescence of the film growth resulting in different nucleation densities at the surface [66, 67]. Of note, a correlation between elastic moduli and porosity [68-70] is inferred, and it can be assumed that anodised ITO films will possess enhanced flexibility due to their high-packing density relative to non-anodised films [70], an important consideration in next-generation neuroelectrode design. Interestingly, it was noted that a current density of 0.4 mA cm^{-2} resulted in anodised ITO films with fewer internal voids.

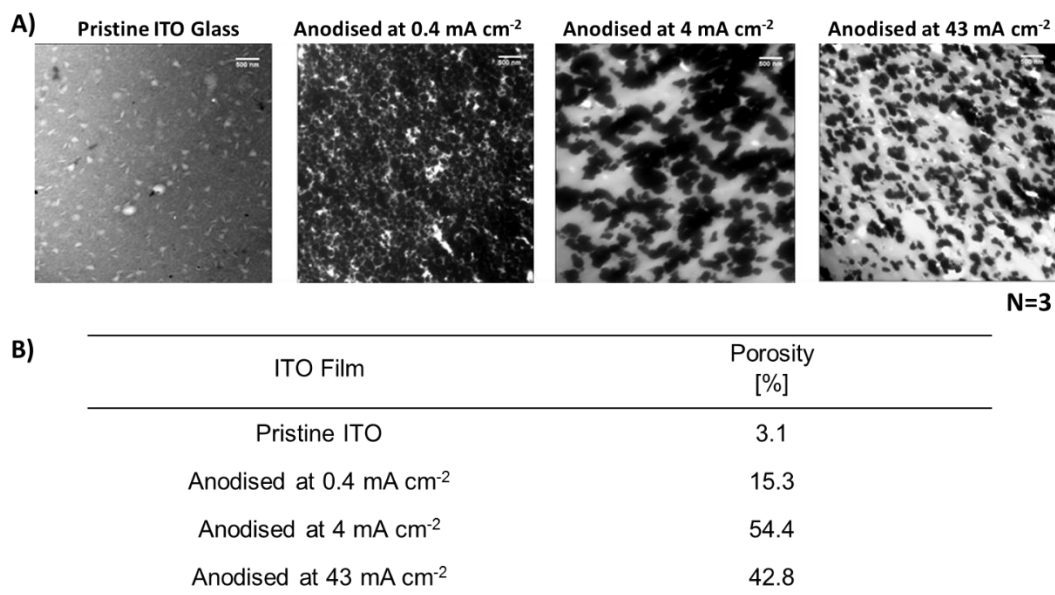


Figure 2.7 Morphological characterisation of the anodised ITO films. A) TEM images showing the structure and distribution of each of the anodised films and the pristine ITO glass control, scale bar = 500 nm B) Tabulated porosity percentages values for each of the experimental groups as an indication of the compactness of the particles forming each film.

Anodisation processes resulted in significant increases in surface roughness (R_a) relative to pristine ITO films as a function of current density (**Figure 2.7B**). Films formed with current densities of 0.4 mA cm^{-2} exhibited an average roughness of 19 nm over $10 \mu\text{m}^2$, and an average roughness of 81 nm and 61 nm when formed at 4 mA cm^{-2} and 43 mA cm^{-2} respectively. Conversely, pristine ITO films possessed a R_a of 1 nm over $10 \mu\text{m}^2$. A similar trend was also observed for mean nodule diameter,

which increased from 89 nm in current densities of 0.4 mA cm⁻² to 152 nm and 112 nm in films formed with current densities of 4 mA cm⁻² and 43 mA cm⁻² respectively (**Table 2.2**).

Table 2.2 Physical properties of anodised ITO films formed with different deposition currents. Values of experimental thickness and mean particle diameter of pristine and anodised films formed with 0.4 mA cm⁻², 4 mA cm⁻² and 43 mA cm⁻² current densities over a constant time of 450 seconds. The data represent the mean of 15 measurements for film thickness plus >200 measurements for particle diameter. Results are ±SD, N=3.

ITO Film	Average Thickness [nm]	Mean Particle Diameter [nm]
Pristine ITO Glass	750 ±	86 ± 17
Anodised at 0.4 mA cm ⁻²	109.7 ± 4	89 ± 26
Anodised at 4 mA cm ⁻²	934.5 ± 35	152 ± 78
Anodised at 43 mA cm ⁻²	937.8 ± 47	112 ± 55

Similarly, an abrupt increase in film thickness was observed in films formed with current densities of 4 mA cm⁻² and 43 mA cm⁻² indicating that the maximum rate of anodisation deposition is limited by the electrolyte diffusion rate [65]. The limiting current density to attain approximately 100 per cent efficiency of film deposition can be determined theoretically by calculating the maximum rate at which the ions diffuse to the cathode. Our data (**Table 2.2**) proposes that at 4 mA cm⁻² (under our experimental conditions), the threshold for the limiting current density may have already been reached [36, 65] and the observed non-linear increases in particle size, film roughness and the plateau in film thickness could be indications that films formed using a current density of 4 mA cm⁻² under our experimental conditions are associated with a decrease in film growth efficiency. Therefore, it can be assumed that between 4 mA cm⁻² and 43 mA cm⁻² the diffusion limiting current density for ITO anodisation can be found, and that the diffusion kinetics of oxygen and hydrogen at the cathode are insufficient, causing reactions at the anode to stop to conserve electrons.

Similarly, this transition in film thickness was also represented as optical changes to the ITO films. It can be anticipated, according to the Drude model [71], that the changes observed in film morphology derived from the differences in film growth imposed by the explore current densities will impact on the refractive index of films. Optical transmission spectra of the pristine ITO coated glass and the anodised ITO films formed at 0.4 mA cm^{-2} , 4 mA cm^{-2} and 43 mA cm^{-2} current densities were performed to quantify film transparency (**Figure 2.8**). The observed trend in optical transmittance of the anodised ITO films formed at higher current densities (4 mA cm^{-2} and 43 mA cm^{-2}) reflects scattering losses as predicted by the effects of film roughness [72]. The aforementioned faster growth observed in films formed at 4 mA cm^{-2} resulted in the decrease in transmittance of these films.

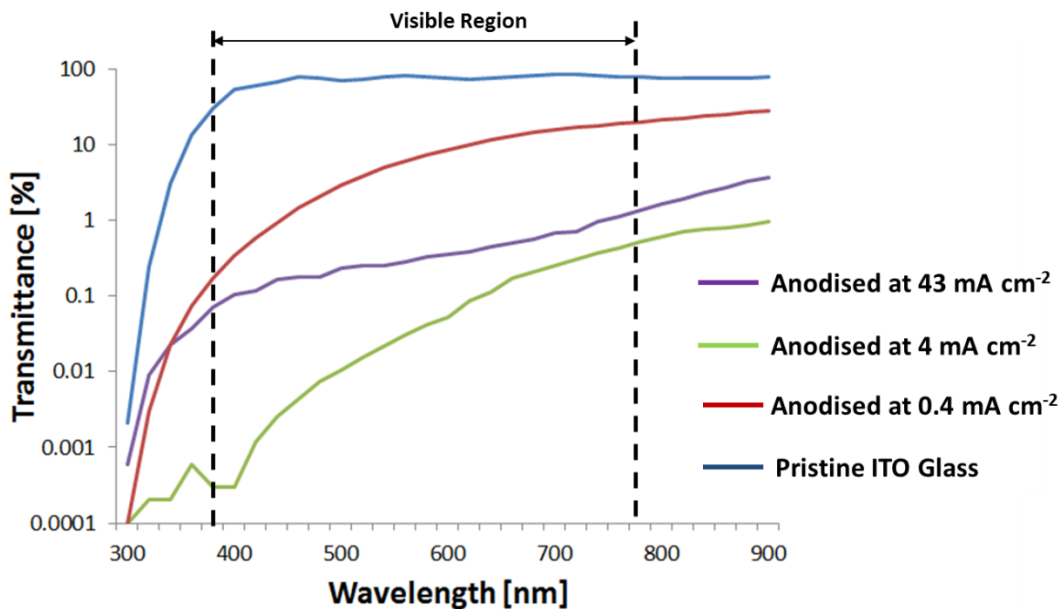


Figure 2.8 Optical transmission spectra of the pristine ITO coated glass and the anodic oxidised films formed at 0.4 mA cm^{-2} , 4 mA cm^{-2} and 43 mA cm^{-2} current densities.

In order to assess the durability and stability of anodised ITO films under physiological conditions, substrates were assessed with an accelerated ageing study that simulated four years of implant equivalence in the body (**Figure 2.9**). Film delamination (**Figure 2.9A**) together with consistent high losses in charge storage

Anodisation of Magnetron-Sputtered Indium-Tin Oxide (ITO) Films

capacity (CSC), 75 % and 74 % were observed in films formed with current densities of 4 mA cm^{-2} and 43 mA cm^{-2} respectively. Conversely, a 55% loss in CSC of ITO films anodised with the lowest current density of 0.4 mA cm^{-2} was observed (**Figure 2.9B**). It is interesting to note that pristine ITO glass also underwent a significant diminution in electrical activity with a 96 % loss in CSC and with pronounced micro-cracks observable by SEM.

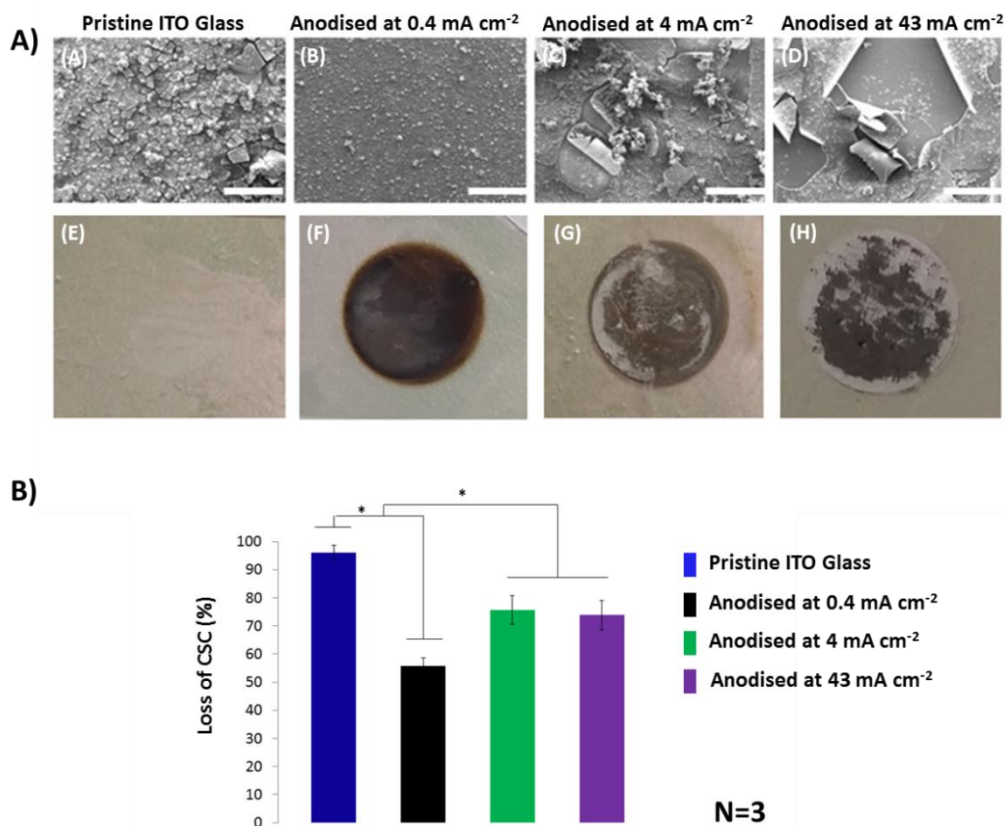


Figure 2.9 The impact of the accelerated ageing study on durability and electrical stability of the anodised ITO films. A) On top, scanning electron micrograms of control pristine ITO glass (A) and ITO anodised films with (B). 0.4 mA cm^{-2} ; (C). 4 mA cm^{-2} ; and (D). 43 mA cm^{-2} current densities. Scale bar = $200 \mu\text{m}$. After four weeks under biologically relevant ageing, important film delamination was observed on anodised films formed using high current densities (4 mA cm^{-2} and 43 mA cm^{-2}). Partial micro-cracks were observed in films formed at 0.4 mA cm^{-2} and control ITO.

On bottom, corresponding photographs showing the final visual appearance of control and anodised films (E-H) after four weeks of ageing study. B) Plot of percentage loss of charge storage capacity (CSC) after four weeks of accelerated ageing study simulating four years of implant equivalence in the body. Important significant differences between the ITO control and the anodised films were observed. The ITO anodised films formed at 0.4 mA cm^{-2} were the most stable films compared to control and to the films formed using high current densities. Results are $\pm \text{STD}$, $\star = p < 0.05$.

The effect of thermal ageing on pristine ITO films perceived here was comparable to those presented by Hamasha and colleagues [73], who also tested ITO under thermal ageing conditions and showed that films became unstable and demonstrated increases in electrical resistance and physical changes. Current research to improve the stability of ITO electrodes has focused on the deposition of multilayers [74], of novel transport and luminescent materials [75] such as polymers [76] and on efficient injection contacts [77]. Conversely, it is reported by Nishimoto et al. [78] that optimal variations in grain-boundary potential caused by oxygen adsorption after annealing TiO_2 structures with ITO can improve thermal stability of pristine ITO. Consequently, surface modifications of thin-films of ITO such as the anodisation process utilised here, may help to explain the enhanced stability observed in anodised films, with the formation of stabilising oxide layers [79].

2.4.2 Chemical characterisation

In **Table 2.3** the XPS survey with the elemental composition of pristine ITO and anodised ITO films using 0.4 mA cm^{-2} , 4 mA cm^{-2} and 43 mA cm^{-2} is reported. The XPS survey spectrum of pristine ITO revealed the presence of prominent indium (In), tin (Sn) and oxide (O) peaks. The atomic percentage for carbon (C) is also relatively high showing a large presence of atmospheric C on the film surface. Similarly, low-current density anodised samples consisted primarily of In, Sn and O. The O concentration was observed to increase significantly in anodised ITO films, increasing from 42% O1s atomic % in pristine ITO films to 49.81% in anodised films formed with current densities of 43 mA cm^{-2} . Conversely, the Sn atomic % is reduced

in anodised ITO films relative to pristine films, which is reportedly due to the leaching of Sn into the electrolyte during the anodisation process [56].

Table 2.3 XPS analysis of the elemental composition of the Pristine ITO and anodised ITO films.

ITO Film	Atomic Composition [%]			
	In3d	O1s	C1s	Sn3d5
Pristine ITO Glass	21.0	42.2	34.6	2.2
Anodised at 0.4 mA cm ⁻²	24.8	43.5	30.3	1.3
Anodised at 4 mA cm ⁻²	23.5	44.5	31.5	1.2
Anodised at 43 mA cm ⁻²	22.8	49.8	26.7	0.8

2.4.3 Electrochemical Characterisation

Figure 2.10A shows cyclic voltammograms for each of the ITO films in 50 mM phosphate buffer before and after anodisation. Surface charge density was approximated through integration of the charge passed within the cathodic region of voltammetric scans, corresponding to charge densities of 49 $\mu\text{C cm}^{-2}$, 341 $\mu\text{C cm}^{-2}$, 15 $\mu\text{C cm}^{-2}$ and 15 $\mu\text{C cm}^{-2}$ for pristine ITO films and films subjected to anodisation at 0.4 mA cm⁻², 4 mA cm⁻² and 43 mA cm⁻² current densities respectively (**Table 2.4**). A large increase in charge density was observed in ITO films subjected to anodisation at 0.4 mA cm⁻², by almost one order of magnitude, compared to pristine ITO films. This is likely due to the greater surface coverage as indicated by SEM and AFM analysis. Interestingly, a three-fold reduction in charge density was observed for ITO films subjected to anodisation at current densities of 4 mA cm⁻² and 43 mA cm⁻² compared to the pristine ITO glass (**Figure 2.10A**) despite increased surface roughness. However, this electrical profile is consistent with the high porosity percentages calculated for these films (**Figure 2.7**). No appreciable difference in charge density was observed in any of the ITO substrates when tested in physiological-like saline solution [48] compared to 50 mM phosphate buffer solution.

Anodisation of Magnetron-Sputtered Indium-Tin Oxide (ITO) Films

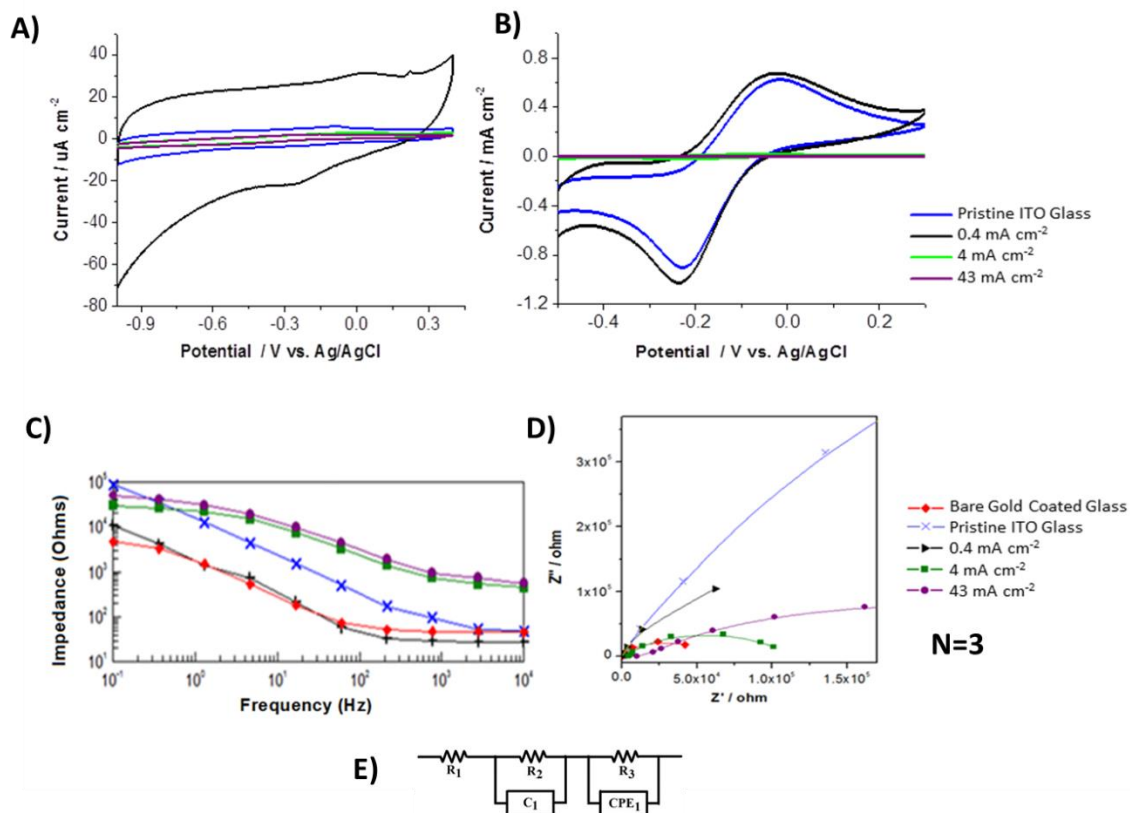


Figure 2.10 Electrochemical analysis of anodised films. Cyclic voltammograms of ITO (blue) and ITO anodised films formed with current densities; 0.4 mA cm⁻² (black), 4 mA cm⁻² (green) and 43 mA cm⁻² (purple). CVs recorded in 50mM phosphate buffer, scan rate 100 mV s⁻¹ A) and in 50mM phosphate buffer containing 2mM [Ru(NH3)6]3+ B), scan rate 100 mV s⁻¹. Bode C) and Nyquist D) plots comparing the EIS spectra of pristine ITO glass (blue filled asterisks), bare gold glass (red filled diamonds), and anodised ITO films formed using 0.4 mA cm⁻² (black filled triangles), 4 mA cm⁻² (green filled squares) and 43.mA cm⁻² (purple filled circles). (E) represents the electrical equivalent circuit used to analyse experimental data.

Table 2.4 Electrochemical characteristics of ITO anodised films. Non-faradaic charge density evaluated from cathodic region of cyclic voltammograms recorded in 50 mM phosphate buffer at 0.1 V s⁻¹ scan rate (Potential range: -1 V to 0.4 V vs. Ag/AgCl). Faradaic charge density and peak current density (*i_{pa}*) evaluated from voltammograms recorded in 50mM phosphate buffer containing 2 mM [Ru(NH₃)₆]₃⁺ at 0.1 V s⁻¹ scan rate.

ITO Film	Non-faradaic Charge Density [μC cm ⁻²]	Faradaic Charge Density [mC cm ⁻²]	E°' [V]	<i>i_{pa}</i> [mA cm ⁻²]	D _o [cm ² s ⁻¹]
Pristine ITO	49	1.43	-0.13	0.62	4.62 × 10 ⁻⁶
Anodised at 0.4 mA cm ⁻²	341	1.45	-0.13	0.77	8.37 × 10 ⁻⁶
Anodised at 4 mA cm ⁻²	15	0.04	-0.14	0.02	6.92 × 10 ⁻⁹
Anodised at 43 mA cm ⁻²	15	-	-	-	-

Comparative electrochemical impedance profiles for films are shown in the Bode diagram (**Figure 2.10C**) and Nyquist plot (**Figure 2.10D**). Within frequency ranges of 10⁻¹ – 10⁴ Hz, ITO anodised films formed at a current density of 0.4 mA cm⁻² displayed the lowest impedance profiles, moderately lower than those recorded for the pristine ITO films and close to the impedance observed for gold coated glass films. This indicates that changes in chemical composition and/or morphology induced by the 0.4 cm⁻² current density anodisation process do not appear to diminish the conductive properties of the ITO electrode. This is significant as alternative electrochemical treatments have been shown to greatly decrease the conductivity of ITO electrodes [56, 58-61]. However, an increase in impedance of one order of magnitude was observed for films formed at high current densities (4 mA cm⁻² and 43 mA cm⁻²), revealing an inverse relationship between electrical conductivity and the anodisation current density applied.

The experimental data of ITO anodised films were fitted to an equivalent circuit (**Figure 2.10E**) consisting of three resistors (R₁, R₂, R₃), a capacitor (C₁) and a constant phase element (CPE₁), in accordance with previous studies [80-82]. In this circuit, R₁ is the solution resistance; and R₂ and C₁ are associated with space charge layer resistance and space charge layer capacitance, respectively. The double layer

capacitance is denoted as CPE_1 and R_3 is ascribed to the resistance of ITO films (**Table 2.5**). The simulated data confirmed that the lowest resistance of $8.3 \text{ k}\Omega \text{ cm}^{-2}$ for the ITO anodised films formed at a current density of 0.4 mA cm^{-2} when compared with the resistance of $9.8 \text{ k}\Omega \text{ cm}^{-2}$ for pristine ITO coated glass. The detrimental effect of high current densities on the conductivity was also observed in the calculated resistance of $22.8 \text{ k}\Omega \text{ cm}^{-2}$ and $209.1 \text{ k}\Omega \text{ cm}^{-2}$ for 4 mA cm^{-2} and 43 mA cm^{-2} current densities respectively.

Table 2.5 Summary of the calculated resistance values (R_3) for each of the anodised ITO films after equivalent circuit analysis.

ITO Film	Resistance (R_3) [$\text{k}\Omega \text{ cm}^{-2}$]
Pristine ITO Glass	9.8 ± 0.3
Anodised at 0.4 mA cm^{-2}	8.3 ± 0.6
Anodised at 4 mA cm^{-2}	22.8 ± 2.6
Anodised at 43 mA cm^{-2}	209.1 ± 9.2

To further evaluate the electrochemical characteristics of the ITO anodised films, a ruthenium hexamine ($[\text{Ru}(\text{NH}_3)_6]^{3+}$) redox probe was employed to examine faradaic redox response within a biologically relevant potential range (-0.4 to $+0.2 \text{ V}$ vs. Ag/AgCl) (**Figure 2.10B**). With pristine ITO films, $[\text{Ru}(\text{NH}_3)_6]^{3+}$ undergoes a one electron redox reaction (redox potential (E°) = -0.13 V vs. Ag/AgCl), yielding an anodic peak current (i_{pa}) of 0.62 mA cm^{-2} and a faradaic charge density of 1.3 mC cm^{-2} (**Table 2.4**). A slight increase of i_{pa} and faradaic charge density is observed with ITO films formed through anodisation at 0.4 mA cm^{-2} , possibly due to the increased surface roughness. This shows that although the non-faradaic charge density is greater with these films, the increased surface roughness does not translate into a greater electrochemically active surface area than that of the relatively smooth non-anodised ITO film. Kraft et. al. [56] observed a similar response using $[\text{Fe}(\text{CN})_6]^{3-}$ as a redox probe, where non-faradaic current (charge density) increased after ITO electrode anodisation while faradaic current remained essentially constant. A large decrease of i_{pa} and faradaic charge density is evident in ITO films subjected to anodisation with current densities greater than 0.4 mA cm^{-2} , accompanied by a slight

decrease in E° of *ca.* 10 mV for the $\text{Ru}^{3+/2+}$ redox couple (**Table 2.4**). The difference in E° may result from variation in chemisorption sites within the electrode film which can influence redox probe stability [83]. The voltammetric response observed for ITO films anodised at 43 mA cm^{-2} is characteristic of a highly resistive surface with no evidence of heterogeneous electron transfer between the electrode and the redox probe [84].

Scan rate studies (**Figure 2.11**) revealed a linear dependence of i_{pa} vs. $v^{1/2}$ (v = scan rate) for all ITO films (with the exception of ITO anodised films formed with current densities of 43 mA cm^{-2}), indicative of a semi-infinite planar diffusional response described by the Randles-Sevcik equation [85]. Diffusion coefficients (D_0), evaluated from the linear portion of i_{pa} vs. $v^{1/2}$, are shown in **Table 2.4**. D_0 values in the order of $10^{-6} \text{ cm}^2 \text{ s}^{-1}$ were calculated for $[\text{Ru}(\text{NH}_3)_6]^{3+}$ at both pristine ITO and ITO films formed through anodisation at 0.4 mA cm^{-2} in a phosphate buffer. Again, a decrease of D_0 , by approximately three orders of magnitude is evident for ITO films subjected to anodisation with current densities of 4 mA cm^{-2} and 43 mA cm^{-2} , further corroborating the insulating nature of films prepared at anodising current densities greater than 0.4 mA cm^{-2} .

Anodisation of Magnetron-Sputtered Indium-Tin Oxide (ITO) Films

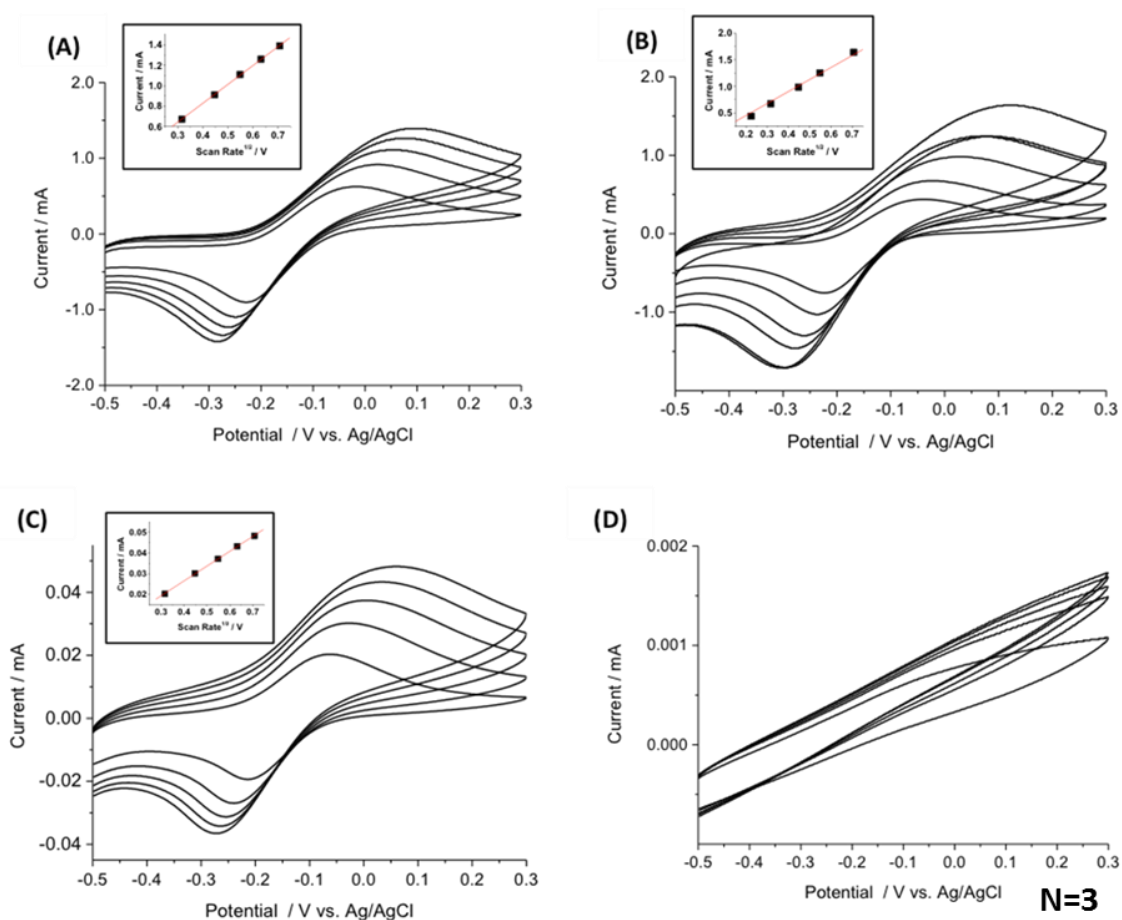


Figure 2.11 Cyclic voltammograms of (A) pristine ITO glass, and anodised ITO films formed at current densities of (B) 0.4 mA cm^{-2} , (C) 4 mA cm^{-2} and (D) 43 mA cm^{-2} , in 50 mM phosphate buffer, pH 7.8, containing 2mM $[\text{Ru}(\text{NH}_3)_6]^{3+}$. Scan rates are 500, 400, 300, 200, and 100 mV s^{-1} , from outside inwards. (Inset: Plot of the square root of scan rate versus anodic peak (*i*_{pa}) currents).

Interestingly, the presence of the PSS ionomer was critical for the anodisation process and ITO thin-films subjected to anodic oxidation under ambient conditions in a 1X phosphate-buffered saline solution were associated with a linear increase in impedance profile as a function of current density (**Figure 2.12**).

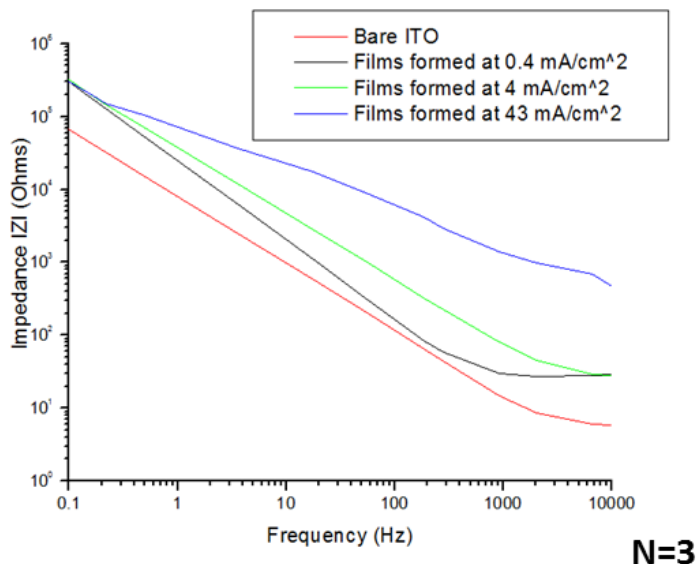


Figure 2.12 The presence of the polymer PSS in the solution is important for the anodisation process. Films formed without the presence of PSS at 0.4 mA cm^{-2} , 4 mA cm^{-2} and 43 mA cm^{-2} current densities revealed a linear increase in impedance compared to pristine ITO.

2.4.4 Biological Characterisation

Nanoscale signaling modality has been shown to have a profound effect on cell viability, proliferation and on cell attachment in the material's space [51, 86, 87]. Because the application of different current densities for the anodisation of ITO films resulted in defined nanoscale morphological changes, the cellular interfacial response has been analysed as a function of roughness. With this in mind, the effects of films formed at 0.4 mA cm^{-2} , 4 mA cm^{-2} and 43 mA cm^{-2} current densities, which in order exhibit an average of roughness of 19 nm, 81 nm and 61 nm respectively, on human neuroblastoma SH-SY5Y cell adhesion and proliferation were assessed *in vitro*. These were then compared to pristine ITO coated glass with an experimental average roughness of 1 nm (**Figure 2.13A**). After periods of one, seven and fourteen days, cells were stained with calcein (live) and ethidium homodimer (dead) to establish cell viability. All experimental and control films were non-toxic to SH-SY5Y cells. However, significant differences were observed at day fourteen with respect to cell viability. Cells grown on films with the lowest roughness profile (formed at the

Anodisation of Magnetron-Sputtered Indium-Tin Oxide (ITO) Films

lowest current density 0.4 mA cm^{-2} ; $R_a = 19 \text{ nm}$ over $10 \text{ }\mu\text{m}^2$) maintained 86% viability relative to control films at day one (**Figure 2.13B**). Similarly, when analysed with Alamar Blue assay by 24h (**Figure 2.13C**), the SH-SY5Y population cultured on anodised ITO films was comparable to cells cultured on control pristine ITO coated glass. While by days seven and fourteen cells cultured on all experimental anodised films demonstrated a marked decreasing trend in metabolic activity, the anodised films with 19 nm roughness (formed at 0.4 mA cm^{-2} current density) showed an overall significant higher metabolic activity of 87% by day seven and 78 % by day fourteen, respectively compared to 61 nm and 81 film's roughness profiles and pristine ITO control substrates. Overall, anodised ITO films possessing a R_a 81 nm, (the highest roughness profile), showed a significant decrease in metabolic activity relative to cells cultured on control ITO coated glass and on anodised films with 19 nm roughness.

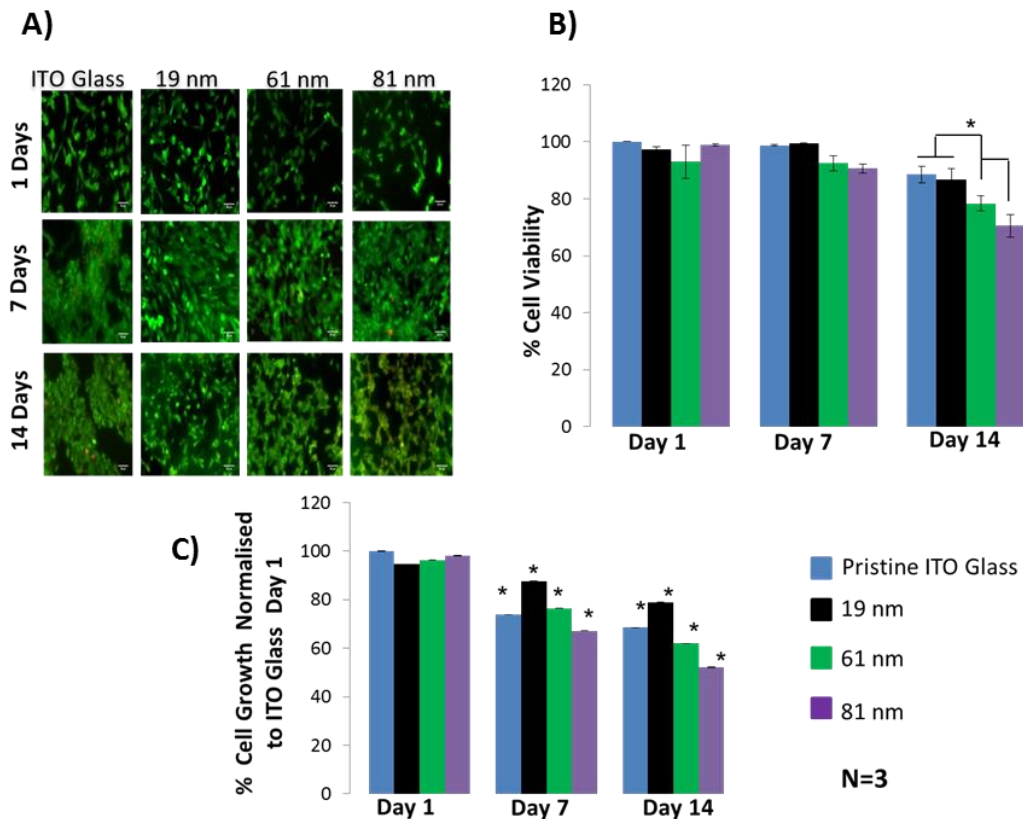


Figure 2.13 Cytocompatibility analysis of anodised ITO films of different roughness (R_a) formed by varying the current density. Fluorescent images of SH-

Anodisation of Magnetron-Sputtered Indium-Tin Oxide (ITO) Films

SY5Y cells following one, seven and fourteen days in culture on anodised films displaying 19 nm, 61 nm and 81 nm over 10 μm^2 (R_a) roughness relative to pristine ITO control (R_a 1 nm over 10 μm^2). Green, live; red, dead. Bar = 50 μm A). A significant ($p < 0.05$) decrease in cell viability was observed in anodised films with an average roughness of 61 nm and 81 nm relative to control and 19 nm film roughness. B). Metabolic activity of SH-SY5Y cells compared with pristine ITO coated glass control as measured by the AlamarBlue assay ($p < 0.05$) C). Metabolic activity was significantly elevated in cells cultured on anodised ITO films with 19 nm roughness relative to anodised films with 61 and 81 nm roughness respectively by day seven and day fourteen. Results are \pm STD, $\star = p < 0.05$.

These results are similar to those of Fan et al. [88]. In their work, they have reported on the cell proliferation of neural cells cultured on silicon wafers possessing different levels of surface roughness. It was concluded that the Si wafers with surface R_a ranging from 20 to 50 nm promoted a significantly higher cell proliferation. Conversely, on surfaces with a R_a less than approx. 10 nm and on rough surfaces with R_a above 70 nm, cell metabolic activity was reported to be significantly lower. It is noteworthy that even though cell proliferation and viability depend on cell type and substrate composition, it is apparent that neurons do not readily attach on excessively smooth ($R_a=10$ nm) or rough surfaces ($R_a = 250$ nm) [89].

Tissues can be described as complex nanoscale composites that impact morphological and mechanical features to the resident cellular constituents. Previous studies show that nano topography influences cellular function and focal adhesion (FA) formation *in vitro* [86, 90] and may be employed to modulate the dynamic interface between materials and cell/tissues. With an awareness of this, cell attachment to the anodised ITO films was quantified through immunofluorescent labelling of the FA associated protein paxillin [91] (**Figure 2.14A-D**). At day one, cells cultured on all experimental films and control pristine ITO glass were associated with an overall average of approximately fourteen focal adhesions per cell. By day seven, SH-SY5Y cells cultured on pristine ITO control presented a significant increase in FA numbers per cell, an average of 25 focal adhesions per cell, compared to all the experimental anodised ITO films with an average number of seventeen FAs per cell. Interestingly,

trends in FA numbers were reversed in cells cultured on the pristine ITO control group by day seven which demonstrated a significant reduction in FA number by day fourteen (**Figure 2.14E**). Conversely, previous studies have reported a disruption to cell adhesion by nano rough surfaces with similar roughness profiles [86, 92] and a decrease in cell viability; however, FA quantification was not performed in these studies. Specifically, it was noted by Brunetti *et al.* [86] that cellular adhesion was significantly increased on regions of low (smooth) roughness.

Independent of the surface roughness, it was interesting to note an increased number of FAs in SH-SY5Y cells cultured on all anodised films relative to SH-SY5Y cells cultured on pristine ITO coated glass by day fourteen [93]. It was hypothesised that the enhanced number of FA observed in SH-SY5Y cells cultured on anodised ITO films relative to pristine ITO may be as a result of the anodisation process inducing differential protein adsorption [94, 95]. Studies into the influence of surface chemistry on protein adsorption through etching and deposition techniques [96], plasma treatment [97] and anodisation processes [98] indicate enhanced ECM protein adsorption as a function of oxygen content [94, 99, 100], also observed here in anodised ITO films.

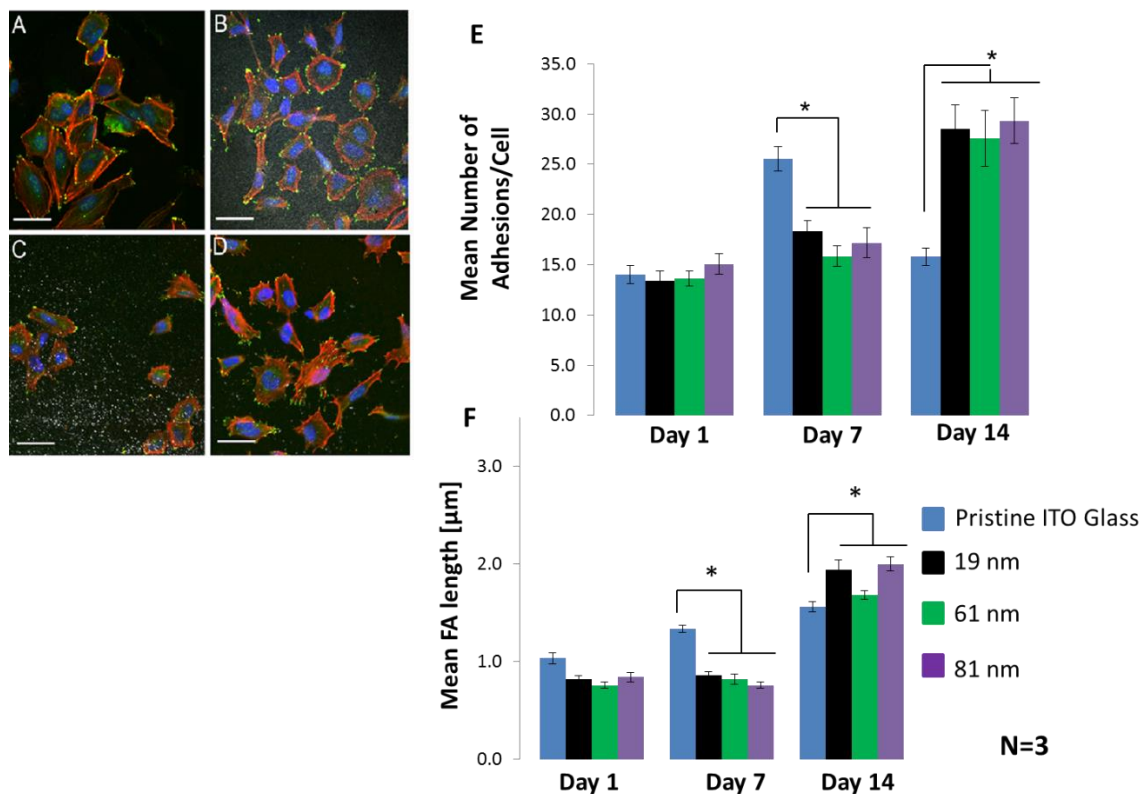


Figure 2.14 Focal adhesion formation of SH-SY5Y cell grown roughness. Immunofluorescent imaging was employed to quantify FA length and number in cells cultured on pristine ITO coated glass and experimental anodised films of different roughness (A-D), (green: paxillin, red: actin, blue: nucleus, bar: 40 μm). Cells cultured on control ITO coated glass generated less FA complexes over time, whilst this trend was reversed in cells on experimental anodised ITO films of all roughness (E). SH-SY5Y cells grown on 19 nm, and 81 nm roughness of anodised films were associated with a significant increase in FA length relative to cells cultured on pristine ITO coated glass ($R_a = 1 \text{ nm}$). There was a significant reduction in FA length of the cells cultured on 61 nm roughness compared to the cells grown on 19 nm, and 81 nm experimental roughnesses (F). For all analysis, results are $\pm \text{STD}$, $\star = p < 0.05$.

Similarly, FA length was observed to be significantly greater in cells cultured on pristine ITO control substrates than in cells cultured on anodised films by day seven. By day fourteen, the FA length in the experimental anodised films with the lowest

and highest roughness profiles (19 nm and 81 nm) was significantly higher than the length of FAs in cells cultured on pristine ITO control substrates (**Figure 2.14F**). A significant reduction in FA length was noted, however, in cells cultured on R_a film roughness of 61 nm over $10 \mu\text{m}^2$. This reduction in FA reinforcement may be related to the particle diameter and nano features with lateral dimensions of approx. 100 nm that have been shown to be disruptive to integrin clustering [90, 101] an effect which is lost by reducing or increasing the feature dimensions, an effect also demonstrated here.

To gain further insight into cell adhesion, the length of the FAs was sub-grouped in focal complexes (FXs) measuring $<1\mu\text{m}$ in length and FAs proper, measuring between 1-5 μm . FXs were most abundant in cells cultured on all experimental roughnesses and pristine ITO coated glass substrates on days one and seven. By day fourteen, cells cultured on anodised ITO films with roughness of 19 nm, 61 nm, and 81 nm over $10 \mu\text{m}^2$ demonstrated reduced FX frequency, and a similar FA distribution profile with lengths ranging from 1 μm to 4.5 μm . However, cells cultured on control ITO substrates were associated with a reduction in FA frequency (**Figure 2.15**). It was interesting to note that over a period of fourteen days in culture, cells demonstrated a progressive shift from nascent and unstable focal complexes to more stable focal adhesions. Hence, it can be inferred that the influence of film roughness is a predominant factor in the observed increase in focal adhesion frequency together with the concept of increased oxygen content to protein adsorption owing to the anodisation process.

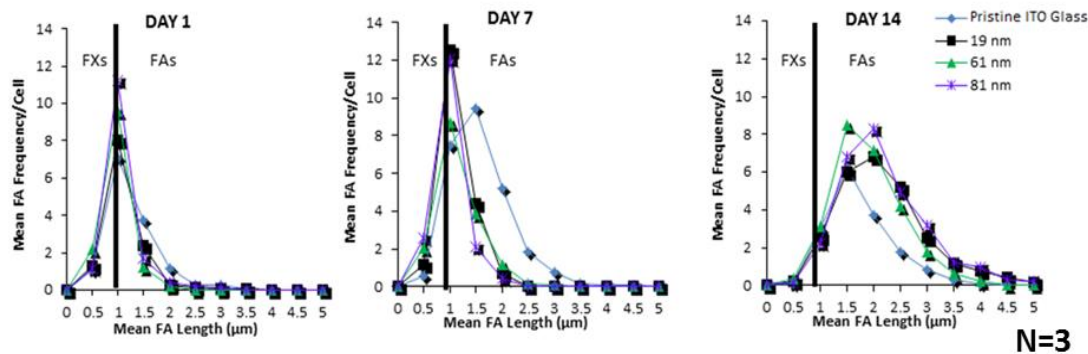


Figure 2.15 Focal adhesions were sub-grouped into focal adhesions proper (FAs) and nascent focal complexes (FX). FXs were the predominant adhesion complex subtype observed on all anodised ITO films and the pristine ITO coated glass up to day seven. However, FXs were displaced by the FA subtype by day fourteen in cells cultured on all experimental and control materials. A significant increase in the mean number of focal adhesions per cell on all of the experimental anodised ITO films compared to control pristine ITO group was observed on day fourteen.

In order to assess the potential functional response of neuronal populations to implanted anodised ITO thin-film devices *in vitro*, and the potential for induction of a reactive astrocyte phenotype, the functional response of a primary VM cells culture was assessed via an in-house protein microarray assay. Spotted antibodies for proteins associated with astrocyte reactivity, cell adhesion and mechanotransduction utilised in this study are outlined in **Table 2.1** Antibodies were printed at a range of concentrations ($0.1 - 1 \text{ mg mL}^{-1}$) and assessed for retained function and optimal print concentration by incubation with a fluorescently labelled protein lysate from VM cells cultured for 21 days on all anodised films and pristine ITO control (**Figure 2.4**).

Owing to the construction of the gliosis antibody microarray, an unsupervised clustering of all experimental films normalised by control pristine ITO was performed (**Figure 2.16**). This analysis clearly defined a group between the anodised films with nano roughness of 61 nm and 81 nm respectively, and a single cluster for the films formed with the lowest roughness profile of 19 nm (formed at 0.4 mA cm^{-2} current density); sharing only 1% similarity with the rest of the experimental substrates. As gliosis is dependent on the bioelectrochemical as well as physicochemical

Anodisation of Magnetron-Sputtered Indium-Tin Oxide (ITO) Films

properties of the implanted material, it was remarkable to notice that the resulting roughness factor of the anodised films was predominant on the differential intensity expression of the antibodies evaluated.

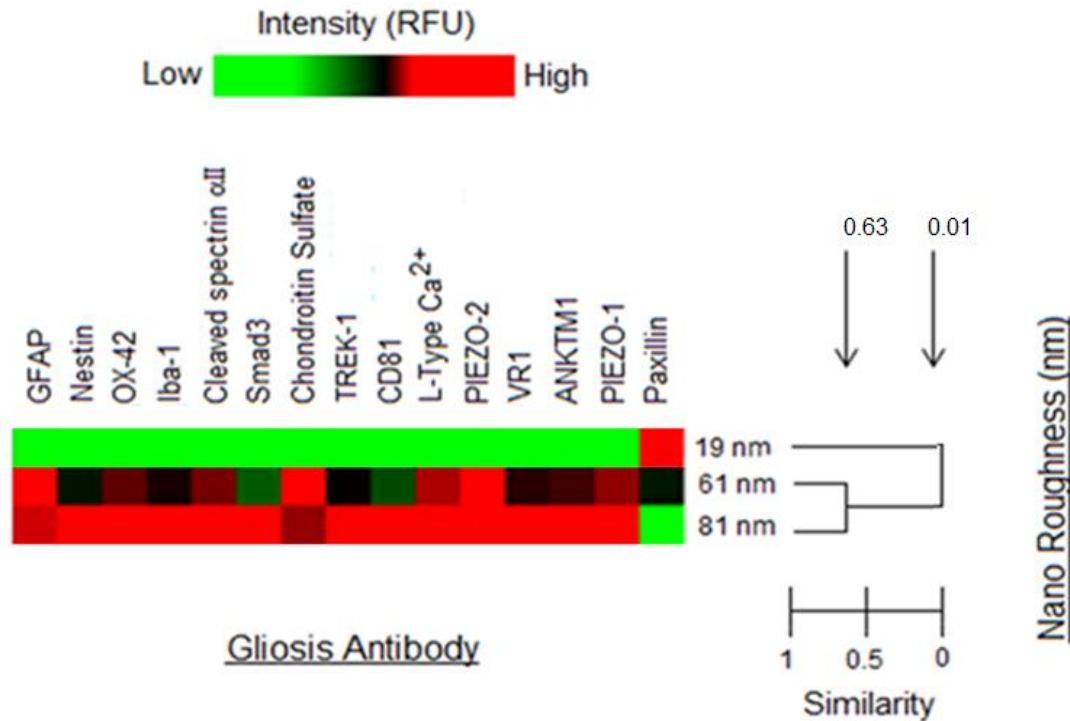


Figure 2.16 Unsupervised clustering of all experimental anodised films normalised by control pristine ITO. This analysis clearly defined a group between the anodised films with nano roughness of 61 nm and 81 nm respectively, and a single cluster for the films formed with the lowest roughness profile of 19 nm; sharing only 1% similarity with the rest of the experimental substrates. The gliosis response of the films formed with 0.4 mA cm^{-2} current density which exhibit the lowest roughness profile of 19 nm showed a remarkable intensity downregulation of reactive astrocytes, microglia and calcium influx markers. The resulting roughness factor of the anodised films was predominant on the differential intensity expression of the antibodies evaluated. $N=3$, 18 data points

The hallmarks of glial scar formation are multifactorial; in the developed antibody microarray gliosis was studied from the diverse and interwoven response of microglia and astrocytes [102, 103], and from the changes of transient calcium currents that

affect overall homeostasis and astrocytes reactivity [104]. Overall, ITO anodised films formed with current densities of 0.4 mA cm^{-2} (films with 19 nm roughness) showed significant downregulation of the gliosis response relative to VM populations cultured on other anodised ITO films. Specifically, downregulation in the intensity of OX42/Iba1 (microglia), GFAP and Nestin (reactive astrocytes) were observed.

A recent study by Kim et al. [105] has shown that coupled to the increase in GFAP expression as main marker for reactive astrocytes, further reactivity can be fully characterised by the expression of cleaved spectrin α II. Downregulations in cleaved spectrin α II were also observed in VM populations cultured on ITO anodised films formed with current densities of 0.4 mA cm^{-2} relative to cells cultured on other experimental and control substrates, again indicating the reduced potential of these films to induce a reactive astrocyte phenotype [105].

Interestingly, cleaved spectrin α II is sensitive to calpain-mediated proteolysis, and calpains have been shown to play a central role in the neuro-protection of the CNS and neuron calcium influx [106, 107], changes which may mediate the onset of reactive gliosis.

Cleaved spectrin α II protein is directly linked to the regulation of intracellular Ca^{2+} concentrations, and it was noted that together with the downregulation of this protein, only VM cells cultured on films formed with 19 nm roughness (formed at 0.4 mA cm^{-2} current density) exhibited a low expression of L-type Ca^{2+} and the mechano-gated ion channel PIEZO 2. These observations are intriguing as an upregulation in voltage-gated calcium channels (VGCCs) such as L-type Ca^{2+} have been known to induce reactive astrogliosis [104]. Furthermore, the calcium regulating mechanosensitive protein PIEZO 2 is known to play a role in the regulation of calcium-permeability, which may relate to cell membrane damage [108-110]. It is of importance to indicate the observed downregulation of TREK 1 expression on ITO films anodised with 0.4 mA cm^{-2} and that optimal function of astrocytes homeostasis is mediated by K^+ channels [111] such as TREK 1, which has been shown to help set the negative resting membrane potential of astrocytes and regulate astrocyte reactivity [112]. Moreover, downregulation in protein markers for gliosis such as Smad3 [113],

Chondroitin Sulfate [114] and the TRP [115] family channels such as VR1[116] and ANKTM1 [117], proteins linked to inflammation and the attenuated gliosis response were observed in VM cells cultured on ITO films anodised with 0.4 mA cm^{-2} .

In order to validate cell studies performed with SH-SY5Y cells, migration proteins such as CD 81 (TAPA) and Paxillin were also concurrently assessed in VM populations. CD 81 is a member of the tetraspan family of proteins, and is involved both in cell adhesion and the machinery of migration [118] and in relation to glial scar formation, CD 81 has been found to have a defined relation to reactive astrocytes expression. Critically, previous studies have shown that upregulation of CD 81 is a prominent characteristic of glial scar formation [119, 120]. Moreover observed downregulation in the expression of CD 81 and upregulations in the expression of paxillin are consistent with observed modulation to FA formation in SH-SY5Y cells and suggest that the roughness of anodised ITO films has an effect on focal adhesion frequency and cell adhesion.

2.4.5 Functional Characterisation

The ability of anodised ITO to interface neuronal circuit formation was subsequently explored via patch-clamp analysis. In particular, due to the favourable electrochemical and phenotypical responses of VM cells to these anodised films the functional response was explored using primary rat hippocampal mature neurons on ITO anodised at the lowest current density (0.4 mA cm^{-2}) via two functional indicators: network formation and synaptic activity [50].

Rat hippocampal cells, from which primary neuronal cultures were grown and maintained for eight to ten days on ITO anodised films formed at a current density of 0.4 mA cm^{-2} , were compared to control cultures grown on poly-L-ornithine coated glass coverslips. Hippocampal neuron maturation and viability were assessed using single-cell recordings (see Materials and Methods section 2.3.7). Visually identified neurons from the two culture groups were patch clamped under voltage clamp modality to measure the cell passive membrane properties which are known indicators of neuronal health [121]. These parameters (input resistance and membrane capacitance) did not differ ($P=0.2$ and $P=0.4$ for input resistance and cell capacitance,

respectively) when measured in the two culture conditions (see bar plots in **Figure 2.17C**). The synapse formation and activity after *in vitro* growth of neurons were investigated by measuring the occurrence of spontaneous postsynaptic currents (PSCs) in both culture groups. The appearance of PSCs provided clear evidence of functional synapse formation which is a widely accepted index of network efficacy [50].

Figure 2.17A shows representative current tracings of the recorded electrical activity. PSC amplitude and frequency were measured from neurons grown in control and 0.4 mA cm⁻² anodised ITO films. As summarised in the bar plots of **Figure 2.17B**, these values were not statistically different (P=0.9 and P=0.3, amplitude and frequency, respectively) in the two groups of cultures and were consistent with those measured in other studies testing the permissive nature of manufactured interfaces [122]. The impact on cells of the modified substrate is, therefore, negligible. In **Figure 2.17D** the cellular composition of control and anodised ITO film hippocampal cultures is shown, assessed by immunofluorescence markers [54] for astrocytes (GFAP) and neurons (β -tubulin III). It was observed that both β -tubulin III and GFAP immunoreactive cells in all growing conditions (**Figure 2.17D** left and right panels) and both cell groups were represented in a proportion that is comparable in all experimental groups (quantified by measuring the cell density, bar plot in **Figure 2.17E**; P=0.4, 30 visual fields per condition, three different culture series). Thus, cell survival and the global network size were not affected by ITO anodised film formed at current density of 0.4 mA cm⁻².

Anodisation of Magnetron-Sputtered Indium-Tin Oxide (ITO) Films

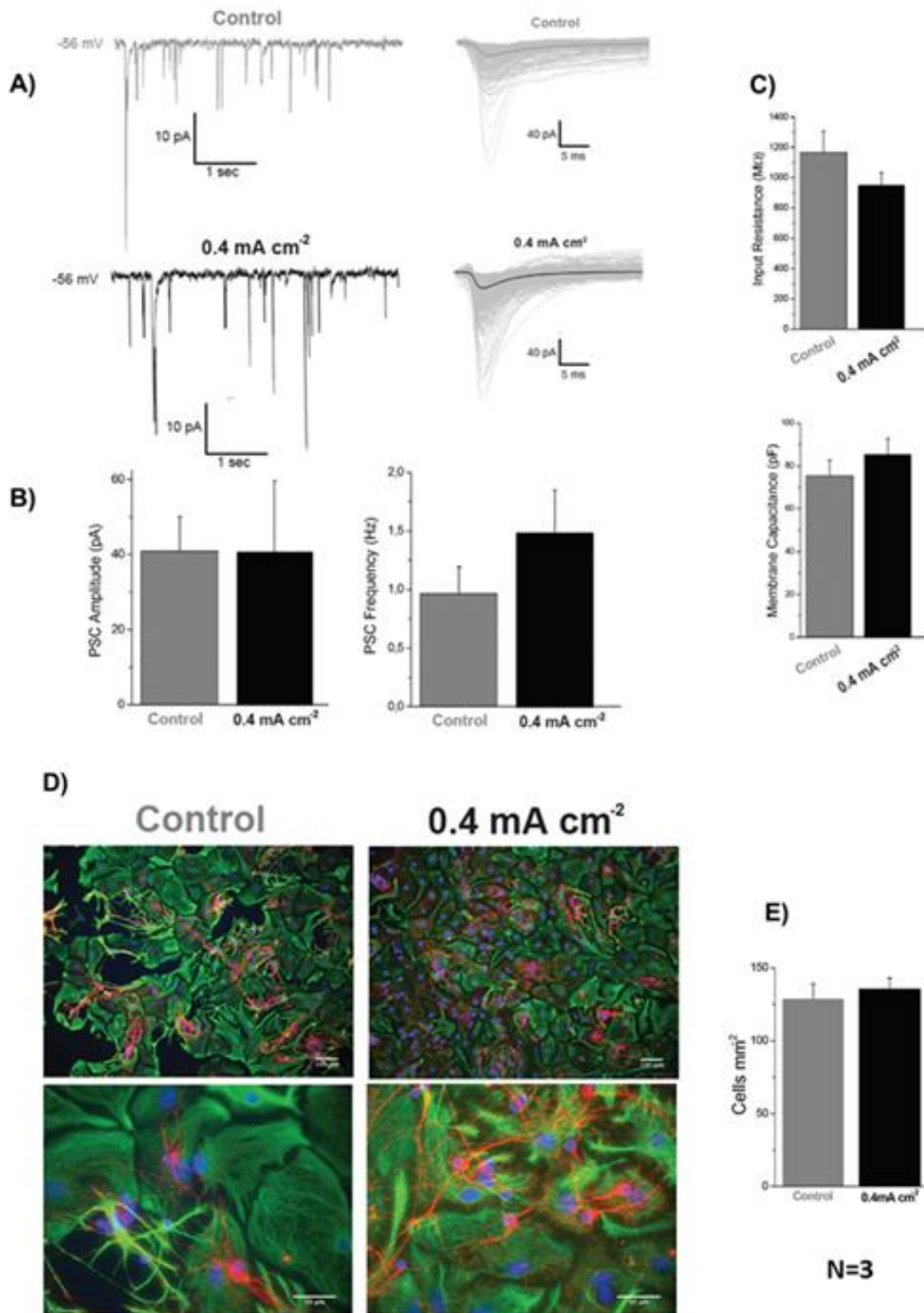


Figure 2.17 Synaptic network formation on anodised film formed at a current density of 0.4 mA cm⁻². A) Left, current tracings from two sample neurons (in grey control and in black anodised film) showing heterogeneous post-synaptic currents (PSCs; inward deflections) recorded at a holding potential of -56 mV. Right,

Superimposed traces show isolated PSCs recorded from Control (top; the average is superimposed in grey) and 0.4 mA cm⁻² (bottom; the average is superimposed in black) neurons. Bar plots in B) summarise PSC amplitude (left) and PSC frequency (right) values. Although not statistically significant, on anodised films PSC frequency was slightly higher (0.9 ± 0.6 Hz in controls and 1.5 ± 0.9 Hz in anodised films, N=8 and N=7, respectively), while the average values for PSC amplitude were similar (40.8 ± 25.9 pA controls and 40.5 ± 50.7 pA in anodised films). C) Bar plots summarise the values measured for the input resistance (top, 1195±368 MΩ controls and 946±229 MΩ anodised films) and membrane capacitance (bottom, 75±20 pF controls and 85±19 pF anodised film). D) Fluorescent micrographs of immune-labelled cultures, control (left) and anodised films (right), at low (top panels, objective 10×) and high (bottom panels objective 40×) magnifications. Neurons are visualised by anti β-tubulin III, in red, glial cells by anti-GFAP, in green and nuclei are visualised by Hoeschst, in blue. The plots in E) summarise neuronal densities in all conditions.

To assess the ability of ITO anodised films formed at a current density of 0.4 mA cm⁻² to transfer sufficient charge for cellular depolarisation, primary cultures of VM cells were grown on films for 60 days and stimulated with biphasic pulses of 2V cm⁻², 0.1s duration at a frequency of 0.2 Hz. Cells were observed to generate calcium transients in response to the stimulus via 0.4 mA cm⁻² anodised ITO films, while the same stimulus did not elicit any response in pristine ITO control cultures (**Figure 2.18**). In turn, the spontaneous calcium events of the neurons cultured on the 0.4 mA cm⁻² anodised ITO films represent the ongoing synaptic activity after material stimulation, further suggesting functional synaptic connections formed in the culture system [123]. Moreover, calcium transients were also visible when using primary hippocampal mature neurons, cultured on 0.4 mA cm⁻² anodised ITO films (**Figure 2.19**).

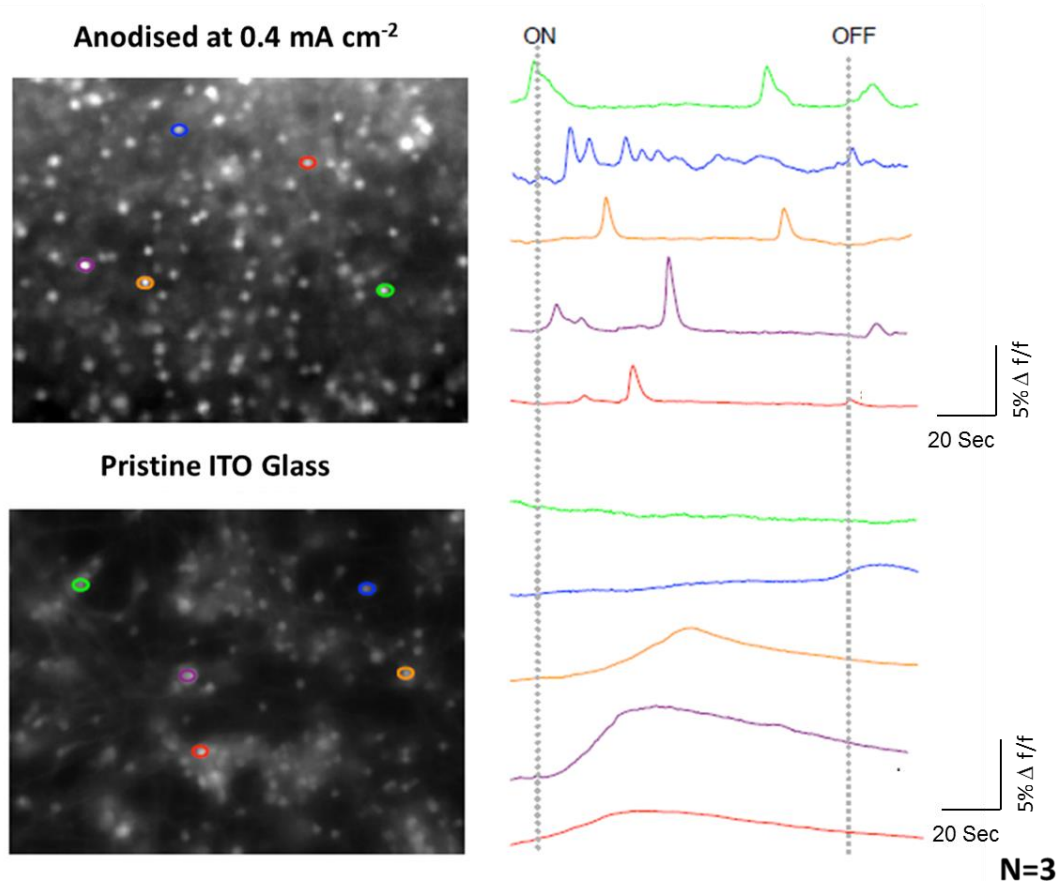


Figure 2.18 Calcium imaging and substrate stimulation. Left snapshots of representative fields of VM cells grown on anodised ITO film formed at 0.4 mA cm^{-2} (top) and control pristine ITO glass (bottom) and stained with calcium-sensitive fluorescent probe Fluo-4. Five regions of interest (ROI) per image were selected (highlighted in different colours), each representing a single neuron. Right, fluorescence tracings show the appearance of Ca^{2+} episodes, calcium events were measured from the relative ROI in the corresponding recording filed in both conditions (each cell is identified by the colour). Stimulation was delivered to the films as biphasic voltage pulses (2 V cm^{-2} , 0.1 s pulse, 0.2 Hz). Dashed lines highlight the corresponding evoked calcium response in both groups. Note that all selected cells displayed calcium transients in response to the stimulus in the 0.4 mA cm^{-2} condition, while the same stimulus did not elicit any responses in control cultures.

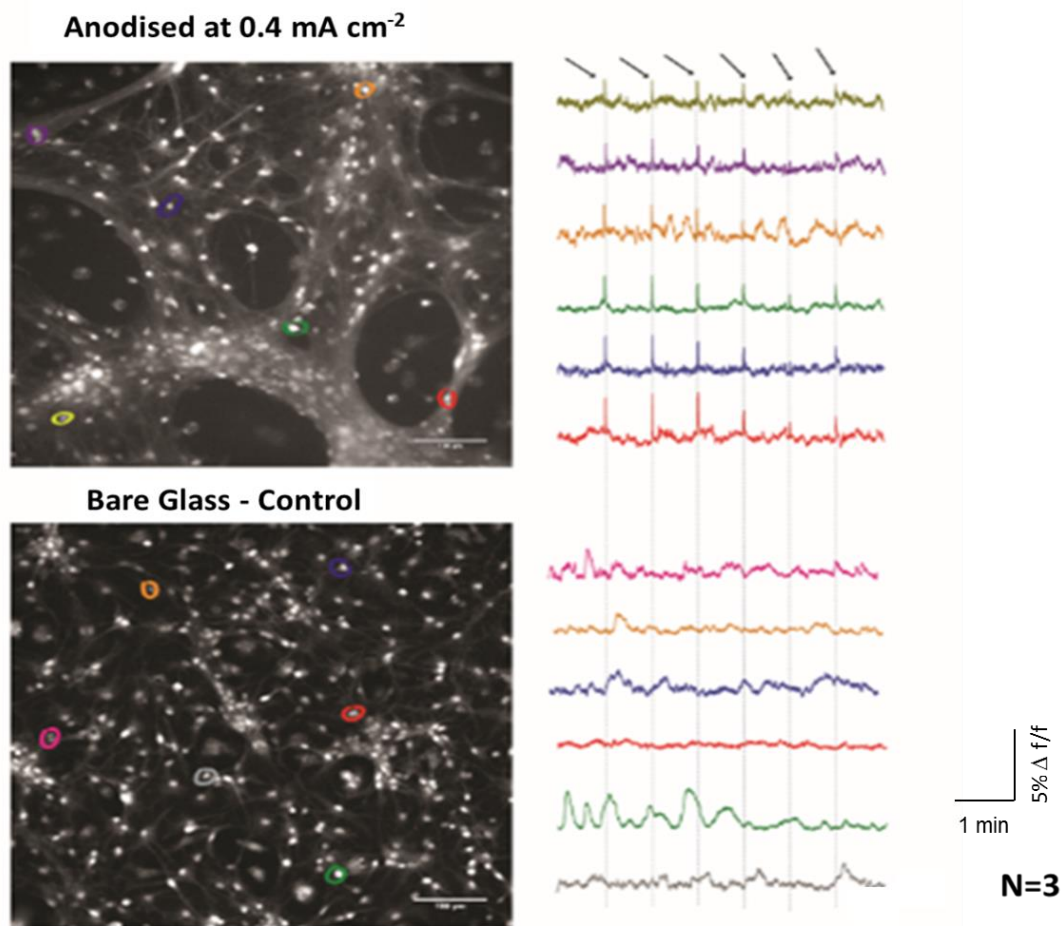


Figure 2.19 Calcium imaging and substrate stimulation. Left, snapshots of representative fields of neuronal cultures grown on 0.4 mA cm^{-2} (top) and control (bottom) and stained with the Oregon Green 488-BAPTA-1 AM. Six regions of interest (ROI) per image were selected (highlighted in different colours), each representing a single neuron, ROIs were selected at least $100 \mu\text{m}$ apart. Right, fluorescence tracings show the appearance of Ca^{2+} episodes, calcium events were measured from the relative ROI in the corresponding recording filed in both conditions (each cell is identified by the colour). In these experiments, voltage stimuli were delivered (every 60 seconds, arrows) via the substrate. Dashed lines highlight the corresponding evoked calcium response in both groups. Note that all selected cells displayed calcium transients in response to the stimulus in the 0.4 mA cm^{-2} condition, while the same stimulus did not elicit any responses in control cultures.

2.5 Conclusion

In this chapter a range of current densities for the anodisation of ITO in an aqueous cytocompatible electrolyte were employed and the effects of anodisation current density on ITO electrochemical, physical and cytocompatibility properties were investigated. Furthermore, anodisation was assessed as a methodology for the formulation of neural interface materials with a focus on reduced cellular reactivity and enhanced neural stimulation capacity.

This work provides a useful bench-mark for anodisation conditions for subsequent studies with neural microelectrodes, micro-patterning and biochemical functionalisation. It was observed that anodisation offers the ability to modify ITO films with differential properties for charge transfer and resistivity may provide a facile approach to the deposition of electrode coatings with differential regions of charge conductance and cellular function capacities. It can be hypothesised that anodisation with varying current densities may be employed to deposit insulator and charge carrier regions on a single electrode system, providing cytocompatible and functional coatings for implantable thin-film ITO devices.

2.6 References

1. Vallejo-Giraldo, C.; Kelly, A.; Biggs, M. J., *Drug Discov. Today* 2014, 19 (1), 88-94. DOI 10.1016/j.drudis.2013.07.022.
2. Durand DM, G. M., Krames E, *J Neural Eng* 2014.
3. Zhang, A.; Lieber, C. M., *Chem. Rev.* 2016, 116 (1), 215-57. DOI 10.1021/acs.chemrev.5b00608.
4. Svennersten, K.; Larsson, K. C.; Berggren, M.; Richter-Dahlfors, A., *Biochim Biophys Acta* 2011, 1810 (3), 276-85. DOI 10.1016/j.bbagen.2010.10.001.
5. Larsson, K. C.; Kjall, P.; Richter-Dahlfors, A., *Biochim Biophys Acta* 2013, 1830 (9), 4334-44. DOI 10.1016/j.bbagen.2012.11.024.
6. Owens, R.; Kjall, P.; Richter-Dahlfors, A.; Cicoira, F., *Biochim Biophys Acta* 2013, 1830 (9), 4283-5. DOI 10.1016/j.bbagen.2013.04.025.

7. Simon, D. T.; Gabrielsson, E. O.; Tybrandt, K.; Berggren, M., *Chem. Rev.* 2016. DOI 10.1021/acs.chemrev.6b00146.
8. Kozai, T. D.; Langhals, N. B.; Patel, P. R.; Deng, X.; Zhang, H.; Smith, K. L.; Lahann, J.; Kotov, N. A.; Kipke, D. R., *Nat Mater* 2012, 11 (12), 1065-73. DOI 10.1038/nmat3468.
9. Mantione, D.; Del Agua, I.; Schaafsma, W.; Diez-Garcia, J.; Castro, B.; Sardon, H.; Mecerreyes, D., *Macromol Biosci* 2016, 16 (8), 1227-38. DOI 10.1002/mabi.201600059.
10. Cogan, S. F., *Annu. Rev. Biomed. Eng.* 2008, 10, 275-309. DOI 10.1146/annurev.bioeng.10.061807.160518.
11. Rose, L. S. R. a. T. L., *Neural Prostheses: Fundamental Studies*. Prentice Hall: Englewood Cliffs, NJ, 1990; p p.25.
12. Vallejo-Giraldo, C.; Pugliese, E.; Larranaga, A.; Fernandez-Yague, M. A.; Britton, J. J.; Trotier, A.; Tadayyon, G.; Kelly, A.; Rago, I.; Sarasua, J. R.; Dowd, E.; Quinlan, L. R.; Pandit, A.; Biggs, M. J., *Nanomedicine (Lond)* 2016, 11 (19), 2547-63. DOI 10.2217/nnm-2016-0075.
13. Zhou, H.; Cheng, X.; Rao, L.; Li, T.; Duan, Y. Y., *Acta Biomater* 2013, 9 (5), 6439-49. DOI 10.1016/j.actbio.2013.01.042.
14. Gregory, O. J.; Luo, Q.; Crisman, E. E., *Thin Solid Films* 2002, 406 (1-2), 286-293. DOI Pii S0040-6090(01)01773-4
Doi 10.1016/S0040-6090(01)01773-4.
15. Faughnan, B. W.; Crandall, R. S., *Top Appl Phys* 1980, 40, 181-211.
16. Meng, L. J.; Li, C. H.; Zhong, G. Z., *J. Lumin.* 1987, 39 (1), 11-17. DOI Doi 10.1016/0022-2313(87)90004-4.
17. Bellingham, J. R.; Mackenzie, A. P.; Phillips, W. A., *Appl. Phys. Lett.* 1991, 58 (22), 2506-2508. DOI Doi 10.1063/1.104858.
18. Luff, B. J.; Wilkinson, J. S.; Perrone, G., *Appl. Opt.* 1997, 36 (27), 7066-7072. DOI Doi 10.1364/Ao.36.007066.

19. Weitz, A. C.; Behrend, M. R.; Lee, N. S.; Klein, R. L.; Chiodo, V. A.; Hauswirth, W. W.; Humayun, M. S.; Weiland, J. D.; Chow, R. H., *J Neurophysiol* 2013, 109 (7), 1979-88. DOI 10.1152/jn.00852.2012.
20. Weitz, A. C.; Behrend, M. R.; Ahuja, A. K.; Christopher, P.; Wei, J.; Wuyyuru, V.; Patel, U.; Greenberg, R. J.; Humayun, M. S.; Chow, R. H.; Weiland, J. D., *J Neural Eng* 2014, 11 (1), 016007.
21. Tanamoto, R.; Shindo, Y.; Miki, N.; Matsumoto, Y.; Hotta, K.; Oka, K., *J Neurosci Methods* 2015, 253, 272-8. DOI 10.1016/j.jneumeth.2015.07.002.
22. Qiu, Q.; Sayer, M.; Kawaja, M.; Shen, X.; Davies, J. E., *J Biomed Mater Res* 1998, 42 (1), 117-27.
23. Petronis, S.; Stangegaard, M.; Christensen, C. B.; Dufva, M., *Biotechniques* 2006, 40 (3), 368-76.
24. Nashimoto, Y.; Takahashi, Y.; Yamakawa, T.; Torisawa, Y. S.; Yasukawa, T.; Ito-Sasaki, T.; Yokoo, M.; Abe, H.; Shiku, H.; Kambara, H.; Matsue, T., *Anal Chem* 2007, 79 (17), 6823-30. DOI 10.1021/ac071050q.
25. Guo, M. L.; Chen, J. H.; Yun, X. B.; Chen, K.; Nie, L. H.; Yao, S. Z., *Bba-Gen Subjects* 2006, 1760 (3), 432-439. DOI 10.1016/j.bbagen.2005.11.011.
26. Selvakumaran, J.; Hughes, M. P.; Keddie, J. L.; Ewins, D. J., *Eng Med Biol Soc Ann* 2002, 261-264. DOI Doi 10.1109/Mmb.2002.1002326.
27. Pluk, H.; Stokes, D.; Lich, B.; Wieringa, B.; Fransen, J., *J Microsc-Oxford* 2009, 233 (3), 353-363. DOI 10.1111/j.1365-2818.2009.03140.x.
28. Bowers, C. M.; Shestopalov, A. A.; Clark, R. L.; Toone, E. J., *ACS Appl Mater Interfaces* 2012, 4 (8), 3932-3937. DOI 10.1021/am300768f.
29. Huang, C. J.; Su, Y. K.; Wu, S. L., *Mater. Chem. Phys.* 2004, 84 (1), 146-150. DOI 10.1016/j.matchemphys.2003.11.021.
30. Ho, P. K. H.; Granstrom, M.; Friend, R. H.; Greenham, N. C., *Adv Mater* 1998, 10 (10), 769-774. DOI Doi 10.1002/(Sici)1521-4095(199807)10:10<769::Aid-Adma769>3.3.Co;2-V.

31. Robinson, J. L.; King, P. F., *J. Electrochem. Soc.* 1961, 108 (1), 36-41. DOI Doi 10.1149/1.2428007.
32. Cabrera, N.; Mott, N. F., *Rep Prog Phys* 1948, 12, 163-184.
33. Cho, S. W.; Jeong, J. G.; Park, S. H.; Cho, M. H.; Jeong, K.; Whang, C. N.; Yi, Y., *Appl. Phys. Lett.* 2008, 92 (21). DOI Artn 213302
10.1063/1.2931697.
34. Schueller, G. R. T.; Taylor, S. R.; Hajcsar, E. E., *J. Electrochem. Soc.* 1992, 139 (10), 2799-2805. DOI Doi 10.1149/1.2068982.
35. Blawert, C.; Dietzel, W.; Ghali, E.; Song, G. L., *Adv Eng Mater* 2006, 8 (6), 511-533. DOI 10.1002/adem.200500257.
36. Diamanti, M. V.; Del Curto, B.; Pedefferri, M., *J. Appl. Biomater. Biomech.* 2011, 9 (1), 55-69. DOI 10.5301/JABB.2011.7429.
37. McNamara, L. E.; Sjostrom, T.; Burgess, K. E. V.; Kim, J. J. W.; Liu, E.; Gordonov, S.; Moghe, P. V.; Meek, R. M. D.; Oreffo, R. O. C.; Su, B.; Dalby, M. J., *Biomaterials* 2011, 32 (30), 7403-7410. DOI 10.1016/j.biomaterials.2011.06.063.
38. Tsuchiya, H.; Macak, J. M.; Ghicov, A.; Taveira, L.; Schmuki, P., *Corros. Sci.* 2005, 47 (12), 3324-3335. DOI 10.1016/j.corsci.2005.05.041.
39. Ghicov, A.; Tsuchiya, H.; Macak, J. M.; Schmuki, P., *Electrochem. Commun.* 2005, 7 (5), 505-509. DOI 10.1016/j.elecom.2005.03.007.
40. Mahshid, S.; Dolati, A.; Goodarzi, M.; Askari, M.; Ghahramaninezhad, A., *Nanotechnology (General) - 217th Ecs Meeting 2010*, 28 (7), 67-74. DOI 10.1149/1.3491775.
41. Tian, T.; Xiao, X. F.; Liu, R. F.; She, H. D.; Hu, X. F., *J. Mater. Sci.* 2007, 42 (14), 5539-5543. DOI 10.1007/s10853-006-1104-6.
42. Bauer, S.; Kleber, S.; Schmuki, P., *Electrochem. Commun.* 2006, 8 (8), 1321-1325. DOI 10.1016/j.elecom.2006.05.030.

43. Swan, E. E. L.; Papat, K. C.; Grimes, C. A.; Desai, T. A., *Journal of Biomedical Materials Research Part A* 2005, 72A (3), 288-295. DOI 10.1002/jbm.a.30223.
44. Foong, T. R. B.; Sellinger, A.; Hu, X., *Acs Nano* 2008, 2 (11), 2250-2256. DOI 10.1021/nn800435n.
45. ASTM, standard guide for accelerated aging of sterile barrier systems for medical devices. In F1980-07 2011.
46. Green, R. A.; Hassarati, R. T.; Bouchinet, L.; Lee, C. S.; Cheong, G. L.; Yu, J. F.; Dodds, C. W.; Suaning, G. J.; Poole-Warren, L. A.; Lovell, N. H., *Biomaterials* 2012, 33 (25), 5875-86. DOI 10.1016/j.biomaterials.2012.05.017.
47. Hukins, D. W.; Mahomed, A.; Kukureka, S. N., *Med Eng Phys* 2008, 30 (10), 1270-4. DOI 10.1016/j.medengphy.2008.06.001.
48. Wei, X. F.; Grill, W. M., *J. Neural Eng.* 2009, 6 (4). DOI Artn 046008 10.1088/1741-2560/6/4/046008.
49. Green, R. A.; Lovell, N. H.; Wallace, G. G.; Poole-Warren, L. A., *Biomaterials* 2008, 29 (24-25), 3393-9. DOI 10.1016/j.biomaterials.2008.04.047.
50. Cellot, G.; Toma, F. M.; Varley, Z. K.; Laishram, J.; Villari, A.; Quintana, M.; Cipollone, S.; Prato, M.; Ballerini, L., *J Neurosci* 2011, 31 (36), 12945-53. DOI 10.1523/JNEUROSCI.1332-11.2011.
51. Biggs, M. J.; Richards, R. G.; McFarlane, S.; Wilkinson, C. D.; Oreffo, R. O.; Dalby, M. J., *J R Soc Interface* 2008, 5 (27), 1231-42. DOI 10.1098/rsif.2008.0035.
52. Smith, P. K.; Krohn, R. I.; Hermanson, G. T.; Mallia, A. K.; Gartner, F. H.; Provenzano, M. D.; Fujimoto, E. K.; Goeke, N. M.; Olson, B. J.; Klenk, D. C., *Analytical biochemistry* 1985, 150 (1), 76-85.
53. Gerlach, J. Q.; Kilcoyne, M.; Joshi, L., *Analytical Methods* 2014, 6 (2), 440-449. DOI 10.1039/C3AY40936H.
54. Bosi, S.; Rauti, R.; Laishram, J.; Turco, A.; Lonardoni, D.; Nieuw, T.; Prato, M.; Scaini, D.; Ballerini, L., *Sci Rep* 2015, 5, 9562. DOI 10.1038/srep09562.

55. Folcher, G.; Cachet, H.; Froment, M.; Bruneaux, J., *Thin Solid Films* 1997, 301 (1-2), 242-248. DOI Doi 10.1016/S0040-6090(97)00024-2.
56. Kraft, A.; Hennig, H.; Herbst, A.; Heckner, K. H., *J. Electroanal. Chem.* 1994, 365 (1-2), 191-196. DOI Doi 10.1016/0022-0728(93)03056-U.
57. Shao, Y.; Xiao, X.; Wang, L. Y.; Liu, Y.; Zhang, S. D., *Adv Funct Mater* 2014, 24 (26), 4170-4175. DOI 10.1002/adfm.201400263.
58. Matveeva, E., *J. Electrochem. Soc.* 2005, 152 (9), H138-H145. DOI 10.1149/1.1984348.
59. Senthilkumar, M.; Mathiyarasu, J.; Joseph, J.; Phani, K. L. N.; Yegnaraman, V., *Mater. Chem. Phys.* 2008, 108 (2-3), 403-407. DOI 10.1016/j.matchemphys.2007.10.030.
60. Liu, L.; Yellinek, S.; Valdinger, I.; Donval, A.; Mandler, D., *Electrochim Acta* 2015, 176, 1374-1381. DOI 10.1016/j.electacta.2015.07.129.
61. Stotter, J.; Show, Y.; Wang, S. H.; Swain, G., *Chem Mater* 2005, 17 (19), 4880-4888. DOI 10.1021/cm050762z.
62. Castro-Rodriguez, R.; Oliva, A. I.; Sosa, V.; Caballero-Briones, F.; Pena, J. L., *Appl. Surf. Sci.* 2000, 161 (3-4), 340-346. DOI Doi 10.1016/S0169-4332(99)00574-7.
63. Kavei, G.; Gheidari, A. M., *J Mater Process Tech* 2008, 208 (1-3), 514-519. DOI 10.1016/j.jmatprotec.2008.01.024.
64. Yao, C.; Webster, T. J., *J Nanosci Nanotechnol* 2006, 6 (9-10), 2682-2692. DOI 10.1166/jnn.2006.447.
65. Vanhumbecck, J. F.; Proost, J., *Corros. Rev.* 2009, 27 (3), 117-204. DOI Doi 10.1515/Corrrev.2009.27.3.117.
66. Paul, A.; Wingbermuehle, J., *Appl. Surf. Sci.* 2006, 252 (23), 8151-8155. DOI 10.1016/j.apsusc.2005.10.056.
67. Facchetti, A.; Yoon, M. H.; Marks, T. J., *Adv Mater* 2005, 17 (14), 1705-1725. DOI 10.1002/adma.200500517.

68. Lee, S.; Kwon, J.-Y.; Yoon, D.; Cho, H.; You, J.; Kang, Y. T.; Choi, D.; Hwang, W., *Nanoscale research letters* 2012, 7 (1), 1.
69. Asmani, M.; Kermel, C.; Leriche, A.; Ourak, M., *J. Eur. Ceram. Soc.* 2001, 21 (8), 1081-1086. DOI [http://dx.doi.org/10.1016/S0955-2219\(00\)00314-9](http://dx.doi.org/10.1016/S0955-2219(00)00314-9).
70. Zeng, K.; Zhu, F.; Hu, J.; Shen, L.; Zhang, K.; Gong, H., *Thin Solid Films* 2003, 443 (1), 60-65.
71. Solieman, A.; Aegerter, M. A., *Thin Solid Films* 2006, 502 (1-2), 205-211. DOI 10.1016/j.tsf.2005.07.277.
72. Montecchi, M.; Montereali, R. M.; Nichelatti, E., *Thin Solid Films* 2001, 396 (1-2), 262-273.
73. Hamasha, M. M.; Dhakal, T.; Alzoubi, K.; Albahri, S.; Qasaimeh, A.; Lu, S.; Westgate, C. R., *Journal of Display Technology* 2012, 8 (7), 385-390. DOI 10.1109/JDT.2011.2176532.
74. Tang, C. W.; VanSlyke, S. A., *Appl. Phys. Lett.* 1987, 51 (12), 913-915.
75. Haskal, E. I., *Synthetic Met* 1997, 91 (1), 187-190. DOI [http://dx.doi.org/10.1016/S0379-6779\(97\)04013-7](http://dx.doi.org/10.1016/S0379-6779(97)04013-7).
76. Jung, H.; Chung, W.; Lee, C. H.; Kim, S. H., *J Nanosci Nanotechnol* 2012, 12 (7), 5407-11.
77. Haskal, E.; Curioni, A.; Seidler, P.; Andreoni, W., *Appl. Phys. Lett.* 1997, 71 (9), 1151-1153.
78. Nishimoto, N.; Yamada, Y.; Ohnishi, Y.; Imawaka, N.; Yoshino, K., *physica status solidi (a)* 2013, 210 (3), 589-593.
79. Turak, A., *Dewetting Stability of ITO Surfaces in Organic Optoelectronic Devices*. In *Optoelectronics - Advanced Materials and Devices*, Ballato, S. L. P. a. J. M., Ed. 2013.
80. Bejital, T.; Ramji, K.; Kessman, A.; Sierros, K.; Cairns, D., *Mater. Chem. Phys.* 2012, 132 (2), 395-401.

81. Serantoni, M.; Cunnane, V. J., *J. Electroanal. Chem.* 2003, 548, 49-67.
82. Hung-Ji, L.; Der-Yuh, L.; Jenq-Shinn, W.; Chu-Shou, Y.; Wu-Ching, C.; Wei-Hsuan, L.; Jyh-Shyang, W., *Japanese Journal of Applied Physics* 2009, 48 (4S), 04C122.
83. Donley, C.; Dunphy, D.; Paine, D.; Carter, C.; Nebesny, K.; Lee, P.; Alloway, D.; Armstrong, N. R., *Langmuir* 2002, 18 (2), 450-457. DOI 10.1021/la011101t.
84. Keil, R. G., *J. Electrochem. Soc.* 1986, 133 (7), 1375-1379.
85. Bard, A. J., & Faulkner, L. R. *Fundamentals and Applications*, New York, Wiley, 2002.
86. Brunetti, V.; Maiorano, G.; Rizzello, L.; Sorce, B.; Sabella, S.; Cingolani, R.; Pompa, P. P., *Proc Natl Acad Sci U S A* 2010, 107 (14), 6264-9. DOI 10.1073/pnas.0914456107.
87. Buttiglione, M.; Vitiello, F.; Sardella, E.; Petrone, L.; Nardulli, M.; Favia, P.; d'Agostino, R.; Gristina, R., *Biomaterials* 2007, 28 (19), 2932-2945. DOI DOI 10.1016/j.biomaterials.2007.02.022.
88. Fan, Y. W.; Cui, F. Z.; Hou, S. P.; Xu, Q. Y.; Chen, L. N.; Lee, I. S., *J Neurosci Methods* 2002, 120 (1), 17-23. DOI Pii S0165-0270(02)00181-4
Doi 10.1016/S0165-0270(02)00181-4.
89. Khan, S. P.; Auner, G. G.; Newaz, G. M., *Nanomed.* 2005, 1 (2), 125-9. DOI 10.1016/j.nano.2005.03.007.
90. Biggs, M. J. P.; Richards, R. G.; Gadegaard, N.; McMurray, R. J.; Affrossman, S.; Wilkinson, C. D. W.; Oreffo, R. O. C.; Dalby, M. J., *Journal of Biomedical Materials Research Part A* 2009, 91A (1), 195-208. DOI Doi 10.1002/Jbm.A.32196.
91. Schaller, M. D., *Oncogene* 2001, 20 (44), 6459-72. DOI 10.1038/sj.onc.1204786.
92. Kim, M. H.; Park, M.; Kang, K.; Choi, I. S., *Biomater Sci-Uk* 2014, 2 (2), 148-155. DOI Doi 10.1039/C3bm60255a.

93. Kang, K.; Kim, M. H.; Park, M.; Choi, I. S., *J Nanosci Nanotechnol* 2014, 14 (1), 513-521. DOI DOI 10.1166/jnn.2014.8764.
94. Sriram, G.; Patil, P.; Bhat, M. P.; Hegde, R. M.; Ajeya, K. V.; Udachyan, I.; Bhavya, M.; Gatti, M. G.; Uthappa, U. T.; Neelgund, G. M., *Journal of Nanomaterials* 2016, 2016, 2.
95. Wälivaara, B.; Aronsson, B.-O.; Rodahl, M.; Lausmaa, J.; Tengvall, P., *Biomaterials* 1994, 15 (10), 827-834.
96. Myung, S. W.; Ko, Y. M.; Kim, B. H., *Japanese Journal of Applied Physics* 2014, 53 (11S), 11RB01.
97. Recek, N.; Jaganjac, M.; Kolar, M.; Milkovic, L.; Mozetič, M.; Stana-Kleinschek, K.; Vesel, A., *Molecules* 2013, 18 (10), 12441-12463.
98. Sharma, A.; McQuillan, A. J.; Sharma, L. A.; Waddell, J. N.; Shibata, Y.; Duncan, W. J., *J Mater Sci Mater Med* 2015, 26 (8), 221. DOI 10.1007/s10856-015-5555-7.
99. Bai, Z.; Filiaggi, M. J.; Sanderson, R. J.; Lohstreter, L. B.; McArthur, M. A.; Dahn, J. R., *J Biomed Mater Res A* 2010, 92 (2), 521-32. DOI 10.1002/jbm.a.32398.
100. Shi, W.; Shen, Y.; Ge, D.; Xue, M.; Cao, H.; Huang, S.; Wang, J.; Zhang, G.; Zhang, F., *J. Membr. Sci.* 2008, 325 (2), 801-808.
101. Biggs, M. J.; Richards, R. G.; Dalby, M. J., *Nanomed.* 2010, 6 (5), 619-33. DOI 10.1016/j.nano.2010.01.009.
102. Karve, I. P.; Taylor, J. M.; Crack, P. J., *Br J Pharmacol* 2016, 173 (4), 692-702. DOI 10.1111/bph.13125.
103. Tykhomyrov, A.; Pavlova, A.; Nedzvetsky, V., *Neurophysiology* 2016, 48 (1), 54-71.
104. Burgos, M.; Pastor, M. D.; Gonzalez, J. C.; Martinez-Galan, J. R.; Vaquero, C. F.; Fradejas, N.; Benavides, A.; Hernandez-Guijo, J. M.; Tranque, P.; Calvo, S., *Glia* 2007, 55 (14), 1437-48. DOI 10.1002/glia.20555.

105. Kim, J. H.; Kwon, S. J.; Stankewich, M. C.; Huh, G. Y.; Glantz, S. B.; Morrow, J. S., *Exp Mol Pathol* 2016, 100 (1), 1-7. DOI 10.1016/j.yexmp.2015.11.005.
106. Du, S.; Rubin, A.; Klepper, S.; Barrett, C.; Kim, Y. C.; Rhim, H. W.; Lee, E. B.; Park, C. W.; Markelonis, G. J.; Oh, T. H., *Exp. Neurol.* 1999, 157 (1), 96-105. DOI <http://dx.doi.org/10.1006/exnr.1999.7041>.
107. Liu, J.; Liu, M. C.; Wang, K. K. W., *Sci. Signal.* 2008, 1 (14), re1-re1. DOI 10.1126/stke.114re1.
108. Sajja, V. S.; Ereifej, E. S.; VandeVord, P. J., *Neurosci Lett* 2014, 570, 33-7. DOI 10.1016/j.neulet.2014.03.072.
109. Coste, B.; Mathur, J.; Schmidt, M.; Earley, T. J.; Ranade, S.; Petrus, M. J.; Dubin, A. E.; Patapoutian, A., *Science* 2010, 330 (6000), 55-60. DOI 10.1126/science.1193270.
110. Dubin, A. E.; Schmidt, M.; Mathur, J.; Petrus, M. J.; Xiao, B.; Coste, B.; Patapoutian, A., *Cell reports* 2012, 2 (3), 511-7. DOI 10.1016/j.celrep.2012.07.014.
111. Olsen, M., *Methods Mol Biol* 2012, 814, 265-81. DOI 10.1007/978-1-61779-452-0_18.
112. Wu, X.; Liu, Y.; Chen, X.; Sun, Q.; Tang, R.; Wang, W.; Yu, Z.; Xie, M., *J. Mol. Neurosci.* 2013, 49 (3), 499-506.
113. Wang, Y.; Moges, H.; Bharucha, Y.; Symes, A., *Exp. Neurol.* 2007, 203 (1), 168-184.
114. Pekny, M.; Pekna, M., *Biochimica et Biophysica Acta (BBA)-Molecular Basis of Disease* 2016, 1862 (3), 483-491.
115. Ellis, A.; Bennett, D. L., *British journal of anaesthesia* 2013, 111 (1), 26-37. DOI 10.1093/bja/aet128.
116. Davis, J. B.; Gray, J.; Gunthorpe, M. J.; Hatcher, J. P.; Davey, P. T.; Overend, P.; Harries, M. H.; Latcham, J.; Clapham, C.; Atkinson, K.; Hughes, S. A.; Rance, K.;

Grau, E.; Harper, A. J.; Pugh, P. L.; Rogers, D. C.; Bingham, S.; Randall, A.; Sheardown, S. A., *Nature* 2000, 405 (6783), 183-7. DOI 10.1038/35012076.

117. Story, G. M.; Peier, A. M.; Reeve, A. J.; Eid, S. R.; Mosbacher, J.; Hricik, T. R.; Earley, T. J.; Hergarden, A. C.; Andersson, D. A.; Hwang, S. W.; McIntyre, P.; Jegla, T.; Bevan, S.; Patapoutian, A., *Cell* 2003, 112 (6), 819-29.

118. Tejera, E.; Rocha-Perugini, V.; Lopez-Martin, S.; Perez-Hernandez, D.; Bachir, A. I.; Horwitz, A. R.; Vazquez, J.; Sanchez-Madrid, F.; Yanez-Mo, M., *Mol Biol Cell* 2013, 24 (3), 261-73. DOI 10.1091/mbc.E12-09-0642.

119. Song, B. K.; Geisert, G. R.; Vázquez-Chona, F.; Geisert, E. E., *Neurosci Lett* 2003, 338 (1), 29.

120. Peduzzi, J. D.; Grayson, T. B.; Fischer, F. R.; Geisert, E. E., Jr., *Exp Neurol* 1999, 160 (2), 460-8. DOI 10.1006/exnr.1999.7234.

121. Carp, J. S., *J Neurophysiol* 1992, 68 (4), 1121-32.

122. Fabbro, A.; Scaini, D.; Leon, V.; Vazquez, E.; Cellot, G.; Privitera, G.; Lombardi, L.; Torrisi, F.; Tomarchio, F.; Bonaccorso, F.; Bosi, S.; Ferrari, A. C.; Ballerini, L.; Prato, M., *Acs Nano* 2016, 10 (1), 615-23. DOI 10.1021/acsnano.5b05647.

123. Jimbo, Y.; Robinson, H. P.; & Kawana, A., *IEEE transactions on biomedical engineering*, 1993, 40(8), 804-810.

CHAPTER 3

TOPOGRAPHICALLY FUNCTIONALISED POLY(3,4-ETHYLENEDIOXYTHIOPHENE):P-TOLUENE SULPHONATE (PEDOT:PTS) NEUROELECTRODES VIA MICROIMPRINT LITHOGRAPHY

3.1 Preamble

After undergoing the unexpected journey with the anodisation process of ITO, and with newly acquired electropolymerisation basics, and equipped with a brand new Potentiostat, I started to explore poly(3,4-ethylenedioxythiophene):p-toluene sulphonate (PEDOT:PTS) coatings as functional neuroelectrode coatings.

At this new stage, the knowledge of relevant current density for electrochemical deposition from my previous work with ITO became useful and the variation of new parameters started again, with an aim to electrodeposit PEDOT:PTS.

Within the neuroengineering community there is a consensus that the induction of selective adhesion and regulated cellular interaction at the tissue-electrode interface can significantly enhance device functionality *in vivo*. In particular, topographical modification holds promise for the development of functionalised neural interfaces to modulate initial cell adhesion and the subsequent evolution of gliosis, minimising the onset of a pro-inflammatory glial phenotype, to provide long-term stability. Herein, a low-temperature microimprint-lithography technique for the development of micro-topographically functionalised neuroelectrode interfaces in electrodeposited PEDOT:PTS is described and assessed *in vitro*.

Important contribution was received from:

- Calaresu, Ivo., Ballerini, L. performed calcium imaging using Hippocampi cells.
- Farid, Nazar., O'Connor, G. micro-machining of platinum microelectrodes.
- Jingyuan Zhu., Palma, M. performed AFM-TUNA measurements

Hypothesis: Topographical functionalisation of PEDOT:PTS electrode coatings with arrays of micropits will increase the electrode active surface area and will enhance electrode integration by minimising astrocyte cell adhesion and the onset of

subsequent astrocyte reactivity. This will provide long-term stability and enhanced charge transfer for neural simulation

3.2 Introduction

Implantable stimulation and recording devices have received significant attention in biomedical engineering and have brought great success in the treatment of central nervous system disorders including paralysis [1], epilepsy [2] and Parkinson's disease [3, 4]. In order to achieve chronic functionality and integration with surrounding tissue however, neural electrodes should present a degree of biomimicry and provide electrical (ionic), chemical and physicochemical properties analogous to neural tissues, with an ultimate goal of mitigating electrode deterioration via reactive host cell response and glial scar-induced encapsulation [3, 5-8].

From this perspective the field of neuroelectrode engineering has encouraged the use of alternative electroactive materials over conventional metallic strategies such as gold and platinum [9, 10] as an approach to immobilise biological molecules [11, 12] or to promote physicochemical mimicry through soft or topographically rough interfaces [13, 14]. Specifically, semiconducting polymers [6, 15-20], including polypyrrole (PPy) [21-23] and poly(3,4-ethylenedioxythiophene) (PEDOT) [24-26], and their hybrids [27, 28] have been employed widely in neural engineering because of their versatility as electrode coatings through electrodeposition processes [29, 30], and have been employed to enhance the neuroelectrode electrochemical profile [26, 31], and provide a platform for chemical [32-34], and morphological [35-38] functionalisation to meet particular biomimicry requirements [39-42].

Ongoing studies into topographical functionalisation strategies of the neural interface have explored the micro [43-45] to the nanoscale [46, 47] and have shown promise, in promoting a low impedance profile of implantable electrodes through effects on electrode surface area [46, 48, 49]. Recent studies indicate the cytocompatibility of conducting and semiconducting polymers *in vitro* and *in vivo* and the realisation that electrodeposited conducting coatings present a nano-rough surface has led to speculation that topography may play a role in directing the inflammatory response to implanted electrodes by modulating cell function through altering integrin

distribution [50], and differential cell adhesion [51, 52]. In particular nanotopographically functionalised materials have been shown to influence the activation of intrinsic cellular processes that lead to more quiescent or reactive cell phenotypes in the onset of a pro-inflammatory response [46, 50-53] and glial scar formation [54, 55].

Ordered arrays of lithography fabricated nanopit substrates have been consistently shown in previous work to disrupt cell adhesion *in vitro* by direct or indirect modulation of focal adhesion formation [51, 52]. Recent *in vitro* studies exploring topographical modification have been successful in controlling astrocyte adhesion while promoting high neuron integration as strategies to reduce gliosis [14, 56, 57]. Although neural cells are reported to produce sparse and small focal adhesions [58], it has been shown that astrocytes are adhesion dependent [59], and when presented with a biomaterial, will form a monolayer in culture, providing neurons with physicochemical cues, to modulate neural processes extension [57]. Consequently, the ability to control astrocyte adhesion and promote a reduction of the reactive astrocyte phenotype at the electrode interface is critical to support neuronal outgrowth [60], and reduce glial scar formation [54]. Critically, microscale isotropic pit topographies of 1 μm in depth have been reported to modulate astrocytes adhesion *in vitro* [61].

In this chapter, PEDOT:PTS coated microelectrodes were topographically functionalised with ordered micro-pit arrays using a novel low-temperature three-step die imprinting lithography process, as a strategy to enhance electrode functionality, cytocompatibility and promote selective adhesion in neural stimulation applications. The physical, electrochemical and cytocompatibility effects of topographically functionalised microelectrodes were herein explored *in vitro*. Our results elucidate important topographical effects with regard to microelectrode functionality, cytocompatibility and astrogliosis towards the generation of neural interfaces with superior electrical and biological characteristics.

3.3 Materials and Methods

3.3.1 Fabrication of Microelectrode Arrays

Ultra-short laser operating at 10 kHz and 1030 nm wavelength with 500 fs pulses duration was used to generate a microelectrode shadow mask in a Polyimide film of 0.05 mm thickness. Polyimide samples were placed on a 3D computer controlled stage (Aerotech) which enabled changes in the sample position with micrometre accuracy. The laser was focused on the sample with a 100 mm focal length lens and the scanning system was coupled to the machining stage through combination of different reflectors and mirrors. The laser spot diameter was found to be 25 μm and ablation threshold 0.56 Jcm^{-2} . To avoid the melting of Polyimide, a laser fluence of 0.6 Jcm^{-2} just above the threshold and 200 laser scans were used in drawing the electrode circuit design through the Polyimide film.

Through-mask sputtering of platinum was achieved with a EMSCOPE SC500 at 25 mA for twenty minutes. Resulting platinum electrode thickness was measured to be 69.27 nm \pm 0.01 and resulted in an electrode size of 287.67 \pm 0.08 μm in width.

3.3.2 Imprinting and Die Fabrication

Micro-topographically functionalised PEDOT:PTS coated electrode were made in a three-step process of photo-lithography, nickel die fabrication, and temperature low imprinting process.

3.3.2.1 Photo Lithography

100 mm diameter silicon-wafers were first cleaned using the [ozone / DI-water / dilute-HF acid] cleaning process on a Semitool SAT spray-acid cleaning-tool. The wafers were then coated with photoresist (Fujifilm HiPR6512) and the mask pattern exposed on an Ultratech 1500 stepper, after which the photoresist was developed using Fujifilm OPD5262 developer. A number of different masks were used to give various diameter patterns. The wafers were then dry-etched to the required depth for each pattern using a [SF_6 / C_4F_8] plasma on an STS-ASE dry-etch tool. After dry-etching, the photoresist was removed by a combination of O_2 plasma ashing plus Piranha (H_2SO_4 / H_2O_2) wet-strip.

3.3.2.2 Nickel Die

This technique has been described previously [51, 52]. Briefly, nickel dies were made directly from the patterned resist samples. A thin (50-nm) layer of Ni-V was sputter coated on the samples. That layer acted as an electrode in the subsequent electroplating process. The dies were plated to a thickness of ca. 300 nm. For more information about the procedure, see reference [62].

3.3.2.3 Imprinting Process

PEDOT:PTS coated electrodes were imprinted by a low temperature imprinting process. Before the imprinting, the processed nickel die master was cut into 1 cm × 1 cm pieces, each piece acting as an individual stamp. The polymeric PEDOT:PTS coated electrodes were placed in a desiccator 24 hours prior to the imprinting process and then taken one by one to be processed. Using a hydraulic press machine (Carver, Inc), the nickel die stamp was then pressed against the PEDOT:PTS coated electrode, previously placed on pressing paralleled plates, using a compressive force of 1.9 tons cm⁻² for fifteen minutes at room temperature.

Flattened controlled non-patterned PEDOT:PTS coated electrodes were processed by pressing a thick mirror glass stamps against the PEDOT:PTS coated electrode, applying a compressive force of 1.9 tons cm⁻² for fifteen minutes at room temperature.

3.3.3 Physical Characterisation

3.3.3.1 Surface Morphology

Scanning electron microscopy (SEM) was carried out using a Hitachi S-4700 Cold Field Emission Gun Scanning Electron Microscope (CFE-SEM). The SEM images were taken using an accelerating voltage of 15 kV and spot current of 10 μA.

Scanning electron microscopy for biological samples was carried out using a Hitachi S-4700 Cold Field Emission Gun Scanning Electron Microscope (CFE-SEM). Cells on experimental electrodes were stabilised in 4% paraformaldehyde with 1% sucrose in 0.1 M piperazine-N,N'-bis(2-ethanesulfonic acid) (PIPES) buffer at pH 7.4 for five minutes. Further, samples were fixed permanently in 2.5% glutaraldehyde for

Topographically Functionalised Poly(3,4-Ethylenedioxythiophene):P-Toluene Sulphonate (PEDOT:PTS) Neuroelectrodes Via Microimprint Lithography

five minutes in PIPES buffer and rinsed three times for two minutes in PIPES buffer. Additional contrasting of the cell was accomplished by staining with 1% osmium tetroxide in PIPES for one hour at 22°C and then rinsed in distilled water for one minute. After this, cells on experimental electrodes were dehydrated through an ethanol/distilled water series (50, 60, 70, 80, 90, 96 and 100%) followed by a hexamethyldisilazane (HDMS) or Acetone/Ethanol series (25, 50, 75 and 100 %). The samples were then left to dry fully and mounted on aluminium stubs, and coated with 10nm layer of gold (Au).

For surface 3D plots and roughness analysis, Atomic Force Microscopy (AFM) was performed as detailed in [7]. All measurements were taken on a Vico Dimension 3100 AFM using TESPA Tips (NanoWorld) (Si <8 nm tip radius, 42 N/m spring constant, 320 kHz nominal resonance frequency), in tapping mode over an area of 10 μm^2 with a 0.5 - 1 Hz scan rate.

3.3.3.2 Thickness Measurements

The thickness of the polymeric PEDOT:PTS coating was measured using a Zygo Newview 100 surface profilometer controlled by MicroPlus software as detailed in [7]. Briefly, a pattern of bright and dark lines - fringes was created as incoming light was split from the limited region between the sample film and the bare platinum electrode. This pattern difference was translated to calculate the height information, resulting in the thickness of the polymeric coatings.

3.3.4 Chemical Characterisation

X-ray photoelectron spectroscopy (XPS) spectra were acquired on a Kratos AXIS 165 spectrometer XPS system with X-Ray Gun mono Al K α 1486.58 eV; 150 W (10 mA, 15kV), for all scans with the following parameters: sample temperature in a range of 20-30 °C with a pass energy of 160°eV for survey spectra and 20°eV for narrow regions and steps of 1 eV for survey and 0.05 eV for regions with dwell times of 50 ms and 100 ms for regions and sweeps for survey of ~35, and for narrow regions of 6-40. The C1s line at 284.8 eV was used as charge reference. Spectra were collected in the normal way to the surface direction with an analysis area of 60 microns. XPS

Topographically Functionalised Poly(3,4-Ethylenedioxythiophene):P-Toluene Sulphonate (PEDOT:PTS) Neuroelectrodes Via Microimprint Lithography

detection limit is estimated to be ~0.1 at%. For the data processing, the construction and peak fitting of synthetic peaks in narrow region spectra was done using a Shirley type background and the synthetic peaks were of a mixed Gaussian-Lorentzian type. Relative sensitivity factors used are from CasaXPS library containing Scofield cross-sections.

3.3.5 Electrochemical Characterisation

3.3.5.1 Preparation of PEDOT:PTS Samples

The electrodeposition of PEDOT:PTS coatings was conducted under ambient conditions according to methods described previously [63]. Briefly, a solution of 0.05M EDOT (Sigma Aldrich, Ireland) and 0.1 M PTS (Sigma Aldrich, Ireland, 70,000 g/mol MW) was prepared in a 50/50 vol.% mixture of acetonitrile and water. The electrolyte solution was placed in an in-house fabricated electrochemical cell, connected to a Princeton Applied Research Potentiostat/Galvanostat model 2273 controlled with Power Suite software. An in-house-fabricated platinum microelectrode probe array and a platinum foil (Goodfellow) were used as the working electrode (WE) and counter-electrode (CE) respectively. A saturated 3 M KCl Ag/AgCl reference electrode (RE) (Bioanalytical Systems) was employed. Galvanostatic electrodeposition was performed and the efficiency of coating, i.e. the amount of polymer deposited on the electrodes, was controlled by the total charge passing during the electrodeposition. When the deposition was finalised, the coated electrodes were soaked in deionised water for 24 hours to remove excess of electrolyte and subsequently dried for use. For cell studies, PEDOT:PTS was electrodeposited on electrodes with areas of 1.6 cm² to facilitate *in vitro* manipulations.

3.3.5.2 Electrochemical Measurements

Cyclic voltammetry was performed as previously described in [7] using a Princeton Applied Research Potentiostat/Galvanostat model 2273 running with Power Suite software. Measurements were recorded in a custom-made electrochemical cell containing the microelectrode as working electrode, an Ag/AgCl reference electrode (3 M KCl) (Bioanalytical Systems) and a platinum foil counter electrode

Topographically Functionalised Poly(3,4-Ethylenedioxythiophene):P-Toluene Sulphonate (PEDOT:PTS) Neuroelectrodes Via Microimprint Lithography

(Goodfellow) in 1X phosphate-buffered saline (PBS). Cyclic voltammograms (CVs) were run in the potential range from -1.0 V to 0.4 V at a scan rate of 0.1 V s⁻¹. The charge storage capacity (CSC) was calculated by integrating the area enclosed by the voltammogram.

Electrical impedance spectroscopy (EIS) was performed using a Princeton Applied Research Potentiostat/Galvanostat model 2273 running with Power Suite software with a three-electrode set-up. The measurements were carried out in a frequency range of 0.1 Hz to 100 kHz with an AC sine wave of 40 mV amplitude applied with 0 V DC offset. The results were presented on Bode and Nyquist plots and compared to those of bare platinum microelectrodes and coated gold microelectrodes, to exclude the effect of electrode thickness when compared to PEDOT:PTS coated microelectrodes. The data fitting analysis was performed using EIS Spectrum Analyser 1.0 software with the application of the Powell algorithm.

Electroactive surface area (ESA) measurements for each microelectrode were done through cyclic voltammetry scans performed in 2.5 mol cm⁻³ K₄[Fe(CN)₆] 0.1 M KCl solution, in the potential range from -1.0 V to 0.4 V at a scan rate of 0.1 V s⁻¹. The enlargement factor was calculated based on the change in the electroactive surface area with a bare platinum microelectrode as a reference. ESA was estimated according to the Randles-Sevcik equation: [64, 65]

$$i_p = 2.69 \cdot 10^5 AD^{1/2} n^{3/2} v^{1/2} C \quad \text{Equation 3.1}$$

where i_p is the reduction/oxidation peak current (A), n is the number of electrons contributing to the redox reaction, A is the area of the electrode (cm²), D is the diffusion coefficient of Fe(CN)₆⁴⁻ in KCl solution (6.3·10⁻⁶ cm² s⁻¹) [66], C is the concentration of the Fe(CN)₆⁴⁻ in the bulk solution (mol cm⁻³) and v is the scan rate (V s⁻¹). The measurements were performed in triplicate; the results were expressed as a mean ± standard deviation.

The electrochemical stability of microelectrodes was determined as described previously in [8]. Briefly, cyclic voltammetry was performed before and after electrical stability measurements and used to calculate the percentage of loss in

Topographically Functionalised Poly(3,4-Ethylenedioxythiophene):P-Toluene Sulphonate (PEDOT:PTS) Neuroelectrodes Via Microimprint Lithography

charge storage capacity by comparing the CSC of the 1st and 500th cycles. The measurements were performed in triplicate; the results were expressed as a mean \pm standard deviation.

Force-controlled current-voltage (I-V) characteristics were recorded employing conductive-AFM (C-AFM) (in PeakForce Tuna mode, PF Tuna, Bruker). Samples were imaged under ambient conditions with a Bruker Dimension Icon microscope, with a NanoScope IV control unit and PF-TUNA add-on module. One sapphire substrate with gold contact was used to connect samples to form the electric circuit. I-V curves were recorded at selective positions on the sample surface. C-AFM tips (coated with Platinum/Iridium) were used as the mobile counter electrode to contact the single-walled carbon nanotubes – (SWCNTs) PeakForce-TUNA tips, Bruker. For a schematic of the set-up, see **Figure 3.1**. The voltage bias was ramped between -500mV and 500mV. The data was then analysed by NanoScope Analysis (version 1.5, Bruker) and Matlab (version 2016 a).

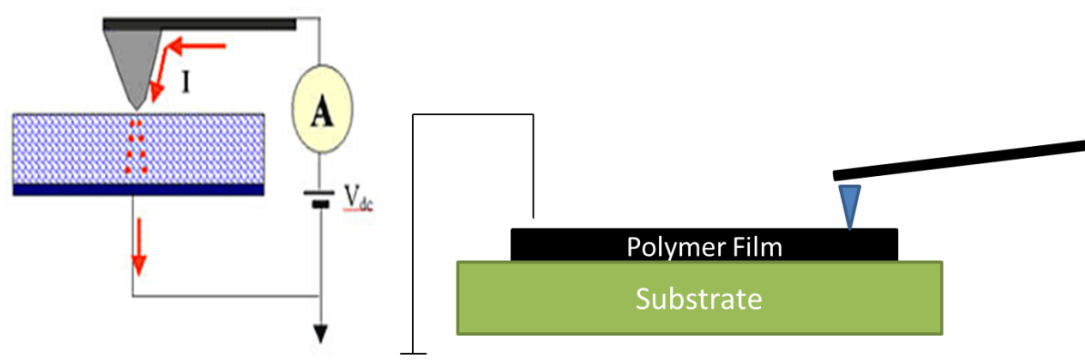


Figure 3.1 Schematic of conductive AFM (PF-TUNA) used for the evaluation of the micro-functionalised microelectrodes conductive profile. By using the moving probe as mobile electrode, the current was flowing through the metal-coated tip and the conducting sample which was grounded.

3.3.6 Biological Characterisation

3.3.6.1 Cell Culture

Primary cultures of ventral mesencephalic neurons (VM) were obtained from the mesencephalon of embryonic Sprague–Dawley rats according to methods previously

Topographically Functionalised Poly(3,4-Ethylenedioxythiophene):P-Toluene Sulphonate (PEDOT:PTS) Neuroelectrodes Via Microimprint Lithography

described by Vallejo-Giraldo et al. [7]. Briefly, the ventral mesencephalon were dissected from embryonic fourteen-day rat brains and then mechanically dissociated with a pipette until the tissue was dispersed. Cells were grown in a humidified atmosphere of 5% CO₂ at 37°C and culture in media (Dulbecco's modified Eagle's medium/F12, 33 mM D-glucose, 1 % L-glutamine, 1% PS, 1 % FCS, supplemented with 2 % B27). Controls and experimental groups were cultured for three, seven and ten days in six well culture plates and sterilised in 70% ethanol for two hours, and subsequently washed repeatedly with Hank's balanced salt solution (HBSS) and/or molecular biology grade water (Sigma). Prior to plating, samples and controls were coated with poly-lysine (PLL) (Sigma). They were then rinsed three times with molecular biology grade water and left to dry overnight. 50,000 cells cm⁻² were plated on each electrode, and then 3 ml of the culture medium was added to each well and half of the volume was replaced with fresh media every two days for a period of ten days.

For the inflammatory control, primary VM cells were cultured on sterile Thermanox® Plastic Coverslips with 13 mm diameter (NUNCTM brand products). 50,000 cells cm⁻² were plated on each coverslip, and grown in a humidified atmosphere of 5% CO₂ at 37°C and culture in media (Dulbecco's modified Eagle's medium/F12, 33 mM D-glucose, 1 % L-glutamine, 1% PS, 1 % FCS, supplemented with 2 % B27). 3 ml of the culture medium was added to each well and, after two days in culture, the cells were stimulated with IL-1β (10 ng mL⁻¹) prepared in plating media to a final volume of 3 ml and half of the volume was changed every two days for a period of ten days. Data for the optimisation of the different concentration of IL-1β as inflammatory stimuli on VM cells cultures is shown in **Figure 3.2** with the analysis of the production of reactive oxygen species (ROS), CellROX® and in **Figure 3.3** with the quantification of activated microglia using methods for morpho-functional analysis described in [67], respectively.

Topographically Functionalised Poly(3,4-Ethylenedioxythiophene):P-Toluene Sulphonate (PEDOT:PTS) Neuroelectrodes Via Microimprint Lithography

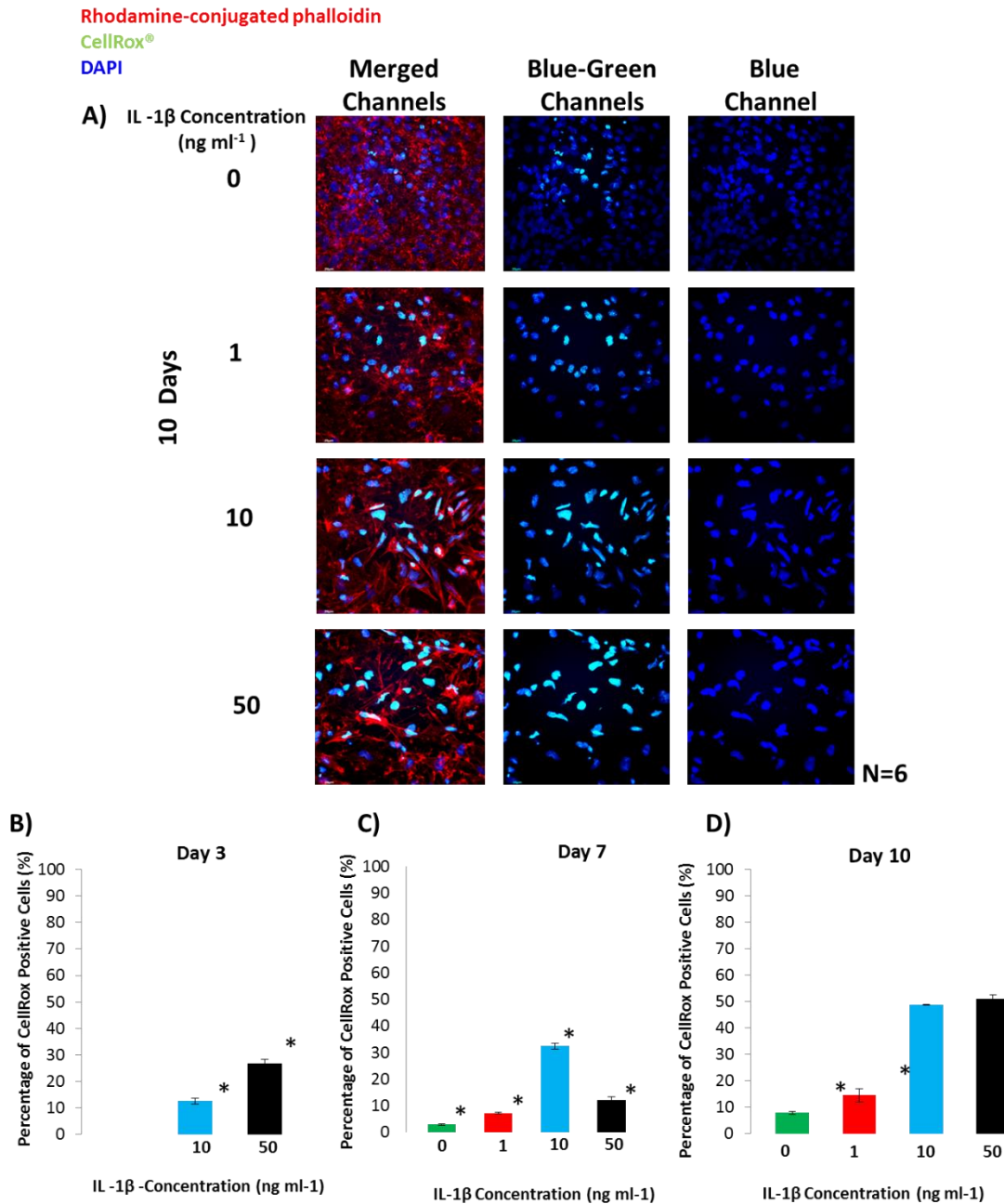


Figure 3.2 CellROX® expression on primary ventral mesencephalic (VM) mixed cell population grown on sterile Thermanox® Plastic Coverslips with 13 mm diameter (NUNCTM brand products). Cultures were stimulated with interleukin-1 β (IL-1 β) at 1, 10 and 50 ng ml⁻¹ and control. A) Fluorescent images of VM mixed cell population grown on sterile Thermanox® Plastic Coverslip over a period of three, seven and ten days showing CellROX® expression in green, actin in red rhodamine-

Topographically Functionalised Poly(3,4-Ethylenedioxythiophene):P-Toluene Sulphonate (PEDOT:PTS) Neuroelectrodes Via Microimprint Lithography

conjugated phalloidin and nuclei in blue, DAPI. Bar = 20 μm , objective 60 \times magnification. (B-D) show the percentage of CellROX[®] nuclei colocalisation quantified after stimulus with interleukin-1 β (IL-1 β) at 1, 10 and 50 ng ml^{-1} and control. Elevated levels of CellROX[®] on VM mixed cell population were seen after a stimulus of 10 ng ml^{-1} of IL-1 β and 50 ng ml^{-1} over ten days in culture, resulting in an increase of oxidative stress species presence as a response of inflammation. $\star = p < 0.05$.

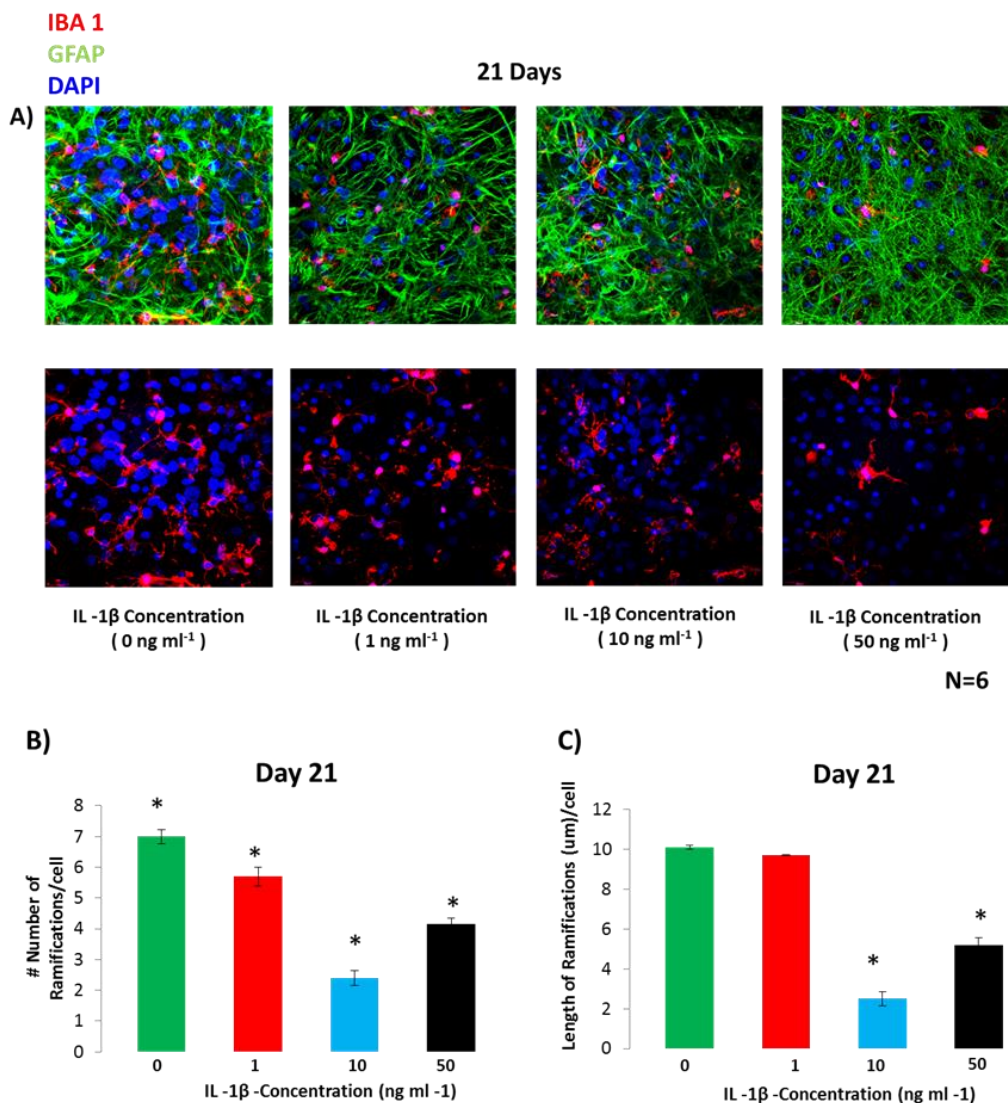


Figure 3.3 Morphological characterisation of activated microglia population from primary ventral mesencephalic (VM) mixed cells under stimulus of interleukin- 1 β (IL-1 β) at 1, 10 and 50 ng ml^{-1} and control concentrations after 21 days in culture.

Topographically Functionalised Poly(3,4-Ethylenedioxythiophene):P-Toluene Sulphonate (PEDOT:PTS) Neuroelectrodes Via Microimprint Lithography

A) *Fluorescent images of astrocytes and microglia from VM mixed cell population grown on sterile Thermanox® Plastic Coverslips with 13 mm diameter (NUNCTM) brand products over a period of 21 days. Astrocytes are visualised by anti-GFAP, in green and microglia are visualised by Iba-1, in red, and nuclei are visualised by DAPI, in blue. Bar = 20 µm, objective 60× magnification. The number of microglia ramifications B) and their length C) were quantified following methods detailed in [67] as indicators of activated microglia. Significant differences ($p < 0.05$) were observed in the number and length of microglia ramifications cultured under stimulus of 10 ng ml⁻¹ IL-1β compared to controls and to the other IL-1β concentrations used. Overall, microglia morphologies under stimulus of 10 ng ml⁻¹ IL-1β resemble microglia amoeboid morphologies. ★ = $p < 0.05$.*

Dissociated hippocampal neurons were obtained from P1 to P4-old Wistar rats as previously reported [68]. Prior to plating, samples of pristine PEDOT:PTS and microtopographically functionalised PEDOT:PTS coated electrodes and control bare platinum were sterilised by repeated (three) ten minutes-long washes with DI H₂O followed by five minutes-long washes in ethanol, both solutions were previously filtered with 0.22 µm cutoff filter (Merck Millipore). Cultured cells were incubated at 37 °C, 5 % CO₂ in culture medium composed of Neurobasal-A (Thermo Fischer) containing B27 2 % (Gibco) Glutamax 10 mM and Gentamycin 0.5 µM (Gibco), and used for experiments at eight–ten days *in vitro* (DIV).

Ethical Statement (Primary hippocampal cultures)

All experiments were performed in accordance with the EU guidelines (2010/63/UE) and Italian law (decree 26/14) and were approved by the local authority veterinary service and by our institution (SISSA-ISAS) ethical committee. Every effort was made to minimise animal suffering and to reduce the number of animals used. Animal use was approved by the Italian Ministry of Health, in accordance with the EU Recommendation 2007/526/CE.

3.3.6.2 Immunofluorescent Labelling

Indirect double-immunofluorescent labelling was performed to visualise neurons and astrocyte cell populations as described by Vallejo-Giraldo et al. [8]. Briefly, VM cells on experimental and control substrates were fixed with 4% paraformaldehyde and 1% of sucrose for twenty minutes at room temperature at the time point. Once fixed, the samples were washed with PBS and permeabilised with buffered 0.5% Triton X-100 within a buffered isotonic solution (10.3 g sucrose, 0.292 g NaCl, 0.06 g MgCl₂, 0.476 g HEPES buffer, 0.5 ml Triton X-100, in 100 ml water, pH 7.2) at 4°C for five minutes. Non-specific binding sites were blocked with 1% bovine serum albumin (BSA) in PBS at 37°C for 30 minutes and subsequently incubated for two hours with a 1:200 concentration anti-gial fibrillary acidic protein (GFAP) antibody produced in mouse (Sigma, 1:200) and 1:500 concentration anti-β-Tubulin III antibody produced in rabbit (Sigma, 1:500). Samples were washed three times with 0.05% Tween 20/PBS and then incubated for one hour in the secondary antibody Alexa Fluor® 488 goat anti-Mouse IgG / IgA / IgM (H+L) (Molecular probes 1:500) combined with the secondary antibody Alexa Fluor® 594 goat anti-Rabbit IgG (H+L) (Molecular probes, 1:500). Samples were washed with PBS (five minutes ×3) and mounted on microscope cover slides and counterstained with slowfade^R gold antifade reagent with DAPI for nuclear staining.

Indirect double-immunofluorescent labelling was performed to visualise focal adhesion sites and astrocytes following the fixation and permeabilisation processes detailed above. In this case the samples were incubated for two hours with a 1:200 concentration anti-Paxillian (Rb mAb to Paxillin (Y113) (Life Technologies, 1:200) and with a 1:200 concentration GFAP antibody produced in mouse (Sigma, 1:200). Samples were washed three times with 0.05% Tween 20/PBS and then incubated for one hour in the secondary antibody Alexa Fluor® 488 goat anti-Mouse IgG / IgA / IgM (H+L) (Molecular probes 1:500) combined with the secondary antibody Alexa Fluor® 594 goat anti-Rabbit IgG (H+L) (Molecular probes, 1:100). Samples were washed with PBS (five minutes ×3) and mounted on microscope cover slides and counterstained with slowfade^R gold antifade reagent with DAPI for nuclear staining.

Topographically Functionalised Poly(3,4-Ethylenedioxythiophene):P-Toluene Sulphonate (PEDOT:PTS) Neuroelectrodes Via Microimprint Lithography

Indirect double-immunofluorescent labelling for microglia and astrocytes on inflamed controls was performed using the same methods detailed above. Samples were incubated for two hours with GFAP antibody produced in mouse (Sigma, 1:200) at a concentration of 1:200 and with anti-rabbit Iba1 (Wako, 1:1000) with a concentration of 1:1000. Samples were washed three times with 0.05% Tween 20/PBS and then incubated for one hour in the secondary antibody Alexa Fluor® 488 goat anti-Mouse IgG / IgA / IgM (H+L) (Molecular probes 1:500) combined with the secondary antibody Alexa Fluor® 594 goat anti-Rabbit IgG (H+L) (Molecular probes, 1:1000). Samples were washed with PBS (five minutes ×3) and mounted on microscope cover slides and counterstained with slowfade^R gold antifade reagent with DAPI for nuclear staining.

The production of reactive oxygen species (ROS) on inflamed controls was visualised using an assay kit, CellROX® Green Reagent, for oxidative stress detection (2.5 mM; Thermo Fisher Scientific - C10444). CellROX® Green Reagent was diluted in HBSS for a final concentration of 5 µM (working solution) that was prepared fresh every time used. During use, this working solution was kept in the dark at 37 °C. After removing cell media, CellROX® Green Reagent was added on each sample and incubated at 37 °C for 30 minutes. After incubation, each sample was fixed and permeabilised using methods described above. One hour incubation in rhodamine-conjugated phalloidin (Life Technologies, 1:100) prepared in 1% BSA in PBS was followed next for F-actin staining. After being washed with PBS (five minutes ×3), samples were mounted with slowfade^R gold antifade reagent with DAPI for nuclear staining and image within 24 hours. CellROX® Green was visualised using FTIC channel.

3.3.6.3 Microscopy and Image Analysis

After immunostaining, samples were viewed with an Olympus Fluoview 1000 Confocal Microscope at a fixed scan size of 1024 by 1024 at a ratio 1:1. Cell analysis was performed as described in [8]. At least twenty images at 60× magnification were taken at random from each experimental group and controls. Cell density was analysed by counting the total number of labelled nuclei corresponding to neurons

Topographically Functionalised Poly(3,4-Ethylenedioxythiophene):P-Toluene Sulphonate (PEDOT:PTS) Neuroelectrodes Via Microimprint Lithography

and astrocytes in an area of $212\ \mu\text{m} * 212\ \mu\text{m}$. Neurite length was quantified by analysing nine random fields of view of three different technical replicas from three different samples using established stereological methods [69]. The formula used was: neurite length = $n * T * \pi / 2$, where n is the number of times neurites intersect grid lines and T = distance between gridlines (taking magnification into account) as described in [70]. Cell area of astrocytes was recorded from the green channel using the threshold function to generate particles that were manually dispersed across the image until good coverage was achieved. The total number of focal adhesion points per cell and their length were quantified by direct scoring with a 4 pixel-wide line on the FITC channel as previously described in [7] using ImageJ software (National Institutes of Health, USA).

3.3.6.4 Cytokine Inflammatory Panel

The cytokine multiplex assay was performed on primary VM cell mixed population supernatants collected at three, seven and ten days in culture grown on all experimental groups, controls and inflamed control. ELISA pro-inflammatory panel 2 (Rat) (Meso Scale Discovery, UK) cytokine (IL-6, IL-1 β , TNF- α , IFN- γ , KC/GRO, IL-4, IL-5, IL-13, IL-10) assays were performed according to the manufacturer's instructions, using six replicas and without adjustments to the recommended standard curve, and sample dilutions. Briefly, 150 μL of blocker H was added on each well of ELISA pro-inflammatory plate and incubated at room temperature with fast shaking for one hour. In parallel, in a separate provided plate, an initial 1:2 dilution of samples and culture media was prepared and put under shaking for fifteen minutes. The ELISA pro-inflammatory plate was then washed three times with at least 150 μL of wash buffer (PBS with 0.05% Tween20) and subsequently, the diluted sample mixed from the additional plate provided was transferred to the ELISA pro-inflammatory plate with the addition of 25 μL of diluent 40. Incubation at room temperature with shaking for two hours was then carried out. The ELISA pro-inflammatory plate was further washed three times with PBS-tween20, and 25 μL of 1X detection antibody solution was added in each well and incubated at room temperature with shaking for two hours. The ELISA pro-inflammatory plate was

Topographically Functionalised Poly(3,4-Ethylenedioxythiophene):P-Toluene Sulphonate (PEDOT:PTS) Neuroelectrodes Via Microimprint Lithography

washed three times and further added 150 μL of 2X read buffer T in each well for plate reading using the QuickPlex SQ 120 multiplexing instrument from MSD.

The STRING (search Tool for the Retrieval of Interacting Genes) database <http://string-db.org> search was performed for known protein interactions adopting a confidence score >0.7 as the threshold to assess associations.

3.3.7 Calcium Imaging

Hippocampal dissociated cultures were loaded with cell permeable Ca^{2+} dye Oregon Green 488 BAPTA-1 AM (Molecular Probes); 10 μL DMSO (Sigma-Aldrich) was added to the stock 50 μg of the dye and cultures were incubated with a final concentration of 4 μM for 30 min at 37 $^{\circ}\text{C}$, 5 % CO_2 , as detailed previously in [7]. Samples were therefore placed in a recording chamber mounted on an inverted microscope (Nikon Eclipse Ti-U). Cultures were continuously superfused at 5 mL min^{-1} rate and at room temperature with extracellular solution of composition (mM): 150 NaCl, 4 KCl, 2 CaCl_2 , 1 MgCl_2 , 10 HEPES, 10 glucose (pH was adjusted to 7.4 with NaOH 1M; osmolarity 300 mOsm). Ca^{2+} dye was excited at 488 nm with a mercury lamp; excitation light was separated from the light emitted from the sample using a 395 nm dichroic mirror and ND filter (1/32). Oregon loaded cultures were observed with a 20 \times objective (0.45 NA PlanFluor) and images were continuously acquired (exposure time 150 ms) using an ORCA-Flash4.0 V2 sCMOS camera (Hamamatsu). The imaging system was controlled by an integrated imaging software (HCLive) and the camera was set to operate on 2048 \times 2048 pixels at binning four. After ten minutes of spontaneous activity recording, 1 μM TTX (a voltage-gated, fast Na^+ channel blocker; Latoxan) was added to confirm the neuronal nature of the recorded signals. Three fields from each sample (two samples per condition) were recorded and 20 ± 4 cells from each recording were selected by drawing regions of interest (ROIs) around cell bodies. Images were analysed with image processing package Fiji; and Clampfit software (pClamp suite, 10.4 version; Axon Instruments) in off-line mode [68]. The difference was computed between peaks consecutive onset times, to obtain the inter-event interval (IEI). Intracellular Ca^{2+} transients were expressed as fractional amplitude increase ($\Delta F/F_0$, where F_0 is the baseline

fluorescence level and ΔF is the rise over baseline); the onset time of neuronal activation was determined by detecting those events in the fluorescence signal that exceed at least five times the standard deviation of the noise.

3.3.8 Statistical Analysis

All data presented here was confirmed using at least three replicates for each of the test groups and control groups. The results are expressed as the mean of the values \pm standard error of the mean. One-way ANOVA followed by a Bonferroni test were performed to determine the statistical significance ($p < 0.05$), unless otherwise stated.

3.4 Results and Discussion

3.4.1 Physical Characterisation

A range of techniques has been explored to create defined microstructures on electrode surfaces [71], including laser ablation [72, 73], focused ion beam [74, 75], sputter etching [76, 77], reactive ion etching [78, 79], deep reactive ion etching [80, 81], hot embossing [82, 83], and electron beam lithography [84, 85]. Complementary to these techniques, imprint lithography is an especially attractive approach due to its simplicity, non-destructive character and feasibility of patterning large areas with features down to 10 nm using elevated temperature and/or pressure processes to transfer a pattern into typically thermoplastic materials [86-89]. Regarding the variation of imprinting methods, direct die imprinting is of particular interest as patterns are transferred via a stamp/die in a single imprint process [90]. However, the quality of the pattern transfer depends on relatively high temperatures and pressures [90, 91] and silanisation steps are also required to facilitate the separation of the die and imprinted material [92-95].

A study by Tan et al. [96] shows the imprinting process of non-thermoplastic materials such as PEDOT and chitosan using plasticisers. Imprinting of PEDOT and chitosan films from the poly(dimethylsiloxane) mold was achieved at a pressure of 10 kPa and 25 °C by controlled addition of glycerol as a plasticiser. In this case, the added glycerol was used to increase the chain mobility of the polymers, resulting in lower imprinting temperature and low pressures.

Topographically Functionalised Poly(3,4-Ethylenedioxythiophene):P-Toluene Sulphonate (PEDOT:PTS) Neuroelectrodes Via Microimprint Lithography

Further, a room temperature nanoimprint lithography process was shown by Pisignano and colleagues [97] with the nanoimprinting of patterns in organic semiconductors with poor thermoplastic properties.

A focus of this work was to develop a low-temperature, simple imprinting method to reproduce lithographically fabricated well-defined and ordered topographies into PEDOT:PTS electrodeposited electrode coatings. Critically this approach preserves the ability to introduce coupled biochemical functionalisation – an approach which has been explored extensively with PEDOT functionalised microelectrodes [98-101]. Arrays of pits possessing a diameter of $\sim 1 \mu\text{m}$ a pitch of $\sim 2 \mu\text{m}$ and depth of $\sim 1 \mu\text{m}$ were initially fabricated via photolithography which was used as a mask for a Ni (Nickel) electroforming process as described previously [51]. Fabricated negative Ni masters were used as hard stamps to replicate the original topography into electrodeposited PEDOT:PTS coatings via an imprint process applying 1.9 tons per cm^2 for fifteen minutes to achieve high quality pattern transfer conducted at room temperature. To facilitate substrate separation, a dehydration-assisted process was employed to enhance the cohesion of PEDOT:PTS and prevent topography disruption during the separation step, ensuring high pattern transfer as first described by Yang et al. [83] who also used the dehydration-assisted method for the imprinting of spin-coated PEDOT:PSS nanogratings for photovoltaic applications. In this way, silanisation steps were avoided as they caused neural cell death to our cultures due to insufficient evaporation of fluorides [102, 103].

Experimentally, the micro-imprinting process is outlined in **Figure 3.4**. Representative SEM micrographs of the nickel die used in the imprinting process and the resulting well-ordered arrays of micro-pits in the micro-topographically functionalised PEDOT:PTS coated microelectrodes with respective dimensions are indicated in **Figure 3.5A**. The calculated thickness of the electrodeposited PEDOT:PTS coating was of $1.22 \pm 0.12 \mu\text{m}$.

Topographically Functionalised Poly(3,4-Ethylenedioxythiophene):P-Toluene Sulphonate (PEDOT:PTS) Neuroelectrodes Via Microimprint Lithography

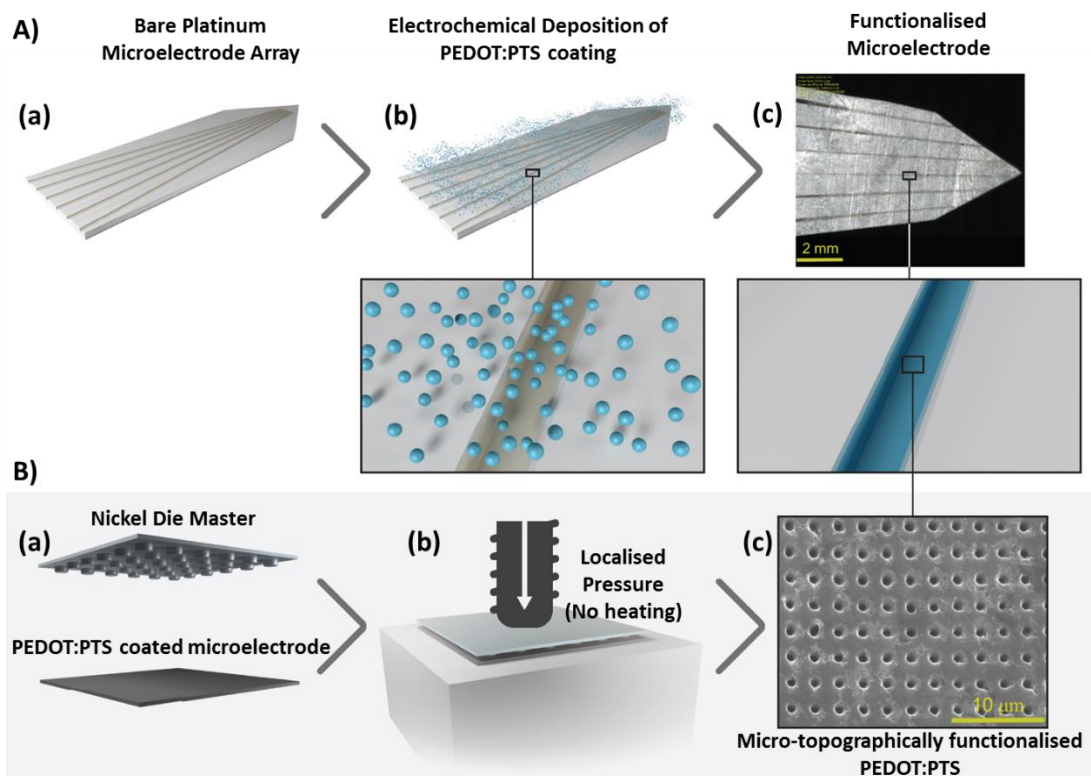


Figure 3.4 Microelectrode functionalisation process. Upper panel A) describes the sequential steps taken on the bare platinum electrodes (a) electrodeposition of PEDOT:PTS coating (b), followed by the optical micrograph of the coated PEDOT:PTS microelectrode ready for the functionalisation with the topography (c) Scale bar= 2mm, 10×. Bottom panel B) outlines the low temperature three-step die imprinting lithography process. This process starts with the micro-pit nickel die master and the PEDOT:PTS coated electrode (a). The nickel die was then pressed against the PEDOT:PTS coated microelectrode at a localised constant pressure of 1.9 tons per cm² for fifteen minutes at room temperature using parallel pressing plates. Finally, a scanning electron micrograph (SEM) of the micro-topographically functionalised PEDOT:PTS coated microelectrode is shown (c).

Topographically Functionalised Poly(3,4-Ethylenedioxythiophene):P-Toluene Sulphonate (PEDOT:PTS) Neuroelectrodes Via Microimprint Lithography

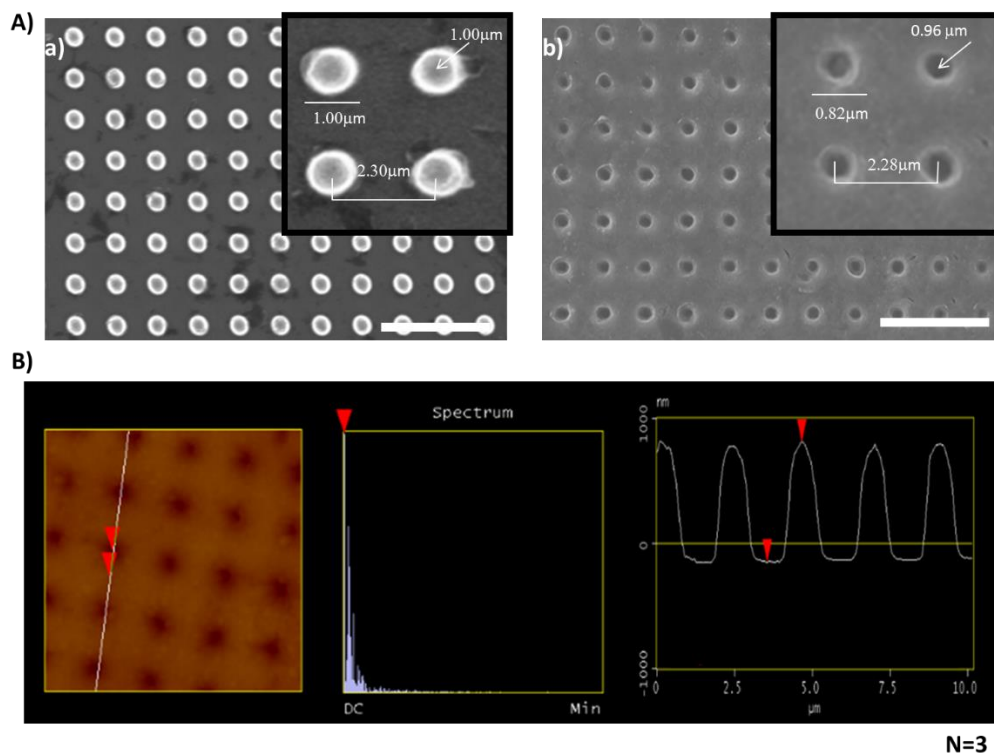


Figure 3.5 *Micro-topographically functionalised microelectrodes.* Upper panel A) Scanning electron micrographs (SEM) of the nickel die master utilised for the low temperature three-step die imprinting lithography process (a) the micro-topographically functionalised substrate with ordered array of micro-pits produced on PEDOT:PTS coated microelectrodes by low temperature three-step die imprinting lithography process (b). Scale bar = 10 μm. In the insets, the pit, interpit and depth dimensions are detailed. B) Atomic-force microscopy (AFM) sectional analysis of the micro-topographically functionalised PEDOT:PTS coated microelectrode over a region of 10 μm² area reflecting the vertical distance of the pit patterned transferred of 0.96 ± 0.07 μm. Fifteen measurements were taken from three different replicas. Results are ± STD.

Following imprinting, PEDOT:PTS microelectrodes were micro-topographically functionalised with arrays of pits with a diameter of 0.82 ± 0.07 μm and interpit spacing of 2.28 ± 0.06 μm. The depth was confirmed by AFM analysis (**Figure 3.5B**) indicating vertical distances of 0.96 ± 0.07 μm and high fidelity pattern transfer using a low temperature three-step die imprinting lithography process. No Ni residues from

Topographically Functionalised Poly(3,4-Ethylenedioxythiophene):P-Toluene Sulphonate (PEDOT:PTS) Neuroelectrodes Via Microimprint Lithography

the die master on the micro-topographically functionalised PEDOT:PTS coated microelectrodes were present after the imprinting process (**Table 3.1**).

Table 3.1 X-ray photoelectron spectroscopy (XPS) analysis of the elemental composition of the micro-topographically functionalised PEDOT:PTS coated microelectrodes looking at the nickel residual presence from nickel die master used in the low temperature three-step die imprinting lithography process. Ni 2p atomic percentage was at the noise level. N=3.

Micro-topographically functionalised PEDOT:PTS coated microelectrode	Atomic Composition [%]							
	C 1s	O 1s	Ni 2p	S 2p	N 1s	Na 1s	P 2p	Cl 2p
	70.52	16.63	0.18	1.76	10.32	0.18	0.42	0.00

The topographical profiles of micro-imprinted PEDOT:PTS coated microelectrodes were subsequently analysed by AFM and results presented relative to pristine PEDOT:PTS and to a PEDOT:PTS coated microelectrode flattened via imprinting with a planar glass substrate, these control groups serving as pristine electrodeposited PEDOT:PTS surface and a topographically planar PEDOT:PTS surface respectively. A sputtered platinum (Pt) group was also used as a representative electrode control material (images shown in **Figure 3.6**). Representative SEM and AFM images of experimental groups are depicted in **Figure 3.7(A-B)**. Micro-topographically functionalised PEDOT:PTS coated microelectrodes resulted in a non-significant decrease in surface roughness (R_a) relative to pristine PEDOT:PTS coated microelectrode but in a significant increase when compared to the control flattened PEDOT:PTS coated microelectrodes (**Table 3.2**). Pristine PEDOT:PTS coated microelectrodes exhibited an average roughness of 85 nm over 10 μm^2 , and an average roughness of 53 nm and 76 nm was noted on flattened and micro-topographically functionalised electrodes respectively. All PEDOT:PTS coated electrodes exhibited a significant increase in surface roughness (R_a) relative to Pt microelectrodes, which possessed an experimental R_a of 2 nm over 10 μm^2 [49].

Topographically Functionalised Poly(3,4-Ethylenedioxythiophene):P-Toluene Sulphonate (PEDOT:PTS) Neuroelectrodes Via Microimprint Lithography

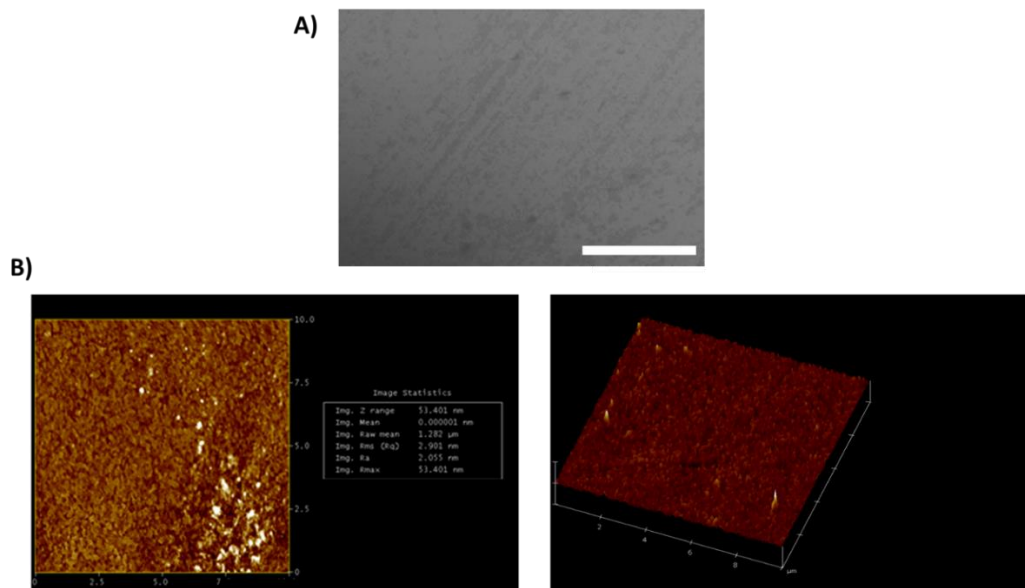


Figure 3.6 Bare platinum (Pt) morphological characterisation. A). Scanning electron micrograph (SEM) of bare platinum (Pt) microelectrodes, and corresponding mean surface roughness (R_a) B). Scale bar = $3\mu\text{m}$.

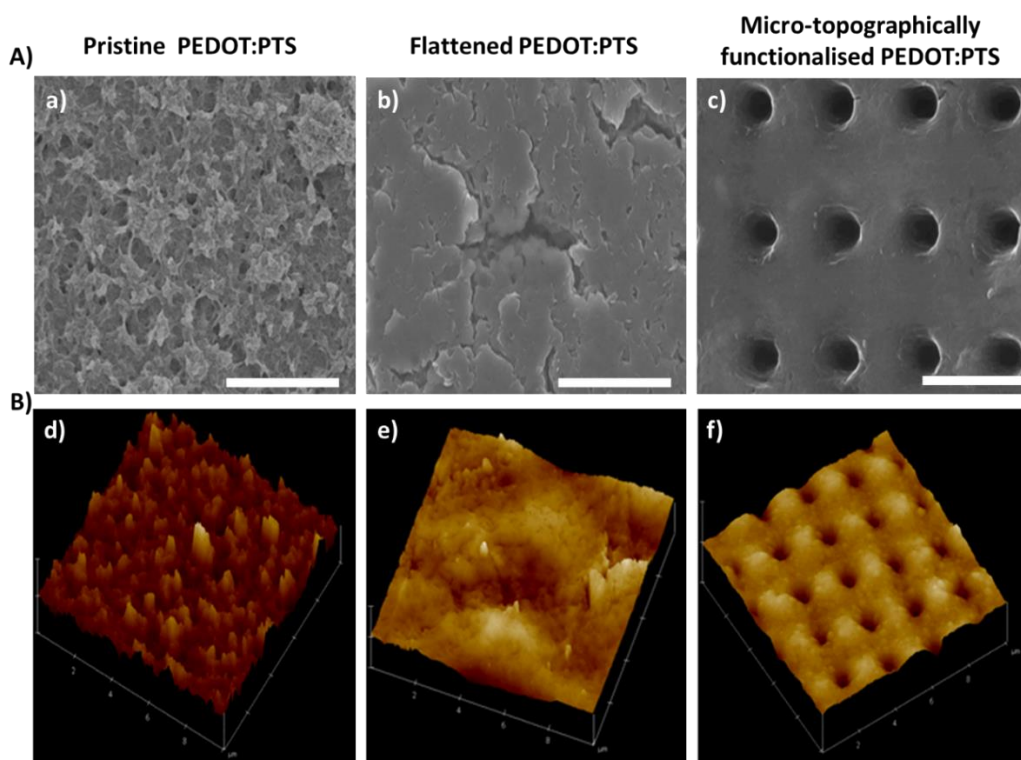


Figure 3.7 Microelectrode morphological physical characterisation. Upper panel A). Scanning electron micrographs (SEM) (a-c) of pristine PEDOT:PTS, flattened

Topographically Functionalised Poly(3,4-Ethylenedioxythiophene):P-Toluene Sulphonate (PEDOT:PTS) Neuroelectrodes Via Microimprint Lithography

PEDOT:PTS and the micro-topographically functionalised PEDOT:PTS coated microelectrodes. Scale bar = 3 μ m. B) Corresponding surface plots (d-f) of pristine PEDOT:PTS, flattened PEDOT:PTS and the micro-topographically functionalised microelectrodes on 10 μ m² regions.

Table 3.2 Microelectrode physical properties. Values of experimental mean surface roughness (R_a) and mean surface area (SA) measurements over 10 μ m² regions. The data represent the mean of 15 measurements from three different replicas. Results are \pm SD, $N=3$.

Microelectrodes	Average Roughness R_a [nm]	Average Surface Area [nm ²]
Bare platinum (Pt)	1.96 \pm 0.22	1.05 E+10 \pm 35.35 E+06
Pristine PEDOT:PTS	85.16 \pm 16.94	1.74 E+10 \pm 93.34 E+06
Flattened PEDOT:PTS	52.59 \pm 6.16	1.32 E+10 \pm 71.42 E+06
Micro-topographically functionalised PEDOT:PTS	76.10 \pm 17.21	2.35 E+10 \pm 51.77 E+06

The micro-imprinting process resulted in a reduction in R_a of the inter-pit surface to levels similar to flattened PEDOT:PTS electrodes, indicating that the application of the mechanical imprinting eliminated nano-roughness while producing micro-roughness [104]. Significantly, the calculated physical surface area of the micro-topographically functionalised PEDOT:PTS coated microelectrodes was of 2.35 E+10 \pm 51.77 E+06 nm², 1.74 E+10 \pm 93.34 E+06 nm² for the pristine PEDOT:PTS coated microelectrodes 1.32 E+10 \pm 71.42 E+06 nm² for the flattened PEDOT:PTS coated microelectrodes and 1.05 E+10 \pm 35.35 E+06 nm² for sputtered Pt electrodes indicating that through micro-imprinting the surface area of electrodeposited PEDOT:PTS was significantly increased relative to nano-rough pristine electrodeposited materials and uncoated Pt electrodes as shown in **Table 3.2**. These results suggest that micro-imprinting functionalisation of PEDOT:PTS coated microelectrodes can be employed to induce a 135.06 % greater surface area relative to pristine PEDOT:PEDOT coated microelectrodes and a 178.03 % greater surface

Topographically Functionalised Poly(3,4-Ethylenedioxythiophene):P-Toluene Sulphonate (PEDOT:PTS) Neuroelectrodes Via Microimprint Lithography

area relative to flattened control microelectrodes. Critically, micro-topographically modified PEDOT:PTS coated microelectrodes represented a 223.81 % increase in surface area over that of Pt microelectrodes.

3.4.2 Electrochemical Characterisation

Topographical surface modification of the neural electrodes has shown promise in improving the electrochemical performance through high aspect ratio structures, increasing the active surface area of the electrodes [13, 71]. The electrochemical performance and the evaluation of the resulting effective-active surface area of the functionalised microelectrodes were subsequently assessed. To allow comparison, the evaluation of the electrical profile of the in-house fabricated sputtered Pt microelectrodes was compared to topographically and non-topographically modified electrodeposited PEDOT:PTS electrodes and to electrodeposited gold coated microelectrodes with a similar experimental coating thickness of the as-formed PEDOT:PTS coatings, which possessed an approximated thickness of $1.21 \pm 0.08 \mu\text{m}$ and $1.22 \pm 0.12 \mu\text{m}$, respectively.

Figure 3.8A shows CVs for each of the experimental and control groups in PBS evaluated in a microelectrode area of 0.287 mm^2 . The increase in CSC (**Table 3.3**), which was approximated through the integration of the charge passed within one CV scan, confirmed the presence of highly conducting PEDOT:PTS coatings with improvement in the electrochemical performance of the microelectrodes over that of bare platinum and gold coated microelectrode controls [105, 106]. In addition, and owing to the topographical functionalisation, further enhancement of electrical performance was observed over that of the CSC of the PEDOT:PTS coated microelectrodes. The highest CSC was obtained with the micro-topographically functionalised PEDOT:PTS coated microelectrodes with a capacitance of $131.01 \pm 8.05 \mu\text{C mm}^{-2}$ followed by the pristine PEDOT:PTS coated microelectrodes with a CSC of $48.82 \pm 0.49 \mu\text{C mm}^{-2}$ and finally the controlled non-patterned surface, flattened PEDOT:PTS coated microelectrodes, with a CSC of $19.09 \pm 0.77 \mu\text{C mm}^{-2}$ (**Table 3.2**). Of note is that these wide ranges of the aforementioned CSC values suggest that film structure plays a major role in determining the capacitance; more

Topographically Functionalised Poly(3,4-Ethylenedioxythiophene):P-Toluene Sulphonate (PEDOT:PTS) Neuroelectrodes Via Microimprint Lithography

specifically, this may be related to the role of volumetric capacitance largely impacted in the flattened PEDOT:PTS coated microelectrodes [107]. The flattening geometry may be limiting the volume fraction of the coating, hence limiting the favourable packing of the polymeric coating for facile ion transport affecting the capacitance [107].

In addition, and together with the increased charge storage capacity, micro-topographically functionalised PEDOT:PTS coated microelectrodes resulted in a significantly increased effective electroactive surface area when compared to pristine PEDOT:PTS coated microelectrodes and even further when compared with the bare platinum and gold coated microelectrodes. The electroactive surface area was measured using a redox probe ($2.5 \text{ mol dm}^{-3} \text{ K}_4[\text{Fe}(\text{CN})_6]$ in 0.1 M KCl) solution and estimated according to the Randles-Sevcik equation (*Equation 3.1*). **Figure 3.8B** shows that it is enough to deposit an electroactive PEDOT:PTS layer on the surface of Pt microelectrodes to observe a significant three-fold increase in effective surface area, also reported in previous studies into electroactive polymers [108-110]. Further, micro-imprinting functionalisation resulted in a significant two-fold increase enhancement of the electroactive surface area relative to pristine PEDOT:PTS coated microelectrodes. Likewise, the micro-topographically functionalised PEDOT:PTS coated microelectrodes induced a significant six-fold increase in effective surface area relative to Pt microelectrodes and a significant five-fold increase relative to gold coated microelectrodes. It is noteworthy, that relative electrode surface area between bare platinum and gold coated microelectrode controls were not significantly different.

Topographically Functionalised Poly(3,4-Ethylenedioxythiophene):P-Toluene Sulphonate (PEDOT:PTS) Neuroelectrodes Via Microimprint Lithography

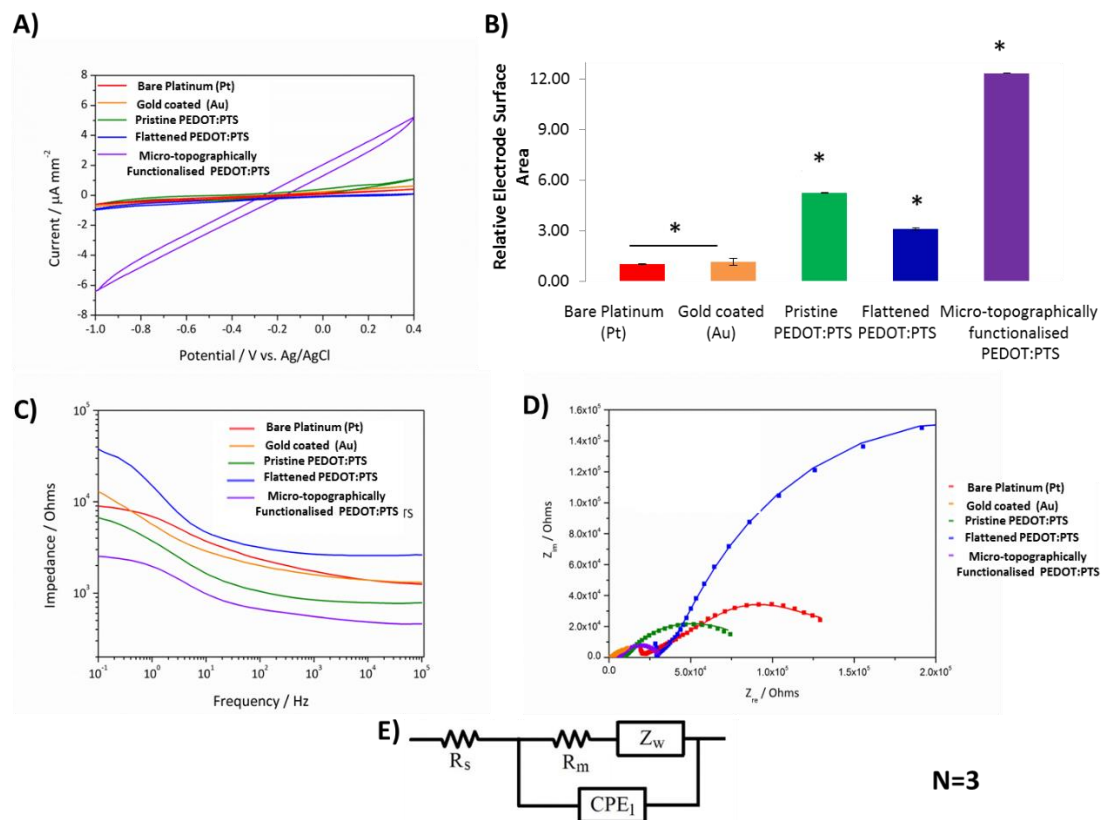


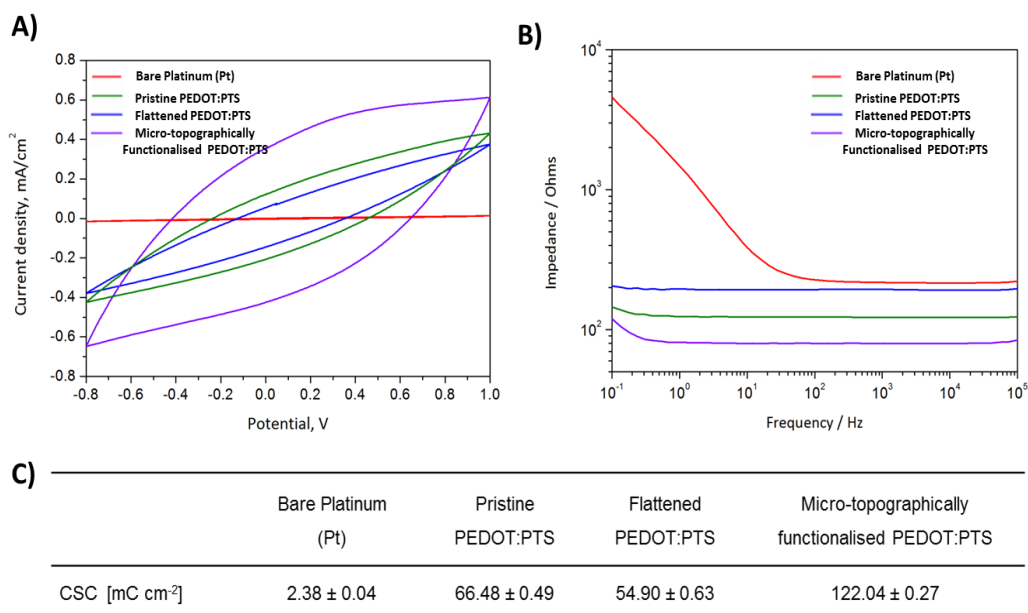
Figure 3.8 Electrochemical analysis of functionalised PEDOT:PTS coated microelectrodes. A) Cyclic voltammograms (CVs) bare platinum (Pt) and gold coated (Au) microelectrodes and pristine PEDOT:PTS, flattened PEDOT:PTS and micro-topographically functionalised PEDOT:PTS coated microelectrodes. CVs were recorded in 0.01 M phosphate-buffered saline (PBS) at a scan rate of 100 mV s^{-1} . B) Relative electrode surface area calculated based on cyclic voltammograms (CVs) in $2.5 \text{ mol dm}^{-3} \text{ K}_4[\text{Fe}(\text{CN})_6]$ in 0.1 M KCl solution at a scan rate of 100 mV s^{-1} . The relative electrode surface area was estimated according to the Randles-Sevcik equation and the bare platinum (Pt) microelectrode was used as a reference. C) and Nyquist D) plots comparing the EIS spectra of bare platinum (Pt) and gold coated (Au) microelectrodes and pristine PEDOT:PTS, flattened PEDOT:PTS and micro-topographically functionalised PEDOT:PTS coated microelectrodes. E) represents the electrical equivalent circuit used to analyse experimental data. Results are $\pm \text{STD}$, $\star = p < 0.05$.

Table 3.3 Electrochemical performance and stability of functionalised PEDOT:PTS coated microelectrodes. The initial and the final charge storage capacity (CSC) was evaluated from the cathodic region of cyclic voltammograms (CVs) recorded in 1X phosphate-buffered saline (PBS) at 100 mV s⁻¹ scan rate (Potential range: -1 V to 0.4 V vs. Ag/AgCl). The corresponding loss was calculated after 500 cycles. Results are \pm SD, N=3.

	Bare Platinum (Pt)	Gold Coated (Au)	Pristine PEDOT:PTS	Flattened PEDOT:PTS	Micro-topographically functionalised PEDOT:PTS
Initial CSC [μ C mm ⁻²]	15.57 \pm 0.66	25.12 \pm 0.66	48.82 \pm 0.49	19.09 \pm 0.77	131.01 \pm 8.05
Final CSC [μ C mm ⁻²]	4.36 \pm 0.17	15.79 \pm 0.31	31.01 \pm 0.11	0.38 \pm 0.04	96.41 \pm 22.23
Electroactivity loss [%]	72.10 \pm 1.61	37.17 \pm 0.23	36.50 \pm 0.41	98.10 \pm 1.52	26.42 \pm 6.33

Following PEDOT:PTS coated microelectrode flattening via imprinting with a planar glass substrate, microelectrode effective surface area was significantly decreased relative to both micro-topographically functionalised and pristine PEDOT:PTS coated microelectrodes. This is due to an overall reduction of microelectrode surface area and lower R_a when compared to the pristine and PEDOT:PTS functionalised microelectrodes. However, flattened PEDOT:PTS microelectrodes still possessed a significantly increased electroactive surface area relative to bare platinum and gold coated microelectrodes [49]. The evolution of electroactive surface area is of importance for microelectrodes, especially because the currents measured with implanted neural recording devices are in the range of μ A or below [111-113]. This, together with the non-typical shape of CVs [114], makes the process of optimisation of microelectrode modification a challenging task. Complimentary data obtained with larger electrodes (1.6 cm²) as part of the optimisation process for this work is presented in **Figure 3.9**.

Topographically Functionalised Poly(3,4-Ethylenedioxythiophene):P-Toluene Sulphonate (PEDOT:PTS) Neuroelectrodes Via Microimprint Lithography



N=3

Figure 3.9 *Electrochemical analysis of functionalised PEDOT:PTS coated macro electrode (1.6 cm²). A) Cyclic voltammograms (CVs) bare platinum (Pt) and pristine PEDOT:PTS, flattened PEDOT:PTS and micro-topographically functionalised PEDOT:PTS coated electrodes. CVs were recorded in 1X phosphate-buffered saline (PBS) at a scan rate of 100 mV s⁻¹. B) Bode plots comparing the EIS spectra of bare platinum (Pt) and pristine PEDOT:PTS, flattened PEDOT:PTS and micro-topographically functionalised PEDOT:PTS coated electrodes. C) Table summarising the charge storage capacity (CSC) of large bare platinum (Pt) and pristine PEDOT:PTS, flattened PEDOT:PTS and micro-topographically functionalised PEDOT:PTS coated electrodes. CSC was evaluated from the cathodic region of cyclic voltammograms (CVs) recorded in 1X phosphate-buffered saline (PBS) at 100 mV s⁻¹ scan rate (Potential range: -1 V to 0.4 V vs. Ag/AgCl). Results are ± STD, ★ = p < 0.05.*

Comparative electrochemical impedance spectroscopy (EIS) profiles of all experimentally modified microelectrodes are presented in the form of a Bode diagram (**Figure 3.8C**) and Nyquist plot (**Figure 3.8D**). Overall, micro-topographically functionalised PEDOT:PTS microelectrodes exhibited the lowest impedance profile

Topographically Functionalised Poly(3,4-Ethylenedioxythiophene):P-Toluene Sulphonate (PEDOT:PTS) Neuroelectrodes Via Microimprint Lithography

within the frequency range of 0.1 Hz to 100 kHz, lower than that of pristine PEDOT:PTS microelectrodes and significantly lower than that of gold coated and bare platinum microelectrodes. This indicates the superior electrical performance of electrodes subjected to micro-topographical functionalisation and the diminishing effect of the process of PEDOT:PTS flattening on the electrochemical properties of microelectrodes, due to an important impact of the former on volumetric changes of the coating [107].

The detailed insight into the process of charge transport was possible by the simulation of EIS data with an equivalent electrical circuit. As shown in **Figure 3.8E**, a Randles equivalent circuit [115, 116] was indicated as the most appropriate and was used to fit the impedance data. The parameters of the equivalent circuit included the solution resistance (R_s), resistance of microelectrodes (R_m), constant phase element (CPE_1) and the diffusion impedance (Z_w) (replaced with CPE_2 in the case of flattened PEDOT:PTS coated microelectrodes and gold coated microelectrodes). The simulated data confirmed the lowest resistance of micro-topographically functionalised PEDOT:PTS coated microelectrode ($3.11 \pm 0.13 \text{ k}\Omega$), when compared to pristine ($12.01 \pm 1.53 \text{ k}\Omega$) and flattened ($357.77 \pm 14.64 \text{ k}\Omega$) PEDOT:PTS coated microelectrodes, as well as bare platinum ($40.28 \pm 0.63 \text{ k}\Omega$) and gold coated ($23.61 \pm 1.28 \text{ k}\Omega$) microelectrodes. The summary of resistance calculated values is tabulated in **Table 3.4**.

The range of impedance as well as the magnitude of resistance achieved by micro-topographically functionalised PEDOT:PTS microelectrodes place them among the surface-materials suitable for use in neural stimulation and recording [117, 118].

Table 3.4 Summary of the calculated resistance values (R_m) of bare platinum (Pt) and gold coated (Au) microelectrodes and pristine PEDOT:PTS, flattened PEDOT:PTS and micro-topographically functionalised PEDOT:PTS coated microelectrodes after equivalent circuit analysis. Results are \pm STD. $N=3$.

	Bare Platinum (Pt)	Gold Coated (Au)	Pristine PEDOT:PTS	Flattened PEDOT:PTS	Micro-topographically functionalised PEDOT:PTS
R_m , [kOhms]	40.28 ± 0.63	23.61 ± 1.28	12.01 ± 1.53	357.77 ± 14.64	3.11 ± 0.13

To further confirm the effects of micro-pit topographical functionalisation on enhancing the electrical performance of the PEDOT:PTS coated microelectrode through an increase in surface area, force-controlled current-voltage (I-V) spectra were recorded employing conductive-AFM (C-AFM) (in PeakForce Tuna mode, PF Tuna, Bruker) using a system detailed in **Figure 3.1**.

Figure 3.10(A-B) shows the surface topography and the corresponding distribution of the electrical profile at the nanoscale level within a micro-topographically functionalised PEDOT:PTS coated microelectrode. The comparative I-V curves detailed in **Figure 3.10B** provide additional insights into the role of the micro-pit topography in generating lower resistance profiles of the PEDOT:PTS relative to non-imprinted peri-pit regions. This effect is likely due to a differential response in potential across the pit, resulting in a linear increase in current compared to a steady response seen on the I-V relationship from the non-patterned region.

Topographically Functionalised Poly(3,4-Ethylenedioxythiophene):P-Toluene Sulphonate (PEDOT:PTS) Neuroelectrodes Via Microimprint Lithography

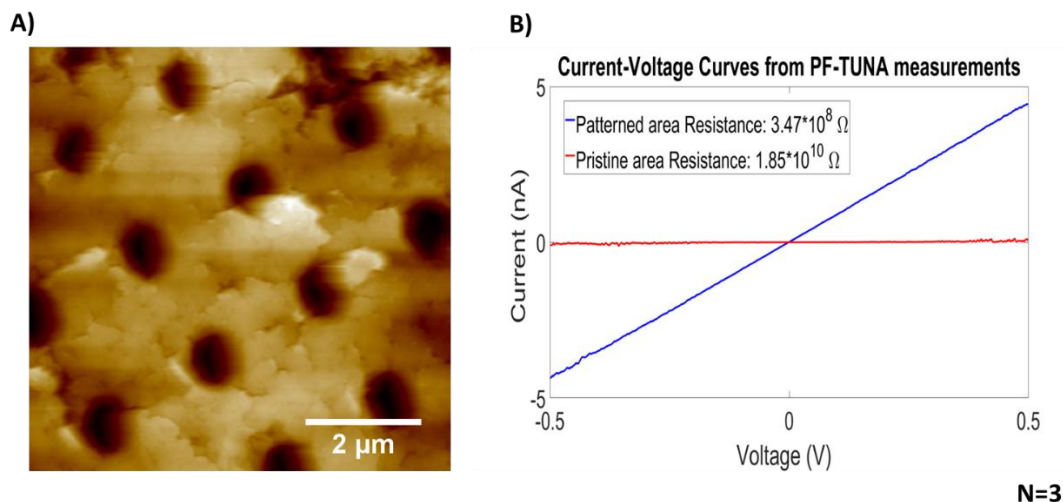


Figure 3.10 Conductive-AFM (C-AFM) (in PeakForce Tuna mode, PF Tuna, Bruker) of micro-topographically functionalised PEDOT:PTS coated microelectrodes. A) C-AFM micrograph of micro-topographically functionalised PEDOT:PTS coated microelectrode used for analysis. B) I-V curves were recorded at selective positions, non-patterned region and patterned region (pit) on the micro-topographically functionalised microelectrode. C-AFM tips (coated with Platinum/Iridium) were used as the mobile counter electrode to contact the SWCNTs (PeakForce-TUNA tips, Bruker). For a schematic of the set-up, see Figure 3.1. The voltage bias was ramped between -500mV and 500mV. The data was then analysed by NanoScope Analysis (version 1.5, Bruker) and Matlab (version 2016 a).

In order to determine the stability of PEDOT:PTS functionalised microelectrodes, substrates were subjected to 500 cycles of continuous potentiodynamic stimulation with the aim of testing, under working conditions, the durability and the electrochemical robustness of the potential neural electrodes [8, 119, 120]. The loss in electroactivity of the microelectrodes was calculated as a percentage based on CSCs recorded before and after stability studies (**Table 3.3**). A high loss in CSC was observed for Pt sputtered microelectrodes due to the thickness differences, with a 72 % loss. In contrast, with a comparable working thickness obtained with gold coated microelectrode, a significantly lower percentage loss of 37 % was observed which was similar to the percentage loss obtained with PEDOT:PTS coated microelectrodes.

Topographically Functionalised Poly(3,4-Ethylenedioxythiophene):P-Toluene Sulphonate (PEDOT:PTS) Neuroelectrodes Via Microimprint Lithography

Significantly, flattened PEDOT:PTS coated microelectrodes were associated with an diminution of performance, with a loss of 98 %. Overall, superior electrochemical stability and robustness was observed with micro-topographically functionalised PEDOT:PTS coated microelectrodes with an electroactivity loss of 26 %. This stability effect, coupled with the high effective surface area and the low impedance profiles, identifies the micro-topographically functionalised PEDOT:PTS coated microelectrodes developed here, as functionalised microelectrodes with potential in neural stimulation and recording performance.

3.4.3 Biological Characterisation

Neural interfaces that promote neural integration, with a minimal inflammation response are persistent challenges within the realms of biomaterials and neural engineering. Even though the cellular response to topography is undoubtedly cell specific, it has been shown that topographical modifications may contribute significantly to answer the challenges of selective cell adhesion and modulated cell behavior to reduce gliosis at the material-tissue interface [121].

The neural response to micro-pit topographies replicated in PEDOT:PTS coated 1.6 cm² Pt electrodes was evaluated using primary VM mixed neural cell population *in vitro* **Figure 3.11**.

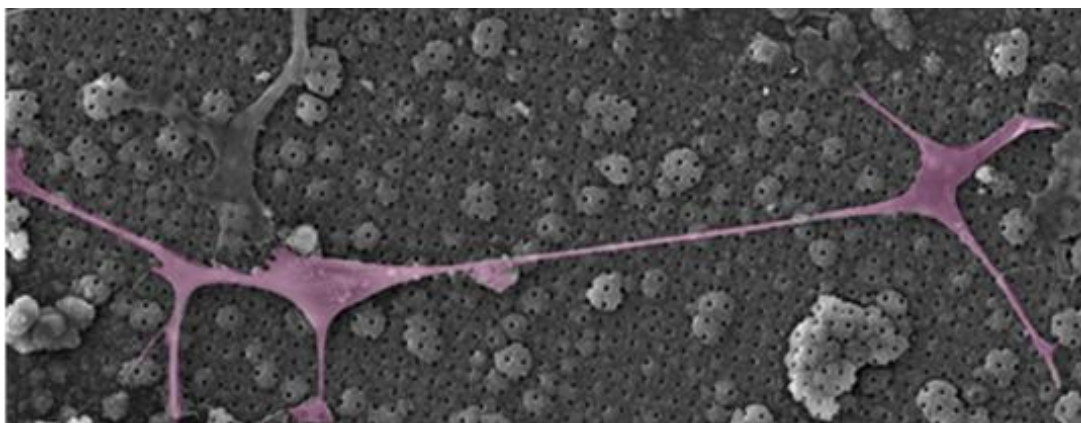


Figure 3.11 *Ventral mesencephalic cells (VM) adhered on micro-topographically functionalised electrodes. Scanning electron micrograph (SEM) of primary VM mixed cell population adhered on micro-topographically functionalised PEDOT:PTS coated electrodes. Scale bar= 50 μ m.*

Topographical functionalisation to modulate differential cell adhesion and the observation that flat or non-structured electrodes surfaces favour astrocyte adhesion has been reported previously [14, 56, 122]. A recent study by Seker and colleagues [56] demonstrated the efficacy of nanotopographical modification of the electrode surface in reducing focal adhesion formation in astrocytes while maintaining neural integration on np-Au surfaces. Conversely, Qi et al. [123] showed that micro-patterned topographies, with dimensions ranging from 2 μm - 10 μm , influence the differentiation of adult neural stem cells (ANSCs) into neurons, and may discourage the differentiation of astrocytes.

Figure 3.12A shows representative fluorescent micrographs of VM derived mixed cultures of neurons and astrocytes cultured on experimental and control electrodes. All groups were evaluated over a period of three, seven and ten days in culture. The persistence of neurons and astrocytes on each of the experimental and control groups as a function of time is presented in **Figure 3.12B**. The percentage cell density of astrocytes and neurons on each assessed group initially indicated that flattened PEDOT:PTS electrodes induced a significant linear increase of astrocytic presence as a function of time, with a subsequent significant decrease in neuronal presence relative to all experimental and the bare platinum control substrates. By day ten, the flattened PEDOT:PTS coated electrodes exhibited an astrocyte presence of 97.67 % and a 2.32 % neuron presence. Interestingly, pristine PEDOT:PTS coated electrodes induced a significant decrease in astrocytic presence and a significant increase in neuron cell populations present at each time point relative to all the experimental and control groups. Following ten days in culture, the astrocyte and neuron presence on pristine PEDOT:PTS coated electrodes was 46.39 % and 53.60% respectively. Furthermore, when comparing the neuron and astrocyte cell density populations with control platinum and micro-topographically functionalised PEDOT:PTS coated electrodes, an identical trend with no statistical difference was observed for differential neuron or astrocytes density over time. Following ten days in culture, the astrocyte population on control platinum and micro-topographically PEDOT:PTS coated electrodes was recorded at 61.97 % and 62.46 % respectively, 16% greater than that on pristine PEDOT:PTS coated electrodes.

Topographically Functionalised Poly(3,4-Ethylenedioxythiophene):P-Toluene Sulphonate (PEDOT:PTS) Neuroelectrodes Via Microimprint Lithography

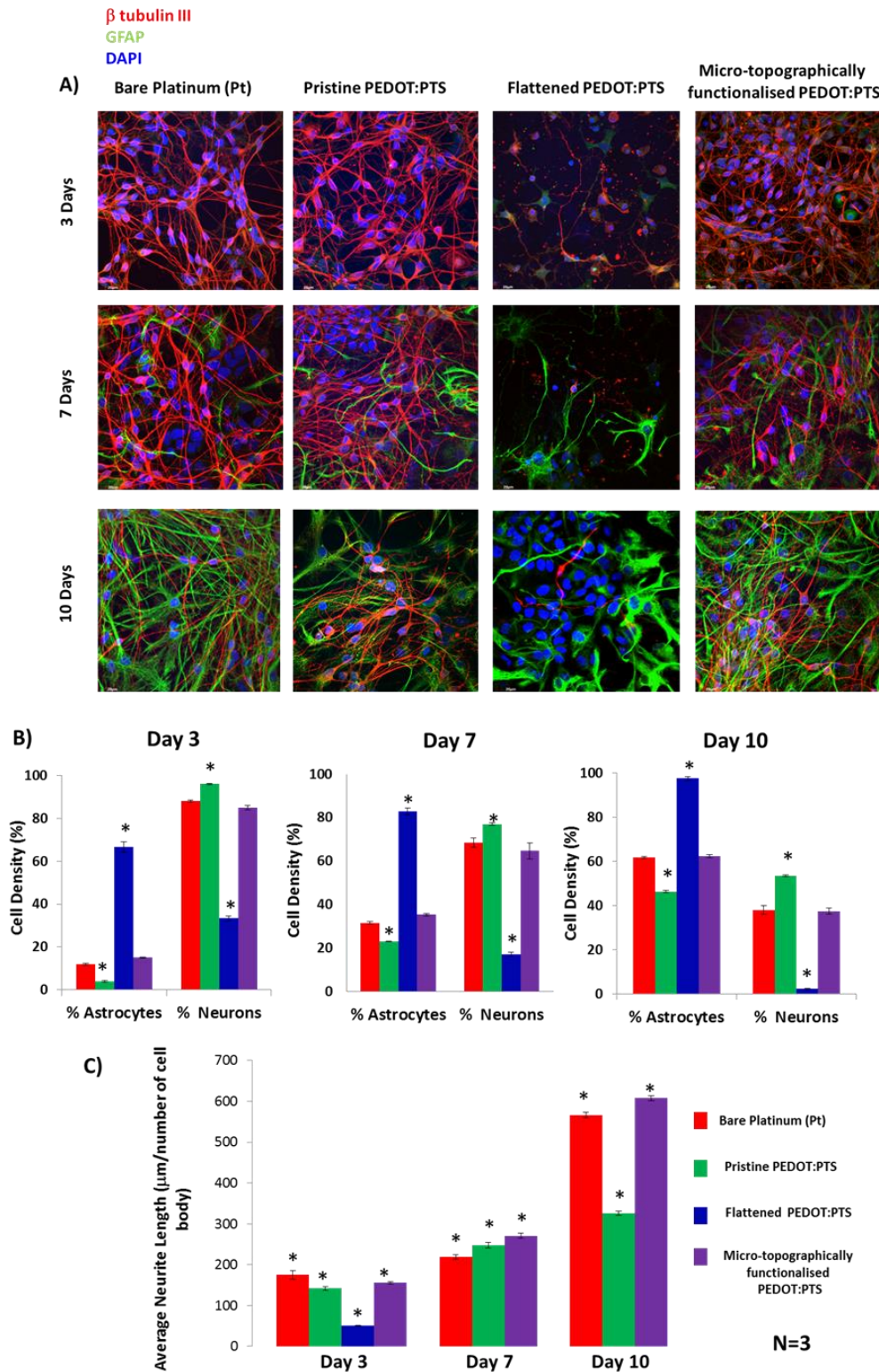


Figure 3.12 Cytocompatibility of functionalised electrodes. A) Fluorescent images of primary ventral mesencephalic (VM) mixed cell population grown on each of the

Topographically Functionalised Poly(3,4-Ethylenedioxythiophene):P-Toluene Sulphonate (PEDOT:PTS) Neuroelectrodes Via Microimprint Lithography

bare platinum (Pt) and functionalised PEDOT:PTS coated electrodes for three, seven and ten days in culture. Neurons are visualised by anti β -tubulin III, in red, astrocyte cells by anti-GFAP, in green and nuclei are visualised by DAPI, in blue. Bar = 20 μ m, objective 60 \times magnification. Cell density (%) analysis of astrocytes and neurons presence on each of the electrodes is presented in B). An overall significant ($p < 0.05$) decrease in viability of neurons and astrocytes density was observed in flattened PEDOT:PTS coated electrodes. Neural length analysis of electrodes presented in C) showed with significant ($p < 0.05$) longer neurite lengths the neurons grown on micro-topographically functionalised PEDOT:PTS coated electrodes. ★ = $p < 0.05$.

In conjunction with cell density, as an indicator of cell viability neurite length on experimental and control substrates was also analysed (**Figure 3.12C**). At day three, a significant decrease in neural length was observed on all experimental groups relative to Pt electrodes on which mean neurite length was $175.08 \mu\text{m} \pm 10.55$. This trend was lost by day seven and a linear increase in length as a function of electrode surface area was observed. However, neurite length on mechanical flattened control samples could not be quantified due to a significant reduction in neuron presence, making the application of the stereology method used for the quantification of length invalid.

Further significant differences in neural length were observed by day ten, with significant neurite elongation exhibited in cells cultured on micro-topographically functionalised PEDOT:PTS electrodes ($607.68 \mu\text{m} \pm 5.53$) relative to Pt control ($566.36 \mu\text{m} \pm 6.35$) and pristine PEDOT:PTS coated electrodes ($325.76 \mu\text{m} \pm 4.66$).

These results indicate that pristine PEDOT:PTS coatings do not enhance astrocyte proliferation and adhesion relative to control Pt electrodes and that micropatterning of PEDOT:PTS coatings can be employed to significantly enhance neurite length *in vitro*. Conversely, mechanically flattened PEDOT:PTS coated electrodes induced overall poor viability of the primary mixed VM cell population relative to all other experimental conditions [14, 122]. That neurons cultured on pristine PEDOT:PTS coated electrodes exhibited a higher frequency but with significantly shorter neural

processes relative to Pt electrodes and micro-topographically functionalised PEDOT:PTS coated electrodes may suggest that network development in ventral mesencephalic derived neurons is not entirely supported on nano-roughened, pristine electrodes [124, 125]. Critically, VM derived glial cells promote neuronal survival and neurite growth by releasing growth factors and providing an ideal biochemical milieu *in vitro* for neuronal development [124]. Thus, although pristine PEDOT:PTS coated electrodes were associated with a significant reduction in astrocyte density and promoted more neural coverage relative to cell population ratios observed on bare platinum and micro-topographically functionalised PEDOT:PTS coated electrodes, this phenomenon did not translate into the development of an extensively interconnected functional neural network. Rather, it may suggest the onset of a pro-inflammatory response [124]. Neurite length was significantly increased on the micro-topographically functionalised PEDOT:PTS coated electrodes by day ten relative to all experimental groups, suggesting that neurons may benefit from the presence of an underlying glia network and a morphological response to micro-topographical features may be manifest in enhanced neurite extension. This observation is supported by previous research into topographical features supporting neural outgrowth through supportive cues [84, 126-128]. Also, it can be inferred that neurite extension on micro-topographically functionalised PEDOT:PTS coated electrodes may suggest a reduced inflammatory environment from the glial interactions relative to all experimental and control groups [124].

In order to assess the reactivity of astrocytes (the key players in astrogliosis) on fabricated electrodes, the mean cellular area was quantified as a morphological indicator of a reactive astrocyte phenotype again using a primary VM mixed cell culture. Critically, morphological analysis of astrocyte populations has been shown repeatedly to provide helpful insights into resting or activated functional states in astrogliosis, considering astrocytic heterogeneity [129, 130]. Furthermore, to assess modulated astrocyte morphology and adhesion on experimental electrodes, GFAP immunofluorescent labelling was conducted in conjunction with Paxillin labelling, a key focal adhesion protein (**Figure 3.13A**). It has been shown *in vitro* that in 2D cultures neurons will grow on the dorsal surface and extend processes along

topographical cues provided by an astrocyte monolayer [57]. Consequently, it has been suggested that astrocyte presence on an implanted electrode is critical to support neural integration and neurite outgrowth [60] rather, it is the reduction of a reactive astrocyte phenotype presence that is a potential functionalisation strategy in minimising astrogliosis in peri-electrode glial scar formation [54].

Representative fluorescent micrographs of isolated astrocytes from the mixed primary VM cell cultures grown on controls Pt, and experimental PEDOT:PTS functionalised electrodes were captured over three, seven and ten days in culture (**Figure 3.13A**). **Figure 3.13B** represents the distribution of astrocyte cell areas as a function of GFAP staining over time. The distribution of the astrocyte cell area is significantly shifted towards a greater astrocyte cell area on Pt electrodes relative to pristine PEDOT:PTS, flattened PEDOT:PTS and micro-topographically functionalised PEDOT:PTS coated electrodes. By day ten, the frequency of astrocyte cell areas between the ranges of $450 \mu\text{m}^2$ and $2250 \mu\text{m}^2$ on Pt electrodes was significantly increased. Astrocyte cultured on pristine PEDOT:PTS, flattened PEDOT:PTS and micro-topographically functionalised PEDOT:PTS coated electrodes, however, exhibited a bio-modal distribution of cell area, with significant peaks also observed in the $50\text{-}350 \mu\text{m}^2$ cell area range. Interestingly, micro-topographically functionalised PEDOT:PTS coated electrodes were associated with the lowest astrocyte area distribution when compared to control and experimental substrates at all time points. It was observed by day ten that the 80 % of the astrocyte cell areas were confined within the ranges of $100 \mu\text{m}^2$ and $1250 \mu\text{m}^2$. These findings are particularly important as it has been shown that the variations in overall astrocytic cell area underlie reactivity implications over time [129, 131, 132], where enlarged astrocytes areas may translate into moderate and/or severe reactive astrogliosis [131].

Topographically Functionalised Poly(3,4-Ethylenedioxythiophene):P-Toluene Sulphonate (PEDOT:PTS) Neuroelectrodes Via Microimprint Lithography

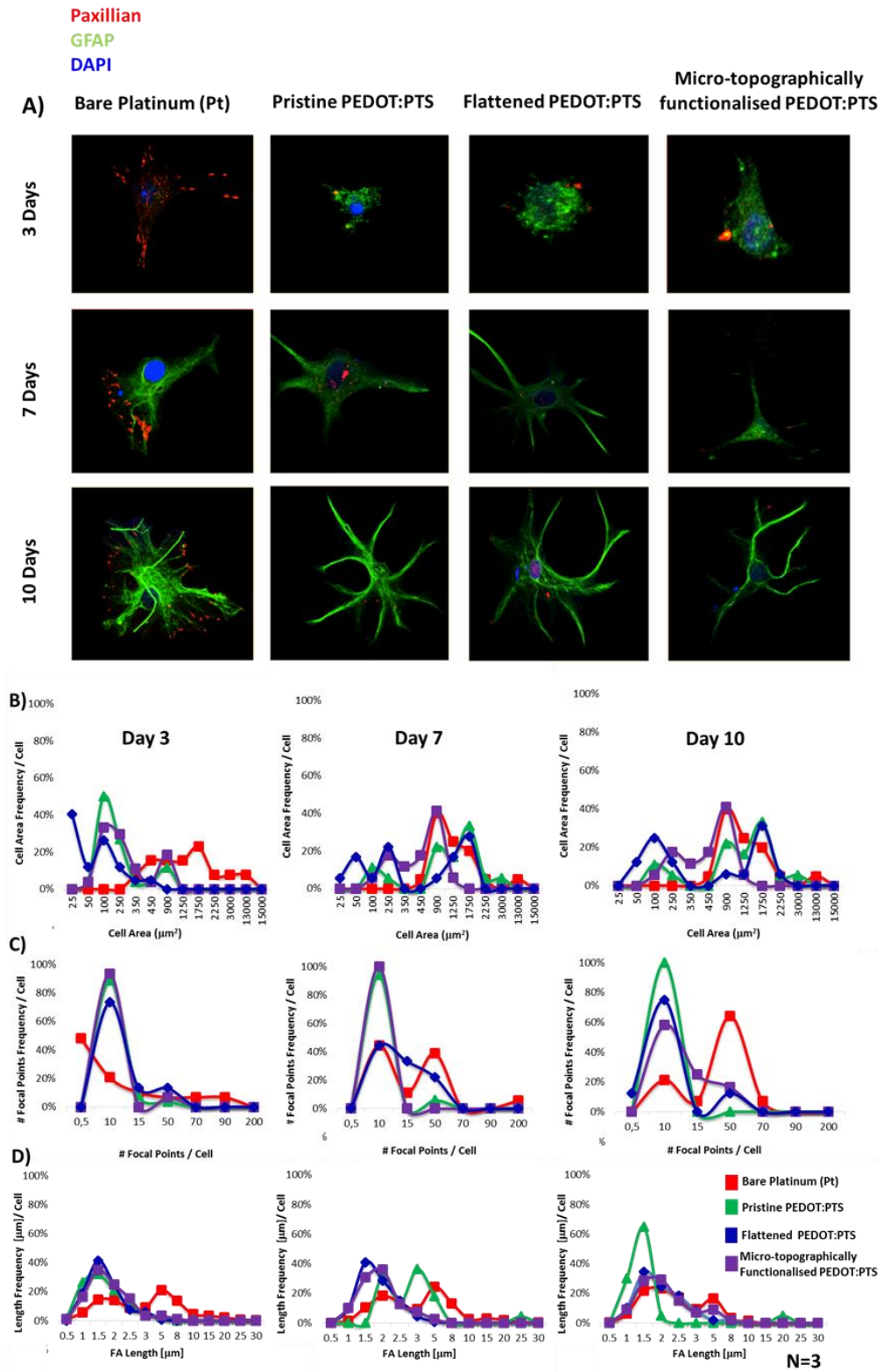


Figure 3.13 Morpho-adhesion characteristics of astrocyte presence in the functionalised electrodes towards astrocyte reactivity indication. A) Selective

Topographically Functionalised Poly(3,4-Ethylenedioxythiophene):P-Toluene Sulphonate (PEDOT:PTS) Neuroelectrodes Via Microimprint Lithography

fluorescent images of astrocytes from primary ventral mesencephalic (VM) mixed cell population grown on each of the bare platinum (Pt) and functionalised PEDOT:PTS coated electrodes for three, seven and ten days in culture. Astrocytes are visualised by anti-GFAP, in green, formation of focal adhesion contacts by anti-Paxillin, in red and nuclei are visualized by DAPI, in blue. Bar = 20 μm , objective 60 \times magnification. Frequency distribution in time (three, seven, and ten days) of cytoplasm astrocyte areas (μm^2) on bare platinum (Pt) and functionalised PEDOT:PTS coated electrodes is presented in B). The frequency distribution of astrocyte areas on micro-topographically functionalised PEDOT:PTS coated electrodes showed the lowest frequencies over time. C) represents the frequency distribution of the astrocyte focal adhesion contact numbers per cell and their corresponding length frequency distribution over time in D).

Of further interest is the observation that the increased frequency of astrocytes with enlarged cell areas observed on bare platinum, pristine PEDOT:PTS and flattened coated electrodes is associated with a reduction in neural outgrowth relative to neurons cultured on micro-functionalised PEDOT:PTS electrodes, again pointing to a reactive astrocyte induced disruption of network evolution. This effect was largely accentuated on flattened PEDOT:PTS coated electrodes.

In order to evaluate perturbation of assessed electrode topography on astrocyte adhesion and to draw parallels between reactive astrocyte phenotype and focal adhesion formation, quantification of mean cellular focal adhesion number and length was carried out (**Figure 3.13C-D**). The regulation of focal adhesion formation in adherent cells such as astrocytes, involves complex recruitment of integrin-dependent signaling pathways mainly mediated by non-receptor tyrosine kinases, markedly by focal adhesion kinase (FAK) [133]. Further, it has been shown that mediated signaling through FAK/Paxillin in astrocytes plays an important role in astrocyte cell morphology, where a reduction of tyrosine phosphorylation and paxillin expression is related to the stellation of astrocytes [134-136]. However, in pathological situations, astrocytes no longer adopt a stellar appearance but become hypertrophic in morphology, and are associated with increased focal adhesion

signaling, so-called reactive astrocytes [137-140]. Certainly, cell-adhesion is mainly controlled through cell-substrate interactions, where topographies have been shown to play an essential role [50].

Analysis of the distribution of FA frequency and length in astrocytes on bare platinum electrodes indicated that at day three 70% of the astrocytes exhibited ten focal adhesion contacts per astrocyte with lengths ranging between 0.5 μm and 10 μm . By day ten, a significant increase in astrocytes adhesion was observed with 70% of the astrocytes exhibiting between 15 and 70 focal adhesion points per cell with maintained focal adhesion lengths between the ranges of 0.5 μm and 8 μm compared to day three. These results suggest a decrease of cell motility owing to the higher number of focal adhesion contacts per cell, but further to the stable lengths achieved [52], results that in light of the augmented astrocytic cell areas observed on these electrodes, showed the development of more focal adhesion contacts suggesting the presence of a more reactive astrocyte phenotype. In addition, bare platinum (R_a : 2 nm) commonly used in neural electrodes, does not allow for the selective control of cell adhesion (**Figure 3.13B**), which together with its mechanical rigidity, may account for the overall higher reactive astrocyte presence than that of more compliant conducting polymeric coated electrodes [141] .

On the other hand, the pristine PEDOT:PTS coated electrodes, the flattened PEDOT:PTS coated electrodes, and the micro-topographically functionalised PEDOT:PTS coated electrodes, were associated with similar astrocyte adhesion over time, with overall focal adhesion numbers significantly less than those observed on bare platinum electrodes.

By day ten, more than 80% of the astrocytes on both, pristine PEDOT:PTS and the flattened PEDOT:PTS coated electrodes, presented a mean value of fifteen focal adhesions per cell. Conversely, micro-topographically functionalised PEDOT:PTS coated electrodes, induced significant modulation to the distribution of the number of astrocyte focal adhesion with 38% of the astrocyte population exhibiting an increase in the mean number of focal adhesions per cell of between 15 and 50 focal adhesions per astrocyte. This observation together with the comparatively lower astrocyte areas

observed on the micro-topographically functionalised PEDOT:PTS coated electrodes, may allude to a differential effect in astrocyte adhesion and a reduction in reactive astrocytes presence as a function of micro-topographical modification. The length of the astrocyte focal adhesion points did not change significantly over time on flattened PEDOT:PTS coated electrodes and on micro-topographically functionalised PEDOT:PTS coated electrodes, with lengths confined between the ranges of 0.5 μm and 5 μm . In contrast, pristine PEDOT:PTS coated electrodes resulted in shorter astrocyte focal adhesion contact lengths between the ranges of 1 μm and 1.5 μm by day ten.

It has been shown by our studies in other fields that ordered nanopits topographies are proposed to impair focal adhesion formation by disrupting integrin activation and clustering, an effect enhanced at the microscale length [50, 51, 56, 59]. Indeed, experimentally this work has shown that PEDOT:PTS coated electrodes functionalised with a micro-pit topography have a significant influence on reactive astrocyte adhesion. Furthermore, these findings present opportunities to study reactive astrocyte presence through cytoskeleton-linked proteins signaling mechanisms controlling astrocyte phenotype.

Understanding the glia interactions as key contributors in the glial scar formation is essential [54] and in addition to influencing cytoskeleton-linked proteins, substrate topography has been previously shown to affect cellular function and the synthesis of cytokines and signaling molecules in neural cells [142, 143]. To elucidate further the roles of topographical functionalisation on the neural response *in vitro*, changes in the expression of pro-inflammatory cytokines and chemokine factors were assessed via multiplex ELISA analysis. Currently, few studies have examined the effect of topographical functionalisation on the glial cell functional response in complex mixed cell cultures [84]. With this in mind, glial-derived cytokines and chemokine factors such as IFN- γ , TNF- α , IL-6, IL-5, and KC/GRO, involved in mediating neuronal-glia interactions and modulation of reactive astrogliosis were selected for analysis [144-149]. The release profiles were compared between each of the experimental groups, controls and with an additional inflammatory control group, VM cells cultured on

Thermanox® Plastic Coverslips (tissue culture plastic) which received a stimulus of interleukin-1beta (IL-1 β) at a dose of 10 ng ml⁻¹. Complementary data for the optimisation of the different concentrations of IL-1 β as inflammatory stimuli on VM cells cultures is shown in **Figure 3.2** with the analysis of the production of reactive oxygen species (ROS), CellROX® and in **Figure 3.3** with the quantification of activated microglia using methods for morpho-functional analysis described in [67], respectively.

The secretion of pro-inflammatory cytokines and chemokine factors in mixed cell populations cultured on all experimental and control groups is presented in **Figure 3.14**. It is interesting to note that even though there is a linear increase in the release profile of IFN- γ in mixed cultures exposed to inflamed control conditions and when cultured on flattened PEDOT:PTS coated electrodes over time, Pt electrodes and pristine PEDOT:PTS coated electrodes followed a trend over time that was similar and constant, with no statistical differences noted between the expression profile of IFN- γ at day three and day ten respectively (**Figure 3.14A**). Importantly, the lowest release profile of IFN- γ was observed with the micro-topographically functionalised PEDOT:PTS coated electrodes, with a maintained overall low and statistically significant release of this cytokine relative to all experimental and control groups by day ten. This cytokine is reportedly a crucial immunological player as it regulates relevant genes for cell function and cell programming [150]. Studies have shown that IFN- γ has a unique action on astrocytes, inducing pro-inflammatory activities and enhancing astrocyte-immunoreactivity [148, 151]. In a similar manner, TNF- α cytokine is known to act in synergy with IFN- γ [152], showing a similar release trend on day seven and day ten respectively relative to the release profiles of IFN- γ on these days (**Figure 3.14B**). Over time, a linear decrease in TNF- α release was observed in all groups and controls, except for on the inflamed control group that presented a consistently high release profile of TNF- α . By day ten, a significantly higher release profile of TNF- α was observed in the inflamed control group which was comparable to that observed in VM cells cultured on flattened PEDOT:PTS coated electrodes. Control Pt, pristine PEDOT:PTS and micro-topographically

functionalised PEDOT:PTS groups, were associated with a significant reduction in TNF- α synthesis and cells cultured on topographically functionalised PEDOT:PTS coated electrodes produced significantly less TNF- α than Pt control and other PEDOT:PTS experimental groups. These results indicate an activated response from astrocytes and microglia respectively, with their coordinated involvement in the host response at the material interface [148, 152]. Furthermore, the micro-pit topography utilised here also induced a reduced glial cell inflammatory response via CXCL-1, also known as KC/GRO (**Figure 3.14C**). CXCL-1 is associated with neutrophil recruitment, to a site of inflammation [153], and a study by Rubio and colleagues [153] showed that astrocytes, as an early cell component of the neuro-immune response, produced CXCL-1 in the chemoattraction of the neutrophils and monocytes in neuro-inflammatory diseases. In this work, it was observed that by day ten, in contrast to a relatively high release profile of CXCL-1 from the inflammatory control conditions, an overall significantly lower release response of CXCL-1 was exhibited by VM populations cultured on the micro-topographically PEDOT:PTS functionalised electrodes, a response maintained up to day ten in culture.

In primary mixed cultures, such as in the VM cells used in this research, as a consequence of the orchestrated release of cytokines and growth factors in neuronal-glial interactions [148], there is a synergistic effect that allows them to work as co-stimulatory molecules to potentiate immune interactions, in this case at the local neuron-glial unit, with a resulting increase of specific cytokines response such as IL-6 [147, 148, 154].

Topographically Functionalised Poly(3,4-Ethylenedioxythiophene):P-Toluene Sulphonate (PEDOT:PTS) Neuroelectrodes Via Microimprint Lithography

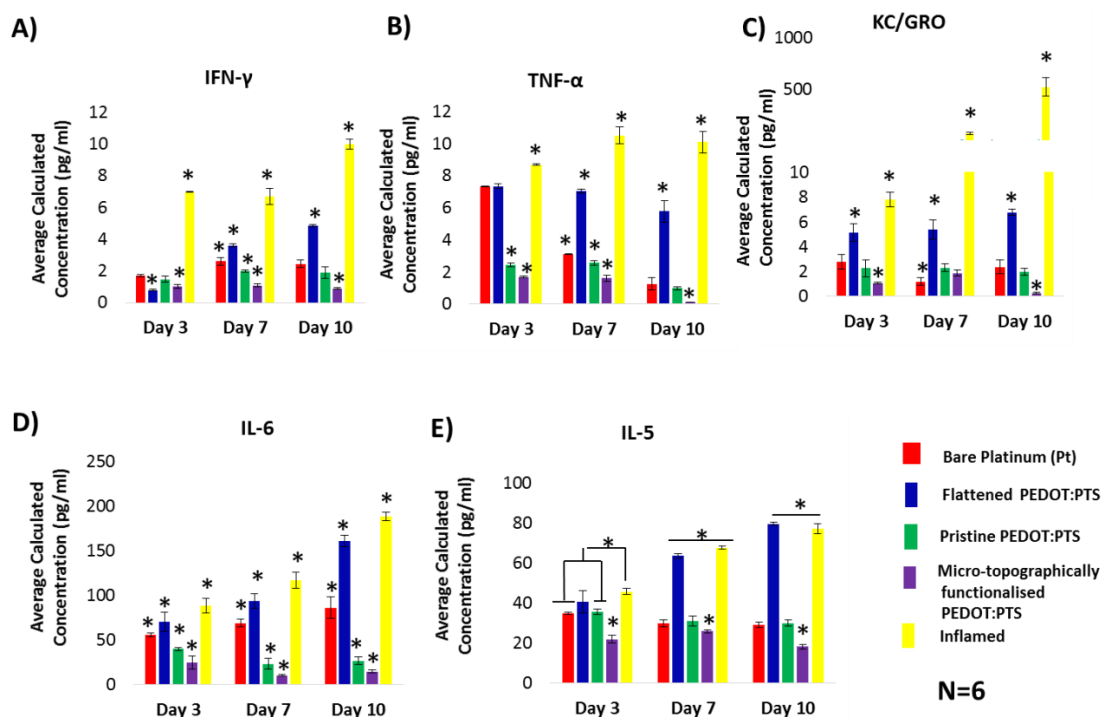


Figure 3.14. Comparative gliosis derived cytokines and chemokine factor profiling for interferon- γ (IFN- γ ;A), tumor necrosis factor- α (TNF- α ;B), chemokine factor CXCL-1 (KC/GRO;C), interleukin-6 (IL-6;D) and interleukin-5 (IL-5;E). The release expression of each of the signaling molecules is analysed from primary ventral mesencephalic (VM) mixed cell population supernatants collected at day three, seven and ten days on bare platinum (Pt) and functionalised PEDOT:PTS coated electrodes. An important effect is seen on the micro-topographically functionalised PEDOT:PTS coated electrodes, which presented significantly and consistently low release profiles for each cytokine and chemokine factor analysed. Results are \pm STD, $\star = p < 0.05$.

At day three (**Figure 3.14D**), IL-6, which plays a vital role in immune regulation and is produced by astrocytes, microglia and neurons in injury-inflamed milieu [155-159], showed a significantly potentiated release profile in the inflammatory control group, relative to an observed significant linear decrease in the release profile in VM cells cultured on all control and experimental electrode substrates. On day seven, comparatively significant increases in the release levels of IL-6 were observed on pristine and micro-topographically functionalised PEDOT:PTS electrodes relative to

Topographically Functionalised Poly(3,4-Ethylenedioxythiophene):P-Toluene Sulphonate (PEDOT:PTS) Neuroelectrodes Via Microimprint Lithography

day three on bare platinum electrodes, flattened PEDOT:PTS coated electrodes and on the inflamed control, with significantly lower levels of IL-6 released VM cells cultured on micro-topographically functionalised PEDOT:PTS electrodes, maintained up to day ten.

Similar release trends in the expression levels of IL-5 were also observed (**Figure 3.14E**), an important and often overlooked pro-inflammatory cytokine that has been shown to be produced by astrocytes and microglia *in vitro* [147, 158]. Further, IL-5 has been shown to induce nerve growth factor (NGF) secretion by astrocytes [161, 162]. Again, the released IL-5 concentrations from micro-topographically functionalised PEDOT:PTS coated electrodes showed significant lower release profiles when compared to all groups, controls and inflamed control respectively at all time points.

Cytokines protein interactions adopting a confidence score >0.7 as the threshold to assess associations was performed and are detailed in **Figure 3.15**. These results are particularly important, and suggest that the cytokine expression profiles observed from VM cells cultured on micro-topographically functionalised electrodes supports an overall neural-glial interaction at the electrode, associated with minimised reactive gliosis over time [163]. Indeed, this work has shown experimentally that the micro-topographically functionalised PEDOT:PTS coated electrodes here developed reduced the cytokine mechanisms of astrogliosis *in vitro*. This response was accentuated relative to bare platinum electrodes and pristine PEDOT:PTS coated electrodes, but further stressed when compared to flattened PEDOT:PTS coated electrodes, which resulted in the promotion of a more pro-inflammatory cytokine release and chemokine factors, reflected in the poor VM cell viability and outgrowth.

Topographically Functionalised Poly(3,4-Ethylenedioxythiophene):P-Toluene Sulphonate (PEDOT:PTS) Neuroelectrodes Via Microimprint Lithography

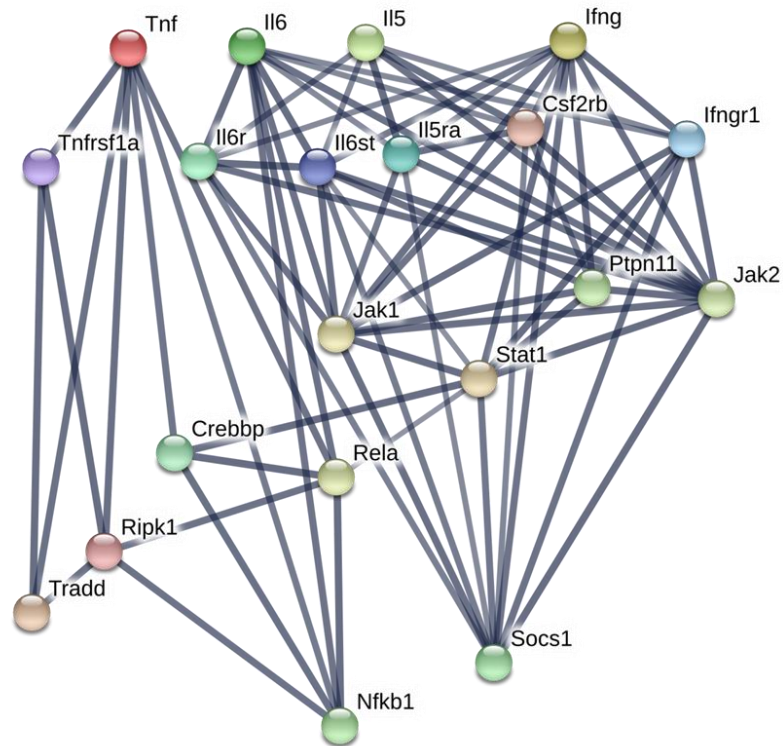


Figure 3.15 *Molecular network induced by cytokines TNF α , IL-6, IL-5 and IFN γ secreted by primary ventral mesencephalic (VM) mixed cells. Each node represents a single protein molecule encoded by genes. Coloured nodes indicate query proteins and first shell of interactors. The lines between the nodes indicate high confidence (>0.7) predicted interactions based on experimentally determined databases, co-expression, and co-occurrence.*

3.4.4 Calcium Imaging

To evaluate the neuronal network activity and functionality of the neuronal population grown on the electrodes, mature explanted primary rat hippocampal neurons were used. Importantly, the VM neuronal population used throughout this work is dissociated from embryos at age E14. As such, the capacity of neuron firing and neuronal networking activity of these embryonic neurons are known to happen after several weeks to months *in vitro*. However, mature neuronal population, such as the hippocampi neurons, present functional neuronal network after seven to ten days in culture offering an important advantage to embryonic cells in terms of culture

Topographically Functionalised Poly(3,4-Ethylenedioxythiophene):P-Toluene Sulphonate (PEDOT:PTS) Neuroelectrodes Via Microimprint Lithography

times. This not only allows the evaluation of continuous several electrodes, but further offers the possibility of addressing questions and potential future problems of instrumentation in short time windows.

Figure 3.16 shows preliminary data of the functional neural network as calcium transits from the rat hippocampal neurons cultured on the micro-pits PEDOT:PTS and pristine PEDOT:PTS coated electrodes as well as Pt electrodes, respectively. **Figure 3.16A** shows the snapshot of the neurons selected for the measurements. Similar occurrence of spontaneous calcium events were observed in all electrodes, showing ongoing synaptic activity (**Figure 3.16B**). However, it is interesting to note that the micro-topographically functionalised PEDOT:PTS coated electrodes generated calcium influx of higher magnitude. **Figure 3.16C** presents the inter event interval (IEI) values for the different electrodes. Further on-going analysis is being performed to elucidate the network activity of the neurons cultured on the functionalised micro-pits electrodes compared to the other electrodes evaluated. In addition, the functional characterisation (substrate stimulation) of the micro-pits functionalised electrodes is also under way.

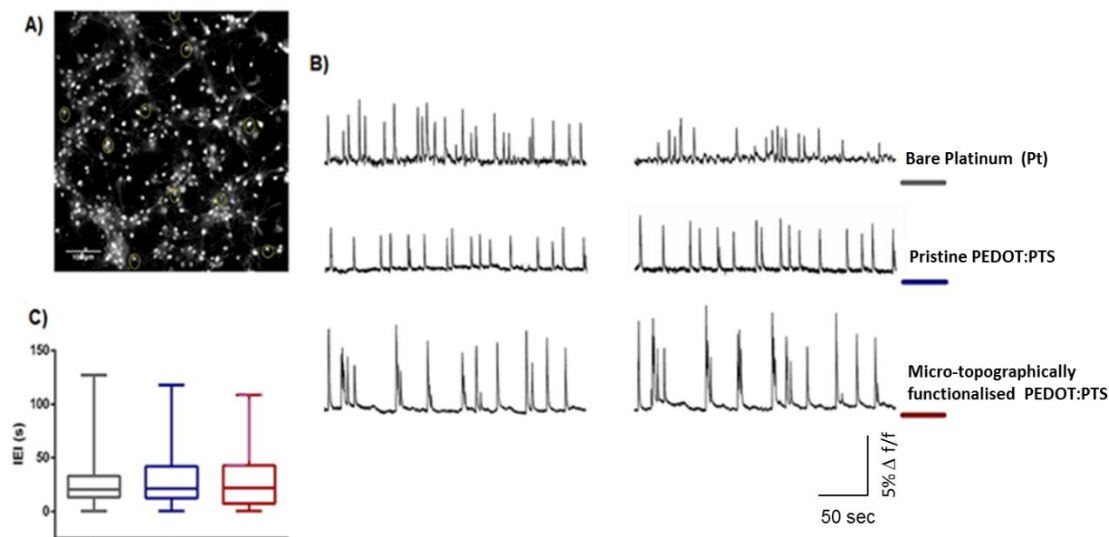


Figure 3.16 Neuronal network activity in bare platinum (Pt), pristine PEDOT:PTS and micro-topographically functionalised PEDOT:PTS coated electrodes. A) snapshot of representative field used for Ca^{2+} imaging recording with highlighted regions of interest (ROI), indicating the neurons selected for the measurements. B)

spontaneous repetitive Ca^{2+} events (two sample neurons were selected from the same field for each electrode) recorded in hippocampal cultures grown on the three different conditions. C) inter event interval (IEI) values are summarised for the different electrodes. Note the similar occurrence of spontaneous calcium events, due to ongoing synaptic activity.

3.5 Conclusion

The paradigm of neuroelectrode functionalisation is the maintenance of electrode functionality and a controlled inflammatory response [164, 165]. Micro-pit topographical functionalised PEDOT:PTS coated electrodes were assessed as a methodology for the design of functionalised neural interface materials with a focus on reduced astrocyte reactivity, enhanced neural integration and functional capacity.

Topographical functionalised PEDOT:PTS electrodes induced a significant reduction in electrical impedance and an increase in charge storage capacity and effective surface area, while maintaining electrode stability. Furthermore, the role of the micro-topographically modified PEDOT:PTS coated electrodes in reducing the characteristic phenotype associated with astrogliosis in complex primary mixed cell cultures was assessed from the evident morphological changes in cell area, the functional promotion of neural network activity, focal adhesion formation, and the release of pro-inflammatory cytokines and chemokine factors.

A low temperature imprint-lithography technique developed in this work for the micro-topographically functionalised neuroelectrode interfaces provides a useful bench-mark for subsequent studies with neural microelectrodes, and the development of dual functionalisation with biological molecules on as-formed conducting polymer coatings.

3.6 References

1. Lahr, J.; Schwartz, C.; Heimbach, B.; Aertsen, A.; Rickert, J.; Ball, T., J. Neural Eng. 2015, 12 (4), 043001.
2. Vanleer, A. C.; Blanco, J. A.; Wagenaar, J. B.; Viventi, J.; Contreras, D.; Litt, B., J. Neural Eng. 2016, 13 (2), 026015.

Topographically Functionalised Poly(3,4-Ethylenedioxythiophene):P-Toluene Sulphonate (PEDOT:PTS) Neuroelectrodes Via Microimprint Lithography

3. Fattahi, P.; Yang, G.; Kim, G.; Abidian, M. R., *Adv Mater* 2014, 26 (12), 1846-1885.
4. Durand, D. M.; Ghovanloo, M.; Krames, E., *J. Neural Eng.* 2014, 11 (2), 020201.
5. Zhou, Z.; Yu, P.; Geller, H. M.; Ober, C. K., *Biomacromolecules* 2013, 14 (2), 529-537.
6. Aregueta-Robles, U. A.; Woolley, A. J.; Poole-Warren, L. A.; Lovell, N. H.; Green, R. A., 2014.
7. Catalina Vallejo-Giraldo, N. P. P., Anuradha R. Pallipurath, John; O'Connell, J. D. H., Parvaneh Mokarian-Tabari, Alexandre Trotier, Katarzyna; Krukiewicz, G. O.-A., Eugenia Pugliese, Laura Ballerini, Michelle Kilcoyne,; Eilís Dowd, L. R. Q., Abhay Pandit, Paul Kavanagh and Manus Jonathan Paul; Biggs, *Adv Funct Mater* 2017.
8. Vallejo-Giraldo, C.; Pugliese, E.; Larranaga, A.; Fernandez-Yague, M. A.; Britton, J. J.; Trotier, A.; Tadayyon, G.; Kelly, A.; Rago, I.; Sarasua, J. R.; Dowd, E.; Quinlan, L. R.; Pandit, A.; Biggs, M. J., *Nanomedicine (Lond)* 2016, 11 (19), 2547-63. DOI 10.2217/nmm-2016-0075.
9. Agnew, W. F.; McCreery, D. B., *Neural Prostheses: Fundamental Studies*. Prentice Hall: 1990.
10. Cogan, S. F., *Annu. Rev. Biomed. Eng.* 2008, 10, 275-309. DOI 10.1146/annurev.bioeng.10.061807.160518.
11. Rousche, P. J.; Pellinen, D. S.; Pivin, D. P., Jr.; Williams, J. C.; Vetter, R. J.; Kipke, D. R., *IEEE Trans Biomed Eng* 2001, 48 (3), 361-71. DOI 10.1109/10.914800.
12. Mantione, D.; Del Agua, I.; Schaafsma, W.; Diez-Garcia, J.; Castro, B.; Sardon, H.; Mecerreyes, D., *Macromol Biosci* 2016, 16 (8), 1227-38. DOI 10.1002/mabi.201600059.

Topographically Functionalised Poly(3,4-Ethylenedioxythiophene):P-Toluene Sulphonate (PEDOT:PTS) Neuroelectrodes Via Microimprint Lithography

13. Boehler, C.; Stieglitz, T.; Asplund, M., *Biomaterials* 2015, 67, 346-353. DOI <http://dx.doi.org/10.1016/j.biomaterials.2015.07.036>.
14. Chapman, C. A. R.; Chen, H.; Stamou, M.; Biener, J.; Biener, M. M.; Lein, P. J.; Seker, E., *ACS Appl Mater Interfaces* 2015, 7 (13), 7093-7100. DOI 10.1021/acsami.5b00410.
15. Asplund, M.; Nyberg, T.; Inganas, O., *Polym Chem-Uk* 2010, 1 (9), 1374-1391. DOI 10.1039/c0py00077a.
16. Green, R. A.; Baek, S.; Poole-Warren, L. A.; Martens, P. J., *Sci Technol Adv Mat* 2010, 11 (1), 014107. DOI 10.1088/1468-6996/11/1/014107.
17. Green, R. A.; Lovell, N. H.; Wallace, G. G.; Poole-Warren, L. A., *Biomaterials* 2008, 29 (24), 3393-3399.
18. Balint, R.; Cassidy, N. J.; Cartmell, S. H., *Acta Biomater* 2014, 10 (6), 2341-2353.
19. Mario Cheong, G. L.; Lim, K. S.; Jakubowicz, A.; Martens, P. J.; Poole-Warren, L. A.; Green, R. A., *Acta Biomater* 2014, 10 (3), 1216-1226. DOI <http://dx.doi.org/10.1016/j.actbio.2013.12.032>.
20. Vallejo-Giraldo, C.; Kelly, A.; Biggs, M. J. P., *Drug Discov. Today* 2014, 19 (1), 88-94. DOI 10.1016/j.drudis.2013.07.022.
21. Shi, Y.; Pan, L.; Liu, B.; Wang, Y.; Cui, Y.; Bao, Z.; Yu, G., *Journal of Materials Chemistry A* 2014, 2 (17), 6086-6091.
22. Zhang, W.; Yang, F. K.; Pan, Z.; Zhang, J.; Zhao, B., *Macromol Rapid Commun* 2014, 35 (3), 350-354.
23. Xu, H.; Holzwarth, J. M.; Yan, Y.; Xu, P.; Zheng, H.; Yin, Y.; Li, S.; Ma, P. X., *Biomaterials* 2014, 35 (1), 225-235.
24. King, Z. A.; Shaw, C. M.; Spanninga, S. A.; Martin, D. C., *Polymer (Guildf)* 2011, 52 (5), 1302-1308. DOI 10.1016/j.polymer.2011.01.042.

Topographically Functionalised Poly(3,4-Ethylenedioxythiophene):P-Toluene Sulphonate (PEDOT:PTS) Neuroelectrodes Via Microimprint Lithography

25. Martin, D. C.; Wu, J.; Shaw, C. M.; King, Z.; Spanninga, S. A.; Richardson-Burns, S.; Hendricks, J.; Yang, J., *Polym. Rev. (Philadelphia, PA, U. S.)* 2010, 50 (3), 340-384. DOI 10.1080/15583724.2010.495440.
26. Castagnola, V.; Descamps, E.; Lecestre, A.; Dahan, L.; Remaud, J.; Nowak, L. G.; Bergaud, C., *Biosens. Bioelectron.* 2015, 67, 450-457.
27. Wu, F.; Sun, M.; Jiang, W.; Zhang, K.; Xie, A.; Wang, Y.; Wang, M., *Journal of Materials Chemistry C* 2016, 4 (1), 82-88.
28. Xiao, H.; Zhang, M.; Xiao, Y.; Che, J., *Colloids and Surfaces B: Biointerfaces* 2015, 126, 138-145.
29. Fonner, J. M.; Forciniti, L.; Nguyen, H.; Byrne, J. D.; Kou, Y. F.; Syeda-Nawaz, J.; Schmidt, C. E., *Biomed Mater* 2008, 3 (3), 034124. DOI 10.1088/1748-6041/3/3/034124.
30. Cui, X.; Lee, V. A.; Raphael, Y.; Wiler, J. A.; Hetke, J. F.; Anderson, D. J.; Martin, D. C., *J Biomed Mater Res* 2001, 56 (2), 261-72.
31. Abidian, M. R.; Corey, J. M.; Kipke, D. R.; Martin, D. C., *Small* 2010, 6 (3), 421-9. DOI 10.1002/sml.200901868.
32. Wolfs, M.; Darmanin, T.; Guittard, F., *Surf. Coat. Technol.* 2014, 259, 594-598.
33. Culebras, M.; Gomez, C.; Cantarero, A., *Journal of Materials Chemistry A* 2014, 2 (26), 10109-10115.
34. Oyman, G.; Geyik, C.; Ayranci, R.; Ak, M.; Demirkol, D. O.; Timur, S.; Coskunol, H., *Rsc Adv* 2014, 4 (96), 53411-53418.
35. Zhu, Z.; Mankowski, T.; Balakrishnan, K.; Shikoh, A. S.; Touati, F.; Benammar, M. A.; Mansuripur, M.; Falco, C. M., *ACS Appl Mater Interfaces* 2015, 7 (30), 16223-16230.
36. Wei, B.; Liu, J.; Ouyang, L.; Kuo, C.-C.; Martin, D. C., *ACS Appl Mater Interfaces* 2015, 7 (28), 15388-15394.

Topographically Functionalised Poly(3,4-Ethylenedioxythiophene):P-Toluene Sulphonate (PEDOT:PTS) Neuroelectrodes Via Microimprint Lithography

37. Deng, H.; Lin, L.; Ji, M.; Zhang, S.; Yang, M.; Fu, Q., *Prog Polym Sci* 2014, 39 (4), 627-655.
38. Uppalapati, D.; Boyd, B. J.; Garg, S.; Travas-Sejdic, J.; Svirskis, D., *Biomaterials* 2016, 111, 149-162.
39. Vara, H.; Collazos-Castro, J. E., *ACS Appl Mater Interfaces* 2015, 7 (48), 27016-27026. DOI 10.1021/acsami.5b09594.
40. Kim, D. H.; Wiler, J. A.; Anderson, D. J.; Kipke, D. R.; Martin, D. C., *Acta Biomater* 2010, 6 (1), 57-62. DOI 10.1016/j.actbio.2009.07.034.
41. Asplund, M.; Thaning, E.; Lundberg, J.; Sandberg-Nordqvist, A. C.; Kostyszyn, B.; Ingnas, O.; von Holst, H., *Biomed Mater* 2009, 4 (4), 045009. DOI 10.1088/1748-6041/4/4/045009.
42. George, P. M.; Lyckman, A. W.; LaVan, D. A.; Hegde, A.; Leung, Y.; Avasare, R.; Testa, C.; Alexander, P. M.; Langer, R.; Sur, M., *Biomaterials* 2005, 26 (17), 3511-9. DOI 10.1016/j.biomaterials.2004.09.037.
43. Pearce, T. M.; Williams, J. C., *Lab Chip* 2007, 7 (1), 30-40.
44. HajjHassan, M.; Chodavarapu, V.; Musallam, S., *Sensors* 2008, 8 (10), 6704-6726.
45. Donoghue, J. P., *Nat Neurosci* 2002, 5, 1085-1088.
46. Kotov, N. A.; Winter, J. O.; Clements, I. P.; Jan, E.; Timko, B. P.; Campidelli, S.; Pathak, S.; Mazzatenta, A.; Lieber, C. M.; Prato, M., *Adv Mater* 2009, 21 (40), 3970-4004.
47. Brüggemann, D.; Michael, K. E.; Wolfrum, B.; Offenhäusser, A., *International Journal of Nano and Biomaterials* 17 2012, 4 (2), 108-127.
48. Cui, X.; Hetke, J. F.; Wiler, J. A.; Anderson, D. J.; Martin, D. C., *Sensors and Actuators A: Physical* 2001, 93 (1), 8-18.
49. Asplund, M.; Nyberg, T.; Ingnäs, O., *Polym Chem-Uk* 2010, 1 (9), 1374-1391.

Topographically Functionalised Poly(3,4-Ethylenedioxythiophene):P-Toluene Sulphonate (PEDOT:PTS) Neuroelectrodes Via Microimprint Lithography

50. Biggs, M. J. P.; Richards, R. G.; Dalby, M. J., *Nanomedicine: Nanotechnology, Biology and Medicine* 2010, 6 (5), 619-633.
51. Biggs, M. J.; Richards, R. G.; Gadegaard, N.; McMurray, R. J.; Affrossman, S.; Wilkinson, C. D.; Oreffo, R. O.; Dalby, M. J., *J Biomed Mater Res A* 2009, 91 (1), 195-208. DOI 10.1002/jbm.a.32196.
52. Biggs, M. J.; Richards, R.; Gadegaard, N.; Wilkinson, C.; Dalby, M., *J Orthop. Res.* 2007, 25 (2), 273-282.
53. Morgan, J. T.; Murphy, C. J.; Russell, P., *Exp. Eye Res.* 2013, 115, 1-12.
54. Sofroniew, M. V., *Trends Neurosci.* 2009, 32 (12), 638-647.
55. Polikov, V. S.; Tresco, P. A.; Reichert, W. M., *J Neurosci Methods* 2005, 148 (1), 1-18. DOI <http://dx.doi.org/10.1016/j.jneumeth.2005.08.015>.
56. Chapman, C. A.; Wang, L.; Chen, H.; Garrison, J.; Lein, P. J.; Seker, E., *Adv Funct Mater* 2016.
57. Ereifej, E. S.; Matthew, H. W.; Newaz, G.; Mukhopadhyay, A.; Auner, G.; Salakhutdinov, I.; VandeVord, P. J., *Journal of Biomedical Materials Research Part A* 2013, 101 (6), 1743-1757.
58. Tawil, N.; Wilson, P.; Carbonetto, S., *The Journal of Cell Biology* 1993, 120 (1), 261-271. DOI 10.1083/jcb.120.1.261.
59. Biggs, M. J. P.; Dalby, M. J., *Proc Inst Mech Eng H* 2010, 224 (12), 1441-1453.
60. Turner, D. A.; Adamson, D. C., *J. Neuropathol. Exp. Neurol.* 2011, 70 (3), 167-176.
61. Turner, A. M.; Dowell, N.; Turner, S. W.; Kam, L.; Isaacson, M.; Turner, J. N.; Craighead, H. G.; Shain, W., *J Biomed Mater Res* 2000, 51 (3), 430-41.
62. Gadegaard, N.; Mosler, S.; Larsen, N. B., *Macromol. Mater. Eng.* 2003, 288 (1), 76-83.

Topographically Functionalised Poly(3,4-Ethylenedioxythiophene):P-Toluene Sulphonate (PEDOT:PTS) Neuroelectrodes Via Microimprint Lithography

63. Baek, S.; Green, R. A.; Poole-Warren, L. A., *Acta Biomater* 2014, 10 (7), 3048-3058.
64. Wen, M.; Liu, H.; Zhang, F.; Zhu, Y.; Liu, D.; Tian, Y.; Wu, Q., *Chem. Commun.* 2009, (30), 4530-4532. DOI 10.1039/B907379E.
65. Bard, A. J.; Faulkner, L. R.; Leddy, J.; Zoski, C. G., *Electrochemical methods: fundamentals and applications*. Wiley New York: 1980; Vol. 2.
66. Stevens, N.; Rooney, M.; Bond, A.; Feldberg, S., *The Journal of Physical Chemistry A* 2001, 105 (40), 9085-9093.
67. Torres-Platas, S. G.; Comeau, S.; Rachalski, A.; Dal Bo, G.; Cruceanu, C.; Turecki, G.; Giros, B.; Mechawar, N., *J Neuroinflammation* 2014, 11 (1), 12.
68. Rauti, R.; Lozano, N.; León, V.; Scaini, D.; Musto, M.; Rago, I.; Ulloa Severino, F. P.; Fabbro, A.; Casalis, L.; Vázquez, E., *Acs Nano* 2016, 10 (4), 4459-4471.
69. O'Keeffe, G. W.; Dockery, P.; Sullivan, A. M., *J. Neurocytol.* 2004, 33 (5), 479-488. DOI 10.1007/s11068-004-0511-y.
70. Kavanagh, E. T.; Loughlin, J. P.; Herbert, K. R.; Dockery, P.; Samall, A.; Doyle, K. M.; Gorman, A. M., *Biochem Biophys Res Commun* 2006, 351 (4), 890-895. DOI 10.1016/j.bbrc.2006.10.104.
71. Leber, M.; Shandhi, M.; Hogan, A.; Solzbacher, F.; Bhandari, R.; Negi, S., *Appl. Surf. Sci.* 2016, 365, 180-190.
72. Corey, J.; Wheeler, B.; Brewer, G., *IEEE Trans. Biomed. Eng.* 1996, 43 (9), 944-955.
73. Chung, C.-K.; Tseng, S.-F.; Hsiao, W.-T.; Chiang, D.; Lin, W.-C., *JOURNAL OF LASER MICRO NANOENGINEERING* 2016, 11 (3), 395-399.
74. Thakar, R.; Weber, A. E.; Morris, C. A.; Baker, L. A., *Analyst* 2013, 138 (20), 5973-82. DOI 10.1039/c3an01216f.

Topographically Functionalised Poly(3,4-Ethylenedioxythiophene):P-Toluene Sulphonate (PEDOT:PTS) Neuroelectrodes Via Microimprint Lithography

75. Bass, R. B.; Clark, W. W.; Zhang, J. Z.; Lichtenberger, A. W., *IEEE Transactions on Applied Superconductivity* 2001, 11 (1), 92-94. DOI 10.1109/77.919292.
76. Moulin, E.; Bittkau, K.; Ghosh, M.; Bugnon, G.; Stuckelberger, M.; Meier, M.; Haug, F.-J.; Hüpkens, J.; Ballif, C., *Sol. Energy Mater. Sol. Cells* 2016, 145, 185-192.
77. Herth, E.; Algré, E.; Rauch, J. Y.; Gerbedoen, J. C.; Defrance, N.; Delobelle, P., *physica status solidi (a)* 2016, 213 (1), 114-121.
78. Khaldi, A.; Maziz, A.; Plesse, C.; Soyer, C.; Vidal, F.; Cattan, E., *Sensors and Actuators B: Chemical* 2016, 229, 635-645.
79. Li, Z.; Chen, Y.; Zhu, X.; Zheng, M.; Dong, F.; Chen, P.; Xu, L.; Chu, W.; Duan, H., *Nanotechnology* 2016, 27 (36), 365302.
80. Ma, S.; Xia, Y.; Wang, Y.; Ren, K.; Luo, R.; Song, L.; Chen, X.; Chen, J.; Jin, Y., *Journal of Vacuum Science & Technology B, Nanotechnology and Microelectronics: Materials, Processing, Measurement, and Phenomena* 2016, 34 (5), 052002.
81. Wulz, T.; Canfield, B. K.; Davis, L. M.; Spanier, S.; Lukosi, E., *Diamond Relat. Mater.* 2017, 74, 108-113. DOI <http://dx.doi.org/10.1016/j.diamond.2017.02.018>.
82. Hof, L. A.; Guo, X.; Seo, M.; Wüthrich, R.; Greener, J., *Micromachines* 2017, 8 (1), 29.
83. Ereifej, E. S.; Cheng, M. M.-C.; Mao, G.; VandeVord, P. J., *J Neurosci Methods* 2013, 217 (1), 17-25.
84. Gomez, N.; Lee, J. Y.; Nickels, J. D.; Schmidt, C. E., *Adv Funct Mater* 2007, 17 (10), 1645-1653. DOI 10.1002/adfm.200600669.
85. Hoshino, T.; Miyazako, H.; Nakayama, A.; Wagatsuma, A.; Mabuchi, K., *Sensors and Actuators B: Chemical* 2016, 236, 659-667.
86. Zhang, L.; Ducharme, S.; Li, J., *Appl. Phys. Lett.* 2007, 91 (17), 172906.

Topographically Functionalised Poly(3,4-Ethylenedioxythiophene):P-Toluene Sulphonate (PEDOT:PTS) Neuroelectrodes Via Microimprint Lithography

87. Chen, Y.; Ohlberg, D. A.; Li, X.; Stewart, D. R.; Stanley Williams, R.; Jeppesen, J. O.; Nielsen, K. A.; Stoddart, J. F.; Olynick, D. L.; Anderson, E., *Appl. Phys. Lett.* 2003, 82 (10), 1610-1612.
88. Jingfeng, S.; Haidong, L.; Shumin, L.; Li, T.; Alexei, G.; Stephen, D., *Nanotechnology* 2016, 27 (1), 015302.
89. Yang, Y.; Lee, K.; Mielczarek, K.; Hu, W.; Zakhidov, A., *Nanotechnology* 2011, 22 (48), 485301.
90. Hourdakis, E.; Nassiopoulou, A. G., *IEEE Trans. Electron Devices* 2016, 63 (2), 746-750.
91. Kim, J.; Wubs, K.; Bae, B.-S.; Kim, W. S., *Sci Technol Adv Mat* 2012, 13 (3), 035004.
92. Ferrari, A.; Cecchini, M.; Dhawan, A.; Micera, S.; Tonazzini, I.; Stabile, R.; Pisignano, D.; Beltram, F., *Nano Lett.* 2011, 11 (2), 505-511.
93. Franco, D.; Milde, F.; Klingauf, M.; Orsenigo, F.; Dejana, E.; Poulidakos, D.; Cecchini, M.; Koumoutsakos, P.; Ferrari, A.; Kurtcuoglu, V., *Biomaterials* 2013, 34 (5), 1488-1497.
94. Franco, D.; Klingauf, M.; Bednarzik, M.; Cecchini, M.; Kurtcuoglu, V.; Gobrecht, J.; Poulidakos, D.; Ferrari, A., *Soft Matter* 2011, 7 (16), 7313-7324.
95. Schiff, H.; Saxer, S.; Park, S.; Padeste, C.; Pielers, U.; Gobrecht, J., *Nanotechnology* 2005, 16 (5), S171.
96. Tan, L.; Kong, Y.; Pang, S.; Yee, A., *Journal of Vacuum Science & Technology B: Microelectronics and Nanometer Structures Processing, Measurement, and Phenomena* 2004, 22 (5), 2486-2492.
97. Pisignano, D.; Persano, L.; Raganato, M. F.; Visconti, P.; Cingolani, R.; Barbarella, G.; Favaretto, L.; Gigli, G., *Adv Mater* 2004, 16 (6), 525-529.
98. Collazos-Castro, J. E.; Hernández-Labrado, G. R.; Polo, J. L.; García-Rama, C., *Biomaterials* 2013, 34 (14), 3603-3617.

Topographically Functionalised Poly(3,4-Ethylenedioxythiophene):P-Toluene Sulphonate (PEDOT:PTS) Neuroelectrodes Via Microimprint Lithography

99. Bhagwat, N.; Murray, R. E.; Shah, S. I.; Kiick, K. L.; Martin, D. C., *Acta Biomater* 2016, 41, 235-246.
100. Alves-Sampaio, A.; García-Rama, C.; Collazos-Castro, J. E., *Biomaterials* 2016, 89, 98-113. DOI <http://dx.doi.org/10.1016/j.biomaterials.2016.02.037>.
101. Kim, D. H.; Richardson-Burns, S. M.; Hendricks, J. L.; Sequera, C.; Martin, D. C., *Adv Funct Mater* 2007, 17 (1), 79-86.
102. Shuhua, X.; Ziyou, L.; Ling, Y.; Fei, W.; Sun, G., *Mediat. Inflamm.* 2012, 2012, 102954. DOI 10.1155/2012/102954.
103. Strunecka, A.; Blaylock, R. L.; Strunecky, O., *Journal of Applied Biomedicine* 2016, 14 (3), 171-176. DOI <http://dx.doi.org/10.1016/j.jab.2016.04.001>.
104. Donoso, M.; Méndez-Vilas, A.; Bruque, J.; González-Martin, M., *Int. Biodeterior. Biodegrad.* 2007, 59 (3), 245-251.
105. Krukiewicz, K.; Zak, J. K., *J. Mater. Sci.* 2014, 49 (16), 5738-5745. DOI 10.1007/s10853-014-8292-2.
106. Krukiewicz, K.; Jarosz, T.; Zak, J. K.; Lapkowski, M.; Ruszkowski, P.; Bobkiewicz-Kozłowska, T.; Bednarczyk-Cwynar, B., *Acta Biomater* 2015, 19, 158-65. DOI 10.1016/j.actbio.2015.03.006.
107. Rivnay, J., Leleux, P., Ferro, M., Sessolo, M., Williamson, A., Koutsouras, D.A., Khodagholy, D., Ramuz, M., Strakosas, X., Owens, R.M. and Benar, C., *Science advances*, 2015, 1(4), e1400251.
108. Ludwig, K. A.; Langhals, N. B.; Joseph, M. D.; Richardson-Burns, S. M.; Hendricks, J. L.; Kipke, D. R., *J. Neural Eng.* 2011, 8 (1), 014001.
109. Abidian, M. R.; Martin, D. C., *Biomaterials* 2008, 29 (9), 1273-1283.
110. Abidian, M. R.; Ludwig, K. A.; Marzullo, T. C.; Martin, D. C.; Kipke, D. R., *Adv Mater* 2009, 21 (37), 3764-3770.
111. Molina, A.; González, J.; Laborda, E.; Wang, Y.; Compton, R. G., *Phys Chem Chem Phys* 2011, 13 (32), 14694-14704.

Topographically Functionalised Poly(3,4-Ethylenedioxythiophene):P-Toluene Sulphonate (PEDOT:PTS) Neuroelectrodes Via Microimprint Lithography

112. Rehacek, V.; Hotovy, I.; Vojs, M.; Mika, F., *Microsystem Technologies* 2008, 14 (4-5), 491-498.
113. Lin, Z.; Ino, K.; Shiku, H.; Matsue, T., *Chem. Commun.* 2010, 46 (4), 559-561.
114. Orozco, J.; Fernández-Sánchez, C.; Jiménez-Jorquera, C., *Sensors* 2010, 10 (1), 475-490.
115. Olowu, R. A.; Arotiba, O.; Mailu, S. N.; Waryo, T. T.; Baker, P.; Iwuoha, E., *Sensors* 2010, 10 (11), 9872-9890.
116. Ma, X.; Yue, G.; Wu, J.; Lan, Z.; Lin, J.-Y., *Rsc Adv* 2015, 5 (54), 43639-43647.
117. Wei, W.; Song, Y.; Wang, L.; Zhang, S.; Luo, J.; Xu, S.; Cai, X., *Microsystems & Nanoengineering* 2015, 1.
118. Arcot Desai, S.; Gutekunst, C.-A.; Potter, S. M.; Gross, R. E., *Front. Neuroengineering* 2014, 7, 16.
119. Zhang, H.; Shih, J.; Zhu, J.; Kotov, N. A., *Nano Lett.* 2012, 12 (7), 3391-3398.
120. Mandal, H. S.; Knaack, G. L.; Charkhkar, H.; McHail, D. G.; Kastee, J. S.; Dumas, T. C.; Peixoto, N.; Rubinson, J. F.; Pancrazio, J. J., *Acta Biomater* 2014, 10 (6), 2446-2454.
121. Nikkhah, M.; Edalat, F.; Manoucheri, S.; Khademhosseini, A., *Biomaterials* 2012, 33 (21), 5230-46. DOI 10.1016/j.biomaterials.2012.03.079.
122. Cesca, F.; Limongi, T.; Accardo, A.; Rocchi, A.; Orlando, M.; Shalabaeva, V.; Di Fabrizio, E.; Benfenati, F., *Rsc Adv* 2014, 4 (86), 45696-45702. DOI 10.1039/C4RA08361J.
123. Qi, L.; Li, N.; Huang, R.; Song, Q.; Wang, L.; Zhang, Q.; Su, R.; Kong, T.; Tang, M.; Cheng, G., *PLoS One* 2013, 8 (3), e59022.

Topographically Functionalised Poly(3,4-Ethylenedioxythiophene):P-Toluene Sulphonate (PEDOT:PTS) Neuroelectrodes Via Microimprint Lithography

124. Fan, C.; Wang, H.; Chen, D.; Cheng, X.; Xiong, K.; Luo, X.; Cao, Q., *Neural regeneration research* 2014, 9 (2), 119.
125. Sun, W.; Incitti, T.; Migliaresi, C.; Quattrone, A.; Casarosa, S.; Motta, A., *J Tissue Eng Regen Med* 2015.
126. Runge, M. B.; Dadsetan, M.; Baltrusaitis, J.; Ruesink, T.; Lu, L.; Windebank, A. J.; Yaszemski, M. J., *Biomacromolecules* 2010, 11 (11), 2845-2853. DOI 10.1021/bm100526a.
127. Kang, G.; Borgens, R. B.; Cho, Y., *Langmuir* 2011, 27 (10), 6179-6184. DOI 10.1021/la104194m.
128. Shi, X.; Xiao, Y.; Xiao, H.; Harris, G.; Wang, T.; Che, J., *Colloids and Surfaces B: Biointerfaces* 2016, 145, 768-776. DOI <http://dx.doi.org/10.1016/j.colsurfb.2016.05.086>.
129. Gottipati, M. K.; Kalinina, I.; Bekyarova, E.; Haddon, R. C.; Parpura, V., *Nano Lett.* 2012, 12 (9), 4742-4747.
130. Ben Haim, L.; Rowitch, D. H., *Nat Rev Neurosci* 2017, 18 (1), 31-41. DOI 10.1038/nrn.2016.159.
131. Sofroniew, M. V.; Vinters, H. V., *Acta Neuropathol.* 2010, 119 (1), 7-35. DOI 10.1007/s00401-009-0619-8.
132. Oberheim, N. A.; Goldman, S. A.; Nedergaard, M., *Astrocytes: Methods and Protocols* 2012, 23-45.
133. Beggs, H. E.; Schahin-Reed, D.; Zang, K.; Goebbels, S.; Nave, K. A.; Gorski, J.; Jones, K. R.; Sretavan, D.; Reichardt, L. F., *Neuron* 2003, 40 (3), 501-14.
134. Ramakers, G. J.; Moolenaar, W. H., *Exp Cell Res* 1998, 245 (2), 252-62. DOI 10.1006/excr.1998.4224.
135. Koyama, Y.; Yoshioka, Y.; Matsuda, T.; Baba, A., *Glia* 2003, 43 (2), 185-9. DOI 10.1002/glia.10240.

Topographically Functionalised Poly(3,4-Ethylenedioxythiophene):P-Toluene Sulphonate (PEDOT:PTS) Neuroelectrodes Via Microimprint Lithography

136. Padmanabhan, J.; Clayton, D.; Shelanski, M. L., *J. Neurobiol.* 1999, 39 (3), 407-22.
137. Paco, S.; Hummel, M.; Plá, V.; Sumoy, L.; Aguado, F., *BMC Genomics* 2016, 17 (1), 304.
138. Montgomery, D. L., *Vet. Pathol.* 1994, 31 (2), 145-67. DOI 10.1177/030098589403100201.
139. Cregg, J. M.; DePaul, M. A.; Filous, A. R.; Lang, B. T.; Tran, A.; Silver, J., *Exp. Neurol.* 2014, 0, 197-207. DOI 10.1016/j.expneurol.2013.12.024.
140. Gilmour, A. D.; Goding, J.; Poole-Warren, L. A.; Thomson, C. E.; Green, R. A. In *In vitro biological assessment of electrode materials for neural interfaces*, 2015 7th International IEEE/EMBS Conference on Neural Engineering (NER), 22-24 April 2015; 2015; pp 450-453.
141. Baek, S., Green, R. A., & Poole-Warren, L. A., *Journal of Biomedical Materials Research Part A*, 2014, 102(8), 2743-2754.
142. Kripparamanan, R.; Aswath, P.; Zhou, A.; Tang, L.; Nguyen, K. T., *J Nanosci Nanotechnol* 2006, 6 (7), 1905-1919.
143. Sonam, S.; Sathe, S. R.; Yim, E. K.; Sheetz, M. P.; Lim, C. T., *Sci Rep-Uk* 2016, 6, 20415.
144. John, G. R.; Lee, S. C.; Brosnan, C. F., *The Neuroscientist* 2003, 9 (1), 10-22. DOI 10.1177/1073858402239587.
145. Farina, C.; Aloisi, F.; Meinl, E., *Trends Immunol.* 2007, 28 (3), 138-45. DOI 10.1016/j.it.2007.01.005.
146. Streit, W. J.; Hurley, S. D.; McGraw, T. S.; Semple-Rowland, S. L., *J Neurosci Res* 2000, 61 (1), 10-20. DOI 10.1002/1097-4547(20000701)61:1<10::aid-jnr2>3.0.co;2-e.
147. Brück, D.; Wenning, G. K.; Stefanova, N.; Fellner, L., *Neurobiol. Dis.* 2016, 85, 262-274.

Topographically Functionalised Poly(3,4-Ethylenedioxythiophene):P-Toluene Sulphonate (PEDOT:PTS) Neuroelectrodes Via Microimprint Lithography

148. Aloisi, F.; Borsellino, G.; Caré, A.; Testa, U.; Gallo, P.; Russo, G.; Peschle, C.; Levi, G., *Int. J. Dev. Neurosci.* 1995, 13 (3), 265-274.
149. Lins, C.; Borojevic, R., *Growth Factors* 2001, 19 (3), 145-152.
150. Torres-Platas, S. G.; Comeau, S.; Rachalski, A.; Dal Bo, G.; Cruceanu, C.; Turecki, G.; Giros, B.; Mechawar, N., *J Neuroinflammation* 2014, 11 (1), 12.
151. Schroder, K.; Hertzog, P. J.; Ravasi, T.; Hume, D. A., *J. Leukoc. Biol.* 2004, 75 (2), 163-189.
152. Miljkovic, D.; Momcilovic, M.; Stojanovic, I.; Stosic-Grujicic, S.; Ramic, Z.; Mostarica-Stojkovic, M., *J Neurosci Res* 2007, 85 (16), 3598-606. DOI 10.1002/jnr.21453.
153. Cavalcanti, Y. V. N.; Brelaz, M. C. A.; Neves, J. K. d. A. L.; Ferraz, J. C.; Pereira, V. R. A., *Pulmonary medicine* 2012, 2012.
154. Rubio, N.; Sanz-Rodriguez, F., *Virology* 2007, 358 (1), 98-108.
155. Roy, M.; Richard, J.-F.; Dumas, A.; Vallières, L., *J Neuroinflammation* 2012, 9 (1), 18.
156. Erta, M.; Quintana, A.; Hidalgo, J., *Int J Biol Sci* 2012, 8 (9), 1254-1266.
157. Hariri, R. J.; Chang, V. A.; Barie, P. S.; Wang, R. S.; Sharif, S. F.; Ghajar, J. B., *Brain Res* 1994, 636 (1), 139-142.
158. Ma, X.; Reynolds, S. L.; Baker, B. J.; Li, X.; Benveniste, E. N.; Qin, H., *The Journal of Immunology* 2010, 184 (9), 4898-4906.
159. Chiang, C.-S.; Stalder, A.; Samimi, A.; Campbell, I., *Dev. Neurosci.* 1994, 16 (3-4), 212-221.
160. Fattori, E.; Lazzaro, D.; Musiani, P.; Modesti, A.; Alonzi, T.; Ciliberto, G., *Eur. J. Neurosci.* 1995, 7 (12), 2441-2449.
161. Sawada, M.; Suzumura, A.; Itoh, Y.; Marunouchi, T., *Neurosci Lett* 1993, 155 (2), 175-178.

Topographically Functionalised Poly(3,4-Ethylenedioxythiophene):P-Toluene Sulphonate (PEDOT:PTS) Neuroelectrodes Via Microimprint Lithography

162. Awatsuji, H.; Furukawa, Y.; Hirota, M.; Murakami, Y.; Nii, S.; Furukawa, S.; Hayashi, K., *J Neurosci Res* 1993, 34 (5), 539-545.
163. Brodie, C., *FEBS Lett* 1996, 394 (2), 117-120.
164. Scarisbrick, I. A.; Radulovic, M.; Burda, J. E.; Larson, N.; Blaber, S. I.; Giannini, C.; Blaber, M.; Vandell, A. G., 2012.
165. Padmanabhan, J.; Kyriakides, T. R., *Wiley Interdisciplinary Reviews: Nanomedicine and Nanobiotechnology* 2015, 7 (3), 355-370.

CHAPTER 4

ANALYSIS OF THE NEUROTROPIC AND ANTI-INFLAMMATORY EFFECTS OF NEUROELECTRODE FUNCTIONALISATION WITH A HEPARAN SULPHATE MIMETIC

4.1 Preamble

In parallel with the topographical functionalisation, biological functionalisation was also carried out. In this case, the role of glycosaminoglycans (GAGs) mimetics in neural interfaces was studied, in conjunction with the expertise of Dulce Papy-Garcia and her team. This phase involved a lot of back and forward within experimental steps. But it was this, in fact, which allowed the formulation of new ideas and raised further mechanistic questions around the observations.

Further in the search for biomimicry of the properties analogous to neural tissues, and with an ultimate goal of mitigating electrode deterioration via reactive host cell response and glial scar formation, the bio-functionalisation of PEDOT:PTS neural coating is here presented using a heparan mimetic termed F6. A sulphated mimetic polyanion, with a potential role in neuromodulation in neurodegenerative diseases, and used here for the first time as neural coating.

Important contribution was received from:

- *Ouidja., M, Huynh., MB, Papy-Garcia.,D*: F6 synthesis and binding experiments.
- *Kilcoyne., M, Flannery.,A*: lectin experiments.
- *R Pallipurath., A, McNamara.,K., Syed., T*: performed Raman and XPS chemical analysis.

Hypothesis: The use of a sulphated heparan mimetic polyanion termed F6 can be employed as a potential biological dopant for neural interfaces leading to enhanced electrode integration, and a minimised glial response through an indirect neurotropic effect of F6 mediated by growth factor binding.

4.2 Introduction

Chronic biocompatibility of an implantable neural device can be enhanced through biomimicry strategies to recapitulate the physicochemical and biochemical properties of neural tissues, with an ultimate goal of mitigating electrode deterioration via a reactive host response [1-5]. The single most detrimental factor in chronic electrode stability is mediated through an adverse peri-electrode tissue response characterised by glial scar formation and electrode encapsulation, causing a reduction in signal strength and local death of adjacent neurons [5-9]. In order to develop meaningful neuromodulation systems and stable brain-machine interfaces there is a clinical need to reduce tissue encapsulation and improve long-term neuroelectrode function through enhanced integration *in situ* [10].

Conducting polymers acting as interfacial neuroelectrode coatings, provide excellent opportunities for functional modification due to their versatile chemistry and simple synthesis approaches [11-13] allowing the preparation of electroactive biointerfaces with tuned electrochemical [14, 15], topographical [16-18] and biochemical [19-21] properties.

Of particular interest, poly(3,4-ethylenedioxythiophene) (PEDOT) derived biomaterials have received considerable interest in the bioengineering of neural implants and devices due to their relatively stability properties [10, 22-24], as well as their superior biocompatibility properties, which can be tailored through the immobilisation of biological elements [2, 25-28] and anti-inflammatory drugs into the polymer matrix [20, 29-31].

In particular, the therapeutic potential of glycosaminoglycans (GAGs) - naturally occurring heteropolysaccharide molecules associated with core protein or lipid molecules, as bio-functional approaches to neurospecific biomaterials has been recently explored [28, 32-36]. This focus on GAG functionalisation has stemmed from the elucidation that GAG species play key roles in the extracellular matrix (ECM) as a major reservoir of growth factors [37-39] and as biological regulators of cellular growth, differentiation and regenerative processes [40-43].

Of particular interest in neural regeneration is the sulphated proteoglycan, heparan sulphate (HS) that, through binding growth factors, plays a critical role in regulating inflammatory responses [43-49] and has shown marked efficacy as a therapeutic functionalisation approach within a broad spectrum of tissue engineering and implantable device applications [40, 50-60].

Accordingly, new avenues of research, focused on the development of synthetic heparan mimetic (HM) chemistries have been initiated to develop stable bioactive glycans for neural engineering applications [35, 61-64]. Of specific interest for the development of neuroelectrode glycofunctionalisation approaches is the formulation of HMs with inherent glycanase resistance, which can circumvent the prolonged inflammation profile and perturbed remodeling of the ECM associated with degraded HS [49, 52, 65-67].

In this chapter, a PEDOT:PTS conducting polymer was doped with a HM termed F6 [44, 68], a polyanion molecule, structurally modified from polymeric dextran and shown to mediate internalisation and propagation of specific proteopathic proteins [60]. The effects of PEDOT:PTS:F6 functionalisation on the physical, electrochemical and biological properties of platinum (Pt) microelectrodes were subsequently evaluated *in vitro*.

This work acts as a first step towards the use of HM biological dopants, to enhance neuroelectrode functionality, to promote neural outgrowth and to maintain minimal glial scar formation *in vitro* at the neural-interface. Further, this study opens new possibilities for the evaluation of glycan mimetics in neuroelectrode functionalisation.

4.3 Materials and Methods

4.3.1 Physical Characterisation

4.3.1.1 Surface Morphology

Scanning electron microscopy (SEM) was carried out using a Hitachi S-4700 Cold Field Emission Gun Scanning Electron Microscope (CFE-SEM). The SEM images were taken using an accelerating voltage of 15 kV and spot current of 10 μ A.

Analysis of the Neurotropic and Anti-inflammatory Effects of Neuroelectrode Functionalisation with a Heparan Sulphate Mimetic

For roughness analysis, Atomic Force Microscopy (AFM) was performed as detailed in [5]. All measurements were taken on a Vico Dimension 3100 AFM using TESPA Tips (NanoWorld) (Si <8 nm tip radius, 42 N/m spring constant, 320 kHz nominal resonance frequency), in tapping mode over an area of 10 μm^2 with a 0.5 - 1 Hz scan rate.

4.3.1.2 Thickness Measurements

The thickness of the polymeric PEDOT:PTS and PEDOT:PTS:F6 coatings was measured using a Zygo Newview 100 surface profilometer controlled by MicroPlus software as detailed in [5]. Briefly, a pattern of bright and dark lines - fringes was created as incoming light was split from the limited region between the sample coating and the metal part of the electrode. This pattern difference was translated to calculate the height information.

4.3.2 Chemical Characterisation

4.3.2.1 Contact Angle Measurement

Contact angles analysis with water droplets was performed using a custom made goniometer connected to an Infinity Camera 2 and operated with Infinity Analyse software. Contact angles were measured at three different points per sample in at least three samples per group. The images taken were calibrated using the measured width of the needle, and through the Infinity Analyse software a curve which was fitted to the arc of the drop to find the radius (R), as well as the length (L) of the base of the drop (from corner to corner).

The equation used to calculate the contact angle is shown below (*Equation 4.1*), where a (-) negative sign was used for hydrophilic surfaces and (+) sign was used for hydrophobic surfaces.

$$\theta = 90 \pm \frac{\left(180 - \left(2 * \text{Arcsin} \left(\frac{1}{\frac{L}{R}} \right) \right) \right)}{2} \quad \text{Equation 4.1}$$

4.3.2.2 Attenuated Total Reflectance Infra-Red Spectroscopy (ATR-IR)

Fourier transform mid infrared spectra in the range of 650-3600 cm^{-1} , with a resolution of 4 cm^{-1} and four integrated scans, were collected on a diamond/ZnSe window using a Perkin Elmer Spectrum 400 fitted with an ATR reflectance attachment.

4.3.2.3 Raman Spectroscopy

Raman spectra were collected using the Renishaw Invia micro-Raman spectrometer (static acquisition centered at 800 cm^{-1} , 1 cm^{-1} resolution, 10s exposure time, 1% laser power, 785 nm laser, 4-5 μm spatial resolution, 12 μm penetration depth). Raman mapping was carried out using the same setup, where 81 spectra were collected at 5 μm intervals in a 60 \times 60 μm grid. All spectra were normalised to account for variation in sample height on the intensity. Component DLS analysis was carried out using the Renishaw Wire 4.2 software to identify spectral contributions from different components.

4.3.2.4 X Ray Photoelectron Spectroscopy

X-ray photoelectron spectroscopy (XPS) spectra were acquired on a Kratos AXIS 165 spectrometer XPS system with X-Ray Gun mono Al $\text{K}\alpha$ 1486.58 eV; 150 W (10 mA, 15kV), for all scans with the following parameters: sample temperature in a range of 20-30 $^{\circ}\text{C}$ with a pass energy of 160 eV for survey spectra and 20 eV for narrow regions and steps of 1 eV for survey and 0.05 eV for regions with dwell times of 50 ms and 100 ms for regions and sweeps for survey of \sim 35, and for narrow regions of 6-40. The C1s line at 284.8 eV was used as charge reference. Spectra were collected in the normal way to the surface direction with an analysis area of 60 microns. XPS detection limit is estimated to be \sim 0.1 at%. For the data processing, the construction and peak fitting of synthetic peaks in narrow region spectra was done using a Shirley type background and the synthetic peaks were of a mixed Gaussian-

Lorentzian type. Relative sensitivity factors used are from CasaXPS library containing Scofield cross-sections.

4.3.3 Electrochemical Characterisation

4.3.3.1 Preparation of PEDOT:PTS and PEDOT:PTS:F6 samples

The electrodeposition of poly(3,4-ethylenedioxythiophene):p-toluene sulfonate (PEDOT:PTS) was conducted under ambient conditions according to methods described previously [23]. Briefly, a solution of 0.05M EDOT (Sigma Aldrich, Ireland) and 0.1 M PTS (Sigma Aldrich, Ireland, 70,000 g mol⁻¹ MW) was prepared in a 50/50 vol.% mixture of acetonitrile and water. The same prepared electrolyte with increasing concentrations of heparan sulphate mimetic F6, i.e. 1 µg ml⁻¹, 10 µg ml⁻¹, 50 µg ml⁻¹, 100 µg ml⁻¹ and 1000 µg ml⁻¹ was used for the electrodeposition of the functionalised PEDOT:PTS:F6 coatings. F6 has a MW of 9900 g mol⁻¹ (Da). The electrolyte solution was placed in an in-house fabricated electrochemical cell, connected to a Princeton Applied Research Potentiostat/Galvanostat model 2273 controlled with Power Suite software. Parylene-C insulated Platinum/Iridium concentric microelectrodes (MicroProbes for Life Science) and a platinum foil (Goodfellow) were used as the working electrode (WE) and counter-electrode (CE) respectively. A saturated 3 M KCl Ag/AgCl reference electrode (RE) (Bioanalytical Systems) was employed. Galvanostatic electrodeposition was performed and the efficiency of coating, i.e. the amount of polymer deposited on the electrodes, was controlled by the total charge passing during the electrodeposition. When the deposition was finalised, the pristine PEDOT:PTS coated electrodes were soaked in deionized water (DI) for 24 hours to remove excess of electrolyte and subsequently dried for use. The PEDOT:PTS:F6 coated electrodes were soaked in Hank's balanced salt solution (HBSS) for two hours. For cell studies, pristine PEDOT:PTS and PEDOT:PTS:F6 were electrodeposited on electrodes with areas of 1.6 cm² to facilitate *in vitro* manipulations.

To determine the total amount of F6 incorporated into PEDOT:PTS polymer, the electrochemical deposition was carried out by means of CH Instruments 400c

Electrochemical Workstation equipped with time-resolved electrochemical quartz crystal microbalance in a standard three-electrode setup, employing CHI125 gold crystal as a working electrode, Ag/AgCl reference electrode and a platinum foil counter electrode.

The change of mass of the electrode resulting from the electrodeposition of pristine PEDOT:PTS or PEDOT:PTS:F6 coatings, respectively, was calculated based on frequency change (Δf) as given by the Sauerbrey equation (**Equation 4.2**) [69]:

$$\Delta f = \frac{-2f_0^2}{A(\mu\rho)^{1/2}} \Delta m \quad \text{Equation 4.2}$$

where f_0 is the resonant frequency of the fundamental mode of the crystal, A is the area of the gold disk coated onto the crystal (0.205 cm^2), ρ is the density of the crystal (2.648 g cm^{-3}) and μ is the shear modulus of quartz ($2.947 \cdot 10^{11} \text{ g cm}^{-1} \text{ s}^{-2}$). For 8 MHz crystal, 1 Hz change in frequency corresponds to a mass change of 1.4 ng.

4.3.3.2 Electrochemical Measurements

Cyclic voltammetry (CV) was performed as previously described in [5] using a Princeton Applied Research Potentiostat/Galvanostat model 2273 running with Power Suite software. Measurements were recorded in a custom-made electrochemical cell containing the Parylene-C insulated Platinum/Iridium concentric microelectrode as working electrode, an Ag/AgCl reference electrode (3 M KCl) (Bioanalytical Systems) and a platinum foil counter electrode (Goodfellow) in 1X phosphate-buffered saline (PBS). Cyclic voltammograms were run in the potential range from -0.8 V to 1 V at a scan rate of 0.1 V s^{-1} . The charge storage capacity (CSC) was calculated by integrating the area enclosed by the voltammogram.

Electrical impedance spectroscopy (EIS) was performed using a Princeton Applied Research Potentiostat/Galvanostat model 2273 running with Power Suite software with a three-electrode set-up. The measurements were carried out at a frequency range of 0.1 Hz to 100 kHz with an AC sine wave of 40 mV amplitude applied with 0 V DC offset. The results were presented on Bode and Nyquist plots and compared to those of bare Platinum/Iridium microelectrodes. The data fitting analysis was

Analysis of the Neurotropic and Anti-inflammatory Effects of Neuroelectrode Functionalisation with a Heparan Sulphate Mimetic

performed using EIS Spectrum Analyser 1.0 software with the application of the Powell algorithm.

The electrochemical stability of pristine PEDOT:PTS and PEDOT:PTS:F6 microelectrodes was done by performing cyclic voltammetry before and after 1000 stimulation cycles, corresponding to the cumulative stimulus used for the active release studies, biphasic potential pulse consisting of a 5-second application of a reduction potential (-0.5 V) followed by a 5-second application of an oxidative potential (+0.5 V). The percentage of loss in charge storage capacity was calculated by comparing the CSC of the 1st and 1000th cycles. All measurements were performed in triplicate; the results were expressed as a mean \pm standard deviation.

4.3.4 Biological Characterisation

4.3.4.1 Bioactivity Elution Profiles

To enable quantitative monitoring of the amount of eluted molecule, F6 was tagged with a fluorescent marker, Cy5. The concentration of released F6 was then measured by means of a plate reader working in a fluorometric mode with the excitation wavelength at 675 nm and the emission wavelength at 690 nm. The calibration curve (**Figure 4.1**) was plotted for the fluorescence versus F6 concentration (where y is the fluorescence and x is the concentration in $\mu\text{g ml}^{-1}$). A linear relationship was observed between $0.5 \mu\text{g ml}^{-1}$ and $500 \mu\text{g ml}^{-1}$ satisfying the equation $y = 1.35 x + 2.56$ ($R^2 = 0.9994$).

Analysis of the Neurotropic and Anti-inflammatory Effects of Neuroelectrode Functionalisation with a Heparan Sulphate Mimetic

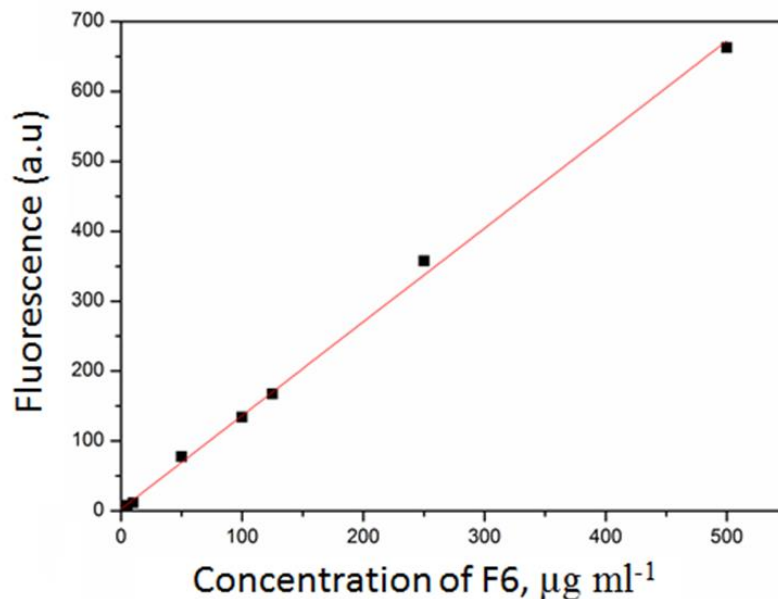


Figure 4.1 Calibration curve showing the linear relationship of the fluorescence heparan sulphate mimetic-F6 -Cy5 tagged versus its concentration. A linear relationship is observed between $0.5 \mu\text{g ml}^{-1}$ and $500 \mu\text{g ml}^{-1}$ satisfying the equation $y = 1.35x + 2.56$ ($R^2 = 0.9994$).

- Passive Release Model

F6 elution in a spontaneous, passive mode was studied for the period of 21 days with the concentration measurements performed on a daily basis. To simulate *in vivo* conditions, PEDOT:PTS:F6 coated electrodes were immersed in phosphate-buffered saline solution (1X PBS), placed on a shaker and kept at a temperature of 37°C . Two $100 \mu\text{l}$ samples of the supernatant were taken from each sample and analysed by a plate reader working in fluorometric mode. Each time, $200 \mu\text{l}$ of a fresh PBS solution was added to the sample to keep the total amount of supernatant at a constant level (2 ml). The continual addition of a fresh solution enabled the sink conditions to be maintained, i.e. prevented the saturation of the solution with F6.

- Active Release Model

The active release of F6 was triggered electrically through a biphasic potential pulse, consisting of a 5-second application of a reduction potential (-0.5 V) followed by a 5-second application of an oxidative potential (+0.5 V). The active release was studied for a period of 21 days with the concentration measurements performed on a daily basis. The electrical trigger consisting of 50 stimulation cycles was applied every daily. Two 100 μ l samples of the supernatant were taken from each sample and analysed by a plate reader working in a fluorometric mode. Each time, 200 μ l of a fresh PBS solution was added to the sample to keep the total amount of supernatant constant (1 ml).

4.3.5 Cell Culture

Primary cultures of ventral mesencephalic neurons (VM) were obtained from the mesencephalon of embryonic Sprague–Dawley rats according to methods previously described by Vallejo-Giraldo et al. [5]. Briefly, the ventral mesencephalon were dissected from embryonic fourteen-day rat brains and then mechanically dissociated with a pipette, until the tissue was dispersed. Cells were grown in a humidified atmosphere of 5% CO₂ at 37°C and culture in media (Dulbecco's modified Eagle's medium/F12, 33 mM D-glucose, 1 % L-glutamine, 1% PS, 1 % FCS, supplemented with 2 % B27). Controls and experimental groups were cultured for three, seven and ten days in six well culture plates and sterilised in 70% ethanol for two hours, and subsequently washed repeatedly with HBSS and/or molecular biology level water (Sigma). Prior to plating, samples and controls were coated with poly-lysine (PLL) (Sigma). They were then rinsed three times with molecular biology level water and left to dry overnight. 50,000 cells cm⁻² were plated on each electrode, and then 3 ml of the culture medium was added to each well and half of the volume was replaced with fresh media every two days for a period of ten days.

For the inflammatory control, primary VM cells were cultured on sterile Thermanox® Plastic Coverslips with 13 mm diameter (NUNC™ brand products). 50,000 cells cm⁻² were plated on each coverslip, and grown in a humidified atmosphere of 5% CO₂ at 37°C and culture in media (Dulbecco's modified Eagle's

Analysis of the Neurotropic and Anti-inflammatory Effects of Neuroelectrode Functionalisation with a Heparan Sulphate Mimetic

medium/F12, 33 mM D-glucose, 1 % L-glutamine, 1% PS, 1 % FCS, supplemented with 2 % B27). 3 ml of the culture medium was added to each well and, after two days in culture, the cells were stimulated with IL-1 β (10 ng mL⁻¹) prepared in plating media to a final volume of 3 ml and half of the volume was changed every two days for a period of ten days.

4.3.6 Immunofluorescent Labelling

Indirect double-immunofluorescent labelling was performed to visualise neurons and astrocyte cell populations as described previously [70]. Briefly, VM cells on experimental and control substrates were fixed with 4% paraformaldehyde and 1% of sucrose for twenty minutes at room temperature at the time point. Once fixed, the samples were washed with PBS and permeabilised with buffered 0.5% Triton X-100 within a buffered isotonic solution (10.3 g sucrose, 0.292 g NaCl, 0.06 g MgCl₂, 0.476 g HEPES buffer, 0.5 ml Triton X 100, in 100 ml water, pH 7.2) at 4°C for five minutes. Non-specific binding sites were blocked with 1% bovine serum albumin (BSA) in PBS at 37°C for 30 minutes and subsequently incubated for two hours with a 1:200 concentration anti-glial fibrillary acidic protein (GFAP) antibody produced in mouse (Sigma, 1:200) and 1:500 concentration anti- β -Tubulin III antibody produced in rabbit (Sigma, 1:500). Samples were washed three times with 0.05% Tween 20/PBS and then incubated for one hour in the secondary antibody Alexa Fluor® 488 goat anti-Mouse IgG / IgA / IgM (H+L) (Molecular probes 1:500) combined with the secondary antibody Alexa Fluor® 594 goat anti-Rabbit IgG (H+L) (Molecular probes, 1:500). Samples were washed with PBS (five minutes \times 3) and mounted on microscope cover slides and counterstained with slowfade^R gold antifade reagent with DAPI for nuclear staining.

4.3.7 Microscopy and Image Analysis

After immunostaining, samples were viewed with an Olympus Fluoview 1000 Confocal Microscope at a fixed scan size of 1024 by 1024 at a ratio 1:1. Cell analysis was performed as described in [70]. At least twenty images at 60 \times magnification were taken at random from each experimental group and controls. Cell density was analysed by counting the total number of labelled nuclei corresponding to neurons

Analysis of the Neurotropic and Anti-inflammatory Effects of Neuroelectrode Functionalisation with a Heparan Sulphate Mimetic

and astrocytes in an area of $212 \mu\text{m} * 212 \mu\text{m}$. Neurite length was quantified by analysing nine random fields of view of three different technical replicas from three different samples using established stereological methods [71]. The formula used was: neurite length = $n * T * \pi / 2$, where n is the number of times neurites intersect grid lines and T = distance between gridlines (taking magnification into account) as described in [72].

4.3.8 Cytokine Inflammatory Panel

Cytokine multiplex assay was performed on primary VM cell mixed population supernatants collected at three, seven and ten days in culture grown on all experimental groups, controls and inflamed control. ELISA pro-inflammatory panel 2 (Rat) (Meso Scale Discovery, UK) cytokine (IL-6, IL-1 β , TNF- α , IFN- γ , KC/GRO, IL-4, IL-5, IL-13, IL-10) assays were performed according to the manufacturer's instructions, using six replicas and without adjustments to the recommended standard curve, and sample dilutions. Briefly, 150 μL of blocker H was added on each well of ELISA pro-inflammatory plate and incubated at room temperature with fast shaking for one hour. In parallel, in a separately provided plate, an initial 1:2 dilution of samples and culture media was prepared and put under shaking for fifteen minutes. The ELISA pro-inflammatory plate was then washed three times with at least 150 μL of wash buffer (PBS 1X with 0.05% Tween20) and subsequently, the diluted sample mixed from the additional plate provided was transferred to the ELISA pro-inflammatory plate with the addition of 25 μL of diluent 40. Incubation at room temperature with shaking for two hours was then carried out. The ELISA pro-inflammatory plate was further washed three times with PBS-Tween20, and 25 μL of 1X detection antibody solution was added in each well and incubated at room temperature with shaking for two hours. The ELISA pro-inflammatory plate was washed three times and further added 150 μL of 2X read buffer T in each well for plate reading using the QuickPlex SQ 120 multiplexing instrument from MSD.

4.3.9 Glycosaminoglycans Competition Assay Towards FGF-2 and VEGF Binding

F6 molecule [60], Heparin, HS and polymeric dextran (Sigma-Aldrich) binding to basic fibroblast growth factor (FGF-2, R&D systems) and Vascular Endothelial

Analysis of the Neurotropic and Anti-inflammatory Effects of Neuroelectrode Functionalisation with a Heparan Sulphate Mimetic

Growth Factor 165 (VEGF165, Promokine) were evaluated by an ELISA based competition assay as previous described [73]. 96 well ELISA plates were coated with a 2 $\mu\text{g mL}^{-1}$ heparin-bovine serum albumin (BSA) conjugate solution prepared as previously described in [74]. Briefly, after washing with 0.05% Tween 20/PBS, wells were saturated with 3% BSA in PBS. Then, FGF-2 (10 ng mL^{-1}) and F6 molecule, heparin, HS or dextran, (in a concentration dependent manner; 0.001, 0.01, 0.1 1, 10 and 100 $\mu\text{g mL}^{-1}$) were simultaneously added to wells. After one hour incubation at room temperature, wells were washed and the growth factors remaining bound to the heparin conjugates were detected by incubation with the corresponding antibody (R&D systems) followed by a peroxidase-labelled secondary antibody (Jackson ImmunoResearch). Peroxidase activity measurement was performed with the 3,3',5,5'-tetramethylbenzidine (TMB) substrate of the Peroxidase Activity Detection Kit (PierceTM) following fabricant indications. FGF-2 and VEGF bindings to the heparin-BSA conjugate were considered as reference binding (100%).

4.3.10 Protein Antibody Microarray and Lectin Array

4.3.10.1 Protein Extraction of Primary VM Cell Mixed Population and Labelling

For protein extraction and collection, samples were carefully placed on ice and the cells were washed twice with ice-cold PBS, pH 7.4. After the complete aspiration of ice-cold PBS, 100 μl of cold RIPA lysis buffer (Sigma) supplemented with 1% of protease inhibitors (Life Science-Roche) and 1% of phosphatase inhibitors cocktails I & III (Sigma) was added. Thereafter, the adherent cells were scraped off from each of the experimental groups and controls using Corning® cell scrapers and then the cell suspension was gently transferred into microcentrifuge tubes and placed on ice. Microcentrifuge tubes were centrifuged for fifteen minutes at 14,000 rpm at 4 °C, and afterwards gently removed from the centrifuge and placed on ice. Without disturbing the pellet, the supernatant was carefully aspirated and placed in a fresh clean tube, kept on ice, and stored at -80 °C to be quantified by bicinchoninic acid (BCA) protein assay kit [75] according to manufacturer's instructions using a bovine serum albumin standard curve (ThermoFisher Scientific). The pellet was discarded.

Analysis of the Neurotropic and Anti-inflammatory Effects of Neuroelectrode Functionalisation with a Heparan Sulphate Mimetic

Protein supernatants were then labelled with Alexa Fluor® 555 carboxylic acid succinimidyl ester (AF555) (ThermoFisher Scientific) essentially as previously described [76]. All processes were carried out in the dark. In brief, approximately 0.5 mg of each sample by protein concentration was incubated with approximately 50 µg of AF555 in 250 mM sodium bicarbonate, pH 8.2 for two hours at room temperature in the dark. Excess label was removed and buffer was exchanged with PBS, pH 7.4 by centrifugation through 3 kDa molecular weight cut off centrifugal filters (Amicon Ultra®, Millipore, Dublin, Ireland). Absorbance at 555 and 280 nm was measured for labelled samples and calculations were performed according to manufacturer's instructions using an arbitrary extinction coefficient of 100,000 and molecular mass of 100,000 to enable quantification of relative protein concentration and label substitution efficiency. Labelled samples were stored at 4 °C protected from light.

4.3.10.2 Construction of Antibody and Lectin Hybrid Microarray

All commercial antibodies (**Table 4.1**) were buffer exchanged in to PBS and quantified by BCA assay. A panel of 15 antibodies and 26 pure unlabelled lectins (**Table 4.2**) were printed in PBS, pH 7.4 on Nexterion® H amine reactive, hydrogel coated glass slides (Schott AG, Mainz, Germany) using a SciFLEXARRAYER S3 piezoelectric printer (Scienion, Berlin, Germany) under constant humidity (62% +/- 2%) and a constant temperature of 20°C essentially as previously described [5, 76]. The lectins were printed at 0.5 mg mL⁻¹ in PBS supplemented with 1 mM of their respective haptenic monosaccharides (**Table 4.2, Figure 4.2**) while antibodies were printed at concentrations between 0.1 – 1.0 mg mL⁻¹ in PBS (**Table 4.1, Figure 4.2**). Antibodies and lectins were printed in replicates of six and each feature was printed using approximately 1 nL using an uncoated 90 µm glass nozzle with eight replicate subarrays printed per microarray slide. After printing, slides were incubated in a humidity chamber overnight at room temperature to facilitate complete conjugation. The slides were then blocked in 100 mM ethanolamine in 50 mM sodium borate, pH 8.0, for one hour at room temperature. Slides were washed in PBS with 0.05% Tween® 20 (PBS-T) three times for three minutes each wash, followed by one wash

Analysis of the Neurotropic and Anti-inflammatory Effects of Neuroelectrode
Functionalisation with a Heparan Sulphate Mimetic

in PBS, dried by centrifugation (470 x g, five minutes) and then stored with desiccant at 4 °C until use.

Table 4.1 Summary of all the commercial antibodies used for the gliosis antibody microarray.

Order	Probe	Conc [mg mL ⁻¹]	Information	Company	Catalogue Number
1	Anti-Glial Fibrillary Acidic Protein (GFAP)	0.25	Mouse anti-rat immunoglobulins, monoclonal	Sigma®	G3893
2	Nestin (Rat-401)	0.5	Mouse anti-rat immunoglobulins, monoclonal	SantaCruz®	sc-33677
3	CD81 (H-121)	1	Rabbit anti-rat immunoglobulins, polyclonal	SantaCruz®	sc-9158
4	Integrin alphaM (OX42)	1	Mouse anti-rat immunoglobulins, monoclonal	SantaCruz®	sc-53086
5	Anti Iba1	2.5	Rabbit anti-rat immunoglobulins, polyclonal	WAKO®	019-19741
6	Paxillin antibody [Y113]	0.5	Rabbit anti-rat immunoglobulins, monoclonal	Abcam	ab32084
7	cleaved spectrin alpha II (h1186)	0.5	Rabbit anti-rat immunoglobulins, polyclonal	SantaCruz®	sc-23464
8	Anti-Smad3 antibody [EP568Y]	1	Rabbit anti-rat immunoglobulins, monoclonal	Abcam	ab40854
9	Anti-Chondroitin Sulfate antibody	0.1	Mouse anti-rat immunoglobulins, monoclonal	Sigma®	C8035
10	PBS		Phosphate buffered saline, pH 7.4		
11	Anti-rat_0.5	0.5	Rabbit anti-rat immunoglobulins, polyclonal	DAKO	
12	Anti-sheep_0.5	0.5	Rabbit anti-sheep immunoglobulins, polyclonal	DAKO	
13	VR1 (H-150)	1	Rabbit anti-human immunoglobulins, polyclonal	SantaCruz®	sc-20813
14	Anticorps L-type Ca ⁺⁺ CP α1C (H-280)	0.5	Rabbit anti-human immunoglobulins, polyclonal	SantaCruz®	sc-25686
15	PIEZO1 Antibody (N- 15)	1	Goat anti-human immunoglobulins, monoclonal	SantaCruz®	sc-164319

Analysis of the Neurotropic and Anti-inflammatory Effects of Neuroelectrode
Functionalisation with a Heparan Sulphate Mimetic

16	PIEZO2 Antibody (G-20)	1	Rabbit anti-human immunoglobulins, polyclonal	SantaCruz®	sc-84763
17	ANKTM1 (C-19)	0.5	Goat anti-human immunoglobulins, polyclonal	SantaCruz®	sc-32353
18	TREK-1 Antibody (C-20)	1	Goat anti-human immunoglobulins, polyclonal	SantaCruz®	sc-11557
19	Anti β -Tubulin III (TUBB3)	0.1	Rabbit anti-rat immunoglobulins, polyclonal	Sigma®	T2200
20	Anti β -Tubulin III (TUBB3)	0.25	Rabbit anti-rat immunoglobulins, polyclonal	Sigma®	T2200
21	Anti β -Tubulin III (TUBB3)	0.5	Rabbit anti-rat immunoglobulins, polyclonal	Sigma®	T2200
22	Anti β -Tubulin III (TUBB3)	0.75	Rabbit anti-rat immunoglobulins, polyclonal	Sigma®	T2200
23	Anti β -Tubulin III (TUBB3)	1	Rabbit anti-rat immunoglobulins, polyclonal	Sigma®	T2200

Table 4.2 Lectins, their sources, common names, binding specificities, print sugars and the manufacturer.

Abbreviation	Source	Species	Common name	General binding specificity	Print sugar	Supplier
AIA (Jacalin)	Plant	<i>Artocarpus integrifolia</i>	Jack fruit lectin	Gal, Gal- β -(1,3)-GalNAc (sialylation independent)	Gal	EY Labs
SJA	Plant	<i>Sophora japonica</i>	Pagoda tree lectin	β -GalNAc	Gal	EY Labs
DBA	Plant	<i>Dolichos biflorus</i>	Horse gram lectin	α -GalNAc	Gal	EY Labs
WFA	Plant	<i>Wisteria floribunda</i>	Japanese wisteria lectin	GalNAc/sulfated GalNAc	Gal	EY Labs
HPA	Animal	<i>Helix pomatia</i>	Edible snail lectin	α -GalNAc	Gal	EY Labs
ACA	Plant	<i>Amaranthus caudatus</i>	Amaranthin	Sialylated/Gal- β -(1,3)-GalNAc	Lac	Vector Labs
GS-II	Plant	<i>Griffonia simplicifolia</i>	Griffonia/B andeiraea lectin-II	GlcNAc	GlcNAc	EY Labs
sWGA	Plant	<i>Triticum vulgare</i>	Succinyl WGA	GlcNAc	GlcNAc	EY Labs
NPA	Plant	<i>Narcissus pseudonarcissus</i>	Daffodil lectin	α -(1,6)-Man	Man	EY Labs

Analysis of the Neurotropic and Anti-inflammatory Effects of Neuroelectrode
Functionalisation with a Heparan Sulphate Mimetic

GNA	Plant	<i>Galanthus nivalis</i>	Snowdrop lectin	Man- α -(1,3)-linked	Man	EY Labs
Con A	Plant	<i>Canavalia ensiformis</i>	Jack bean lectin	α -Man / α -Glc	Man	EY Labs
Lch-B	Plant	<i>Lens culinaris</i>	Lentil isolectin B	α -Man, core fucosylated, agalactosylated biantennary N-glycans	Man	EY Labs
Lch-A	Plant	<i>Lens culinaris</i>	Lentil isolectin A	α -Man / α -Fuc	Man	EY Labs
PSA	Plant	<i>Pisum sativum</i>	Pea lectin	Branched α -Man, core fucosylated trimannosyl N-glycans	Man	EY Labs
WGA	Plant	<i>Triticum vulgare</i>	Wheat germ agglutinin	NeuAc/GlcNAc	GlcNAc	EY Labs
MAA	Plant	<i>Maackia amurensis</i>	Maackia agglutinin	Sialic acid- α -(2,3)-linked	Lac	EY Labs
SNA-I	Plant	<i>Sambucus nigra</i>	Sambucus lectin-I	Sialic acid- α -(2,6)-linked	Lac	EY Labs
RCA-I/120	Plant	<i>Ricinus communis</i>	Castor bean lectin-I	Gal- β -(1,4)-GlcNAc	Gal	Vector Labs
CAA	Plant	<i>Caragana arborescens</i>	Pea tree lectin	Complex oligosaccharides	Lac	EY Labs
ECA	Plant	<i>Erythrina cristagalli</i>	Cocks comb/coral tree lectin	Gal- β -(1,4)-GlcNAc oligomers, LacNAc	Lac	EY Labs
AAL	Fungi	<i>Aleuria aurantia</i>	Orange peel fungus lectin	Fuc- α -(1,6)-linked > Fuc- α -(1,3)- and - α -(1,2)-linked	Fuc	EY Labs
LTA	Plant	<i>Lotus tetragonolobus</i>	Lotus lectin	Fuc- α -(1,3)-linked	Fuc	EY Labs
UEA-I	Plant	<i>Ulex europaeus</i>	Gorse lectin-I	Fuc- α -(1,2)-linked	Fuc	EY Labs
MPA	Plant	<i>Maclura pomifera</i>	Osage orange lectin	Terminal Gal- β -(1,3)-GalNAc > GalNAc- α -(1,6)-Gal	Gal	EY Labs
VRA	Plant	<i>Vigna radiate</i>	Mung bean lectin	Terminal α -Gal	Gal	EY Labs
MOA	Fungi	<i>Marasmius oreades</i>	Fairy ring mushroom lectin	Terminal α -Gal	Gal	EY Labs

Analysis of the Neurotropic and Anti-inflammatory Effects of Neuroelectrode Functionalisation with a Heparan Sulphate Mimetic

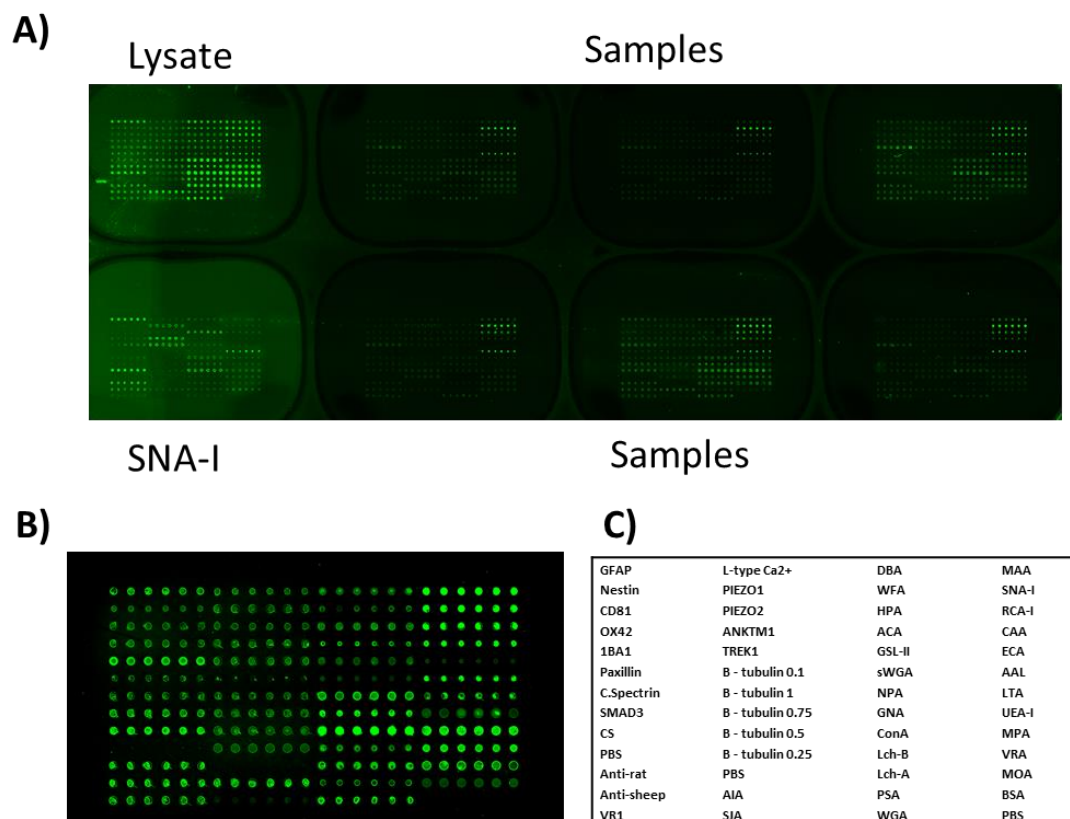


Figure 4.2 Images from a representative scanned microarray slide after incubation and washing. A) Incubations were carried out on three replicate microarray slides. Alexa Fluor® 555 labelled healthy rat brain lysate (5 mg mL^{-1}) and SNA-I lectin (10 mg mL^{-1}) were used as controls to confirm retained antibody performance and printing, respectively, and were incubated in two separate subarrays on every slide. B) Individual subarray from a representative scanned microarray slide after incubation with healthy rat brain lysate and subsequent washing. The subarrays were printed with antibodies and lectins in replicates of six following the order detailed in C).

4.3.10.3 Profiling Samples on Hybrid Microarrays, Data Extraction and Analysis

All incubations were carried out under dark conditions. Microarray slides were incubated as previously described [5, 76]. Initially, one labelled sample was titrated ($2.5 - 15 \text{ } \mu\text{g mL}^{-1}$) to determine optimal signal to noise ratio and all samples were subsequently incubated for one hour at $23 \text{ } ^\circ\text{C}$ at $5 \text{ } \mu\text{g mL}^{-1}$ in Tris-buffered saline

Analysis of the Neurotropic and Anti-inflammatory Effects of Neuroelectrode Functionalisation with a Heparan Sulphate Mimetic

(TBS; 20 mM Tris-HCl, 100 mM NaCl, 1 mM CaCl₂, 1 mM MgCl₂, pH 7.2) with 0.05% Tween® 20 (TBS-T). All microarray experiments were carried out using three replicate slides. AF555-labelled healthy rat brain lysate (5 µg mL⁻¹) and tetramethylrhodamine-(TRITC)-labelled SNA-I lectin (10 µg mL⁻¹) were incubated in two separate subarrays on every slide to confirm retained antibody performance and printing, respectively (**Figure 4.2**). After incubation, slides were washed three times in TBS-T for three minutes per wash, once in TBS and then centrifuged dry as above. Dried slides were scanned immediately on an Agilent G2505 microarray scanner using the Cy3 channel (532 nm excitation, 90% PMT, 5 µm resolution) and intensity data was saved as a .tif file. The antibodies and lectins conjugated to the microarray surface were verified to remain active for at least one month after printing and all incubations were carried out within that timeframe.

Data extraction from .tif files was performed essentially as previously described [5, 76]. Data were normalised to the mean of three replicate microarray slides (subarray by subarray using subarray total intensity, N= 3, 18 data points). Unsupervised hierarchical clustering of normalised data was performed using Hierarchical Clustering Explorer v3.0 (<http://www.cs.umd.edu/hcil/hce/hce3.html>) using the parameters no pre-filtering, complete linkage, and Euclidean distance. Statistical analysis was performed as detailed in the section 4.3.11.

4.3.11 Statistical Analysis

All data presented here was confirmed using at least three replicates for each of the test groups and control groups. The results are expressed as the mean of the values ± standard error of the mean. One-way ANOVA followed by a Bonferroni test were performed to determine the statistical significance (p<0.05), unless otherwise stated.

4.4 Results and Discussion

The use of GAGs as dopants within an electrodeposited polymer not only endows the resulting polymer with bioactivity, but as charged biomolecules, also act as counterions in the electrochemical polymerisation process [28, 36]. Experimentally, this study employed a PEDOT derivative, modified through the incorporation of the HM - F6, a polysulphated molecule which acted as a biological co-dopant for the

Analysis of the Neurotropic and Anti-inflammatory Effects of Neuroelectrode Functionalisation with a Heparan Sulphate Mimetic

formulation of glycan functionalised neural interfaces [52, 60, 77, 78]. F6 was originally described by Papy- Garcia et al. as a functionalised dextran derivative with resistance to glycanase degradation [44]. F6, together with the conventional sulphonate anion PTS, was incorporated in the matrix of PEDOT through a co-doping electropolymerisation process. The chemical structure of the F6 molecule and a proposed pictorial representation of PEDOT:PTS:F6 functionalisation on the physico-electrical and biological properties through F6 interaction are shown in **Figure 4.3**.

Initially, an optimisation process to assess the therapeutic concentration of F6 was conducted with concentrations of 1, 10, 50, 100 and 1000 $\mu\text{g ml}^{-1}$ incorporated into cell culture media over a period of ten days in culture. Cell viability effects using primary ventral mesencephalic mixed neural cell population grown *in vitro* are presented in **Figure 4.4**. Live/dead analysis indicated maintained cell viability when F6 was present in the cell culture media at concentrations below 50 $\mu\text{g ml}^{-1}$, a range that was replicated in F6 functionalised PEDOT:PTS films electrodeposited from an electrolyte/EDOT solution containing 1000 $\mu\text{g ml}^{-1}$ of F6 (**Table 4.3**).

Analysis of the Neurotropic and Anti-inflammatory Effects of Neuroelectrode Functionalisation with a Heparan Sulphate Mimetic

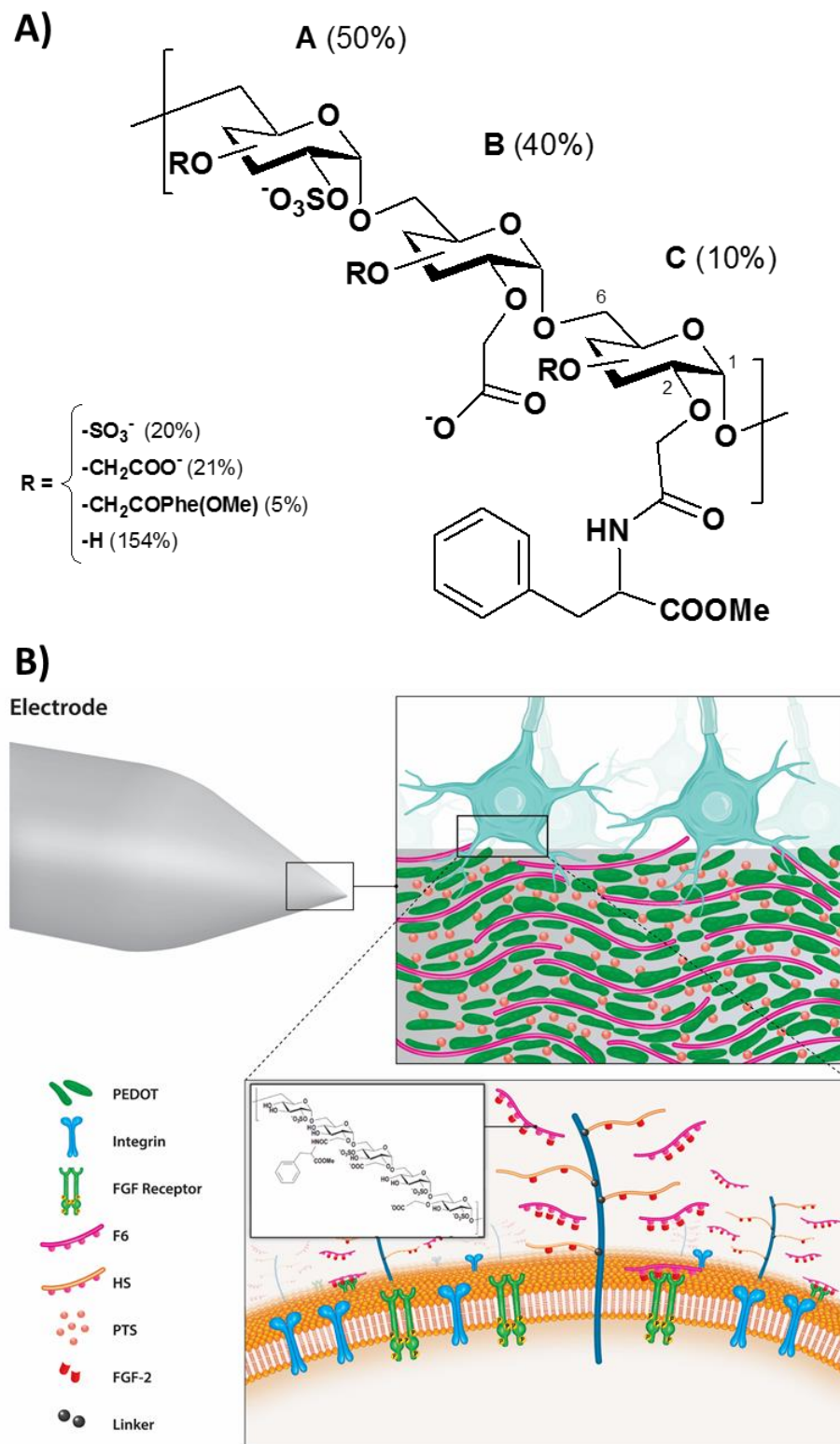


Figure 4.3 Biochemical functionalisation of the neuroelectrode surface with PEDOT:PTS:F6 thin films. A) F6 is a dextran T5 (M_w 5,000 Daltons) derivative

Analysis of the Neurotropic and Anti-inflammatory Effects of Neuroelectrode
Functionalisation with a Heparan Sulphate Mimetic

containing sulphate, carboxymethyl, and phenylalanine methyl ester groups. For an easy representation, three differently substituted glucosidic units (A, B, and C) are depicted and arranged in an arbitrary combination. The relative content of each unit was calculated according to the nature of the group substituted at position 2 of each unit (C2). R represents the proportion of each substituted group at C3 and C4, which total substitution corresponds to 200%. F6 was synthesised and analysed as in [44].

B) Pictorial representation of PEDOT:PTS:F6 functionalised electrodes from the electrophysical arrangement to the cell level interaction with growth factors binding, i.e FGF-2.

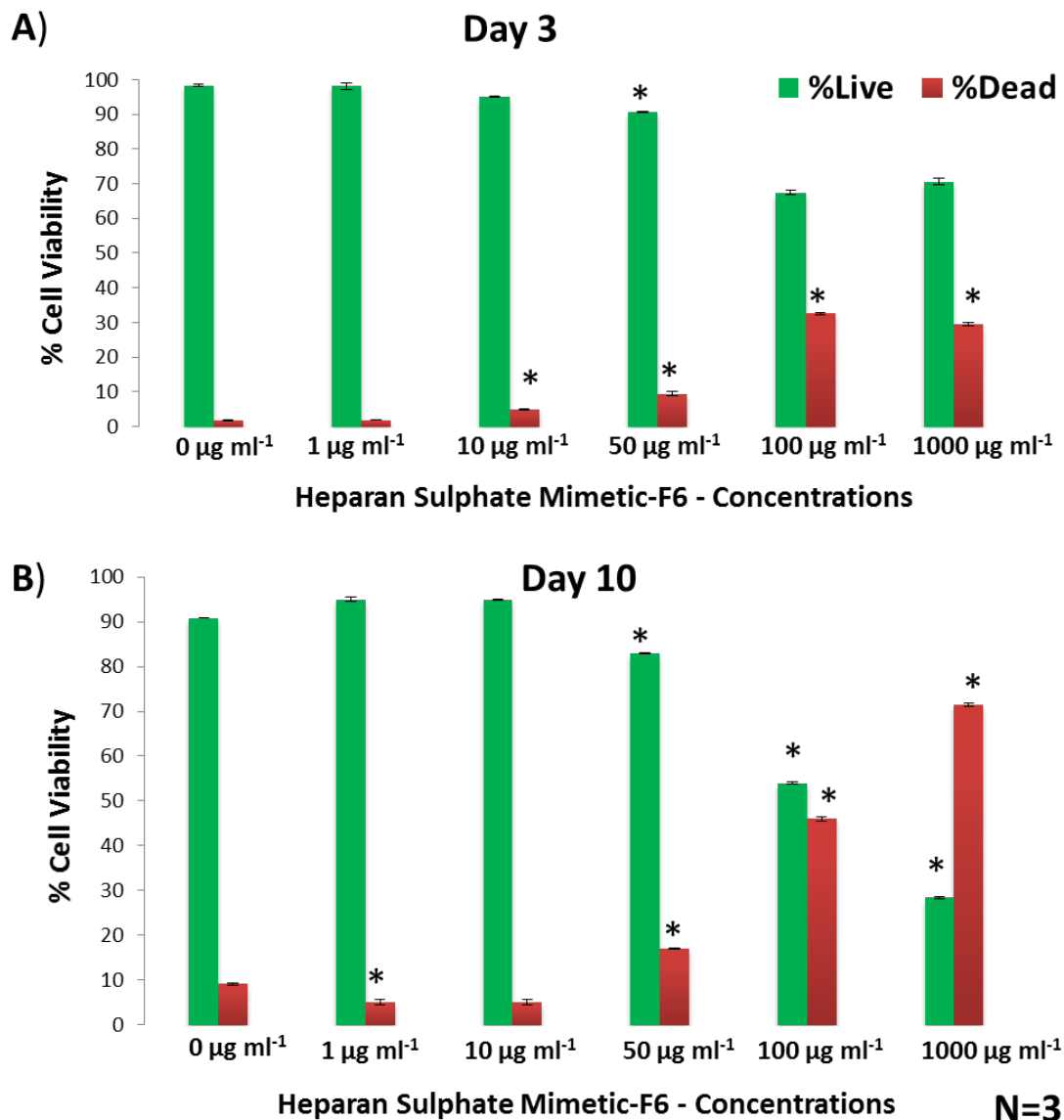


Figure 4.4 *Cytocompatibility effects of heparan sulphate mimetic-F6 – concentrations in solution.* Live and dead assay was carried out using primary ventral mesencephalic (VM) mixed neural cell population under the presence of bulk F6 at 1, 10, 50, 100 and 1000 µg ml⁻¹. An early time of three days in culture A) and late time of ten days B) were evaluated. A maintained cell viability was achieved when bulk F6 was present in the cell culture media at concentrations below 50 µg ml⁻¹. Results are ± STD. ★ = $p < 0.05$.

Table 4.3 *Passive mode concentration profile of heparan sulphate mimetic-F6 released from PEDOT:PTS:F6 coated electrodes at a concentration of 1, 10, 50, 100 and 1000 $\mu\text{g ml}^{-1}$ for a period of 21 days. Results are \pm STD. N=3*

		PEDOT:PTS:F6 at 1000 $\mu\text{g ml}^{-1}$	PEDOT:PTS:F6 at 100 $\mu\text{g ml}^{-1}$	PEDOT:PTS:F6 at 50 $\mu\text{g ml}^{-1}$	PEDOT:PTS:F6 at 10 $\mu\text{g ml}^{-1}$	PEDOT:PTS:F6 at 1 $\mu\text{g ml}^{-1}$
Concentration of Heparan Sulphate Mimetic F6 Released from PEDOT:PTS polymeric Matrix [$\mu\text{g ml}^{-1}\text{cm}^{-2}$]	3 days	5.6 \pm 1.8	2.1 \pm 0.7	2.5 \pm 1.1	1.8 \pm 0.4	1.4 \pm 0.4
	7 days	8.0 \pm 3.5	3.9 \pm 1.1	3.5 \pm 1.4	3.5 \pm 0.4	1.8 \pm 0.7
	10 days	10.2 \pm 3.2	5.6 \pm 2.5	6.0 \pm 1.4	4.9 \pm 0.7	3.2 \pm 1.4
	Total amount of F6 released over 21 days	11.7 \pm 2.8	5.6 \pm 3.5	6.0 \pm 1.8	6.7 \pm 0.7	5.3 \pm 1.8

Additionally, PEDOT:PTS films electrodeposited from an electrolyte/EDOT solution containing 1000 $\mu\text{g ml}^{-1}$ of F6 were found to possess the highest mass of immobilised F6 within the polymer matrix as assessed via Electrochemical Quartz Crystal Microbalance (EQCM) **Figure 4.5**. Taken together, the optimal F6 electrolyte/EDOT solution concentration selected for subsequent analysis was 1000 $\mu\text{g ml}^{-1}$, denoted hereon as “PEDOT:PTS:F6” in this chapter. PEDOT:PTS doped with a non-sulphated polymeric dextran was also employed as a control group to understand further the effect of sulphation pattern provided by F6. This was incorporated during the electrodeposition process of EDOT at the same concentration of F6, 1000 $\mu\text{g ml}^{-1}$.

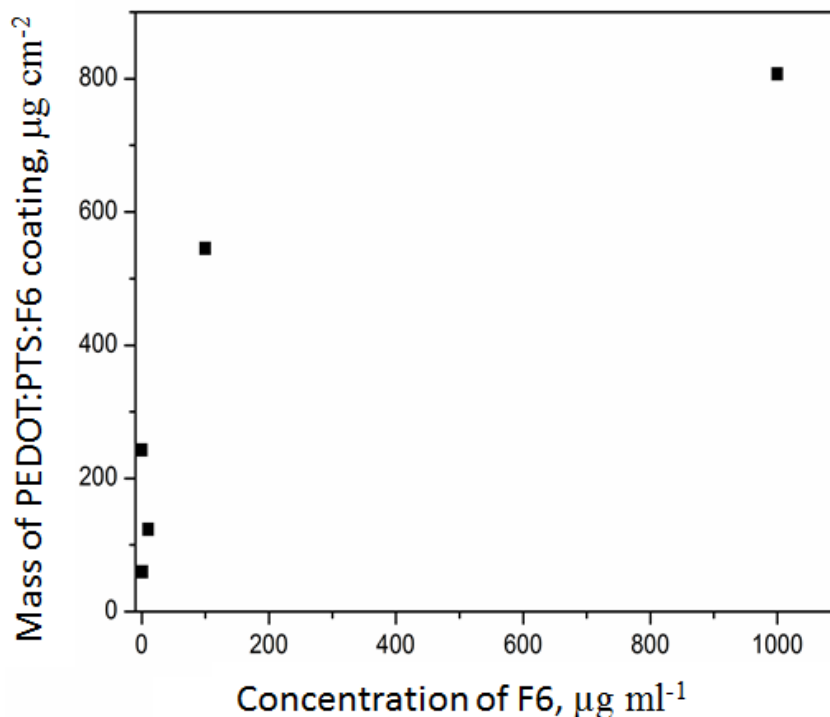


Figure 4.5 Electrochemical quartz crystal microbalance (EQCM) measurements of the masses recorded of PEDOT:PTS:F6 coatings at 1, 10, 50, 100 and 1000 $\mu\text{g ml}^{-1}$. PEDOT:PTS:F6 at 1000 $\mu\text{g ml}^{-1}$ of heparan sulphate mimetic- F6 was found to possess the highest mass immobilised of F6 within the polymer matrix with a mass recorded of 807.2 $\mu\text{g cm}^{-2}$.

4.4.1 Physical and Chemical Characterisation

Electrodeposition of PEDOT:PTS:F6 onto concentric Platinum/Iridium (PtIr) microelectrodes was confined to the conducting surfaces and did not result in an increase of electrode area at the macroscale. Representative SEM micrographs of the bare PtIr A) and the PEDOT:PTS:F6 coated microelectrodes B) are indicated in **Figure 4.6**. The experimental values of the roughness and thickness profiles for the pristine PEDOT:PTS coatings and the functionalised PEDOT:PTS:F6 coatings at different F6 concentrations are detailed in **Table 4.4**. The average roughness, R_a of electrodeposited PEDOT:PTS:F6 films, was observed to decrease in a non-linear concentration dependent manner, but all electrodeposited PEDOT:PTS:F6 films

possessed higher R_a values relative to pristine PEDOT:PTS films, a phenomenon reported previously with biological doping of PEDOT derivatives [79]. It should be noted that relative to pristine PEDOT:PTS coatings, electrodeposited PEDOT:PTS:F6 electrode coatings possessed a denser and more uniform surface topography with more island-like particles, whereas films formulated with F6 concentrations $< 1000 \mu\text{g ml}^{-1}$ possessed a less uniform and more porous surface structure with easy-to-observe aggregates (**Figure 4.7A**). PEDOT:PTS:F6 coatings (formed at $1000 \mu\text{g ml}^{-1}$, the highest F6 concentration used), however, presented a more homogeneous structure, where the aggregates tend to form regular structures. Thus, the ability of the polymeric-F6 to aggregate within the electrodeposition process may explain the differential topographical roughness and the building layers in thickness of the coatings with changes in F6 concentrations [79, 80]. In addition, a saturation value was reached for both measurements at a concentration of $50 \mu\text{g ml}^{-1}$ of F6 within the polymeric matrix, which in these films the clustered-like aggregates were comparatively larger than those observed in the other experimental samples (**Figure 4.7A**). Further, these physical observations taken in conjunction with FT-MIR spectra data indicate that with an increase in the concentration of F6 within the PEDOT:PTS polymer (**Figure 4.7B**), the IR bands become noticeably sharper, owing to an increase in rigidity by restriction of conformational freedom [81].

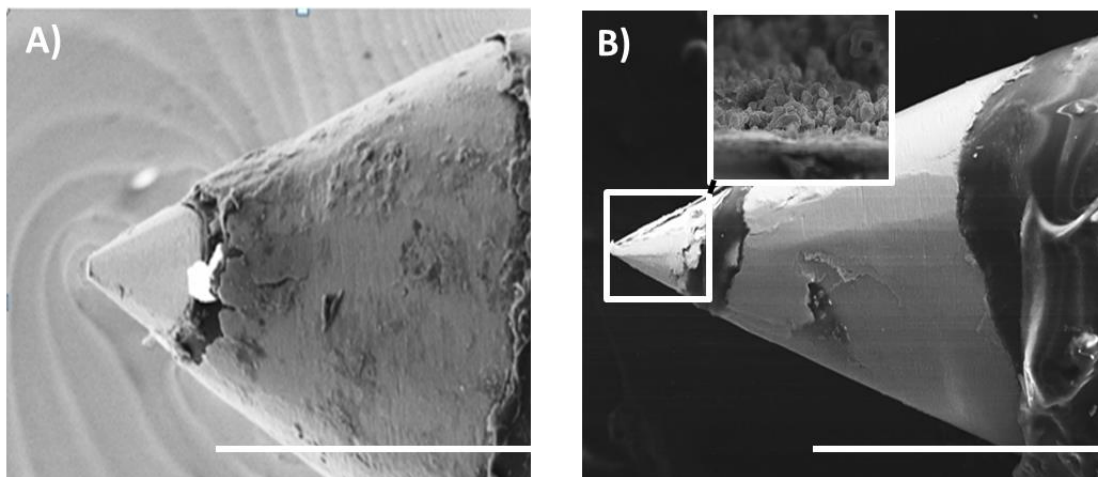


Figure 4.6 Scanning electron micrographs (SEM) of the bare platinum/iridium (PtIr) microelectrode A) and PEDOT:PTS:F6 coated microelectrode B) are shown,

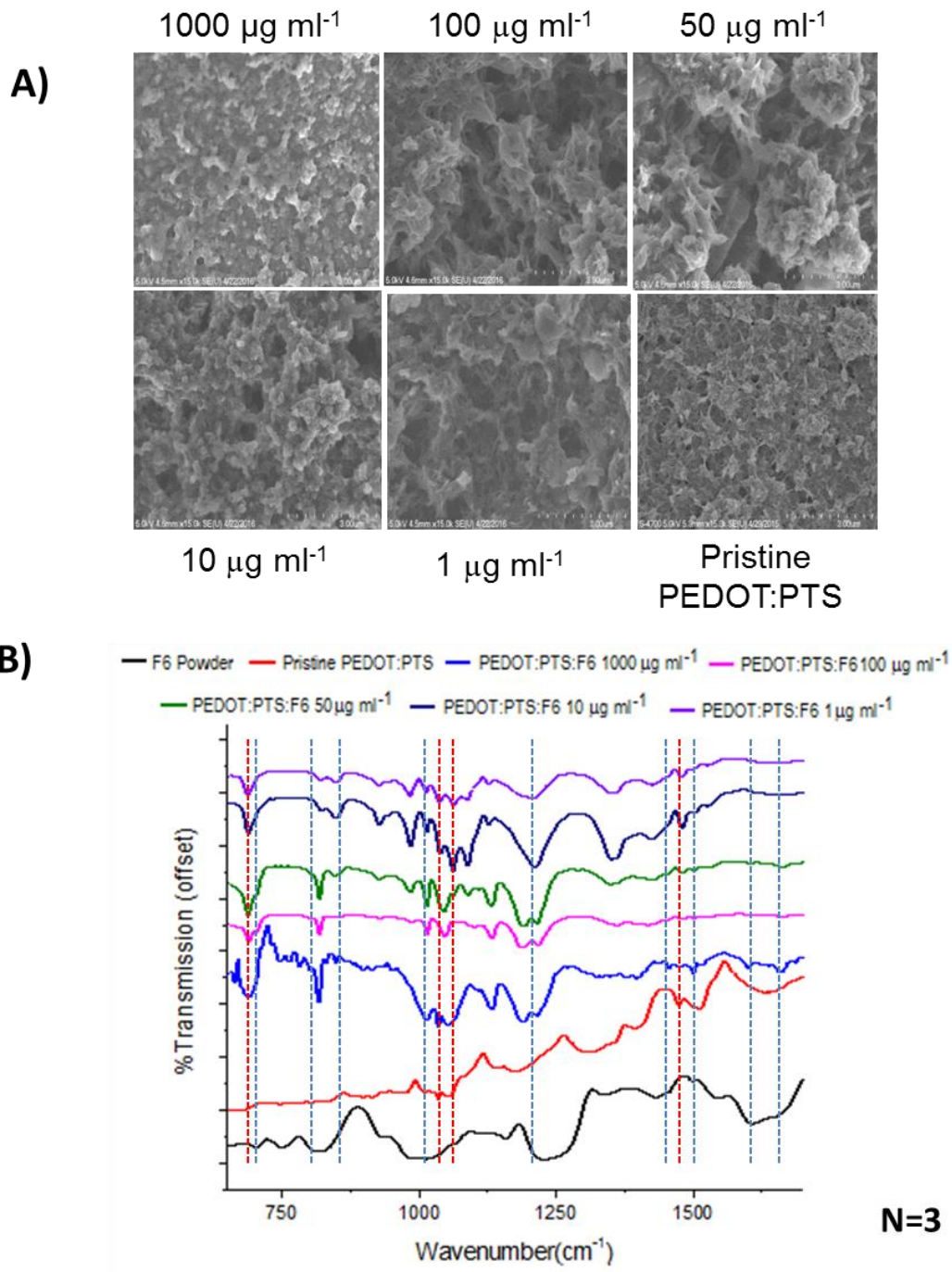
Analysis of the Neurotropic and Anti-inflammatory Effects of Neuroelectrode
Functionalisation with a Heparan Sulphate Mimetic

respectively. Scale bar = 200 μm . In the inset, the PEDOT:PTS:F6 coating is detailed, showing the nodular formation of electrodeposited coatings.

Table 4.4 Values of experimental mean surface roughness (R_a) and mean thickness measurements of pristine PEDOT:PTS coated microelectrodes and PEDOT:PTS:F6 coated microelectrodes at 1, 10, 50, 100 and 1000 $\mu\text{g ml}^{-1}$ of heparan sulphate mimetic-F6. The data represent the mean of 15 measurements from three different replicas. Results are \pm SD, $N=3$.

Electrodes	Average Roughness R_a [nm]	Thickness [nm]
Pristine PEDOT:PTS	85.16 ± 16.94	1210.01 ± 0.08
PEDOT:PTS :F6 1 $\mu\text{g ml}^{-1}$	160.59 ± 11.92	1374.02 ± 0.37
PEDOT:PTS :F6 10 $\mu\text{g ml}^{-1}$	167.00 ± 25.12	1619.00 ± 0.41
PEDOT:PTS :F6 50 $\mu\text{g ml}^{-1}$	181.40 ± 28.73	784.80 ± 0.24
PEDOT:PTS :F6 100 $\mu\text{g ml}^{-1}$	150.35 ± 9.65	2167.30 ± 0.31
PEDOT:PTS :F6 1000 $\mu\text{g ml}^{-1}$	104.72 ± 6.64	2404.22 ± 0.53

Analysis of the Neurotropic and Anti-inflammatory Effects of Neuroelectrode Functionalisation with a Heparan Sulphate Mimetic



Amide stretching at 1730 cm^{-1} is missing in the case of F6, as there is only a 5% substitution, so it may not be strong enough. No exclusive NH for F6 either - too weak perhaps. The sulphate peaks are also not known to occur frequently.

Figure 4.7 Morphological changes with different concentrations of F6. A) Scanning electron micrographs (SEM) of pristine PEDOT:PTS coated microelectrodes and the PEDOT:PTS:F6 coated microelectrodes at 1, 10, 50, 100 and $1000 \mu\text{g ml}^{-1}$ of

Analysis of the Neurotropic and Anti-inflammatory Effects of Neuroelectrode Functionalisation with a Heparan Sulphate Mimetic

heparan sulphate mimetic-F6. B) FT-MIR spectra of powdered F6 (black), pristine PEDOT:PTS coated microelectrodes (red) and PEDOT:PTS:F6 coated microelectrodes at 1, 10, 50, 100 and 1000 $\mu\text{g ml}^{-1}$ of F6. Blue dotted lines show bands that belong to only F6, while red dotted lines show bands contributed by just PEDOT:PTS polymer. It can be seen that with an increase in the concentration of F6 in the PEDOT:PTS matrix, the bands become sharper suggesting a greater rigidity in the structure.

In order to assess F6 incorporation into electrodeposited PEDOT:PTS:F6 and pristine PEDOT:PTS films extensive chemical characterisation of coated microelectrodes was performed (**Figure 4.8A-I**). Surface wettability of the electrodeposited films was assessed through contact angle analysis via an in-house developed goniometer. Pristine PEDOT:PTS coated microelectrodes were associated with a water contact angle of $15.92^\circ \pm 2.91$, indicating the high hydrophilicity of the coatings [82]. Through the incorporation of F6, the water contact angle was observed to decrease to $<5^\circ$ accompanied by a rapid spreading of the water drop, indicating that the hydrophilicity of the electrodeposited films was significantly increased through doping with F6, potentially due to the presence of sulphate groups at the film surface, increasing polar interaction with the water droplet (**Figure 4.8A**) [82]. Furthermore, the observed increase in PEDOT:PTS film roughness associated with F6 doping relative to pristine PEDOT:PTS coatings complements the observation of increased wettability of these coatings [83, 84].

Analysis of the Neurotropic and Anti-inflammatory Effects of Neuroelectrode Functionalisation with a Heparan Sulphate Mimetic

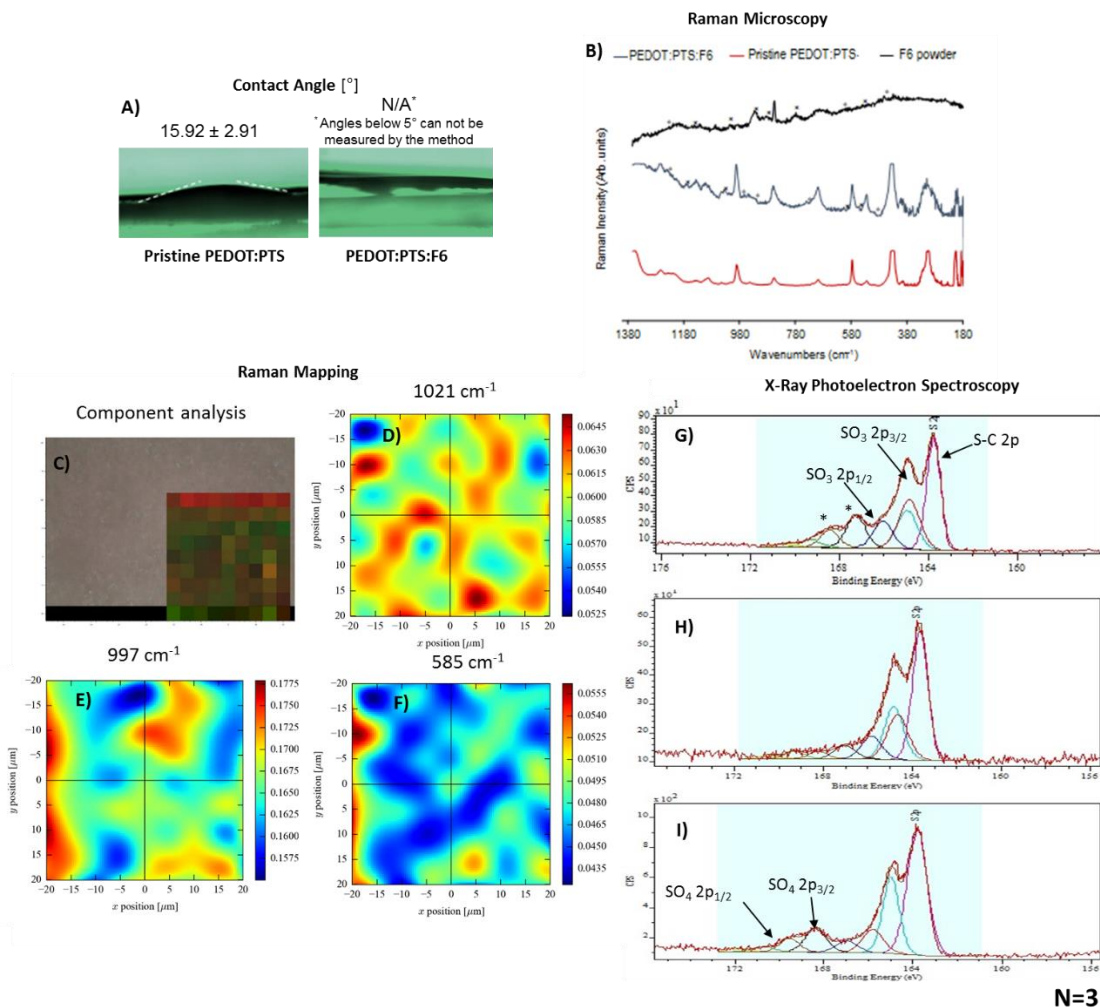


Figure 4.8 Chemical characterisation of the PEDOT:PTS:F6 coated microelectrode. A) Contact angle on pristine PEDOT:PTS and PEDOT:PTS:F6 coated microelectrodes, showing the decrease in a water contact angle suggesting an increase in hydrophilicity. B) Raman spectra of PEDOT:PTS microelectrodes, with and without incorporated F6, and powdered F6. Peaks assigned solely to F6 are indicated by an * on the pure F6 and of PEDOT:PTS:F6 coated microelectrodes spectra. (C-F) Raman mapping of pristine PEDOT:PTS and PEDOT:PTS:F6 coated microelectrodes. C) shows the component DLS analysis, where red pixels represent the F6 component and green pixels represent the PEDOT:PTS component. D) and E) show the intensity of the Raman bands at 1021 cm⁻¹ and 997 cm⁻¹, respectively, and indicate the presence of F6 evenly distributed on coated PEDOT:PTS microelectrodes. F) shows the band intensity at 585 cm⁻¹ and indicates the presence

of PEDOT:PTS in the coating. (G-I) X-ray photoelectron spectra of G) pristine PEDOT:PTS, H) PEDOT:PTS:Dextran, and I) PEDOT:PTS:F6 coated microelectrodes, showing the presence of sulphur in various chemical environments corresponding to S-C bonding ($2p$ neutral state) and $2p_{3/2}$ and $2p_{1/2}$ states in both sulphonates and sulphates. The * in G) denotes the presence of possible impurities from the electrolyte.

Raman spectral analysis also indicated the presence of F6 in electrodeposited PEDOT:PTS:F6 coated microelectrodes (**Figure 4.8 B**). Peaks were observed at 997 cm^{-1} and 1021 cm^{-1} corresponding to C-C stretches and C-H deformations also observed in pristine F6. Peaks marked with * indicate that the microelectrode had measurable amounts of F6 incorporated into the PEDOT:PTS:F6 coating. The tentative assignments of peaks in the Raman spectra are shown in **Table 4.5**. Peaks observed at 816 cm^{-1} and 848 cm^{-1} , visible in both Raman and FT-MIR spectra (**Figure 4.7B**), also confirm the presence of the F6 on the PEDOT:PTS:F6 coated microelectrodes. These bands correspond to E-E and E-A fragment γ C-H deformations, respectively, in the dextran moiety [85]. Other peaks corresponding to F6 are indicated by blue dotted lines, and bands corresponding to the pristine PEDOT:PTS polymer are marked by red dotted lines in the IR spectra (**Figure 4.7B**). A peak at 1180 cm^{-1} is masked by a broad peak in spectra recorded from the two lower concentrations of F6, but emerges as a sharp peak as the F6 concentration increases. This band corresponds to C-O stretching [86]. Peaks at 928 cm^{-1} in F6 (**Figure 4.7B**) and 915 cm^{-1} in dextran (**Figure 4.9**) suggest the presence of the C1 glucopyranosol conformation [85]. The presence of a peak at 800 cm^{-1} assigned to dextran suggests the presence of less than 5% alpha (1,3) glucoside bonds, making it highly linear [84] (**Figure 4.9**). The tentative assignments of peaks in the ATR-IR spectra are summarised in **Table 4.6**.

Analysis of the Neurotropic and Anti-inflammatory Effects of Neuroelectrode
Functionalisation with a Heparan Sulphate Mimetic

Table 4.5 Tentative assignments of the peaks observed in the Raman spectra.

F6 Powder	Pristine PEDOT:PTS	PEDOT:PTS:F6	Tentative assignments
	197, 205	209	C-S stretching in PEDOT
240, 410	299, 327, 394	311, 389	CO ₂ out-of-plane deformation
420, 462	430, 496, 518	443, 492, 518	CO ₂ rocking deformation
	549, 589	564	CO ₂ out-of-plane deformation / SO ₂ scissoring
	602	601	CO ₂ in-plane deformation
687	687	691	Sextant ring deformation in phenylalanine like fragment
774	715	733	Aromatic C-H deformation / E-E Fragment γ C-H deformation in dextran / C-O-C symmetric stretches in cyclic esters
812			
844	848	847	E-A Fragment γ C-H deformation in dextran
875			A-E Fragment γ C-H deformation in dextran
892			
915		915	A-A fragment γ C-H deformation in dextran
997	937, 984	944, 962, 997	C-C vs
	1007	1010	Sulphonate bands (S=O) vs
1026	1037	1021	C-H def.
1056	1084	1049, 1085	C-C and C-N vs
1116		1106	C-C and C-C-N vs
1144, 1203	1128	1126, 1161, 1194	C-O vs in alcohols and phenols
1218, 1226	1212, 1227	1234	C=S vs
1286, 1292	1256, 1288	1274, 1296	C-O vs in carboxylic acid derivatives
1305, 1317			

Analysis of the Neurotropic and Anti-inflammatory Effects of Neuroelectrode Functionalisation with a Heparan Sulphate Mimetic

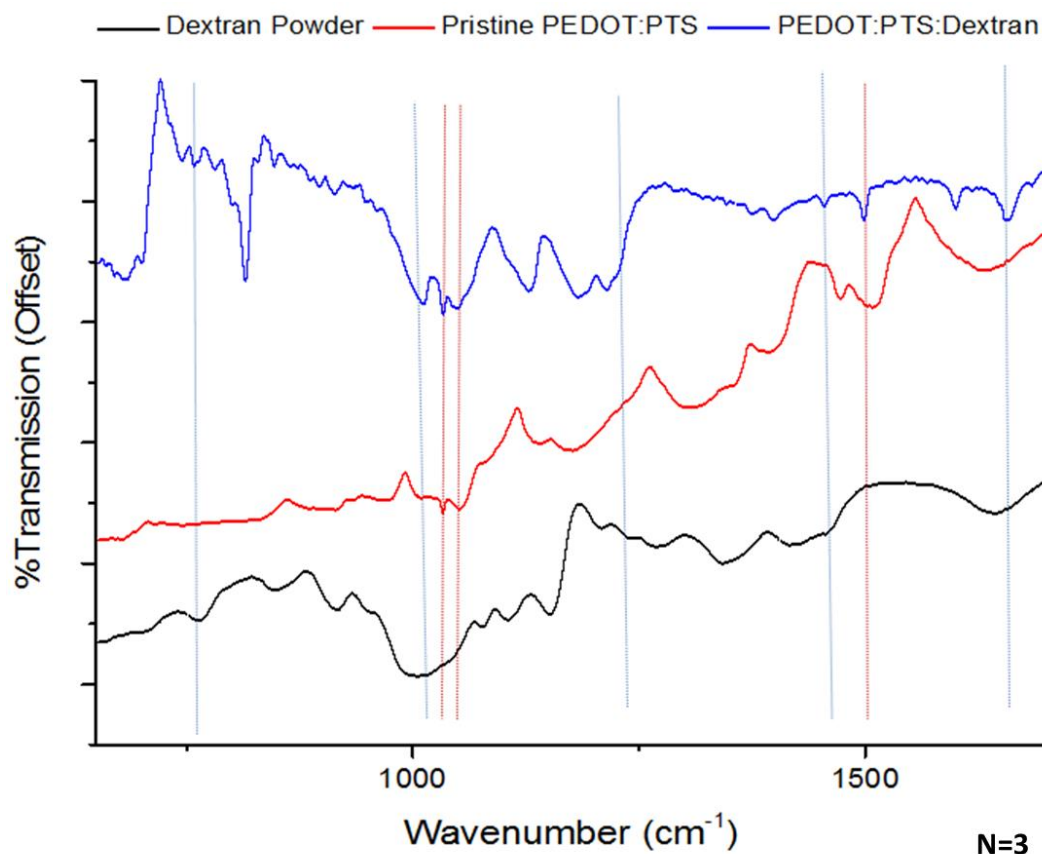


Figure 4.9 FT-MIR spectra of powdered dextran (black), pristine PEDOT:PTS coated microelectrodes (red) and PEDOT:PTS:Dextran coated microelectrodes. Blue dotted lines show bands that belong to only dextran, while red dotted lines show bands contributed just by PEDOT:PTS matrix.

Table 4.6 Tentative assignments of the peaks observed in the ATR-IR spectra.

Pristine PEDOT:PTS	F6 Powder	PEDOT:PTS:F6	Dextran Powder	PEDOT:PTS:Dextran	Tentative Assignments	
		664		659	Quad. deformation	Ring
	671	674, 680	670	671, 679, 684	Sextant deformation in phenylalanine	ring in
		685, 689				
	700, 751	710, 729, 745 757, 763	705, 762	700, 731, 744 758, 762	Aromatic deformation	C-H
	811	780, 816	816	780, 800, 815	E-E Fragment deformation in dextran / C-O-C symmetric stretches	γ C-H in cyclic

Analysis of the Neurotropic and Anti-inflammatory Effects of Neuroelectrode
Functionalisation with a Heparan Sulphate Mimetic

		829, 837, 848	847	828, 846	esters
		864, 878	867, 874	864, 873	E-A Fragment γ C-H deformation in dextran
917	928	887, 896 913, 930	915	887, 896 914, 919	A-E Fragment γ C-H deformation in dextran
975	980	949	950	935, 949, 960	A-A fragment γ C-H deformation in dextran
	1002	1012	1014	1011	C-C v_s
1032		1033		1033	Sulphonate bands (S=O) v_s
1050	1068	1049	1040, 1069	1050	C-H def.
	1104	1106	1107		C-C and C-N v_s
1138, 1174	1171	1122, 1183	1157	1128, 1181	C-C and C-C-N v_{as}
	1223	1213	1208, 1238	1214, 1224	C-O v_s in alcohols and phenols
				1258	C=S v_s
1298	1260, 1330	1268	1272	1288, 1292	C-O vs (also observed in carboxylic acid derivatives)
		1310, 1321 1331, 1346	1343	1321, 1331 1347	
1356		1359	1359	1360	O-H bending (in plane)
	1379	1378		1375	CH ₃ umbrella deformation
1394		1395		1399	Sulphonate bands (S=O) v_{as}
1453, 1472	1420, 1447	1438, 1454	1416, 1458	1432, 1438	CH ₂ and CH ₃ deformations
1493	1498	1471, 1480		1498	
1509	1540	1500, 1516	1502	1518, 1533	
1625	1605	1548, 1567	1560	1550, 1567	Aromatic C=C v_s
		1599		1577, 1600, 1618	
	1649	1637	1649	1640, 1650	H ₂ O vibrations
	1666	1660, 1684	1659	1655, 1684	C=O stretches
		2820, 2845		2822, 2844	C-H alliphatic v_s
		2869		2870	
2969, 2999	2955	2920, 2924 2973, 2998	2916	2967, 2991	C-H Aromatic v_s
3268		3053, 3287		3069	H ₂ O vibrations
3347	3499	3361, 3471	3300	3361, 3475	
3661		3665, 3673		3653, 3660 3672, 3691 3758	OH v_s

Further, Raman mapping followed by component DLS analysis was performed to identify the F6 and the PEDOT:PTS components in electrodeposited films. The 585

cm^{-1} band corresponds to SO_2 scissoring vibrations from PEDOT:PTS polymer, while bands at 997 cm^{-1} and 1021 cm^{-1} correspond to C-C stretches and C-H deformations observed in F6. **Figure 4.8C** shows a component analysis of these bands, where red pixels represent the F6 component and green pixels represent the PEDOT:PTS component, suggesting a uniform distribution of the F6 within the PEDOT:PTS:F6 coated microelectrodes. On comparing **Figure 4.8D** to **Figure 4.8E** and **Figure 4.8F**, a greater contribution from the C-H deformation in PEDOT:PTS:F6 films relative to the PEDOT:PTS films was observed. The highest-intensity contributions however were from the C-C stretches (**Figure 4.8E**). These results successfully confirmed the presence of F6 on the surface of the PEDOT:PTS:F6 coated microelectrodes, with the increase in hydrophilicity observed from the contact-angle studies attributed to the sulphate groups from F6 being presented at the polymer surface.

Sulphate group vibrations are known to be weak and do not always appear in vibrational spectra, especially in the presence of other strongly absorbing groups [86, 87]. Therefore, to discern the chemical composition of PEDOT:PTS:F6 coating surface, X-ray photoelectron spectroscopy (XPS) analysis was conducted. **Figure 4.8(G-I)** show the surface analysis of pristine PEDOT:PTS, PEDOT:PTS:Dextran and the PEDOT:PTS:F6 coated microelectrodes, respectively. All coated electrodes were associated with XPS peaks corresponding to neutral S, arising from the S-C bonds in PEDOT (163.7 eV) (**Figure 4.8G**) [88], and peaks arising from the $2p_{3/2}$ and $2p_{1/2}$ states of the sulphonates present in PTS (164.7 and 165.2 eV) (**Figure 4.8H**) [89]. The presence of peaks arising from the $2p_{3/2}$ and $2p_{1/2}$ states of the sulphates from F6 (168.5 and 169.4 eV) were also observed (**Figure 4.8I**) [90]. This peak is not present in the PEDOT:PTS:Dextran coated electrodes, while there appears to be some sulphate impurity in the pristine PEDOT:PTS coated electrodes, which could be from the electrolyte or formed during the electrodeposition process. The positions of C peaks and the relative compositions can be found in **Figure 4.10**.

Analysis of the Neurotropic and Anti-inflammatory Effects of Neuroelectrode Functionalisation with a Heparan Sulphate Mimetic

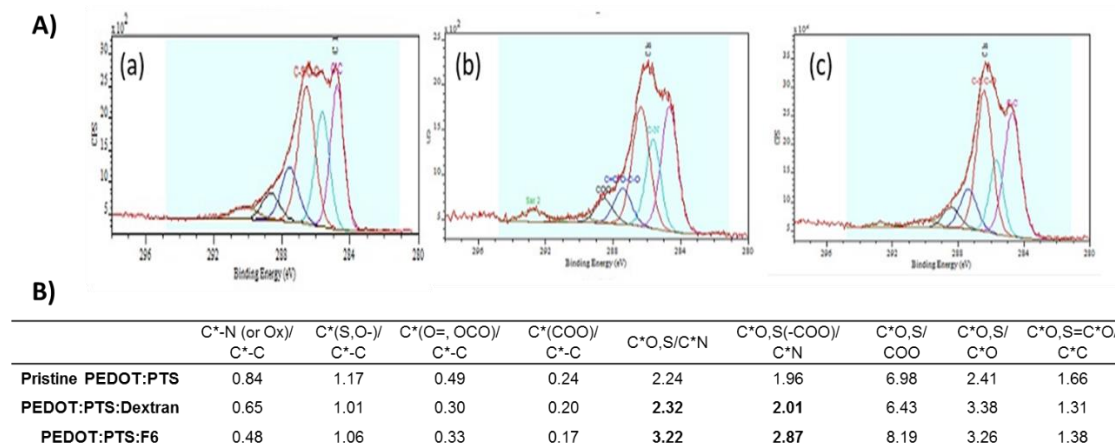


Figure 4.10 The positions of C peaks and the relative compositions. A) X-ray photoelectron spectra of (a) pristine PEDOT:PTS coated microelectrode, (b) PEDOT:PTS:Dextran coated microelectrode, and (c) PEDOT:PTS:F6 coated microelectrode showing the presence of carbon in various oxidation states. The C-N bond cannot be used to discern the percentage of alanine moiety present as a substitution on heparan sulphate mimetic-F6, because trace amounts of acetonitrile from the electrolyte could be present contributing to this peak in all three coated microelectrodes. C* denotes partially oxidised carbon. Table giving the relative atomic percentages of these bonds in coated microelectrodes is presented in B) the relative increase in the percentages of C*O,S/C*N and C*O,S(-COO)/C*N bonds between PEDOT:PTS:Dextran and PEDOT:PTS:F6 (highlighted in bold), shows the increase in N possibly due to presence of phenylalanine component in F6.

The data presented above reports on the super-hydrophilic chemical character of the PEDOT:PTS:F6 coated microelectrodes owing to the successful incorporation of F6 compared to pristine PEDOT:PTS coatings. This favourable chemical surface character of the PEDOT:PTS:F6 coating is important for material performance towards the development of mimetic neural coatings.

4.4.2 Electrochemical Characterisation

The selection of dopants and their ionic nature are of particular importance in electrochemical deposition, and the formulation of electrically stable conducting

polymers as neuroelectrode coatings [33, 91-95] and ultimately impact upon the materials physico-chemical, electrical and biological characteristics [33, 96].

Although a number of studies have shown that the incorporation of biomolecules as dopants within a conducting polymer can initiate biological responses *in vitro* [2, 25, 27, 28, 34, 36, 97], a majority of these studies also note an associated deterioration in the conducting polymer electrochemical properties relative to pristine polymers or polymers doped with inorganic ionic species [32, 95, 98, 99]. Research to date on the electrochemical effects of doping conducting polymers with biochemical molecules has not been extended to the effect of HS mimetic incorporation into PEDOT derivatives. However, initial physicochemical analysis indicated that PEDOT:PTS:F6 electrode coatings presented a significantly rougher, super-hydrophilic surface relative to pristine PEDOT:PTS coating, suggesting that PtIr microelectrodes coated with this chemistry would exhibit an enhanced charge transfer capability and neural stimulation efficacy.

To assess the electroactivity and electrochemical stability of electrodeposited chemistries, CV was performed with PtIr, pristine PEDOT:PTS and PEDOT:PTS:F6 coated microelectrodes, recorded in PBS with microelectrodes possessing a surface area of 0.054 mm² (**Figure 4.11A**). CV curves of PEDOT:PTS:F6 coated microelectrodes demonstrated defined oxidation – reduction peaks and demonstrated a strong capacitive behavior, especially within the potential range from -0.2 V to 0.8 V (vs. Ag/AgCl), when compared to PEDOT formed in the presence of conventional sulphonate anion PTS only. Of note, the additional redox peaks observed in the CV curve of PEDOT:PTS:F6 coated microelectrodes may further suggest the pseudocapacitance behaviour of these electrodes [100]. This may be attributed to the super-hydrophilic character of the PEDOT:PTS:F6 coating, which provides more active sites to fully utilise the coating surface for more efficient ion transport, therefore suggesting an active electrolyte interaction at the surface [100, 101].

As reported previously [102-104], PEDOT coatings have a strong beneficial effect on the CSC of metallic microelectrodes, and a significant increase in the CSC was observed following electrodeposition of PEDOT:PTS onto PtIr microelectrodes, from

Analysis of the Neurotropic and Anti-inflammatory Effects of Neuroelectrode Functionalisation with a Heparan Sulphate Mimetic

$99.7 \pm 17.2 \mu\text{C mm}^{-2}$ ($9.9 \pm 1.7 \text{ mC cm}^{-2}$) for bare PtIr microelectrodes to $697.9 \pm 23.7 \mu\text{C mm}^{-2}$ ($69.8 \pm 2.4 \text{ mC cm}^{-2}$) for pristine PEDOT:PTS coated microelectrodes (**Table 4.7**). The incorporation of F6 induced a further significant increase in the CSC of coated PtIr microelectrodes, to a value of $899.5 \pm 1.6 \mu\text{C mm}^{-2}$ ($89.9 \pm 0.2 \text{ mC cm}^{-2}$). Critically this observed CSC was substantially higher than those recorded with other conducting polymer-based systems employed in neural applications, e.g. surfactant-templated ordered PEDOT (26.7 mC cm^{-2}) [105], PEDOT-CNT (70 mC cm^{-2}) [106] and PEDOT:PSS (75.6 mC cm^{-2}) [103].

Impedance spectra of PEDOT:PTS:F6 and pristine PEDOT:PTS coated microelectrodes and a control PtIr microelectrode group were obtained via a three electrode set-up to assess the effects of F6 doping on film resistance **Figure 4.11B**. The Bode plot indicates that PEDOT:PTS:F6 coated microelectrodes exhibited the lowest impedance profile in the low frequency range (below 1 Hz). For the rest of the evaluated frequencies (1 Hz to 100K Hz), PEDOT:PTS:F6 coated microelectrodes and pristine PEDOT:PTS coated microelectrodes show similar profiles, and a significant decrease in impedance relative to uncoated microelectrodes in the 0.1 Hz to 1K Hz range. Further, bare PtIr microelectrodes at higher frequencies (1 Hz to 100K Hz) presented low impedance values, while the ionic conduction behaviour of the pristine PEDOT:PTS and PEDOT:PTS:F6 coated microelectrodes evolve towards higher impedance magnitudes at this range of frequencies. This, in turn, relates to the relaxation phenomena shown by the polymeric coated microelectrodes at the lower frequencies where they presented a marked electrolytic/capacitance behaviour, leading to higher impedance values at high frequencies [107, 108]. However, due to the complex character of the impedance response, which is typical for microelectrodes and microelectrode arrays [109], Nyquist plots were generated to compare the resistance of the electrodes (**Figure 4.11C**). These plots display both amplitude and phase angle on a single plot using frequency as a parameter, and, when fitted with an appropriate equivalent electrical circuit, can be used to provide the quantification of electrical properties of all elements of the circuit. Through detailed analysis of the Nyquist plots, it was possible to report on the charge transport mechanism and to extract solution resistance from the overall impedance profile and

study only the parameters related to the properties of electrodeposited coatings [36]. The equivalent circuit for pristine PEDOT:PTS and PEDOT:PTS:F6 coated microelectrodes included bulk solution resistance of the polymer and the electrolyte (R_1), double layer capacitance (C_1), resistance of the electrolyte (R_2), constant phase element (CPE), charge transfer (R_3) and Warburg impedance of the polymer coating (W), second capacitor element (C_2) as well as charge transfer resistor (R_4), (**Figure 4.11D**) as described previously [110]. In the case of bare PtIr microelectrodes, the equivalent circuit was the same except for the Warburg impedance element as the polymer coating was not present (**Figure 4.11E**). The simulation data confirmed the lowest resistance profile of PEDOT:PTS:F6 coated microelectrodes ($17.0 \pm 3.5 \text{ k}\Omega$), when compared to pristine PEDOT:PTS ($41.9 \pm 2.1 \text{ k}\Omega$) and bare PtIr ($591.9 \pm 144.8 \text{ k}\Omega$) microelectrodes (**Table 4.7**).

It can be hypothesised that F6 acted as a stable dopant for PEDOT, as observed with electrodeposited PEDOT:PSS, for which positively charged PEDOT oligomers are attached to the negatively charged, high molecular weight PSS, resulting in the stacked arrangement of polythiophene rings responsible for high conductivity of the material [111, 112]. Similarly, it can be hypothesised that the F6 counterion enhances the self-arrangement of growing PEDOT chains with more defined oligomers than occurs in the presence of PTS alone [15, 111, 112]. It can also be argued that the morphological and super-hydrophilicity properties of the PEDOT:PTS:F6 coated microelectrodes, further increase the availability of sites for charge transfer and contribute to the observed improvement in CSC of PEDOT:PTS:F6 coated microelectrodes relative to pristine PEDOT:PTS coated microelectrodes which are represented by the increased conductivity of the PEDOT:PTS:F6 coated microelectrodes [15, 82, 113]. The benefit of F6 as the counterion for the functionalised PEDOT:PTS:F6 coating is here shown with the potential of a structure-electronic surface that lays foundation for future coating-electrode design.

Analysis of the Neurotropic and Anti-inflammatory Effects of Neuroelectrode Functionalisation with a Heparan Sulphate Mimetic

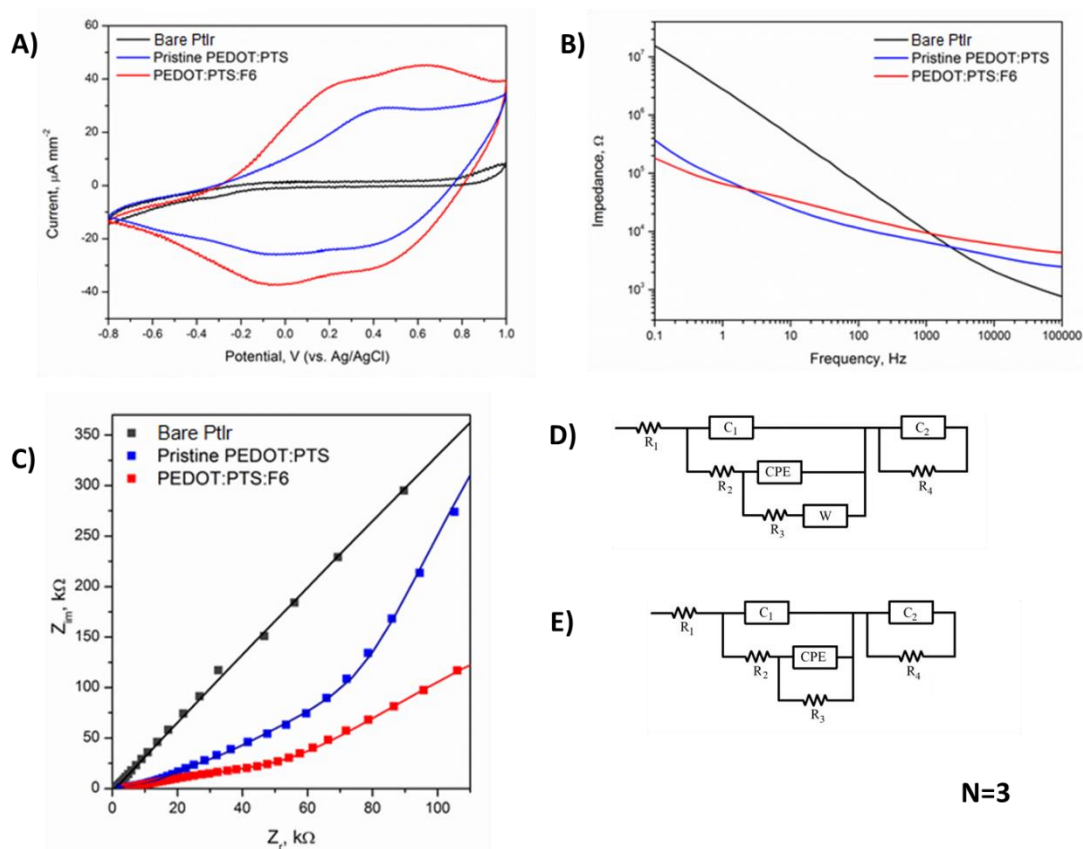


Figure 4.11 Electrochemical analysis of PEDOT:PTS:F6 coated microelectrodes.

A) Cyclic voltammograms (CVs) of bare Platinum/Iridium (PtIr) microelectrodes, pristine PEDOT:PTS and PEDOT:PTS:F6 coated microelectrodes. CVs were recorded in 1X phosphate-buffered saline (PBS) at a scan rate of 100 mV s⁻¹. Bode B) and Nyquist C) plots comparing the EIS spectra of bare Platinum/Iridium (PtIr) microelectrodes, pristine PEDOT:PTS, and PEDOT:PTS:F6 coated microelectrodes. D) and E) represent the electrical equivalent circuit used to analyse experimental data of the coated microelectrodes and bare Platinum/Iridium (PtIr) microelectrodes, respectively. Results are ± STD.

Table 4.7 Electrochemical performance of PEDOT:PTS:F6 coated microelectrodes. The charge storage capacity (CSC) was evaluated from the cathodic region of cyclic voltammograms (CVs) recorded in 1X phosphate-buffered saline (PBS) at 100 mV s⁻¹ scan rate (potential range: -0.8 V to 1 V vs. Ag/AgCl). The

Analysis of the Neurotropic and Anti-inflammatory Effects of Neuroelectrode Functionalisation with a Heparan Sulphate Mimetic

calculated resistance values (R_3) of bare Platinum/Iridium (PtIr) microelectrodes, pristine PEDOT:PTS and PEDOT:PTS:F6 coated microelectrodes after equivalent circuit analysis. Results are \pm STD. $N=3$

	CSC, [$\mu\text{C mm}^{-2}$]	R_3 [k Ω]
PtIr	99.7 \pm 17.2	591.9 \pm 144.8
Pristine PEDOT:PTS	697.9 \pm 23.7	41.9 \pm 2.1
PEDOT:PTS:F6	899.5 \pm 1.6	17.0 \pm 3.5

4.4.3 Biological Characterisation

The aim of reducing inflammation while promoting neural tissue integration and maintaining device functionality represents a paradigm of the field of bio-interface engineering [21, 30, 98, 114-120]. GAGs, as key components of the ECM architecture, and as charged biomolecules that can act as counterions in the electrochemical polymerisation of conducting polymers, represent ideal dopants for the formulation of functional conducting polymer interfaces to modulate cellular function and tissue homeostasis [121, 122].

In particular, the HM F6 has been shown previously to present efficacy in the regulation of neurodegenerative diseases including the tauopathies and synucleinopathies *in vitro* and *in vivo* by blocking the internationalisation and propagation of protein aggregates [60]. Therefore, it was the hypothesis of this work that through the incorporation of the F6 as co-dopant for EDOT electrical polymerisation biomimetic coatings could be developed to promote neural integration and minimise the inflammatory response associated with reactive gliosis *in vitro*.

Initially, to determine a release profile of the HS mimetic F6 from the PEDOT:PTS polymer and to understand the bioactivity of the F6 in subsequent *in vitro* culture studies, the elution profile of PEDOT:PTS:F6 coated electrodes was assessed through a spontaneous passive mode over a period of 21 days simulating *in vivo* conditions (constant agitation under 37° degrees), (**Figure 4.12**). The spontaneous elution profile shows an initial burst of the F6 taking place within the first three days of the experiment with observed eluted F6 concentrations of 5.9 $\mu\text{g ml}^{-1} \text{cm}^{-2}$, followed by a

slow increase by day seven to reach a plateau with a released concentration of F6 of $11.1 \mu\text{g ml}^{-1} \text{cm}^{-2}$ by day twelve. This behavior is consistent with the commonly observed pattern of spontaneous passive release of biomolecules from polymeric matrices observed by others [21, 123, 124], a trend associated with the elution of the active molecules from the near-surface region of the matrix.

Further, and in recognition of the excellent electrochemical properties of the PEDOT:PTS:F6 coatings, these results were compared to an electrically active mode of F6 release from bio-functionalised coated electrodes to evaluate the effective release of F6 in response to a therapeutically relevant voltage pulse (**Figure 4.12**). It has been shown that when bioactive counterions enter a polymeric conducting matrix and under electrical stimulation regimes, the matrix expands and when they exit it contracts, called electrochemical actuators [125]. Thus, the extent of expansion or contraction of the electroactive controlled system allows, for spatial and temporal release modes to be achieved [125, 126]. PEDOT:PTS:F6 coated microelectrodes were subjected to a biphasic potential pulse of 5-second duration to apply a reduction potential (-0.5 V) followed by a 5-second application of an oxidative potential (+0.5 V). Stimulation conditions mimicked those of the passive study but under a stimulation regime of 50 cycles (corresponding to 500 s) every day over a period 21 days (approx. 1000 stimulations in total) [31, 127-129].

In contrast to the spontaneous passive release of F6, with electrically triggered PEDOT:PTS:F6 coated electrodes the concentration of F6 increased linearly over time and to reach a concentration of $44.7 \mu\text{g ml}^{-1} \text{cm}^{-2}$ by day 20, a concentration that was shown to promote high cell viability (**Figure 4.4**) when added unbound into culture. Interestingly, the F6 released from electrically active electrodes exhibited a release profile similar to that of the electrically passive electrodes until day seven. Following this initial period, bi-phasic stimulation induced a linear release of significantly higher amounts of F6 than those of electrically passive electrodes. Thus, it is the substantial amount, especially when comparing the time of active stimulus application (3 hours) to the total time of passive release (504 hours). Evaluation of F6 release triggered by electrical stimulus revealed the active contribution of 66% to the

Analysis of the Neurotropic and Anti-inflammatory Effects of Neuroelectrode Functionalisation with a Heparan Sulphate Mimetic

totally eluted mass in 0.6 % of the total time. It follows that by modification of the electrode stimulation parameters, it may be possible to temporally control the release profile of F6, to maximise the therapeutic potential *in vivo* or to prolong the elution period [127], important considerations for future work into developing functionalisation approaches for long term applications.

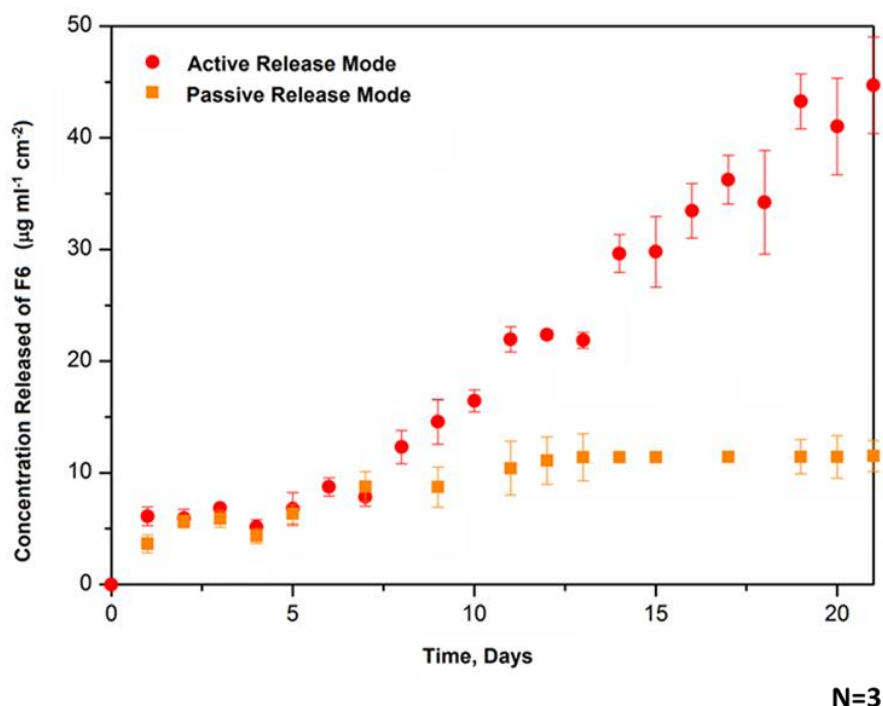


Figure 4.12 Concentration profile of heparan sulphate mimetic- F6 released from PEDOT:PTS:F6 coated electrodes in the passive (orange squares) and active (red dots) modes for a period of 21 days under simulating *in vivo* conditions (constant agitation under 37° degrees). For the active release mode, 50 stimulation cycles were applied every day over 21 days which resulted in approx. 1000 stimulations over this period. The stimulation regime was a biphasic potential pulse, consisting of a 5-second application of a reduction potential (-0.5 V) followed by a 5-second application of an oxidative potential (+0.5 V). Results are \pm STD.

To further assess stability of the electrochemical performance of the coated microelectrodes, pristine PEDOT:PTS and PEDOT:PTS:F6 coated microelectrodes and bare PtIr microelectrodes were subjected to 1000 continuous stimulation cycles corresponding to the cumulative stimulus used for the active release mode of the F6.

Analysis of the Neurotropic and Anti-inflammatory Effects of Neuroelectrode Functionalisation with a Heparan Sulphate Mimetic

The final performance of the microelectrodes was evaluated in terms of changes in charge storage capacity after stimulation as detailed in **Figure 4.13**. Electrodes exhibited maintained electrical integrity after electrical stimulation conditions, with the incorporation of the F6 within the PEDOT matrix.

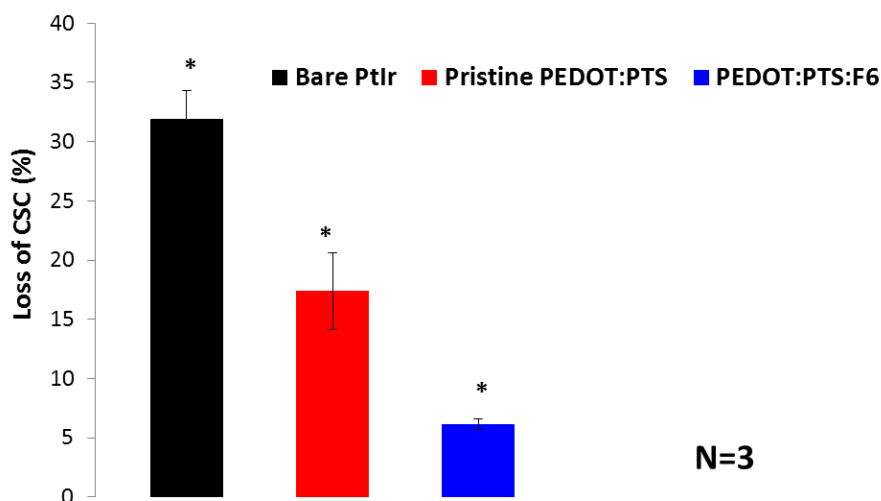


Figure 4.13 *Electrical stability of the PEDOT:PTS:F6 microelectrodes. Plot of percentage loss of charge storage capacity (CSC) after 1000 continuous stimulation cycles of biphasic potential pulses, consisting of a 5-second application of a reduction potential (-0.5 V) followed by a 5-second application of an oxidative potential (+0.5 V). Important significant differences between the bare Platinum/Iridium (PtIr) microelectrodes and the PEDOT-based coated microelectrodes were observed. PEDOT:PTS:F6 coated microelectrodes were the most stable followed by pristine PEDOT:PTS coated microelectrodes and bare Platinum/Iridium (PtIr) microelectrodes after. Results are \pm STD, $\star = p < 0.05$.*

The bioactivity of PEDOT:PTS:F6 coatings was evaluated *in vitro* with planar 1.6 cm² platinum (Pt) coated electrodes using a primary ventral mesencephalic (VM) mixed neural cell population. A non-sulphated polymeric dextran was also used as negative control to understand the effect of the sulphation pattern provided by the mimetic on cell function. A sputtered platinum (Pt) group was also used in the *in vitro* studies as a representative electrode control material.

Figure 4.14A shows representative fluorescent micrographs of VM derived mixed cultures of neurons and astrocytes cultured on experimental and control electrodes. All groups were evaluated over a period of three, seven and ten days in culture. The persistence of neurons and astrocytes on each of the experimental and control groups as a function of time is presented in **Figure 4.14B**. It was evident that electrodes subjected to the electrodeposition of PEDOT:PTS doped with non-sulphated polymeric dextran (PEDOT:PTS:Dextran) induced an overall marked increase in astrocyte density, accompanied with a significant decrease in neuronal presence as a function of time. A trend that contrasted significantly to all other experimental groups and to Pt control substrates. By day ten, the PEDOT:PTS:Dextran coated electrodes exhibited an astrocytes presence of 92.86 % and a neurons presence of 7.15 %. In contrast, a maintained significant lower presence of astrocytes on PEDOT:PTS:F6 coated electrodes over that of Pt control and pristine PEDOT:PTS coated electrodes was consistently observed over time, findings that were coupled with an interesting and significantly higher presence of neural density on these electrodes at each time point relative to all the experimental and control groups. By day ten, the recorded percentage of astrocytic cell density on the PEDOT:PTS:F6 coated electrodes was 42.86 % with a percentage of neuron presence of 57.14%, followed by pristine PEDOT:PTS coated electrodes with a 46.39 % astrocytes presence and a 53.60 % neuron presence and Pt controls with 61.97% astrocytes presence and 38.03% neural density.

In conjunction with cell density, as an indicator of cell viability, neurite length on experimental and control substrates was also analysed (**Figure 4.14C**). At day three, similar neural lengths were observed in neurons cultured on pristine PEDOT:PTS coated electrodes and PEDOT:PTS:F6 coated electrodes with neural lengths of $142.21 \mu\text{m} \pm 4.21$ and $149.60 \mu\text{m} \pm 7.45$ respectively. Neurite length was significantly lower than those of neurons cultured on Pt electrodes on which mean neurite length was of $175.08 \mu\text{m} \pm 10.55$, but significantly higher than the neurite length observed on the PEDOT:PTS:Dextran coated electrodes of $18.85 \mu\text{m} \pm 3.15$. This trend was lost by day seven and neurite lengths were significantly increased on PEDOT:PTS:F6 coated electrodes relative to Pt control and PEDOT:PTS coated

Analysis of the Neurotropic and Anti-inflammatory Effects of Neuroelectrode Functionalisation with a Heparan Sulphate Mimetic

electrodes. However, neurite length on the non-sulphated polymeric dextran PEDOT:PTS:Dextran control samples could not be quantified at the subsequent time points due to a significantly reduced neuron presence, rendering the application of the stereology method used for the quantification of length invalid.

Additional significant differences in neural length were observed by day ten, with significant neurite elongation exhibited in cells cultured on the PEDOT:PTS:F6 coated electrodes ($589.20 \mu\text{m} \pm 2.90$) relative to bare platinum control ($566.36 \mu\text{m} \pm 6.35$) and pristine PEDOT:PTS coated electrodes ($325.76 \mu\text{m} \pm 4.66$).

Analysis of the Neurotropic and Anti-inflammatory Effects of Neuroelectrode Functionalisation with a Heparan Sulphate Mimetic

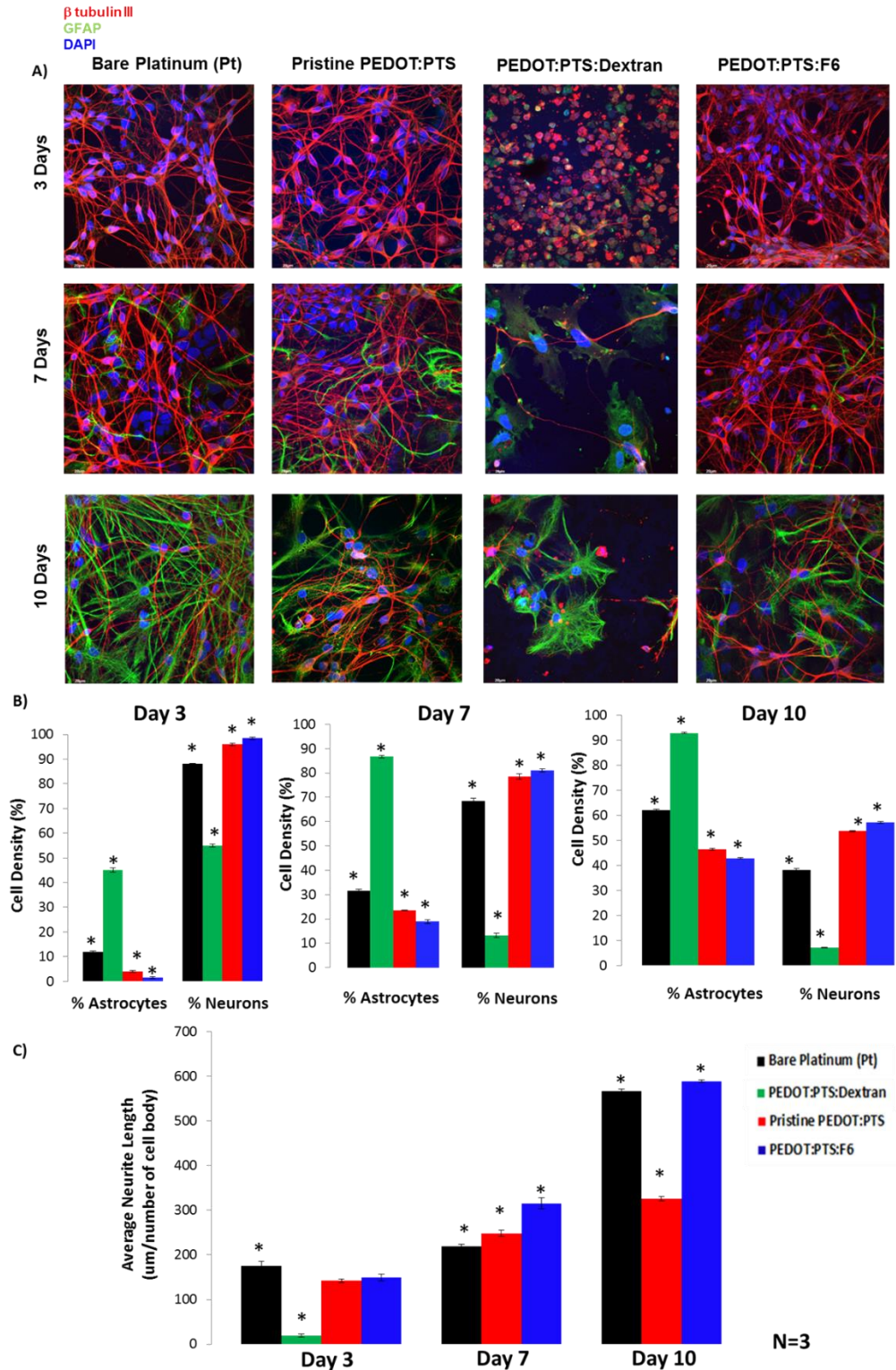


Figure 4.14 Cytocompatibility of PEDOT:PTS:F6 coated electrodes. A) Fluorescent images of primary ventral mesencephalic (VM) mixed cell population grown on each

Analysis of the Neurotropic and Anti-inflammatory Effects of Neuroelectrode
Functionalisation with a Heparan Sulphate Mimetic

of the bare platinum (Pt) electrodes and pristine PEDOT:PTS, PEDOT:PTS:Dextran and PEDOT:PTS:F6 coated electrodes for three, seven and ten days in culture. Neurons are visualised by anti β -tubulin III, in red, astrocyte cells by anti-GFAP, in green and nuclei are visualised by DAPI, in blue. Bar = 20 μ m, objective 60 \times magnification. Cell density (%) analysis of astrocytes and neurons presence on each of the electrodes is presented in B). An overall significant ($p < 0.05$) enhancement in viability of neurons was observed in PEDOT:PTS:F6 coated electrodes. Neural length analysis of electrodes presented in C) showed with significant ($p < 0.05$) longer neurite lengths the neurons grown on PEDOT:PTS:F6 coated electrodes, suggesting on an overall neurotrophic effect of these electrodes owing to the presence of heparan sulphate mimetic-F6. Results are \pm STD. $\star = p < 0.05$.

These results show that the PEDOT:PTS:Dextran coated electrodes overall induced poor viability of the primary VM neural population relative to pristine PEDOT:PTS coated electrodes and functionalised PEDOT:PTS:F6 coated electrodes, resulting, as a consequence, in an over proliferation of astrocytes. Moreover, this finding has implications for the role of sulphation on the modulation of neural survival, as seen by others [36, 130-132]. In fact the incorporation of the F6 within the PEDOT:PTS polymer matrix showed that these coatings do not enhance astrocyte proliferation and adhesion relative to control Pt and to pristine PEDOT:PTS coated electrodes for up to ten days in culture, rather, the presence of F6 significantly enhanced neuron survival and supported neurite extension of the mesencephalic neuros *in vitro* relative to all experimental and control groups. Therefore, a neurotrophic effect imparted by F6 incorporated in the PEDOT:PTS polymer matrix is suggested.

Further, the synthesis of pro-inflammatory cytokines from VM populations was assessed *in vitro* to support the inflammatory modulatory effect of F6 when incorporated in the PEDOT:PTS matrix. Chemokines IFN- γ , TNF- α , IL-6, IL-5, and KC/GRO were selected for analysis, signaling factors involved in mediating neuronal-glia interactions [133, 134] [65, 135-139]. The release profiles were compared across the experimental groups, controls and with an additional inflammatory control group, VM cells cultured on Thermanox® Plastic Coverslips

Analysis of the Neurotropic and Anti-inflammatory Effects of Neuroelectrode
Functionalisation with a Heparan Sulphate Mimetic

(tissue culture plastic) which received a stimulus of interleukin-1beta (IL-1 β) at a dose of 10 ng ml⁻¹. Optimisation of different concentrations of IL-1 β as inflammatory stimuli on VM cells cultures is shown in **Chapter 3**.

The secretion of pro-inflammatory cytokines and chemokine factors in mixed cell populations cultured on all experimental and control groups is presented in **Figure 4.15A-E**.

Analysis of the Neurotropic and Anti-inflammatory Effects of Neuroelectrode Functionalisation with a Heparan Sulphate Mimetic

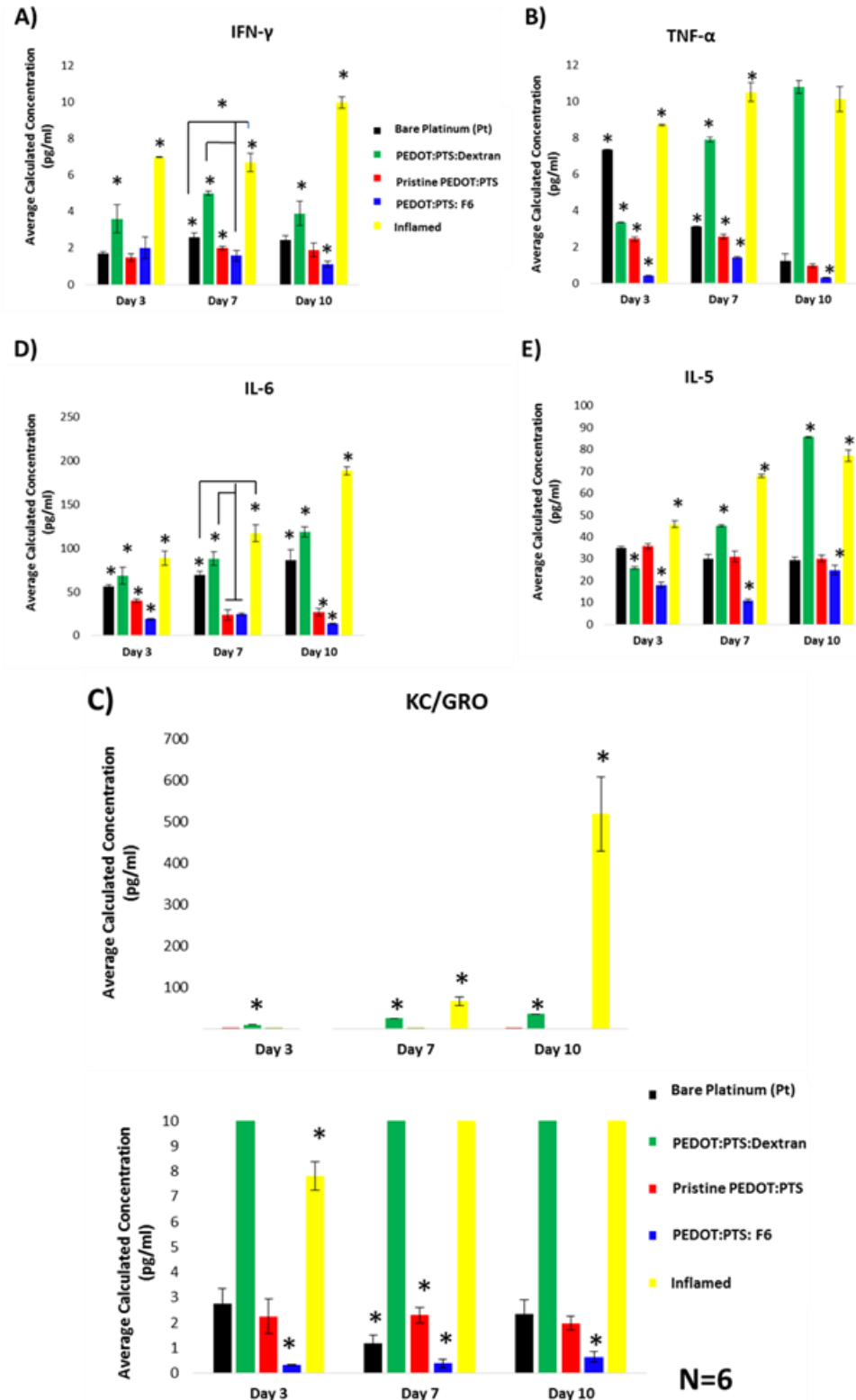


Figure 4.15 Comparative pro-inflammatory derived cytokines and chemokine factor profiling for interferon- γ (IFN- γ ;A), tumor necrosis factor- α (TNF- α ;B),

chemokine factor CXCL-1 (KC/GRO;C), interleukin-6 (IL-6;D) and interleukin-5 (IL-5;E). The release expression of each of the signaling molecules is analysed from primary ventral mesencephalic (VM) mixed cell population supernatants collected at day three, seven and ten days on bare platinum (Pt) electrodes, pristine PEDOT:PTS, PEDOT:PTS:Dextran and PEDOT:PTS:F6 coated electrodes. An important effect is seen on the PEDOT:PTS functionalised with the heparan sulphate mimetic-F6 coated electrodes, which presented significantly low release profiles for each cytokine and chemokine factor analysed after ten days in culture. Results are \pm STD, $\star = p < 0.05$.

Figure 4.15A-B show the release profiles of IFN- γ and TNF- α , respectively. These cytokines are known to act in synergy [140-142], and showed a similar release profile. It was observed that the release of IFN- γ from VM cells cultured on PEDOT:PTS:F6 coated electrodes underwent a linear decrease with time, and was significantly lower by day ten relative to IFN- γ synthesis on Pt control, PEDOT:PTS based-coated electrodes, and inflamed control, respectively. Interestingly, the IFN- γ release profile of VM cells cultured on Pt and pristine PEDOT:PTS coated electrodes was maintained at comparatively similar levels by day ten. Further, PEDOT:PTS:Dextran coated electrodes induced the second highest VM release profile of IFN- γ after that of cells cultured on the inflamed control. Conversely, TNF- α release profiles showed an overall linear decrease with time from VM cells cultured on bare Pt electrodes, pristine PEDOT:PTS and PEDOT:PTS:F6 coated electrodes, yet cells cultured under inflamed conditions and on PEDOT:PTS:Dextran control groups presented a consistent increase in TNF- α release. By day ten, a significantly higher release profile of TNF- α was observed with VM cells cultured on the PEDOT:PTS:Dextran coated electrodes which was comparable to that observed in VM cells cultured under inflamed control conditions. Control Pt, pristine PEDOT:PTS and PEDOT:PTS:F6 groups, were associated with a significant reduction in TNF- α synthesis, with an overall significantly lower TNF- α expression by the cells cultured on the functionalised PEDOT:PTS:F6 electrodes.

VM cell expression of the chemoattractive factor CXCL1 [143, 144] also known as KC/GRO, was significantly reduced at all time points when cultured on

Analysis of the Neurotropic and Anti-inflammatory Effects of Neuroelectrode Functionalisation with a Heparan Sulphate Mimetic

PEDOT:PTS:F6 coated electrodes relative to all experimental and control groups (**Figure 4.15C**). In contrast, a significantly higher production of KC/GRO was observed with control PEDOT:PTS:Dextran coated electrodes and with the inflamed group.

Further, an increase in the secretion of cytokines IL-6 [145, 146] (**Figure 4.15D**) and IL-5 [147-149] (**Figure 4.15E**), as result of the co-stimulatory cross-talk of cell-cell interactions produced by the nature of the mixed VM populations was observed, indicating the biological protection offered by the PEDOT:PTS:F6 coated electrodes relative to control Pt electrodes, pristine PEDOT:PTS and PEDOT:PTS:Dextran coated electrodes, and inflamed control respectively. Also, the release expression of IL-6 and IL-5 by the VM populations cultured on the PEDOT:PTS:Dextran coated electrodes, reflects on the overall promotion of a more pro-inflammatory milieu, which relates to the poor VM cell viability and neural outgrowth observed on these electrodes.

The modulation of cytokine and chemokine activity in VM populations cultured on PEDOT:PTS functionalised with F6 indicates the protective effect of F6 on matrix proteins from protease activities [35, 44], which translates to an enhanced availability [40, 54, 65, 144] of neurotropic growth factors.

Considerable research has shown that the ECM presents a spatial network of functional GAGs moieties located on proteoglycans which are present at the cell surface [151-152] and exert biological activities by interacting with a broad spectrum of protein ligands including growth factors, cytokines and ECM proteins [152]. The molecular mechanism of GAGs like HS that mediate cell signaling has been extensively studied, and a high binding affinity for FGF-2 promotes the formation of a stable tertiary signal complex [153]. HS-protein binding processes are known to be mediated by specific sulphation patterns that recognise protein binding sites [154] and promote cellular signaling processes including cell proliferation and differentiation [73] and more specifically, they play essential roles in inflammation [65, 155], wound healing [156], angiogenesis [157] and anticoagulation [158, 159]. Of note, all these processes are not mediated by a single generic HS polysaccharide,

but by many different HS species which differ in their sulphated disaccharide profile. Here F6, a chemically modified molecule from the HM library was synthesised with a 0.7 (70%) statically available sulphate substitution (dsS) along the saccharidic chains of a sulphation pattern on 2-O-sulphated in percentage (**Figure 4.3**). These structural properties of F6 have particularly important correlations with the findings within this work and it can be hypothesised that the neurotrophic and neuroprotective effects observed with PEDOT:PTS:F6 coated electrodes were potentiated through binding with the anionic characteristics of F6. In consequence, potentialise the binding with secreted neurotropic growth factors such as FGF-2 [151, 152, 160] and VEGF [161, 162].

FGF-2 has been shown to promote neural survival and the development of ventral midbrain neurons with a neurotrophic function that enhances neural networking, neural outgrowth and guidance [163-166]. Moreover, VEGF has been shown to promote neuroprotection indirectly by activating the proliferation of glia and by promoting neurogenesis and neuronal patterning in mixed embryonic VM cultures [167, 168].

Therefore, as a proof of concept study, the binding capacity of F6 with FGF-2 and VEGF were assessed with a competitive binding affinity assay as previously described [73] (**Figure 4.16**). The binding potential of F6 and other exogenous GAGs HS and heparin to FGF-2 and VEGF was assessed within the limits of F6 concentrations that were previously shown to maintain high cell viability (**Figure 4.4**) when added unbound into the culture medium. Heparin was used as a biochemical control (100% relative effect), and naturally occurring HS as relevant physiological control. Dextran was further used as a non-sulphated GAG control.

Analysis of the Neurotropic and Anti-inflammatory Effects of Neuroelectrode Functionalisation with a Heparan Sulphate Mimetic

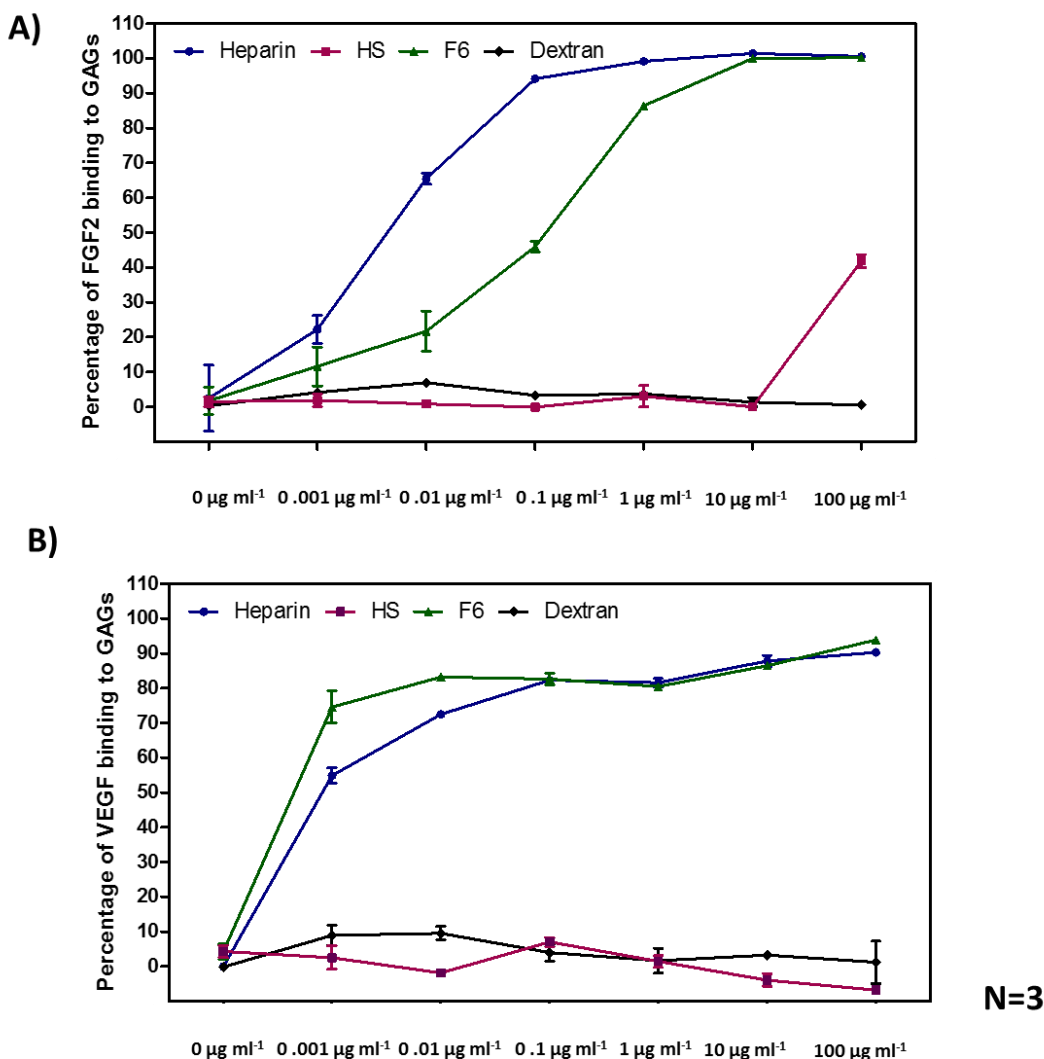


Figure 4.16 Glycosaminoglycans competition assay towards FGF-2 and VEGF binding. F6 shows a strong binding capacity to FGF2 and VEGF in a heparin-like manner.

Figure 4.16 (A-B) shows the binding of F6 to FGF-2 and VEGF respectively. It is interesting to observe that F6 binds to both growth factors in a heparin-like manner, suggesting the presence of structural binding motifs with 2-O-sulfated and 6-O-sulfated domains for the binding with FGF-2 and VEGF growth factors, respectively [169-172]. But further, this data suggests that F6 adopts a favourable molecular conformation in solution that facilitate the recognition of important biological growth

factors compared to the physiological control HS. The introduction of hydrophobic moieties in polyanions, as is the case of the L-phenylalanine methyl ester in F6, can be expected to increase their affinity for proteins and participate in the control of the conformational changes associated to pathogenesis [78]. Our results suggest that there is a structural rationale for the binding potential of F6 to the studied growth factors. This rationale can be used to analyse these activities through recognition studies using molecular and conformational analysis.

Overall, these findings are particularly important for neuroelectrode coating designs with biological dopants as they not only show an overall reduction of inflammation profiling while promoting neural growth through a mechanistic binding with growth factors *in vitro*, but further open up the study of glycan mimetics to potentiate matrix-therapeutics strategies at the neural-tissue interface.

Complementary to the cytokine-protection response, and as part of a synergistic approach with an in-house gliosis antibody microarray as previously detailed in [5], the neuroprotective effect of the PEDOT:PTS:F6 coated electrodes was further evaluated in the context of gliosis, a process shown to decrease adjacent neurons from the electrode *in vitro* and *in vivo* conditions [5-9]. Details of the antibodies used and their corresponding optimised concentrations are in **Table 4.1**.

Unsupervised clustering of the expression of pro-gliosis proteins was performed with VM cells cultured on all experimental and control groups and an additional inflamed control for three days (**Figure 4.17A**) and for ten days *in vitro*. (**Figure 4.17B**).

Analysis of the Neurotropic and Anti-inflammatory Effects of Neuroelectrode Functionalisation with a Heparan Sulphate Mimetic

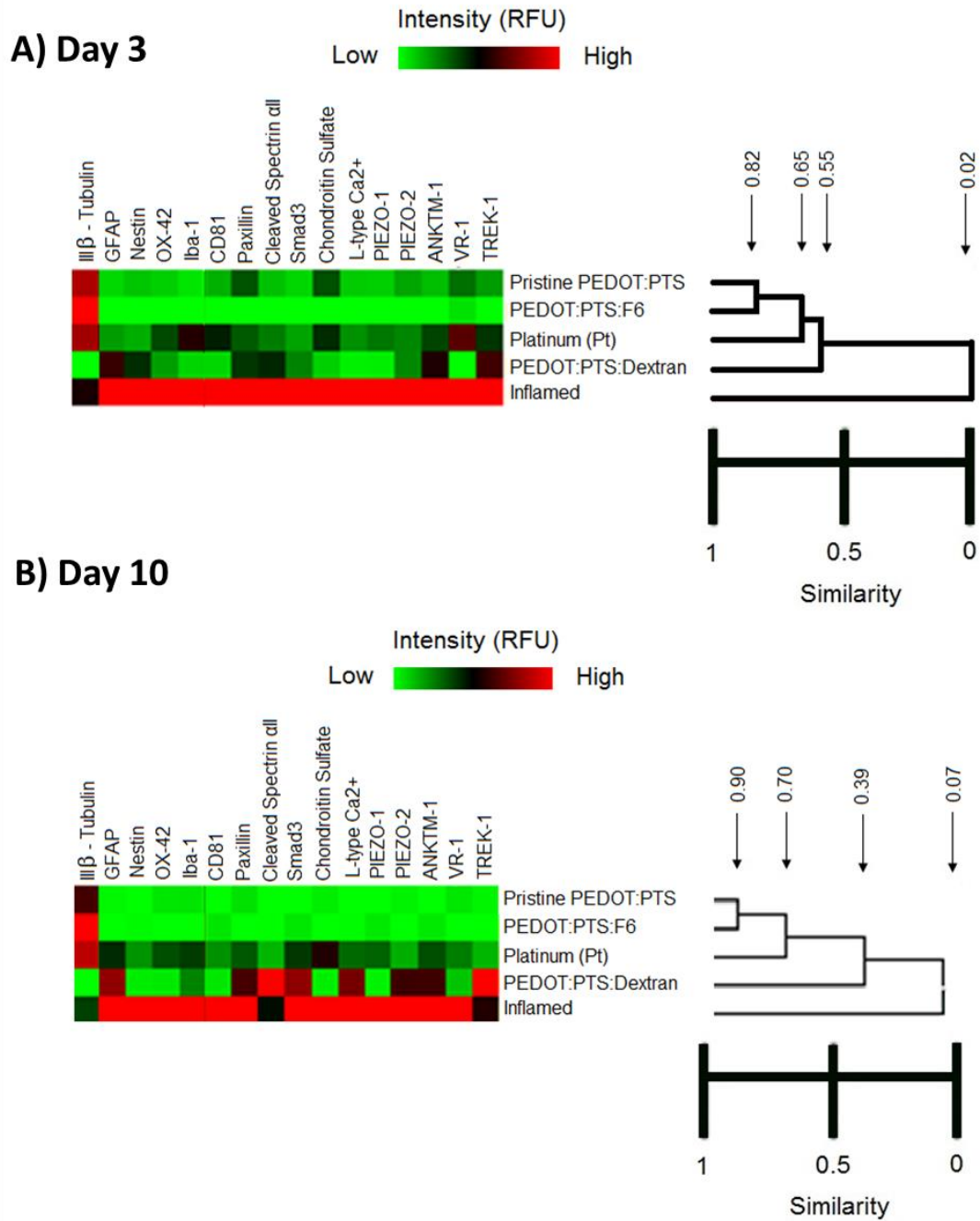


Figure 4.17 Unsupervised clustering of all experimental and control groups and inflamed control, respectively. This analysis clearly defined interestingly hierarchical clusters between experimental sulphated groups: the chemical sulphated pristine PEDOT:PTS coated electrodes and the biological modified PEDOT:PTS:F6 coated electrodes with the heparan sulphate mimetic-F6, and between controls groups with non-sulphated patterns: control material bare platinum, the negative

Analysis of the Neurotropic and Anti-inflammatory Effects of Neuroelectrode Functionalisation with a Heparan Sulphate Mimetic

control for sulphation PEDOT:PTS:Dextran coated electrodes and tissue culture plastic as inflamed control, at both days three A) and ten B) respectively. PEDOT:PTS:F6 coated electrodes showed a remarkable intensity downregulation of reactive astrocytes, microglia and calcium influx markers with an important upregulation of neural response compared to all groups and controls at day three and day ten, respectively. N = 3, 18 data points.

This analysis defined groups with hierarchical similarities between cells cultured on experimental sulphated groups, the chemically sulphated pristine PEDOT:PTS coated electrodes and the biological modified PEDOT:PTS:F6 coated electrodes with F6, followed by control groups with non-sulphated patterns, i.e. control Pt, the negative control for sulphation PEDOT:PTS:Dextran coated electrodes and finally tissue culture plastic as inflamed control, at both three and ten days.

By day three, PEDOT:PTS:F6 coated electrodes induced a marked downregulation in the expression of pro-gliosis proteins relative to all experimental, and inflamed controls. Specifically reductions were observed in the expression of OX42/Iba1 (microglia) [173], GFAP and Nestin (reactive astrocytes) [174, 175], gliosis specific markers such as cleaved spectrin α II [176], Smad3 [177], Chondroitin Sulphate [178] and CD 81 [179, 180], as well as from the changes of transient calcium seen by the expression of L-type Ca^{2+} [181], PIEZO-2 [182], K^+ channels such as TREK 1 [183], and in the low intensity of proteins linked to inflammation such as VR1 [184] and ANKTM1 [185]. Interestingly, by day three a high expression of the neural marker III β Tubulin was observed relative to all experimental, controls and inflamed groups (**Figure 4.17A**). By day ten although PEDOT:PTS:F6 coated electrodes shared a 90% protein expression similarity with the pristine PEDOT:PTS coated electrodes, a significant increase in the expression of β -tubulin was observed, indicating a relative increase in the presence of VM neurons on PEDOT:PTS:F6 functionalised electrodes (**Figure 4.17B**). These findings are consistent with the noticeable neural survival observed on the PEDOT:PTS:F6 coated electrodes (**Figure 4.14B**) and with the suggested neurotropic effect of F6 relative to all experimental, control and inflamed groups. Further and owing to the multifactorial markers of the hallmark of gliosis

Analysis of the Neurotropic and Anti-inflammatory Effects of Neuroelectrode Functionalisation with a Heparan Sulphate Mimetic

evaluated here with the microarray, the results also allude to the overall low inflammation profile offered by the PEDOT:PTS:F6 functionalised electrodes F6.

In contrast, the negative control for glycan sulphation, the PEDOT:PTS:Dextran coated electrodes, exhibited the lowest intensity of the neural marker, III β Tubulin compared to all experimental, and control groups except the inflamed control, at day three and further maintained by day ten. Interestingly, PEDOT:PTS:Dextran coated electrodes induced a GFAP expression profile similar to that of VM cells cultured under inflamed control conditions, but induced a marked differential intensity in the expression of the K^+ ion channel TREK 1 relative to all experimental and control groups. This suggest a disruption of astrocyte K^+ homeostasis, which has been shown to help set the negative resting membrane potential of astrocytes and regulate astrocyte reactivity [186], an effect that is reflected in the over-proliferation of astrocytes observed on these coated electrodes relative to PEDOT:PTS:F6, pristine PEDOT:PTS coated electrodes and Pt controls (**Figure 4.14B**).

Coupled with this, marked upregulations in the expression of cleaved spectrin α II relative to the inflamed control group [176], together with a high expression in Smad3 [177], and paxillian, an adhesion marker used for the healthy stellation of astrocytes [187-189], indicated an overall significant influence on reactive astrocyte adhesion on PEDOT:PTS:Dextran electrodes relative to PEDOT:PTS:F6 and pristine PEDOT:PTS coated electrodes and Pt control electrodes. The further reduced expression of OX42/Iba1 and VR1, markers for microglia [190], and increased expression of ion channel proteins (L-type V [181] and PIEZO-2 [159]) by day ten, may reflect the overall pro-inflammatory nature of PEDOT:PTS:Dextran coated electrodes relative to PEDOT:PTS:F6, pristine PEDOT:PTS coated electrodes and Pt control.

Experimentally, it has been demonstrated that the HS mimetic F6, when incorporated in a PEDOT:PTS polymer matrix, is able to enhance neuron survival and support neural outgrowth while maintaining a low inflammatory and low gliosis micro-environment *in vitro*.

Analysis of the Neurotropic and Anti-inflammatory Effects of Neuroelectrode Functionalisation with a Heparan Sulphate Mimetic

In order to assess the effects of F6 on the glycosylation profile of labelled protein preparations VM populations, a lectin binding assay employing 26 lectins was conducted following three and ten days of culture. Relative fluorescence intensity (RFU) values for lectins that exceeded approximately five times the average median background (1,000 RFU) were considered to have undergone glycan binding and were contributed to the glycosylation pattern.

A marked binding intensity with the lectins SNA-I and AAL was observed in all experimental and control groups (*Figure 4.18*), which indicated the presence of α -(2,6)-linked sialic acid and fucosylation, respectively (*Table 4.2*). AAL has a binding specificity with high affinity for α -(1,6)-linked fucose (Fuc) residues which are found on the chitobiose core of N-linked oligosaccharides, and can also bind with much lower affinity to α -(1,3)- and α -(1,2)-linked Fuc [191, 192] (*Table 4.2*). Interestingly, α -(2,3)-linked sialic acid has been previously shown to be the most abundant sialic acid linkage present in total brain tissue protein [193]. The predominance of α -(2,6)-linked sialic acid in the VM cell protein preparations may be characteristic of the particular type compared to total tissue.

Analysis of the Neurotropic and Anti-inflammatory Effects of Neuroelectrode Functionalisation with a Heparan Sulphate Mimetic

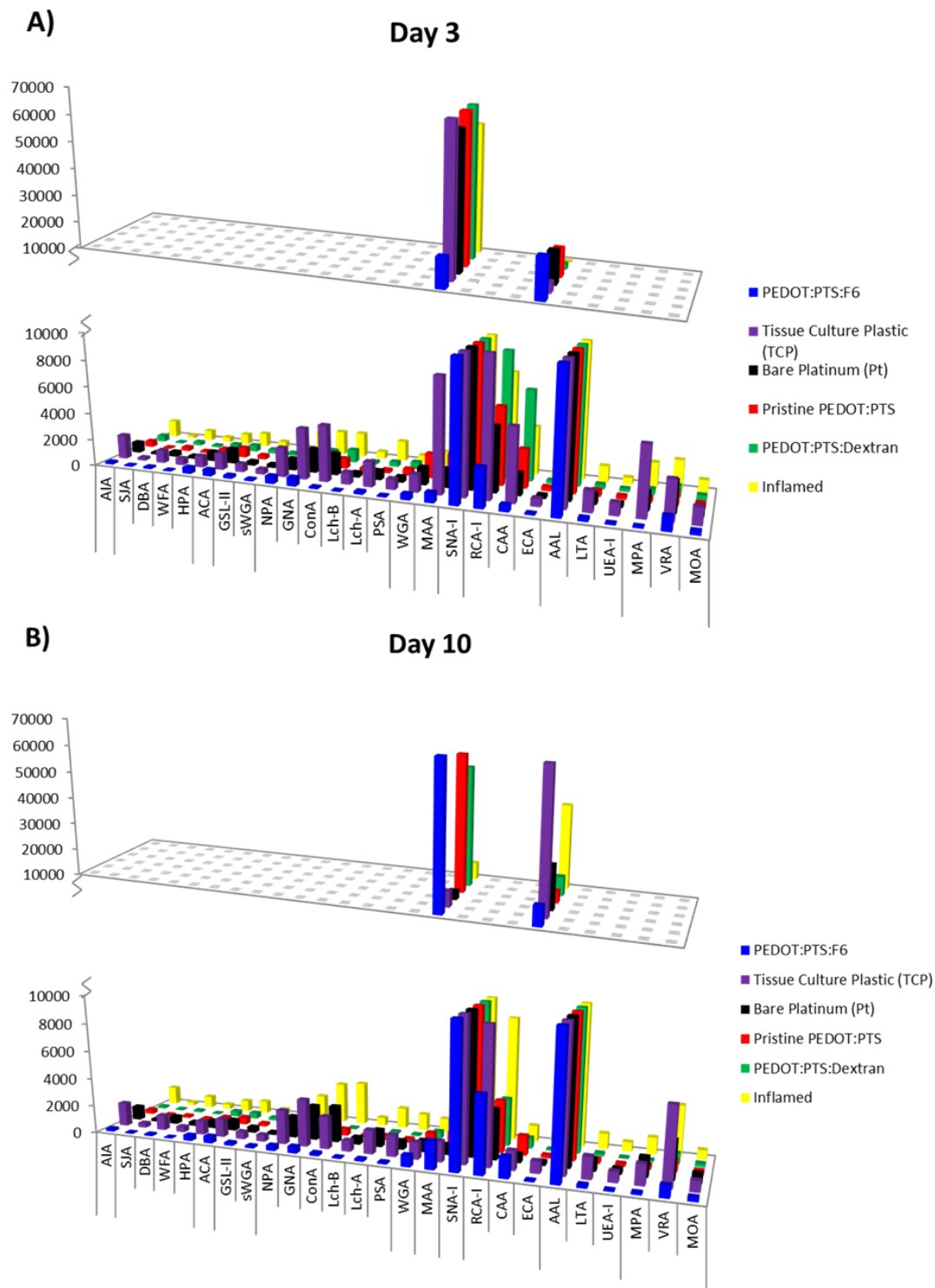


Figure 4.18 Histograms representing the differences in recognition of printed lectins by each of the experimental groups and controls at day three A) and day seven B) respectively. Microarray experiments were carried out using three replicate

Analysis of the Neurotropic and Anti-inflammatory Effects of Neuroelectrode Functionalisation with a Heparan Sulphate Mimetic

slides. The subarrays were printed with each lectin following the order detailed in Figure 4.2 and incubated with fluorescently labelled protein preparations. Results are average \pm standard error. $N = 3$, 18 data points

At day three VM cells cultured on all experimental and control groups exhibited glycosylation profiles with a high binding affinity to SNA-I and AAL, which presented differential low binding affinity on inflamed and tissue culture plastic controls and on PEDOT:PTS:Dextran coated electrodes relative to VM cells culture on Pt controls and pristine PEDOT:PTS, with the highest binding observed in VM cells cultured on PEDOT:PTS:F6 coated electrodes (**Figure 4.18A**). Further, VM cells cultured on PEDOT:PTS:F6 functionalised electrodes, exhibited almost equally intense binding for SNA-I and AAL, with SNA-I binding intensities significantly lower than all other experimental and control groups. Critically, glycoprotein sialylation is known to play a role in modulating the excitability of voltage-gated ion channels, and in mediating cellular adhesion [194, 195]. Moreover, sialic acids can function as ligands for sialic acid-specific receptors, such as siglecs and selectins, facilitating cellular communication and signaling with roles in inflammation [194, 196] and cell fate [197].

Fucosylation, as identified through high binding affinity to AAL has a roles in mediating interactions with selectins and α -(1,6)-linked fucosylation is a common modification of the rat brain N-linked oligosaccharides [193]. This motif has been shown to play an important role in regulating cell neurite formation [198] while a loss of α -(1,6)-fucosylation has been shown to decrease hippocampal potentiation [199]. Interestingly, the observed higher binding affinity for α -(1,6)-fucosylation (AAL) in VM cells cultured on PEDOT:PTS:F6 coated electrode relative to all experimental and control groups may suggest the early trophic effect of F6.

By day ten all experimental conditions were associated with a reduction in SNA-I binding efficiency relative to day three, except for VM cells cultured on PEDOT:PTS:F6 coated electrodes, which exhibited increased SNA-I binding (**Figure 4.18B**). This binding intensity was comparable to all other experimental and control groups at day three. This result may suggest a role for glycoprotein sialylation in

modulating the excitability of voltage-gated ion channels [194, 195]. The promotion of sialic acid expression through electrode functionalisation with the synthetic HS mimetic may be as a response of neuronal control and network excitability through electrical signalling, providing adequate conditions for the appropriate function of neurons and synapses [200, 201]. This data can be further correlated with the downregulation of voltage-gated ion channels observed by the VM cells cultured on the functionalised electrodes, followed by pristine PEDOT:PTS coated electrodes compared to all controls at day ten (**Figure 4.17B**). In turn, impairment of K^+ buffering currents by the altered high expression of TREK-1 channels by astrocytes on PEDOT:PTS:Dextran coated electrodes by day ten, may contribute, particularly to the high sialic acid content observed on these electrodes [202-204]. Results that suggest the importance of orchestrated variable sets of ion channels for homeostasis [205]. Furthermore, the maintained expression of AAL binding for 1,6-fucosylation may suggest to an overall temporal-regulation of intracellular signalling and neural homeostasis offered by the presence of the HS mimetic.

4.5 Conclusion

In the search for biomimicry of the neuroelectrode interface, and with an ultimate goal of mitigating electrode deterioration via reactive host cell response and glial scar formation, PEDOT:PTS electrode coatings were functionalised with a heparan mimetic as a biological dopant for the first time.

The use of F6 as a dopant within PEDOT:PTS electroactive coatings significantly reduced the electrochemical resistance and increased the charge storage capacity of PtIr electrodes, while maintaining electrode stability. Together, neuroprotective and neurotrophic effects were observed *in vitro* with a significant reduction in the inflammatory and gliosis profile noted in a complex primary mixed cell VM culture accompanied by neurogenesis and neurogenesis of the mesencephalic neurons. These trophic characteristics can be explained by the potentiation of synthetic HS mimetic-F6, in the binding of FGF-2 and VEGF growth factors to the functionalised peri-electrode region.

Analysis of the Neurotropic and Anti-inflammatory Effects of Neuroelectrode Functionalisation with a Heparan Sulphate Mimetic

Bio-functionalisation of neural electrodes with PEDOT:PTS:F6 coatings show promise as a functional approach to promote the integration of implanted electrodes through the attenuation of glial scar response and through promoting a neuroprotective response *in vitro*. This work further promotes the exploration of further glycan mimetics to potentiate matrix-therapeutics strategies at the neural-tissue interface.

4.6 References

1. Durand, D. M.; Ghovanloo, M.; Krames, E., *Journal of neural engineering* 2014, 11 (2), 020201.
2. Kim, D. H.; Richardson-Burns, S. M.; Hendricks, J. L.; Sequera, C.; Martin, D. C., *Advanced Functional Materials* 2007, 17 (1), 79-86.
3. Agnew, W. F.; McCreery, D. B., *Neural prostheses: fundamental studies*. Prentice hall: 1990.
4. Luan, L.; Wei, X.; Zhao, Z.; Siegel, J. J.; Potnis, O.; Tuppen, C. A.; Lin, S.; Kazmi, S.; Fowler, R. A.; Holloway, S., *Science Advances* 2017, 3 (2), e1601966.
5. Vallejo-Giraldo, C.; Pampaloni, N. P.; Pallipurath, A. R.; Mokarian-Tabari, P.; O'Connell, J.; Holmes, J. D.; Trotier, A.; Krukiewicz, K.; Orpella-Aceret, G.; Pugliese, E., *Advanced Functional Materials* 2017.
6. Asplund, M.; Boehler, C.; Stieglitz, T., 2014.
7. McConnell, G. C.; Rees, H. D.; Levey, A. I.; Gutekunst, C.-A.; Gross, R. E.; Bellamkonda, R. V., *Journal of neural engineering* 2009, 6 (5), 056003.
8. Polikov, V. S.; Su, E. C.; Ball, M. A.; Hong, J.-S.; Reichert, W. M., *Journal of Neuroscience Methods* 2009, 181 (2), 170-177. DOI <https://doi.org/10.1016/j.jneumeth.2009.05.002>.
9. Polikov, V. S.; Block, M. L.; Fellous, J.-M.; Hong, J.-S.; Reichert, W. M., *Biomaterials* 2006, 27 (31), 5368-5376.
10. Vallejo-Giraldo, C.; Kelly, A.; Biggs, M. J., *Drug discovery today* 2014, 19 (1), 88-94.

Analysis of the Neurotropic and Anti-inflammatory Effects of Neuroelectrode
Functionalisation with a Heparan Sulphate Mimetic

11. Aqrawe, Z.; Montgomery, J.; Travas-Sejdic, J.; Svirskis, D., Trends in Biotechnology 2017, 35 (2), 93-95. DOI <https://doi.org/10.1016/j.tibtech.2016.06.007>.
12. Ravichandran, R.; Sundarrajan, S.; Venugopal, J. R.; Mukherjee, S.; Ramakrishna, S., Journal of the Royal Society Interface 2010, rsif20100120.
13. Hackett, A. J.; Malmström, J.; Travas-Sejdic, J., Progress in Polymer Science 2017.
14. Admassie, S.; Elfwing, A.; Inganäs, O., Advanced Materials Interfaces 2016.
15. Rivnay, J.; Inal, S.; Collins, B. A.; Sessolo, M.; Stavrinidou, E.; Strakosas, X.; Tassone, C.; Delongchamp, D. M.; Malliaras, G. G., Nature communications 2016, 7.
16. Uppalapati, D.; Boyd, B. J.; Garg, S.; Travas-Sejdic, J.; Svirskis, D., Biomaterials 2016, 111, 149-162.
17. Wu, F.; Sun, M.; Jiang, W.; Zhang, K.; Xie, A.; Wang, Y.; Wang, M., Journal of Materials Chemistry C 2016, 4 (1), 82-88.
18. Hardy, J. G.; Khaing, Z. Z.; Xin, S.; Tien, L. W.; Ghezzi, C. E.; Mouser, D. J.; Sukhavasi, R. C.; Preda, R. C.; Gil, E. S.; Kaplan, D. L., Journal of Biomaterials Science, Polymer Edition 2015, 26 (17), 1327-1342.
19. Bhagwat, N.; Murray, R. E.; Shah, S. I.; Kiick, K. L.; Martin, D. C., Acta biomaterialia 2016, 41, 235-246.
20. Park, S. J.; Lee, Y. J.; Heo, D. N.; Kwon, I. K.; Yun, K.-S.; Kang, J. Y.; Lee, S. H., Sensors and Actuators B: Chemical 2015, 215, 133-141.
21. Abidian, M. R.; Kim, D. H.; Martin, D. C., Advanced materials 2006, 18 (4), 405-409.
22. Alves-Sampaio, A.; García-Rama, C.; Collazos-Castro, J. E., Biomaterials 2016, 89, 98-113.
23. Baek, S.; Green, R. A.; Poole-Warren, L. A., Acta biomaterialia 2014, 10 (7), 3048-3058.

Analysis of the Neurotropic and Anti-inflammatory Effects of Neuroelectrode
Functionalisation with a Heparan Sulphate Mimetic

24. Du, Z. J.; Luo, X.; Weaver, C. L.; Cui, X. T., *Journal of Materials Chemistry C* 2015, 3 (25), 6515-6524.
25. Eles, J. R.; Vazquez, A. L.; Snyder, N. R.; Lagenaur, C.; Murphy, M. C.; Kozai, T. D.; Cui, X. T., *Biomaterials* 2017, 113, 279-292.
26. Collazos-Castro, J. E.; Hernández-Labrado, G. R.; Polo, J. L.; García-Rama, C., *Biomaterials* 2013, 34 (14), 3603-3617.
27. Povlich, L. K.; Cho, J. C.; Leach, M. K.; Corey, J. M.; Kim, J.; Martin, D. C., *Biochimica et Biophysica Acta (BBA)-General Subjects* 2013, 1830 (9), 4288-4293.
28. Mantione, D.; del Agua, I.; Schaafsma, W.; Diez-Garcia, J.; Castro, B.; Sardon, H.; Mecerreyes, D., *Macromolecular bioscience* 2016, 16 (8), 1227-1238.
29. Krukiewicz, K.; Cichy, M.; Ruszkowski, P.; Turczyn, R.; Jarosz, T.; Zak, J. K.; Lapkowski, M.; Bednarczyk-Cwynar, B., *Materials Science and Engineering: C* 2017, 73, 611-615.
30. Boehler, C.; Kleber, C.; Martini, N.; Xie, Y.; Dryg, I.; Stieglitz, T.; Hofmann, U.; Asplund, M., *Biomaterials* 2017, 129, 176-187.
31. Catt, K.; Li, H.; Hoang, V.; Beard, R.; Cui, X. T., *Nanomedicine: Nanotechnology, Biology and Medicine* 2017.
32. Aregueta-Robles, U. A.; Woolley, A. J.; Poole-Warren, L. A.; Lovell, N. H.; Green, R. A., *Frontiers in Neuroengineering* 2014, 7 (15). DOI 10.3389/fneng.2014.00015.
33. Asplund, M.; Nyberg, T.; Inganäs, O., *Polymer Chemistry* 2010, 1 (9), 1374-1391.
34. Asplund, M.; Thaning, E.; Lundberg, J.; Sandberg-Nordqvist, A.; Kostyszyn, B.; Inganäs, O.; von Holst, H., *Biomedical Materials* 2009, 4 (4), 045009.
35. Wang, M.; Liu, X.; Lyu, Z.; Gu, H.; Li, D.; Chen, H., *Colloids Surf B Biointerfaces* 2017, 150, 175-182. DOI 10.1016/j.colsurfb.2016.11.022.

Analysis of the Neurotropic and Anti-inflammatory Effects of Neuroelectrode
Functionalisation with a Heparan Sulphate Mimetic

36. Asplund, M.; von Holst, H.; Inganas, O., *Biointerphases* 2008, 3 (3), 83-93.
DOI Doi 10.1116/1.2998407.
37. Hay, E. D., *Cell biology of extracellular matrix*. Springer Science & Business Media: 2013.
38. Juliano, R. L.; Haskill, S., *Journal of Cell Biology* 1993, 120, 577-577.
39. SELIKTAR, D., *Annals of the New York Academy of Sciences* 2005, 1047 (1), 386-394.
40. Ikeda, Y.; Charef, S.; Ouidja, M.-O.; Barbier-Chassefière, V.; Sineriz, F.; Duchesnay, A.; Narasimprakash, H.; Martelly, I.; Kern, P.; Barritault, D., *Biomaterials* 2011, 32 (3), 769-776.
41. Daamen, W. F.; van Moerkerk, H. T.; Hafmans, T.; Buttafoco, L.; Poot, A. A.; Veerkamp, J. H.; van Kuppevelt, T. H., *Biomaterials* 2003, 24 (22), 4001-9.
42. Geutjes, P. J.; Daamen, W. F.; Buma, P.; Feitz, W. F.; Faraj, K. A.; Kuppevelt, T. H., *Tissue engineering* 2007, 279-295.
43. Tillman, J.; Ullm, A.; Madihally, S. V., *Biomaterials* 2006, 27 (32), 5618-5626.
44. Papy-Garcia, D.; Barbier-Chassefière, V.; Rouet, V.; Kerros, M.-E.; Klochendler, C.; Tournaire, M.-C.; Barritault, D.; Caruelle, J.-P.; Petit, E., *Macromolecules* 2005, 38 (11), 4647-4654.
45. Horonchik, L.; Tzaban, S.; Ben-Zaken, O.; Yedidia, Y.; Rouvinski, A.; Papy-Garcia, D.; Barritault, D.; Vlodaysky, I.; Taraboulos, A., *Journal of Biological Chemistry* 2005, 280 (17), 17062-17067.
46. Turnbull, J.; Powell, A.; Guimond, S., *Trends in cell biology* 2001, 11 (2), 75-82.
47. Fugedi, P., *Mini reviews in medicinal chemistry* 2003, 3 (7), 659-667.
48. Nakato, H.; Kimata, K., *Biochimica Et Biophysica Acta (BBA)-General Subjects* 2002, 1573 (3), 312-318.

Analysis of the Neurotropic and Anti-inflammatory Effects of Neuroelectrode
Functionalisation with a Heparan Sulphate Mimetic

49. Taylor, K. R.; Gallo, R. L., *The FASEB Journal* 2006, 20 (1), 9-22.
50. Chevalier, F.; Lavergne, M.; Negroni, E.; Ferratge, S.; Carpentier, G.; Gilbert-Sirieix, M.; Sineriz, F.; Uzan, G.; Albanese, P., *Stem Cell Res* 2014, 12 (3), 703-15. DOI 10.1016/j.scr.2014.03.001.
51. Frescaline, G.; Boudierlique, T.; Mansoor, L.; Carpentier, G.; Baroukh, B.; Sineriz, F.; Trouillas, M.; Saffar, J.-L.; Courty, J.; Lataillade, J.-J., *Tissue Engineering Part A* 2013, 19 (13-14), 1641-1653.
52. Tong, M.; Zbinden, M. M.; Hekking, I. J.; Vermeij, M.; Barritault, D.; Van Neck, J. W., *Wound repair and regeneration* 2008, 16 (2), 294-299.
53. Barbier-Chassefière, V.; Garcia-Filipe, S.; Yue, X.; Kerros, M.; Petit, E.; Kern, P.; Saffar, J.; Papy-Garcia, D.; Caruelle, J.; Barritault, D., *Journal of Biomedical Materials Research Part A* 2009, 90 (3), 641-647.
54. Barritault, D.; Caruelle, J. In *Regenerating agents (RGTAs): a new therapeutic approach*, *Annales pharmaceutiques francaises*, 2006; pp 135-144.
55. Colombier, M.; Lafont, J.; Blanquaert, F.; Caruelle, J.; Barritault, D.; Saffar, J., *Cells Tissues Organs* 1999, 164 (3), 131-140.
56. Rouet, V.; Meddahi-Pellé, A.; Miao, H. Q.; Vlodaysky, I.; Caruelle, J. P.; Barritault, D., *Journal of Biomedical Materials Research Part A* 2006, 78 (4), 792-797.
57. Friand, V.; Haddad, O.; Papy-Garcia, D.; Hlawaty, H.; Vassy, R.; Hamma-Kourbali, Y.; Perret, G.-Y.; Courty, J.; Baleux, F.; Oudar, O., *Glycobiology* 2009, 19 (12), 1511-1524.
58. Albanese, P.; Caruelle, D.; Frescaline, G.; Delbé, J.; Petit-Cocault, L.; Huet, E.; Charnaux, N.; Uzan, G.; Papy-Garcia, D.; Courty, J., *Experimental hematology* 2009, 37 (9), 1072-1083.
59. Papy-Garcia, D.; Albanese, P., *Glycoconj J* 2017, 34 (3), 377-391. DOI 10.1007/s10719-017-9773-8.

Analysis of the Neurotropic and Anti-inflammatory Effects of Neuroelectrode
Functionalisation with a Heparan Sulphate Mimetic

60. Holmes, B. B.; DeVos, S. L.; Kfoury, N.; Li, M.; Jacks, R.; Yanamandra, K.; Ouidja, M. O.; Brodsky, F. M.; Marasa, J.; Bagchi, D. P.; Kotzbauer, P. T.; Miller, T. M.; Papy-Garcia, D.; Diamond, M. I., *Proceedings of the National Academy of Sciences* 2013, 110 (33), E3138-E3147. DOI 10.1073/pnas.1301440110.
61. Tremblay, P.; Aisen, P.; Garceau, D., *Alzheimer's & Dementia: The Journal of the Alzheimer's Association* 1 (1), S2. DOI 10.1016/j.jalz.2005.06.033.
62. Ernst, B.; Magnani, J. L., *Nat Rev Drug Discov* 2009, 8 (8), 661-677.
63. Mehanna, A.; Mishra, B.; Kurschat, N.; Schulze, C.; Bian, S.; Loers, G.; Irintchev, A.; Schachner, M., *Brain* 2009, awp128.
64. Wang, M.; Lyu, Z.; Chen, G.; Wang, H.; Yuan, Y.; Ding, K.; Yu, Q.; Yuan, L.; Chen, H., *Chemical Communications* 2015, 51 (84), 15434-15437.
65. Parish, C. R., *Nature Reviews Immunology* 2006, 6 (9), 633-643.
66. Bishop, J. R.; Schuksz, M.; Esko, J. D., *Nature* 2007, 446 (7139), 1030-1037.
67. Bame, K. J., *Glycobiology* 2001, 11 (6), 91R-98R.
68. Papy-Garcia, D.; Huynh, M. B.; Soussi-Yanicostas, N.; Vozari, R.; Sineriz, F.; Yanicostas, C., *Method of diagnosis, prognostic or treatment of neurodegenerative diseases*. Google Patents: 2014.
69. Krukiewicz, K.; Bednarczyk-Cwynar, B.; Turczyn, R.; Zak, J. K., *Electrochimica Acta* 2016, 212, 694-700.
70. Vallejo-Giraldo, C.; Pugliese, E.; Larranaga, A.; Fernandez-Yague, M. A.; Britton, J. J.; Trotier, A.; Tadayyon, G.; Kelly, A.; Rago, I.; Sarasua, J. R.; Dowd, E.; Quinlan, L. R.; Pandit, A.; Biggs, M. J., *Nanomedicine (Lond)* 2016, 11 (19), 2547-63. DOI 10.2217/nnm-2016-0075.
71. O'Keeffe, G. W.; Dockery, P.; Sullivan, A. M., *Journal of Neurocytology* 2004, 33 (5), 479-488. DOI 10.1007/s11068-004-0511-y.

Analysis of the Neurotropic and Anti-inflammatory Effects of Neuroelectrode
Functionalisation with a Heparan Sulphate Mimetic

72. Kavanagh, E. T.; Loughlin, J. P.; Herbert, K. R.; Dockery, P.; Samall, A.; Doyle, K. M.; Gorman, A. M., *Biochemical and Biophysical Research Communications* 2006, 351 (4), 890-895. DOI 10.1016/j.bbrc.2006.10.104.
73. Huynh, M. B.; Villares, J.; Díaz, J. E. S.; Christiaans, S.; Carpentier, G.; Ouidja, M. O.; Sissoeff, L.; Raisman-Vozari, R.; Papy-Garcia, D., *Neurobiology of aging* 2012, 33 (5), 1005. e11-1005. e22.
74. Najjam, S.; Gibbs, R. V.; Gordon, M. Y.; Rider, C. C., *Biochemical Society Transactions* 1997, 25 (1), 3S-3S.
75. Smith, P. K.; Krohn, R. I.; Hermanson, G.; Mallia, A.; Gartner, F.; Provenzano, M.; Fujimoto, E.; Goetze, N.; Olson, B.; Klenk, D., *Analytical biochemistry* 1985, 150 (1), 76-85.
76. Saldova, R.; Kilcoyne, M.; Stöckmann, H.; Martín, S. M.; Lewis, A. M.; Tuite, C. M.; Gerlach, J. Q.; Le Berre, M.; Borys, M. C.; Li, Z. J., *Methods* 2017, 116, 63-83.
77. Adjou, K. T.; Simoneau, S.; Sales, N.; Lamoury, F.; Dormont, D.; Papy-Garcia, D.; Barritault, D.; Deslys, J. P.; Lasmezas, C. I., *J Gen Virol* 2003, 84 (Pt 9), 2595-603. DOI 10.1099/vir.0.19073-0.
78. Ouidja, M.-O.; Petit, E.; Kerros, M.-E.; Ikeda, Y.; Morin, C.; Carpentier, G.; Barritault, D.; Brugère-Picoux, J.; Deslys, J.-P.; Adjou, K., *Biochemical and biophysical research communications* 2007, 363 (1), 95-100.
79. Krukiewicz, K.; Zawisza, P.; Herman, A. P.; Turczyn, R.; Boncel, S.; Zak, J. K., *Bioelectrochemistry* 2016, 108, 13-20.
80. Raposo, M., Lobo, R. F. M., Pereira-Da-Silva, M. A., Faria, R. M., & Oliveira, O. N, *ISE 10 Proceedings - 10th International Symposium*, 1999, 533-536.
81. Barth, A., *Biochimica et Biophysica Acta* 2007, 1767 (9), 1073 - 1101. DOI <https://doi.org/10.1016/j.bbabbio.2007.06.004>.
82. Darmanin, T.; Guittard, F., *Progress in Polymer Science* 2014, 39 (4), 656-682.

Analysis of the Neurotropic and Anti-inflammatory Effects of Neuroelectrode
Functionalisation with a Heparan Sulphate Mimetic

83. Lampin, M.; Warocquier-Clérout, R.; Legris, C.; Degrange, M.; Sigot-Luizard, M., *Journal of Biomedical Materials Research Part A* 1997, 36 (1), 99-108.
84. Ashoka, S.; Saleema, N.; Sarkar, D., *Journal of Alloys and Compounds* 2017, 695, 1528-1531.
85. Cakić, M.; Nikolić, G.; Ilić, L.; Stanković, S., *Chemical Industry and Chemical Engineering Quarterly* 2005, 11 (2), 74-78.
86. Socrates, G., *Infrared and Raman Characteristic Group Frequencies: Tables and Charts Third Edition* ed.; John Wiley and sons 2001.
87. Davies, M.; Binns, J.; Melia, C.; Hendra, P.; Bourgeois, D.; Church, S.; Stephenson, P., *International journal of pharmaceutics* 1990, 66 (1-3), 223-232.
88. Gardella Jr, J. A.; Ferguson, S. A.; Chin, R. L., *Applied spectroscopy* 1986, 40 (2), 224-232.
89. Lindberg, B.; Hamrin, K.; Johansson, G.; Gelius, U.; Fahlman, A.; Nordling, C.; Siegbahn, K., *Physica Scripta* 1970, 1 (5-6), 286.
90. Littlejohn, D.; Chang, S.-G., *Journal of Electron Spectroscopy and Related Phenomena* 1995, 71 (1), 47-50.
91. Ismail, Y. A.; Martinez, J. G.; Al Harrasi, A. S.; Kim, S. J.; Otero, T. F., *Sensors and Actuators B-Chemical* 2011, 160 (1), 1180-1190. DOI DOI 10.1016/j.snb.2011.09.044.
92. Green, R. A.; Hassarati, R. T.; Goding, J. A.; Baek, S.; Lovell, N. H.; Martens, P. J.; Poole-Warren, L. A., *Macromolecular Bioscience* 2012, 12 (4), 494-501. DOI DOI 10.1002/mabi.201100490.
93. Guimard, N. K.; Gomez, N.; Schmidt, C. E., *Progress in polymer science* 2007, 32 (8), 876-921.
94. Fonner, J. M.; Forciniti, L.; Nguyen, H.; Byrne, J. D.; Kou, Y.-F.; Syeda-Nawaz, J.; Schmidt, C. E., *Biomedical Materials* 2008, 3 (3), 034124.

Analysis of the Neurotropic and Anti-inflammatory Effects of Neuroelectrode
Functionalisation with a Heparan Sulphate Mimetic

95. Green, R. A.; Lovell, N. H.; Poole-Warren, L. A., *Acta Biomaterialia* 2010, 6 (1), 63-71. DOI <http://dx.doi.org/10.1016/j.actbio.2009.06.030>.
96. King, Z. A.; Shaw, C. M.; Spanninga, S. A.; Martin, D. C., *Polymer* 2011, 52 (5), 1302-1308. DOI DOI 10.1016/j.polymer.2011.01.042.
97. Collazos-Castro, J. E.; Hernandez-Labrado, G. R.; Polo, J. L.; Garcia-Rama, C., *Biomaterials* 2013, 34 (14), 3603-17. DOI 10.1016/j.biomaterials.2013.01.097.
98. Krukiewicz, K.; Zak, J., *Journal of Materials Science* 2014, 49 (16).
99. Poole-Warren, L.; Lovell, N.; Baek, S.; Green, R., *Expert review of medical devices* 2010, 7 (1), 35-49.
100. Mai, L. Q., Minhas-Khan, A., Tian, X., Hercule, K. M., Zhao, Y. L., Lin, X., & Xu, X., *Nature communications*, 2012, 4, 2923-2923.
101. Zanin, H., Saito, E., Ceragioli, H. J., Baranauskas, V., & Corat, E. J., *Materials Research Bulletin*, 2014, 49, 487-493.
102. Lamont, C. A.; Winther-Jensen, O.; Winther-Jensen, B., *Journal of Materials Chemistry B* 2015, 3 (43), 8445-8448.
103. Wilks, S. J.; Richardson-Burns, S. M.; Hendricks, J. L.; Martin, D. C.; Otto, K. J., *Frontiers in neuroengineering* 2009, 2.
104. Szauer, T., *Progress in Organic Coatings*, 1982, 10(2), 171-183.
105. Pethrick, R. A., & Hayward, D., *Progress in Polymer Science*, 27(9), 1983-2017.
106. Luo, X.; Weaver, C. L.; Zhou, D. D.; Greenberg, R.; Cui, X. T., *Biomaterials* 2011, 32 (24), 5551-5557.
107. Venkatraman, S.; Hendricks, J.; King, Z. A.; Sereno, A. J.; Richardson-Burns, S.; Martin, D.; Carmena, J. M., *IEEE Transactions on Neural Systems and Rehabilitation Engineering* 2011, 19 (3), 307-316.
108. Yang, J.; Kim, D. H.; Hendricks, J. L.; Leach, M.; Northey, R.; Martin, D. C., *Acta Biomaterialia* 2005, 1 (1), 125-136.

Analysis of the Neurotropic and Anti-inflammatory Effects of Neuroelectrode
Functionalisation with a Heparan Sulphate Mimetic

109. Kim, G. H.; Kim, K.; Nam, H.; Shin, K.; Choi, W.; Shin, J. H.; Lim, G., *Sensors and Actuators B: Chemical* 2017, 252, 152-158. DOI <http://dx.doi.org/10.1016/j.snb.2017.04.142>.
110. Ates, M.; Sarac, A. S., *Progress in Organic Coatings* 2009, 65 (2), 281-287.
111. Diah, A. W.; Quirino, J. P.; Belcher, W.; Holdsworth, C. I., *Electrophoresis* 2014, 35 (14), 1976-1983.
112. Kirchmeyer, S.; Reuter, K., *Journal of Materials Chemistry* 2005, 15 (21), 2077-2088.
113. Xu, L.; Chen, W.; Mulchandani, A.; Yan, Y., *Angewandte Chemie International Edition* 2005, 44 (37), 6009-6012.
114. Jeon, G.; Yang, S. Y.; Byun, J.; Kim, J. K., *Nano Letters* 2011, 11 (3), 1284-1288. DOI [Doi 10.1021/NL104329y](https://doi.org/10.1021/NL104329y).
115. Esrafilzadeh, D.; Razal, J. M.; Moulton, S. E.; Stewart, E. M.; Wallace, G. G., *J Control Release* 2013. DOI [10.1016/j.jconrel.2013.01.022](https://doi.org/10.1016/j.jconrel.2013.01.022).
116. Yue, Z.; Moulton, S. E.; Cook, M.; O'Leary, S.; Wallace, G. G., *Adv Drug Deliv Rev* 2013, 65 (4), 559-69. DOI [10.1016/j.addr.2012.06.002](https://doi.org/10.1016/j.addr.2012.06.002).
117. Ge, J.; Neofytou, E.; Cahill III, T. J.; Beygui, R. E.; Zare, R. N., *ACS nano* 2011, 6 (1), 227-233.
118. Chikar, J. A.; Hendricks, J. L.; Richardson-Burns, S. M.; Raphael, Y.; Pfingst, B. E.; Martin, D. C., *Biomaterials* 2012, 33 (7), 1982-1990.
119. Boulahneche, S.; Jijie, R.; Barras, A.; Chekin, F.; Singh, S. K.; Bouckaert, J.; Medjram, M. S.; Kurungot, S.; Boukherroub, R.; Szunerits, S., *Journal of Materials Chemistry B* 2017.
120. Löffler, S.; Melican, K.; Nilsson, K.; Richter-Dahlfors, A., *Journal of internal medicine* 2017.
121. Singh, M.; Chandrasekaran, E.; Cherian, R.; Bachhawat, B., *Journal of neurochemistry* 1969, 16 (7), 1157-1162.

Analysis of the Neurotropic and Anti-inflammatory Effects of Neuroelectrode
Functionalisation with a Heparan Sulphate Mimetic

122. Hsieh-Wilson, L. C., 2016.
123. Wadhwa, R.; Lagenaur, C. F.; Cui, X. T., *Journal of Controlled Release* 2006, 110 (3), 531-541.
124. Green, R. A.; Lovell, N. H.; Wallace, G. G.; Poole-Warren, L. A., *Biomaterials* 2008, 29 (24-25), 3393-9. DOI 10.1016/j.biomaterials.2008.04.047.
125. Abidian, M. R., Kim, D. H., & Martin, D. C., *Advanced materials*, 2006, 18(4), 405-409.
126. Abidian, M. R., & Martin, D. C., *Advanced Functional Materials*, 2009, 19(4), 573-585.
127. Weaver, C. L.; LaRosa, J. M.; Luo, X.; Cui, X. T., *ACS nano* 2014, 8 (2), 1834-1843.
128. Thompson, B. C.; Moulton, S. E.; Ding, J.; Richardson, R.; Cameron, A.; O'leary, S.; Wallace, G. G.; Clark, G. M., *Journal of Controlled Release* 2006, 116 (3), 285-294.
129. Ghasemi-Mobarakeh, L.; Prabhakaran, M. P.; Morshed, M.; Nasr-Esfahani, M. H.; Baharvand, H.; Kiani, S.; Al-Deyab, S. S.; Ramakrishna, S., *Journal of tissue engineering and regenerative medicine* 2011, 5 (4).
130. Dow, K.; Riopelle, R.; Kisilevsky, R., *Cell and tissue research* 1991, 265 (2), 345-351.
131. Clement, A. M.; Sugahara, K.; Faissner, A., *Neuroscience letters* 1999, 269 (3), 125-128.
132. Richardson-Burns, S. M.; Hendricks, J. L.; Foster, B.; Povlich, L. K.; Kim, D.-H.; Martin, D. C., *Biomaterials* 2007, 28 (8), 1539-1552.
133. John, G. R.; Lee, S. C.; Brosnan, C. F., *The Neuroscientist* 2003, 9 (1), 10-22. DOI 10.1177/1073858402239587.
134. Gulati, K.; Poluri, K. M., *Glycoconjugate journal* 2016, 33 (1), 1-17.

Analysis of the Neurotropic and Anti-inflammatory Effects of Neuroelectrode
Functionalisation with a Heparan Sulphate Mimetic

135. Farina, C.; Aloisi, F.; Meinl, E., *Trends Immunol* 2007, 28 (3), 138-45. DOI 10.1016/j.it.2007.01.005.
136. Streit, W. J.; Hurley, S. D.; McGraw, T. S.; Semple-Rowland, S. L., *J Neurosci Res* 2000, 61 (1), 10-20. DOI 10.1002/1097-4547(20000701)61:1<10::aid-jnr2>3.0.co;2-e.
137. Brück, D.; Wenning, G. K.; Stefanova, N.; Fellner, L., *Neurobiology of disease* 2016, 85, 262-274.
138. Aloisi, F.; Borsellino, G.; Caré, A.; Testa, U.; Gallo, P.; Russo, G.; Peschle, C.; Levi, G., *International journal of developmental neuroscience* 1995, 13 (3), 265-274.
139. Lins, C.; Borojevic, R., *Growth Factors* 2001, 19 (3), 145-152.
140. Cavalcanti, Y. V. N.; Brelaz, M. C. A.; Neves, J. K. d. A. L.; Ferraz, J. C.; Pereira, V. R. A., *Pulmonary medicine* 2012, 2012.
141. Henry-Stanley, M. J.; Zhang, B.; Erlandsen, S. L.; Wells, C. L., *Cytokine* 2006, 34 (5), 252-259. DOI <http://dx.doi.org/10.1016/j.cyto.2006.05.008>.
142. Parish, C. R., *Nature immunology* 2005, 6 (9), 861-862.
143. Rubio, N.; Sanz-Rodriguez, F., *Virology* 2007, 358 (1), 98-108.
144. Sheng, G. J.; Oh, Y. I.; Chang, S.-K.; Hsieh-Wilson, L. C., *Journal of the American Chemical Society* 2013, 135 (30), 10898-10901.
145. Erta, M.; Quintana, A.; Hidalgo, J., *Int J Biol Sci* 2012, 8 (9), 1254-1266.
146. Joyce, J. A., *Cancer cell* 2005, 7 (6), 513-520.
147. Awatsuji, H.; Furukawa, Y.; Hirota, M.; Murakami, Y.; Nii, S.; Furukawa, S.; Hayashi, K., *Journal of neuroscience research* 1993, 34 (5), 539-545.
148. Sawada, M.; Suzumura, A.; Itoh, Y.; Marunouchi, T., *Neuroscience letters* 1993, 155 (2), 175-178.
149. Lipscombe, R. J.; Nakhoul, A.-M.; Sanderson, C. J.; Coombe, D. R., *Journal of leukocyte biology* 1998, 63 (3), 342-350.

Analysis of the Neurotropic and Anti-inflammatory Effects of Neuroelectrode
Functionalisation with a Heparan Sulphate Mimetic

150. Kim, S.-H.; Turnbull, J.; Guimond, S., *Journal of Endocrinology* 2011, 209 (2), 139-151.
151. Roberts, R.; Gallagher, J.; Spooncer, E.; Alien, T.; Bloomfield, F.; Dexter, T. M., *Nature* 1988, 332 (6162), 376-378.
152. Weiss, R. J.; Esko, J.; Tor, Y., *Organic & Biomolecular Chemistry* 2017.
153. Chu, C. L.; Goerges, A. L.; Nugent, M. A., *Biochemistry* 2005, 44 (36), 12203-12213.
154. Huynh, M. B.; Morin, C.; Carpentier, G.; Garcia-Filipe, S.; Talhas-Perret, S.; Barbier-Chassefière, V.; van Kuppevelt, T. H.; Martelly, I.; Albanese, P.; Papy-Garcia, D., *Journal of Biological Chemistry* 2012, 287 (14), 11363-11373.
155. Severin, I. C.; Soares, A.; Hantson, J.; Teixeira, M.; Sachs, D.; Valognes, D.; Scheer, A.; Schwarz, M. K.; Wells, T. N.; Proudfoot, A. E., *Frontiers in immunology* 2012, 3.
156. Olczyk, P.; Mencner, Ł.; Komosinska-Vassev, K., *BioMed research international* 2015, 2015.
157. Stringer, S., *The role of heparan sulphate proteoglycans in angiogenesis*. Portland Press Limited: 2006.
158. Liu, J.; Pedersen, L. C., *Applied microbiology and biotechnology* 2007, 74 (2), 263-272.
159. Shworak, N. W.; Kobayashi, T.; de Agostini, A.; Smits, N. C., *Progress in molecular biology and translational science* 2010, 93, 153-178.
160. Nurcombe, V.; Ford, M. D.; Wildschut, J. A.; Bartlett, P. F., *SCIENCE-NEW YORK THEN WASHINGTON*- 1993, 260, 103-103.
161. Rosenstein, J. M.; Krum, J. M.; Ruhrberg, C., *Organogenesis* 2010, 6 (2), 107-114.

Analysis of the Neurotropic and Anti-inflammatory Effects of Neuroelectrode
Functionalisation with a Heparan Sulphate Mimetic

162. Yasuhara, T.; Shingo, T.; Kobayashi, K.; Takeuchi, A.; Yano, A.; Muraoka, K.; Matsui, T.; Miyoshi, Y.; Hamada, H.; Date, I., *European Journal of Neuroscience* 2004, 19 (6), 1494-1504. DOI 10.1111/j.1460-9568.2004.03254.x.
163. Baron, O.; Ratzka, A.; Grothe, C., *Journal of Comparative Neurology* 2012, 520 (17), 3949-3961.
164. Bikfalvi, A.; Klein, S.; Pintucci, G.; Rifkin, D. B., *Endocrine reviews* 1997, 18 (1), 26-45.
165. Jensen, P.; Pedersen, E. G.; Zimmer, J.; Widmer, H. R.; Meyer, M., *Brain Res* 2008, 1218, 13-20. DOI 10.1016/j.brainres.2008.04.039.
166. Caldwell, M. A.; Svendsen, C. N., *Experimental Neurology* 1998, 152 (1), 1-10. DOI <http://dx.doi.org/10.1006/exnr.1998.6815>.
167. Ogunshola, O. O.; Antic, A.; Donoghue, M. J.; Fan, S.-Y.; Kim, H.; Stewart, W. B.; Madri, J. A.; Ment, L. R., *Journal of Biological Chemistry* 2002, 277 (13), 11410-11415.
168. Jin, K.; Zhu, Y.; Sun, Y.; Mao, X. O.; Xie, L.; Greenberg, D. A., *Proceedings of the National Academy of Sciences* 2002, 99 (18), 11946-11950.
169. Kreuger, J.; Salmivirta, M.; Sturiale, L.; Giménez-Gallego, G.; Lindahl, U., *Journal of Biological Chemistry* 2001, 276 (33), 30744-30752.
170. Ferreras, C.; Rushton, G.; Cole, C. L.; Babur, M.; Telfer, B. A.; van Kuppevelt, T. H.; Gardiner, J. M.; Williams, K. J.; Jayson, G. C.; Avizienyte, E., *The Journal of Biological Chemistry* 2012, 287 (43), 36132-36146. DOI 10.1074/jbc.M112.384875.
171. Ishihara, M.; Takano, R.; Kanda, T.; Hayashi, K.; Hara, S.; Kikuchi, H.; Yoshida, K., *The Journal of Biochemistry* 1995, 118 (6), 1255-1260.
172. Taipale, J.; Keski-Oja, J., *The FASEB Journal* 1997, 11 (1), 51-59.
173. Giulian, D.; Li, J.; Li, X.; George, J.; Rutecki, P. A., *Developmental neuroscience* 1994, 16 (3-4), 128-136.

Analysis of the Neurotropic and Anti-inflammatory Effects of Neuroelectrode
Functionalisation with a Heparan Sulphate Mimetic

174. Karve, I. P.; Taylor, J. M.; Crack, P. J., *Br J Pharmacol* 2016, 173 (4), 692-702. DOI 10.1111/bph.13125.
175. Tykhomyrov, A.; Pavlova, A.; Nedzvetsky, V., *Neurophysiology* 2016, 48 (1), 54-71.
176. Kim, J. H.; Kwon, S. J.; Stankewich, M. C.; Huh, G. Y.; Glantz, S. B.; Morrow, J. S., *Exp Mol Pathol* 2016, 100 (1), 1-7. DOI 10.1016/j.yexmp.2015.11.005.
177. Wang, Y.; Moges, H.; Bharucha, Y.; Symes, A., *Experimental neurology* 2007, 203 (1), 168-184.
178. Pekny, M.; Pekna, M., *Biochimica et Biophysica Acta (BBA)-Molecular Basis of Disease* 2016, 1862 (3), 483-491.
179. Song, B. K.; Geisert, G. R.; Vázquez-Chona, F.; Geisert, E. E., *Neuroscience letters* 2003, 338 (1), 29.
180. Peduzzi, J. D.; Grayson, T. B.; Fischer, F. R.; Geisert, E. E., Jr., *Exp Neurol* 1999, 160 (2), 460-8. DOI 10.1006/exnr.1999.7234.
181. Burgos, M.; Pastor, M. D.; Gonzalez, J. C.; Martinez-Galan, J. R.; Vaquero, C. F.; Fradejas, N.; Benavides, A.; Hernandez-Guijo, J. M.; Tranque, P.; Calvo, S., *Glia* 2007, 55 (14), 1437-48. DOI 10.1002/glia.20555.
182. Sajja, V. S.; Ereifej, E. S.; VandeVord, P. J., *Neurosci Lett* 2014, 570, 33-7. DOI 10.1016/j.neulet.2014.03.072.
183. Olsen, M., *Methods Mol Biol* 2012, 814, 265-81. DOI 10.1007/978-1-61779-452-0_18.
184. Davis, J. B.; Gray, J.; Gunthorpe, M. J.; Hatcher, J. P.; Davey, P. T.; Overend, P.; Harries, M. H.; Latcham, J.; Clapham, C.; Atkinson, K.; Hughes, S. A.; Rance, K.; Grau, E.; Harper, A. J.; Pugh, P. L.; Rogers, D. C.; Bingham, S.; Randall, A.; Sheardown, S. A., *Nature* 2000, 405 (6783), 183-7. DOI 10.1038/35012076.

Analysis of the Neurotropic and Anti-inflammatory Effects of Neuroelectrode
Functionalisation with a Heparan Sulphate Mimetic

185. Story, G. M.; Peier, A. M.; Reeve, A. J.; Eid, S. R.; Mosbacher, J.; Hricik, T. R.; Earley, T. J.; Hergarden, A. C.; Andersson, D. A.; Hwang, S. W.; McIntyre, P.; Jegla, T.; Bevan, S.; Patapoutian, A., *Cell* 2003, 112 (6), 819-29.
186. Wu, X.; Liu, Y.; Chen, X.; Sun, Q.; Tang, R.; Wang, W.; Yu, Z.; Xie, M., *Journal of Molecular Neuroscience* 2013, 49 (3), 499-506.
187. Ramakers, G. J.; Moolenaar, W. H., *Exp Cell Res* 1998, 245 (2), 252-62. DOI 10.1006/excr.1998.4224.
188. Koyama, Y.; Yoshioka, Y.; Matsuda, T.; Baba, A., *Glia* 2003, 43 (2), 185-9. DOI 10.1002/glia.10240.
189. Padmanabhan, J.; Clayton, D.; Shelanski, M. L., *J Neurobiol* 1999, 39 (3), 407-22.
190. Kraft, A. D.; Harry, G. J., *International journal of environmental research and public health* 2011, 8 (7), 2980-3018.
191. Matsumura, K.; Higashida, K.; Hata, Y.; Kominami, J.; Nakamura-Tsuruta, S.; Hirabayashi, J., *Analytical biochemistry* 2009, 386 (2), 217-221.
192. Manimala, J. C.; Roach, T. A.; Li, Z.; Gildersleeve, J. C., *Angewandte Chemie* 2006, 118 (22), 3689-3692.
193. Zamze, S.; Harvey, D. J.; Chen, Y. J.; Guile, G. R.; Dwek, R. A.; Wing, D. R., *The FEBS Journal* 1998, 258 (1), 243-270.
194. Scott, H.; Panin, V. M., N-glycosylation in regulation of the nervous system. In *Glycobiology of the Nervous System*, Springer: 2014; pp 367-394.
195. Wielgat, P.; Braszko, J. J., *Cellular Immunology* 2012, 273 (1), 17-22. DOI <http://dx.doi.org/10.1016/j.cellimm.2011.12.002>.
196. Schnaar, R. L.; Gerardy-Schahn, R.; Hildebrandt, H., *Physiological Reviews* 2014, 94 (2), 461-518.
197. Zhuo, Y.; Bellis, S. L., *Journal of Biological Chemistry* 2011, 286 (8), 5935-5941.

Analysis of the Neurotropic and Anti-inflammatory Effects of Neuroelectrode
Functionalisation with a Heparan Sulphate Mimetic

198. Gu, W.; Fukuda, T.; Isaji, T.; Hashimoto, H.; Wang, Y.; Gu, J., *The FASEB Journal* 2013, 27 (10), 3947-3958.
199. Gu, W.; Fukuda, T.; Isaji, T.; Hang, Q.; Lee, H.-h.; Sakai, S.; Morise, J.; Mitoma, J.; Higashi, H.; Taniguchi, N., *Journal of Biological Chemistry* 2015, 290 (28), 17566-17575.
200. Isaev, D.; Isaeva, E.; Shatskih, T.; Zhao, Q.; Smits, N. C.; Shworak, N. W.; Khazipov, R.; Holmes, G. L., *The Journal of neuroscience : the official journal of the Society for Neuroscience* 2007, 27 (43), 11587-94. DOI 10.1523/jneurosci.2033-07.2007.
201. Ednie, A. R.; Bennett, E. S., *Comprehensive Physiology* 2012.
202. Araque, A.; Navarrete, M., *Philosophical Transactions of the Royal Society B: Biological Sciences* 2010, 365 (1551), 2375-2381. DOI 10.1098/rstb.2009.0313.
203. Seifert, G.; Schilling, K.; Steinhäuser, C., *Nature reviews. Neuroscience* 2006, 7 (3), 194.
204. Bennett, E. S., *The Journal of Physiology* 2002, 538 (Pt 3), 675-690. DOI 10.1113/jphysiol.2001.013285.
205. Faber, E. S. L.; Sah, P., *The Neuroscientist* 2003, 9 (3), 181-194. DOI 10.1177/1073858403009003011.

CHAPTER 5**FUTURE DIRECTIONS**

In this thesis, findings on the physicochemical functionalisation of a metal oxide and topographical and biological functionalisation strategies of conducting polymers were provided in the context of neurospecific biomaterials, shedding light on the valuable impact of multi-functionalised strategies for biomedical applications (*Figure 5.1*). However, it is important to recognise that each biomaterial platform is appropriate for further work, mechanistic questions and different directions towards multidisciplinary approaches.

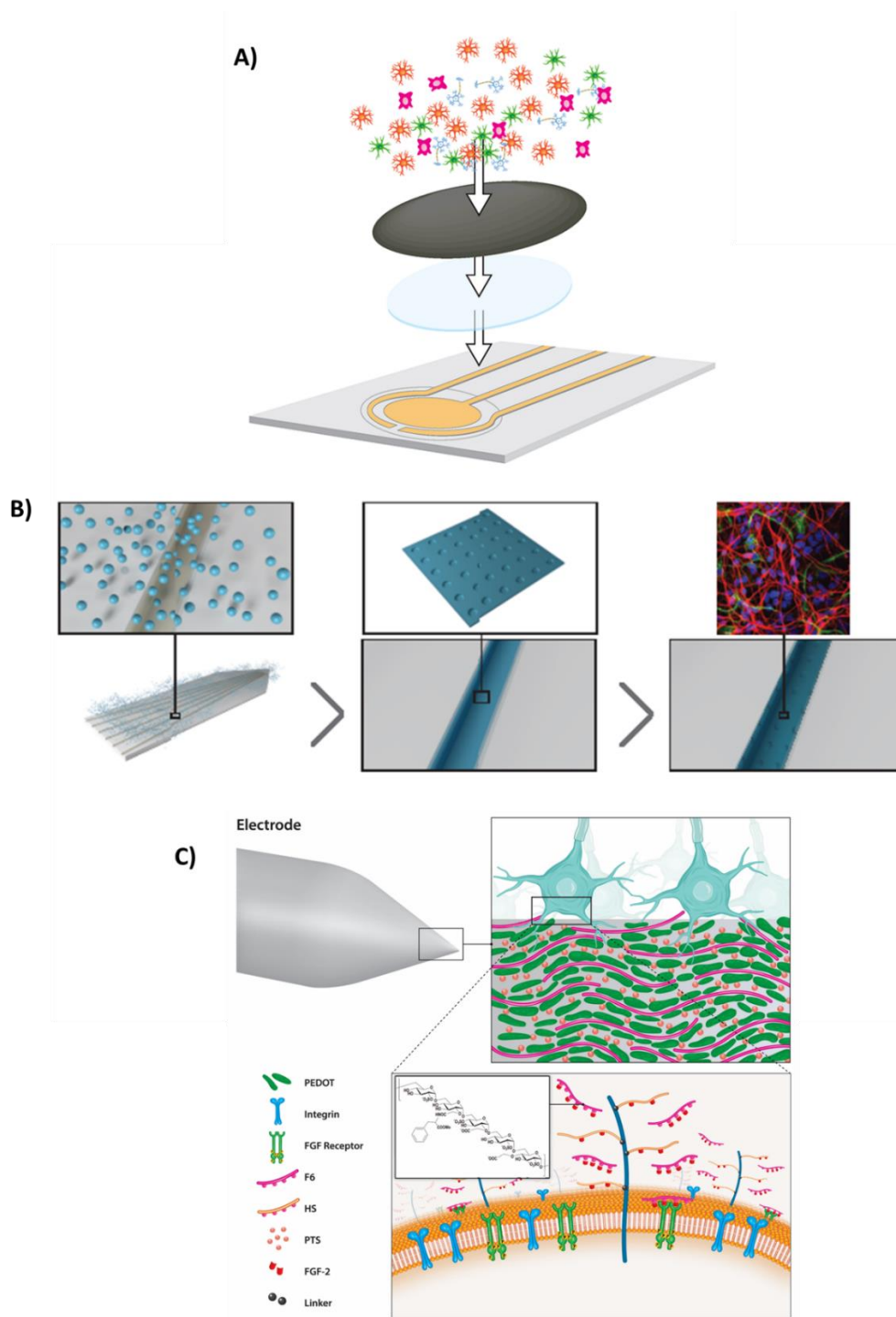


Figure 5.1 *Multidisciplinary approaches for neural interfaces applications. A) Anodisation of ITO, B) Micro-pit and C) GAG-mimetic functionalised electrodes, respectively, as electrochemical, surface morphology, and cytocompatibility strategies for the generation of neural interfaces with superior electrical and biological characteristics.*

5.1 Platform Development

5.1.1 Dual Functionalisation

As complementary work to the topographical and biological functionalisation strategies of PEDOT-based materials achieved with this work, a dual functionalisation approach using these platforms combined is proposed next. The involvement of both topographical and biological processes in the success or failure of the neural interface requires interdisciplinary efforts to solve a complex problem (*Figure 5.2*).

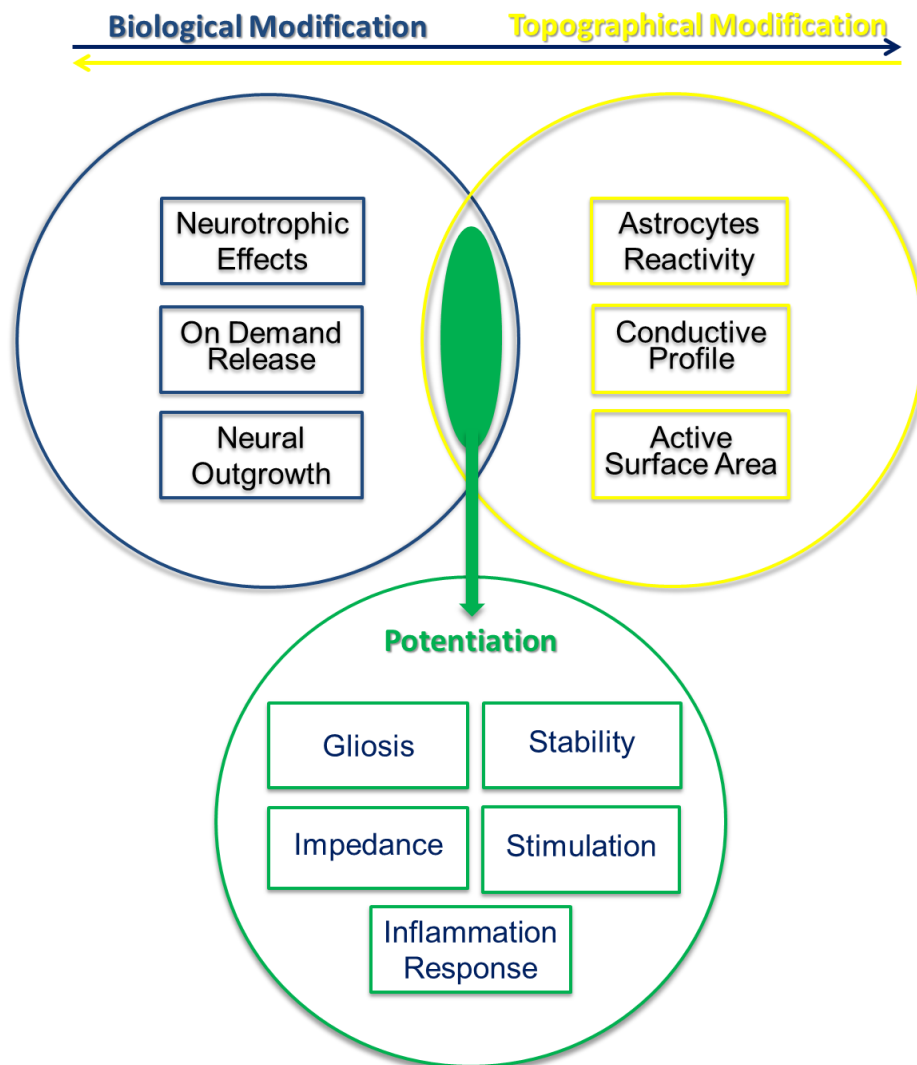


Figure 5.2 Involvement of both biological and topographical functionalisation strategies as interdisciplinary efforts for neural interface applications.

Biological systems to improve neuroelectrode stability through enhanced charge transfer capacity, increased neurite outgrowth, reduced gliosis potential with a modulated inflammatory response could be achieved with the overall synergic effects offered by the functionalisation approaches in a combinatorial approach. This is proposed to potentiate the physicochemical and biological effects observed in the work of this thesis. As this end-point was anticipated, the micro-imprinting protocol was optimised at room-temperature to ensure compatibility with doped biological molecules. It can be hypothesised that initial stability and selective cell adhesion at the electrode interface can be realised through topographical functionalisation and that stable electrode performance through an attenuated inflammation profile and a reduction in reactive gliosis may be further promoted through glycochemical functionalisation, as observed with the heparin mimetic F6. Critically, PEDOT:PTS doping with F6 induced marked neurotrophic and neuroprotective effects *in vitro*, with a proposed mechanism of action derived through F6 binding with neurotropic growth factors. Moreover, future work will focus on dual functionalisation approaches coupled with on-demand release of doped bioactive agents.

5.1.2 The influence of Electrochemical Modification on the Surface Properties of ITO (Chapter 2).

Taking into account that the anodisation of ITO using current density of 0.4 mA cm^{-2} resulted in anodised ITO films with fewer internal voids, it can be assumed that anodised ITO films will possess enhanced flexibility due to their high-packing density relative to non-anodised films, an important consideration in next-generation neuroelectrode design. Then, the effects of anodisation of the biocompatibility and electrochemical properties of sputtered ITO films on flexible-less stiff materials, such as polyethylene terephthalate (PET), polyimide (PI), parylene C, and polydimethylsiloxane (PDMS) can be explored next towards minimising flexible cuff microelectrodes and differences in mechanical strength between neural tissue and the electrode surface. Further, using the flexible microelectrodes and the favourable surface chemistry of the anodised ITO films as a function of oxygen content observed with this work, will be interesting to propose a complete focused study on ECM protein adsorption on these microelectrodes. These platforms may constitute

biomaterials for the modulation of cell behaviour from the protein - ionic availability at the surface, resulting in identification of particular cues for bioengineering the interface with control of chemical, morphophysical, and electrical properties. Together with the flexible bioelectronics of the ITO microelectrodes and with the differential presentation of protein/ions at surface, these platforms will allow local modulation of cell viability, growth and substrate adhesion. This, in fact, may have an important impact on electrophysiological recording functionality and *in vivo* translation. **Figure 5.3.**

In addition, and although we found a favourable response with a single aqueous electrolyte, the effects of anodisation in the presence of biocompatible ionic liquids is an interesting step forward of this work.

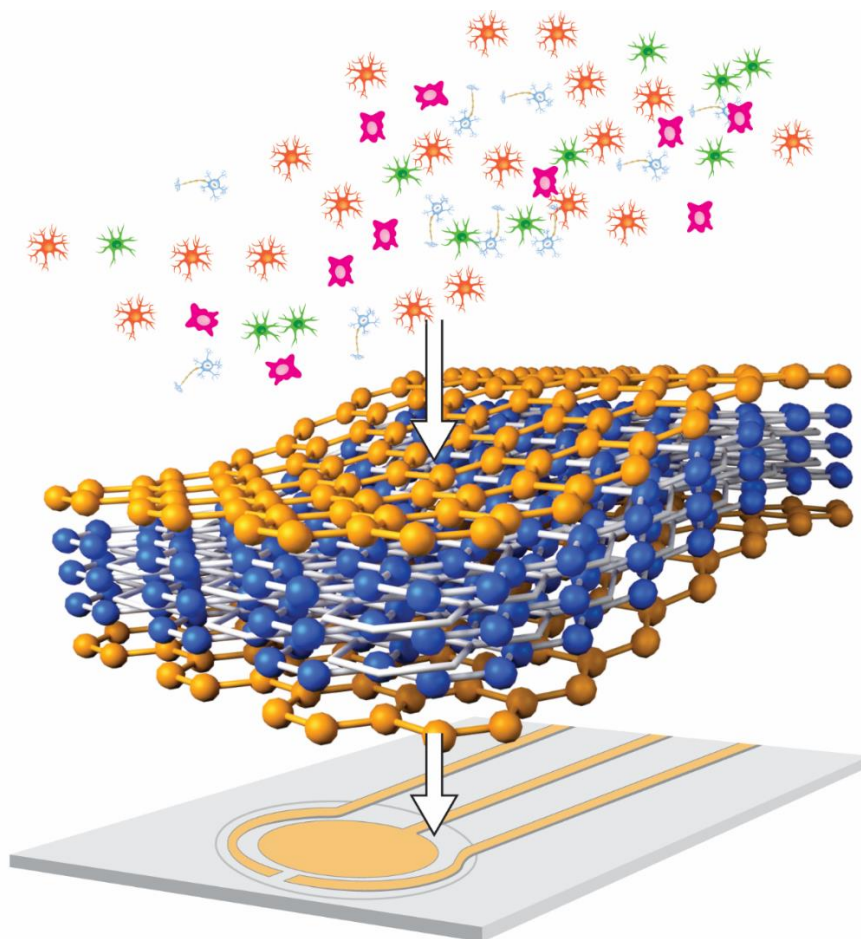


Figure 5.3 Pictorial representation of flexible ITO microelectrode arrays for the fabrication of anodised electrodes

5.1.3 Topographical Cues for The Modulation of Reactive Astrocyte Phenotype and Neurite outgrowth for Neural Interfaces Application (Chapter 3)

As a complementary approach for the micro-pits topography utilised in this thesis, the use of grooves and pillars is proposed using the low temperature imprinting lithography developed here to transfer these patterns. This differential array of topographies will constitute a mechanistic study towards understanding astrocyte adhesion, particularly reactive astrocyte adhesion, through focal adhesion studies on different topographies, and their response at the level of adhesion complexes or adaptor proteins to recruit key components of their signal transduction machinery to specific subcellular responses. This future research will help to elucidate the process of reactive astrocytes adhesion at the electrode from the actin-cytoskeleton phosphorylation cascades of these adherent cells. A custom-made protein array is under way, designed by members of Bigg’s lab to help with this process. **Figure 5.4.**

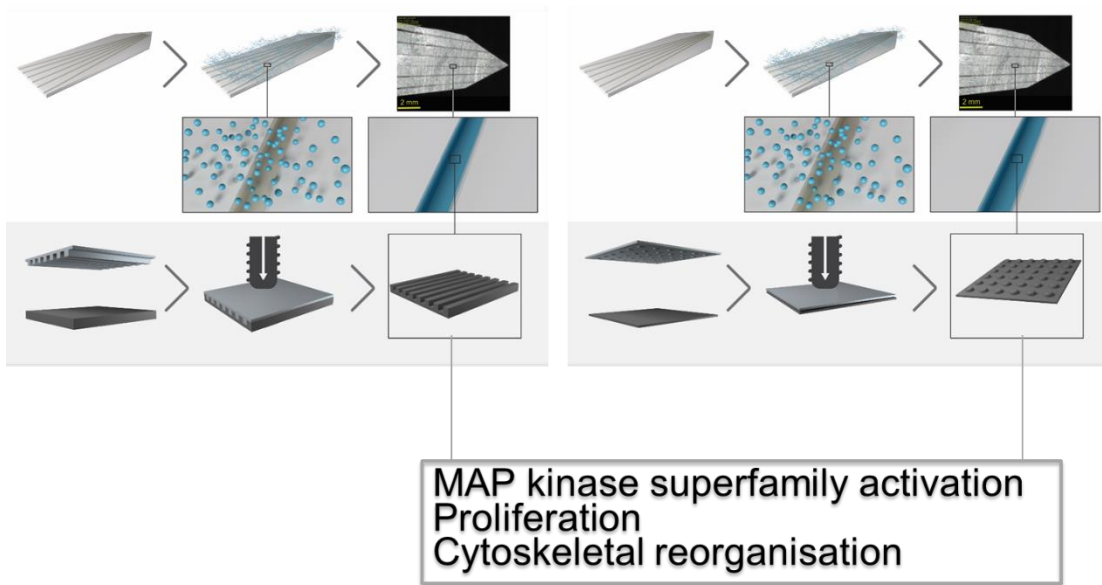


Figure 5.4 Schematic of the fabrication process for the topographical functionalisation of conducting polymer coatings for the modulation of reactive astrocytes adhesion and function to be further evaluated through signalling and interaction pathways.

5.1.3.1 The Neural response to Topographically Functionalised Neuroelectrode Surfaces with Vertical Silicon Nanowires (*Manuscript in preparation*)

Biologically relevant nanosurfaces which mimic the biological length scale may prevent an adverse host response via the modulation of protein adsorption, cell adhesion and the onset of a pro-inflammatory glial phenotype. Nanotopographical functionalisation that integrates increased surface conductivity with enhanced host integration is advantageous in neuroelectrode functionality to provide long-term stability and enhanced charge transfer, for neural simulation and recording.

In particular, topographical modification holds much promise for the development of chemically stable FDA approved materials in neuroelectrode development with enhanced integration potential. A facile technology to fabricate nanotopographically functionalised neuroelectrode interfaces composed of vertical silicon nanowires by a block copolymer mask technique to enhance electrical conductivity and to serve as potent modulators of cellular adhesion and proliferation was assessed. In particular, this process circumvents the need for expensive and time consuming top-down processes for the fabrication of topographically functionalised interfaces. Surface functionalisation with sub-20 nm silicon nanowires, causes a significant reduction in electrical impedance and increased photosensitivity relative to planar Si surfaces. Furthermore, a reactive ion etching process was employed to modify the nanowire heights from 40 nm to 1 μm , and marked increases in electrode electrochemical and photoelectric properties were noted. It was observed that although nanowire functionalisation enhanced key physicochemical properties of silicon neuroelectrode systems, sub-20 nm nanowires adversely impacted on neuronal cell growth and function *in vitro* through the down-regulation of key neuronal growth factors. Critically, this study contributes to a deeper understanding of cellular interactions with nanoscale neural interfaces and their role in the development of topographically functionalised neuroelectrode systems with enhanced chronic functionality. Future studies should focus on transferring this developed process to relevant biomaterials with enhanced conducting properties, i.e. platinum and platinum/iridium alloys. But further to potentiate these topographical features in flexible conductive polymer

composites towards flexible bioelectronics with topographical roles for implantation.

Figure 5.5.

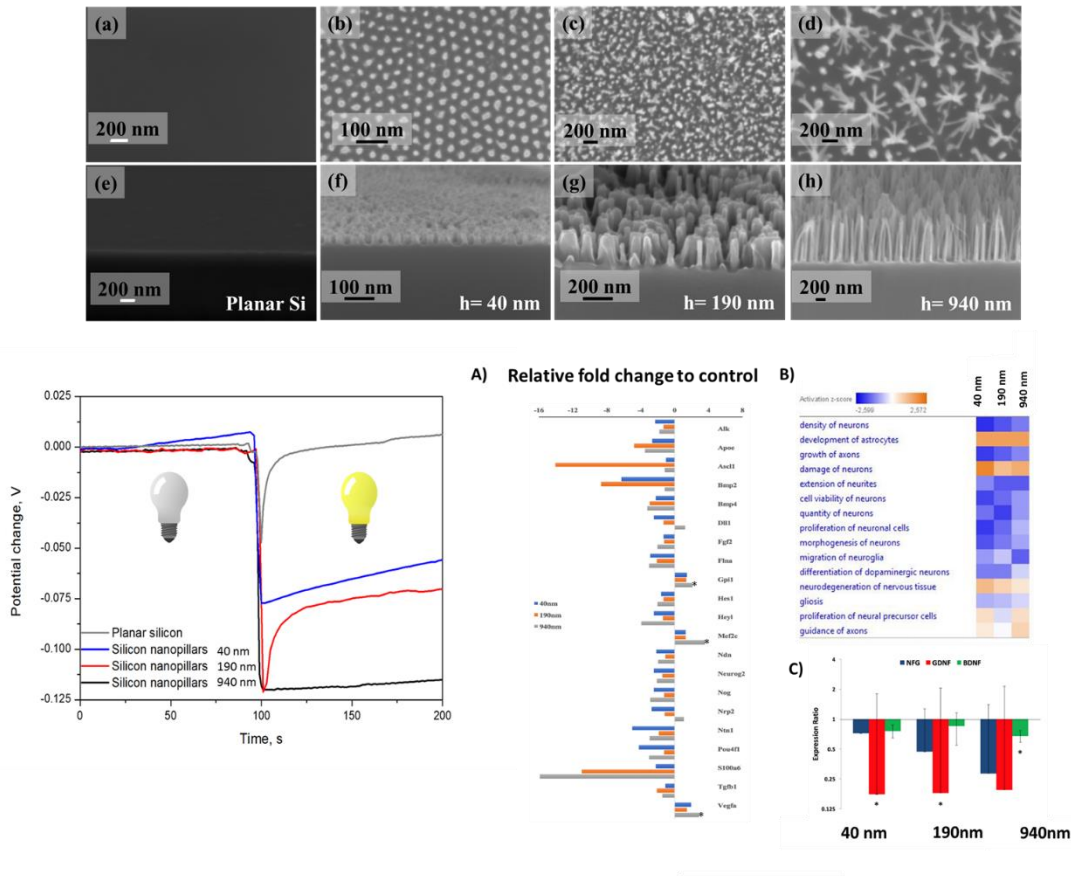


Figure 5.5 The neural response to topographically functionalised neuroelectrode surfaces with vertical silicon nanowires.

5.1.4 Chemically Modified Conducting Coatings for Neural Applications (Chapter 4).

Although PEDOT doping approaches were found to induce significant effects on cell function, it may be interesting to explore precise functionalisation approaches using chemical immobilisation of the biological dopants on the backbone of the polymer or explore radical polymerisation techniques for attaching customised polymers by ‘grafting to’ or ‘grafting from’ the conductive polymer backbone. This in fact, may provide a versatile toolbox to propose systems for combined studies of electrical stimuli and the coupling of glycanic mimetics. Composition, length and thickness of the grafts will be an interesting initial start point to control cell-interaction, but further

providing possibilities for matching of mechanical properties, enhanced electrical properties and bioactivity.

Since it has been presented in this work that the structural orientation and conformation of the mimetics may regulate binding and therefore increasing bioavailabilities, studies with other glycanic mimetics can be at the base of more efficient therapeutic applications controlling the structure features for *in vivo* application in neural interfaces (**Figure 5.6**).

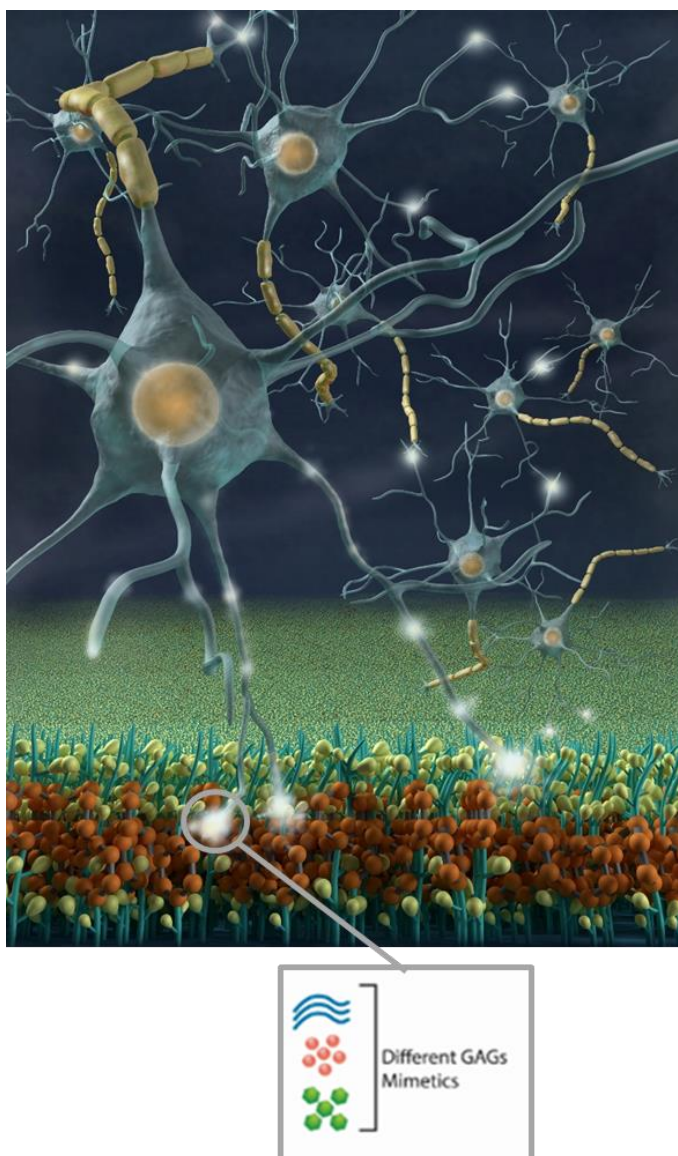


Figure 5.6 Biomimetic conducting coatings for the presentation of glycochemistries at the neural interface.

5.1.5 *Ex vivo* Whole Rat Brain Slice Model

With the prospect of elucidating functionality of these modification approaches in a complex biological system, and in particular assessing the long term performance of the electrode-tissue interface, *ex vivo*, and *in vivo* models need to be developed and further applied.

Primary *in vitro* cell cultures allow the assessment of survival, maintenance of morphology, and function as well as analysis of the influence of toxic or protective biochemicals to be studied. However, isolated cells do not reflect the nature of the organism due to the isolation and lack of contact with other cells. Thus, organotypic cultures have been found to be an important step forward in simulating more *in vivo*-like situations [1, 2]. **Figure 5.7.**

In this future work, organotypic whole brain slices from postnatal rats at an age of 11 days (P11) are proposed to be initially cultured for 7, 14 and 21 days and stained for specific cell markers. These include microglia, astrocytes, dopaminergic neurons and general neurons to assess the viability of the organotypic whole brain slices as an *ex vivo* brain slice model for neural-electrode applications.

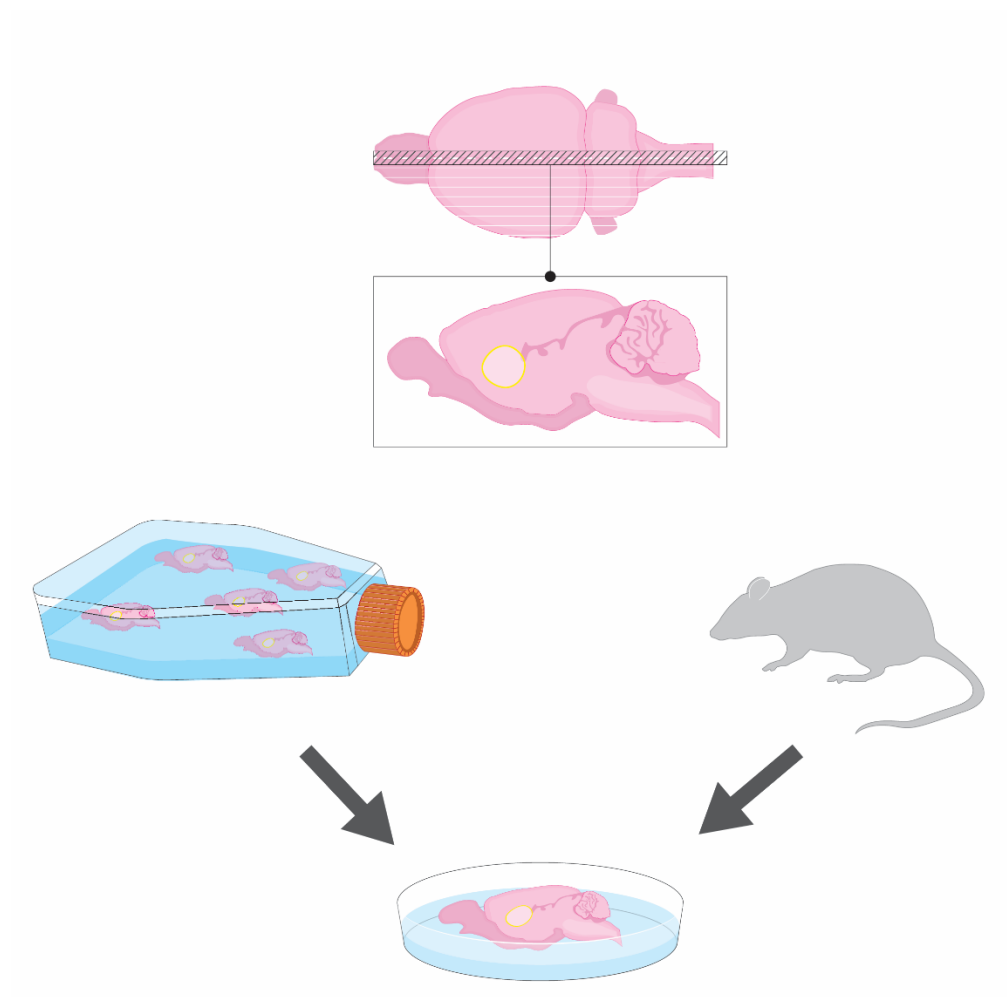


Figure 5.7 Organotypic whole brain slice cultures as *ex vivo* models. Brain slice cultures can be effective models of neurodegenerative diseases and an important translational step forward in simulating more *in vivo*-like conditions.

Preliminary data obtained from organotypic whole brain slices is presented below. The initial aim of this work was to obtain viable and reproducible whole brain sagittal slices and optimise a culture protocol.

In this preliminary work, an important contribution was received from a master's student, Mrs Laura Judge, with the quantification of the immunofluorescent images as part of her master project, and from the PhD student Mr Enrico Bagnoli, with the cutting of the whole brain slices.

5.1.5.1 Material and Methods

- Brain Slice Culture

Brain sagittal sections from P11 rat brain were cut and prepared using a LEICA vibratome. Slices obtained were 400 μm in thickness. Postnatal rat pups of day ten and twelve are recommended because of their better morphology, increased survival and resistance to mechanical trauma during slide preparation [1]. A graphical representation of whole brain slice is shown in **Figure 5.8**. It can be observed that the slices effectively maintained their cryoarchitecture.

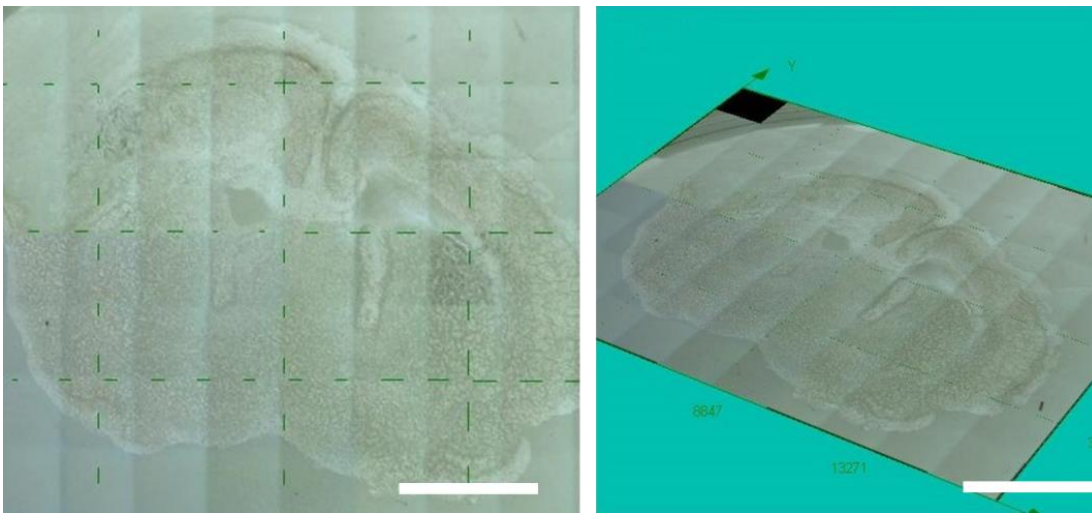


Figure 5.8 Whole brain sagittal slice after 21 days in culture. In a unique slice many anatomical structures are conserved. Scale bar =5 mm.

The whole brain slices were kept in culture for three weeks. Brain slices were grown in a humidified atmosphere of 5% CO_2 at 37°C and culture in media (Dulbecco's modified Eagle's medium/F12, 33 mM D-glucose, 1 % L-glutamine, 1% PS, 1 % FCS, supplemented with 2 % B27). All the samples were cultured for 7, 14, 21 days in sterile cell culture inserts of 0.4 μm , 30 mm diameter (Millicell®). Two whole brain slices were plated on each insert, and then 1.5 ml of the culture medium was added to each insert and changed with fresh media every two days for a period of 21 days.

- Immunofluorescent Labelling

After 21 days in culture, the whole slices were stained with 20 μ l of Fluorescein Diacetate (FDA) (Sigma) at a concentration of 1:100 followed by 20 μ l of Propidium Iodide (PI) (Invitrogen) at a concentration of 1:10, to establish viability. The membranes around the slices were cut carefully and placed in 35 mm glass petri dishes. After 30 seconds with the staining solution, this was removed and replaced with 500 μ l of PBS to be imaged. FTIC and PI filters respectively were used.

As a complementary assay for the evaluation of toxicity of the brain slices, Lactate Dehydrogenase (LDH) analyse was performed, using the established method adapted by Dr Una Fitzgerald's group. See **Appendix 1** for the protocol used.

To visualise astrocytes, general neurons, microglia and Tyrosine Hydroxylase (TH) neurons at each time point (7, 14 and 21 days), slices were fixed using 10% Neutral Formalin Buffer (NFB) for two hours followed by three washes with PBS. The membranes around the slices were cut carefully to reduce the amount of reagent used, and then placed on glass petri dishes. Slices were blocked and permeabilised for one hour with 10% normal goat serum (NGS) and Triton X-100 at 0.4%. Note: NGS was replaced with 10% horse serum when using the Iba1 goat antibody to visualise microglia. By indirect double-immunofluorescent labelling, the slices were incubated with primary antibody in NGS (2.5%) Triton X-100 (0.1%) in PBS (or 2.5% horse serum for IBA1) for 48 hours at 4°C. Expression of dopamine by the presence of TH and general neurons with β -tubulin III were evaluated with Anti-Tyrosine Hydroxylase (TH) (MAB318, Merck Millipore, 1:1000), and anti- β -Tubulin III antibody produced in rabbit (Sigma, 1:500), respectively. Expression of astrocytes and microglia were evaluated, respectively with a 1:200 concentration anti-gial fibrillary acidic protein (GFAP) antibody produced in mouse (Sigma, 1:200) and with anti-rabbit Iba1 (Wako, 1:1000) with a concentration of 1:1000. Samples were washed three times with PBS for fifteen minutes and then incubated overnight at 4°C in the secondary solution antibodies. Note: the secondary antibody solution was in NGS (2.5%) Triton X-100 (0.1%) in PBS. A secondary antibody Alexa Fluor® 488 goat anti-Mouse IgG / IgA / IgM (H+L) (Molecular probes) at a concentration of

1:1000 for TH neurons and 1:500 for astrocytes respectively was used. Secondary antibodies Alexa Fluor® 594 goat anti-Rabbit IgG (H+L) (Molecular probes) were used at a concentration of 1:1000 for microglia and 1:500 for general neurons. Samples were washed with PBS (fifteen minutes ×3) and mounted with counterstained with slowfade^R gold antifade reagent with DAPI for nuclear staining.

- Microscopy and Image Analysis

After immunostaining, samples were viewed with an Olympus Fluoview 1000 Confocal Microscope at a fixed scan size of 1024 by 1024 at a ratio 1:1. A minimum of twenty random images at 10× magnification for live and dead analysis and at 40× magnification for immunohistochemistry analysis were taken from each time point.

The cells were quantified using an unbiased stereological sampling method [3]. The top and right lines of each square were the inclusion lines. Cells that hit the lines or were close to the lines were counted [4, 5]. The number of dopaminergic neurons and microglia at 14 days and 21 days were quantified by analysing five random fields of view of three different images. Note: Day seven cultures were not used for quantification because the slices were too thick to be imaged and further analysed.

- Statistical Analysis

All data presented was confirmed using two replicates for each of time points analysed. The results are expressed as the mean of the values ± standard deviation.

5.1.5.2 Preliminary Results: Important Observations

Whole brain sagittal slices were successfully cultured over a period of 7, 14 and 21 days. However, whole brain culture at day seven showed a very thick composition attributed to the initial section thickness selected (400 µm). Then, this initial time point was not included in the analyses owing to the difficulty of imaging of the structural composition of the slice. However, this resulted in an important initial thickness for subsequent experiments.

Figure 5.9A shows representative fluorescent micrographs of the whole brain slices. Overall, the slice viability was achieved after 21 days with 64 % of general tissue viability (**Figure 5.9B**). A result that coupled with the decreased levels of LDH

production over time show that after 21 days in culture, the whole brain slices have achieved a stable and highly viable state with low tissue damage (**Figure 5.9C**). This is particularly important because this preliminary data may suggest that after 21 days, the maturation and stabilisation of the slice are reached when cut at an initial thickness of 400 μm . Thus, from this time point onwards the evaluation in culture of electrodes and treatments can be applied and further analysis can be carried out.

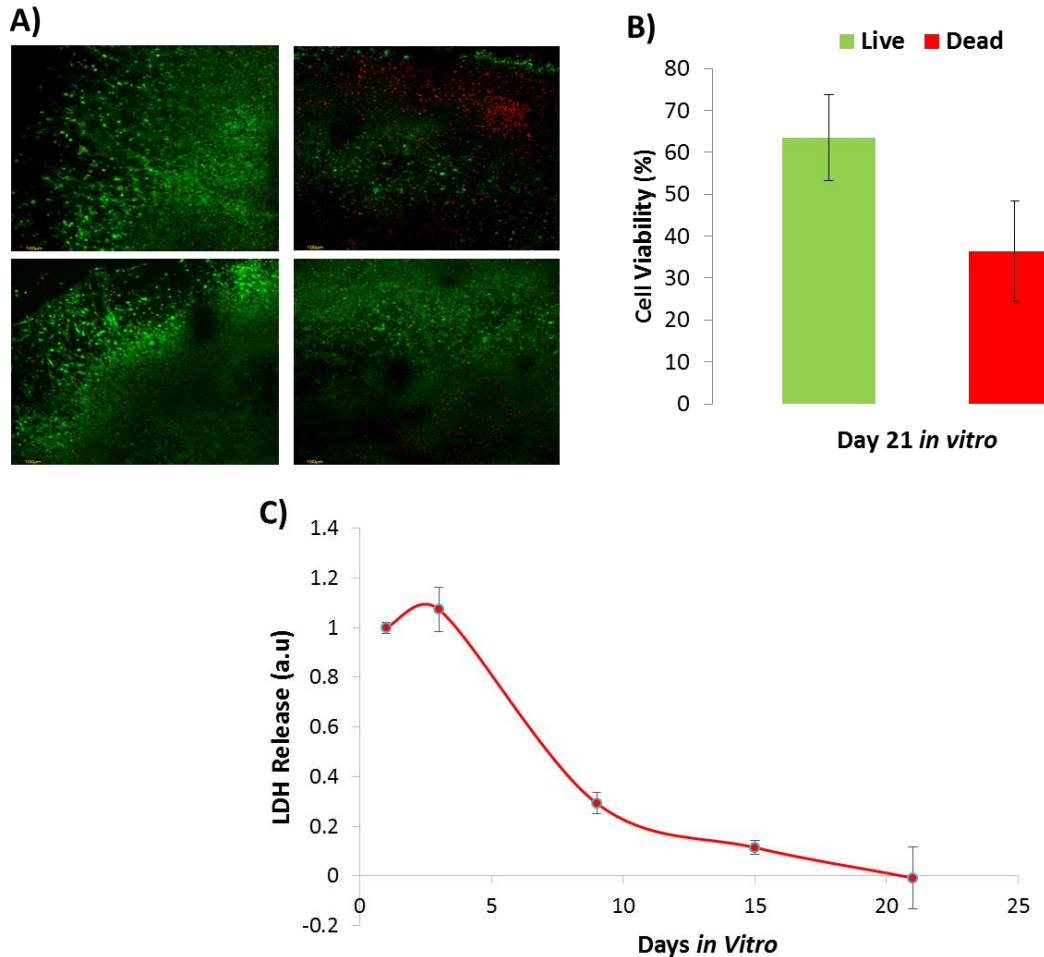


Figure 5.9 Characterisation of whole brain slice viability. A) Fluorescent micrographs showing the overall tissue viability at day 21 in culture through the live/dead assay B) and LDH analysis in C) Live cells are shown in green, dead cells in red. Scale bar 100 μm .

Further analysis showed difference in the quantification of dopaminergic neurons presence between day 14 and day 21 evaluated at the striatum region (**Figure 5.10A-**

B). This is interesting as this may coincide with the fact that dopaminergic nigrostriatal pathway when using P11 pups develops during the first to second week [6]. At day 21 in culture, the dopaminergic neurons present showed fibrous and interconnecting morphology [6]. This region was in fact, chosen, as a particularly interesting anatomical area for future development of Parkinson models using brain slices.

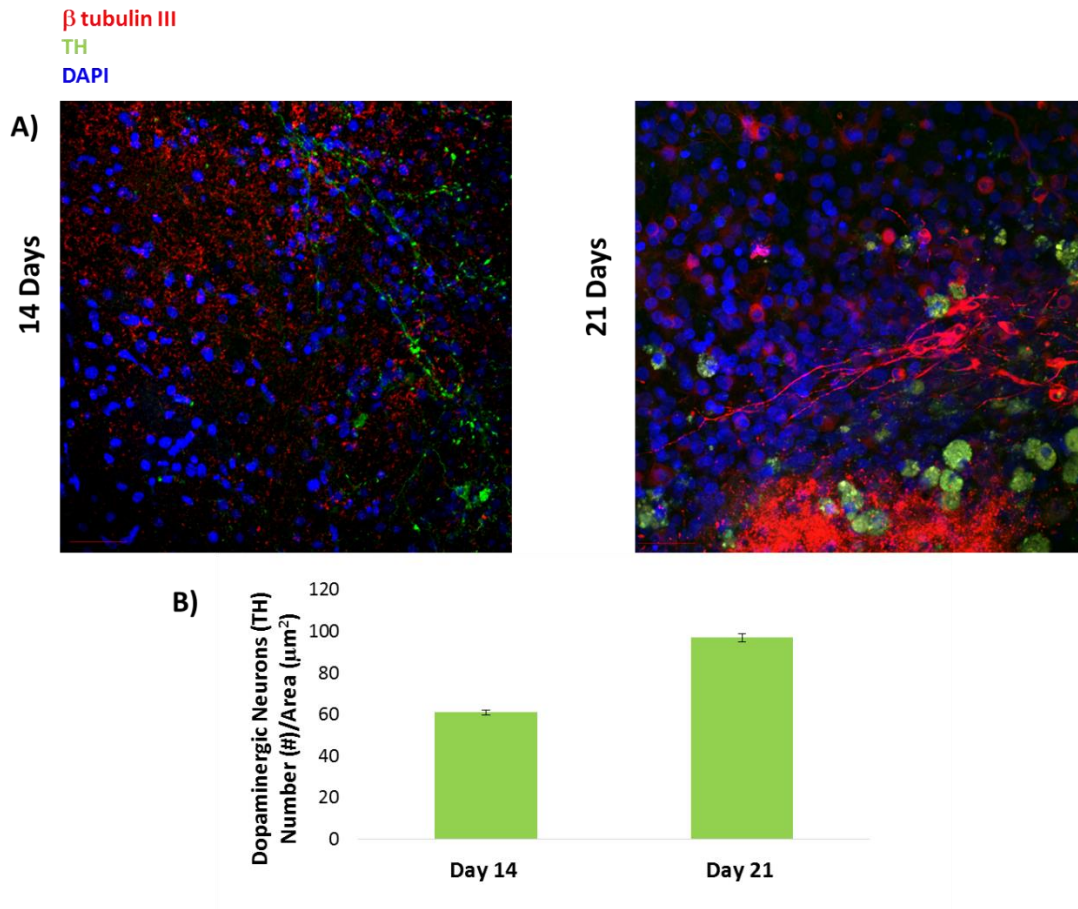


Figure 5.10 Immunohistochemical characterisation of striatum region from a whole brain slice cultures. A) Representative images demonstrating the presence of general neuronal and dopaminergic neurons at 14 and 21 days in culture B). Scale bar= 40 μm .

In addition, the quantification of microglia presence in the whole brain slice showed a difference in the microglia cell number between day 14 and day 21 (**Figure 5.11A-B**). However, further microglia length analysis of the ramification per cell presented

in *Figure 5.11C*, showed that there is an increase in frequency of microglia ramifications with lengths greater between 5 μm and 15 μm between these days. These preliminary results show that the lengths of the ramification of the microglia at day 14 are clustered between 0 μm and 7.5 μm lengths. By day 21, the distribution of the lengths is more confined between 5 μm and 10 μm . This is an observation that may indicate a less inflammatory microglia morphology over time. This preliminary data contributes and correlates with the overall low toxicity seen in the whole brain slices over time.

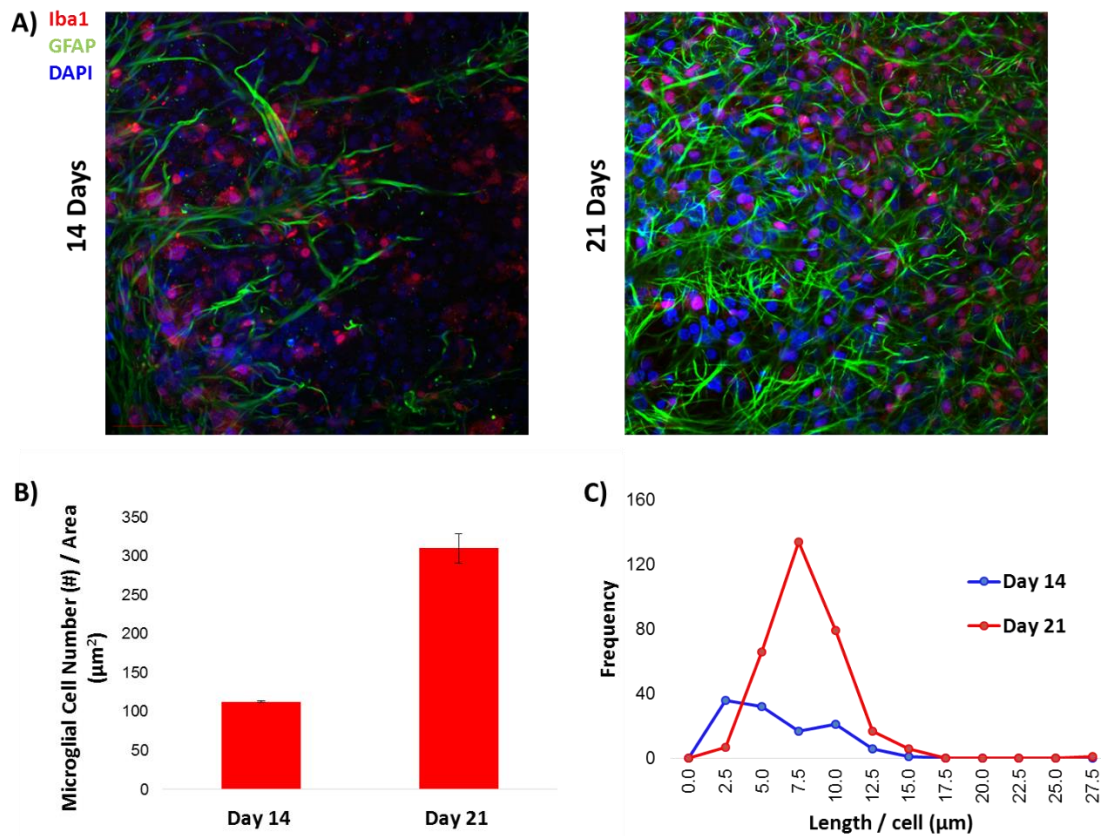


Figure 5.11 Immunohistochemical characterisation of whole brain slice cultures of microglial presence. A) Representative images demonstrating the presence of astrocytes (in green) and microglia (in red). A presence of microglia in the whole brain slice was observed by day 21 in culture B). Length analysis of the microglia ramifications showed that there is an increase in length over time C). Scale bar= 40 μm .

These preliminary results shed light on important considerations such as initial thickness of the slices and correlation for optimal time in culture for their maturation and stabilisation. This will, in fact, dictate the functional cellular architecture of the slices as an initial *ex vivo* model and screening tool. It is asserted by Humpel et al. that functional whole brain slices can be obtained at 110 μm thickness [7]. There may be space to optimise the thickness to achieve a functional cellular architecture whilst still maintaining a 3D dimensional anisotropic.

5.2 References

1. Cho, S.; Wood, A.; Bowlby, M. R., *Curr. Neuropharm.* 2007, 5 (1), 19-33.
2. Gähwiler, B.; Capogna, M.; Debanne, D.; McKinney, R.; Thompson, S., *Trends Neurosci.* 1997, 20 (10), 471-477.
3. O’Keeffe, G. W.; Dockery, P.; Sullivan, A. M., *Journal of neurocytology* 2004, 33 (5), 479-488.
4. Li, C.; Yang, S.; Chen, L.; Lu, W.; Qiu, X.; Gundersen, H. J. G.; Tang, Y., *The Anatomical Record* 2009, 292 (10), 1648-1655.
5. Şimşek, N.; Altunkaynak, B. Z.; Ünal, D.; Can, S.; Malkoç, I.; Ünal, B., *The Eurasian journal of medicine* 2009, 41 (2), 84.
6. Franke, H.; Schelhorn, N.; Illes, P., *Neurochem Int* 2003, 42 (5), 431-439.
7. Humpel, C., *Neuroscience* 2015, 305, 86-98.

APPENDICES

APPENDIX 1:

LDH VIABILITY ASSAY

APPENDIX 2:

ARTICLE. PREPARATION OF CYTocompatible ITO
NEUROELECTRODES WITH ENHANCED ELECTROCHEMICAL
CHARACTERISTICS USING A FACILE ANODIC OXIDATION PROCESS

APPENDIX 3:

ARTICLE. POLYHYDROXYALKANOATE/CARBON NANOTUBE
NANOCOMPOSITES: FLEXIBLE ELECTRICALLY CONDUCTING
ELASTOMERS FOR NEURAL APPLICATIONS

APPENDIX 4:

CONFERENCE ARTICLE. ELECTROCHEMICAL ANALYSIS OF
ACCELERATED AGING OF PEDOT-PTS COATED SCREEN-PRINTED
ELECTRODES

APPENDIX 5:

ARTICLE. NANOSCALE NEUROELECTRODE MODIFICATION VIA SUB-20
NM SILICON NANOWIRES THROUGH SELF-ASSEMBLY OF BLOCK
COPOLYMERS

**APPENDIX 1:
LDH VIABILITY ASSAY**

Table of Contents

Section		Page
1	Background	3
1.1	Reaction	3
1.2	Principle	3
2	Materials	4
3	Reagents Preparation	5
3.1.	Potassium Phosphate Buffer	
3.2	Sodium Hydroxide	
3.3	LDH Standard	
3.4	Sodium Pyruvate	
3.5	NADH	
4	Assay Protocol	6
4.1	Preparation of Standards	6
4.2	Preparation of Samples	6
4.3	Reaction	6
5	Data Analysis	7
6	Notes	8

1. Background

A number of methods have been developed to study cell viability and proliferation in cell culture. Various parameters associated with cell death and proliferation may be used to determine viability. One parameter for cell death is the integrity of the cell membrane.

1.1 LDH Reaction

Lactate dehydrogenase activity is often considered to be a preferred marker for cell death with *in vitro* cell models. LDH is a stable cytoplasmic enzyme present in all cells, and is rapidly released into the cell culture supernatant upon membrane damage or cell lysis.

Quantification of LDH release is a rapid, reliable, and reproducible method for detecting cell toxicity without disrupting or destroying the cells in culture, so they can also be assessed morphologically. .

NADH reactant (not the NAD⁺ product) absorbs light at 340 nm, the course of the reaction can be monitored by the decrease in the 340 nm absorption as reactant is converted to product (Fig. 1). This assay will monitor the drop in absorbance as a function of time when a mixture of sodium pyruvate and NADH is added to an aliquot containing an unknown amount of LDH

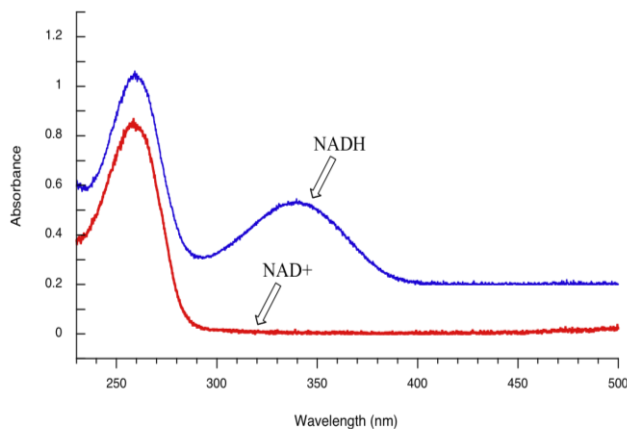
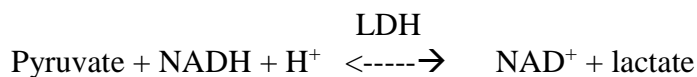


Figure 1: Absorbance spectra of NADH and NAD.

1.2 Principle:

The activity of LDH can be measured as the reduction of pyruvate to lactate. The reduction is coupled to the oxidation of NADH to NAD⁺:



2. Materials

Multi-channel pipette

96-well plate

Spectrophotometer platereader with wavelength 340 nm (uv)

Clean reservoir

Eppendorfs

Ice

3. Reagent Preparation

3.1 0.1 M Potassium Phosphate Buffer (7.5 pH)

- Mix 16 ml solution A and 84 ml of solution B (below)
- Dilute with distilled millipore water to a final volume of 200 ml
- Store for up to 3 months at room temperature
- Solution A & B can be kept indefinitely on the bench at room temperature.

Solution A: 2.72 g KH_2PO_4 per 100 ml (0.2 M)

Solution B: 3.48 g K_2HPO_4 per 100 ml (0.2 M)

3.2 10 mM Sodium Hydroxide (NaOH)

- Prepare 50 mM NaOH in Millipore water.
- Dilute 1/5 to 10 mM
- Store at room temperature indefinitely.

3.3 LDH standard

- Reconstitute contents in 1.8 ml of Potassium Phosphate Buffer
- Store in aliquots at -80°C .
- Only thaw each aliquot once. Do not vortex; mix gently.
- Keep on ice during use.

3.4 Sodium Pyruvate Stock Solution

- Dissolve 0.110 g sodium pyruvate in 50 ml potassium phosphate buffer.
- Store at 4°C for up to 24 months.

3.5 NADH Stock Solution

- Prepare 10 mM NADH in 10 mM NaOH and dilute 1/10 to 1 mM NADH
- Store 1 mM NADH in 2 ml aliquots -80°C until use.
- Keep stock reagent protected from light and desiccated
- Working solutions may be stored up to a day at 4°C .

3.5 Reagent Summary

Table 1: Reagent Summary

Name	MW	Source	Stock	Working	Storage
LDH		Cayman (10009321)	200 mU/ml	Various	Aliquots at -80°C .
Sodium Pyruvate	110.4	Sigma (P8574)	0.02 M (2X)	0.01 M	50 ml tube at $2-8^\circ\text{C}$ for 24 months
NADH	709.4	Sigma (N8129)	1 mM (10X)	0.1 mM	Aliquot at -20°C , dark & desiccated.
Solution A	136.09	Sigma (P3786)	0.2 M	0.2 M	Room temperature
Solution B	174.18	Sigma P5655)	0.2M	0.2 M	Room temperature
NaOH		Sigma	50 mM	10 mM	Room temperature
Triton X-100		Sigma	25%	0.5%	Store at $2-8^\circ\text{C}$.

4. Assay Protocol

4.1 Preparation of LDH Standards

- Obtain 8 eppendorfs and label 1-9
- Add 190 μ l of brain slice culture media (BSCM) into tube 1 and 100 μ l into tubes 2-9.
- Transfer 10 μ l of LDH standard into 1 and mix thoroughly to make a 10 mU/ml LDH solution.
- Serially dilute the standard 1/2 by removing 100 μ l from tube 1 and transferring into tube 2; mix thoroughly (10 mU/ml; first standard). Repeat this procedure for tubes 3-9.
- Do not add any standard to tube 9 (this is the blank).
- Prepare 3 replicates (A, B, C) of LDH standards 2-9 by adding 25 μ l of each LDH standard into triplicate wells of a fresh 96-well test plate (discard standard 1 since there is different ratio of LDH to media)

Table 2: Preparation of solutions for LDH standard curve.

Tube	1	2	3	4	5	6	7	8	9
BSCM	190	100	100	100	100	100	100	100	100
LDH stock	10								
	Mix & add 100 to 2	Mix & add 100 to 3	Mix & add 100 to 4	Mix & add 100 to 5	Mix & add 100 to 6	Mix & add 100 to 7	Mix & add 100 to 8	Mix only.	
Leftover Vol.	100	100	100	100	100	100	100	100	100
LDH mU/ml	10	5	2.5	1.25	0.625	0.313	0.156	0.078	0
Standard ID	(Discarded)	S1	S2	S3	S4	S5	S6	S7	S8

All volumes in μ l.

4.2 Preparation of Samples

A) Sample Storage

- Collect approximately 0.5 ml of culture medium in an eppendorf tube (pre-labelled with well ID) during each media change.
- Keep eppendorfs on ice or transfer to freezer immediately.
- Store culture medium at -20°C until assay.
- As a positive control, expose one well to 0.5% Triton X-100 to lyse cells. LDH medium from this well will be taken as maximal LDH release.

B) Sample Processing

- Allow samples to thaw at room temperature and briefly centrifuge. Once thawed, keep on ice.
- Dilute samples (if required) in BSCM.
- Transfer triplicate samples of 25 μ l into the 96-well plate
- Unused media may be stored short-term at 4°C for subsequent re-analysis.

4.3. LDH Reaction and Measurements

- Prepare working solution (only add NADH just before use): 10 ml sodium pyruvate, 8 ml potassium phosphate buffer and 2 ml NADH.
- Mix working solution by shaking and transfer into clean reservoir

- Using a multichannel pipette, add 175 μ l of working reagent to each well of the 96 well plate containing media samples and standards.
- Mix quickly and gently by tilting plate and then read plate immediately.
- Read the plate at 340 nm every 45 s for 9 minutes.

Table 3: A typical 96-well setup for the LDH assay.

	1	2	3	4	5	6	7	8	9	10	11	12
A	S8	S8	S8	M1	M1	M1	M9	M9	M9	M17	M17	M17
B	S7	S7	S7	M2	M2	M2	M10	M10	M10	M18	M18	M18
C	S6	S6	S6	M3	M3	M3	M11	M11	M11	M19	M19	M19
D	S5	S5	S5	M4	M4	M4	M12	M12	M12	M20	M20	M20
E	S4	S4	S4	M5	M5	M5	M13	M13	M13	M21	M21	M21
F	S3	S3	S3	M6	M6	M6	M14	M14	M14	M22	M22	M22
G	S2	S2	S2	M7	M7	M7	M15	M15	M15	M23	M23	M23
H	S1	S1	S1	M8	M8	M8	M16	M16	M16	M24	M24	M24

Standards (denoted S1-S8, see Table 2) media samples (denoted M, 22 total number), and controls (positive control: 0.5% Triton X denoted T) are assayed in triplicate.

3. Data Analysis

3.1 Organise Data

- Average the absorbance readings of replicate wells of each LDH standard and media samples
- Rearrange data

3.2 Plot Absorbance against Time

- Plot the time course of each standard and sample in Graphpad Prism.
- Inspect the curve and identify a time period where the curves are linear (i.e. r^2 value > 0.9 and exclude others time points from graph)

3.3 Determine Slope (i.e. reaction rate)

- Plot the slopes (from step 3.2) against LDH standards
- Interpolate LDH concentration values of samples using this standard curve

3.4 Statistics

- Determine normality: Analyse – Column Analysis – select all tests – ok
- Go to: results – column stats – check whether data passed/failed test
- If passed: Analyse – Column Analysis – One-way ANOVA – Selected Values – Ok – Select One-way ANOVA and Newman-Keuls post-test – Click the create descriptive output box – ok – results – column stats.

6. Notes:

1. It is not necessary to use a physiological temperature if LDH activity is used for detecting cell membrane damage (i.e. LDH leakage). Instead, measurements may be performed at a constant temperature with an extended incubation time of 1 hr (Kuznetsov and Gnaiger, 2010)
2. Air bubbles interfere with the measurement and must be removed prior to reading, e.g. by quickly moving with a gas flame over the wells, hair dryer or syringe.
3. Two factors in tissue culture medium can contribute to background absorbance: coloured compounds, such as phenol red, in medium and high concentrations of animal serum (it may contain LDH)

**APPENDIX 2:
ARTICLE.
PREPARATION OF CYTOTOXIC ITO
NEUROELECTRODES WITH ENHANCED
ELECTROCHEMICAL CHARACTERISTICS
USING A FACILE ANODIC OXIDATION
PROCESS**

Preparation of Cytocompatible ITO Neuroelectrodes with Enhanced Electrochemical Characteristics Using a Facile Anodic Oxidation Process

Catalina Vallejo-Giraldo, Niccolò Paolo Pampaloni, Anuradha R. Pallipurath, Parvaneh Mokarian-Tabari, John O'Connell, Justin D. Holmes, Alexandre Trotier, Katarzyna Krukiewicz, Gemma Orpella-Aceret, Eugenia Pugliese, Laura Ballerini, Michelle Kilcoyne, Eilís Dowd, Leo R. Quinlan, Abhay Pandit, Paul Kavanagh,* and Manus Jonathan Paul Biggs*

Physicochemical modification of implantable electrode systems is recognized as a viable strategy to enhance tissue/electrode integration and electrode performance in situ. In this work, a bench-top electrochemical process to formulate anodized indium tin oxide (ITO) films with altered roughness, conducting profiles, and thickness is explored. In addition, the influence of these anodized films on neural cell adhesion, proliferation, and function indicates that anodized ITO film cytocompatibility can be altered by varying the anodization current density. Furthermore, ITO-anodized films formed with a current density of 0.4 mA cm^{-2} show important primary neural cell survival, modulation of glial scar formation, and promotion of neural network activity.

morphological, and topographical functionalization has been a major focus of neural engineering over the past five years.^[1,2] A common occurrence following electrode implantation is reactive gliosis and the formation of a glial scar. This encapsulating scar forms at the electrode–tissue interface and accelerates neural loss, increases electrical signal impedance, and thereby compromises the efficacy of a stimulating/recording system in situ.^[1] Biomimetic interfaces with multiple functionalities that facilitate stable charge transfer in vivo while promoting enhanced cell interaction, selection, and attachment

are critical in chronic neuroelectrode functionality and the development of advanced neural stimulation systems and brain/machine interfaces.^[3] In turn, important contributions in organic bioelectronics as neural interface platforms possessing

1. Introduction

The modification of implantable electrodes for neural stimulation and recording through electrochemical, biochemical,

C. Vallejo-Giraldo, A. Trotier, Dr. K. Krukiewicz,^[†] G. Orpella-Aceret, E. Pugliese, Prof. A. Pandit, Dr. M. J. P. Biggs
CÚRAM – Centre for Research in Medical Devices – Galway
Biosciences Research Building
118 Corrib Village, Newcastle, Galway, Ireland
E-mail: manus.biggs@nuigalway.ie

N. P. Pampaloni, Prof. L. Ballerini
Scuola Internazionale Superiore di Studi Avanzati (SISSA)
Via Bonomea, 265, 34136 Trieste, Italy

Dr. A. R. Pallipurath, Dr. P. Kavanagh,^[††]
School of Chemistry
NUI Galway

University Road, Galway, Ireland
E-mail: p.kavanagh@qub.ac.uk

Dr. J. O'Connell, Prof. J. D. Holmes, Dr. P. Mokarian-Tabari
Department of Chemistry
University College Cork
Cork, Ireland

Dr. J. O'Connell, Prof. J. D. Holmes, Dr. P. Mokarian-Tabari
Tyndall National Institute
University College Cork
Cork, Ireland

Dr. J. O'Connell, Prof. J. D. Holmes, Dr. P. Mokarian-Tabari
Centre for Research on Adaptive Nanostructures
and Nanodevices (CRANN) and AMBER Centre
Trinity College Dublin
Dublin 2, Ireland

Dr. M. Kilcoyne
Carbohydrate Signalling Group
Microbiology
School of Natural Sciences
NUI Galway, University Road, Galway, Ireland

Dr. E. Dowd
Department of Pharmacology, Physiology
NUI Galway
University Road, Galway, Ireland

Dr. L. R. Quinlan
Department of Physiology
NUI Galway
University Road, Galway, Ireland

^[†]Present address: Department of Physical Chemistry and Technology of Polymers, Silesian University of Technology, 44-100 Gliwice, Poland

^[††]Present address: School of Chemistry and Chemical Engineering, Queen's University Belfast, David Keir Building, Stranmillis Road, Belfast, BT9 5AG, UK



DOI: 10.1002/adfm.201605035

favorable electrochemical properties for neural recording and stimulation have been reported.^[4–7]

Ongoing strategies in biomimetic design of the neural interface have focused on morphological, mechanical, and biochemical modification of the electrode–tissue interface to reduce tissue damage and promote electrode integration through device miniaturization, the development of flexible polymer systems, and the localized delivery of antifibrotic or neurotropic chemistries.^[8,9] Traditionally, chemically inert conductors such as gold, platinum, and iridium, as well as semiconductors such as silicon, have been widely employed as electrode systems in both clinical and research settings and have been found to perform well under nonchronic settings.^[10,11] Recently, however, nonmetallic electrically conducting biomaterials including inherently conducting polymers and polymer composites have been explored as neuroelectrode alternatives in an effort to promote chronic functionality and enhanced biocompatibility.^[12,13]

In the field of conductive metal oxide electronics, indium tin oxide (ITO) is one of the most intensively investigated materials because of its relatively low electrical resistivity, its optical transparency, and its thermal stability, making it well-suited for use as an electrode or sensor material.^[14] Specifically, ITO thin films have been employed successfully in the fabrication of optoelectronic and electrochromic devices,^[15] electroluminescent devices,^[16] photovoltaic cells,^[17] and waveguide sensors.^[18]

Recent studies indicate the potential of electrically conducting ITO thin films for biosensor applications *in vitro*.^[19–25] Selvakumar et al.^[26] demonstrated the efficacy of ITO electrodes as sensing electrodes *in vitro* for bioassays, and potential physiological measurements. Here it was concluded that ITO offered a compromise between promoting cell growth while adsorbing significantly less protein than titanium control substrates.^[22,27] Further, Tanamoto et al.^[21] developed micropatterned ITO glass electrode devices to facilitate electrical stimulation of neural cells coupled with fluorescent imaging processes. The device was observed to uniformly stimulate multiple single cells with and the authors noted potential *in vivo* applications.

It has been shown that ITO can be physically and chemically modified to locally tailor its electrical and optical properties,^[28] and, in particular, the modification of ITO electrodes with conductive polymer thin films via electropolymerization techniques has been explored as a method to enhance the electrode conductivity.^[29,30] Further, surface treatments such as acid etching^[31] and layer-by-layer assembly^[32] have been used to modulate and alter the performance of ITO for commercial applications. Electrochemical activation or passivation via the anodic oxidation (anodization process)^[33,34] is widely used in biomedical engineering to grow metal oxide dielectrics for electrical devices^[35,36] and to obtain protective and decorative films on metallic surfaces to increase corrosion resistance.^[37] The experimental conditions, *i.e.*, galvanostatic or potentiostatic anodization deposition, electrolyte composition, and deposition time, facilitate the oxidation of ions at the substrate–solution interface to produce thin-film coatings.^[38] Several research groups^[39–46] have demonstrated that the anodic oxidation technique can be employed in conjunction with mask strategies for the generation of biologically passive layers or nanostructures on titanium^[39–44] and alumina^[45,46] to improve cell adhesion and implant integration. Surface modification of ITO via

anodization, however, has not yet been explored as a method to enhance cytocompatibility, cell adhesion, and functionality in implantable systems. Furthermore, the effects of ITO anodization on film electrochemical impedance and topography remain unknown.

In this present comprehensive and systematic study, ITO anodization as a functionalization approach for the generation of cytocompatible and functional thin-film electrodes for potential neural applications is explored for the first time. Anodized ITO thin films were formulated through a facile electrochemical process employing the application of current densities ranging from 0.4 to 43 mA cm⁻². Subsequently, the physical, chemical, electrochemical, and cytocompatibility effects of ITO anodization were explored. Our results elucidate important material effects with regard to anodization current densities on ITO film surface morphology, electrochemistry, and cytocompatibility for the generation of neural interfaces with superior electrical and biological characteristics.

2. Results and Discussion

When subjected to anodic^[47–51] and cathodic^[50–53] polarization, ITO electrodes undergo changes in chemical composition,^[47–53] surface morphology,^[47,48,50–53] conductivity,^[47,48,50–53] and optical transparency.^[49–53] Such effects are largely influenced by (i) the electrochemical parameters selected for electrode polarization and (ii) composition of the electrolyte solution.^[47–53] For example, polarization at high positive potentials (>1.5 V vs saturated calomel electrode) in aqueous electrolyte can cause substantial structural changes to the ITO electrode.^[48] Similarly, polarization in strong acid (1 M HNO₃) or strong base (1 M NaOH) can result in a dramatic reduction in electrochemical activity, electrical conductivity, and optical transparency of the ITO electrode.^[53] Such effects are normally attributed to structural and/or chemical changes within the ITO film induced by the polarization process,^[47,48] which, under harsh electrochemical conditions, may result in partial or complete dissolution of ITO coating.^[47–51]

Here, we report a novel method for the facile fabrication of bioactive ITO substrates with enhanced electrochemical properties as neural interfaces. Due to the detrimental effects on ITO films resulting from anodization in harsh chemical conditions detailed above, we chose to perform the anodization process in a relatively mild electrolyte consisting of 0.01 M phosphate-buffered saline (PBS) and 10 × 10⁻⁶ M poly(sodium 4-styrenesulfonate) (PSS). Constant current densities of 0.4, 4, and 43 mA cm⁻² applied for 450 s were used to prepare modified ITO films through anodization in this electrolyte. The optimization process of the current densities employed in this study is indicated in Figure S1 (Supporting Information).

The following sections describe the physical, chemical, electrochemical, and biocompatibility properties of resulting films.

2.1. Physical Characterization of Anodized ITO Films

Systematic studies of thin-film ITO postdeposition processing in optoelectronic device fabrication have focused on the

processing effects on surface roughness and on the generation of defined nanostructures. To a great extent, techniques such as chemical-bath deposition^[54] and thermal annealing,^[55] respectively, have been utilized to modify film physicochemical properties with resulting films showing considerable morphological changes that translate into the optical transmittance and electrical conductivity. While a number of studies have explored anodization processes to produce microporous titanium oxide films on implant surfaces for orthopedic applications,^[56] the impact of anodization on the physical properties of ITO substrates for neural interfaces has not been investigated thus far.

Figure 1A shows representative scanning electron microscopy (SEM) images of anodized ITO films using 0.4, 4, and 43 mA cm⁻² current densities over a constant time of 450 s, and pristine ITO coated glass as a control substrate. It is interesting to note that pristine ITO films possess a surface morphology composed of a random assembly of nanoparticles that is developed into a nanoparticulate/granular morphology in films anodized under our experimental conditions. The quantification of the degree of nodularity revealed significant differences in nodule diameter when subjected to different deposition current densities. Film growth using higher current densities yielded

less-dense, nonuniform films than those of anodized films formed with lower current densities.^[57]

Experimentally, pristine ITO films reported a mean particle size of 86 nm, films formed with 0.4 mA cm⁻² were associated with a mean particle size of 89 nm; and mean particle diameters of 152 and 112 nm were observed in films formed using 4 and 43 mA cm⁻² current densities, respectively. At 0.4 mA cm⁻², the observed nodular distribution was uniform and compact. However, at 4 and 43 mA cm⁻² current densities, a more clustered grain-like structure and a nonhomogeneous distribution of particles were evident. This trend in distribution was further observed as an increase in porosity percentage in films formed using higher current densities relative to films formed at 0.4 mA cm⁻² and the pristine ITO coated glass (Figure S2, Supporting Information). This suggests that current deposition strongly affects the processes of surface diffusion of atoms, nucleation, and coalescence of the film growth resulting in different nucleation densities at the surface.^[58,59] Noteworthy, a correlation between elastic moduli and porosity^[60–62] is inferred, and it can be assumed that anodized ITO films will possess enhanced flexibility due to their high-packing density relative to nonanodized films,^[62] an important consideration

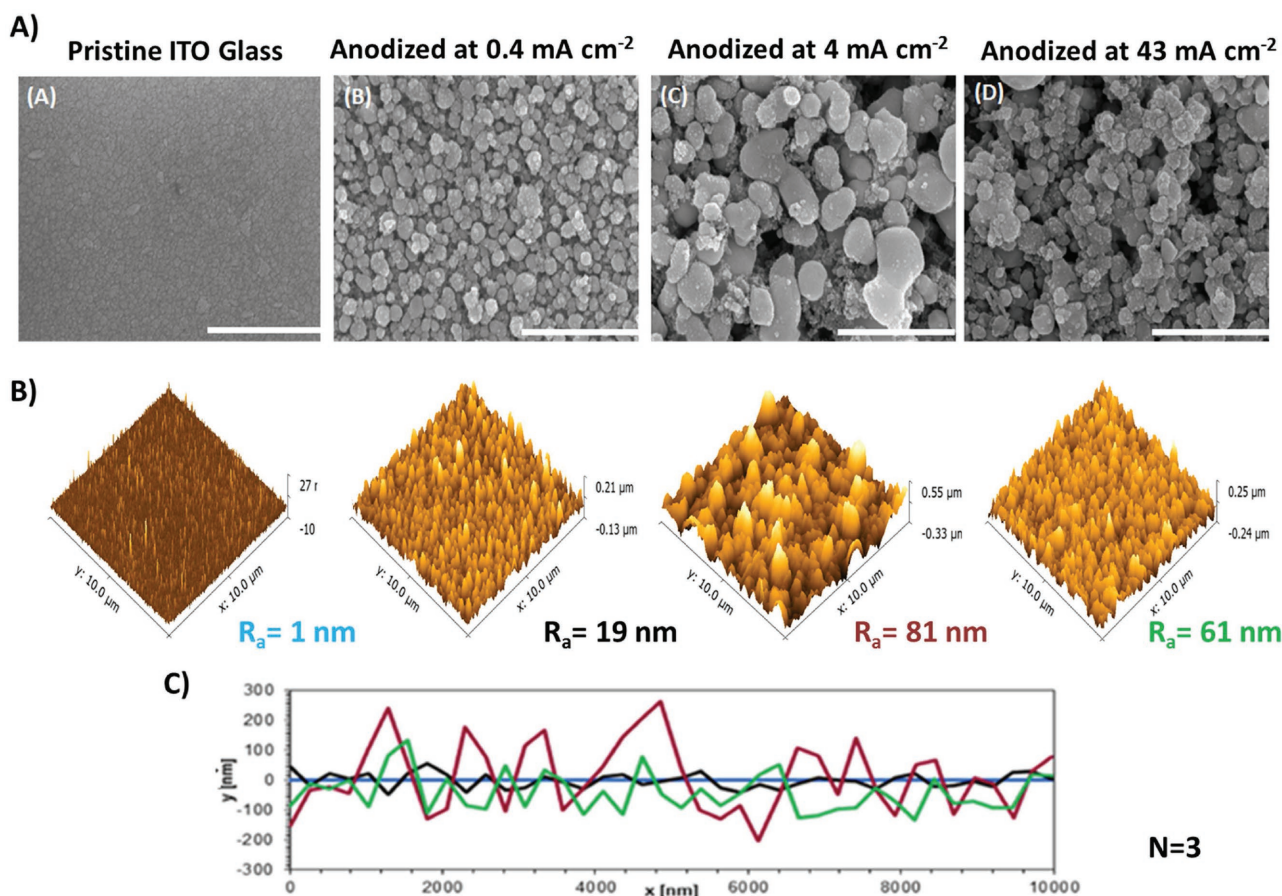


Figure 1. Particle size and distribution are significantly affected by current density. A) Scanning electron micrograms of control pristine ITO coated glass (A) and ITO anodized films electrodeposited with (B) 0.4 mA cm⁻², (C) 4 mA cm⁻², and (D) 43 mA cm⁻² current densities. Scale bar = 1 μm . B) Corresponding roughness (R_a) measurements of the pristine ITO glass and the anodized ITO films with different current densities, 0.4 mA cm⁻², 4 mA cm⁻², and 43 mA cm⁻², and representative line profiles C) from each of the films. R_a indicates the mean surface roughness, calculated on 10 μm^2 regions.

in next-generation neuroelectrode design. Interestingly, it was noted that a current density of 0.4 mA cm^{-2} resulted in anodized ITO films with less internal voids.

Anodization processes resulted in significant increases in surface roughness (R_a) relative to pristine ITO films as a function of current density (Figure 1B). Films formed with current densities of 0.4 mA cm^{-2} exhibited an average roughness of 19 nm over $10 \mu\text{m}^2$, and an average roughness of 81 and 61 nm when formed at 4 and 43 mA cm^{-2} , respectively. Conversely, pristine ITO films possessed an R_a of 1 nm over $10 \mu\text{m}^2$. A similar trend was also observed for mean nodule diameter, which increased from 89 nm in current densities of 0.4 mA cm^{-2} to 152 and 112 nm in films formed with current densities of 4 and 43 mA cm^{-2} , respectively (Table 1).

Similarly, an abrupt increase in film thickness was observed in films formed with current densities of 4 and 43 mA cm^{-2} indicating that the maximum rate of anodization deposition is limited by the electrolyte diffusion rate.^[57] The limiting current density to attain $\approx 100\%$ efficiency of film deposition can be determined theoretically by calculating the maximum rate at which the ions diffuse to the cathode. Our data (Table 1) propose that at 4 mA cm^{-2} (under our experimental conditions), the threshold for the limiting current density may have already been met^[38,57] and the observed nonlinear increases in particle size, film roughness, and the plateau in film thickness could be indications that films formed using a current density of 4 mA cm^{-2} under our experimental conditions are associated with a decrease in film growth efficiency. Therefore, it can be assumed that between 4 and 43 mA cm^{-2} the diffusion limiting current density for ITO anodization can be found, and that the diffusion kinetics of oxygen and hydrogen at the cathode are insufficient, causing reactions at the anode to stop to conserve electrons.

Similarly, this transition in film thickness was also represented as optical changes to the ITO films that changed from a translucent blue-grey to an opaque dark grey (Figure S3, Supporting Information). It can be anticipated, according to the Drude model,^[63] that the changes observed in film morphology derived from the differences in film growth imposed by the explore current densities will impact on the refractive index of films. Optical transmission spectra of the pristine ITO coated glass and the anodized ITO films formed at 0.4 , 4 , and 43 mA cm^{-2} current densities were performed to quantify film transparency (Figure S4, Supporting Information). The observed trend in optical transmittance of the anodized ITO films formed

Table 1. Physical properties of anodized ITO films formed with different deposition currents. Values of experimental thickness and mean particle diameter of pristine and anodized films formed with 0.4 , 4 , and 43 mA cm^{-2} current densities over a constant time of 450 s . The data represent the mean of 15 measurements for film thickness plus >200 measurements for particle diameter. Results are $\pm \text{SD}$, $n = 3$.

ITO film	Average thickness [nm]	Mean particle diameter [nm]
Pristine ITO glass	$750 \pm$	86 ± 17
Anodized at 0.4 mA cm^{-2}	109.7 ± 4	89 ± 26
Anodized at 4 mA cm^{-2}	934.5 ± 35	152 ± 78
Anodized at 43 mA cm^{-2}	937.8 ± 47	112 ± 55

at higher current densities (4 and 43 mA cm^{-2}) reflects scattering losses as predicted by the effects of film roughness.^[64] The aforementioned faster growth observed in films formed at 4 mA cm^{-2} resulted in the decrease in transmittance of these films.

In order to assess the durability and stability of anodized ITO films under physiological conditions, substrates were assessed with an accelerated ageing study that simulated 4 years of implant equivalence in the body (Figure 2). Regarding film delamination (Figure 2A) together with consistent high losses in charge storage capacity (CSC), 75% and 74% were observed in films formed with current densities of 4 and 43 mA cm^{-2} , respectively. Conversely, a 55% loss in CSC of ITO films anodized with the lowest current density of 0.4 mA cm^{-2} was observed (Figure 2B). It is interesting to note that pristine ITO glass also underwent a significant diminution in electrical activity with a 96% loss in CSC and with pronounced micro-cracks observable by SEM.

The effect of thermal ageing on pristine ITO films perceived here was comparable to those presented by Hamasha et al.,^[65] who also tested ITO under thermal ageing conditions and showed that films became unstable and demonstrated increased in electrical resistance and physical changes. Current research to improve the stability of ITO electrodes has focused on the deposition of multilayers,^[66] of novel transport and luminescent materials^[67] such as polymers,^[68] and on efficient injection contacts.^[69] Conversely, it is reported by Nishimoto et al.^[70] that optimal variations in grain-boundary potential caused by oxygen adsorption after annealing TiO_2 structures with ITO can improve thermal stability of pristine ITO. Consequently, surface modifications of thin films of ITO such as the anodization process utilized here may help to explain the enhanced stability observed in anodized films, with the formation of stabilizing oxide layers.^[71]

2.2. Chemical Characterization

In Table 2, the X-ray photoelectron spectroscopy (XPS) survey with the elemental composition of pristine ITO and anodized ITO films using 0.4 , 4 , and 43 mA cm^{-2} is reported. The XPS survey spectrum of pristine ITO revealed the presence of prominent In, Sn, and O peaks. The atomic percentage for C is also relatively high showing a large presence of atmospheric C on the film surface. Similarly, low-current density anodized samples consisted primarily of In, Sn, and O. The O concentration was observed to increase significantly in anodized ITO films, increasing from 42% O1s atomic% in pristine ITO films to 49.81% in anodized films formed with current densities of 43 mA cm^{-2} . Conversely, the Sn atomic% is reduced in anodized ITO films relative to pristine films, which is reportedly due to the leaching of Sn into the electrolyte during the anodization process.^[48]

2.3. Electrochemical Characterization

Figure 3A shows cyclic voltammograms for each of the ITO films in $50 \times 10^{-3} \text{ M}$ phosphate buffer before and after anodization. Surface charge density was approximated through integration of the charge passed within the cathodic region of voltammetric scans, corresponding to charge densities

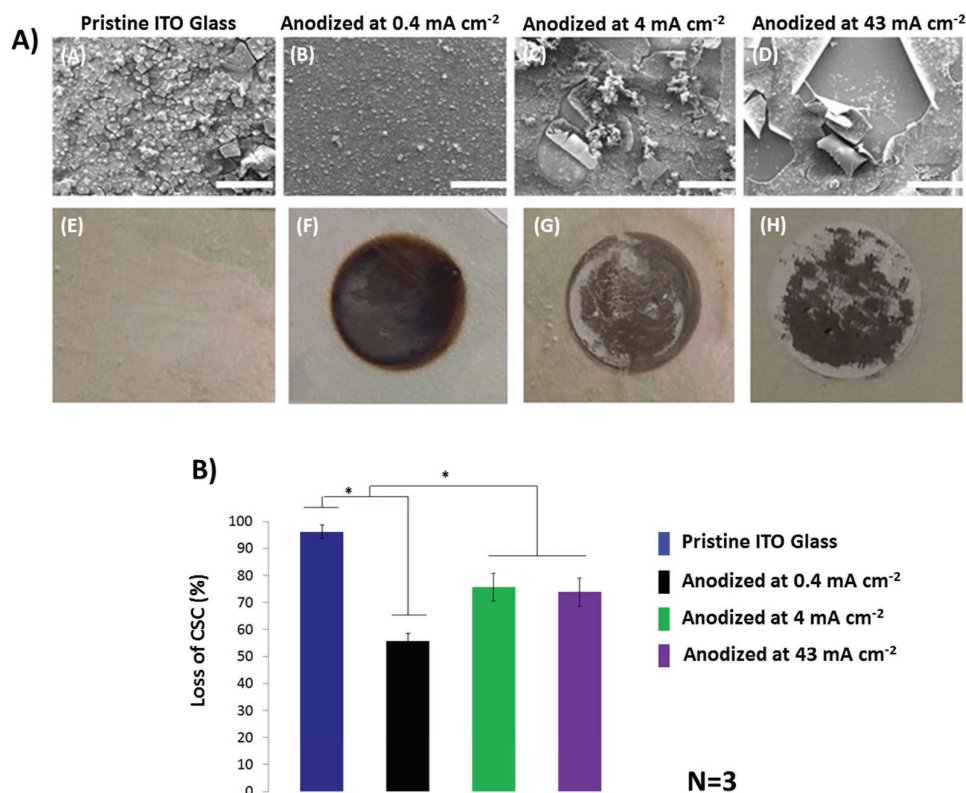


Figure 2. The impact of the accelerated ageing study on durability and electrical stability of the anodized ITO films. A) On top, scanning electron micrograms of control pristine ITO glass (A) and ITO anodized films electrodeposited with (B) 0.4 mA cm⁻², (C) 4 mA cm⁻², and (D) 43 mA cm⁻² current densities. Scale bar = 200 μm. After four weeks under biologically relevant ageing, important film delamination was observed on anodized films formed using high current densities (4 and 43 mA cm⁻²). Partial microcracks were observed in films formed at 0.4 mA cm⁻² and control ITO. On bottom, corresponding photographs showing the final visual appearance of control and anodized films (E)–(H) after four weeks of ageing study. B) Plot of percentage loss of charge storage capacity (CSC) after four weeks of accelerated ageing study simulating four years of implant equivalence in the body. Important significant differences between the ITO control and the anodized films were observed. The ITO anodized films formed at 0.4 mA cm⁻² were the most stable films compared to control and to the films formed using high current densities. Results are ± STD, ★ = *p* < 0.05.

of 49, 341, 15, and 15 μC cm⁻² for pristine ITO films and films subjected to anodization at 0.4, 4, and 43 mA cm⁻² current densities, respectively (Table 3). A large increase in charge density was observed in ITO films subjected to anodization at 0.4 mA cm⁻², by almost one order of magnitude, compared to pristine ITO films. This is likely due to the greater surface coverage as indicated by SEM and atomic force microscopy (AFM) analysis. Interestingly, a threefold reduction in charge density was observed for ITO films subjected to anodization at current densities of 4 and 43 mA cm⁻² compared to the pristine ITO glass (Figure 3A) despite increased surface roughness.

Table 2. XPS analysis of the elemental composition of the pristine ITO and anodized ITO films.

ITO film	Atomic composition [%]			
	In3d	O1s	C1s	Sn3d5
Pristine ITO glass	21.00	42.17	34.62	2.21
Anodized at 0.4 mA cm ⁻²	24.88	43.47	30.34	1.31
Anodized at 4 mA cm ⁻²	23.45	44.53	31.52	1.16
Anodized at 43 mA cm ⁻²	22.75	49.81	26.65	0.78

However, this electrical profile is consistent with the high porosity percentages calculated for these films (Figure S2, Supporting Information). No appreciable difference in charge density was observed in any of the ITO substrates when tested in physiological-like saline solution^[72] compared to 50 × 10⁻³ M phosphate buffer solution.

Comparative electrochemical impedance profiles for films are shown in the Bode diagram (Figure 3C) and Nyquist plot (Figure 3D). Within frequency ranges of 10⁻¹ to 10⁴ Hz, ITO anodized films formed at a current density of 0.4 mA cm⁻² displayed the lowest impedance profiles, moderately lower than those recorded for the pristine ITO films and close to the impedance observed for gold coated glass films. This indicates that changes in chemical composition and/or morphology induced by the 0.4 mA cm⁻² current density anodization process do not appear to diminish the conductive properties of the ITO electrode. This is significant as alternative electrochemical treatments have been shown to greatly decrease the conductivity of ITO electrodes.^[48,50–53] However, an increase in impedance of one order of magnitude was observed for films formed at high current densities (4 and 43 mA cm⁻²), revealing an inverse relationship between electrical conductivity and the anodization current density applied.

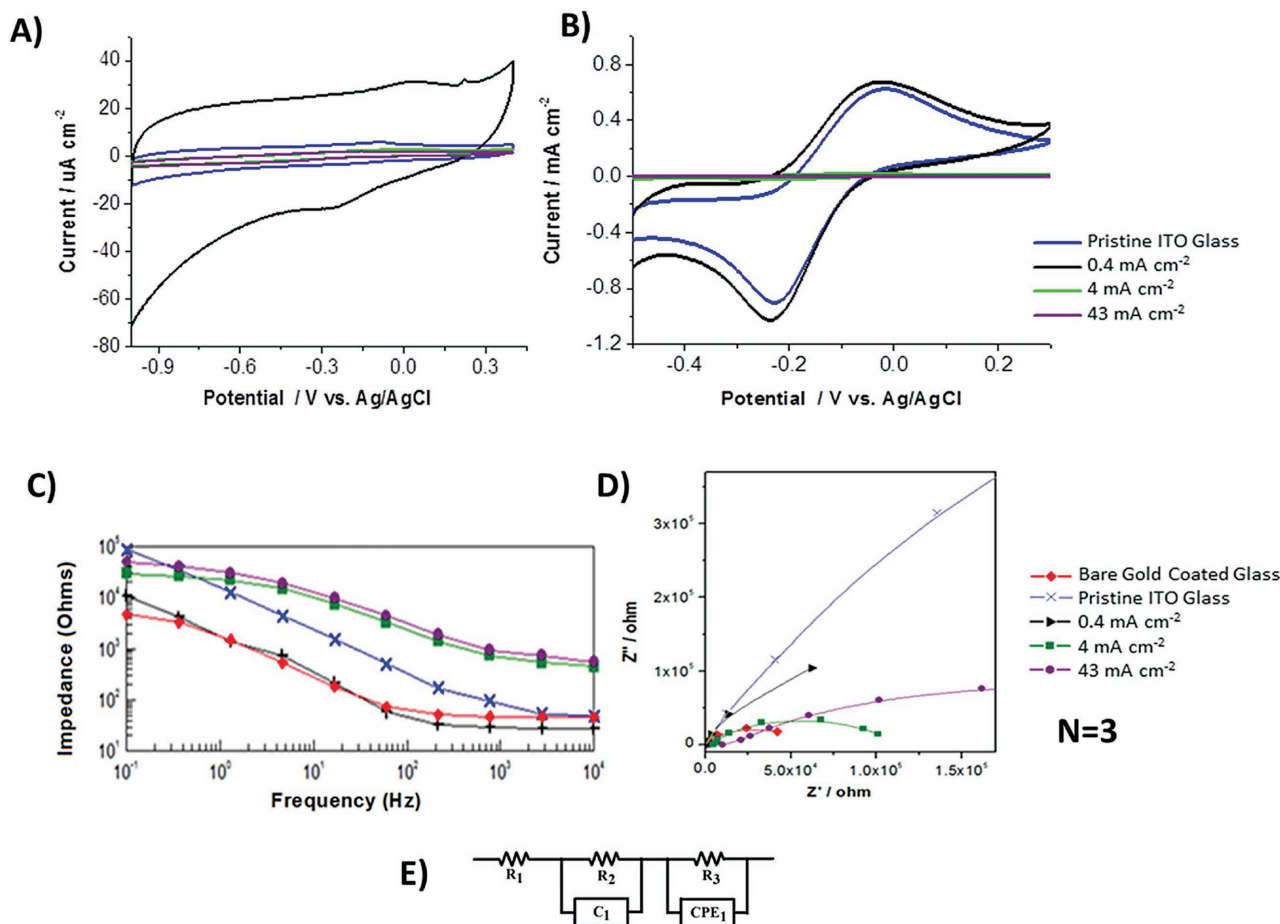


Figure 3. Electrochemical analysis of anodized films. Cyclic voltammograms of ITO (blue) and ITO anodized films formed with current densities; 0.4 mA cm^{-2} (black), 4 mA cm^{-2} (green), and 43 mA cm^{-2} (purple). CVs recorded in $50 \times 10^{-3} \text{ M}$ phosphate buffer, A) scan rate 100 mV s^{-1} and in $50 \times 10^{-3} \text{ M}$ phosphate buffer containing $2 \times 10^{-3} \text{ M}$ $[\text{Ru}(\text{NH}_3)_6]^{3+}$, B) scan rate 100 mV s^{-1} . C) Bode and D) Nyquist plots comparing the EIS spectra of pristine ITO glass (blue-filled asterisks), bare gold glass (red-filled diamonds), and anodized ITO films formed using 0.4 mA cm^{-2} (black-filled triangles), 4 mA cm^{-2} (green-filled squares), and 43 mA cm^{-2} (purple-filled circles). E) The electrical equivalent circuit used to analyze experimental data.

The experimental data of ITO anodized films were fitted to an equivalent circuit (Figure 3E) consisting of three resistors (R_1 , R_2 , and R_3), a capacitor (C_1), and a constant phase element (CPE_1), in accordance with previous studies.^[73–75] In this circuit, R_1 is the solution resistance; and R_2 and C_1 are associated with space charge layer resistance and space charge layer capacitance, respectively. The double-layer capacitance is denoted as CPE_1 and R_3 is ascribed to the resistance of ITO films (Table 4). The simulated data confirmed that the lowest resistance of

$8.3 \text{ k}\Omega \text{ cm}^{-2}$ for the ITO anodized films formed at a current density of 0.4 mA cm^{-2} when compared with the resistance of $9.8 \text{ k}\Omega \text{ cm}^{-2}$ for pristine ITO coated glass. The detrimental effect of high current densities on the conductivity was also observed in the calculated resistance of 22.8 and $209.1 \text{ k}\Omega \text{ cm}^{-2}$ for 4 and 43 mA cm^{-2} current densities, respectively.

To further evaluate the electrochemical characteristics of the ITO anodized films, a ruthenium hexamine ($[\text{Ru}(\text{NH}_3)_6]^{3+}$) redox probe was employed to examine Faradaic redox response

Table 3. Electrochemical characteristics of ITO anodized films. Non-Faradaic charge density evaluated from cathodic region of cyclic voltammograms recorded in $50 \times 10^{-3} \text{ M}$ phosphate buffer at 0.1 V s^{-1} scan rate (potential range: -1 to 0.4 V vs Ag/AgCl). Faradaic charge density and peak current density (i_{pa}) evaluated from voltammograms recorded in $50 \times 10^{-3} \text{ M}$ phosphate buffer containing $2 \times 10^{-3} \text{ M}$ $[\text{Ru}(\text{NH}_3)_6]^{3+}$ at 0.1 V s^{-1} scan rate.

ITO film	Non-Faradaic charge density [$\mu\text{C cm}^{-2}$]	Faradaic charge density [mC cm^{-2}]	E^{ov} [V]	i_{pa} [mA cm^{-2}]	D_o [$\text{cm}^2 \text{ s}^{-2}$]
Pristine ITO	49	1.43	-0.13	0.62	4.62×10^{-6}
Anodized at 0.4 mA cm^{-2}	341	1.45	-0.13	0.67	8.37×10^{-6}
Anodized at 4 mA cm^{-2}	15	0.04	-0.14	0.02	6.92×10^{-9}
Anodized at 43 mA cm^{-2}	15	–	–	–	–

Table 4. Summary of the calculated resistance values (R_3) for each of the anodized ITO films after equivalent circuit analysis.

ITO film	Resistance (R_3) [k Ω cm $^{-2}$]
Pristine ITO glass	9.8 \pm 0.3
Anodized at 0.4 mA cm $^{-2}$	8.3 \pm 0.6
Anodized at 4 mA cm $^{-2}$	22.8 \pm 2.6
Anodized at 43 mA cm $^{-2}$	209.1 \pm 9.2

within a biologically relevant potential range (−0.4 to +0.2 V vs Ag/AgCl) (Figure 3B). With pristine ITO films, [Ru(NH₃)₆]³⁺ undergoes a one electron redox reaction (redox potential (E°) = −0.13 V vs Ag/AgCl), yielding an anodic peak current (i_{pa}) of 0.62 mA cm $^{-2}$ and a Faradaic charge density of 1.3 mC cm $^{-2}$ (Table 3). A slight increase of i_{pa} and Faradaic charge density is observed with ITO films formed through anodization at 0.4 mA cm $^{-2}$, possibly due to the increased surface roughness. This shows that although the non-Faradaic charge density is greater with these films, the increased surface roughness does not translate into a greater electrochemically active surface area than that of the relatively smooth nonanodized ITO film. Kraft et al.^[48] observed a similar response using [Fe(CN)₆]^{3−} as a redox probe, where non-Faradaic current (charge density) increased after ITO electrode anodization while Faradaic current remained essentially constant. A large decrease of i_{pa} and Faradaic charge density is evident in ITO films subjected to anodization with current densities greater than 0.4 mA cm $^{-2}$, accompanied by a slight decrease in E° of \approx 10 mV for the Ru^{3+/2+} redox couple (Table 3). The difference in E° may result from variation in chemisorption sites within the electrode film, which can influence redox probe stability.^[76] The voltammetric response observed for ITO films anodized at 43 mA cm $^{-2}$ is characteristic of a highly resistive surface with no evidence of heterogeneous electron transfer between the electrode and the redox probe.^[77]

Scan rate studies (Figure S5, Supporting Information) revealed a linear dependence of i_{pa} versus $\nu^{1/2}$ (ν = scan rate) for all ITO films (with the exception of ITO anodized films formed with current densities of 43 mA cm $^{-2}$), indicative of a semi-infinite planar diffusional response described by the Randles–Sevcik equation.^[78] Diffusion coefficients (D_0), evaluated from the linear portion of i_{pa} versus $\nu^{1/2}$, are shown in Table 3. D_0 values in the order of 10 $^{-6}$ cm s $^{-1}$ were calculated for [Ru(NH₃)₆]³⁺ at both pristine ITO and ITO films formed through anodization at 0.4 mA cm $^{-2}$ in a phosphate buffer. Again, a decrease of D_0 , by approximately three orders of magnitude, is evident for ITO films subjected to anodization with current densities of 4 and 43 mA cm $^{-2}$, further corroborating the insulating nature of films prepared at anodizing current densities greater than 0.4 mA cm $^{-2}$.

Interestingly, the presence of the PSS ionomer was critical for the anodization process and ITO thin films subjected to anodic oxidation under ambient conditions in a 0.01 M phosphate-buffered saline solution were associated with a linear increase in impedance profile as a function of current density (Figure S6, Supporting Information).

2.4. Biological Characterization

Nanoscale signaling modality has been shown to have a profound effect on cell viability, proliferation, and on cell attachment in the material's space.^[79–81] Because the application of different current densities for the anodization of ITO films resulted in defined nanoscale morphological changes, the cellular interfacial response has been analyzed based as a function of roughness. With this in mind, the effects of films formed at 0.4, 4, and 43 mA cm $^{-2}$ current densities, which in order exhibit an average of roughness of 19, 81, and 61 nm, respectively, on human neuroblastoma SH-SY5Y cell adhesion and proliferation were assessed in vitro. These were then compared to pristine ITO coated glass with an experimental average roughness of 1 nm (Figure 4A). After periods of 1, 7, and 14 d, cells were stained with calcein (live) and ethidium homodimer (dead) to establish cell viability. All experimental and control films were nontoxic to SH-SY5Y cells. However, significant differences were observed at day 14 with respect to cell viability. Cells grown on films with the lowest roughness profile (formed at the lowest current density 0.4 mA cm $^{-2}$; R_a = 19 nm over 10 μ m²) maintained 86% viability relative to control films at day 1 (Figure 4B). Similarly, when analyzed with alamarBlue Assay by 24 h (Figure 4C), the SH-SY5Y population cultured on anodized ITO films was comparable to cells cultured on control pristine ITO coated glass. While by days 7 and 14 cells cultured on all experimental anodized films demonstrated a marked decreasing trend in metabolic activity, the anodized films with 19 nm roughness (formed at 0.4 mA cm $^{-2}$ current density) showed an overall significant higher metabolic activity of 87% by day 7 and 78% by day 14, respectively, compared to 61 and 81 nm films' roughness profiles and pristine ITO control substrates. Overall, anodized ITO films possessing an R_a 81 nm (the highest roughness profile) showed a significant decrease in metabolic activity relative to cells cultured on control ITO coated glass and on anodized films with 19 nm roughness.

These results are similar to those of Fan et al.^[82] In their work, they have reported on the cell proliferation of neural cells cultured on silicon wafers possessing different levels of surface roughness. It was concluded that the Si wafers with surface R_a ranging from 20 to 50 nm promoted a significantly higher cell proliferation. Conversely, on surfaces with an R_a less than \approx 10 nm and on rough surfaces with R_a above 70 nm, cell metabolic activity was reported to be significantly lower. It is noteworthy that even though cell proliferation and viability depend on cell type and substrate composition, it is apparent that neurons do not readily attach on excessively smooth (R_a = 10 nm) or rough surfaces (R_a = 250 nm).^[83]

Tissues can be described as complex nanoscale composites that impact morphological and mechanical features to the resident cellular constituents. Previous studies show that nanotopography influences cellular function and focal adhesion (FA) formation in vitro^[79,84] and may be employed to modulate the dynamic interface between materials and cell/tissues. With an awareness of this, cell attachment to the anodized ITO films was quantified through immunofluorescent labeling of the FA associated protein paxillin^[85] (Figure 5A–D). At day 1, cells cultured on all experimental films and control pristine ITO glass were associated with an overall average of \approx 14 focal adhesions

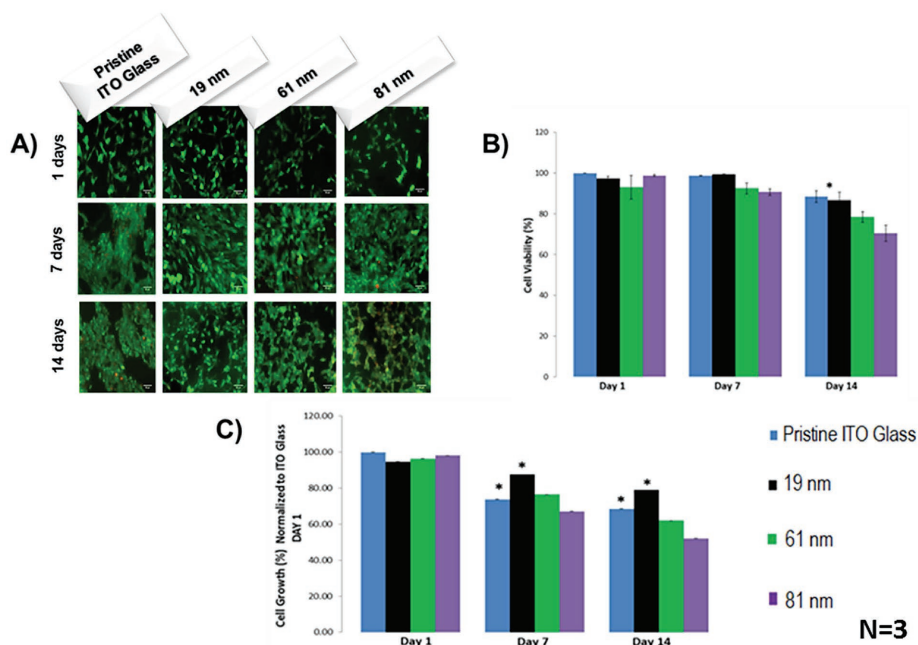


Figure 4. Cytocompatibility analysis of anodized ITO films of different roughness (R_a) formed by varying the current density. A) Fluorescent images of SH-SY5Y cells following 1, 7, and 14 d in culture on anodized films displaying 19, 61, and 81 nm over $10 \mu\text{m}^2$ (R_a) roughness relative to pristine ITO control (R_a 1 nm over $10 \mu\text{m}^2$). Green, live; red, dead. Bar = $50 \mu\text{m}$. B) A significant ($p < 0.05$) decrease in cell viability was observed in anodized films with an average roughness of 61 and 81 nm relative to control and 19 nm film roughness. C) Metabolic activity of SH-SY5Y cells compared with pristine ITO coated glass control as measured by the alamarBlue Assay ($p < 0.05$), $n = 3$. Metabolic activity was significantly elevated in cells cultured on anodized ITO films with 19 nm roughness relative to anodized films with 61 and 81 nm roughness, respectively, by days 7 and 14. Results are \pm STD, $\star = p < 0.05$.

per cell. By day 7, SH-SY5Y cells cultured on pristine ITO control presented a significant increase in FA numbers per cell, an average of 25 focal adhesions per cell, compared to all the experimental anodized ITO films with an average number of 17 FAs per cell. Interestingly, trends in FA numbers were

reversed in cells cultured on the pristine ITO control group by day 7, which demonstrated a significant reduction in FA number by day 14 (Figure 5E). Conversely, previous studies have reported a disruption to cell adhesion by nanorough surfaces with similar roughness profiles^[79,86] and a decrease in cell viability; however,

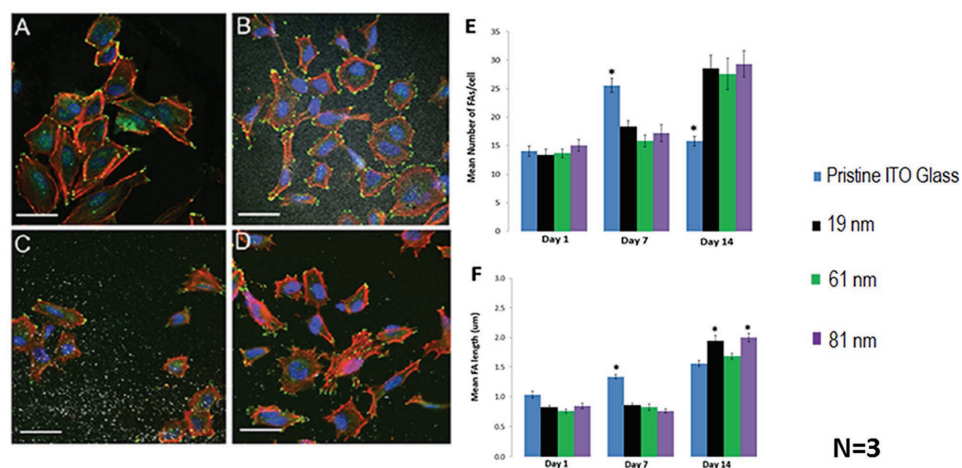


Figure 5. Focal adhesion formation of SH-SY5Y cell grown roughness. A–D) Immunofluorescent imaging was employed to quantify FA length and number in cells cultured on pristine ITO coated glass and experimental anodized films of different roughness (green: paxillin, red: actin; blue: nucleus, bar: $40 \mu\text{m}$). E) Cells cultured on control ITO coated glass generated less FA complexes over time, while this trend was reversed in cells on experimental anodized ITO films of all roughness. SH-SY5Y cells grown on 19 and 81 nm roughness of anodized films were associated with a significant increase in FA length relative to cells cultured on pristine ITO coated glass ($R_a = 1 \text{ nm}$). F) There was a significant reduction in cell adhesion on 61 nm roughness compared to the cells grown on 19 and 81 nm experimental roughnesses. For all analysis, results are \pm STD, $\star = p < 0.05$.

FA quantification was not performed in these studies. Specifically, it was noted by Brunetti et al.^[79] that cellular adhesion was significantly increased on regions of low (smooth) roughness.

Independent of the surface roughness, it was interesting to note an increased number of FAs in SH-SY5Y cells cultured on all anodized films relative to SH-SY5Y cells cultured on pristine ITO coated glass by day 14.^[87] We hypothesize that the enhanced number of FA observed in SH-SY5Y cells cultured on anodized ITO films relative to pristine ITO may be as a result of the anodization process inducing differential protein adsorption.^[88,89] Studies into the influence of surface chemistry on protein adsorption through etching and deposition techniques,^[90] plasma treatment,^[91] and anodization processes^[92] indicate enhanced extracellular matrix (ECM) protein adsorption as a function of oxygen content,^[88,93,94] also observed here in anodized ITO films.

Similarly, FA length was observed to be significantly greater in cells cultured on pristine ITO control substrates than in cells cultured on anodized films by day 7. By day 14, the FA length in the experimental anodized films with the lowest and highest roughness profiles (19 and 81 nm) was significantly higher than the length of FAs in cells cultured on pristine ITO control substrates (Figure 5F). A significant reduction in FA length was noted, however, in cells cultured on R_a film roughness of 61 nm over $10 \mu\text{m}^2$. This reduction in FA reinforcement may be related to the particle diameter and nanofeatures with lateral dimensions of ≈ 100 nm that have been shown to be disruptive to integrin clustering,^[84,95] an effect which is lost by reducing or increasing the feature dimensions, an effect also demonstrated here.

To gain further insight into cell adhesion, the length of the FAs was subgrouped in focal complexes (FXs) measuring $<1 \mu\text{m}$ in length and FAs proper, measuring between 1 and $5 \mu\text{m}$. FXs were most abundant in cells cultured on all experimental roughnesses and pristine ITO coated glass substrates on days 1 and 7. By day 14, cells cultured on anodized ITO films with roughness of 19, 61, and 81 nm over $10 \mu\text{m}^2$ demonstrated reduced FX frequency, and a similar FA distribution profile with lengths ranging from 1 to $4.5 \mu\text{m}$. However, cells cultured on control ITO substrates were associated with a reduction in FA frequency (Figure 6). It was interesting to note that over a period of 14 d in culture, cells demonstrated a progressive shift from nascent and unstable focal complexes to more stable focal adhesions. Hence, it can be inferred that the influence of film roughness is a predominant factor in the observed increase in

focal adhesion frequency together with the concept of increased oxygen content to protein adsorption owing to the anodization process.

In order to assess the potential functional response of neuronal populations to implanted anodized ITO thin-film devices in vitro, and the potential for induction of a reactive astrocyte phenotype, the functional response of a primary ventral mesencephalic (VM cells) coculture was assessed via an in-house protein microarray assay. Spotted antibodies for proteins associated with astrocyte reactivity, cell adhesion, and mechanotransduction utilized in this study are outlined in Table S1 (Supporting Information). Antibodies were printed at a range of concentrations ($0.1\text{--}1 \text{ mg mL}^{-1}$) and assessed for retained function and optimal print concentration by incubation with a fluorescently labeled protein lysate from VM cells cultured for 21 d on all anodized films and pristine ITO control (Figure S8, Supporting Information).

Owing to the construction of the gliosis antibody microarray, an unsupervised clustering of all experimental films normalized by control pristine ITO was performed (Figure 7). This analysis clearly defined a group between the anodized films with nanoroughness of 61 and 81 nm, respectively, and a single cluster for the films formed with the lowest roughness profile of 19 nm (formed at 0.4 mA cm^{-2} current density); sharing only 1% similarity with the rest of the experimental substrates. As gliosis is dependent on the bioelectrochemical as well as physicochemical properties of the implanted material it was remarkable to notice that the resulting roughness factor of the anodized films was predominant on the differential intensity expression of the antibodies evaluated.

The hallmarks of glial scar formation are multifactorial; in the developed antibody microarray gliosis was studied from the diverse and interwoven response of microglia and astrocytes,^[96,97] and from the changes of transient calcium currents that affect overall homeostasis and astrocyte reactivity.^[98] Overall, ITO anodized films formed with current densities of 0.4 mA cm^{-2} (films with 19 nm roughness) showed significant downregulation of the gliosis response relative to VM populations cultured on other anodized ITO films. Specifically, downregulation in the intensity of OX42/Iba1 (microglia), glial-fibrillary acidic protein (GFAP), and Nestin (reactive astrocytes) was observed.

A recent study by Kim et al.^[99] has shown that coupled to the increase in GFAP expression as main marker for reactive

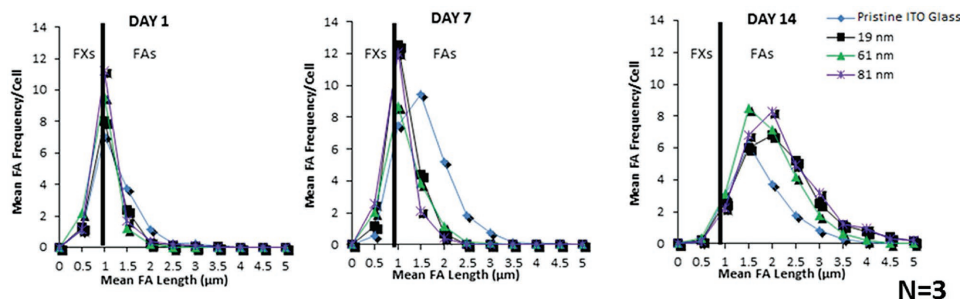


Figure 6. Focal adhesions were subgrouped into focal adhesions (FAs) proper and nascent focal complexes (FX). FXs were the predominant adhesion complex subtype observed on all anodized ITO films and the pristine ITO coated glass up to day 7. However, FXs were displaced by the FA subtype by day 14 in cells cultured on all experimental and control materials. A significant increase in the mean number of focal adhesions per cell on all of the experimental anodized ITO films compared to control pristine ITO group was observed on day 14, $n = 3$.

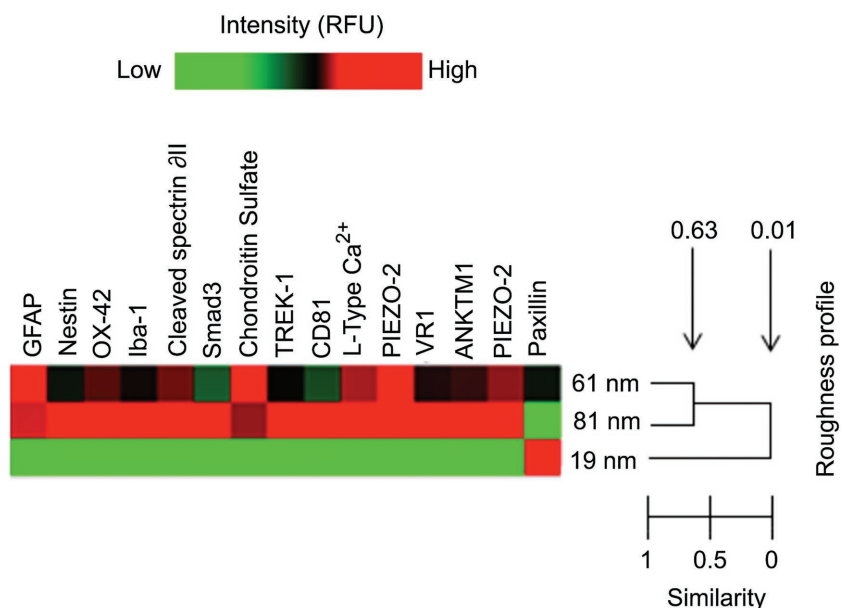


Figure 7. Unsupervised clustering of all experimental anodized films normalized by control pristine ITO. This analysis clearly defined a group between the anodized films with nanoroughness of 61 and 81 nm, respectively, and a single cluster for the films formed with the lowest roughness profile of 19 nm; sharing only 1% similarity with the rest of the experimental substrates. The gliosis response of the films formed with 0.4 mA cm^{-2} current density, which exhibit the lowest roughness profile of 19 nm, showed a remarkable intensity downregulation of reactive astrocytes, microglia and calcium influx markers. The resulting roughness factor of the anodized films was predominant on the differential intensity expression of the antibodies evaluated.

astrocytes, further reactivity can be fully characterized by the expression of cleaved spectrin α II. Downregulations in cleaved spectrin α II were also observed in VM populations cultured on ITO anodized films formed with current densities of 0.4 mA cm^{-2} relative to cells cultured on other experimental and control substrates, again indicating the reduced potential of these films to induce a reactive astrocyte phenotype.^[99]

Interestingly, cleaved spectrin α II is sensitive to calpain-mediated proteolysis, and calpains have been shown to play a central role in the neuroprotection of the CNS and neuron calcium influx^[100,101] changes in which may mediate the onset of reactive gliosis.

Cleaved spectrin α II protein is directly linked to the regulation of intracellular Ca^{2+} concentrations, and it was noted that together with the downregulation of this protein, only VM cells cultured on films formed with 19 nm roughness (formed at 0.4 mA cm^{-2} current density) exhibited a low expression of L-type Ca^{2+} and the mechano-gated ion channel PIEZO 2. These observations are intriguing as an upregulation in voltage-gated calcium channels such as L-type Ca^{2+} has been known to induce reactive astrogliosis.^[98] Furthermore, the calcium regulator mechanosensitive protein PIEZO 2 is known to play a role in the regulation of calcium permeability, which may relate to cell membrane damage.^[102–104] It is of importance to indicate the observed downregulation of TREK 1 expression on ITO films anodized with 0.4 mA cm^{-2} and that optimal function of astrocytes homeostasis is mediated by K^+ channels^[105] such as TREK 1, which has been shown to help set the negative resting membrane potential of astrocytes and regulate

astrocyte reactivity.^[106] Moreover, downregulation in protein markers for gliosis such as Smad3,^[107] chondroitin sulfate^[108] and the TRP^[109] family channels such as VR1^[110] and ANKTM1^[111] proteins linked to inflammation and the attenuated gliosis response were observed in VM cells cultured on ITO films anodized with 0.4 mA cm^{-2} .

In order to validate cell studies performed with SH-SY5Y cells migration proteins such as CD 81 (TAPA) and paxillin were also concurrently assessed in VM populations. CD 81 is a member of the tetraspan family of proteins and is involved both in cell adhesion and the machinery of migration^[112] and in relation to glial scar formation, CD 81 has been found to have a defined relation to reactive astrocytes expression. Critically, previous studies have shown that upregulation of CD 81 is a prominent characteristic of glial scar formation.^[113,114] Moreover observed downregulation in the expression of CD 81 and upregulations in the expression of paxillin are in accordance with observed modulation to FA formation in SH-SY5Y cells and suggest that the roughness of anodized ITO films has an effect on focal adhesion frequency and cell adhesion.

2.5. Functional Characterization

The ability of anodized ITO to interface neuronal circuit formation was subsequently explored via patch-clam analysis. In particular, due to the favorable electrochemical and phenotypical responses of VM cells to these anodized films the functional response was explored using explanted primary neurons on ITO anodized at the lowest current density (0.4 mA cm^{-2}) via two functional indicators: network formation and synaptic activity.^[115] Rat hippocampal cells, from which primary neuronal cultures were grown and maintained for 8 to 10 d on ITO anodized films formed at a current density of 0.4 mA cm^{-2} , were compared to control cultures grown on poly-L-ornithine coated glass coverslips. Hippocampal neuron maturation and viability were assessed using single-cell recordings (see subsection “*Electrophysiological Recordings*” in the Experimental Section). Visually identified neurons from the two culture groups were patch clamped under voltage clamp modality to measure the cell passive membrane properties that are known indicators of neuronal health.^[116] These parameters (input resistance and membrane capacitance) did not differ ($P = 0.221$ and $P = 0.369$ for input resistance and cell capacitance, respectively) when measured in the two culture conditions (see bar plots in **Figure 8C**). We investigated synapse formation and activity after in vitro growth of neurons by measuring the occurrence of spontaneous postsynaptic currents (PSCs) in both culture groups. The appearance of PSCs provided clear evidence of functional synapse formation, which is a widely accepted index of network efficacy.^[115]

Figure 8A shows representative current tracings of the recorded electrical activity. PSC amplitude and frequency were measured from neurons grown in control and 0.4 mA cm^{-2} anodized ITO films. As summarized in the bar plots of Figure 8B, these values were not statistically different ($P = 0.988$ and $P = 0.247$, amplitude and frequency, respectively) in the two groups of cultures and were consistent with those measured in other studies testing the permissive nature of manufactured interfaces.^[117] The impact on cells of the modified substrate is, therefore, negligible. In Figure 8D, the cellular composition of control and anodized ITO film hippocampal cultures is shown, assessed by immunofluorescence markers^[118] for astrocytes (GFAP) and neurons (β -tubulin III). It was observed both β -tubulin III and GFAP immunoreactive cells in all growing conditions (Figure 8D left and right panels) and both cell groups were represented in a proportion that is comparable in all experimental groups (quantified by measuring the cell density, bar plot in Figure 8E; $P = 0.415$, 30 visual fields per condition, three different culture series). Thus cell survival and the global network size were not affected by ITO anodized film formed at current density of 0.4 mA cm^{-2} .

To assess the ability of ITO anodized films formed at a current density of 0.4 mA cm^{-2} to transfer sufficient charge for cellular depolarization, primary cultures of VM cells were grown on films for 60 d and stimulated with biphasic pulses of 2 V cm^{-2} , 0.1 s duration at a frequency of 0.2 Hz . Cells were observed to generate calcium transients in response to the stimulus via 0.4 mA cm^{-2} anodized ITO films, while the same stimulus did not elicit any response in pristine ITO control cultures. Representative traces of changes in background subtracted Fluo4 fluorescence intensity from individual regions of interest were acquired (Figure 9) (representative videos of the stimulation via 0.4 mA cm^{-2} (Video S1, Supporting Information) and pristine ITO controls (Video S2, Supporting Information) using VM cells are available in the Supporting Information). Moreover, calcium transients were also visible when using primary hippocampal neurons, cultured on 0.4 mA cm^{-2} anodized ITO films (Figure S9, Supporting Information).

3. Conclusion

Here we employed a range of current densities for the anodization of ITO in an aqueous cytocompatible electrolyte and investigated the effects of anodization current density on ITO electrochemical, physical, and cytocompatibility properties. Furthermore we assessed anodization as a methodology for the formulation of neural interface materials with a focus on reduced cellular reactivity and enhanced neural stimulation capacity.

This work provides a useful benchmark for anodization conditions for subsequent studies with neural microelectrodes, micropatterning, and biochemical functionalization. It was observed that anodization offers the ability to modify ITO films with differential properties for charge transfer and resistivity may provide a facile approach to the deposition of electrode coatings with differential regions of charge conductance and cellular function capacities. It can be hypothesized that anodization with varying current densities may be employed to deposit insulator and charge carrier regions on a single

electrode system, providing cytocompatible and functional coatings for implantable thin-film ITO devices.

4. Experimental Section

Anodic Oxidation of ITO: The anodic oxidation of ITO was conducted under ambient conditions in a solution of $10 \times 10^{-6} \text{ M}$ PSS (Sigma-Aldrich, Ireland, $70\,000 \text{ g mol}^{-1} M_w$) prepared in a 0.01 M PBS solution with a platinum foil as a counter electrode (cathode). The electrolyte solution was placed in an in-house fabricated electrochemical cell, connected to a Princeton Applied Research Potentiostat/Galvanostat model 2273 controlled with Power Suite software. Pristine ITO coated glass slides were purchased from Diamond Coatings, UK. These were provided as thin films sputtercoated onto glass substrates with a nominal thickness of 750 nm and a sheet resistivity of $8\text{--}10 \text{ Ohms sq}^{-1}$. Pristine ITO coated glass slides were individually cleaned in acetone, dried with a stream of nitrogen, and moved to a desiccating chamber to remove moisture for 24 h prior to use. Galvanostatic anodization was performed applying constant current densities of 0.4 , 4 , and 43 mA cm^{-2} over a constant time of 450 s to pristine ITO coated glass. A schematic representation of the anodization process is presented in Figure S10 (Supporting Information).

Physical Characterization—Surface Morphology: SEM was carried out using a Hitachi S-4700 Cold Field Emission Gun Scanning Electron Microscope. The SEM images were taken using an accelerating voltage of 15 kV and spot current of $10 \text{ }\mu\text{A}$. Gold sputtering was carried out before testing the samples using an EMSCOPE SC500 to deposit 10 nm of gold.

AFM was performed to analyze the roughness of the samples. All measurements were taken on a Veeco Dimension 3100 AFM using TESPA Tips (NanoWorld) ($\text{Si} < 8 \text{ nm}$ tip radius, 42 N m^{-1} spring constant, 320 kHz nominal resonance frequency), in tapping mode over an area of 10 and $10 \text{ }\mu\text{m}^2$, respectively, with a $0.5\text{--}1 \text{ Hz}$ scan rate.

Transmission Electron Microscopy (TEM) was performed using an H-7000 electron microscope to analyze inner particle distribution of the films. The samples were fixed into Epon base low viscosity resin (Agar Scientific R1078) so as to release the samples from the glass surface slide and be embedded in the resin. Thereafter, all samples were sectioned at 100 nm thickness and collected on Formvar-carbon 200 mesh copper grids (Agar Scientific—62200N-200 Square Mesh Nickel 3.95 mm). Images were taken at 75 kV with direct magnification of $20\,000\times$.

Physical Characterization—Thickness Measurements: The thickness of the anodized films was measured using a Zygo Newview 100 surface profilometer controlled by MicroPlus software. A pattern of bright and dark lines—fringes was created as incoming light was split from the limited region between the anodized film and the pristine ITO glass. This pattern difference was translated to calculate the height information, resulting in the thickness of the film. The size of the testing area was 1.6 cm^2 .

Physical Characterization—UV-Visible Spectroscopy: The optical transmittance of the ITO coated glass and the anodized films was assessed by using a Thermo Scientific Varios-Kan Flash microplate reader at the visible-light wavelengths ($400\text{--}800 \text{ nm}$).

Physical Characterization—Stability and Durability through Accelerated Ageing Study: The stability of the pristine ITO glass and the anodized ITO films was determined using a long-term passive degradation through accelerated ageing study. Following the ASTM international guidelines for accelerated aging of medical devices^[119] as well as the procedure detailed by Green et al.^[120] and Hukins et al.^[121] the experimental parameters were determined using Equation (1)

$$t_{37} = t_T \times Q10^{(T-37)/10} \quad (1)$$

where t_{37} is the simulated time at $37 \text{ }^\circ\text{C}$, t_T shows time samples are placed at the elevated temperature, T is the elevated temperature, and $Q10$ is the accelerated factor equal to 2.0 as per the ASTM specification.

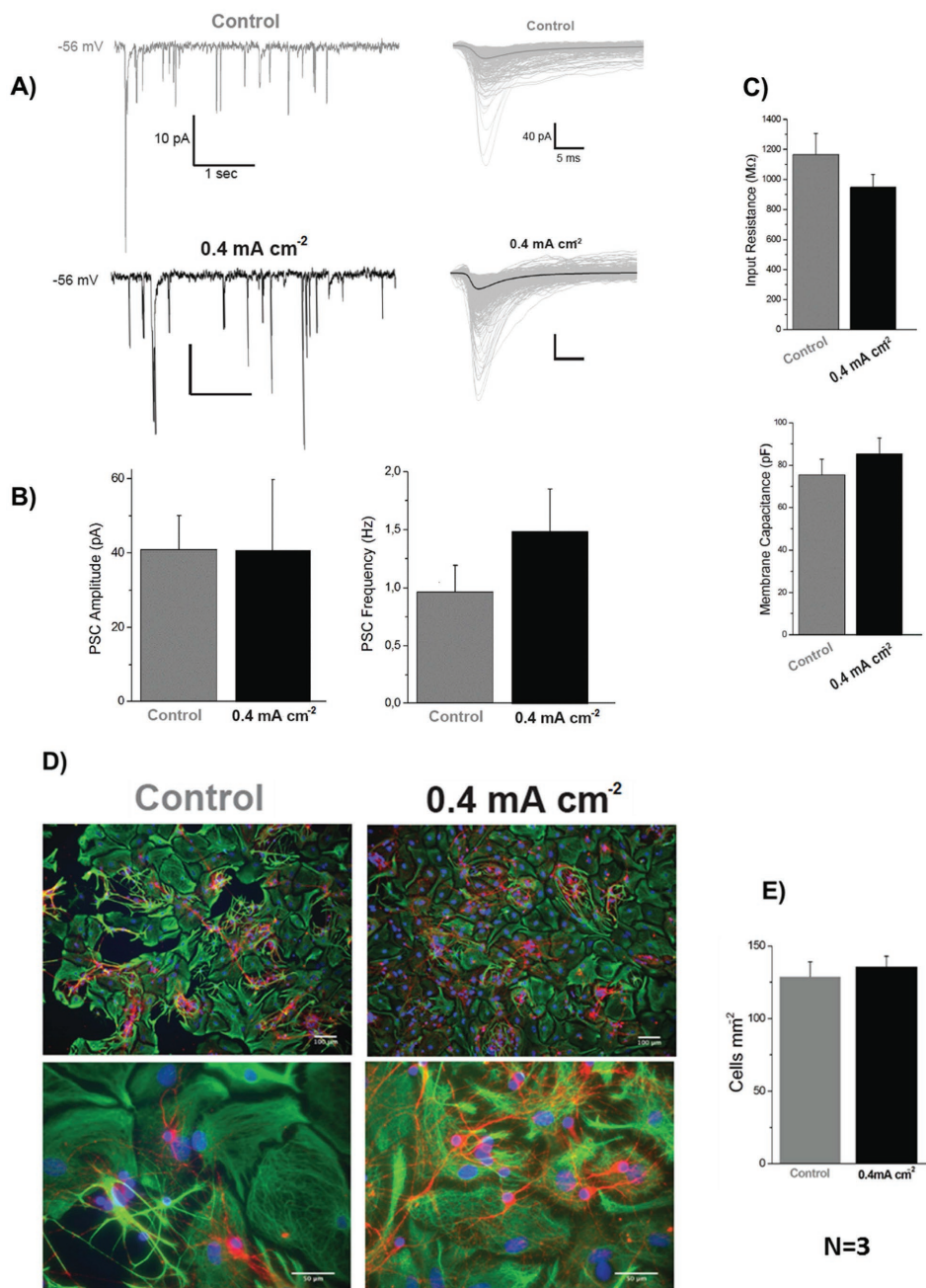


Figure 8. Synaptic network formation on anodized film formed at a current density of 0.4 mA cm^{-2} . A) Left, current tracings from two sample neurons (in grey control and in black anodized film) showing heterogeneous postsynaptic currents (PSCs; inward deflections) recorded at a holding potential of -56 mV . Right, Superimposed traces show isolated PSCs recorded from control (top; the average is superimposed in grey) and 0.4 mA cm^{-2} (bottom; the average is superimposed in black) neurons. B) Bar plots summarize PSC amplitude (left) and PSC frequency (right) values. Although not statistically significant, on anodized films PSC frequency was slightly higher ($0.96 \pm 0.65 \text{ Hz}$ in controls and $1.48 \pm 0.97 \text{ Hz}$ in anodized films, $n = 8$ and $n = 7$, respectively), while the average values for PSC amplitude were similar ($40.8 \pm 25.9 \text{ pA}$ controls and $40.5 \pm 50.7 \text{ pA}$ in anodized films). C) Bar plots summarize the values measured for the input resistance (top, $1195 \pm 368 \text{ M}\Omega$ controls and $946 \pm 229 \text{ M}\Omega$ anodized films) and membrane capacitance (bottom, $75 \pm 20 \text{ pF}$ controls and $85 \pm 19 \text{ pF}$ anodized films). D) Fluorescent micrographs of immune-labeled cultures, control (left) and anodized films (right), at low (top panels, objective 10 \times) and high (bottom panels objective 40 \times) magnifications. Neurons are visualized by anti β -tubulin III, in red, glial cells by anti-GFAP, in green, and nuclei are visualized by Hoechst, in blue. E) The plots summarize neuronal (left) and glial (right) densities in all conditions.

Three experimental replicas for each group were placed in an oven at $95 \text{ }^\circ\text{C}$ and immersed in 0.9% saline for four weeks simulating 1560 d (four years) of implantation. Cyclic voltammetry was performed before and after the ageing study and used to calculate the percentage of

loss in CSC. SEM pictures were taken after the ageing study to show morphological changes. The SEM sample preparation and imaging were performed following the details in the subsection “Physical Characterization—Surface Morphology” of this section.

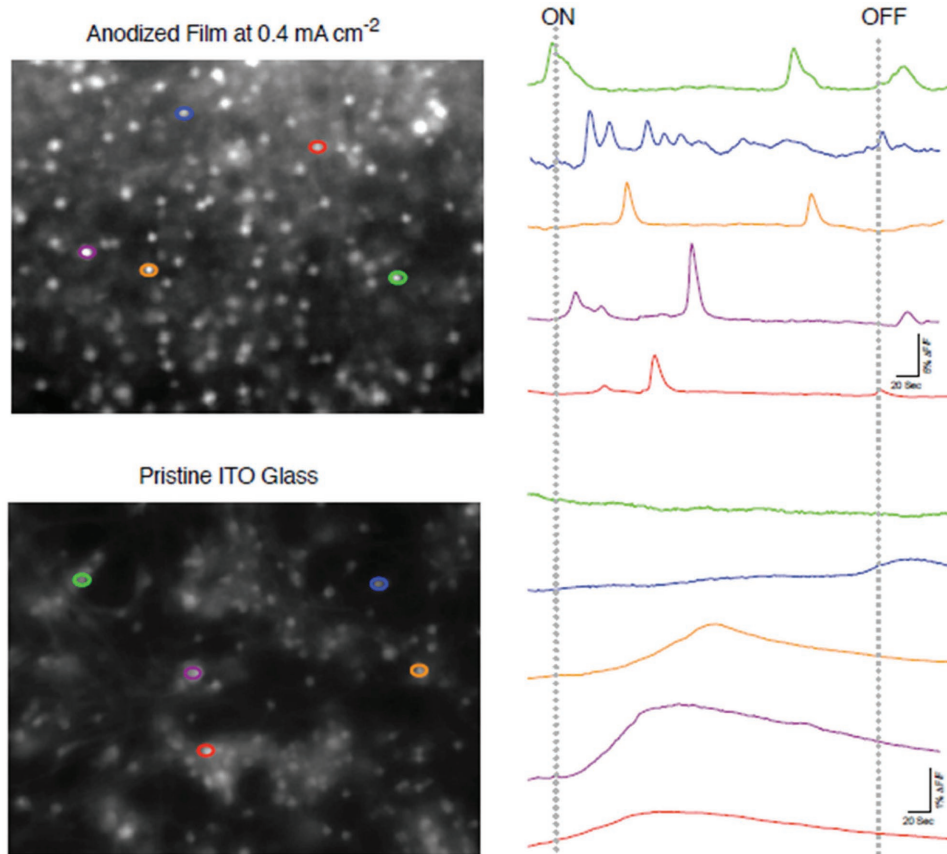


Figure 9. Calcium imaging and substrate stimulation. Left snapshots of representative fields of VM cells grown on anodized ITO film formed at 0.4 mA cm^{-2} (top) and control pristine ITO glass (bottom) and stained with calcium-sensitive fluorescent probe Fluo-4. Five regions of interest (ROI) per images were selected (highlighted in different colors), each representing a single neuron. Right, fluorescence tracings show the appearance of Ca^{2+} episodes, calcium events were measured from the relative ROI in the corresponding recording filed in both conditions (each cell is identified by the color). Stimulation was delivered to the films as biphasic voltage pulses (2 V cm^{-2} , 0.1s pulse, 0.2 Hz). Dashed lines highlight the corresponding evoked calcium response in both groups. Note that all selected cells displayed calcium transients in response to the stimulus in the 0.4 mA cm^{-2} condition, while the same stimulus did not elicit any responses in control cultures.

Chemical Characterization: XPS spectra were acquired on an Oxford Applied Research Escabase XPS system equipped with a CLASS VM 100 mm mean radius hemispherical electron energy analyzer with a triple-channel detector arrangement in an analysis chamber with a base pressure of 5.0×10^{-10} mbar. Survey scans were acquired between 0 and 1100 eV with a step size of 0.7 eV, dwell time of 0.5 s, and pass energy of 100 eV. Core level scans were acquired at the applicable binding energy range with a step size of 0.1 eV, dwell time of 0.5 s, and pass energy of 50 eV averaged over 50 scans. A non-monochromated Mg- $\text{K}\alpha$ X-ray source at 200 W power was used for all scans. All spectra were acquired at a take-off angle of 90° with respect to the analyzer axis and were charge corrected with respect to the C 1s photoelectric line by rigidly shifting the binding energy scale to 285 eV. Data were processed using CasaXPS software where a Shirley background correction was employed and peaks were fitted to Voigt profiles. To ensure accurate quantification, atomic sensitivity factors were taken from the instrument spectrum acquisition software and manually input into the data processing software.

Electrochemical Characterization—Electrochemical Measurements: Cyclic voltammetry was performed using a CH Instruments 620 series potentiostat. Measurements were recorded in a custom-made electrochemical cell (2 mL volume) containing the pristine ITO coated glass as working electrode (1.6 cm^2), an Ag/AgCl reference electrode (3 M KCl) (Bioanalytical Systems), and a platinum foil counter electrode (Goodfellow) in $50 \times 10^{-3} \text{ M}$ phosphate buffer solution (pH 7.8) or saline

solution.^[72] Prior to measurements, solutions were purged with N_2 to avoid O_2 reduction at low potentials ($< -0.4 \text{ V vs Ag/AgCl}$).

Electrical impedance spectroscopy (EIS) was performed using a Princeton Applied Research Potentiostat/Galvanostat model 2273 running with Power Suite software with a four-electrode setup as described in ref. [12]. Briefly, the signal was to the anodized films with a surface area of 1.6 cm^2 , along with a platinum foil counter-electrode (CE) and controlled by a saturated Ag/AgCl reference electrode. An AC sine wave of 40 mV amplitude was applied with 0 V DC offset. The impedance magnitude and phase angle were calculated at 1, 10, 100, 1000, and 10 000 Hz, as it is reported that most of the neural cell communication occurs between 300 Hz and 1 kHz.^[122]

Values were presented on Bode and Nyquist plots and compared to those of a pristine ITO coated glass slide and to bare gold coated glass. The data fitting analysis was performed using EIS Spectrum Analyzer 1.0 software.

Biological Characterization—Cell Culture: The human neuroblastoma cell line SH-SY5Y was cultured in Dulbecco's modified Eagle's medium nutrient mixture F12 (DMEM/F12) medium and supplemented with 10% fetal bovine serum, 1% penicillin/streptomycin (PS), and all-*trans* retinoic acid (RA) at a final concentration of $10 \times 10^{-6} \text{ M}$ for differentiation into a neuronal phenotype. Immunofluorescence micrographs showing the neuronal phenotype of SH-SY5Y as a response to RA supplementation are shown in Figure S7 (Supporting Information).

To control the surface area of culture, the pristine ITO coated glass and the anodized films were placed in customized silicone Ace O-rings with wall dimension of 1.78 mm and internal diameter (I.D) of 10.8 mm and were sealed around the borders of the surface area with silicone elastomer (Sylgard 184). The materials were placed in six well culture plates and sterilized by 100% ethanol for 2 h, and subsequently washed repeatedly with Hank's balanced salt solution (HBSS) and incubated overnight at 37 °C, 5% CO₂ for neural cell culture. A quantity of 50 000 or 2000 cells cm⁻² was plated on each film, and then 200 µL of the culture medium was added to each well, and changed with fresh media every day for a period of 1, 7, or 14 d. Control Thermanox Plastic Coverslips with 13 mm diameter (NUNC brand products) were also bonded with silicone Ace O-rings as above.

Primary hippocampal cultures were prepared from 2 to 3 d postnatal (P₂–P₃) rats as previously reported by Cellot et al.^[115] Briefly, hippocampi were dissected and enzymatically digested. Cells were plated on poly-L-ornithine coated glass coverslips (control) or on anodized ITO substrates formed at 0.4 mA cm⁻² current density. Coverslips were placed in petri dishes and cultured in serum-containing medium in a 5% CO₂-humidified incubator for 8–10 d. Cell morphology was analyzed by immunofluorescence experiments and epifluorescence microscopy to gain insights into cell health and shape. Briefly, cell densities were quantified at 20× (0.5 NA) magnification using a DM6000 Leica microscope (Leica Microsystems GmbH, Wetzlar, Germany), with random sampling of visual fields (713 × 532 µm).

Cell Culture—Ethical Statement: All experiments were performed in accordance with the European (EU) guidelines (2010/63/UE) and Italian law (decreto 26/14) and were approved by the local authority veterinary service and by our institution (SISSA-ISAS) ethical committee. Every effort was made to minimize animal suffering and to reduce the number of animals used. Animal use was approved by the Italian Ministry of Health, in accordance with the EU Recommendation 2007/526/CE.

Primary cultures of VM neurons were obtained from the mesencephalon of embryonic Sprague-Dawley rats according to methods previously described by Vallejo-Giraldo et al.^[12] Briefly, the ventral mesencephalon was dissected from embryonic 14 d rat brains and then mechanically dissociated with a pipette, until the tissue was dispersed. Cells were grown in a humidified atmosphere of 5% CO₂ at 37 °C and culture in media (Dulbecco's modified Eagle's medium/F12, 33 × 10⁻³ M D-glucose, 1% L-glutamine, 1% PS, 1% fetal calf serum (FCS), supplemented with 2% B27). The pristine ITO glass and the anodized films were cultured for 21 d in six well culture plates and sterilized in 70% ethanol for 2 h, and subsequently washed repeatedly with HBSS. They were then rinsed three times with deionized (DI) water and left to dry overnight. A quantity of 50 000 cells cm⁻² was plated on each film, and then 3 mL of the culture medium was added to each well and changed with fresh media every 2 d for a period of 21 d.

Biological Characterization—Metabolic Analysis: The alamarBlue Assay (Life Technologies, UK) was used to assess cell metabolism and was carried out at days 1, 7, and 14. For this purpose, 10% of the alamarBlue solution was added to the culture media, in accordance with the provided protocols. Sample absorbance was measured in a 96-well plate at 544 excitation and 590 emission wave lengths using a Thermo Scientific Varios-Kan Flash microplate reader.

Biological Characterization—Immunofluorescent Labeling: Indirect double-immunofluorescent labeling was performed to visualize focal adhesion sites. SH-SY5Y cells on experimental and control substrates were fixed with 4% paraformaldehyde and 1% of sucrose for 15 min at room temperature (RT) at each time point. Once fixed, the samples were washed with PBS and permeabilized with buffered 0.5% Triton X-100 within a buffered isotonic solution (10.3 g sucrose, 0.292 g NaCl, 0.06 g MgCl₂, 0.476 g (4-(2-hydroxyethyl)-1-piperazineethanesulfonic acid) HEPES buffer, 0.5 mL Tri-ton-X-100, in 100 mL water, pH 7.2) at 4 °C for 5 min. Nonspecific binding sites were blocked with 1% bovine serum albumin (BSA) in PBS at 37 °C for 5 min and subsequently incubated for 2 h with a 1:100 concentration anti-vinculin (Rb mAb to Paxillin (Y113) (Life Technologies, 1:100). Samples were washed three times with 0.05% Tween 20, PBS and then incubated for 1 h in the

secondary antibody Alexa Fluor 488 goat anti-Rabbit IgG (H+L) (Life Technologies, 1:100) combined with rhodamine-conjugated phalloidin (Life Technologies, 1:100) to stain F-actin. Nonspecific charges (e.g., remaining aldehyde) were neutralized with 0.5% Tween 20/PBS (5 min ×3) to minimize background labeling. Samples were mounted on microscope cover slides and counterstained with SlowFade Gold antifade reagent with 4',6-diamidino-2-phenylindole (DAPI) for nuclear staining.

For immunofluorescence experiments on primary hippocampal neurons, cultures were fixed with 4% formaldehyde (prepared from fresh paraformaldehyde) in PBS for 60 min at RT and then washed in PBS. The samples were permeabilized with 0.3% Triton-X-100 and subsequently incubated with primary antibodies for 30 min at room temperature, washed with PBS and incubated with secondary antibodies for 45 min. Cultures were then mounted in Vectashield (Vector Laboratories) on 1 mm thick microscope slides. To visualize neurons, rabbit anti β-tubulin III, 1:250 (Sigma), primary antibody was used and Alexa 594 goat anti-rabbit secondary antibody, 1:500 (Invitrogen); to visualize astrocytes mouse anti GFAP 1:250 (Sigma) primary antibody was used and Alexa 488 goat anti-mouse secondary antibody 1:500 (Invitrogen), and Hoechst 1:10 000 (Invitrogen) was used to visualize cell nuclei.

Expression of dopamine by the presence of tyrosine hydroxylase (TH) in human neuroblastoma cell line SH-SY5Y cultures was evaluated by indirect double-immunofluorescent labeling as detailed for the visualization of focal adhesion sites in this section. SH-SY5Y cells on experimental and control ITO substrates were incubated for 2 h with a 1:1000 concentration anti-Anti-TH (MAB318, Merck Millipore, 1:1000) washed three times with 0.05% Tween 20, PBS and then incubated for 1 h in the secondary antibody Alexa Fluor 488 (Life Technologies, 1:1000) combined with rhodamine-conjugated phalloidin (Life Technologies, 1:100) to stain F-actin. Samples were mounted on microscope cover slides and counterstained with SlowFade Gold antifade reagent with DAPI for nuclear staining.

Biological Characterization—Microscopy and Image Analysis: After immunostaining, samples were viewed with an Olympus IX 81 fluorescence microscope with filters for fluorescein isothiocyanate (FITC) (excitation 490 nm; emission 520 nm), Texas Red (excitation 596 nm; emission 615 nm), and DAPI (excitation 358 nm; emission 461 nm). At least 20 randomly selected images at 60× magnification were taken from each test group and the control group. The total number of focal adhesion points per cell and their length were quantified by direct scoring with a 4-pixel-wide line on the FITC channel as previously described in ref. [81] using ImageJ software (National Institutes of Health, USA) (Figure S11, Supporting Information).

Cell densities were quantified at 20× (0.5 NA) magnification using a DM6000 Leica microscope (Leica Microsystems GmbH, Wetzlar, Germany), with random sampling of seven to ten fields (713 × 532 µm; control and anodized film, n = 3 culture series).

Protein Antibody Microarray—Protein Extraction: For protein extraction and collection, samples were carefully placed on ice and the cells were washed twice with cold PBS 1X. After the complete aspiration of cold PBS 1X, 100 µL of cold lysis buffer was added. The lysis buffer was composed of radioimmunoprecipitation (RIPA) lysis buffer (Sigma) supplemented with 1% of protease inhibitors (Life Science-Roche) and 1% of phosphatase inhibitors cocktails I & III (Sigma). Thereafter, the adherent cells were scraped off using Corning cell scrapers (Sigma) and then the cell suspension was gently transferred into microcentrifuge tubes and placed on ice. Microcentrifuge tubes were centrifuged for 15 min at 14 000 rpm at 4 °C, and afterward gently removed from the centrifuge and placed on ice. Without disturbing the pellet, the supernatant was carefully aspirated and placed in a fresh clean tube, kept on ice, and stored at -80 °C to be quantified. The pellet was discarded.

Protein Antibody Microarray—Protein Quantification: Protein quantification of the pristine ITO glass and the ITO anodized films was done using Bio-Rad Protein Assay Dye Reagent (#5000006). As per manufacturer's instructions, the dye working solution was prepared and filtered in a concentration of 1:4 in distilled water followed by the preparation of protein standard BSA at concentrations of 0.25, 0.5, 0.75,

and 0.9 mg mL⁻¹. After this, 5 μ L of each BSA standard and sample solution were mixed in a clean, dry tube together with 250 μ L of dye working solution. This solution was vortexed and incubated for 5 min at RT and finally read using NanoDrop 8000 software with the Protein Bradford module.

Protein Antibody Microarray—Construction of Gliosis Antibody Microarray: Nexterion slide H microarray slides were purchased from Schott AG (Mainz, Germany). Alexa Fluor 555 carboxylic acid succinimidyl ester was obtained from Life Technologies (Carlsbad, CA, USA).

Protein samples were labeled with Alexa Fluor 555 carboxylic acid succinimidyl ester according to manufacturer's instructions. Excess label was removed and buffer was exchanged with PBS, pH 7.4, by centrifugation through 3 kDa molecular weight cutoff filters. Absorbance at 555 and 280 nm was measured for labeled samples and calculations were performed according to manufacturer's instructions using an arbitrary extinction coefficient of 100 000 and molecular mass of 100 000 to enable quantification of relative protein concentration and label substitution efficiency.

All commercial antibodies (Table S1, Supporting Information) were buffer exchanged into PBS and quantified by bicinchoninic acid (BCA) assay.^[123] Antibodies were diluted to print concentration in PBS and printed in six replicates on Nexterion H amine reactive, hydrogel coated glass slides using a SciFLEXARRAYER S3 piezoelectric printer (Scienion, Berlin, Germany) under constant humidity (62% \pm 2%) at 20 °C. Each feature was printed using \approx 1 nL of diluted antibody using an uncoated 90 μ m glass nozzle with eight replicated subarrays per microarray slide. After printing, slides were incubated in a humidity chamber overnight at room temperature to facilitate complete conjugation. The slides were then blocked in 100 \times 10⁻³ M ethanolamine in 50 \times 10⁻³ M sodium borate, pH 8.0, for 1 h at room temperature. Slides were washed in PBS with 0.05% Tween 20 (PBS-T) three times for 2 min each wash followed by one wash in PBS, dried by centrifugation (470 \times g, 5 min), and then stored with desiccant at 4 °C until use.

Incubations were carried out in the dark. Microarray slides were incubated essentially as previously described.^[124] Initially, one labeled sample was titrated (2.5–15 μ g mL⁻¹) for optimal signal-to-noise ratio and all samples were subsequently incubated for 1 h at 23 °C at 5 μ g mL⁻¹ in Tris-buffered saline (TBS; 20 \times 10⁻³ M Tris-HCl, 100 \times 10⁻³ M NaCl, 1 \times 10⁻³ M CaCl₂, 1 \times 10⁻³ M MgCl₂, pH 7.2) with 0.05% Tween 20 (TBS-T). All microarray experiments were carried out using three replicate slides. Alexa Fluor 555 labeled healthy rat brain lysate (5 μ g mL⁻¹) and soybean agglutinin lectin (10 μ g mL⁻¹) were incubated in two separate subarrays on every slide to confirm retained antibody performance and printing, respectively (Figure S8, Supporting Information). After incubation, slides were washed three times in TBS-T for 2 min per wash, once in TBS and then centrifuged dry as above. Dried slides were scanned immediately on an Agilent G2505 microarray scanner using the Cy3 channel (532 nm excitation, 90% photomultiplier tubes (PMT), 5 μ m resolution) and intensity data were saved as a .tif file. Antibody microarrays were verified to remain active for at least 2 weeks after printing and all incubations were carried out within that timeframe.

Data extraction from .tif files was performed essentially as previously described.^[124] Data were normalized to the mean of three replicate microarray slides (subarray-by-subarray using subarray total intensity, $n = 3$, 18 data points). Unsupervised hierarchical clustering of normalized data was performed using Hierarchical Clustering Explorer v3.0 (<http://www.cs.umd.edu/hcil/hce/hce3.html>) using the parameters no prefiltering, complete linkage, and Euclidean distance. Statistical analysis was performed as detailed in subsection "Calcium Imaging and Substrate Stimulation".

Electrophysiological Recordings: Single whole-cell recordings were obtained at RT with pipettes (5–7 M Ω) containing (in \times 10⁻³ M): 120 K gluconate, 20 KCl, 10 HEPES, 10 ethylene glycol-bis(beta-aminoethyl ether)-N,N,N',N'-tetraacetic acid (EGTA), 2 MgCl₂, 2 Na₂ATP, pH 7.3; osmolarity was adjusted to 300 mOsm. The extracellular solution contained (in \times 10⁻³ M): 150 NaCl, 4 KCl, 1 MgCl₂, 2 CaCl₂, 1 MgCl₂, 10 HEPES, 10 glucose (all Sigma), pH 7.4. Coverslips with cultures were positioned in a Perspex chamber mounted on an inverted microscope

(Eclipse TE-200, Nikon, Japan). Data were collected by Multiclamp 700B patch amplifier (Axon CNS, Molecular Devices) and digitized at 10 kHz with the pClamp 10.2 acquisition software (Molecular Devices LLC, US). The spontaneous synaptic activity was recorded clamping the membrane voltage at -56 mV holding potential (not corrected for liquid junction potential, which was 14 mV). All recorded events were analyzed offline with the AxoGraph 1.4.4 (Axon Instrument) event detection software (Axon CNS, Molecular Devices).

Calcium Imaging and Substrate Stimulation: Stimulation of anodized films formed at 0.4 mA cm⁻² was performed with two different primary cultures: primary cultures of VM neurons and primary hippocampal neurons.

Changes in intracellular calcium (Ca²⁺) primary cultures of VM neurons were measured as described previously.^[12] Briefly, cells grown on pristine ITO glass as a control and on ITO anodized films formed at 0.4 mA cm⁻² were loaded with the calcium-sensitive fluorescent probe Fluo-4 AM (Life Technologies) (5 \times 10⁻⁶ M in dimethyl sulfoxide (DMSO)) for 30 min at 37 °C, washed, followed by 30 min at 37 °C in the dark. After dye loading was completed, cells were bathed in culture media (Dulbecco's modified Eagle's medium/F12, 33 \times 10⁻³ M D-glucose, 1% L-glutamine, 1% PS, 1% FCS, supplemented with 2% B27) and transferred to a custom built chamber that allowed electrical stimulation to be applied directionally to the films. Stimulation was achieved by the delivery of biphasic voltage pulses, using a software controlled constant voltage stimulator connected to the chamber via Pt contacts. The chamber was mounted on the stage of a Zeiss Axiovert 200 inverted microscope. The microscope was equipped with a 10 position Orbit I filterwheel (Improvision), for excitation (488 nm) and emission (510 nm low-pass (LP) filter). The emission light was collected every second with an Orca 285 camera (Hamamatsu). The system was controlled by the Openlab system version 5.5. Changes in Ca²⁺_i in response to external electrical stimulation were expressed as changes in background subtracted fluorescence intensity expressed as $\Delta F/F_0$ (F_0 is the baseline fluorescence level and ΔF is the rise over baseline).

For Ca²⁺ imaging experiments using primary hippocampal neurons, cultures were loaded with cell permeable Ca²⁺ dye Oregon Green 488 BAPTA-1 AM (Molecular Probes) in DMSO (Sigma-Aldrich) with a final concentration of 4 \times 10⁻⁶ M for 20 min at 37 °C in the cell culture incubator.^[118] The samples were then placed in a recording chamber mounted on an inverted microscope (Nikon TE-200) where they were continuously superfused at RT with the extracellular solution (see subsection "Electrophysiological Recordings"). Cultures were observed with a 20 \times objective (0.45 NA, PlanFluor, Nikon). Images (1024 \times 1024 pixels) were acquired continuously for 7 min (at 6.67 frame s⁻¹) by a Hamamatsu Orca-Flash 4.0 digital camera, exciting the Ca²⁺ dye with a 488 nm wavelength light generated by a mercury lamp. Excitation light was separated from the light emitted from the sample using a 395 nm dichroic mirror and ND filter (1/16). Images of emitted fluorescence $>$ 480 nm were displayed on a color monitor controlled by an integrating imaging software package (HC Image, Hamamatsu) using a personal computer. Recorded images were analyzed offline with the Clampfit software (pClamp suite, 10.2 version; Axon Instruments). Intracellular Ca²⁺ transients were expressed as fractional amplitude increase ($\Delta F/F_0$, where F_0 is the baseline fluorescence level and ΔF is the rise over baseline); the onset time of neuronal activation determined by detecting those events in the fluorescence signal that exceed at least five times the standard deviation of the noise. For stimulation, voltage stimuli were delivered using a Constant Voltage Isolated Stimulator (DS2A-Mk.II, Digitimer, England) connected to silver electrodes through insulated silver wires. One electrode was placed in contact with the upper part of the anodized film formed at 0.4 mA cm⁻² or glass (control) sample in a dry environment; the reference electrode was in the extracellular solution. Under such conditions, neurons could only be extracellularly stimulated through the electrolyte-anodized film interface. During Ca²⁺ imaging recording session, 500 ms long high voltage was delivered (1/60 s).

Statistical Analysis: All data presented here were confirmed using at least three replicates for each of the test groups and control group.

The results are expressed as the mean of the values \pm standard error of the mean. One-way ANOVA followed by a Bonferroni test was performed to determine the statistical significance ($p < 0.05$), unless otherwise stated.

For the hippocampal cultures electrophysiology and immunofluorescence analysis, all values from samples subjected to the same experimental protocols were pooled and expressed as mean \pm SD with n = number of cells, unless otherwise specified. Where not otherwise indicated, statistically significant differences between data sets were assessed by Student's t -test (after validation of variances homogeneity by Levene's test) for parametric data at a minimum significance level of $p < 0.05$.

Supporting Information

Supporting Information is available from the Wiley Online Library or from the author.

Acknowledgements

This research was supported in part by a research grant from the Science Foundation Ireland (SFI) and was cofunded under the European Regional Development Fund under Grant Number 13/RC/2073. M. J. P. Biggs is also an SFI, Starting Investigator SIRG COFUND fellow (Grant No. 11/SIRG/B2135). The authors would like to acknowledge the Advanced Materials and BioEngineering Research (AMBER) and the Science Foundation Ireland (SFI) for funding through SFI-AMBER (Grant No. SFI 12/RC/2278 AMBER). The authors would like to acknowledge the joint funding received from the Irish Research Council through IRC New Foundation Scheme/Nano Surface project, the NUI Galway microscopy suite, and David Connolly for microscopy support. The authors are grateful to Pierce Lalor and Ruther Levey for help in the TEM analysis.

Received: September 27, 2016

Revised: January 16, 2017

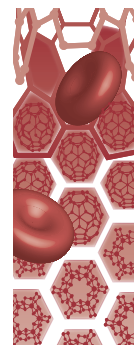
Published online:

- [1] C. Vallejo-Giraldo, A. Kelly, M. J. Biggs, *Drug Discovery Today* **2014**, *19*, 88.
- [2] G. M. Durand Dm, E. Krames, *J. Neural Eng.* **2014**, *11*, 020201.
- [3] A. Zhang, C. M. Lieber, *Chem. Rev.* **2016**, *116*, 215.
- [4] K. Svennersten, K. C. Larsson, M. Berggren, A. Richter-Dahlfors, *Biochim. Biophys. Acta* **2011**, *1810*, 276.
- [5] K. C. Larsson, P. Kjall, A. Richter-Dahlfors, *Biochim. Biophys. Acta* **2013**, *1830*, 4334.
- [6] R. Owens, P. Kjall, A. Richter-Dahlfors, F. Cicoira, *Biochim. Biophys. Acta* **2013**, *1830*, 4283.
- [7] D. T. Simon, E. O. Gabriellsson, K. Tybrandt, M. Berggren, *Chem. Rev.* **2016**, DOI: 10.1021/acs.chemrev.6b00146, *116*, 13009.
- [8] T. D. Kozai, N. B. Langhals, P. R. Patel, X. Deng, H. Zhang, K. L. Smith, J. Lahann, N. A. Kotov, D. R. Kipke, *Nat. Mater.* **2012**, *11*, 1065.
- [9] D. Mantione, I. Del Agua, W. Schaafsma, J. Diez-Garcia, B. Castro, H. H. Sardon, D. Mecerreyes, *Macromol. Biosci.* **2016**, *16*, 1227.
- [10] S. F. Cogan, *Annu. Rev. Biomed. Eng.* **2008**, *10*, 275.
- [11] Rose LSRaTL, *Neural Prostheses: Fundamental Studies*, Prentice Hall, Englewood Cliffs, NJ **1990**.
- [12] C. Vallejo-Giraldo, E. Pugliese, A. Larranaga, M. A. Fernandez-Yague, J. J. Britton, A. Trotier, G. Tadjon, A. Kelly, I. Rago, J. R. Sarasua, E. Dowd, L. R. Quinlan, A. Pandit, M. J. Biggs, *Nanomedicine (Lond)* **2016**, *11*, 2547.
- [13] H. Zhou, X. Cheng, L. Rao, T. Li, Y. Y. Duan, *Acta Biomater.* **2013**, *9*, 6439.
- [14] O. J. Gregory, Q. Luo, E. E. Crisman, *Thin Solid Films* **2002**, *406*, 286.
- [15] B. W. Faughnan, R. S. Crandall, *Top. Appl. Phys.* **1980**, *40*, 181.
- [16] L. J. Meng, C. H. Li, G. Z. Zhong, *J. Lumin.* **1987**, *39*, 11.
- [17] J. R. Bellingham, A. P. Mackenzie, W. A. Phillips, *Appl. Phys. Lett.* **1991**, *58*, 2506.
- [18] B. J. Luff, J. S. Wilkinson, G. Perrone, *Appl. Opt.* **1997**, *36*, 7066.
- [19] A. C. Weitz, M. R. Behrend, N. S. Lee, R. L. Klein, V. A. Chiodo, W. W. Hauswirth, M. S. Humayun, J. D. Weiland, R. H. Chow, *J. Neurophysiol.* **2013**, *109*, 1979.
- [20] A. C. Weitz, M. R. Behrend, A. K. Ahuja, P. Christopher, J. Wei, V. Wuyyuru, U. Patel, R. J. Greenberg, M. S. Humayun, R. H. Chow, J. D. Weiland, *J. Neural Eng.* **2014**, *11*, 016007.
- [21] R. Tanamoto, Y. Shindo, N. Miki, Y. Matsumoto, K. Hotta, K. Oka, *J. Neurosci. Methods* **2015**, *253*, 272.
- [22] Q. Qiu, M. Sayer, M. Kawaja, X. Shen, J. E. Davies, *J. Biomed. Mater. Res.* **1998**, *42*, 117.
- [23] S. Petronis, M. Stangegaard, C. B. Christensen, M. Dufva, *Biotechniques* **2006**, *40*, 368.
- [24] Y. Nashimoto, Y. Takahashi, T. Yamakawa, Y. S. Torisawa, T. Yasukama, T. ITO-Sasaki, M. Yokoo, H. Abe, H. Shiku, H. Kambara, T. Matsue, *Anal. Chem.* **2007**, *79*, 6823.
- [25] M. L. Guo, J. H. Chen, X. B. Yun, K. Chen, L. H. Nie, S. Z. Yao, *Biochim. Biophys. Acta: Gen. Subjects* **2006**, *1760*, 432.
- [26] J. Selvakumaran, M. P. Hughes, J. L. Keddie, D. J. Ewins, *Eng. Med. Biol. Soc. Ann.* **2002**, *261*, DOI: 10.1109/Mmb.2002.1002326.
- [27] H. Pluk, D. Stokes, B. Lich, B. Wieringa, J. Franssen, *J. Microsc.-Oxford* **2009**, *233*, 353.
- [28] C. M. Bowers, A. A. Shestopalov, R. L. Clark, E. J. Toone, *ACS Appl. Mater. Interfaces* **2012**, *4*, 3932.
- [29] B. Wei, J. Liu, L. Ouyang, C. C. Kuo, D. C. Martin, *ACS Appl. Mater. Interfaces* **2015**, *7*, 15388.
- [30] J. Arjomandi, D. Raoufi, F. Ghamari, *J. Phys. Chem. C* **2016**, *120*, 18055.
- [31] C. J. Huang, Y. K. Su, S. L. Wu, *Mater. Chem. Phys.* **2004**, *84*, 146.
- [32] P. K. H. Ho, M. Granstrom, R. H. Friend, N. C. Greenham, *Adv. Mater.* **1998**, *10*, 769.
- [33] J. L. Robinson, P. F. King, *J. Electrochem. Soc.* **1961**, *108*, 36.
- [34] N. Cabrera, N. F. Mott, *Rep. Prog. Phys.* **1948**, *12*, 163.
- [35] S. W. Cho, J. G. Jeong, S. H. Park, M. H. Cho, K. Jeong, C. N. Whang, Y. Yi, *Appl. Phys. Lett.* **2008**, *92*, 213302.
- [36] G. R. T. Schueller, S. R. Taylor, E. E. Hajcsar, *J. Electrochem. Soc.* **1992**, *139*, 2799.
- [37] C. Blawert, W. Dietzel, E. Ghali, G. L. Song, *Adv. Eng. Mater.* **2006**, *8*, 511.
- [38] M. V. Diamanti, B. Del Curto, M. Pedferri, *J. Appl. Biomater. Biomech.* **2011**, *9*, 55.
- [39] L. E. Mcnamara, T. Sjoström, K. E. Burgess, J. J. Kim, E. Liu, S. Gordonov, P. V. Moghe, R. M. Meek, R. O. Oreffo, B. Su, M. J. Dalby, *Biomaterials* **2011**, *32*, 7403.
- [40] H. Tsuchiya, J. M. Macak, A. Ghicov, L. Taveira, P. Schmuki, *Corros. Sci.* **2005**, *47*, 3324.
- [41] A. Ghicov, H. Tsuchiya, J. M. Macak, P. Schmuki, *Electrochem. Commun.* **2005**, *7*, 505.
- [42] S. Mahshid, A. Dolati, M. Goodarzi, M. Askari, *Nanotechnology (General) -217th Ecs Meeting* **2010**, *28*, 67.
- [43] T. Tian, X. F. Xiao, R. F. Liu, H. D. She, X. F. Hu, *J. Mater. Sci.* **2007**, *42*, 5539.
- [44] S. Bauer, S. Kleber, P. Schmuki, *Electrochem. Commun.* **2006**, *8*, 1321.
- [45] E. E. L. Swan, K. C. Popat, C. A. Grimes, T. A. Desai, *J. Biomed. Mater. Res., Part A* **2005**, *72A*, 288.
- [46] T. R. B. Foong, A. Sellinger, X. Hu, *ACS Nano* **2008**, *2*, 2250.
- [47] G. Folcher, H. Cachet, M. Froment, J. Bruneaux, *Thin Solid Films* **1997**, *301*, 242.
- [48] A. Kraft, H. Hennig, A. Herbst, K. H. Heckner, *J. Electroanal. Chem.* **1994**, *365*, 191.

- [49] Y. Shao, X. Xiao, L. Y. Wang, Y. Liu, S. D. Zhang, *Adv. Funct. Mater.* **2014**, *24*, 4170.
- [50] E. Matveeva, *J. Electrochem. Soc.* **2005**, *152*, H138.
- [51] M. Senthilkumar, J. Mathiyarasu, J. Joseph, K. L. N. Phani, V. Yegnaraman, *Mater. Chem. Phys.* **2008**, *108*, 403.
- [52] L. Liu, S. Yellinek, I. Valding, A. Donval, D. Mandler, *Electrochim. Acta* **2015**, *176*, 1374.
- [53] J. Stotter, Y. Show, S. H. Wang, G. Swain, *Chem. Mater.* **2005**, *17*, 4880.
- [54] R. Castro-Rodriguez, A. I. Oliva, V. Sosa, F. Caballero-Briones, J. L. Pena, *Appl. Surf. Sci.* **2000**, *161*, 340.
- [55] G. Kavei, A. M. Gheidari, *J. Mater. Process. Technol.* **2008**, *208*, 514.
- [56] C. Yao, T. J. Webster, *J. Nanosci. Nanotechnol.* **2006**, *6*, 2682.
- [57] J. F. Vanhumbecq, J. Proost, *Corros. Rev.* **2009**, *27*, 117.
- [58] A. Paul, J. Wingbermuehle, *Appl. Surf. Sci.* **2006**, *252*, 8151.
- [59] A. Facchetti, M. H. Yoon, T. J. Marks, *Adv. Mater.* **2005**, *17*, 1705.
- [60] S. Lee, J.-Y. Kwon, D. Yoon, H. Cho, J. You, Y. T. Kang, D. Choi, W. Hwang, *Nanoscale Res. Lett.* **2012**, *7*, 18.
- [61] M. Asmani, C. Kermel, A. Leriche, M. Ourak, *J. Eur. Ceram. Soc.* **2001**, *21*, 1081.
- [62] K. Zeng, F. Zhu, J. Hu, L. Shen, K. Zhang, H. Gong, *Thin Solid Films* **2003**, *443*, 60.
- [63] A. Solieman, M. A. Aegerter, *Thin Solid Films* **2006**, *502*, 205.
- [64] M. Montecchi, R. M. Montecchi, E. Nichelatti, *Thin Solid Films* **2001**, *396*, 262.
- [65] M. M. Hamasha, T. Dhakal, K. Alzoubi, S. Albahri, A. Qasaimah, S. Lu, C. R. Westgate, *J. Disp. Technol.* **2012**, *8*, 385.
- [66] C. W. Tang, S. A. Vanslyke, *Appl. Phys. Lett.* **1957**, *51*, 913.
- [67] E. I. Haskal, *Synth. Met.* **1997**, *91*, 187.
- [68] H. Jung, W. Chung, C. H. Lee, S. H. Kim, *J. Nanosci. Nanotechnol.* **2012**, *12*, 5407.
- [69] E. Haskal, A. Curioni, P. Seidler, W. Andreoni, *Appl. Phys. Lett.* **1997**, *71*, 1151.
- [70] N. Nishimoto, Y. Yamada, Y. Ohnishi, N. Imawaka, K. Yoshino, *Phys. Status Solidi A* **2013**, *210*, 589.
- [71] A. Turak, InTech, Dewetting Stability of ITO Surfaces in Organic Optoelectronic Devices, in *Optoelectronics—Advanced Materials and Devices*, **2013**, Ballato, S.L.P.a.J.M. ., DOI:10.5772/3463.
- [72] X. F. Wei, W. M. Grill, *J. Neural Eng.* **2009**, *6*, 046008.
- [73] T. Bejital, K. Ramji, A. Kessman, K. Sierros, D. Cairns, *Mater. Chem. Phys.* **2012**, *132*, 395.
- [74] M. Serantoni, V. J. Cunnane, *J. Electroanal. Chem.* **2003**, *548*, 49.
- [75] L. Hung-Ji, L. Der-Yuh, W. Jenq-Shinn, Y. Chu-Shou, C. Wu-Ching, L. Wei-Hsuan, W. Jyh-Shyang, *Jpn. J. Appl. Phys.* **2009**, *48*, 04C122.
- [76] C. Donley, D. Dunphy, D. Paine, C. Carter, K. Nebesny, P. Lee, D. Alloway, N. R. Armstrong, *Langmuir* **2002**, *18*, 450.
- [77] R. G. Keil, *J. Electrochem. Soc.* **1986**, *133*, 1375.
- [78] A. J. F. Bard, *Electrochemical Methods: Fundamentals and Applications*, Wiley, New York **1980**.
- [79] V. Brunetti, G. Maiorano, L. Rizzello, B. Sorce, S. Sabella, R. Cingolani, P. P. Pompa, *Proc. Natl. Acad. Sci. USA* **2010**, *107*, 6264.
- [80] M. Buttiglione, F. Vitiello, E. Sardella, L. Petrone, M. Nardulli, P. Favia, R. d'Agostino, R. Cristina, *Biomaterials* **2007**, *28*, 2932.
- [81] M. J. Biggs, R. G. Richards, S. Mcfarlane, C. D. Wilkinson, R. O. Oreffo, M. J. Dalby, *J. R. Soc. Interface* **2008**, *5*, 1231.
- [82] Y. W. Fan, F. Z. Cui, S. P. Hou, Q. Y. Xu, L. N. Chen, I. S. Lee, *J. Neurosci. Methods* **2002**, *120*, 17.
- [83] S. P. Khan, G. G. Auner, G. M. Newaz, *Nanomedicine* **2005**, *1*, 125.
- [84] M. J. P. Biggs, R. G. Richards, N. Gadegaard, R. J. McMurray, S. Affrossman, C. D. W. Wilkinson, R. O. C. Oreffo, M. J. Dalby, *J. Biomed. Mater. Res., Part A* **2009**, *91A*, 195.
- [85] M. D. Schaller, *Oncogene* **2001**, *20*, 6459.
- [86] M. H. Kim, M. Park, K. Kang, I. S. Choi, *Biomater Sci-Uk* **2014**, *2*, 148.
- [87] K. Kang, M. H. Kim, M. Park, I. S. Choi, *J. Nanosci. Nanotechnol.* **2014**, *14*, 513.
- [88] G. Sriram, P. Patil, M. P. Bhat, R. M. Hegde, K. V. Ajeya, I. Udachyan, M. B. Bhavya, M. G. Gatti, U. T. Uthappa, G. M. Neelgund, H. Y. Jung, T. Altalhi, M. D. M. Kurkuri, *J. Nanomater.* **2016**, *2*, 24.
- [89] B. Wälivaara, B.-O. Aronsson, M. Rodahl, J. Lausmaa, P. Tengvall, *Biomaterials* **1994**, *15*, 827.
- [90] S. W. Myung, Y. M. Ko, B. H. Kim, *Jpn. J. Appl. Phys.* **2014**, *53*, 11R. B.01.
- [91] N. Recek, M. Jaganjac, M. Kolar, L. Milkovic, M. Mozetič, K. Stana-Kleinschek, A. Vesel, *Molecules* **2013**, *18*, 12441.
- [92] A. Sharma, A. J. Mcquillan, L. A. Sharma, J. N. Waddell, Y. Shibata, W. J. Duncan, *J. Mater. Sci.: Mater. Med.* **2015**, *26*, 221.
- [93] Z. Bai, M. J. Filiaggi, R. J. Sandersen, L. B. Lohstreter, M. A. Mcarthur, J. R. Dahn, *J. Biomed. Mater. Res., Part A* **2010**, *92*, 521.
- [94] W. Shi, Y. Shen, D. Ge, M. Xueb, H. Cao, S. Huang, J. Wang, G. Zhang, F. Zhang, *J. Membr. Sci.* **2008**, *325*, 801.
- [95] M. J. Biggs, R. G. Richards, M. J. Dalby, *Nanomedicine* **2010**, *6*, 619.
- [96] I. P. Karve, J. M. Taylor, P. J. Crack, *Br. J. Pharmacol.* **2016**, *173*, 692.
- [97] A. Tykhomyrov, A. Pavlova, V. Nedzvetsky, *Neurophysiology* **2016**, *48*, 54.
- [98] M. Burgos, M. D. Pastor, J. C. Gonzalez, J. R. Martinez-Galan, C. F. Vaquero, N. Fradejas, A. Benavides, J. M. Hernández-Guijo, P. Tranque, S. P. K. Calvo, *Glia* **2007**, *55*, 1437.
- [99] J. H. Kim, S. J. Kwon, M. C. Stankewich, G. Y. Huh, S. B. Glantz, J. S. Morrow, *Exp. Mol. Pathol.* **2016**, *100*, 1.
- [100] S. Du, A. Rubin, S. Klepper, C. Barrett, Y. C. Kim, H. W. Rhim, E. B. Lee, C. W. Park, G. J. Markelonis, T. H. Oh, *Exp. Neurol.* **1999**, *157*, 96.
- [101] J. Liu, M. C. Liu, K. K. W. Wang, *Sci. Signaling* **2008**, *1*, re1.
- [102] V. S. Sajja, E. S. Ereifej, P. J. Vandevord, *Neurosci. Lett.* **2014**, *570*, 33.
- [103] B. Coste, J. Mathur, M. Schmidt, T. J. Earley, S. Ranade, M. J. Petrus, A. E. Dubin, A. Patapoutian, *Science* **2010**, *330*, 55.
- [104] A. E. Dubin, M. Schmidt, J. Mathur, M. J. Petrus, B. Xiao, B. Coste, A. Patapoutian, *Cell Rep.* **2012**, *2*, 511.
- [105] M. Olsen, *Methods Mol. Biol.* **2012**, *814*, 265.
- [106] X. Wu, Y. Liu, X. Chen, Q. Sun, R. Tang, W. Wang, Z. Yu, M. Xie, *J. Mol. Neurosci.* **2013**, *49*, 499.
- [107] Y. Wang, H. Moges, Y. Bharucha, A. Symes, *Exp. Neurol.* **2007**, *203*, 168.
- [108] M. Pekny, M. Pekna, *Biochim. Biophys. Acta: Mol. Basis Disease* **2016**, *1862*, 483.
- [109] A. Ellis, D. L. Bennett, *Br. J. Anaesth.* **2013**, *111*, 26.
- [110] J. B. Davis, J. Gray, M. J. Gunthorpe, J. P. Hatcher, P. T. Davey, P. Overend, M. H. Harries, J. Latcham, C. Clapham, K. Atkinson, S. A. Hughes, K. Rance, E. Grau, A. J. Harper, P. L. Pugh, D. C. Rogers, S. Bingham, A. Randall, S. A. Sheardown, *Nature* **2000**, *405*, 183.
- [111] G. M. Story, A. M. Peier, A. J. Reeve, S. R. Eid, J. Mosbacher, T. R. Hricik, T. J. Earley, A. C. Hergarden, D. A. Andersson, S. W. Hwang, P. McIntyre, T. Jegla, S. Bevan, A. Patapoutian, *Cell* **2003**, *112*, 819.
- [112] E. Tejera, V. Rocha-Perugini, S. Lopez-Martin, D. Pérez-Hernández, A. I. Bachir, A. R. Horwitz, J. Vázquez, F. Sánchez-Madrid, M. Yáñez-Mo, *Mol. Biol. Cell.* **2013**, *24*, 261.
- [113] B. K. Song, G. R. Geisert, F. Vázquez-Chona, E. E. Geisert, *Neurosci. Lett.* **2003**, *338*, 29.
- [114] J. D. Peduzzi, T. B. Grayson, F. R. Fischer, E. E. Geisert Jr., *Exp. Neurol.* **1999**, *160*, 460.
- [115] G. Cellot, F. M. Toma, Z. K. Varley, J. Laishram, A. Villari, M. Quintana, S. Cipollone, M. Prato, L. Ballerini, *J. Neurosci.* **2011**, *31*, 12945.

- [116] J. S. Carp, *J. Neurophysiol.* **1992**, *68*, 1121.
- [117] A. Fabbro, D. Scaini, V. Leon, E. Vázquez, G. Cellot, G. Privitera, L. Lombardi, F. Torrisi, F. Tomarchio, F. Bonaccorso, S. Bosi, A. C. Ferrari, L. Ballerini, M. Prato, *ACS Nano* **2016**, *10*, 615.
- [118] S. Bosi, R. Rauti, J. Laishram, A. Turco, D. Lonardoni, T. Nieuw, M. Prato, D. Scaini, L. Ballerini, *Sci. Rep.* **2015**, *5*, 9562.
- [119] ASTM, Standard Guide for Accelerated Aging of Sterile Barrier Systems for Medical Devices, *In F1980-07*, **2011**, ASTM International, Conshohocken, PA.
- [120] R. A. Green, R. T. Hassarati, L. Bouchinet, C. S. Lee, G. L. Cheong, J. F. Yu, C. W. Dodds, G. J. Suaning, L. A. Poole-Warren, N. H. Lovell, *Biomaterials* **2012**, *33*, 5875.
- [121] D. W. Hukins, A. Mahomed, S. N. Kukureka, *Med. Eng. Phys.* **2008**, *30*, 1270.
- [122] R. A. Green, N. H. Lovell, G. G. Wallace, L. A. Poole-Warren, *Biomaterials* **2008**, *29*, 3393.
- [123] P. K. Smith, R. I. Krohn, G. T. Hermanson, A. K. Mallia, F. H. Gartner, M. D. Provenzano, E. K. Fujimoto, N. M. Goeke, B. J. Olson, D. C. Klenk, *Anal. Biochem.* **1985**, *150*, 76.
- [124] J. Q. Gerlach, M. Kilcoyne, L. Joshi, *Anal. Methods* **2014**, *6*, 440.
-

**APPENDIX 3:
ARTICLE.
POLYHYDROXYALKANOATE/CARBON
NANOTUBE NANOCOMPOSITES: FLEXIBLE
ELECTRICALLY CONDUCTING
ELASTOMERS FOR NEURAL APPLICATIONS**



Polyhydroxyalkanoate/carbon nanotube nanocomposites: flexible electrically conducting elastomers for neural applications

Aim: Medium chain length-polyhydroxyalkanoate/multi-walled carbon nanotube (MWCNTs) nanocomposites with a range of mechanical and electrochemical properties were fabricated via assisted dispersion and solvent casting, and their suitability as neural interface biomaterials was investigated. **Materials & methods:** Mechanical and electrical properties of medium chain length-polyhydroxyalkanoate/MWCNTs nanocomposite films were evaluated by tensile test and electrical impedance spectroscopy, respectively. Primary rat mesencephalic cells were seeded on the composites and quantitative immunostaining of relevant neural biomarkers, and electrical stimulation studies were performed. **Results:** Incorporation of MWCNTs to the polymeric matrix modulated the mechanical and electrical properties of resulting composites, and promoted differential cell viability, morphology and function as a function of MWCNT concentration. **Conclusion:** This study demonstrates the feasibility of a green thermoplastic MWCNTs nanocomposite for potential use in neural interfacing applications.

First draft submitted: 26 February 2016; Accepted for publication: 4 August 2016; Published online: 12 September 2016

Keywords: elastomeric polymers • MWCNTs • neural interfaces • PHA

Implanted neuroprosthetics and neuroelectrode systems have been under investigation for a number of decades and have been proven to be safe and efficacious as treatments for several neurological disorders as well as for biosensor and stimulation systems [1,2]. Neuroelectrode technologies are typically fabricated from metallic conductors such as platinum, iridium and its oxides, materials that while chemically inert and excellent electrical conductors, are often not intrinsically cytocompatible and do not promote integration with neural tissue [1–3]. The performance of the electrode–tissue interface ultimately rests on the optimization of the material substrate, to enable chronic functionality. The challenge for materials science is to apply biomaterials strategies and develop innovative biocompatible materials that mimic neural tissue characteristics,

cause minimal inflammation and neuronal cell loss, and are retain functionality in chronic settings.

Over the past decade, significant attempts have also been made to enhance chronic neuroelectrode functionality *in situ* through a focus on developing soft electrically conducting polymeric or elastomeric alternatives to metallic implants with the aim of reducing the mechanical mismatch at the tissue/electrode interface [4–7]. These alternatives are in response to the idea that the biomaterial–tissue interface is not a simple static boundary but rather a mechanically and biochemically dynamic region with the potential for chronic inflammation arising from a mismatch in elastic modulus and relative micromotion of the implanted materials [1].

For a majority of neural electrode applications, a threshold material stiffness must be

Catalina Vallejo-Giraldo^{†1,2}, Eugenia Pugliese^{†1,2}, Aitor Larrañaga^{1,3}, Marc A Fernandez-Yague^{1,2}, James J Britton^{1,2}, Alexandre Trotier¹, Ghazal Tadayyon¹, Adriona Kelly^{1,2}, Ilaria Rago⁴, Jose-Ramon Sarasua³, Eilís Dowd^{1,4}, Leo R Quinlan^{1,5}, Abhay Pandit^{1,2} & Manus JP Biggs^{*1,2}

¹CÚRAM – Centre for Research in Medical Devices, National University of Ireland, Galway, Ireland

²Department of Biomedical Engineering, National University of Ireland, Galway, Ireland

³Department of Mining-Metallurgy Engineering & Materials Science & POLYMAT, School of Engineering, University of the Basque Country (UPV/EHU) 480130 Bilbao, Spain

⁴Department of Physics, University of Trieste, Via Valerio 2-34127, Trieste, Italy

⁵Department of Pharmacology, National University of Ireland, Galway, Ireland

⁶Department of Physiology, National University of Ireland, Galway, Ireland

*Author for correspondence: manus.biggs@nuigalway.ie

[†]Authors contributed equally

maintained in order for the implant to penetrate the neural tissue to the final insertion point, a process in itself associated with an acute tissue response, characterized by glial scar formation and electrode encapsulation. Critically, chronic neuroelectrode micromotion persistent with nonfloating electrode systems can contribute to a chronic peri-electrode inflammatory response *in vivo* [1,8].

Although the brain's shear modulus is reported to be in a range between 200 kPa and 1.5 MPa [9] and soft polymers such as polydimethylsiloxane (PDMS) possess an elastic modulus of between 100 kPa and 3 MPa [10,11], elastomeric polymers may offer a viable strategy to reduce the mechanical mismatch at the neuroelectrode interface [12], promoting chronic electrode performance and enhanced integration of the device with the adjacent tissue [1]. Furthermore, relative micromotion can be reduced using flexible materials [13], which can accommodate relative movement, maintaining a mechanically stable tissue/electrode interface, reducing mechanically induced inflammation and improving the electrode charge transfer capability [14]. In turn, the search for flexible biomaterials capable of extending the functional lifetime of implanted electrode systems through optimized mechanical and chemical properties has become a focus of biomedical engineering, with a growing interest in biodegradable thermoplastic elastomers and their electrically conducting composites [15,16].

Polyhydroxyalkanoates (PHAs) are a group of biodegradable and biocompatible polyesters that are synthesized by numerous microorganisms as intracellular carbon and energy storage compounds [17–19]. PHAs can be divided into two main groups depending on the number of carbon atoms in the monomeric units: short chain length PHAs (scl-PHAs), that contain between 3 and 5 carbon atoms (e.g., poly(3-hydroxybutyrate) [P3HB], poly(4-hydroxybutyrate) [P4HB], etc.); and medium chain length PHAs (mcl-PHAs) containing 6–14 carbon atoms (e.g., poly(3-hydroxyhexanoate) [P3HHx], poly(3-hydroxyoctanoate) [P3HO], etc.). With respect to the fabrication of mechanically compliant biomaterials with neural interfacing applications, mcl-PHAs are of particular interest because of their low crystallinity (with melting temperatures of 45–60°C), low glass transition temperatures (T_g between -25 and -50°C), a Young's modulus of 3–70 MPa and up to 500% elongation at break [20]. Additionally, thanks to their thermoplastic nature, they are easily processed via traditional thermoplastic techniques, and composite systems can be prepared to improve the intrinsic properties of the polymer matrix [21,22].

2D electrically conducting nanomaterials such as graphene [23] and carbon nanotubes [24] have generated

considerable interest among the scientific community in recent years. In particular, their novel electrical and physicomaterial properties are the subject of intense research into the development of novel biomaterials with potential application in developing neural interface systems [25–28], and mechanically favorable alternatives to traditional metallic or silicon electrode materials, with equal or superior impedance properties [29]. In particular nanocomposites incorporating multi-walled carbon nanotubes (MWCNTs) have been successfully employed in compliant electrode technologies. These materials have been shown to promote neuronal adhesion, survival and support neurite elongation [30]. Carbon nanotube interfaces also promote spontaneous synaptic activity in neuronal networks, and can be successfully employed to deliver electrical stimulation to neuronal pathways *in vitro* [31,32].

In the present work (Figure 1), MWCNTs were incorporated into a mcl-PHA copolymer based on 3-hydroxyoctanoate and 3-hydroxyhexanoate to develop an electrically conductive elastomeric composite presenting a range of physical-mechanical, electrical and biological properties as a neuroelectrode material.

Materials & methods

Materials

The mcl-PHA employed in this work was synthesized by Neol Biosolutions (Spain) as previously described [33]. Briefly, mcl-PHA was produced by *Pseudomonas putida* strain from octanoic acid and glycerol in a fed-batch fermentation. The dried biomass was extracted using an organic solvent to obtain the raw polymer. To purify the raw material, it was mixed with a nonsolvent, which induced precipitation of the polymer. As determined by gel permeation chromatography, the synthesized mcl-PHA showed a weight-averaged molecular weight of $125 \times 10^3 \text{ g mol}^{-1}$ with a polydispersity index of 1.68. ^{13}C NMR results revealed that the synthesized mcl-PHA was a copolymer based on 94.3 and 5.7% of 3-hydroxyoctanoate and 3-hydroxyhexanoate, respectively.

The MWCNTs were purchased from SouthWest NanoTechnologies, Inc., (OK, USA) and were synthesized by a catalytic chemical vapor deposition (CVD) method (CoMoCAT[®]) at 700–950°C in a flow of pure CO_2 at a total pressure ranging from 1 to 10 atm. The specifications of as received MWCNTs were as follows: outer diameter $10 \pm 1 \text{ nm}$, internal diameter $4.5 \text{ nm} \pm 0.5 \text{ nm}$, length 3–6 μm (transmission electron microscopy), purity >98% (carbon basis), density 2.1 g cm^{-3} at 25°C, bulk density 0.068 g cm^{-3} , specific surface area (Brunauer-Emmett-Teller) $>280\text{--}350 \text{ m}^2\text{g}^{-1}$ and aspect ratio $>250\text{--}550$ (atomic force microscopy).

Formulation & characterization of mcl-PHA/MWCNT films

Formulation of electrically conducting mcl-PHA/MWCNT nanocomposites

The mcl-PHA films containing 0, 0.1, 0.5 and 1 wt.% of MWCNTs were prepared by solvent casting. Predetermined amounts of MWCNTs previously dispersed by ultrasonication in chloroform with a Vibracell VC 505 probe (Sonics and Materials Inc., CT, USA), using a pulse (10s ON, 2s OFF) with an output power of 17 W at 4°C for 2 h were added to a mcl-PHA solution in chloroform (10% w/v). The mixture was further sonicated for an additional 15 min to ensure a good dispersion of MWCNTs within the polymer matrix before casting in Petri dishes. The samples were kept under a fume hood to let the solvent slowly evaporate at room temperature (RT). After 24 h, polymer solutions were transferred to an oven at 55°C for 1 h to eliminate remaining traces of solvent.

Tensile test

The mechanical properties of the mcl-PHA nanocomposites were investigated using a Zwick Roell THIS Z2.5 tensile test system (Zwick GmbH & Co. KG, Ulm, Germany). The samples prepared for the tensile tests were cut from the mcl-PHA/MWCNTs films with a gauge section of 6.5 mm wide x 130 µm thick. The tensile test was conducted using a 100 N load cell at a crosshead speed of 10 mm min⁻¹.

Transmission electron microscopy

MWCNTs samples prepared in chloroform were prepared by depositing one drop of diluted dispersion of MWCNTs onto a lacey carbon grid allowing the samples to dry overnight. Samples were examined with a JEOL JEM-2100 F TEM operated at 200 kV using a Field Emission Electron Gun equipped with a Gatan Ultrascan digital camera and an EDAX Genesis XM 4 energy dispersive x-ray (EDS) analyser (JEOL USA Inc., MA, USA). To obtain high-resolution images, the probe size was set to 1.5 nm. TEM was performed both to characterize the morphology of MWCNTs dispersion by measuring the diameter of aggregates and to evaluate the uniformity of the dispersion.

UV-visible spectroscopy

A Thermo Scientific, Inc. (UK) Varios-Kan Flash microplate reader was used to assess MWCNTs concentrations via light absorbance spectroscopy with a path length of 100 µm. The spectrophotometric values obtained at a defined wavelength region (450 nm) permitted the evaluation of the extinction coefficient using the formula $A = k \cdot C$, where k is the extinction coefficient and C the concentration of MWCNTs (Beer's Law plot).

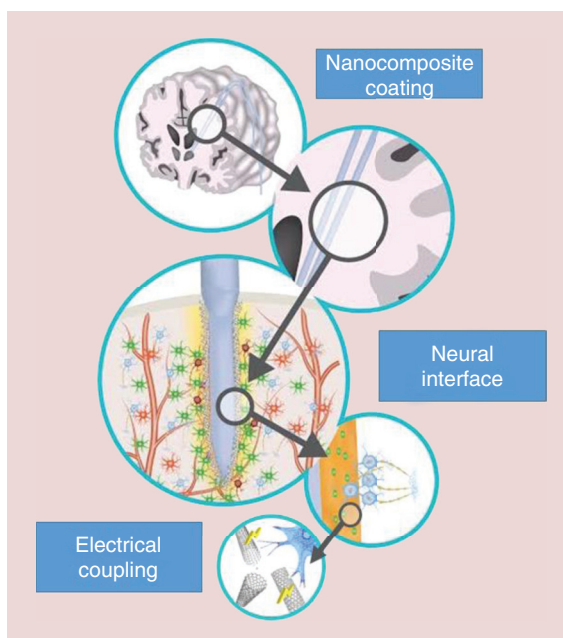


Figure 1. Schematic overview of the challenges associated with neural interfacing technologies.

Implanted electrodes elicit mechanically mediated reactive gliosis and the formation of investing scar tissue. Soft polymeric biomaterials may be employed to reduce the mechanical mismatch and relative micromotion at the electrode–tissue interface.

Electrochemical characterization

Electrical impedance spectroscopy and a potentiodynamic electrochemical assay conducted via cyclic voltammetry, were recorded in a biological electrocell system (Bioanalytical Systems; 1 ml volume) containing the analyzed samples as the working electrode, an Ag/AgCl reference electrode (3 M KCl; Bioanalytical Systems, IN, USA) and a platinum foil counter electrode (Goodfellow, UK) in saline solution prepared as described previously [34]. Measurements were recorded at room temperature using a Princeton Applied Research Potentiostat/Galvanostat model 2273 (Princeton Applied Research, IN, USA). Electrical impedance spectroscopy measurements were performed using a four electrode setup as described previously [35] with an AC sine wave of 40 mV amplitude with 0 V DC offset. The impedance magnitude and phase angle were measured over the frequency range from 0.1 Hz to 100 kHz. Values were presented on a Bode plot and compared with those of a 0.025 mm thick platinum foil (Sigma-Aldrich, Ireland). A second control of a thin-film MWCNT network was also assessed in this study. Carbon nanotubes were grown on silicon wafer chips (SiO₂/Si) substrates following an iron nanoparticle-catalyzed CVD process as described previously [36]. Briefly, an acetylene gas (carbon source) was delivered through a flow meter system in a high-

vacuum reaction chamber in which silicon wafer chips (SiO_2/Si) substrates were located. Chips were made typically around 1–2 cm^2 in size cutting wafers with a diamond cutter and mounted on the heating element inside the chamber. Since CVD-assisted carbon nanotube (CNT) synthesis on a supporting substrate needs a catalytic element, iron was deposited as a thin layer (2–5 nm in thickness) on the silicon chips via electron beam evaporation. CVD process was preceded by sample annealing (4 min at 650–670°C in H_2 atmosphere) in order to reduce iron oxides eventually present on sample surface and to de-wet the iron layer inducing nanoparticle formation. Thereafter, sample temperature was raised to 700°C and acetylene was introduced in the chamber up to a partial pressure of 10–20 mbar. Reaction time was limited to 4 min, resulting in the formation of a uniform network of CNTs of about 10 μm in thickness. Samples were used as removed from the reaction chamber. All electrode surface areas were constant at 0.283 cm^2 .

Cyclic voltammetry was recorded for 100 cycles at a scan rate of 100 mV s^{-1} between -1 V and +0.4 versus Ag/Ag/C. Prior to measurements, solutions were purged with N_2 to avoid O_2 reduction at low potentials. The charge storage capacity (CSC) was calculated by integrating the area enclosed by the voltammogram. The percentage CSC loss was measured by comparing the CSC of the 1st and 100th cycles.

Biological characterization

Ventral mesencephalic neuron culture & seeding

Primary cultures of mesencephalic neurons were obtained from the ventral mesencephalon (VM) of embryonic Sprague–Dawley rats according to methods described previously [37]. Briefly, the VM were dissected from embryonic 14-day rat brains and then mechanically dissociated with a pipette, until the tissue was dispersed. VM Cells were grown in a humidified atmosphere of 5% CO_2 at 37°C and culture in media (Dulbecco's modified Eagle's medium/F12, 33 mM D-glucose, 1% L-glutamine, 1% penicillin/streptomycin, 1% fetal calf serum, supplemented with 2% B27). The mcl-PHA/MWCNTs films were cut to fit in 48-well culture plates and sterilized in 70% ethanol for 2 h, and subsequently washed repeatedly with Hank's balanced salt solution. Prior to plating, samples were coated with poly-lysine (Sigma, Ireland). They were then rinsed three-times with distilled water and left to dry overnight. A quantity of 50,000 cells/ cm^2 was plated on each film, and then 300 μl of the culture medium was added to each well and changed with fresh media every 2 days for a period of 10 days. Control Thermanox® Plastic Coverslips (NUNC™ brand products, Thermo Fisher Scientific Inc, USA) were also

used as internal controls and coated with poly-lysine as above.

Immunofluorescent labeling

Indirect double-immunofluorescent labeling was performed to visualize neurons and astrocytes cell populations. VM cells on experimental and control substrates were fixed with 4% paraformaldehyde and 1% of sucrose for 20 min at room temperature at the time point. Once fixed, the samples were washed with PBS and permeabilized with buffered 0.5% Triton X-100 within a buffered isotonic solution (10.3 g sucrose, 0.292 g NaCl, 0.06 g MgCl_2 , 0.476 g HEPES buffer, 0.5 ml Triton X-100, in 100 ml water, pH 7.2) at 4°C for 5 min. Nonspecific binding sites were blocked with 1% bovine serum albumin in PBS at 37°C for 30 min and subsequently incubated for 2 h with a 1:200 concentration anti-glial fibrillary acidic protein antibody produced in mouse (Sigma, 1:200) and 1:500 concentration anti- β -Tubulin III antibody produced in rabbit (Sigma, 1:500). Samples were washed three-times with 0.05% Tween 20/PBS and then incubated for 1 h in the secondary antibody Alexa Fluor® 488 goat anti-mouse IgG/IgA/IgM (H+L) (molecular probes 1:500) combined with the secondary antibody Alexa Fluor 594 goat anti-rabbit IgG (H+L) (molecular probes, 1:500). Samples were washed with PBS 1 \times (5 min \times 3) and mounted on microscope cover slides and counterstained with Slowfade® Gold Antifade Mountant (Thermo Fisher Scientific Inc, Ireland) with Dapi for nuclear staining.

Microscopy & image analysis

After immunostaining, samples were viewed with an Olympus Fluoview 1000 Confocal Microscope (Olympus America Inc. NY, USA) at a fixed scan size of 1024 by 1024 at a ratio 1:1. At least 20 random images at 60 \times magnification were taken from each test group and the control groups. Cell density was analyzed by counting the total number of labeled nuclei corresponding to neurons and astrocytes in an area of 211.97 $\mu\text{m} \times$ 211.97 μm . Neurite length was quantified by analyzing nine random fields of view of three different technical replicas from three different samples using established stereological methods [38]. The formula used was: neurite length = $n^*T * \pi/2$, where n is the number of times neurites intersect grid lines and T is equal to distance between gridlines (taking magnification into account) as described in [39].

Measurement of intracellular calcium fluctuation through electrical stimulation

Changes in intracellular calcium ($[\text{Ca}^{2+}]_i$) were measured using the calcium-sensitive fluorescent probe

Fluo-4 (Life Technologies, Ireland). Cells grown on the nanocomposites and glass as control were loaded with Fluo-4 AM (5 μM in DMSO) for 30 min at 37°C, washed, followed by 30 min at 37°C in the dark. After dye loading was completed, cells were bathed in culture media (Dulbecco's modified eagle medium/F12, 33 mM D-glucose, 1% L-glutamine, 1% PS, 1% FCS, supplemented with 2% B27) and transferred to a custom built chamber that allows electrical stimulation be applied to the PHA films. Stimulation was achieved by the delivery of biphasic voltage pulses, using a software controlled constant voltage stimulator connected to the chamber via sputter-coated platinum contacts. The chamber was mounted on the stage of a Zeiss Axiovert 200 inverted microscope (Zeiss, Germany). The microscope was equipped with a 10 position Orbit I filter wheel and LP filter for excitation at 488 nm and emission at 510 nm (Perkin Elmer Inc. USA). The emission light was collected every second with an Orca 285 camera (Hamamatsu Photonics K.K, Japan). The system was controlled by the Openlab system version 5.5 (Perkin Elmer Inc. USA). Changes in calcium influx in response to external electrical stimulation were expressed as changes in background subtracted fluorescence intensity.

Statistical analysis

All data presented here were confirmed using at least three replicates for each of the test groups and control group. The results are expressed as the mean of the values \pm standard error of the mean, unless otherwise stated. One-way analysis of variance followed by Bonferroni test was performed to determine the statistical significance ($p < 0.05$), unless otherwise stated.

Results

Physical characterization of MWCNTs dispersion & nanocomposite formulation

Nonsonicated dispersions of MWCNTs in chloroform after 24 h of preparation were clearly inhomogeneous, showing a surface clear zone and sedimented MWCNTs aggregates (Figure 2A [left]). In contrast, dispersions that were sonicated remained homogeneous after 24 h and no CNT precipitates were observed (Figure 2A [right]).

The spectrophotometric values obtained permitted the evaluation of extinction coefficient k (Figure 2B). The attenuation coefficient was obtained for high concentrations of MWCNTs (up to 0.5 wt.%). The attenuation coefficient followed a linear relationship ($R = 99.29\%$) with the MWCNTs concentration showing a value of 8.7 wt.% MWCNTs/cm (wavelength = 450 nm).

Low-magnification TEM (Figure 2C) indicated the absence of aggregates after the sonication process

for any aforementioned concentration of MWCNTs (0.1–1 wt.%). The obtained dispersions were uniform forming a percolated network. No significant damage on the structure of individual MWCNTs was observed (see Figure 2C). MWCNTs were observed to possess well-defined walls, typically ranging from 9 to 14 in number (please refer to Supplementary Figure 1 and Table 1).

Figure 2D shows that incorporation of MWCNTs increased the elastic modulus of the polymeric composites in a concentration-dependent manner. The secant elastic modulus calculated at 2% of elongation was 8.13 ± 0.951 MPa for pristine mcl-PHA, 29.70 ± 0.76 MPa for mcl-PHA with 0.1 wt.% of MWCNTs, 55.30 ± 7.75 MPa for mcl-PHA with 0.5 wt.% MWCNTs and 48.30 ± 1.06 MPa for mcl-PHA with 1.0 wt.% MWCNTs. Statistical analysis was performed using Dunnett's and Fisher's multiple comparisons tests with *** indicating $p < 0.001$.

Electrochemical characterization

Figure 3 shows the electrical impedance properties measured at frequencies from 0.1 Hz to 100 kHz. It was observed that the electrical impedance of all samples decreased with increasing MWCNTs concentration, but this decrease was more pronounced in mcl-PHA/0.5 wt.% MWCNTs (yellow line) followed by mcl-PHA/1 wt.% MWCNTs (blue line) nanocomposites. The results correlate with two main trends. First, the electrical impedance of the pristine mcl-PHA samples (green line) and mcl-PHA/0.1 wt.% MWCNTs (gray line) presented insulator profiles. Second, a reduction in the impedance was observed in mcl-PHA/0.5 wt.% MWCNTs, mcl-PHA/1 wt.% MWCNTs relative to these insulator materials, with an increase of capacitive current. However, the impedance magnitude of all mcl-PHA nanocomposites samples did not possess impedance profiles less than those of pristine MWCNTs networks or platinum at the investigated weight fractions.

A comparison of the electrochemical performance and stability of the mcl-PHA nanocomposites, pristine mcl-PHA and control thin-film MWCNT networks and platinum foil substrates is presented in Table 2. It can be observed that the platinum, control thin-film MWCNT networks and all mcl-PHA nanocomposites followed a linear trend in initial charge storage capacitance (CSC). The greatest CSC was observed in platinum foil samples, with a charge of 8.18 ± 1.27 mC/cm² followed by thin-film MWCNT network controls, with 3.14 ± 0.76 mC/cm², and mcl-PHA/1 wt.% MWCNTs films with 2.96 ± 0.73 mC/cm², 1.85 ± 0.31 mC/cm² for mcl-PHA/0.5 wt.% MWCNTs films, and 0.68 ± 0.06 mC/cm² for mcl-PHA/0.1 wt.%

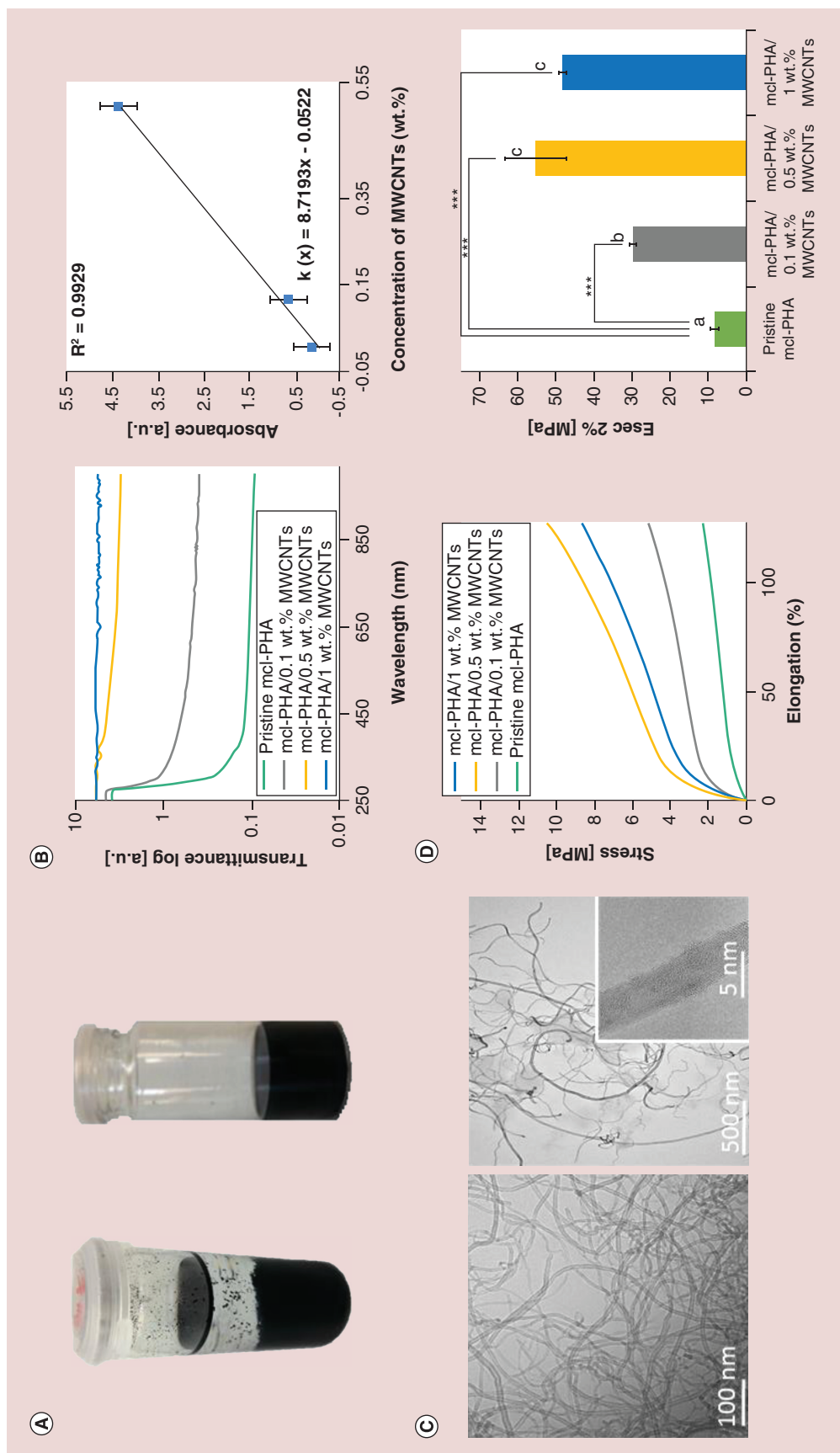


Figure 2. Formulation of polyhydroxyalkanoate/multi-walled carbon nanotube nanocomposites. (A) Dispersion of MWCNTs in chloroform after 24 h with (right) and without (left) ultrasonication process. (B) Absorbance spectroscopy of pristine mcl-PHA and mcl-PHA/MWCNTs nanocomposites with 0.1, 0.5 and 1 wt.% of MWCNTs. Curve showing the extinction coefficient for MWCNTs. The correlation of the curve was 99.29% for $n = 3$ samples (C) TEM images showing uniform dispersion and individual (insert) MWCNTs after ultrasonication process. (D) Stress-strain curves and extracted elastic moduli of pristine mcl-PHA and mcl-PHA/MWCNTs nanocomposites with 0.1, 0.5 and 1 wt.% of MWCNTs indicate the different mechanical behavior between nanocomposite samples. The different letters show statistically significant differences ($p < 0.001$).

*** $p < 0.001$.

mcl-PHA: Medium-chain-length polyhydroxyalkanoate; MWCNT: Multiwalled carbon nanotube.

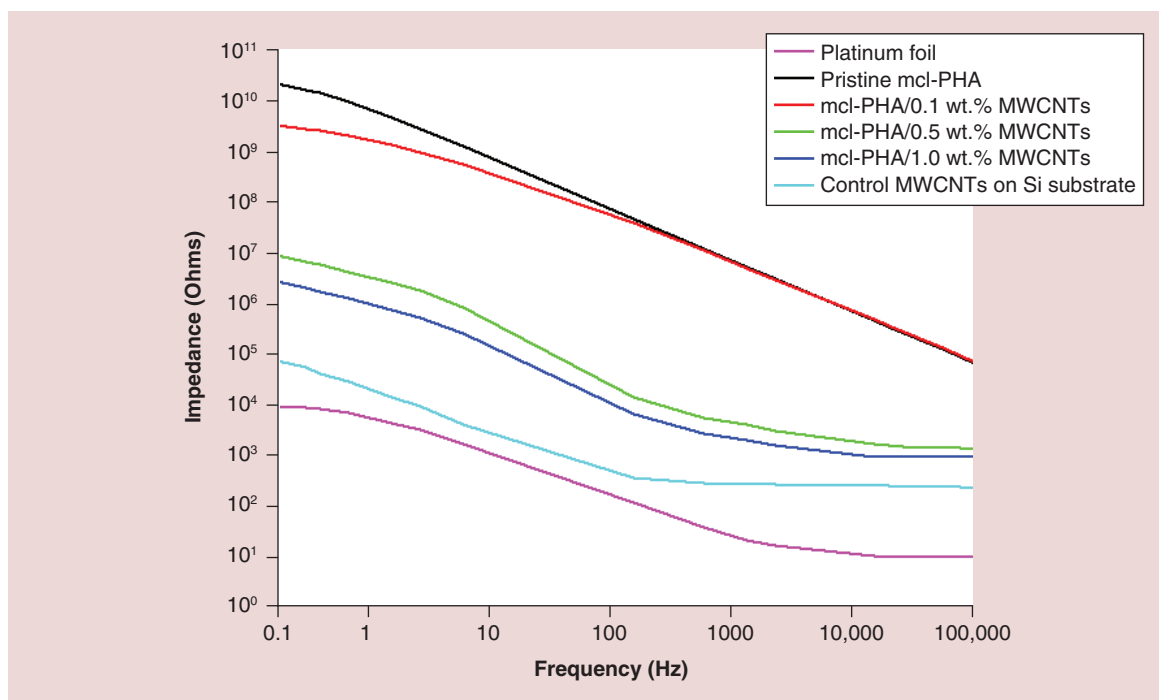


Figure 3. Electrochemical analysis of medium chain length polyhydroxyalkanoates nanocomposites. Bode plot comparing the electrical impedance spectroscopy spectra of platinum foil (purple line), thin-film MWCNT networks (red line) and mcl-PHA nanocomposites: pristine mcl-PHA (green line), mcl-PHA/0.1 wt.% MWCNTs (gray line), mcl-PHA/0.5 wt.% MWCNTs (yellow line) and mcl-PHA/1 wt.% MWCNTs (blue line). mcl-PHA: Medium-chain-length polyhydroxyalkanoate; MWCNT: Multiwalled carbon nanotube.

MWCNTs films. Finally, as expected, the lowest CSC was observed in the non-conductive pristine mcl-PHA films with an initial CSC of $0.06 \text{ mC/cm}^2 \pm 0.03$. With the exception of the final CSC of platinum and MWCNTs controls (CSC of 6.85 ± 1.34 and 1.65 ± 0.91 , respectively), the final CSC values of nano composite films increase with the amount of MWCNTs present following 100 potentiodynamic cycles. The percentage of electroactivity lost calculated for nanocomposite films was non-linear and the mcl-PHA/0.5 wt.% MWCNTs nanocomposites underwent the least electroactivity loss (11.75%), i.e., these films were the

most electrochemically stable relative to other investigated mcl-PHA nano composite and control materials.

Biological characterization

Figure 4 shows representative micrographs of neuron and astrocyte-cell populations cultured on each of the nanocomposites evaluated, and platinum-coated glass as a control group over a period of 10 days in culture. Note that mcl-PHA/0.1 wt.% MWCNTs films were not evaluated *in vitro* as these did not exhibit a significantly different electrical profile relative to unmodified mcl-PHA substrates.

Table 1. The dimensional and chemical properties of the multi-walled carbon nanotubes employed in nanocomposite formulation.

MWCNTs	Evaluated properties
Number of walls	9–14
Wall thickness	$0.35 \pm 0.01 \text{ nm}$
Outer diameter	$11.4 \pm 0.91 \text{ nm}$
Inner diameter	4.61 ± 0.72
Length	3–6 μm
Carbon content	>98%
Aspect ratio	350–400

EDS: Energy-dispersive x-ray spectrometry; MWCNT: Multi-walled carbon nanotube.

Table 2. Electrochemical performance and stability of control pristine multi-walled carbon nanotubes and platinum foil and medium chain length polyhydroxyalkanoate nanocomposites.

Substrate	Initial charge capacity (mC/cm ²)	Final charge capacity (mC/cm ²)	Electroactivity loss (%)
Platinum foil	8.18 ± 1.27	6.85 ± 1.34	16.33%
Control MWCNTs grown on an Si substrate	3.14 ± 0.76	1.65 ± 0.91	47.51%
Pristine mcl-PHA	0.06 ± 0.0	0.04 ± 0.0	28.56%
mcl-PHA/0.1 wt.% MWCNTs	0.68 ± 0.0	0.43 ± 0.22	30.14%
mcl-PHA/0.5 wt.% MWCNTs	1.85 ± 0.31	1.63 ± 0.72	11.75%
mcl-PHA/1.0 wt.% MWCNTs	2.96 ± 0.73	2.42 ± 0.81	18.04%

The initial and the final charge storage capacity evaluated from cathodic region of cyclic voltammograms recorded in saline solution at 0.1 Vs⁻¹ scan rate (potential range: -1-0.4 V vs Ag/AgCl) and corresponding loss during 100 potentiodynamic cycles. Results are ±SD, n = 3. mcl-PHA: Medium-chain-length polyhydroxyalkanoate; MWCNT: Multiwalled carbon nanotube; SD: Standard deviation.

The percentage cell density of astrocytes and neurons on all experimental and control substrates is depicted in Figure 5A. The upper inset tabulation shows the mean number of VM derived neurone and astrocyte cells per unit area of 211.97 μm × 211.97 μm. Significant differences of $p < 0.05$ for Figure 5A are expressed in Table 3. The mcl-PHA nanocomposites were observed to sustain and promote neuronal viability with respect to platinum-coated glass. A significantly lower percentage of neurons (30.4%) was observed on platinum-coated substrates relative to the neuronal presence on pristine mcl-PHA, mcl-PHA/0.5 wt.% MWCNTs and mcl-PHA/1 wt.% MWCNTs samples, which maintained 72.6, 75.4 and 52.9% neuronal populations, respectively. Conversely, platinum-coated glass presented the highest percentage of astrocyte presence (69.6%) relative to pristine mcl-PHA and mcl-PHA nanocomposites. No statistical difference was observed either for differential neurons or astrocytes density for mcl-PHA/0.5 wt.% MWCNTs nanocomposites films relative to pristine mcl-PHA substrates. However, mcl-PHA/1 wt.% MWCNTs samples induced: a significant decrease in neuron density with 52.9% compared with 72.6% for pristine mcl-PHA substrates and 75.4% for mcl-PHA/0.5 wt.% MWCNTs; and a significant increase of astrocyte presence with a 47.1% of astrocyte presence compared with the 27.4 and 24.6% observed on pristine mcl-PHA and mcl-PHA/0.5 wt.% MWCNTs substrates.

Figure 5B shows the neurite length in neurons cultured on pristine mcl-PHA and mcl-PHA nanocomposite films as well as on platinum-coated glass substrates. The neural length was observed to increase from 280.4 ± 5.2 μm on platinum-coated glass to 386.3 ± 6.4 μm on pristine mcl-PHA samples. In particular, mcl-PHA/0.5 wt.% MWCNTs nanocomposites showed a trend similar to that of platinum-coated glass with an average neurite length of 271.0 ± 4.8 μm. As the amount of MWCNTs in the films was increased

from 0.5 to 1 wt.%, the neuronal length significantly decreased relative to the pristine mcl-PHA samples. Overall, mcl-PHA/1 wt.% MWCNTs samples resulted in significantly lower neurite length (187.0 ± 6.7) than that of mcl-PHA/0.5 wt.% MWCNTs nanocomposites and to that of platinum-coated glass substrates.

In order to assess the efficacy of formulated nanocomposites as neural interface biomaterials, representative traces of changes in background subtracted fluorescence intensity from matched individual regions of interest were acquired over 20 s using a biphasic stimulation waveform with 900 mV/cm², 0.003 s pulse (Figure 6). VM neuron cells were observed to generate calcium-mediated signal spikes only upon stimulation with mcl-PHA/0.5 wt.% nanocomposites (Figure 6B). Conversely, calcium influx was not observed in VM-derived neurons cultured on control pristine mcl-PHA or on mcl-PHA/1 wt.% substrates (Figure 6A & C). Platinum-coated glass substrates, although able to induce calcium influx spikes in cultured cells with a higher frequency of excitation (Figure 6D), could not induce calcium influx of the magnitude observed in VM neurons excited with mcl-PHA/0.5 wt.% nanocomposites.

Discussion

Because of their biodegradability, biocompatibility and wide range of physical and mechanical properties, PHA-derived polymers have attracted increasing interest for their use in several biomedical applications (e.g., vascular grafts [40], heart valves [41], and as scaffolds for nerve [42], hard- and soft-tissue engineering [43,44] or as drug-delivery vehicles [45]). Physical and mechanical properties of PHAs are closely related to the length of pendant groups, which extend from the polymer backbones or the distance between the ester linkages. The particular application of PHAs as neurointerfacing material or neuroelectrodes, and in par-

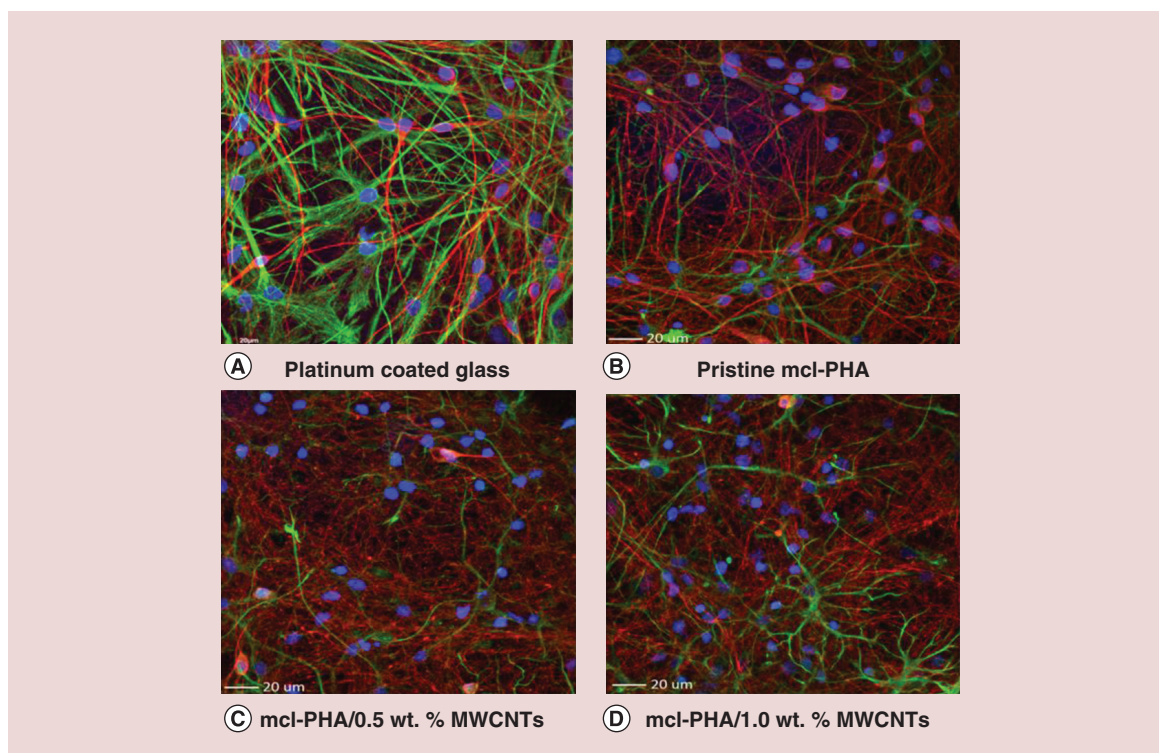


Figure 4. Immunofluorescent micrographs of VM derived neuron and astrocyte populations on experimental and control substrates. Immunofluorescent imaging of β -Tubulin III and GFAP was employed to qualify the number of neurons and astrocytes per unit area and neurite length on platinum-coated glass and experimental nanocomposites (A–D) (green: GFAP, red: β -Tubulin III, blue: nucleus, bar: 20 μ m). GFAB: Glial fibrillary acidic protein.

ticular mcl-PHAs (i.e., those that have between 6 and 14 carbon atoms in their structure) is of special interest due to their low crystallinity, low glass transition temperature and associated low tensile strength and high elongation at break [46].

In order to improve the intrinsic electrical properties of the polymer matrix, mcl-PHA/MWCNTs nanocomposites were prepared. Conducting composites have attracted great attention as potential candidates for implantable neural microelectrodes because of their ability to electrically interface with neural cells [47,48]; and as neuroelectrode materials or coatings with an

aim to decreasing electrical impedance [49–51] and supporting neuronal growth and differentiation [52]. Furthermore, the incorporation of MWCNTs into biodegradable polymers has been widely employed as a strategy to improve the thermal [53], mechanical [54] and electrical [55] properties of implantable biomaterials. In the specific case of PHAs, the addition of carbon nanotubes has resulted in the formulation of nanocomposites with increased elastic moduli and electrical conductivities [56–60]. It is reported that carbon nanotubes can provide a high surface area offering excellent and unique electrical conductivity to polymer com-

Table 3. Significant differences corresponding to the values presented in Figure 5A.

Substrates	Statistical difference
Platinum-coated glass – pristine mcl-PHA	$1.2 \times 10^{-4*}$
Platinum-coated glass – mcl-PHA/0.5 wt.% MWCNTs	$7.8 \times 10^{-5*}$
Platinum-coated glass – mcl-PHA/1.0 wt.% MWCNTs	0.009*
Pristine mcl-PHA – mcl-PHA/0.5 wt.% MWCNTs	1
Pristine mcl-PHA – mcl-PHA/1.0 wt.% MWCNTs	0.020*
mcl-PHA/0.5 wt.% MWCNTs – mcl-PHA/1.0 wt.% MWCNTs	0.009*

mcl-PHA: Medium-chain-length polyhydroxyalkanoate; MWCNT: Multiwalled carbon nanotube.
* $p < 0.05$.

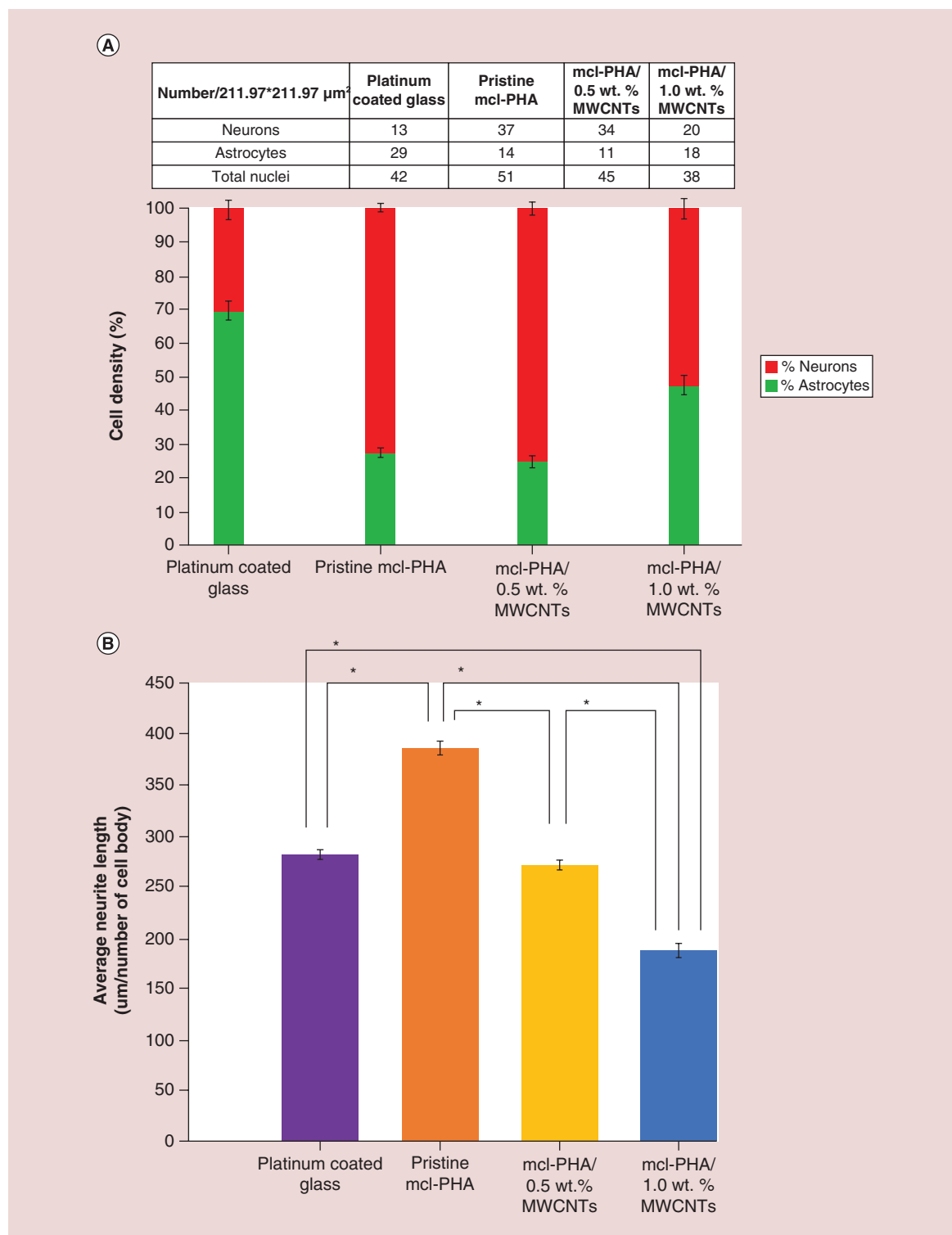


Figure 5. Cytocompatibility analysis of the medium-chain-length nanocomposites over a period of 10 days in culture. (A) Percentage of VM-derived astrocytes and neuronal populations on experimental and control substrates (inset tabulation indicates mean cell number for each condition); (B) length of neuron neurites on control Pt and experimental nano composite films.

posites once they are correctly dispersed [61]. However, due to hydrophobic interactions, MWCNTs tend to

self-associate forming microscale aggregates resulting in poor electrical performance of the nanocomposites.

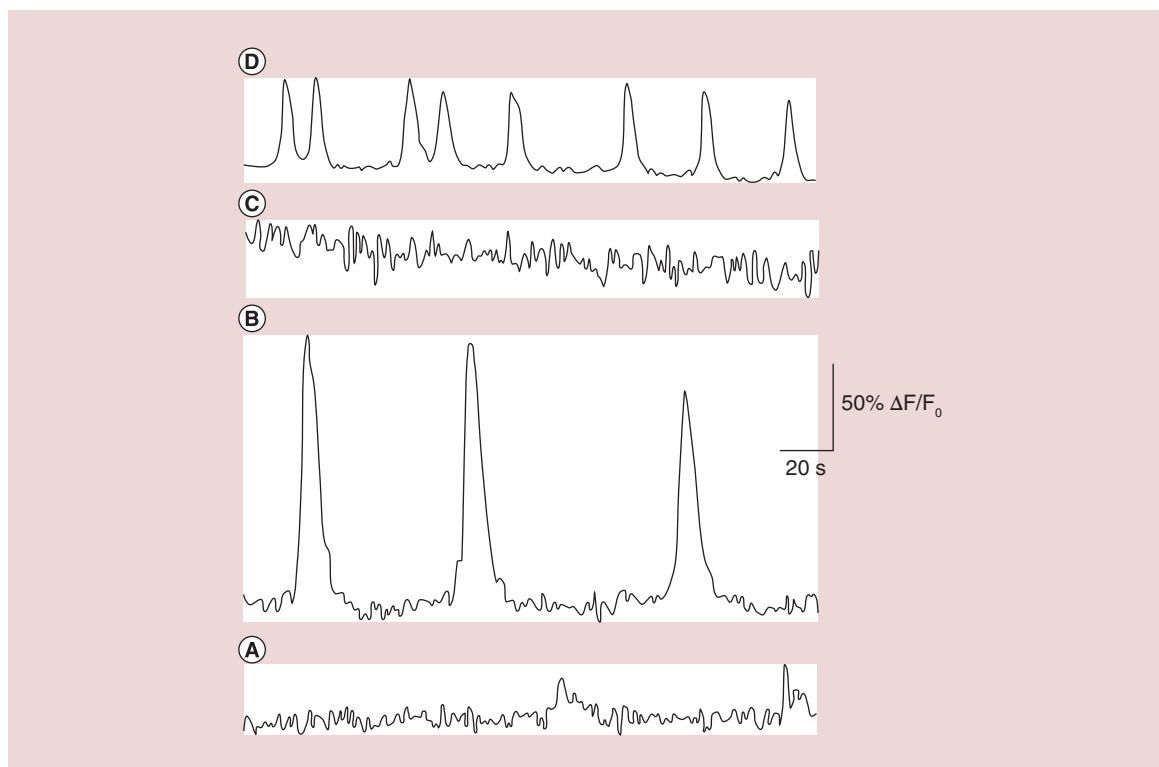


Figure 6. Representative traces showing responses of selected regions of interest (single neurons) to stimulation-induced changes in intracellular calcium. Stimulation was delivered to the films as biphasic voltage pulses (900 mV/cm², 0.003 s pulse, 0.2Hz). Cells were grown on (A) pristine mcl-PHA (B) mcl-PHA/0.5 wt.% MWCNTs and (C) mcl-PHA/1.0 wt.% MWCNTs. (D) Control stimulation experiments were conducted on Pt coated glass. mcl-PHA: Medium-chain-length polyhydroxyalkanoate; MWCNT: Multiwalled carbon nanotube.

In this study, MWCNTs were easily dispersed in CHCl₃ after a relatively short (2 h) period of ultrasonication. Different concentrations (0.1, 0.5 and 1 wt.% of MWCNTs) were dispersed in mcl-PHA and films of approximately 100 μm thickness were obtained. TEM observation enabled the evaluation of microscale disaggregation of MWCNTs and optimization of ultrasonication time and energy. It was observed that after 2 h of sonication at 40% of amplitude, MWCNTs even at high concentrations (Figure 2C) showed a uniform dispersion. In the present work, the elastic modulus of mcl-PHA was significantly increased through the incorporation of MWCNTs, confirming their reinforcing effects on mcl-PHA even at very low concentrations. The enhancement of the mechanical properties in nanocomposites occurs due to the ability of nanoscale reinforcement materials to promote entanglement of polymer chains and through the direct incorporation of highly stiff nanotubes into the soft polymer matrix [22].

Previously it has been reported that if sufficiently distributed in the polymer matrix, MWCNTs have the ability to modify the conductivity of a nanocomposite at very low percolation thresholds (<1 wt.%) [62–65]. The cyclic voltammetry and electrochemical imped-

ance results confirmed that there was a significant enhancement of the electrical conducting properties of mcl-PHA through the incorporation of MWCNTs [66]. The results also confirm the ability of mcl-PHA chains to prevent reagglomeration of the MWCNTs maintaining a suitable dispersion within the nanocomposites once the initial dispersion of pristine MWCNTs has been achieved.

It was observed that with an increase in MWCNTs concentration, the magnitude of impedance was decreased in a frequency-dependent manner. This behavior is consistent with the principle of capacitive reactance being inversely proportional to the frequency and capacitance. At low frequency where the capacitive reactance was more prominent, it was observed that nanocomposites formulated with 0.5 and 1 wt.% of MWCNTs exhibited impedance profiles more closely approaching those of control platinum foil and pristine MWCNTs substrates. This is especially important as it is reported that neural cell communication occurs between 300 Hz and 1 kHz range [67]. Conversely, pristine mcl-PHA and 0.1 wt.% of MWCNTs impedance curves did not demonstrate an impedance plateau with increasing frequency corresponding to a nonconductive profile with high impedance [63].

The loading fraction of 0.1 wt.% of MWCNTs was not sufficient to allow the formation of a conductive network inside the mcl-PHA matrix, resulting in isolated nanotubes and a nonpercolation state. However, by incorporating 0.5 wt.% of MWCNTs, a critical concentration of nanofillers was created in the nanocomposite films resulting in a decrease of impedance by almost three orders of magnitude with respect to the insulating pristine mcl-PHA matrix. Above the percolation threshold, the mcl-PHA/1 wt.% MWCNTs nanocomposites exhibited a further decrease in impedance close to the order of $10^6 \Omega/\text{cm}^2$.

Previous work by Duan *et al.* [68] exploring the dual reinforcement of elastomeric polylactic acid based nanocomposites with graphene nanosheets/MWCNTs nanofillers demonstrated impedance magnitudes of an order of $10^5 \Omega/\text{cm}^2$. Moreover, the incorporation of 0.5 and 1 wt.% of MWCNTs provided the highest surface areas and exhibited the lowest material electrochemical impedances. This was directly related to the observed charge capacities of the samples over 100 cycles, contributing to a double-layer capacitance. Interestingly, previous studies with nanocomposites composed of a common elastomer – PDMS reinforced with CNTs have demonstrated the ability to reliably record neural signals with CNT concentrations in the range of 4%. A study by Jung *et al.* reported that 1.5 wt.% CNT/PDMS composite electrodes exhibited large noise fluctuations, and the P and T waves were not clearly observed. In contrast 4.5 wt.% nanocomposites extracted high-fidelity neural recording *in vitro*. Critically, these electrodes were associated with impedance values orders of magnitude higher than the electrodes employed in this study [69]. Other studies utilizing similar 4% concentrations have also been published, again with electrochemical impedance far higher than the nanocomposite described herein [70]. Critically, in this study percolation state was achieved with CNT concentrations as low as 0.5% and nanocomposites were shown to be efficacious as neural stimulators. This may have arisen from the enhanced neural coupling that is reported with CNTs. Specifically, studies indicate that CNTs are able to directly infiltrate the cell membrane to propagate electrical signals directly to the cell interior, promoting an increase in the efficacy of neural signal transmission [71,72]. In fact, we noted significantly enhanced cell stimulation on our CNT nanocomposites relative to controls.

Controversial data are available about the potential hazard of MWCNTs in biomedical applications [73,74]. However, a detailed study about CNT's effect on the nervous system is still not available. Studies conducted by Misra *et al.* on poly(3-hydroxybutyrate) P(3HB)/MWCNTs and Bioglass® particles compos-

ites indicate that concentrations of 2 wt.% MWCNTs improved the proliferation and adhesion of MG-63 human osteoblast-like cell line, whereas at higher concentration of MWCNTs (4–7 wt.%) toxicity effects were present [75]. Similarly, in the present study, mcl-PHA/0.5 wt.% MWCNTs nanocomposites did not show statistical difference in total neurons and astrocytes persistence with respect to pristine mcl-PHA, or platinum-coated glass.

Further work is required to fully characterize the differences in the dynamics, uniformity and intensity of the cellular response for each of the nanocomposites described. However, it is interesting to note that when VM cells were stimulated with a voltage pulse of $900 \text{ mV}/\text{cm}^2$, 0.00 3s nanocomposites formulated from the mcl-PHA/0.5 wt.% MWCNTs result in the most characteristic physiological type response in these cells. This is also interesting from an inflammatory response point of view, as VM cells cultured on this formulation were observed to possess the lowest fraction of reactive astrocytes relative to all experimental and control groups.

Encouragingly, future studies will focus on topographical modification of the nanocomposite to reduce the electrochemical impedance through topographically mediated increased surface area. Preliminary studies have indicated that this is a feasible avenue of research and through the inclusion of microscale features we have successfully reduced the impedance of the described nanocomposite (Supplementary Figure 2). In combination with this avenue of exploration is the potential that microscale features may significantly modulate cellular function and adhesion, as previously reported [76,77] and it can be hypothesized that topographical modification may represent a powerful approach to reducing both electrochemical impedance and modulating reactive gliosis, a significant bottleneck in neuroelectrode design.

In the present study, the final charge capacities of the mcl-PHA nanocomposites were significantly higher than those of pristine mcl-PHA, and also than that of control MWCNTs. Charges ranged from $2.42 \text{ mC}/\text{cm}^2$ for mcl-PHA/1 wt.% MWCNTs to the insulating behavior of pristine mcl-PHA matrix with a value of $0.04 \text{ mC}/\text{cm}^2$. Importantly, it was observed that overall the mcl-PHA/0.5 wt.% MWCNTs nanocomposites were the most electrochemically stable over the 100 cycles compared with the other nanocomposites and controls, respectively, with a loss of 11.75%.

The family of PHA polymers has exhibited good *in vitro* and *in vivo* biocompatibility as reported previously [78–83]. In particular, mcl-PHA, thanks to the elastomeric properties, has shown better suitability for soft-tissue regeneration than scl-PHA, which is intrin-

sically brittle and stiff [83]. It was shown by J Sun *et al.* that the cytotoxicity of oligohydroxyalkanoates (OHA) toward the mouse fibroblast cell line L929 could be reduced by increasing the OHA side chain length, indicating that mcl-OHAs containing PHA and mcl-PHAs are more biocompatible than scl-PHA [81]. Previous work reported by Xie *et al.* also explored the possibility of enhancing proliferation and differentiation of neuronal stem cells on PHA films coated with recombinant fusion proteins, with respect to uncoated polymer films [84]. Their viability results showed that PHA films, irrespective of biochemical functionalization, had similar distributions in a 3:1 ratio between neurons and astrocytes after 3 days. This finding suggests the intrinsic ability of PHA material to sustain neuronal growth.

In this work, it was confirmed that mcl-PHA is able to promote neuronal cell growth, with respect to platinum-coated glass, which, conversely, presented a high percentage of astrocytes presence. It can be hypothesized that the persistence of neurons on pristine and nanocomposite substrates is influenced by the intrinsic stiffness of the materials. It was interesting to note, however, that mcl-PHA/1 wt.% MWCNTs resulted in a lower percentage of neurons relative to the presence of these cell populations on pristine and mcl-PHA/0.5 wt.% MWCNTs composites, again suggesting the effect of increased rigidity and/or MWCNTs-mediated toxicity toward neurons. This may explain why neural stimulation was not achieved with these nanocomposites.

As a moderately biodegradable polymer it was deemed necessary to assess the degradation rate of mcl-PHA *in vitro*, to evaluate the possibility of CNT elution from the nanocomposite over time. The polymer reveals a very slow degradation rate as can be observed in **Supplementary Figure 3**, and did not lose weight significantly during the hydrolytic degradation study (180 days). To determine the degradation rate (K_{Mw}) as well as half-degradation time ($t_{1/2}$), an exponential relationship between molecular weight and degradation time (validated for biodegradable polyesters degrading under bulk degradation) was employed after measuring the molecular weight of the samples (via gel permeation chromatography) at different time points. The calculated $t_{1/2}$ for mcl-PHA films was 462 days, indicating that 462 days *in vitro* are required for the polymer to reach half of its initial molecular weight and substantiates the observation of the extremely slow degradation by weight measurements.

Analysis of neurons cultured on pristine mcl-PHA films indicated a significant increase in neurite length with respect to neurons cultured on platinum-coated glass, and a linear decrease of neurite length with

MWCNTs concentration. There are some discrepancies about the relationship between neurite outgrowth and substrate stiffness. Willits *et al.* [85] showed an increase in neurite outgrowth in soft collagen gels. In contrast, an equivalent neurite outgrowth on both polyacrylamide and fibrin gel scaffolds of varying compliance was observed by Georges *et al.* [86]. Similarly, Leach *et al.* demonstrated in their study that PC12 neurons display a threshold response to substrates varying in shear modulus from approximately 10^1 – 10^4 Pa. Neurons were able to extend neurites that were more numerous, longer and more branched on stiffer substrates compared with those of softer substrates [87].

In this work, the substantial increase in neurite outgrowth on pristine mcl-PHA compared with the linear decrease in neurite length observed on the mcl-PHA/0.5 wt.% MWCNTs followed by mcl-PHA/1 wt.% MWCNTs nanocomposites reflects a close relationship between neuron's extension and substrate's stiffness. However, the MWCNTs benefits on neurite length cannot be underestimated: findings by Jin *et al.* showed that scaffolds made of Poly l-lactic acid-co-caprolactone coated with CNTs improved neural outgrowth of dorsal root ganglia neurons, with respect to unmodified films [88]. Furthermore, Matsumoto *et al.* showed the stimulation of neurite growth in culture media with functionalized MWCNTs at very low concentrations ranging from 0.11 to 1.7 $\mu\text{g}\cdot\text{ml}^{-1}$ [89]. Therefore, these results together with our findings accentuate the importance of more experimental data to define 'optimal' MWCNTs concentrations that are able to confer electrical charge transfer properties while maintaining the suitable intrinsic mechanical properties of nanocomposite materials for neural extension.

Conclusion

In the present study, mcl-PHA/MWCNTs nanocomposites are proposed as potential neurointerface or neuroelectrode materials. The thermoplastic elastomer behavior of the mcl-PHA employed in this work, which may reduce the mechanical mismatch between the neuroelectrodes and the brain tissue, is clearly altered by the incorporation of MWCNTs. Because of the entanglement of polymer chains promoted by nanofillers and the incorporation of stiff nanotubes into the soft polymer matrix, the stiffness of the polymer matrix gradually increased in a concentration-dependent manner from the initial value of 8.13 MPa for pristine mcl-PHA to approximately 50 MPa for mcl-PHA/1 wt.% MWCNTs nanocomposite. Incorporation of MWCNTs also resulted in a higher conductivity of the studied system. Incorporation of 0.5 wt.% of MWCNTs was enough to shift the behavior of the

samples from resistive to capacitors. Both mechanical and electrical properties are believed to affect the biological response of the cells employed herein. Among the studied systems, mcl-PHA/0.5 wt.% MWCNTs is of particular interest because it promoted neuron maintenance and shows no detrimental modification to neurite length with respect to platinum control or mcl-PHA nanocomposite formulations possessing higher concentrations of MWCNTs. Furthermore, mcl-PHA/0.5 wt.% MWCNTs nanocomposites were able to produce a characteristic neural physiological type response in electrically stimulated VM neuronal populations.

Future perspective

The fabrication of conductive nanocomposites described in the present work lends itself well to the fabrication of castable and mechanically tunable electrically conducting nanocomposites with low CNT concentrations. In addition, studies with microscale pillars indicate that the inclusion of topographical features into the neural interface can reduce electrochemical impedance of the nanocomposite. We expect that the inclusion of nanofeatures in cast mcl-PHA/MWCNTs nanocomposites will enhance the biological responses observed here as well as the mechanical and electrical profiles. Our experimental *in vitro* results

provide important insight for studying astrocyte reactivity toward a better understanding of the glial scar formation at the electrode interface.

Supplementary data

To view the supplementary data that accompany this paper please visit the journal website at: www.futuremedicine.com/doi/full/10.2217/nnm-2016-0075

Financial & competing interests disclosure

MJ Biggs is a Science Foundation Ireland, Starting Investigator SIRG COFUND fellow (grant no. 11/SIRG/B2135). In addition, MJ Biggs is a funded investigator through the CURAM Science Foundation Ireland (grant agreement no. 13/RC/2073). A Larrañaga would like to acknowledge Basque Government (Department of Education, Language Policy and Culture) for a postdoctoral grant. The authors would like to acknowledge the Centre for Microscopy & Imaging funded by National University of Ireland Galway and The Programme for Research in Third-Level Institutions (PRTL), Cycles 4 and 5, National Development Plan 2007–2013, and P Owens for microscopy support. The authors have no other relevant affiliations or financial involvement with any organization or entity with a financial interest in or financial conflict with the subject matter or materials discussed in the manuscript apart from those disclosed.

No writing assistance was utilized in the production of this manuscript.

Executive summary

- A nanocomposite based on multi-walled carbon nanotubes (MWCNTs) and a green thermoplastic elastomer (medium chain length polyhydroxyalkanoate [mcl-PHA]) was prepared as a neurointerface-specific biomaterial.
- The stiffness of mcl-PHA gradually increased with the amount of MWCNTs from approximately 8 MPa (pristine mcl-PHA) to approximately 50 MPa (1 wt.% MWCNTs).
- Incorporation of 0.5 wt.% of MWCNTs allows the formation of a conductive network inside the polymer matrix.
- Pristine mcl-PHA and its MWCNTs composites promoted neuron adhesion (while preventing astrocyte adhesion) with respect to the control substrates (platinum-coated glass).
- Neurite length was significantly increased in neurons cultured on mcl-PHA and mcl-PHA/0.5 wt.% MWCNTs with respect to the control substrates (platinum-coated glass).
- mcl-PHA/0.5 wt.% MWCNTs nanocomposites were able to produce a characteristic neural physiological type response in electrically stimulated VM neuronal populations.

References

Papers of special note have been highlighted as: • of interest; •• of considerable interest

- 1 Vallejo-Giraldo C, Kelly A, Biggs MJP. Biofunctionalisation of electrically conducting polymers. *Drug Discov. Today* 19(1), 88–94 (2014).
- 2 Cogan SF. Neural stimulation and recording electrodes. *Annu. Rev. Biomed. Eng.* 10, 275–309 (2008).
- 3 Rose LSRaTL. *Neural Prostheses: Fundamental Studies*. Prentice Hall, NJ, USA (1990).
- 4 McClain MA, Clements IP, Shafer RH, Bellamkonda RV, Laplaca MC, Allen MG. Highly-compliant, microcable neuroelectrodes fabricated from thin-film gold and PDMS. *Biomed. Microdevices* 13(2), 361–373 (2011).
- 5 Biran R, Martin DC, Tresco PA. The brain tissue response to implanted silicon microelectrode arrays is increased when the device is tethered to the skull. *J. Biomed. Mater. Res. A* 82A(1), 169–178 (2007).
- 6 Asplund M, Nyberg T, Inganas O. Electroactive polymers for neural interfaces. *Polym. Chem-UK* 1(9), 1374–1391 (2010).
- 7 Apollo NV, Maturana MI, Tong W et al. Soft, flexible freestanding neural stimulation and recording electrodes fabricated from reduced graphene oxide. *Adv. Funct. Mater.* 25(23), 3551–3559 (2015).

- 8 Thelin J, Jornell H, Psouni E *et al.* Implant size and fixation mode strongly influence tissue reactions in the CNS. *PLoS ONE* 6(1), e16267 (2011).
- 9 Miller K, Chinzei K, Orssengo G, Bednarz P. Mechanical properties of brain tissue *in-vivo*: experiment and computer simulation. *J. Biomech.* 33(11), 1369–1376 (2000).
- 10 Lotters JC, Olthuis W, Veltink PH, Bergveld P. The mechanical properties of the rubber elastic polymer polydimethylsiloxane for sensor applications. *J. Micromech. Microeng.* 7(3), 145–147 (1997).
- 11 Palchesko RN, Zhang L, Sun Y, Feinberg AW. Development of polydimethylsiloxane substrates with tunable elastic modulus to study cell mechanobiology in muscle and nerve. *PLoS ONE* 7(12), e51499 (2012).
- 12 Keohan F, Wei XFF, Wongsarnpigooon A, Lazaro E, Darga JE, Grill WM. Fabrication and evaluation of conductive elastomer electrodes for neural stimulation. *J. Biomat. Sci-Polym. E* 18(8), 1057–1073 (2007).
- 13 Harris JP, Hess AE, Rowan SJ *et al.* Deployment of mechanically adaptive nanocomposites for intracortical microelectrodes. *J. Neural Eng.* 8(4), 046010 (2011).
- 14 Khodagholy D, Doublet T, Gurfinkel M *et al.* Highly conformable conducting polymer electrodes for *in vivo* recordings. *Adv. Mater.* 23(36), H268–H272 (2011).
- 15 Li Y, Thouas GA, Chen QZ. Biodegradable soft elastomers: synthesis/properties of materials and fabrication of scaffolds. *RSC Adv.* 2(22), 8229–8242 (2012).
- 16 Wang WS, Guo YL, Otaigbe JU. Synthesis, characterization and degradation of biodegradable thermoplastic elastomers from poly(ester urethane)s and renewable soy protein isolate biopolymer. *Polymer* 51(23), 5448–5455 (2010).
- 17 Muhammadi Shabina, Afzal M, Hameed S. Bacterial polyhydroxyalkanoates-eco-friendly next generation plastic: production, biocompatibility, biodegradation, physical properties and applications. *Green Chem. Lett. Rev.* 8(3–4), 56–77 (2015).
- 18 Lee SY. Bacterial polyhydroxyalkanoates. *Biotechnol. Bioeng.* 49(1), 1–14 (1996).
- 19 Lee SY. Plastic bacteria? Progress and prospects for polyhydroxyalkanoate production in bacteria. *Trends Biotechnol.* 14(11), 431–438 (1996).
- 20 Rai R, Keshavarz T, Roether JA, Boccaccini AR, Roy I. Medium chain length polyhydroxyalkanoates, promising new biomedical materials for the future. *Mat. Sci. Eng. R.* 72(3), 29–47 (2011).
- 21 Misra SK, Valappil SP, Roy I, Boccaccini AR. Polyhydroxyalkanoate (PHA)/inorganic phase composites for tissue engineering applications. *Biomacromolecules* 7(8), 2249–2258 (2006).
- Review describing current applications of polyhydroxyalkanoate composites in biomedical fields and the prospect of potential development with optimized properties for tissue-engineering scaffolds.
- 22 Barrett JSF, Abdala AA, Srien F. Poly(hydroxyalkanoate) elastomers and their graphene nanocomposites. *Macromolecules* 47(12), 3926–3941 (2014).
- 23 Novoselov KS, Geim AK, Morozov SV *et al.* Electric field effect in atomically thin carbon films. *Science* 306(5696), 666–669 (2004).
- 24 Iijima S. Helical microtubules of graphitic carbon. *Nature* 354(6348), 56–58 (1991).
- 25 Liu TC, Chuang MC, Chu CY *et al.* Implantable graphene-based neural electrode interfaces for electrophysiology and neurochemistry in *in vivo* hyperacute stroke model. *ACS Appl. Mater. Inter.* 8(1), 187–196 (2016).
- 26 Park DW, Schendel AA, Mikael S *et al.* Graphene-based carbon-layered electrode array technology for neural imaging and optogenetic applications. *Nat. Commun.* 5, 5258 (2014).
- 27 Vitale F, Summerson SR, Aazhang B, Kemere C, Pasquali M. Neural stimulation and recording with bidirectional, soft carbon nanotube fiber microelectrodes. *ACS Nano* 9(4), 4465–4474 (2015).
- 28 Bosi S, Fabbro A, Cantarutti C, Mihajlovic M, Ballerini L, Prato M. Carbon based substrates for interfacing neurons: comparing pristine with functionalized carbon nanotubes effects on cultured neuronal networks. *Carbon* 97, 87–91 (2016).
- 29 Tian HC, Liu JQ, Wei DX *et al.* Graphene oxide doped conducting polymer nanocomposite film for electrode-tissue interface. *Biomaterials* 35(7), 2120–2129 (2014).
- 30 Cellot G, Toma FM, Varley ZK *et al.* Carbon nanotube scaffolds tune synaptic strength in cultured neural circuits: novel frontiers in nanomaterial-tissue interactions. *J. Neurosci.* 31(36), 12945–12953 (2011).
- 31 Lovat V, Pantarotto D, Lagostena L *et al.* Carbon nanotube substrates boost neuronal electrical signaling. *Nano Lett.* 5(6), 1107–1110 (2005).
- 32 Mazzatenta A, Giugliano M, Campidelli S *et al.* Interfacing neurons with carbon nanotubes: electrical signal transfer and synaptic stimulation in cultured brain circuits. *J. Neurosci.* 27(26), 6931–6936 (2007).
- 33 Larrañaga A FJ, Vega A, Etxeberria A, Ronchel C, Adrio JI, Sarasua Jr. Crystallization and its effects on the mechanical properties of a medium chain length polyhydroxyalkanoate. *J. Mech. Behav. Biomed. Mater.* 39, 87–94 (2014).
- 34 Wei XF, Grill WM. Impedance characteristics of deep brain stimulation electrodes *in vitro* and *in vivo*. *J. Neural. Eng.* 6(4), 046008 (2009).
- 35 Peixoto N, Silue T, Vallejo-Giraldo C, Biggs MJ. Electrochemical analysis of accelerated aging of PEDOT-PTS coated screen-printed electrodes. *Biomedical Electronics and Devices* (2016) (In press).
- 36 Cecilia Mattevi CTW, Hofmann S *et al.* In-situ x-ray photoelectron spectroscopy study of catalyst-support interactions and growth of carbon nanotube forests. *J. Phys. Chem* (112), 12207–12213 (2008).
- 37 Hegarty SV, Collins LM, Gavin AM *et al.* Canonical BMP-smad signalling promotes neurite growth in rat midbrain dopaminergic neurons. *NeuroMol. Med.* 16(2), 473–489 (2014).
- 38 O’Keeffe GW, Dockery P, Sullivan AM. Effects of growth/differentiation factor 5 on the survival and morphology of

- embryonic rat midbrain dopaminergic neurones *in vitro*. *J. Neurocytol.* 33(5), 479–488 (2004).
- 39 Kavanagh ET, Loughlin JP, Herbert KR *et al.* Functionality of NGF-protected PC12 cells following exposure to 6-hydroxydopamine. *Biochem. Biophys. Res. Commun.* 351(4), 890–895 (2006).
- 40 Pontailleur M, Illangakoon E, Williams GR *et al.* Polymer-based reconstruction of the inferior vena cava in rat: stem cells or RGD peptide? *Tissue Eng. Pt A* 21(9–10), 1552–1564 (2015).
- 41 Wu S, Liu YL, Cui B, Qu XH, Chen GQ. Study on decellularized porcine aortic valve/poly (3-hydroxybutyrate-co-3-hydroxyhexanoate) hybrid heart valve in sheep model. *Artif. Organs* 31(9), 689–697 (2007).
- 42 Masaeli E, Wieringa PA, Morshed M *et al.* Peptide functionalized polyhydroxyalkanoate nanofibrous scaffolds enhance Schwann cells activity. *Nanomedicine* 10(7), 1559–1569 (2014).
- 43 Wei X, Hu YJ, Xie WP, Li RL, Chen GQ. Influence of poly(3-hydroxybutyrate-co-4-hydroxybutyrate-co-3-hydroxyhexanoate) on growth and osteogenic differentiation of human bone marrow-derived mesenchymal stem cells. *J Biomed. Mater. Res. A* 90A(3), 894–905 (2009).
- 44 Rathbone S, Furrer P, Lubben J, Zinn M, Cartmell S. Biocompatibility of polyhydroxyalkanoate as a potential material for ligament and tendon scaffold material. *J. Biomed. Mater. Res. A* 93A(4), 1391–1403 (2010).
- 45 Barouti G, Jarnouen K, Cammas-Marion S, Loyer P, Guillaume SM. Polyhydroxyalkanoate-based amphiphilic diblock copolymers as original biocompatible nanovectors. *Polym. Chem-Uk* 6(30), 5414–5429 (2015).
- 46 Larranaga A, Fernandez J, Vega A *et al.* Crystallization and its effect on the mechanical properties of a medium chain length polyhydroxyalkanoate. *J. Mech. Behav. Biomed. Mater.* 39, 87–94 (2014).
- 47 Kozai TD, Langhals NB, Patel PR *et al.* Ultrasmall implantable composite microelectrodes with bioactive surfaces for chronic neural interfaces. *Nat. Mater.* 11(12), 1065–1073 (2012).
- **Demonstrates that an integrated composite electrode consisting of a carbon-fibre core can elicit less chronic reactive tissue response.**
- 48 Chen C, Zhang T, Zhang Q *et al.* Three-dimensional BC/PEDOT composite nanofibers with high performance for electrode-cell interface. *ACS Appl. Mater. Interfaces* 7(51), 28244–28253 (2015).
- 49 Baranauskas G, Maggiolini E, Castagnola E *et al.* Carbon nanotube composite coating of neural microelectrodes preferentially improves the multiunit signal-to-noise ratio. *J. Neural Eng.* 8(6), 066013 (2011).
- 50 Lu Y, Li T, Zhao X *et al.* Electrodeposited polypyrrole/carbon nanotubes composite films electrodes for neural interfaces. *Biomaterials* 31(19), 5169–5181 (2010).
- 51 Kim SY, Kim KM, Hoffman-Kim D, Song HK, Palmore GT. Quantitative control of neuron adhesion at a neural interface using a conducting polymer composite with low electrical impedance. *ACS Appl. Mater. Interfaces* 3(1), 16–21 (2011).
- 52 Scapin G, Salice P, Tesconi S, Menna E, De Filippis V, Filippini F. Enhanced neuronal cell differentiation combining biomimetic peptides and a carbon nanotube-polymer scaffold. *Nanomedicine* 11(3), 621–632 (2015).
- 53 Lizundia E, Oleaga A, Salazar A, Sarasua JR. Nano- and microstructural effects on thermal properties of poly (L-lactide)/multi-wall carbon nanotube composites. *Polymer* 53(12), 2412–2421 (2012).
- 54 Obarzanek-Fojt M, Elbs-Glatz Y, Lizundia E, Diener L, Sarasua JR, Bruinink A. From implantation to degradation – are poly (L-lactide)/multiwall carbon nanotube composite materials really cytocompatible? *Nanomedicine* 10(5), 1041–1051 (2014).
- 55 Lizundia E, Sarasua JR, D’angelo F *et al.* Biocompatible poly(L-lactide)/MWCNT nanocomposites: morphological characterization, electrical properties, and stem cell interaction. *Macromol. Biosci.* 12(7), 870–881 (2012).
- 56 Yun SI, Gadd GE, Latella BA, Lo V, Russell RA, Holden PJ. Mechanical properties of biodegradable polyhydroxyalkanoates/single wall carbon nanotube nanocomposite films. *Polym. Bull. (Berlin)* 61(2), 267–275 (2008).
- 57 Mangeon C, Mahouche-Chergui S, Versace DL *et al.* Poly(3-hydroxyalkanoate)-grafted carbon nanotube nanofillers as reinforcing agent for PHAs-based electrospun mats. *React. Funct. Polym.* 89, 18–23 (2015).
- 58 Xu CL, Qiu ZB. Crystallization behavior and thermal property of biodegradable poly(3-hydroxybutyrate)/multi-walled carbon nanotubes nanocomposite. *Polym. Adv. Technol.* 22(5), 538–544 (2011).
- 59 Yun SI, Lo V, Noorman J *et al.* Morphology of composite particles of single wall carbon nanotubes/biodegradable polyhydroxyalkanoates prepared by spray drying. *Polym. Bull. (Berlin)* 64(1), 99–106 (2010).
- 60 Misra SK, Ohashi F, Valappil SP *et al.* Characterization of carbon nanotube (MWCNT) containing P(3HB)/bioactive glass composites for tissue engineering applications. *Acta Biomater.* 6(3), 735–742 (2010).
- 61 Domun N, Hadavinia H, Zhang T, Sainsbury T, Liaghat GH, Vahid S. Improving the fracture toughness and the strength of epoxy using nanomaterials-a review of the current status. *Nanoscale* 7(23), 10294–10329 (2015).
- 62 Logakis E, Pissis P, Pospiech D *et al.* Low electrical percolation threshold in poly(ethylene terephthalate)/multi-walled carbon nanotube nanocomposites. *Eur. Polym. J.* 46(5), 928–936 (2010).
- 63 Battisti A, Skordos AA, Partridge IK. Percolation threshold of carbon nanotubes filled unsaturated polyesters. *Compos. Sci. Technol.* 70(4), 633–637 (2010).
- 64 Chen J, Shi Y-Y, Yang J-H *et al.* A simple strategy to achieve very low percolation threshold via the selective distribution of carbon nanotubes at the interface of polymer blends. *J. Mater. Chem.* 22(42), 22398 (2012).
- 65 Kim IH, Jeong YG. Polylactide/exfoliated graphite nanocomposites with enhanced thermal stability, mechanical modulus, and electrical conductivity. *J. Polym. Sci. Pol. Phys.* 48(8), 850–858 (2010).

- 66 Spitalsky Z, Tasis D, Papagelis K, Galioris C. Carbon nanotube-polymer composites: chemistry, processing, mechanical and electrical properties. *Progr. Polym. Sci.* 35(3), 357–401 (2010).
- 67 Green RA, Lovell NH, Wallace GG, Poole-Warren LA. Conducting polymers for neural interfaces: challenges in developing an effective long-term implant. *Biomaterials* 29(24–25), 3393–3399 (2008).
- 68 Duan JK, Shao SX, Ya-Li, Wang LF, Jiang PK, Liu BP. Polylactide/graphite nanosheets/MWCNTs nanocomposites with enhanced mechanical, thermal and electrical properties. *Iran Polym. J.* 21(2), 109–120 (2012).
- 69 Jung HC, Moon JH, Baek DH *et al.* CNT/PDMS composite flexible dry electrodes for long-term ECG monitoring. *IEEE Trans. Biomed. Eng.* 59(5), 1472–1479 (2012).
- 70 Liu B, Chen Y, Luo Z, Zhang W, Tu Q, Jin X. A novel method of fabricating carbon nanotubes-polydimethylsiloxane composite electrodes for electrocardiography. *J. Biomater. Sci. Polym. Ed.* 26(16), 1229–1235 (2015).
- 71 Bosi S, Rauti R, Laishram J *et al.* From 2D to 3D: novel nanostructured scaffolds to investigate signalling in reconstructed neuronal networks. *Sci. Rep.* 5, 9562 (2015).
- 72 Mazzatenta A, Giugliano M, Campidelli S *et al.* Interfacing neurons with carbon nanotubes: electrical signal transfer and synaptic stimulation in cultured brain circuits. *J. Neurosci.* 27(26), 6931–6936 (2007).
- 73 Belyanskaya L, Weigel S, Hirsch C, Tobler U, Krug HF, Wick P. Effects of carbon nanotubes on primary neurons and glial cells. *Neurotoxicology* 30(4), 702–711 (2009).
- 74 Voge CM, Stegemann JP. Carbon nanotubes in neural interfacing applications. *J. Neural Eng.* 8(1), 011001 (2011).
- 75 Misra SK, Ohashi F, Valappil SP *et al.* Characterization of carbon nanotube (MWCNT) containing P(3HB)/bioactive glass composites for tissue engineering applications. *Acta Biomater.* 6(3), 735–742 (2010).
- 76 Blumenthal NR, Hermanson O, Heimrich B, Shastri VP. Stochastic nanoroughness modulates neuron-astrocyte interactions and function via mechanosensing cation channels. *Proc. Natl Acad. Sci. USA* 111(45), 16124–16129 (2014).
- 77 Qi L, Li N, Huang R *et al.* The effects of topographical patterns and sizes on neural stem cell behavior. *PLoS ONE* 8(3), e59022 (2013).
- 78 Chen GQ, Wu Q. The application of polyhydroxyalkanoates as tissue engineering materials. *Biomaterials* 26(33), 6565–6578 (2005).
- 79 Rathbone S, Furrer P, Lubben J, Zinn M, Cartmell S. Biocompatibility of polyhydroxyalkanoate as a potential material for ligament and tendon scaffold material. *J. Biomed. Mater. Res. A* 93(4), 1391–1403 (2010).
- 80 Shishatskaya EI, Voinova ON, Goreva AV, Mogilnaya OA, Volova TG. Biocompatibility of polyhydroxybutyrate microspheres: *in vitro* and *in vivo* evaluation. *J. Mater. Sci. Mater. Med.* 19(6), 2493–2502 (2008).
- 81 Sun J, Dai Z, Zhao Y, Chen GQ. *In vitro* effect of oligo-hydroxyalkanoates on the growth of mouse fibroblast cell line L929. *Biomaterials* 28(27), 3896–3903 (2007).
- 82 Wampfler B, Ramsauer T, Rezzonico S *et al.* Isolation and purification of medium chain length poly(3-hydroxyalkanoates) (mcl-PHA) for medical applications using nonchlorinated solvents. *Biomacromolecules* 11(10), 2716–2723 (2010).
- 83 Rai R, Keshavarz T, Roether JA, Boccaccini AR, Roy I. Medium chain length polyhydroxyalkanoates, promising new biomedical materials for the future. *Materials Science and Engineering: R: Reports* 72(3), 29–47 (2011).
- 84 Xie H, Li J, Li L, Dong Y, Chen GQ, Chen KC. Enhanced proliferation and differentiation of neural stem cells grown on PHA films coated with recombinant fusion proteins. *Acta Biomater.* 9(8), 7845–7854 (2013).
- **Demonstrates that coated polyhydroxyalkanoate surfaces with biomolecules promote adhesion, proliferation and neural differentiation of rat neuronal stem cells.**
- 85 Willits RK, Skornia SL. Effect of collagen gel stiffness on neurite extension. *J. Biomater. Sci. Polym. Ed.* 15(12), 1521–1531 (2004).
- 86 Georges PC, Miller WJ, Meaney DF, Sawyer ES, Janmey PA. Matrices with compliance comparable to that of brain tissue select neuronal over glial growth in mixed cortical cultures. *Biophys. J.* 90(8), 3012–3018 (2006).
- 87 Leach JB, Brown XQ, Jacot JG, Dimilla PA, Wong JY. Neurite outgrowth and branching of PC12 cells on very soft substrates sharply decreases below a threshold of substrate rigidity. *J. Neural Eng.* 4(2), 26–34 (2007).
- 88 Jin GZ, Kim M, Shin US, Kim HW. Neurite outgrowth of dorsal root ganglia neurons is enhanced on aligned nanofibrous biopolymer scaffold with carbon nanotube coating. *Neurosci. Lett.* 501(1), 10–14 (2011).
- 89 Matsumoto K, Sato C, Naka Y, Whitby R, Shimizu N. Stimulation of neuronal neurite outgrowth using functionalized carbon nanotubes. *Nanotechnology* 21(11), 115101 (2010).

**APPENDIX 4:
CONFERENCE ARTICLE.
ELECTROCHEMICAL ANALYSIS OF
ACCELERATED AGING OF PEDOT-PTS
COATED SCREEN-PRINTED ELECTRODES**

Electrochemical Analysis of Accelerated Aging of PEDOT-PTS Coated Screen-printed Electrodes

Nathalia Peixoto¹, Tjerignimin Silue¹, Catalina Vallejo-Giraldo² and Manus Biggs²

¹Electrical and Computer Engineering, George Mason University, Fairfax, VA, U.S.A.

²Centre for Research in Medical Devices (CURAM), National University of Ireland Galway, Galway, Ireland

Keywords: Implantable Electrodes, Electrode Coating, Stability of Electrode Coatings, Electrochemical Impedance Spectroscopy, Accelerated Aging, Cyclic Voltammetry, Long-term Electrode Testing.

Abstract: We have developed a deposition method that enhances charge delivery of screen printed electrodes by up to six times through electrochemical deposition of poly (3,4-ethylenedioxythiophene):*p*-toluenesulfonate (PEDOT-PTS). In order to elucidate the effects of PEDOT-PTS deposition on the long-term electrochemical characterization of screen-printed electrodes we characterized electrode stability with cyclic voltammetry and impedance spectroscopy at room temperature and at 47 °C. A deposition current of 0.4 mA/cm² guarantees coverage of the working electrode conductive area with no spill of the conductive polymer through the insulating tracks. Control electrodes show charge storage capacity of 0.25 mC. PEDOT-PTS deposited electrodes are stable for over 4 months and present cathodic charge storage capacity of 1.25 mC.

1 INTRODUCTION

The electrode interface continues to be the main puzzle piece in the development of neural coupled devices and implanted sensors. Current challenges are focused on addressing the accumulation of hypertrophic astrocytes, and the development of electrode-investing glial scar tissue (Vallejo-Giraldo et al., 2014), which increases impedance and prevents electrode integration with excitable neural tissues. The development of next-generation electrode technologies is informed by the biological and physico-mechanical considerations of nervous tissues and neural interfaces (Fernandez-Yague, 2015), which has led to advances in the fabrication of high-density microelectrode arrays (Green et al., 2013) and the development of biochemically modified (Kikkawa et al., 2014) and mechanically biomimetic neuroelectrode systems (Ware et al., 2012).

Long-term recording with implanted electrode systems in non-human primates represents a significant bottleneck in the development of brain-computer-coupled devices and of novel medical solutions to neural disorders. Although long-term neural recording has been reported in a handful of studies (Nicollelis et al., 2003) using traditional electrode approaches (parylene-coated microwires),

the controversy of long-term neural recording proliferates due to confounding variables such as handling of the implant, chemical and mechanical properties of implants, surgical technique, and quality of materials implanted, among other fabrication variables.

In order to investigate the mechanisms of electrode failures, *in vitro* experiments are performed with a subset of those variables, under controlled environmental conditions. Previous research from our group, for example, showed that parylene as an insulator would age within 4 months if implanted. However, when parylene is applied in conjunction with ALD (atomic layer deposition) alumina, it demonstrated a four-fold increase in lifetime (Minnikanti et al., 2014). Furthermore, we compared these two kinds of insulations while testing them at relatively high temperatures, or under “accelerated aging” conditions, which allowed us to reliably predict the lifetime of this polymer *in vivo*.

Poly(3,4-ethylenedioxythiophene) (PEDOT) has gained much attention recently (Green et al., 2013, Kim et al., 2014, Mandal et al., 2014), given its biocompatibility, versatility in terms of counter-ion species and high charge storage capacity (Green et al., 2013). Our group has previously investigated several conductive polymers, as well as surface modifications for biological applications (Fernandez-Yague et al.,

2014) and in particular for the development of smart neuroelectrode applications (Mokarian-Tabari et al., 2015).

We hypothesized that we could apply the same principles of testing the material lifetime of electrodes coated with poly(3,4-ethylenedioxythiophene):*p*-toluenesulfonate (PEDOT-PTS) and that electrodeposition of this conducting polymer at the recording surface would enhance their electrochemical properties. In a previous report we have shown that PEDOT was not as stable as iridium oxide when used for stimulation (Peixoto et al., 2009). Here we will address a PEDOT formulation with stable counter-ions and leverage accelerated aging and electrochemical characterization to demonstrate stability of the superficial layers.

In this manuscript we report on the lifetime assessment of such coatings when used for macro screen-printed electrodes. In order to determine stability, we electrodeposit PEDOT-PTS on commercially available low-cost electrodes with a carbon layer as the active material. Those strips, as well as control strips, were subjected to cyclic voltammetry and electrochemical impedance analysis for up to one month at room temperature, and thereafter at elevated temperatures (in our case, 47 °C) for up to three months. The charge delivery capacity of the electrodes is then evaluated, relative to their initial value, and the robustness of coatings determined based on that parameter and on the stability of the modulus and phase angle in impedance profiles.

2 METHODS

Here we describe the utilized substrates, the methods of electrodeposition of PEDOT-PTS, and the electrochemical methods that were utilized in order to characterize the stability of the coatings and of non-coated control samples.

2.1 Substrates and Solutions

Screen-printed paper-based electrodes (Zensor, TE100) were acquired from CH Instruments. Figure 1 shows the as-received electrodes. The counter and working electrode are carbon-based, while the reference electrode is a silver-silver chloride formulation.

All characterizations were performed with electrodes immersed in phosphate buffered saline (Sigma-Aldrich, St. Louis, MO) at 7.4 pH.

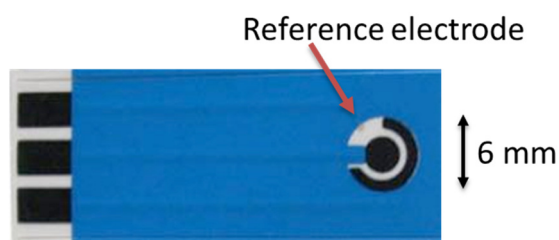


Figure 1: As-received screen-printed electrodes. The active areas are carbon black and silver/silver-chloride. The tabs on the left allow for electrical connection through alligator clips. The active areas are the ring (6mm outer diameter), the center circle (3 mm diameter), and the reference electrode, silver/silver-chloride. The Ag/AgCl is identified by the red arrow. An electrically insulating polymeric cover is identified in blue.

2.2 Electrochemical Deposition

The electrodeposition of PEDOT-PTS films was conducted under ambient conditions. A solution of 0.05 M EDOT (Sigma Aldrich, Ireland) and 0.1 M PTS (Sigma Aldrich, Ireland) was prepared in a 50:50 vol% mixture of acetonitrile and DI water. The electrolyte solution containing the monomeric EDOT was placed in an in-house fabricated electrochemical cell system, as shown in Figure 2. The cell was connected to a Princeton Applied Research electrochemical potentiostat/galvanostat model 2273. The electrochemical apparatus consisted of a four electrode set-up and galvanostatic electrodeposition was performed with 0.03 and 0.64 mA, and providing current densities of 0.4 and 9.014 mA cm⁻²

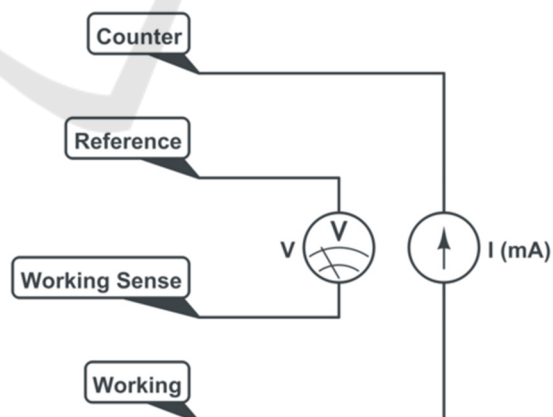


Figure 2: Four-electrode set-up for electrodeposition of PEDOT-PTS onto Zensor TE100 electrodes under galvanostatic conditions. Current is first adjusted according to electrode surface area and then it is applied between working and counter electrodes, while voltage is measured between the sensor (working sense) and reference electrodes.

respectively, over a constant electrodeposition time of 450 seconds. When the deposition was completed, each electrode was soaked in deionized water for 24 h to remove excess electrolyte and unreacted EDOT monomer.

Figure 3 shows magnified images of working electrode following PEDOT-PTS electrodeposition. In this manuscript we discuss results pertaining to the 0.4 mA/cm^2 current deposition, as the higher current showed polymeric coating of the plastic insulation.

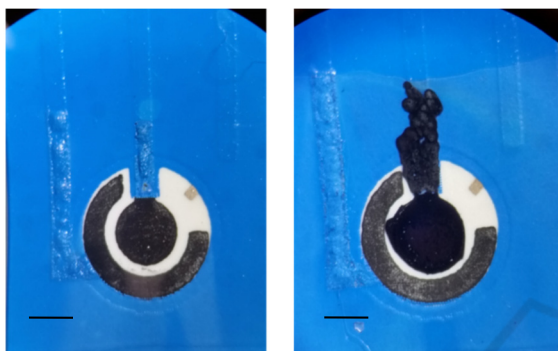


Figure 3: As-deposited screen-printed electrodes. PEDOT-PTS coated electrodes using a current density of 0.4 mA cm^{-2} (left) and PEDOT-PTS coated electrodes using a current density of 9.014 mA cm^{-2} (right). These magnified images show details of the surface of the counter and working electrodes immediately after deposition. Horizontal scale: 3 mm.

2.3 Characterization Techniques

Control electrodes (carbon-based) as well as PEDOT-deposited electrodes were immersed in PBS and characterized over time at $24 \text{ }^\circ\text{C}$ (room temperature) and at $47 \text{ }^\circ\text{C}$. The temperature controller was filled with Aluminium beads and temperature was logged over time with a temperature data-logger. Temperature variation from the heated experiments ($47 \text{ }^\circ\text{C}$) was within $1 \text{ }^\circ\text{C}$ over the course of experiment. A common problem with long-term experiments is the evaporation of the media. We resolved evaporation issues as follows: (a) dental cement was used on the cap of vials; (b) Teflon tape used around the threads; (c) a wet environment was created inside a beaker in order to raise the water vapor pressure and to allow for temperature control through a bead bath. Figure 4 shows a schematic of the setup built and used throughout the characterization experiments.

Electrochemical characterization was performed using a 16 channel multiplexer attached to a CHI660D potentiostat (CH instruments, Bee Cave, TX). The potentiostat, the electrodes, and all cables were kept inside a Faraday cage. The potentiostat is

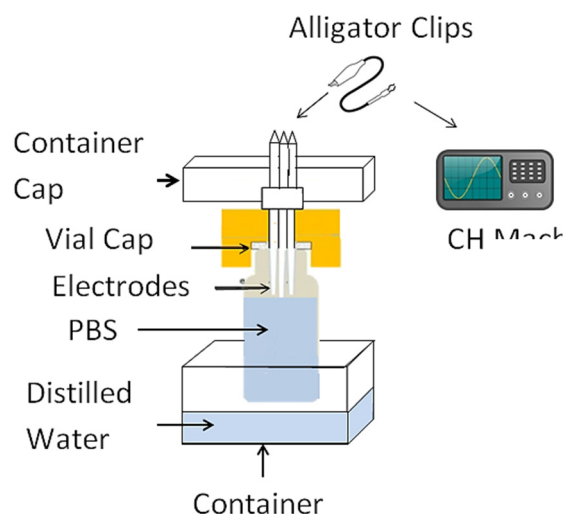


Figure 4: The experimental setup used for long-term characterization of coated and control electrodes. Dental cement was used to seal screen-printed electrodes into electrode cells following PEDOT-PTS deposition. In order to prevent evaporation, vials were filled with phosphate buffered saline. Electrodes were inserted through the vial caps and secured with dental cement. Alligator clips and multi-stranded wires were used to contact the three electrodes to the potentiostat, and the whole vial was kept inside a container with distilled water in order to prevent evaporation. An external environment with saturated humidity guaranteed that no evaporation took place over three months.

connected to a PC, kept outside the cage, through a USB cable. Cyclic voltammetry (CV) is an electrochemical method that entails the application of a voltage between the counter and the working electrode from -0.7 V to 0.7 V while measuring the current through the working electrode, in reference to the silver/silver-chloride electrode. While this test is usually performed continuously, here we ran five periods, at a scan rate of 50 mV/s . Each electrode therefore undergoes five CV cycles and then one EIS test. We have the capability of running up to 16 channels, but we only used 6 of those (3 controls and 3 experimental strips) in order to demonstrate the stability of the coatings for up to two months.

Once a voltammetry cycle was recorded, the current was integrated over half of the period of the voltage applied (for example, from -0.7 V to 0.7 V , or from 0.7 V to -0.7 V) and the charge transferred could be obtained. Because this test was done at low scan rates, it was possible to calculate the *charge storage capacity* of the electrode. More specifically, because integration was applied over the cathodic half of the period, the resulting plot can be referred to as the *cCSC* (cathodic charge storage capacity), given in Coulombs.

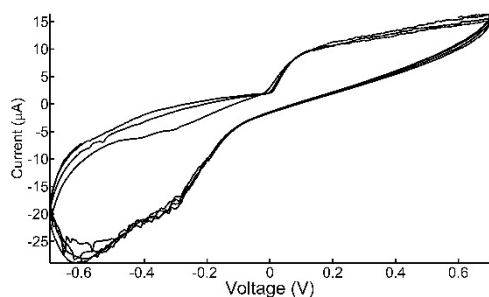


Figure 5: Five cycles of voltammetric spectra of control non-coated carbon electrodes characterized at room temperature, in PBS, with a three-electrode setup, voltage range from -0.7 V to 0.7 V. Current is shown in micro Amperes. Cyclic voltammetry profile was stable for over one week (data not shown).

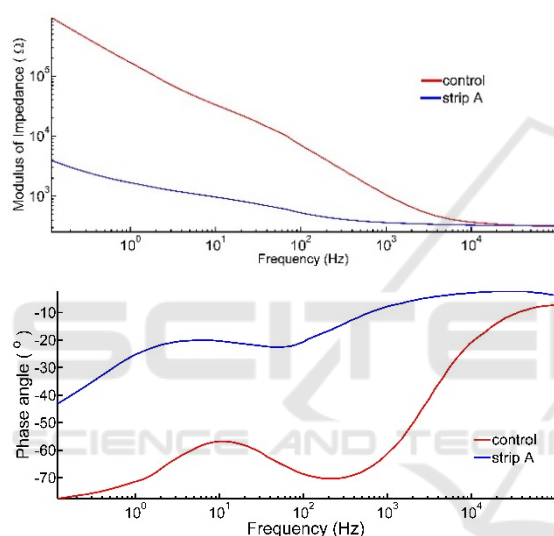


Figure 6: Electrochemical impedance spectroscopy of control and coated electrodes characterized at room temperature, in PBS, with a three-electrode setup. Both impedance modulus (top graph) and phase angle (bottom graph) show a typical profile for carbon black in the control electrode (red curves). For lower frequencies, the electrochemical cell is capacitive (with angles approaching 90 degrees), while for higher frequencies the characteristic resistive phase is seen. This profile was stable over one week (testing period, data not shown). Strip A, in blue, shows lower impedance modulus and a more resistive phase angle than the control electrode.

Electrochemical impedance spectroscopy (EIS) was implemented with a 20 mVrms sinusoidal voltage signal with frequency varying from 0.1 Hz to 100 kHz. Both the modulus and phase were then recorded for one sweep of frequency. Subsequently the electrode was subjected to another cyclic voltammetry (CV) and impedance spectroscopy (EIS) cycle. Throughout 24 hours at least 80 cycles of

these two tests were recorded.

Figure 5 shows a typical CV spectrum for a control electrode. Following one week a similar profile was obtained.

While the CV shows how much charge an electrode could deliver, the impedance profile facilitated the generation of the characteristic circuit component that better describes the interface between the coating and the electrolyte. Figure 6 shows the capacitive nature of the carbon-electrolyte interface at lower frequencies, and the resistive interface at higher frequencies.

3 RESULTS

“As-received” non-coated electrodes ($n=10$) were used as control substrates in order to determine the stability of the cathodic charge storage capacity. This was calculated as a function of the surface area of the working electrode (7 mm^2), and found to be $0.25 \pm 0.10 \text{ mC}$. Due to excessive PEDOT-PTS deposition on the insulated regions when using a current density of 9.014 mA cm^{-2} , we have characterized further only electrodes coated with PEDOT-PTS electrodeposited with a current density of 0.4 mA cm^{-2} , which were assessed for long-term stability *in vitro*.

PEDOT-PTS films deposited at a current density of 0.4 mA cm^{-2} were immersed in PBS and analysed at room temperature for one month, along with three control strips. During this time, approximately 2,000 runs were performed on each electrode. In order to analyze the impedance changes of each electrode, EIS runs for each experimental condition were combined and a mean plot obtained. Figure 7A shows an example of a twenty-four hour interval, for PEDOT-PTS coated electrodes. The stability of the modulus of impedances over time is within one fold for low frequencies (up to 1 Hz) and it is statistically insignificant for frequencies above 10 Hz. Figures 7A and 7B also demonstrate the effects of PEDOT-PTS deposition on the modulus and phase of the low frequency impedance spectrum, reducing the modulus of impedance to less than $10 \text{ k}\Omega$ at frequencies less than 1 Hz. This is in conjunction with a 30 degree angle on the phase of impedance, indicating a more resistive electrode-electrolyte interface.

While the EIS results demonstrated repeatable profiles, the CV spectra presented noise at voltages above 0.4 V and below -0.4 V. However, the profiles were significantly different to those of the non-coated carbon control electrodes (Figure 4), indicating an

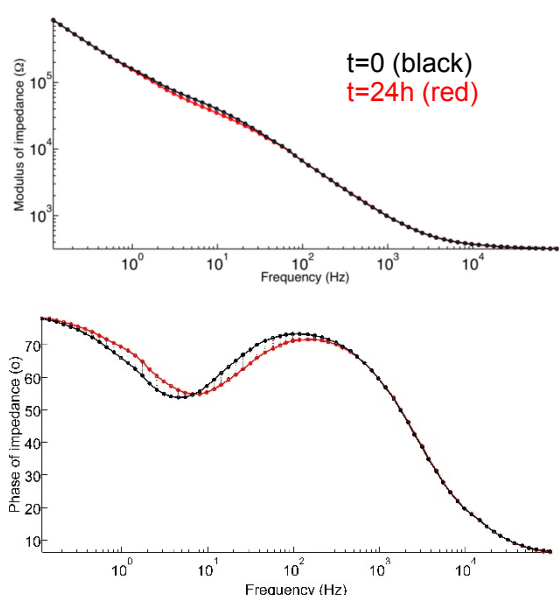


Figure 7: Overlay of electrochemical impedance spectroscopy measurements (modulus) and of phase measurements for PEDOT-PTS coated electrodes. The measurements were obtained at $t=0$ and after 24 hours at room temperature, in PBS, with a three-electrode setup. The modulus of impedance was stable across all frequencies tested (0.1 Hz through 100 kHz) (top graph). The phase was observed to increase by up to 10 degrees between the beginning and end of the test (lower graph).

increased charge transfer capacity (over 1 mC at room temperature), a higher surface area, and a more electrically active material. Figure 8 shows CVs taken at three different times during a 600-hour run at 47°C. Offsets in current are not considered when calculating the cathodic charge storage capacity. In order to measure cCSC the average current per cycle of the voltage is first subtracted from the current. After one month of electrochemical analysis at room temperature, both controls and PEDOT-PTS coated electrodes presented profiles which are not statistically different from the profiles recorded during the initial tests (as shown in figure 7 for impedance profiles). In order to force the aging of the electrodes, the temperature of electrolyte was increased to 47 °C and the cathodic charge storage capacity was assessed for up to two months. At this elevated temperature, the main qualitative difference noted was electrical noise. The impact on the EIS and CV however was minimal. In order to quantify stability, we measured the cCSC for over 1,500 voltammetric cycles. Figure 9 shows a summary of these plots obtained from PEDOT-PTS coated and non-coated electrodes. The standard deviation was not plotted on this graph for clarity.

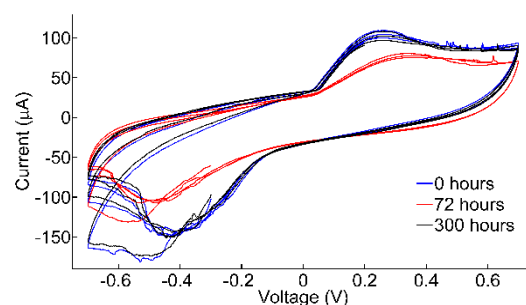


Figure 8: Cyclic voltammetry for PEDOT-PTS coated electrodes characterized at 47°C. Electrodes were immersed in PBS, and the CV recorded using a three-electrode setup, with a scan rate of 50 mV/s. The voltammetry was performed against the reference electrode potential. The blue curve was taken at 0 h (first cycle recorded), red curve at 72 hours, and black curve at 144 hours.

Each electrode was characterized approximately 3 times per hour, for up to 500 hours. There were two interruptions due to power outages, one around the 300-hour mark, and one around the 420-hour mark. This means that we are reporting on approximately 400 hours (non-consecutive). Approximately 1,000 files were generated per electrode and each files was used to extract one cCSC, which was then plotted along the time axis (Figure 9). The mean and standard deviation of the cCSCs for control and PEDOT-PTS electrodes was recorded as 0.26 ± 0.12 mC; 1.25 ± 0.30 mC, respectively.

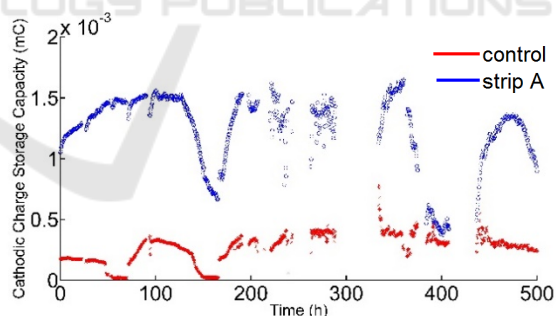


Figure 9: Cathodic charge storage capacity over time for control (red) and PEDOT-PTS coated electrodes (blue and black). The charge storage capacity indicates the stability of the cyclic voltammetry through a combined mean data point. Each number corresponds to a full cycle of a CV performed on the electrode from -0.7 V to 0.7 V at 50 mV/s, against a reference electrode. These experiments were performed in PBS held at 47°C.

4 DISCUSSION

Recently, several groups have demonstrated the

successful deposition of PEDOT-PTS on Platinum substrates for electrical stimulation in neural prosthetics applications (Green et al., 2012, Green et al., 2013) or as conductive films electro-sprayed onto glass substrates (Kim et al., 2104). To our knowledge, this is the first report of a PEDOT-PTS film successfully deposited on Carbon substrates, on commercially available screen-printed electrodes.

We have successfully designed a coating protocol for PEDOT-PTS thin films that can be adjusted in order to obtain varying charge delivery capacities. The charge storage capacity of the films showed a five to seven fold increase over the commercially available carbon coating, and given the surface area of the working electrode (7 mm^2), and the highly non-uniform surface, the cathodic charge storage capacity of $0.25 \pm 0.10 \text{ mC}$ was not surprising. A usual side effect of thin film coatings, and in particular for PEDOT electrodes, is the splitting of layers, also known as delamination, over time. Factors that affect delamination are the dynamic range of the voltage applied during CV tests, the temperature at which the characterizations are performed, the surface roughness and the electrostatic interaction at the material interface.

Delamination can usually be visualized on the surface of the electrode seen as cracks when it is substantial (Green et al., 2012), and it is a significant concern in implantable applications since coating technologies can be important to preserve biocompatibility during chronic recording or stimulation (Vallejo-Giraldo et al.). Critically, when during the onset of delamination, electrochemical methods can point to subtle or microscopic defects that are not readily found microscopically. With the combination of cyclic voltammetry and impedance spectroscopy profiles, it was possible to ascertain over time, the stability of the interface between the working electrode or the electrode coating and an electrolyte.

By characterizing electrodes over several months we demonstrated that the charge and the impedance can vary around a mean value but remained stable *in vitro*. Robustness of the PEDOT-PTS could then be demonstrated at room temperature and when subjected to accelerated aging at elevated temperatures. It can be hypothesized that for applications utilizing implantable PEDOT-PTS coated electrodes, a similar robust behavior can be expected. The original motivation for electrochemical analysis at 47°C was derived from the hypothesis that in general, for every 10 degree increase in temperature, it can be expected that the lifetime of the polymer will decrease by a factor of two. In other

words, given that 10 days is the mean time to failure cited in the literature for implanted PEDOT-PTS coatings (Green et al, 2012), it could be expected that the carbon-based electrodes investigated in this study would fail within 5 days.

The robustness of the screen-printed electrodes was a further unexpected result observed in this exploration and the polymeric insulating coating did not delaminate over the course of three months (total test time) indicating the potential applications of these cost-effective devices for implantable devices.

Future studies will focus on the miniaturization of the deposition area and on validating the stability of PEDOT-PTS coated electrodes in neuronal-glia culture maintained for over three months, while leveraging the electrodes for stimulation and recording of extra-cellular activity.

5 CONCLUSIONS

PEDOT-PTS films, when deposited on Carbon-based substrates, enhance the electrode-electrolyte interface through increasing the charge delivery with a constant surface area. The potential of this coating approach for neuroelectrode applications is further validated through the coating persistence and delamination was not observed for up to two months in age-accelerated conditions. We intend to test miniaturized electrodes with the same coating process, and with neuronal-glia cultures, in order to further characterize PEDOT-PTS for biological applications.

ACKNOWLEDGEMENTS

We acknowledge the participation of our summer students, Kevin Luu (UCSD) and Jose Pahuacho Palomino (GMU), who performed some of the experiments discussed here. M.J. Biggs is a Science Foundation Ireland, Starting Investigator SIRG COFUND fellow (grant agreement no. 11/SIRG/B2135), and a funded investigator through the Science Foundation Ireland Centre for Research in Medical Devices (CÚRAM) (Grant agreement no. 13/RC/2073).

REFERENCES

Fernandez-Yague, Marc A., et al. "Biomimetic approaches in bone tissue engineering: integrating biological and physicochemical strategies." *Advanced drug delivery*

- reviews 84 (2015): 1-29.
- Green, Rylie A., et al. "Substrate dependent stability of conducting polymer coatings on medical electrodes." *Biomaterials* 33.25 (2012): 5875-5886.
- Green, R. A., et al. "Performance of conducting polymer electrodes for stimulating neuroprosthetics." *Journal of neural engineering* 10.1 (2013): 016009.
- Kikkawa, Y. S., T. Nakagawa, L. Ying, Y. Tabata, H. Tsubouchi, A. Ido and J. Ito (2014). "Growth factor-eluting cochlear implant electrode: impact on residual auditory function, insertional trauma, and fibrosis." *J Transl Med* 12: 280.
- Kim, Seul-Gi, et al. "Highly conductive PEDOT: PTS films interfacially polymerized using electro spray deposition and enhanced by plasma doping." *Japanese Journal of Applied Physics* 53.3 (2014): 035501.
- Mandal, Himadri S., et al. "Improving the performance of poly (3, 4-ethylenedioxythiophene) for brain-machine interface applications." *Acta biomaterialia* 10.6 (2014): 2446-2454.
- Minnikanti, Saugandhika, et al. "Lifetime assessment of atomic-layer-deposited Al₂O₃-Parylene C bilayer coating for neural interfaces using accelerated age testing and electrochemical characterization." *Acta biomaterialia* 10.2 (2014): 960-967.
- Mokarian-Tabari, P., C. Vallejo-Giraldo, M. Fernandez-Yague, C. Cummins, M. A. Morris and M. J. P. Biggs (2015). "Nanoscale neuroelectrode modification via sub-20 nm silicon nanowires through self-assembly of block copolymers." *Journal of Materials Science-Materials in Medicine* 26(2).
- Nicolelis, Miguel AL, et al. "Chronic, multisite, multielectrode recordings in macaque monkeys." *Proceedings of the National Academy of Sciences* 100.19 (2003): 11041-11046.
- Peixoto, Nathalia, et al. "Charge storage: stability measures in implantable electrodes." *Engineering in Medicine and Biology Society, 2009. EMBC 2009. Annual International Conference of the IEEE. IEEE, 2009.*
- Vallejo-Giraldo, Catalina, Adriona Kelly, and Manus JP Biggs. "Biofunctionalisation of electrically conducting polymers." *Drug discovery today* 19.1 (2014): 88-94.
- Ware, Taylor, et al. "Three-Dimensional Flexible Electronics Enabled by Shape Memory Polymer Substrates for Responsive Neural Interfaces." *Macromolecular materials and engineering* 297.12 (2012): 1193-1202.

**APPENDIX 5:
ARTICLE.
NANOSCALE NEUROELECTRODE
MODIFICATION VIA SUB-20 nm SILICON
NANOWIRES THROUGH SELF-ASSEMBLY
OF BLOCK COPOLYMERS**

Nanoscale neuroelectrode modification via sub-20 nm silicon nanowires through self-assembly of block copolymers

Parvaneh Mokarian-Tabari · Catalina Vallejo-Giraldo ·
Marc Fernandez-Yague · Cian Cummins ·
Michael A. Morris · Manus J. P. Biggs

Received: 25 July 2014 / Accepted: 15 September 2014
© Springer Science+Business Media New York 2015

Abstract Neuroprosthetic technologies for therapeutic neuromodulation have seen major advances in recent years but these advances have been impeded due to electrode failure or a temporal deterioration in the device recording or electrical stimulation potential. This deterioration is attributed to an intrinsic host tissue response, namely glial scarring or gliosis, which prevents the injured neurons from sprouting, drives neurite processes away from the neuroelectrode and increases signal impedance by increasing the distance between the electrode and its target neurons. To address this problem, there is a clinical need to reduce tissue encapsulation of the electrodes in situ and improve long-term neuroelectrode function. Nanotopographical modification has emerged as a potent methodology for the disruption of protein adsorption and cellular adhesion in vitro. This study investigates the use of block copolymer self-assembly technique for the generation of sub-20 nm nanowire features on silicon substrates. Critically, these nanostructures were observed to significantly reduce electrical impedance and increase conductivity. Human neuroblastoma SH-SY5Y cells cultured on nanowire substrates for up to 14 days were associated with enhanced focal

adhesion reinforcement and a reduction in proliferation. We conclude that nanowire surface modulation may offer significant potential as an electrode functionalization strategy.

1 Introduction

The translation of neuroelectrode-based therapies into long-term clinical solutions is problematic due to soft-tissue scarring, and sub-optimal electrode integration [1], which prevents the injured neurons from regenerating, drives neurite processes away from the neuroelectrodes and increases signal impedance. Inert anti-fouling polymers are commonly used to coat the non-stimulating elements of the electrode, however this material act as a potent dielectric barrier and cannot be employed to reduce glial cell adhesion and scarring on the stimulating surface.

Nanotopographically modified neuroelectrode surfaces may provide excellent opportunities for functional modification, through the modulation of both protein adsorption and cell adhesion to promote electrode integration. Further, nanotopography may be employed to significantly enhance electrode performance by reducing the interfacial impedance. The success or failure of novel neuroelectrode systems hinge on an implanted electrode system that reduces adverse peri-implant encapsulation, reduces neural loss, and receive/target stimulating electrical pulses to from/to the site of interest to achieve maximum therapeutic efficacy.

Highly ordered micro and nanotopographies (<100 nm) have recently been identified as useful in modulating cell adhesion and differentiation [2]. However, a paradigm of nanobiomimetic design is that features with dimensions similar to those of surface bound proteins (~10 nm) can significantly affect protein adsorption and cellular activity

P. Mokarian-Tabari (✉) · C. Cummins · M. A. Morris
Department of Chemistry, Tyndall National Institute,
University College Cork, Cork, Ireland
e-mail: p.mokarian@ucc.ie

P. Mokarian-Tabari · M. A. Morris
Centre for Research on Adaptive Nanostructures and
Nanodevices (CRANN) and AMBER Centre, Trinity College
Dublin, Dublin, Ireland

C. Vallejo-Giraldo · M. Fernandez-Yague · M. J. P. Biggs (✉)
Network of Excellence for Functional Biomaterials (NFB),
National University of Ireland, Galway, Ireland
e-mail: manus.biggs@nuigalway.ie

[3, 4]. Cost effective methodologies for the fabrication of sub-20 nm features are critical for the translation of true nanotechnologies into the clinic, and high-throughput photolithography approaches are rapidly approaching their resolution limitations. Here, we describe a self-assembly process for the production of hexagonally arranged arrays of 20 nm vertical silicon nanowires using a block copolymer, reactive ion etching process and discuss the effect of the surface modifications on cell adhesion and electrical charge transfer in vitro.

2 Results and discussion

2.1 Physicochemical characterisation of silicon substrates

Here we describe the fabrication of sub-20 nm nanowire features in silicon using a block copolymer mask technique. Critically, these nanowire substrates were observed to significantly reduce in the magnitude of electrode impedance due to a significant increase in surface area. Furthermore, preliminary biological observations offer significant insight into the development of next-generation neuroelectrode design.

We used PS-*b*-PEO poly (styrene-*b*-ethylene oxide) block copolymer to make 50 nm thick, nanopatterned, thin films on silicon substrates [5]. The films were exposed to toluene vapor at 50 °C, a common technique known as solvent vapor annealing employed to induce nanophase separation of BCP thin films [6]. Due to the affinity of both polymers with toluene, the chains become mobilised. The phase separation is driven by immiscibility of the two polymer blocks and an ordered dot pattern of hexagonally phase separated polymer is formed (Fig. 1a). The dark dot

domains in (Fig. 1a) are PEO and the matrix polymer is composed of PS. To be able to use this pattern as a mask template on silicon, it is necessary to increase the etch contrast between the polymer and the substrate. This was done by an iron oxide inclusion technique [7].

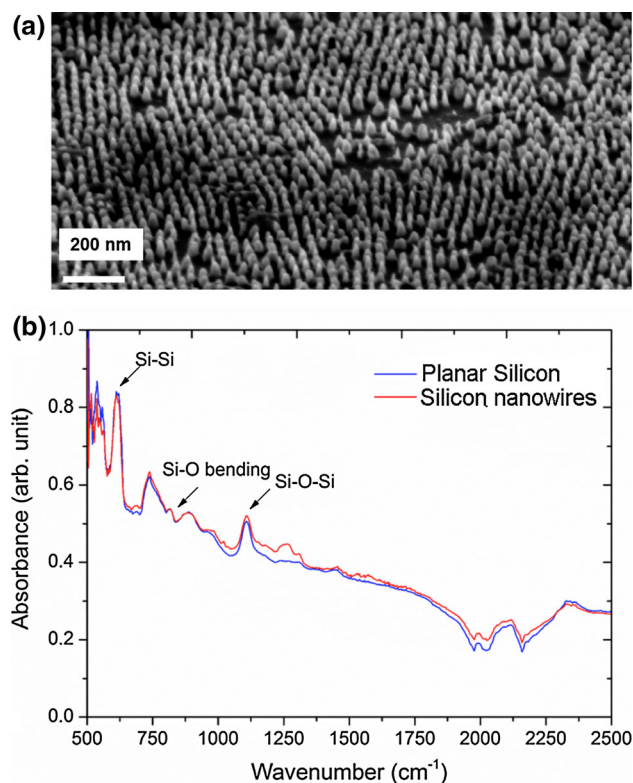


Fig. 2 Si nanowires characterisations. **a** SEM tilted image ($\sim 40^\circ$) of Si nanowires after pattern transfer of iron oxide dot domain (shown in **c**) to Si substrate following 10 s SiO_2 etch ($\text{C}_4\text{F}_8/\text{H}_2$) + 90 s Si etch ($\text{C}_4\text{F}_8/\text{SF}_6$) in ICP/RIE. **b** FT-IR spectra of plain Si and Si nanowire substrate confirms similar surface chemistry

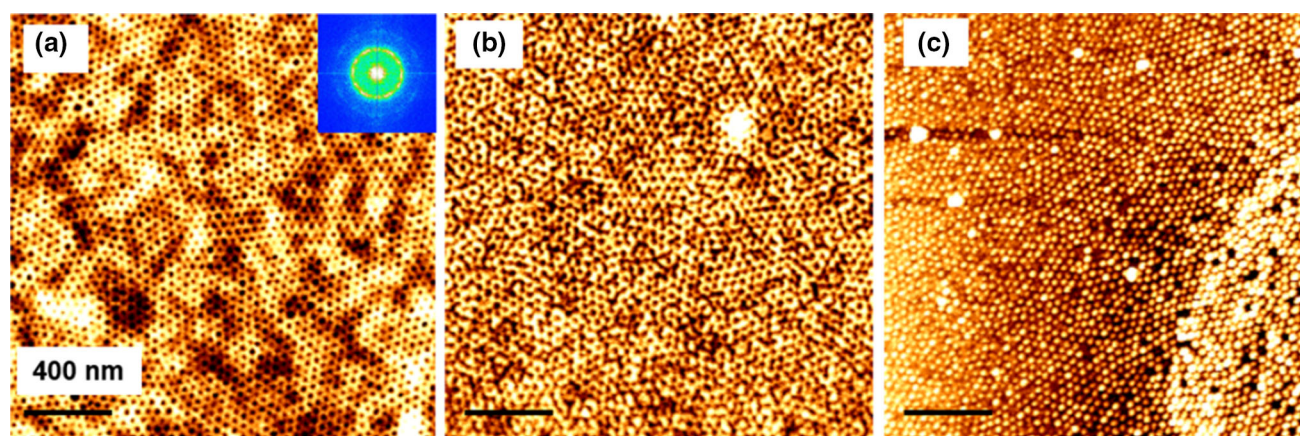


Fig. 1 Block copolymer nanolithography. **a** AFM topographic images of PS-*b*-PEO after annealing. The FFT image indicating a periodicity of 38 nm. **b** After iron oxide inclusion to PEO (dark

domains) to enhance the etch contrast. **c** After UV/Ozone exposure to remove the matrix polymer (PS) and oxidise the precursor. The white domains are iron oxide arrays

After immersing the sample in ethanol for 6 h, an iron nitride III solution was spin cast on PS-*b*-PEO film. The iron nitride immigrates to PEO domains selectively (Fig. 1b). Further exposure of the sample to UV/ozone

leads to oxidation of the domains and also removal of most of the PS matrix (Fig. 1c). The template is then etched using an ICP-RIE plasma reactor. Due to the high etch contrast of iron oxide with silicon, we were able to fabricate high aspect ratio vertical nanowires in silicon. Figure 2a is a 40° tilted SEM image of silicon nanowires after removal of iron oxide. The wires are 20 nm in diameter and 92 ± 11.5 nm in height. With this method it is possible to make high aspect ratio (20:1) vertical nanowires (data not shown). FT-IR spectra shown in (Fig. 2b) provides additional information on the surface chemistry of the substrates and indicates that both planar silicon and the nanopatterned silicon possess identical chemical profiles. Different peaks associated with different bonds are indicated.

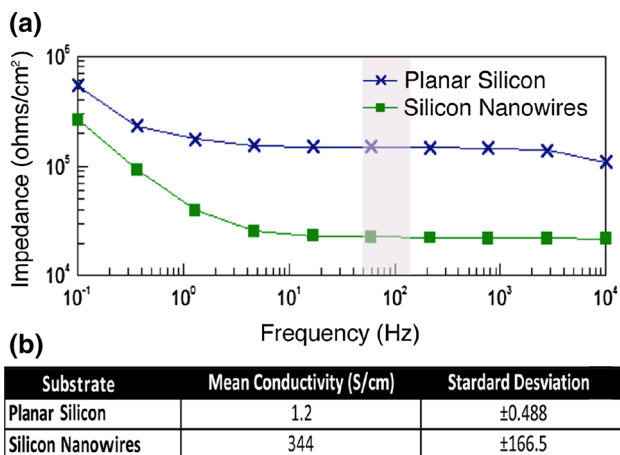


Fig. 3 Analysis of silicon electrical conductivity. **a** Si nanowire substrates were observed to reduce the electrical impedance relative to planar silicon substrates, assessed at 10^{-1} – 10^4 Hz. The reduction in impedance was particularly significant at physiological relevant frequencies (*shaded*) ($n = 3$). Four-point probe analysis indicated a significant increase in substrate conductivity when patterned with silicon nanowires (**b**)

2.2 Electrical characterisation of silicon substrates

For electrical stimulating devices, increases in electrode impedance can affect current delivery, device battery life, and stimulation thresholds [8–10], with current spinal stimulation systems maintaining functionality for less than 5 years in chronic pain patients due to increased tissue impedance, migration or battery failure [11–14]. Furthermore, the volume of tissue stimulation is dependent on the

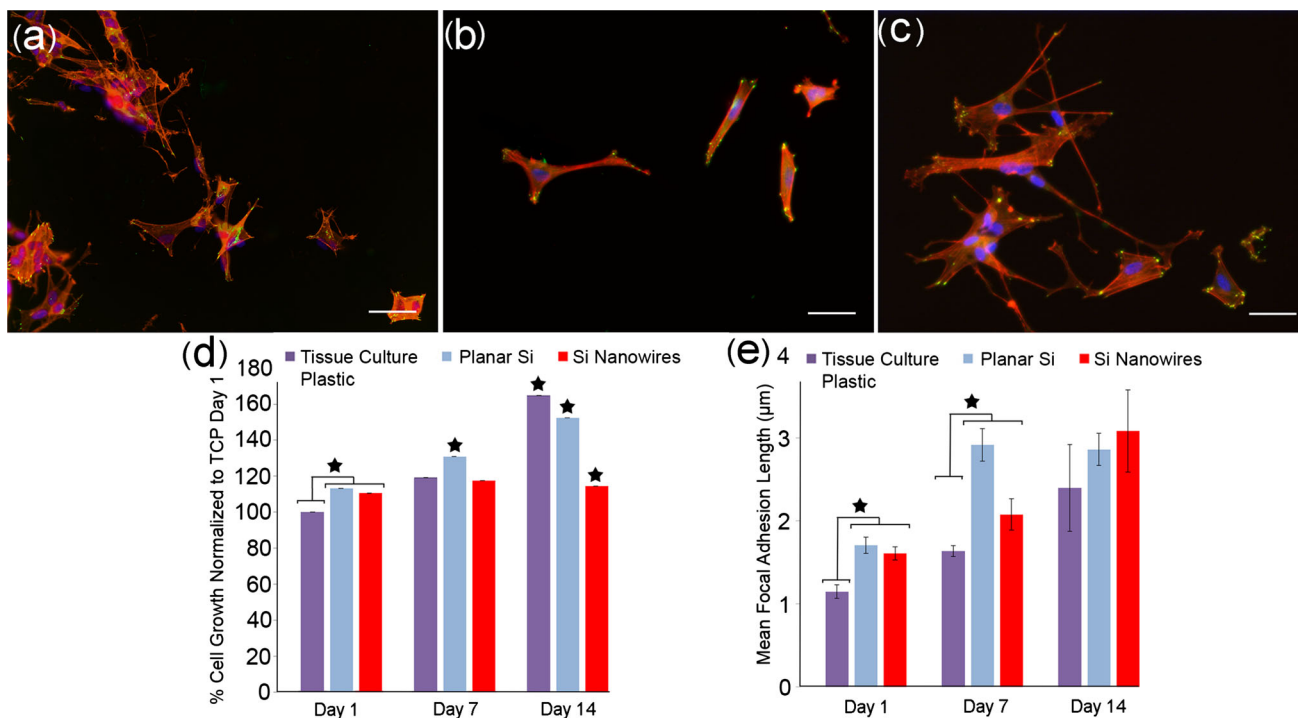


Fig. 4 Human neuroblastoma cell proliferation and adhesion on nanowire substrates. Cells adhered to all experimental substrates. Focal adhesion formation and neurospecific morphology was increased on **c** vertical nanowire substrates relative to **b** planar silicon and **a** control TCP substrates. This was quantified at day analysis of cell proliferation

d indicated that SH-5YSY cells proliferated on nanowire substrates less efficiently than on planar silicon and control TCP substrates. **e** Nanowire substrates promoted neural cell adhesion through the generation of elongated focal adhesions. *Red* actin, *green* paxillin, *blue* DAPI. Bar 50 µm (Color figure online)

electrode–tissue interface impedance when using voltage-controlled stimulation [12, 15].

Electrochemical impedance spectroscopy (EIC) indicated that through surface patterning with nanowire structures the impedance profile of planar silicon can be significantly reduced. In particular, at physiologically relevant electrical frequencies (indicated) this reduction in impedance was by approximately 1 order of magnitude (Fig. 3a). Four-point probe analysis also indicated a significant increase in nanowire substrate conductivity relative to planar silicon substrates (Fig. 3b).

2.3 Cytocompatibility of silicon substrates

Human neuroblastoma SH-SY5Y cells were cultured on experimental and control substrates for up to 14 days and assessed for proliferation and adhesion. SH-SY5Y cells were observed to proliferate on control tissue culture plastic (TCP) and planar silicon substrates but not on nanowire substrates as identified by Alamar blue assay. Immunofluorescent labelling of paxillin and subsequent focal adhesion analysis revealed an increase in focal adhesion reinforcement of both planar and silicon nanowire samples, which was present up to day 14 of culture (Fig. 4).

Neurons do not possess a regenerative capacity and hence proliferation at the cell/neuroelectrode interface will be restricted predominantly to the resident glial and migratory leukocyte populations leading to frustrated phagocytosis, local inflammation and neuron death. Although glial cell adhesion was not assessed in this study, it is interesting to suggest that anti-proliferative surfaces may reduce glial proliferation and subsequent gliosis whilst maintaining intimate contact with interfacial neurites through the promotion of focal adhesion reinforcement.

3 Conclusion

The limited success of long-term spinal stimulation is due to the absence of an innovative anti-scarring system that can promote electrode interaction, reduce encapsulation and improve the therapeutic charge transfer to neural tissue. Reactive tissue and consolidated scar tissue have higher resistive properties than normal tissue [15, 16] and changes in electrode impedance can alter the performance of implantable devices. To address this problem, there is a clinical need to reduce scar-tissue encapsulation in situ and improve long-term neuroelectrode function. It can be hypothesised that the chronic performance of neural interfaces can be enhanced by promoting neuron adhesion to the electrode surface to increase device integration and reduce scar tissue encapsulation. Here vertical silicon nanowire

substrates fabricated via block copolymer templating were evaluated as potent modulators of cellular adhesion and proliferation and significantly improved the material electrical conductivity.

4 Experimental methods

4.1 Sub-20 nm nanowire fabrication

Polystyrene-*b*- ethylene oxide (PS-*b*-PEO) diblock copolymer with average molecular masses of blocks $M_{PS} = 42 \text{ kg mol}^{-1}$ and $M_{PEO} = 11 \text{ kg mol}^{-1}$ and PDI (polydispersity index) of 1.07 was purchased from Polymer Source. A 1 wt% solution of polymer in toluene was prepared. The thin film was spin cast at 2,000 r.p.m. on a *p*-type silicon substrate with a 2 nm native oxide layer on top and annealed at 50 °C exposed to toluene. For metal oxide inclusion the film was immersed in anhydrous ethanol for 6 h at 40 °C to obtain activated PEO domains. A 0.4 % iron (III) nitrate nonahydrate solution in ethanol was spin cast on the film. The sample was exposed to UV/Ozone for 3 h to oxidize the precursor and remove the polystyrene polymer matrix. The iron oxide mask was pattern transferred to the silicon substrate performing a 10 s silicon oxide etch (to remove the native oxide layer) using a combination of tetrafluorocarbon (C_4F_4) and hydrogen gases and 90 s siliconetch using a combination of sulphur hexafluoride (SF_6) and trifluoromethane (CHF_3) gases in an (ICP-RIE) inductively coupled plasma-reactive ion etch machine [17]. The iron oxide was removed by immersion the patterned substrate in a 10 wt% oxalic acid in water solution for 3 h. Surface morphologies were imaged by scanning probe microscopy in tapping mode and scanning electron microscopy. FT-IR was used to characterise the chemistry of the plain silicon and nanotopography pattern silicon surfaces to make sure the chemistry of the both surfaces are similar.

4.2 Electrical conductivity measurements

Resistance of the films was measured using a four-point probe technique on a custom built apparatus. Four locations on the polymeric film were measured in an area of 2 cm^2 .

Electrical impedance spectroscopy (EIS) was performed using a Solartron Instruments controlled by the Z view software with a three electrode set up in a-physiological saline electrolyte buffered with carbonate and phosphate as described in [18]. An AC sine wave of 40 mV amplitude was applied with 0 V DC offset. The impedance magnitude and phase angle were calculated at 1, 10, 100, 1,000, 10,000 Hz [1].

4.3 Cell studies

The human neuroblastoma SH-SY5Y cells were cultured in Dulbeccos modified eagles medium (DMEM), F12 medium and supplemented with 10 % fetal bovine serum and 1 % penicillin/streptomycin (FBS) and all-trans retinoic acid at a final concentration of 10 μM for differentiation into neuronal cell morphology. Cells were seeded onto experimental substrates at a final density of 50,000 cells/ cm^2 . AlamarBlue[®] Assay (Life Technologies, UK) was carried out after 1, 7 and 14 days on each of the samples according to manufacturer guidelines and absorbance was measured at 544 excitation and 590 emission wave lengths using a Thermo Scientific Varios-Kan Flash microplate reader.

Cell cultures were fixed in 4 % paraformaldehyde and 1 % sucrose at days, 1, 7 and 14. Indirect immunofluorescent labelling of paxillin was performed as described previously [19]. The samples were subsequently imaged with an Olympus IX 81 fluorescence microscope.

At least 20 randomly selected images at 20 \times magnification were taken from each tested groups and control groups. The total number of focal adhesion points per cell and their length was directly counted and measured with ImageJ software (National Institutes of Health, USA). All data presented here was confirmed at least using three replicates for each of the tested groups and control groups. The results are expressed as the mean of the values \pm standard error. One way ANOVA followed by Bonferroni test were performed to determine the statistical significance ($P < 0.05$), unless otherwise stated.

Acknowledgments The authors would like to acknowledge (AMBER) Advanced Materials and BioEngineering Research and (SFI) Science Foundation Ireland for funding through SFI-AMBER (Grant No. SFI 12/RC/2278 AMBER). We acknowledge the joint funding received from Irish Research Council through IRC New Foundation Scheme/Nano Surface project. Also the authors thank Advance Microscopy Laboratory (AML)/CRANN for their collaboration and facilities. Bell Labs Ireland thanks the Industrial Development Agency (IDA) Ireland for their financial support. M. J. Biggs is a Science Foundation Ireland, Starting Investigator SIRG COFUND fellow, Grant No. 11/SIRG/B2135.

References

- Green RA, Lovell NH, Wallace GG, Poole-Warren LA. Conducting polymers for neural interfaces: challenges in developing an effective long-term implant. *Biomaterials*. 2008;29:3393–9.
- Dalby MJ, Gadegaard N, Tare R, Andar A, Riehle MO, Herzyk P, et al. The control of human mesenchymal cell differentiation using nanoscale symmetry and disorder. *Nat Mater*. 2007;6:997–1003.
- Hammarin G, Persson H, Dabkowska AP, Prinz CN. Enhanced laminin adsorption on nanowires compared to flat surfaces. *Colloids Surf B*. 2014;122C:85–9.
- Kam KR, Walsh LA, Bock SM, Ollerenshaw JD, Ross RF, Desai TA. The effect of nanotopography on modulating protein adsorption and the fibrotic response. *Tissue Eng Part A*. 2014;20:130–8.
- Mokarian-Tabari P, Collins TW, Holmes JD, Morris MA. Cyclical “Flipping” of morphology in block copolymer thin films. *ACS Nano*. 2011;5:4617–23.
- Sinturel C, Vayer M, Morris M, Hillmyer MA. Solvent vapor annealing of block polymer thin films. *Macromolecules*. 2013;46:5399–415.
- Ghoshal T, Maity T, Godsell JF, Roy S, Morris MA. Large scale monodisperse hexagonal arrays of superparamagnetic iron oxides nanodots: a facile block copolymer inclusion method. *Adv Mater*. 2012;24:2390–7.
- Johnson MD, Otto KJ, Kipke DR. Repeated voltage biasing improves unit recordings by reducing resistive tissue impedances. *IEEE Trans Neural Syst Rehabil Eng*. 2005;13:160–5.
- Dorman MF, Smith LM, Dankowski K, McCandless G, Parkin JL. Long-term measures of electrode impedance and auditory thresholds for the Ineraid cochlear implant. *J Speech Hear Res*. 1992;35:1126–30.
- De Ceulaer G, Johnson S, Yperman M, Daemers K, Offeciers FE, O’Donoghue GM, et al. Long-term evaluation of the effect of intracochlear steroid deposition on electrode impedance in cochlear implant patients. *Otol Neurotol*. 2003;24:769–74.
- Fakhar K, Hastings E, Butson CR, Foote KD, Zeilman P, Okun MS. Management of deep brain stimulator battery failure: battery estimators, charge density, and importance of clinical symptoms. *PLoS One*. 2013;8:e58665.
- Butson CR, Moks CB, McIntyre CC. Sources and effects of electrode impedance during deep brain stimulation. *Clin Neurophysiol*. 2006;117:447–54.
- Kay AD, McIntyre MD, Macrae WA, Varma TR. Spinal cord stimulation—a long-term evaluation in patients with chronic pain. *Br J Neurosurg*. 2001;15:335–41.
- Quigley DG, Arnold J, Eldridge PR, Cameron H, McIvor K, Miles JB, et al. Long-term outcome of spinal cord stimulation and hardware complications. *Stereotact Funct Neurosurg*. 2003;81:50–6.
- Wei XF, Grill WM. Current density distributions, field distributions and impedance analysis of segmented deep brain stimulation electrodes. *J Neural Eng*. 2005;2:139–47.
- Williams JC, Hippensteel JA, Dilgen J, Shain W, Kipke DR. Complex impedance spectroscopy for monitoring tissue responses to inserted neural implants. *J Neural Eng*. 2007;4:410–23.
- Borah D, Shaw MT, Rasappa S, Farrell RA, O’Mahony C, Faulkner CM, et al. Plasma etch technologies for the development of ultra-small feature size transistor devices. *J Phys D*. 2011;44:12.
- Wei XF, Grill WM. Impedance characteristics of deep brain stimulation electrodes in vitro and in vivo. *J Neural Eng*. 2009;6:046008.
- Biggs MJ, Capdevila EP, Vallejo-Giraldo G, Wind S. Cellular response to ferroelectric PVDF-TrFE nanoscale surfaces formed by varying polymer concentration. *Pharm Nanotechnol*. 2014;2:42–8.